The Telecommunications and Data Acquisition Progress Report 42-93

January–March 1988

E. C. Posner
Editor

May 15, 1988

National Aeronautics and
Space Administration

Jet Propulsion Laboratory
California Institute of Technology
Pasadena, California

The Telecommunications and Data Acquisition Progress Report 42-93

January–March 1988

E. C. Posner
Editor

May 15, 1988

National Aeronautics and
Space Administration

Jet Propulsion Laboratory
California Institute of Technology
Pasadena California

The research described in this publication was carried out by the Jet Propulsion Laboratory, California Institute of Technology, under a contract with the National Aeronautics and Space Administration

Preface

This quarterly publication provides archival reports on developments in programs managed by JPL's Office of Telecommunications and Data Acquisition (TDA) In space communications, radio navigation, radio science, and ground-based radio and radar astronomy, it reports on activities of the Deep Space Network (DSN) and its associated Ground Communications Facility (GCF) in planning, in supporting research and technology, in implementation, and in operations Also included is TDA-funded activity at JPL on data and information systems and reimbursable DSN work performed for other space agencies through NASA The preceding work is all performed for NASA's Office of Space Operations (OSO)

In geodynamics, the publication reports on the application of radio interferometry to space geodesy using natural and artificial sources at microwave frequencies In the search for extraterrestrial intelligence (SETI), it reports on implementation and operations for searching the microwave spectrum In solar system radar, it reports on the uses of the Goldstone Solar System Radar for scientific exploration of the planets, their rings and satellites, asteroids, and comets In radio astronomy, the areas of support include spectroscopy, very long baseline interferometry, and astrometry These four programs are performed for NASA's Office of Space Science and Applications (OSSA), with support by the Office of Space Operations for the station support time

Finally, tasks funded under the JPL Director's Discretionary Fund and the Caltech President's Fund which involve the TDA Office are included

This and each succeeding issue of the TDA Progress Report will present material in some, but not necessarily all, of the following categories

OSO Tasks

- DSN Advanced Systems
  - Tracking and Ground-Based Navigation
  - Communications, Spacecraft-Ground
  - Station Control and System Technology
  - Network Data Processing and Productivity
- DSN Systems Implementation
  - Capabilities for Existing Projects
  - Capabilities for New Projects
  - New Initiatives
  - Network Upgrade and Sustaining
- DSN Operations
  - Network Operations and Operations Support
  - Mission Interface and Support
  - TDA Program Management and Analysis
- Communications Implementation and Operations
- Data and Information Systems
- Flight-Ground Advanced Engineering

OSSA Tasks

- Search for Extraterrestrial Intelligence
- Geodynamics
  - Space Geodetic Technical Development
  - Earth Science
- Goldstone Solar System Radar
- Radio Astronomy

Discretionary Funded Tasks

Contents

OSO TASKS
DSN Advanced Systems
TRACKING AND GROUND-BASED NAVIGATION

The Limits of Direct Satellite Tracking With the Global Positioning System (GPS) 1
W I Bertiger and T P Yunck
NASA Code 310-10-61-84-02

Spectral Estimation of Received Phase in the Presence of Amplitude Scintillation 8
V A Vilnrotter, D H Brown, and W J Hurd
NASA Code 310-30-70-84-02

COMMUNICATIONS, SPACECRAFT-GROUND

X-Band Resonant Ring Operation at 450 kW 18
D Hoppe and R Perez
NASA Code 310-20-64-86-02

The Feasibility of the Disturbance Accommodating Controller for Precision Antenna Pointing 27
L L Gresham, F L Lansing, and C N Guiar
NASA Code 310-20-65-63-00

Digital Carrier Demodulation for the DSN Advanced Receiver 45
R Sadr and W J Hurd
NASA Code 310-30-70-84-02

Telemetry SNR Improvement Using the DSN Advanced Receiver With Results for Pioneer 10 64
W J Hurd, D H Brown, V A Vilnrotter, and J D Wiggins
NASA Code 310-30-70-84-02

Advanced Receiver Tracking of Voyager 2 Near Solar Conjunction 75
D H Brown, W J Hurd, V A Vilnrotter, and J D Wiggins
NASA Code 310-30-70-84-02

A New Code for Galileo 83
S Dolinar
NASA Code 310-30-71-83-02

Strawman Optical Reception Development Antenna (SORDA) 97
E L Kerr
NASA Code 310-20-67-59-00

Apparent Brightness of Stars and Lasers 111
B L Schumaker
NASA Code 310-20-67-59-00

Performance Analysis of a Noncoherently Combined Large Aperture Optical Heterodyne Receiver 131
C -C Chen
NASA Code 310-20-67-59-00

Effect of Detector Dead Time on the Performance of Optical Direct-Detection Communication Links 146
C -C Chen
NASA Code 310-20-67-59-00

Efficient Multiplication Algorithms Over the Finite Fields GF(q^m), Where q = 3,5 155
T K Truong, I S Hsu, K M Cheung, and I S Reed
NASA Code 310-30-71-87-02

STATION CONTROL AND SYSTEM TECHNOLOGY

DSS 13 Microprocessor Antenna Controller 163
R M Gosline
NASA Code 310-30-68-87-00

Heat Exchanger Demonstration Expert System 177
D G Bagby and R A Cormier
NASA Code 310-30-68-87-06

A Wideband, High-Resolution Spectrum Analyzer 188
M P Quirk, H C Wilck, M F Garyantes, and M J Grimm
NASA Code 310-30-70-87-04

DSN Systems Implementation

CAPABILITIES FOR EXISTING PROJECTS

2.3-GHz Low-Noise Cryo-FET Amplifier 199
J Loreman
NASA Code 314-30-51-34-30

A Digitally Implemented Phase-Locked Loop Detection Scheme for Analysis of the Phase and Power Stability of a Calibration Tone 207
A C Densmore
NASA Code 889-59-05-84-00

An 8.4-GHz Dual Maser Front End for Parkes Reimplementation 214
D L Trowbridge, J R Loreman, T J Brunzie, and B Jenkins
NASA Code 314-30-66-11-09

CAPABILITIES FOR NEW PROJECTS

The Behavior of a Costas Loop in the Presence of Space Telemetry Signals 229
T M Nguyen
NASA Code 314-40-22-70-08

NETWORK UPGRADE AND SUSTAINING

DSN Very Long Baseline Interferometry System Mark IV-88 239
K M Liewer
NASA Code 314-40-41-81-14

X-Band Noise Temperature Near the Sun at a 34-Meter High Efficiency Antenna 247
T A Rebold, T K Peng, and S D Slobin
NASA Code 314-40-41-81-11

Baseband Assembly Analog-to-Digital Coverter Board 257
I Doerksen and L Howard
NASA Code 314-40-41-91-19

DSN Operations
MISSION INTERFACE AND SUPPORT

Mark IV-85 Mission Support Planning and Future Mission Set 265
R J Amorose
NASA Code 055-10-02-00-96

Determination of the Venus Flyby Orbits of the Soviet Vega Probes Using VLBI Techniques 271
J Ellis and T P McElrath
NASA Code 314-40-22-42-01

Communications Implementation and Operations

New CCIR Report on SETI 280
N F de Groot
NASA Code 315-20-50-00-01

Flight-Ground Advanced Engineering

An Electronically Tuned, Stable 8415-MHz Dielectric Resonator FET Oscillator for Space Applications 292
M Lakshminarayana
NASA Code 315-91-10-12-02

OSSA TASKS
Goldstone Solar System Radar

Goldstone Solar System Radar Performance Analysis 302
E Satorius and S Brokl
NASA Code 314-40-59-31-01

DSS 14 Antenna Calibrations for GSSR/VLA Saturn Radar Experiments 309
C N Guiar, R L Riggs, R Stevens, and M Wert
NASA Code 314-40-31-10-83

The Limits of Direct Satellite Tracking With the Global Positioning System (GPS)

W I Bertiger and T P Yunck
Tracking Systems and Applications Section

Recent advances in high precision differential GPS-based satellite tracking can be applied to the more conventional direct tracking of low earth satellites To properly evaluate the limiting accuracy of direct GPS-based tracking, it is necessary to account for the correlations between the a priori errors in GPS states, Y-bias, and solar pressure parameters These can be obtained by careful analysis of the GPS orbit determination process The analysis indicates that sub-meter accuracy can be readily achieved for a user above 1000 km altitude, even when the user solution is obtained with data taken 12 hours after the data used in the GPS orbit solutions

I. Introduction

In recent years, a variety of differential GPS techniques have been described which promise to deliver decimeter accuracy in tracking low earth satellites [1] – [4] Briefly, the high precision differential GPS techniques involve (1) simultaneous observation of the GPS satellites by a network of 6 to 10 ground receivers and by the user satellite, and (2) simultaneous estimation of GPS satellite states and clocks, the user state, and all receiver clocks

Because of this need for a set of simultaneous GPS observations from both the user vehicle and a global ground network, the high precision differential techniques are somewhat cumbersome and are ill suited to near-real-time autonomous navigation For this reason, we have investigated the limiting performance of direct (nondifferential) GPS-based tracking of low earth satellites, incorporating into this analysis a number of refinements that have emerged in recent years from differential GPS development work

With direct GPS-based tracking (which in fact is the more conventional approach), the user position and the time offset from GPS time are obtained using measurements from only the user receiver The collected GPS metric data, which include pseudorange and carrier phase data, are used together with information about the GPS orbits and clocks provided to the user separately, usually through the GPS broadcast data message Highly accurate direct GPS-based tracking therefore requires highly accurate predetermination of GPS positions and time offsets This predetermination of orbits and clocks is carried out using an extensive set of ground-based observations from a global tracking network

In this respect, differential and direct tracking are rather similar both require data from an on-board receiver and a global ground network The key difference is that with direct tracking, the ground data are reduced independently, some hours in advance, to predetermine the GPS ephemeris and clock offsets The central result of this article is that in making

this separation between ground data processing and on-board data processing, surprisingly little of the advantage of true differential tracking need be lost To see this, we need to understand the correlations arising in the GPS orbit determination process and incorporate these into the analysis of the final user orbit error Failure to do so can result in a substantial overestimation of the user error This fact has generally been overlooked in previous analyses of direct GPS-based tracking

Operationally, high precision direct GPS-based tracking might work as follows

(1) A worldwide network of GPS ground receivers, such as the current Air Force Monitor Stations or the network being established for the differential GPS-based tracking demonstration of NASA's Ocean Topography Experiment (Topex) [1], is used to determine GPS orbits and clock parameters with sub-meter accuracy several hours in advance of user tracking

(2) The GPS states and clock information are then propagated forward several hours, with accuracies that project to roughly 1 m and 10 ns at the time of user tracking, and are transmitted to the user satellite Note that GPS clock accuracy degrades more than position accuracy in this process

(3) The user satellite collects GPS measurements over a relatively short arc, typically 2 to 4 hours, to solve for its position and time offset from GPS time, as well as GPS clock offsets from one GPS reference clock This requires a dynamic solution strategy which can be accurate to sub-meter levels only above 800 to 1000 km where gravity and drag model errors are sufficiently small

II. Analysis

Using covariance analysis, we have evaluated the expected accuracy of the direct user orbit solution and the nature of the error sources In order to explore the limiting accuracy of this technique we have assumed use of the high precision receivers, measurement calibration techniques, and geophysical models that have recently been developed for high precision GPS-based geodesy and differential satellite tracking The dependence of user orbit accuracy on such factors as data arc length, the time interval between the end of the ground data arc and the beginning of the user data arc, and the data type used has also been studied For comparison, results from a differential solution are also presented The Topex satellite, which is scheduled to be launched in 1991 into a 1334-km circular orbit and which will carry a high performance GPS receiver, is assumed for the purposes of this analysis to be the test user satellite Note that real-time on-board precision orbit determination is beyond the scope of the Topex mission

In addition to the assumed state-of-the-art precision of the tracking system, one feature distinguishes this analysis from previous studies of direct GPS-based tracking Analyses of direct GPS-based tracking have generally treated the a priori errors in the components of GPS satellite states—errors which often dominate the final user error—as statistically independent That is, the errors in the GPS state components have generally been represented by diagonal covariance matrices, although it is well known that important correlations between component errors exist The usual reasons for this simplifying assumption are that the full GPS covariance matrices are unavailable or unknown, the analysis software can accept only a diagonal matrix, or both In this study, by first analyzing the GPS satellite orbit determination process, we have been able to generate accurate full error covariance matrices for the GPS ephemerides supplied to the user and to employ these in the user orbit error analysis The result is that the true user orbit error is seen to be consistently, and in most cases substantially, lower than the simpler analysis indicates

All cases examined, both differential and direct, assume a worldwide network of six ground stations (in California, Spain, Brazil, Australia, Japan, and South Africa) and a full constellation of 18 GPS satellites

For the differential solution, pseudorange measurements were assumed to be taken every five minutes from each ground station to all observable GPS satellites above a 10-degree elevation cutoff over a period of 24 hours starting at 1400 hours on March 21, 1986 Typically, 5 to 7 GPS satellites are visible at one time from each ground site Topex was assumed to observe all GPS satellites above a 90-degree zenith angle for only the last two hours of this period Measurement assumptions included 5 cm pseudorange every 5 minutes, a 10-degree elevation cutoff at the ground stations, and a zero-degree elevation cutoff for Topex Note that pseudorange is assumed to be smoothed over the entire 5-minute measurement interval in order to achieve 5 cm precision This level of performance is being routinely achieved by the "Rogue" geodetic receiver now undergoing field testing at the Jet Propulsion Laboratory (JPL) [5]

For the base case direct solution, only the two hours of measurements made by Topex were used The GPS states and associated solar pressure parameters (including a Y-bias), obtained with a preliminary solution using a subset of the 24-hour ground track, were left unadjusted, and the effects of errors in those parameters were considered In order to obtain a realistic covariance matrix for the GPS state and related force parameters used in the consider analysis, the first 20

hours of ground data from the 24-hour arc were used to solve independently for the GPS states, Y-bias, and solar pressure The Y-bias parameter is associated with forces due to unmodeled thermal effects and solar panel misalignments [6]

The covariance matrix was assembled as follows the 20-hour solution produced a computed covariance matrix for the GPS states, Y-bias, and solar pressure at epoch, this covariance matrix depends only upon the random data noise assumed in the solution A consider analysis was then performed to evaluate the effects of troposphere and station location error upon the GPS states, Y-bias, and solar pressure, producing a second covariance matrix due to the consider variables The two covariance matrices were then summed to form a single covariance matrix, containing computed error plus consider error, for use in the analysis of the Topex direct solution

The covariance matrix for GPS states revealed 3-D position errors of about 1 meter when projected into the two-hour Topex data arc This is compatible with the results of recent high precision GPS orbit determination demonstrations conducted under somewhat less favorable conditions [7], [8] In fact, in this analysis the estimated error in Y-bias and solar pressure was somewhat higher than that obtained with multi-day data arcs in the same demonstration program

The details of the measurement schedules for the three solutions–base case Topex direct, Topex differential, and GPS a priori state–are shown in Fig 1 In both the GPS satellite solutions and the Topex differential solution, white noise clock models were used, producing independent clock solutions at each time point with one of the ground clocks used as reference This is a general form of the double differencing technique that is widely used to eliminate receiver and satellite clocks as a source of error In the Topex direct solution, where white noise modeling of all clocks is impossible, only the Topex clock was modeled as white noise, and the GPS clocks were modeled as quadratic functions with one GPS clock serving as reference Extensive experience with real GPS data has shown that the highly stable GPS atomic clocks can be modeled as quadratic functions over many hours with sub-centimeter accuracy (This situation will improve only when the more advanced Block II GPS satellites are deployed in the next few years)

For the direct solution, the three quadratic coefficients (constant bias, rate, and rate-rate) were assumed to be known to 10 ns, 10 ns/(4 hours), and 10 ns/(4 hours)^2, respectively These are in fact rather conservative values, solutions for actual GPS clocks with recent field data have been substantially better [9] Ground receiver location errors were considered at 5 cm per component in the differential solution The zenith troposphere error was considered at 1 cm, an accuracy that requires use of high performance water vapor radiometers at the ground sites Finally, the earth gravity model was considered as an error source for Topex in both the differential and direct solutions For this the covariance matrix associated with the 8 X 8 portion of the PGS3012 gravity model, produced recently by the Goddard Space Flight Center, was used The higher order terms in the gravity covariance do not contribute significantly to the Topex position error for the short 2-hour data arc

III. Results

A. Base Case

In the middle of the 2-hour Topex data arc, the estimated altitude errors are 17 cm for the base case direct solution and 7 cm for the differential solution The RMS altitude errors over the arc are 21 cm and 11 cm The errors as a function of time are shown in Fig 2 for the direct solution and in Fig 3 for the differential solution

To test the importance of using the full a priori covariance matrix, a second consider analysis was conducted using only the diagonal elements of the covariance matrix for GPS states, Y-bias, and solar pressure The resulting Topex position error grew to several meters Clearly, the correlations between the consider parameters must be accounted for to accurately estimate final user errors

B. Dependence on Topex Arc Length

In order to study the effect of data arc length on the Topex direct solution, a number of runs were made employing the same assumptions as the base case but differing in the length of the Topex data arc Figure 4 shows a significant degradation in performance when the arc is reduced to 1 hour and 1/2 hour Nevertheless, a 30-minute data arc gives an altitude accuracy better than 40 cm in the middle of the arc

C. Dependence on Data Type

All cases examined so far have used precision pseudorange (5 cm data noise over 5 minutes) In this section we examine the direct solution method using carrier phase data alone (Fig 5) and carrier phase together with pseudorange (Fig 6) For these cases, carrier phase measurements with 0 5 cm data noise over 5-minute intervals were assumed This noise level is consistent with the JPL "Rogue" receiver [5] Other measurement assumptions were the same as for the base case Figures 5 and 6 show very small computed errors and a slight improvement over the pseudorange base case in the middle of the data arc The RMS errors for carrier and mixed data over the 2-hour data arc are 16 and 23 cm, respectively The larger error in the mixed data type is anomalous and is due to nonoptimal

weighting of the data in the filter With real data, the filter data weights could be adjusted by looking at the residuals to include the effects of mismodeling errors and to bring the total error with the mixed data type below that with either data type alone Here the relative data weights are based only on the expected receiver data noise

D. Dependence on the Time Offset From GPS Data

To study the effect of solving for GPS further in the past, the Topex data arc was progressively moved further away in 2-hour increments In the base case the Topex data arc spanned March 22, 1400–1600 The next arc spanned 1600–1800, the next 1800–2000, and so on The final arc in the series started 12 hours after the end of the arc used for the a priori GPS states All other assumptions were the same as for the base case

The errors due to gravity and the computed errors are similar for all of the five additional test arcs Thus for comparison we show only the errors due to GPS state, Y-bias, and solar pressure As expected, the solution degrades as we move further away from the solution for GPS The degradation is not monotonic, however, for the arcs that are 4 and 6 hours away, performance is actually better than the base case that is only 2 hours away from the solution for GPS states This is consistent with the periodic signature in GPS orbit errors in addition to the general trend of increasing error further from the data arc Figure 7 shows the RMS errors as a function of the time interval between the end of the GPS data arc and the beginning of the user data arc Figure 8 shows the errors over the 2-hour Topex data arc at 2, 6, and 12 hours from the GPS data arc Even after an interval of 12 hours, the RMS error due to GPS state, Y-bias, and solar pressure over the arc is only about 30 cm

IV. Conclusions

Direct GPS-based tracking of low earth orbiters can deliver sub-meter accuracy at altitudes above roughly 1000 km, with the user tracking up to 12 hours after the GPS orbit solutions The major error sources are the predetermined GPS states, Y-bias, solar pressure, and the model for the earth's gravity field In order to obtain a realistic estimate of the accuracy that can be achieved, a full covariance matrix must be used to represent the a priori error in the pre-adjusted parameters

At altitudes lower than 1000 km, significant errors in the force models, principally the models for the gravity field and atmospheric drag, will begin to corrupt the direct dynamic solution Therefore, to maintain high accuracy at lower altitudes, nondynamic (geometric or kinematic) or reduced dynamic strategies must be adopted Such techniques have been evaluated extensively in connection with differential satellite tracking and promise to deliver sub-decimeter accuracy down to the lowest possible altitudes [10], [11] Differential tracking, however, requires simultaneous GPS observations by the user and a global network of ground receivers It remains to investigate the potential performance of the nondynamic and reduced dynamic techniques in direct GPS-based satellite tracking

References

[1] T P Yunck, W G Melbourne, and C L Thornton, "GPS-Based Satellite Tracking System for Precise Positioning," *IEEE Transactions on Geoscience and Remote Sensing*, vol GE-23, no 4, pp 450–457, July 1985

[2] T P Yunck, S C Wu, and J T Wu, "Strategies for Sub-Decimeter Satellite Tracking with GPS," *Proc IEEE Position Location and Navigation Symposium*, vol 86, no CH 2365-5, pp 122–128, November 1986

[3] S C Wu and V J Ondrasik, "Orbit Determination of Low-Altitude Earth Satellites Using GPS RF Doppler," *Proc IEEE Position Location and Navigation Symposium*, pp 85–91, December 1982

[4] S M Lichten, S C Wu, J T Wu, and T P Yunck, "Precise Positioning Capabilities for TOPEX Using Differential GPS Techniques," AAS Paper 85-401, presented at the AAS/AIAA Astrodynamics Specialist Conference, Vail, Colorado, August 12–15, 1985

[5] T K Meehan, T N Munson, J B Thomas, J M Srinivasan, D J Spitzmesser, L E Young, and R E Neilan, "Rogue A New High Accuracy Digital GPS Receiver," presented at the International Union of Geodesy and Geophysics, Vancouver, Canada, August 1987

[6] H M Fliegel, W A Feess, W C Layton, and N W Rhodus, "The GPS Radiation Force Model," in *Proceedings of the First International Symposium on Precise Positioning with the Global Positioning System*, pp 113–120, April 1985

[7] S M Lichten, W I Bertiger, and J S Border, "Precision GPS Orbit Determination Strategies for an Earth Orbiter and Geodetic Tracking System," AAS Paper 87-502, presented at the AAS/AIAA Astrodynamics Specialist Conference, Kalispell, Montana, August 10–13, 1987

[8] S M Lichten and J S Border, "Strategies for High Precision GPS Orbit Determination," *Journal of Geophysical Research*, vol 92, pp 12751–12762, November 10, 1987

[9] S A Stephens, L L Skrumeda, and D M Tralli, "Stochastic Colored-Noise Estimation of Clocks Tropospheres in Analysis of GPS Geodetic Data," *EOS Transactions*, vol 68, p 286, April 21, 1987

[10] T P Yunck and S C Wu, "Non-Dynamic Decimeter Tracking of Earth Satellites Using the Global Positioning System," AIAA Paper 86-0404, presented at the AIAA 24th Aerospace Sciences Meeting, Reno, Nevada, January 1986

[11] S C Wu, T P Yunck, and C L Thornton, "Reduced-Dynamic Technique for Precise Orbit Determination of Low Earth Satellites," AAS Paper 87-410, presented at the AAS/AIAA Astrodynamics Specialist Conference, Kalispell, Montana, August 10–13, 1987

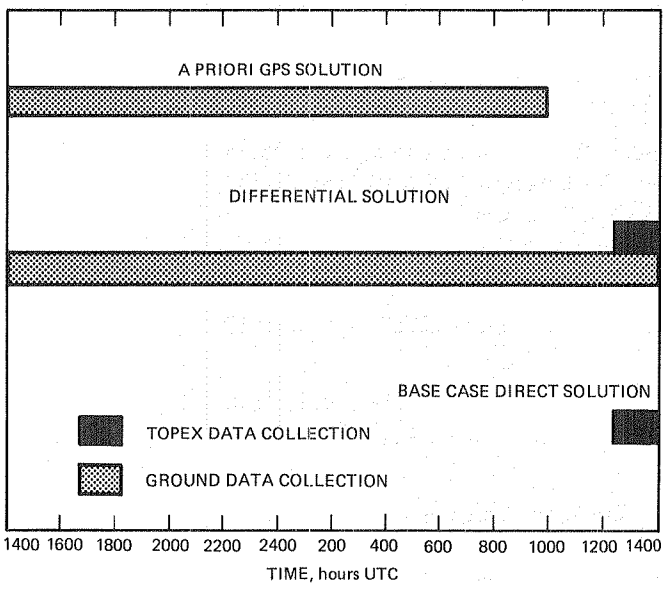

Fig. 1. Basic measurement scenario, March 21–22, 1986

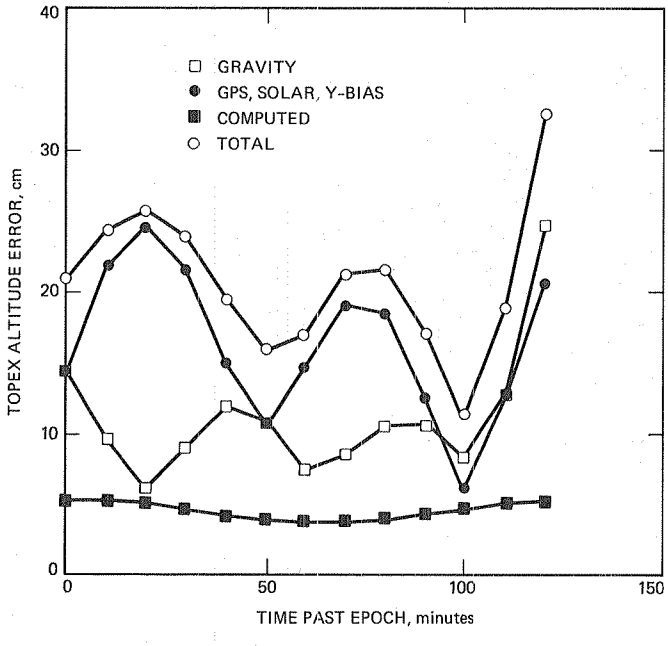

Fig. 2. Base case direct solution, 2-hour arc, pseudorange

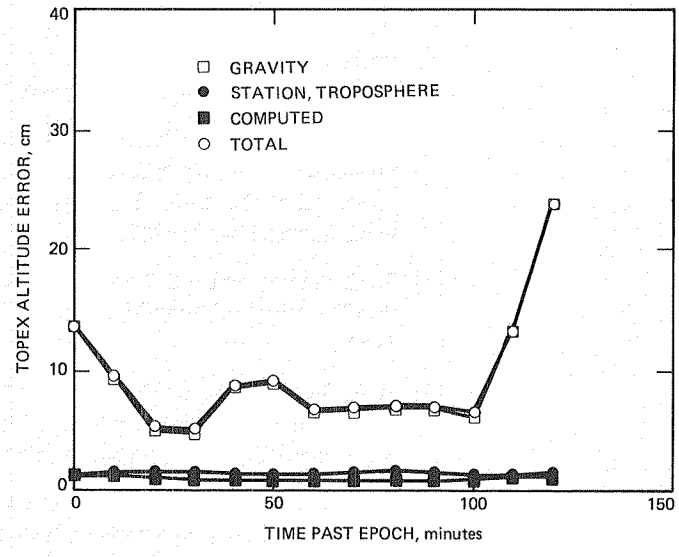

Fig. 3. Differential solution, 2-hour Topex arc, 24-hour GPS arc, pseudorange

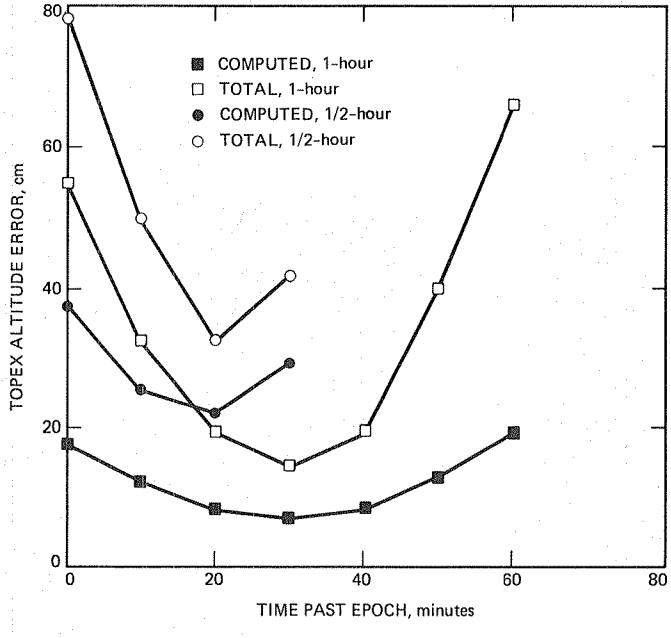

Fig. 4. Accuracy dependence on Topex arc length

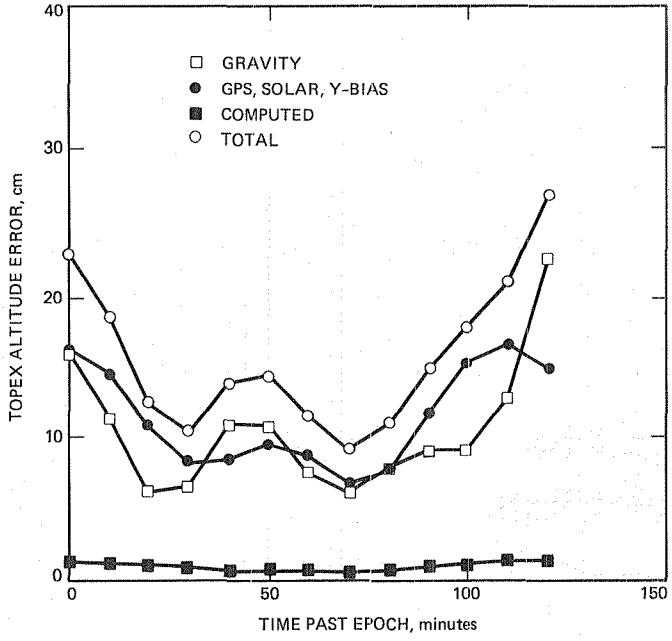

Fig. 5. Direct solution with carrier phase data

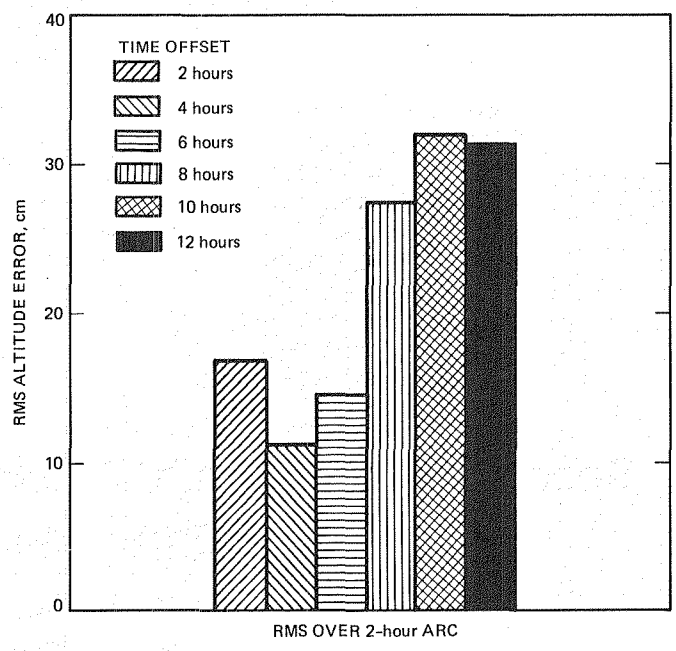

Fig. 7. Variation of RMS Topex altitude error with the time offset from GPS solution arc

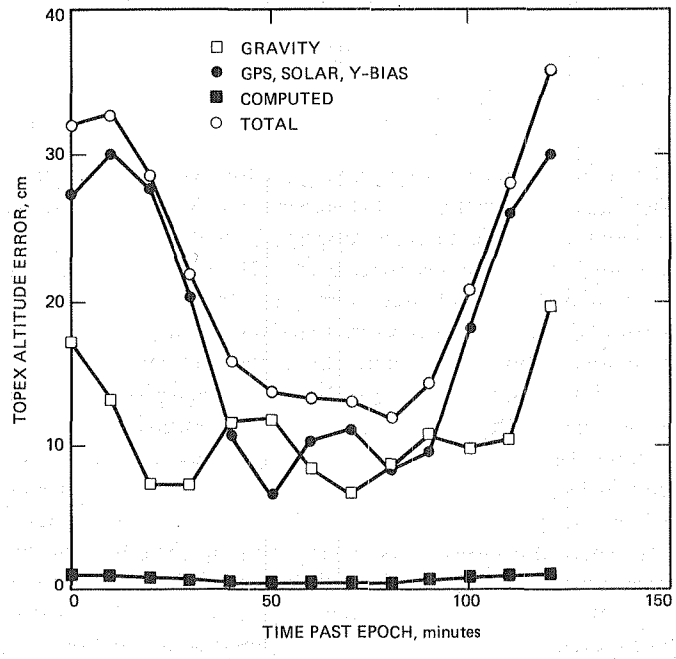

Fig. 6. Direct solution with mixed data types

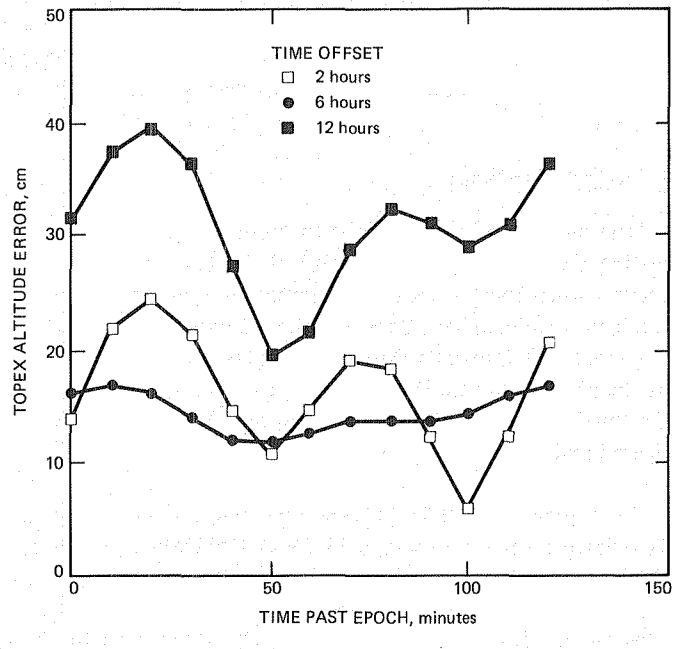

Fig. 8. Errors over a 2-hour period for different time offsets from GPS solution

Spectral Estimation of Received Phase in the Presence of Amplitude Scintillation

V A Vilnrotter, D H Brown, and W J Hurd
Communications Systems Research Section

A technique is demonstrated for obtaining the spectral parameters of the received carrier phase in the presence of carrier amplitude scintillation, by means of a digital phase locked loop Since the random amplitude fluctuations generate time-varying loop characteristics, straightforward processing of the phase detector output does not provide accurate results The method developed here performs a time-varying inverse filtering operation on the corrupted observables, thus recovering the original phase process and enabling accurate estimation of its underlying parameters

I. Introduction

The purpose of this article is to present a method for estimating the power spectral density of the phase of a received carrier, when there is significant amplitude scintillation on the received waveform For example, these conditions occur when the spacecraft transmits through the solar corona Knowledge of the phase spectrum is important for improving carrier tracking through bandwidth optimization, or through more sophisticated real-time adaptive techniques

In a previous article [1] we reported the results of an experiment, carried out at DSS 14 at Goldstone, where the DSN Advanced Receiver was used to track weak signals originating from the Pioneer 10 spacecraft on its way out of the solar system [2] One purpose of the experiment was to optimize the bandwidth of the Advanced Receiver's coherent phase-locked loop in near-real time, thus minimizing the root mean square (rms) phase error and improving the quality of the recovered data The optimization was based on estimates of the phase spectral density and the spectral level of the additive noise, using a robust ad hoc estimator Amplitude fluctuation was not a factor in that experiment More recently, an attempt was made to track Voyager 2, as it travelled behind the solar corona in the latter part of December 1987 [3] A maximum likelihood estimator was developed to obtain improved estimates However, the unexpectedly large amplitude fluctuations encountered near the Sun rendered these parameter estimates questionable, even though phase lock was maintained with the help of the ad hoc estimator A large amount of data was collected and subsequently analyzed In this article, we present the results of the data analysis and demonstrate a technique for obtaining estimates of the relevant spectral parameters, taking into account the effects of the time-varying amplitude Our ultimate goal is to adaptively control loop parameters for the purpose of minimizing phase error, even in the presence of severe amplitude fluctuations

Radio waves propagating through a turbulent medium, such as the solar corona, undergo random changes that often alter their characteristics From the viewpoint of deep space com-

munications, the most significant of these effects are phase and amplitude scintillation, spectral and angular broadening, and Faraday rotation [4] Amplitude and phase scintillation are the most pronounced effects at the 8 4-GHz carrier frequency (X-band) employed by the DSN Scintillations are caused by random inhomogeneities within the propagation channel Amplitude scintillation is basically a diffraction phenomenon, caused by plasma irregularities that are smaller than or roughly equal to the Fresnel zone size at the irregularity The time scale of the amplitude fluctuations due to the solar corona is typically on the order of a second Phase scintillation is primarily a refraction effect, caused by plasma irregularities with different refractive indexes, and different random velocity components along the line of sight The power spectral densities of both phase and amplitude fluctuations obey inverse power relations in certain frequency regions near the carrier frequency, which means that the level of the spectral density is inversely proportional to the frequency difference, raised to some constant power

$$S(f) \simeq S_1 |f|^{-\alpha} \tag{1}$$

For phase spectra, the exponent α due to the solar corona is typically 8/3 or less at small Sun-Earth-probe (SEP) angles [5] The coefficient S_1 is the value of the spectral level at a frequency of 1 Hz from the carrier Oscillator instabilities aboard the spacecraft also generate a power law type spectral density, but with an exponent of $\alpha = 3$ [6] In the current application, we shall assume that plasma effects dominate, and model the spectral density of the phase fluctuations as in Eq (1) in order to obtain the required parameter estimates However, care must be exercised in interpreting the results, since other effects (such as oscillator instability) may not be completely negligible The spectral characteristics of the amplitude fluctuations are less critical, since only the bandwidth of the amplitude fluctuations will be used to estimate the scintillating amplitude

II. The Received Waveform

As the transmitted signal propagates through the solar plasma, it suffers random amplitude and phase distortions that degrade the quality of the received waveform An accurate description of these degradations is the subject of the following paragraphs

A. Signal and Noise Representations

Having propagated through the turbulent channel, the residual component of the transmitted radio wave $s(t)$ can be represented at the receiver as

$$s(t) = \sqrt{2} A(t) \cos(\omega_0 t + \theta(t)) \tag{2}$$

where ω_0 is the carrier frequency in radians per second, $A(t)$ is a random amplitude function describing the channel-induced amplitude scintillation, and $\theta(t)$ is a random phase process, also due to the channel Unfortunately, a perfect measurement of this received waveform cannot be made, because of background radiation and receiver noise Within the frequency band of interest, the sum of all significant noise contributions can be modeled as an equivalent narrowband Gaussian process, with representation

$$n(t) = \sqrt{2} [n_c(t) \cos(\omega_0 t) - n_s(t) \sin(\omega_0 t)] \tag{3}$$

Here $n_c(t)$ and $n_s(t)$ are taken to be independent white Gaussian processes, each with two-sided spectral level $N_0/2$, within the frequency band of interest Thus, the receiver observes the channel-corrupted signal in the presence of additive white Gaussian noise

$$r(t) = s(t) + n(t) \tag{4}$$

Amplitude and phase information may be extracted from the received waveform by means of coherent processing techniques, such as by means of a phase-locked loop in a coherent receiver A coherent receiver estimates the total phase $(\omega_0 t + \theta(t))$, and multiplies the received waveform $r(t)$ by locally generated sinusoids driven by the estimated phase process $\hat{\theta}(t)$ If the estimate is a good approximation to the received phase, then the resulting baseband waveforms can be represented as

$$r_I(t) = A(t) \cos(\phi(t)) + n_I(t) \tag{5a}$$

$$r_Q(t) = A(t) \sin(\phi(t)) + n_Q(t) \tag{5b}$$

where $\phi(t) = \theta(t) - \hat{\theta}(t)$ is the instantaneous phase error, and $n_I(t)$ and $n_Q(t)$ are approximately white Gaussian processes with two-sided spectral level $N_0/2$, independent of each other and of the underlying phase error (this last assumption is valid only if the correlation time of the additive noise is short compared to that of the phase process) The I (or in-phase) signal can be used for amplitude estimation, whereas the Q (or quadrature) signal is generally used for phase control Note that if the phase estimate is accurate so that $|\phi(t)| \ll 1$, then Eqs (5a) and (5b) reduce to

$$r_I(t) \simeq A(t) + n_I(t) \tag{6a}$$

$$r_Q(t) \simeq A(t)\,\phi(t) + n_Q(t) \tag{6b}$$

In particular, the scintillating amplitude $A(t)$ can be estimated under this condition, since the in-phase signal $r_I(t)$ reduces

to the sum of the amplitude function and the equivalent noise, independent of the phase process

In digital systems, the analog waveforms are converted to numerical sequences prior to processing The conversion operation is called sampling It is generally implemented by averaging the analog waveform over intervals that are short compared to the correlation time of the desired component, or by performing other roughly equivalent operations For purposes of analysis it is convenient to adopt the averaging approach, and model the received samples as

$$r_x(t) = \frac{1}{T}\int_{t_1}^{t_1+T} r_x(t)\,dt = s_x(t) + n_x(t) \qquad (7)$$

where x represents either I or Q, $s_I(t) = A(t)$, and $s_Q(t) = A(t)\,\phi(t)$ If the noise correlation time is short compared to the averaging time T, then the variance of either noise sample becomes $N_0/2T$, while its mean value remains zero It is often necessary (or desirable) to resample the original sequence at various points within the system by averaging consecutive samples Because integration is a linear operation, this type of resampling is exactly equivalent to averaging the analog waveform over the longer (resampled) time interval Thus, if L consecutive samples are averaged, the variance of either resulting noise sample becomes $N_0/2LT$ The desired signal component remains essentially undistorted by resampling, provided its correlation time exceeds LT by a significant margin

B. Amplitude Scintillation Spectrum

An example of a scintillating radio wave observed in the presence of additive noise was provided by the Voyager 2 spacecraft as it passed behind the solar corona As an example, we use the data from day-of-year (DOY) 357, corresponding to an SEP angle of about 2 3 degrees, because strong amplitude scintillations were evident The Advanced Receiver tracked the phase with small error, validating our linear model

The received analog waveform was initially sampled at approximately 10 million samples/s, then summed and resampled at a rate of 320 samples/s, yielding a sampling time of $T = 3\ 125$ ms This was the update rate of the digital phase locked loop The observables generated by the coherent loop were further summed and resampled at 40 samples/s, corresponding to a final resampling time of $LT = 0\ 025$ second

A sample sequence of the observables, consisting of 256 consecutive samples, is shown in Fig 1, spanning a time of 6 4 seconds The discrete sample values are connected with straight line segments to aid in visual perception Slow variations in the average amplitude are apparent The significant frequency components of this sequence can be quantified by estimating its power spectral density This was done by means of averaged periodograms, described in detail in Section IV Periodograms can be obtained efficiently using fast Fourier-transform (FFT) algorithms The normalized spectral density estimate of the amplitude shown in Fig 2 was obtained by averaging 100 disjoint sequences of 256 samples each, and dividing by the zero-frequency value It is apparent that the spectrum can be divided into two distinct regions, namely a "high-frequency" region due to the white noise where the spectrum appears flat, and a "low-frequency" region where the signal amplitude fluctuations dominate

An estimate of the amplitude fluctuations may be obtained in real time by passing the received sequence through a low-pass filter with bandwidth great enough to ensure acceptably small distortion in the scintillation spectrum The required filtering operation can be generated by averaging K consecutive samples in a "sliding window" implementation We take the bandwidth of this filter to be the frequency of the first null, namely

$$B_{FN} = (LTK)^{-1} \qquad (8)$$

(Note this is greater than the usual "–3 dB" bandwidth) Observing that there is no significant power in the amplitude scintillations above 2 Hz, we set $B_{FN} = 2$ Hz, for which $K = 1/(2TL) = 20$ The estimated amplitude function $\hat{A}(t)$ is shown in Fig 1, while the spectrum of the filtered estimates is shown in Fig 2, both represented by dashed curves The performance of this rather simple amplitude estimator is not expected to be as good as that of more sophisticated algorithms based on optimum estimation principles However, since the sliding window combines ease of implementation with acceptable performance, it is considered adequate for the purpose of demonstrating the concepts developed in this article

III. Separation of Amplitude and Phase Effects

In this section we describe a technique for reconstructing the noise-corrupted phase process from the recorded phase detector output, effectively removing the random coefficient of the phase due to the scintillating amplitude First we discuss the standard digital phase locked loop (PLL), then we model the loop in the presence of random signal-amplitude variations, and finally we demonstrate the reconstruction of the received phase

A. Linear Time Invariant Phase Locked Loop

The quadrature samples defined in the previous section are used in the Advanced Receiver to drive a digital phase-locked loop, which in turn generates estimates of the received phase process at the loop update rate These estimates control the frequency of a local oscillator operating at, or near, the received carrier frequency, whose output is used to perform the desired downconversion operation With little loss in generality, we shall assume that direct baseband downconversion is performed If the loop is locked, and operating with small instantaneous phase error most of the time, then the linear model yields an accurate description of loop operation

A linear model of the digital phase-locked loop is shown in Fig 3 The loop generates estimates of the received phase sequence, $\hat{\theta}(t)$, and subtracts these estimates from the received phase sequence $\theta(t)$ The received phase consists of three independent components a doppler-induced phase process $d(t)$, transmitter instability $\psi_t(t)$, and a plasma-induced phase process $\psi_p(t)$ Therefore we can write $\theta(t) = d(t) + \psi_t(t) + \psi_p(t)$ The instantaneous phase error, defined as $\phi(t) = \theta(t) - \hat{\theta}(t)$, is multiplied by a slowly varying sequence $A(t)$ representing the plasma-induced amplitude scintillation of the received carrier After adding the equivalent noise sequence $n_Q(t)$, the resulting sequence is filtered by the loop filter The filtered error sequence $e(t)$ controls the frequency of a numerically controlled oscillator (NCO) whose output is also considered to be a phase sequence, sampled at the same rate as the input The phase estimate is the sum of the NCO phase plus an independent random sequence representing NCO drift The observable sequence is denoted by $w(t)$ It is a resampled version of the phase detector sequence which appears at the input to the loop filter Henceforth we assume that $w(t) \simeq y(t)$, because in our case the resampling rate is much greater than the bandwidth of the phase process

B. PLL With Time Varying Signal Amplitude

In analogy with Heaviside's differential operator, it is convenient to define the shift operator S, which operates on an arbitrary sample $x(t)$ according to the rule

$$S^{-k}x(t) = x(t-k) \tag{9}$$

The shift operator allows us to relate the output of a linear filter, defined by the operator $P(S)$, to its input as $y(t) = P(S)\,x(t)$ Since the z-transform of a k-increment delay is z^{-k}, it follows that the transfer function of the above filter in the z-domain is $P(z)$ Making use of the shift-operator concept, the digital loop equations become

$$\phi(t) = \theta(t) - \hat{\theta}(t) \tag{10a}$$

$$y(t) = A(t)\phi(t) + n_Q(t) \tag{10b}$$

$$\hat{\theta}(t) = F(S)N(S)y(t) + \psi_r(t) \tag{10c}$$

Defining the total phase process $\xi(t) = d(t) + \psi_t(t) + \psi_p(t) - \psi_r(t)$, Eq (10) can be solved for the phase error, hence the phase detector output, as

$$\phi(t) = \left\{1 + A(t)F(S)N(S)\right\}^{-1}\xi(t) + \left\{\frac{A(t)F(S)N(S)}{1 + A(t)F(S)N(S)}\right\}\frac{n_Q(t)}{A(t)} \tag{11a}$$

$$y(t) = A(t)\left\{1 + A(t)F(S)N(S)\right\}^{-1}\left[\xi(t) + \frac{n_Q(t)}{A(t)}\right] \tag{11b}$$

Thus, the phase detector output contains a term that depends on the phase $\xi(t)$, and one that depends on the additive noise

C. Reconstruction of the Phase Process

We observe that in Eqs (11a) and (11b) both the phase and additive noise processes are operated on by time-varying operators, due to the fluctuating amplitude $A(t)$ Since the amplitude fluctuations vary slowly compared to both the loop response time and noise correlation time, and since estimates of the amplitude process are available, we may attempt to reconstruct the original processes by passing the phase detector output through a time-varying inverse filter of the form

$$P(S) = \frac{\{1 + \hat{A}(t)F(S)N(S)\}}{\hat{A}(t)} \tag{12a}$$

If $v(t)$ denotes the response of $P(S)$ to $y(t)$, the operation of the filter may be described by the recursion

$$v(t) = \sum_{l=0}^{4} a_l(t)\,y(t-l) + \sum_{l=1}^{2} b_l(t)\,v(t-l) \tag{12b}$$

The coefficients are derived in the Appendix The filter's response to the phase detector output is

$$v(t) = \left\{\frac{1 + \hat{A}(t)F(S)N(S)}{\hat{A}(t)}\right\}y(t) \simeq \xi(t) + \left(\frac{n_Q(t)}{\hat{A}(t)}\right) \tag{13}$$

This is an estimate of the total phase process corrupted by a modified noise sequence That this noise sequence is also white

follows from the following argument over a suitably short time interval, such that channel statistics remain fixed, we can express the amplitude fluctuations as the sum of an average value plus a zero-mean random process

$$\hat{A}(i) = \bar{A} + n_A(i) = \bar{A}\left(1 + \frac{n_A(i)}{\hat{A}}\right) \tag{14a}$$

The modified noise sequence now becomes

$$\frac{n_Q(i)}{\hat{A}(i)} = \frac{n_Q(i)}{\bar{A}\left[1 + \dfrac{n_A(i)}{\bar{A}}\right]} = \frac{n_Q(i)}{\bar{A}}\left[1 - \frac{n_A(i)}{\bar{A}} + \frac{n_A^2(i)}{\bar{A}^2} - + \right]$$

$$\triangleq \frac{n_Q(i)\, n_{eq}(i)}{\bar{A}} \tag{14b}$$

where $n_{eq}(i)$ is the series inside the brackets Assuming that the additive noise is independent of the amplitude process, the autocorrelation function of the modified noise sequence is

$$R_{\left(\frac{n_Q}{\hat{A}}\right)}(k) = (\bar{A})^{-2} R_{n_Q}(k) R_{n_{eq}}(k) \tag{15}$$

For uncorrelated noise samples we have $R_{n_Q}(k) = (N_0/2)\,\delta(k)$, which reduces Eq (15) to

$$R_{\left(\frac{n_Q}{\hat{A}}\right)}(k) = (\bar{A})^{-2}\left(\frac{N_0}{2}\right) R_{n_{eq}}(0)\,\delta(k) \triangleq \frac{N_{0E}}{2}\,\delta(k) \tag{16}$$

Therefore $n_Q(i)/\hat{A}(i)$ is white, with a spectral level corresponding to the coefficient of the Kroenecker delta function The power spectral density of the reconstructed observables consists of spectral contributions from both the phase and the modified noise processes

$$S_v(f) \simeq S_\xi(f) + \frac{N_{0E}}{2} \tag{17}$$

In our application, the contributions of Doppler and receiver phase processes are small The main components of the phase process are due to the solar corona and to transmitter oscillator instabilities Both effects produce a power-law type phase spectrum near the carrier frequency, the first with exponent 8/3 or less, and the second with exponent 3 Thus we expect the observed spectral density to be composed of a constant spectral level due to the inverse-filtered white noise, plus a power law component due to the dominant phase process

The estimated power spectral density for the data sequence under consideration is shown in Fig 4 The white noise component is clearly evident This figure is discussed further in the next section where we consider the problem of estimating the relevant channel parameters from the reconstructed sequence These estimates may be used to monitor channel conditions, or to adaptively match receiver parameters to channel conditions for improved performance

IV. Parameter Estimation

In this section we estimate the parameters of the spectral density of the received phase First we discuss the method used to estimate the spectral density, and then describe the maximum likelihood (ML) algorithm used to estimate its parameters

A. Power Spectral Density Estimation

An extensive body of literature exists on spectral estimation algorithms Here we use a simple but well established approach known as Bartlett's procedure [7] This technique is easy to implement, but yields good results whenever spectral resolution requirements are met with a small fraction of the available samples In particular, estimates of the power spectral density are obtained by averaging independent periodograms, which can be generated by means of efficient FFT algorithms

The periodogram of length N, $I_N(\omega)$, associated with the sequence $v(i)$, is defined as

$$I_N(\omega) = \frac{1}{N}\left|V(e^{j\omega})\right|^2 \tag{18a}$$

where

$$V(e^{j\omega}) = \sum_{i=0}^{N-1} v(i)\, e^{-j\omega i} \tag{18b}$$

is the discrete Fourier transform of the sequence $v(i)$ The use of periodograms in spectral estimation is justified on the grounds that in the limit as N approaches infinity, the expected value of the periodogram approaches the desired power spectral density With $R_v(m)$ the autocorrelation function of v, we have from [7] that if $R_v(m) = 0$ for all $m > m_0$, then

$$\lim_{N\to\infty} E\{I_N(\omega)\} = \lim_{N\to\infty} \sum_{m=-(N-1)}^{N-1} \left(1 - \frac{|m|}{N}\right) R_v(m)\, e^{-j\omega m}$$

$$= S_v(\omega) \tag{19}$$

The FFT generates samples of the periodogram, evaluated at the points $\omega = 2\pi k/N$ With

$$V(k) = V(e^{j\omega})\Big|_{\omega=2\pi k/N} \tag{20a}$$

it follows that

$$I_N(k) = I_N(\omega)\Big|_{\omega=2\pi k/N} \tag{20b}$$

Suppose the observed samples were obtained from a white Gaussian process, and therefore are jointly Gaussian random variables with the autocorrelation function $R_v(m) = R_v(0)\,\delta(m)$ Consequently, the transformed samples $V(k)$ become complex Gaussian random variables The correlation between the transformed samples at frequencies corresponding to k and l can be evaluated directly from the expression

$$\frac{1}{N}\overline{V(k)\,V^*(l)} = \frac{1}{N}\sum_{i=0}^{N-1}\sum_{n=0}^{N-1} \overline{v(i)\,v(n)}\; e^{-j\frac{2\pi}{N}(ki-ln)}$$

$$= \begin{cases} R_v(0) & , \quad k = l \\ 0 & , \quad k \neq l \end{cases} \tag{21}$$

where * denotes conjugation, and the overbar denotes the expectation operator It follows from Eq (21) that the frequency samples are uncorrelated, hence independent by the Gaussian assumption Since for $k = l$ the correlation expression corresponds to the expected value of the periodogram, we conclude that for white processes the periodogram is an unbiased estimator of spectral level

This result may be generalized by observing that any desired spectral characteristics can be obtained by filtering a unity spectral level white sequence with the appropriate linear filter [7] Thus, if the squared magnitude of the frequency response is chosen to be $S_v(\omega)$, the resulting periodogram expressed in terms of $I_{NW}(\omega)$, the periodogram of the white sequence, becomes

$$I_N(\omega) \simeq S_v(\omega)\, I_{NW}(\omega) \tag{22}$$

This expression is not exact because of the transient end effects associated with the filtering of a finite length sequence However, if the sequence is long compared to the memory of the filter, then Eq (22) should yield an accurate representation of the actual spectrum Thus we conclude from Eqs (21) and (22) that the spectral samples remain independent, with magnitudes that approximate the actual spectral level at that frequency It has been shown [7] that the variance of the samples is

$$\mathrm{var}\,(I_N(k)) \simeq S_v^2(k)\left\{1 + \left[\frac{\sin(2\pi k)}{N\sin\left(\frac{2\pi k}{N}\right)}\right]^2\right\} \tag{23}$$

from which it follows that for all $k > 0$, the standard deviation of a periodogram sample is equal to the spectral level The resulting wild fluctuations from one sample to the next render a single periodogram somewhat useless as a spectral level estimator The problem can be ameliorated by averaging a large number of independent periodograms, as originally proposed by Bartlett If M independent periodograms are averaged, the variance at any frequency is reduced by M, while the expected value is preserved Denoting the averaged periodogram samples by $B_N(k)$, we have

$$\lim_{N\to\infty} E\{B_N(k)\} = S_v(k) \tag{24a}$$

$$\mathrm{var}\{B_N(k)\} = M^{-1} S_v^2(k), \qquad k = 1, 2, \quad , N-1 \tag{24b}$$

The spectral density estimate for the data under consideration is shown in Fig 4, obtained by averaging 100 independent periodograms of the reconstructed phase detector output A log-log plot was chosen to facilitate comparison with theory The agreement with the power-law model is evident in the low frequency regions, while dominance of the white noise component occurs at higher frequencies

B. Maximum Likelihood Estimator

The maximum likelihood estimator described here processes independent frequency samples to obtain estimates of the desired spectral parameters, namely the coefficient S_1, the exponent α, and the equivalent noise spectral level $N_{0E}/2$ After some preliminary processing, the channel-induced signal distortions were found to be separately accessible from the in-phase and quadrature samples, corrupted by independent additive noise samples We begin by developing the necessary mathematical models

Since the final spectral estimates are averages of many independent records, the Central Limit Theorem may be invoked for approximating the density of the frequency samples Al-

though each spectral sample is the squared magnitude of a complex Gaussian random variable and therefore is chi-squared distributed with two degrees of freedom, the operation of averaging a large number of independent samples transforms the averages to Gaussian random variables with the mean and variance given by Eq (24) Thus we can model the problem as one of estimating the parameters of a deterministic function g from its noise-corrupted samples y

$$y(k) = g(k, \mathrm{a}) + n_e(k) \tag{25a}$$

$$g(k, \mathrm{a}) = a1 + a2\left(\frac{k}{NT}\right)^{-a3} \tag{25b}$$

Here $n_e(k)$ is an equivalent noise sample representing the estimation error While $n_e(k)$ is zero mean, its variance depends on the square of the spectral level and on the number of samples averaged, as in Eq (24b) Since the frequency samples are assumed to be independent, we can write the joint density of the $N - 1$ samples (excluding the sample at $k = 0$, since this sample cannot possibly obey the power-law relation of Eq (1)) as

$$p(\mathrm{y}|\mathrm{a}) = \prod_{k=1}^{\frac{N}{2}-1} \exp\left\{-\left(\frac{y(k) - g(k)}{\sqrt{2}\,\sigma(k)}\right)^2\right\} (2\pi\sigma^2(k))^{-1/2} \tag{26}$$

with $\mathrm{y} = (y(1), y(2), \ldots, y((N/2 - 1))$, $\mathrm{a} = (a1, a2, a3)$ For our case, $\sigma(k) = g(k)/\sqrt{M}$ Taking the natural log, and keeping only those terms that contain the parameters of interest, the "log-likelihood" function becomes

$$\Lambda(\mathrm{y}) = -\sum_{k=1}^{\frac{N}{2}-1}\left\{ln(g(k)) + \frac{M}{2}\left(\frac{y(k)}{g(k)}\right)^2 - M\,\frac{y(k)}{g(k)}\right\} \tag{27}$$

With $a1 = N_{0E}/2$, $a2 = S_1$, and $a3 = \alpha$, the maximum likelihood estimates are those values that simultaneously maximize Eq (27), for the given observation vector Equivalently, we can find the minimum of the negative of the log-likelihood function This we proceeded to do, using the simplex method of function minimization described by Nelder and Mead [8]

C. Results

The following parameter estimates were obtained for the data taken on DOY 357, at an SEP angle of 2 25 degrees $S_1 = 2\ 13 \times 10^{-3}\ r^2/\mathrm{Hz}$, $\alpha = 2\ 186$, and $N_{0E}/2 = 8\ 77 \times 10^{-4}\ r^2/\mathrm{Hz}$ The exponent compares favorably with theory, which predicts a frequency exponent of less than 8/3 for the phase spectra this close to the Sun The phase spectral coefficient S_1 is also in order-of-magnitude agreement with the measurements in [5], after our result is extrapolated to S-band (2-GHz) frequencies The estimates obtained by the ad hoc estimator, which does not take into account the time-varying nature of the closed-loop transfer function, were $7\ 6 \times 10^{-4}$ for the white noise component and $3\ 7 \times 10^{-2}$ for the phase spectral coefficient, assuming a power-law exponent of 8/3 The importance of our signal reconstruction technique is well demonstrated by this example, since the ad hoc estimate of the spectral coefficient appears to be in error

The degree of complexity required to evaluate the performance of the maximum likelihood estimator by analytical means, such as the Cramer-Rao bound, is beyond the scope and interest of this article However, performance can be easily evaluated by simulation techniques Using the spectral model defined in Eq (25b) with the parameter values $a1 = 8\ 77 \times 10^{-4}$, $a2 = 2\ 13 \times 10^{-3}$, $a3 = 2\ 186$, and adding an independent Gaussian noise sample with the proper variance to each frequency sample, parameter estimates were obtained for 1000 independent simulated spectral densities The sample means agreed well with the modeled values, indicating that unbiased estimates were obtained With obvious notation, the standard deviations of the estimation errors were $\sigma_{a1} = 9\ 3 \times 10^{-6}$, $\sigma_{a2} = 9\ 5 \times 10^{-5}$ and $\sigma_{a3} = 4\ 7 \times 10^{-2}$ Therefore the simulations indicate very good accuracy in the final estimates We must remember, however, that our underlying model is only approximate, since we have assumed a single power-law component to the phase spectrum where in fact there may have been two In addition, other sources of error in preprocessing the data, such as the use of inaccurate amplitude estimates, were not taken into account in the simulations However, we did succeed in demonstrating a useful technique for reconstructing phase spectra from observables corrupted by random amplitude effects

V. Conclusions

Recently, the JPL Advanced Receiver was used to track Voyager 2 as it passed behind the solar corona During tracking, severe fluctuations were noted in the amplitude of the received signal, particularly at small SEP angles Since these fluctuations introduced a corresponding random variation into the transfer function of the tracking loop, previous spectral density estimation techniques that assumed a time-invariant loop became inadequate Thus, a method was developed to extract the desired parameters from the recorded data, taking into account the fluctuating signals

Our approach is based on the observation that random variations in the transfer function could be attributed directly to the fluctuating amplitude, suggesting the use of a time-varying inverse filter to remove these unwanted amplitude effects from

the phase-detector output This required estimates of the random amplitude Since both in-phase and quadrature samples were recorded, the necessary amplitude estimates could be obtained from the in-phase samples, provided the loop remained in lock Thus, we were able to recover the phase error process from the phase-detector output by means of a time-varying inverse filter operation Subsequent spectral analysis and parameter estimation yielded results that agreed both with theory and with measurements made independently by other researchers, confirming the validity of our approach

The ability to obtain real-time estimates of the random amplitude function along with the relevant phase and noise spectral parameters opens up the possibility of adaptive control, where the system parameters are continuously adjusted to achieve optimum performance This would be useful whenever significant amplitude variations occur, as with a wobbling spacecraft antenna, mechanical vibrations at the receiving antenna, solar plasma effects, tropospheric turbulence, etc Perhaps a rudimentary form of an adaptive system could be demonstrated during the upcoming solar occultation of Voyager 2, in January of 1989 Such a demonstration might have a significant impact on future centimeter and millimeter wave DSN system design, where fluctuations in received signal strength due to atmospheric effects may be routinely encountered

References

[1] V A Vilnrotter, W J Hurd, and D H Brown, "Optimized Tracking of RF Carriers With Phase Noise, Including Pioneer 10 Results," *TDA Progress Report 42-91*, vol July–September 1987, Jet Propulsion Laboratory, Pasadena, California, pp 141–157, November 15, 1987

[2] D H Brown and W J Hurd, "DSN Advanced Receiver Breadboard Description and Test Results" *TDA Progress Report 42-89*, vol January–March 1987, Jet Propulsion Laboratory, Pasadena, California, pp 48–66, May 15, 1987

[3] D H Brown, W J Hurd, V A Vilnrotter, and J D Wiggins, "Advanced Receiver Tracking of Voyager 2 Near Solar Conjunction," *TDA Progress Report 42-93*, vol January–March 1988, Jet Propulsion Laboratory, Pasadena, California, May 15, 1988

[4] J W Armstrong et al , *The Deep Space Network – A Radio Communications Instrument for Deep Space Exploration*, JPL Publication 82-104, Jet Propulsion Laboratory, Pasadena, California, July 15, 1983

[5] R Woo and J W Armstrong, "Spacecraft Radio Scattering Observations of the Power Spectrum of Electron Density Fluctuations in the Solar Wind," *J Geophys Res* , vol 84, no A12, pp 7288–7296, 1979

[6] R Gagliardi, *Introduction to Communications Engineering*, New York John Wiley & Sons, 1978

[7] A V Oppenheim and R W Schafer, *Digital Signal Processing*, Englewood Cliffs, New Jersey Prentice-Hall, 1975

[8] J A Nelder and R Mead "A Simplex Method for Function Minimization," *Computer J* , vol 7, pp 308–313, 1965

[9] S Aguirre and W J Hurd, "Design and Performance of Sampled Data Loops for Subcarrier and Carrier Tracking," *TDA Progress Report 42-79*, vol July–September 1984, Jet Propulsion Laboratory, Pasadena, California, pp 81–95, November 15, 1984

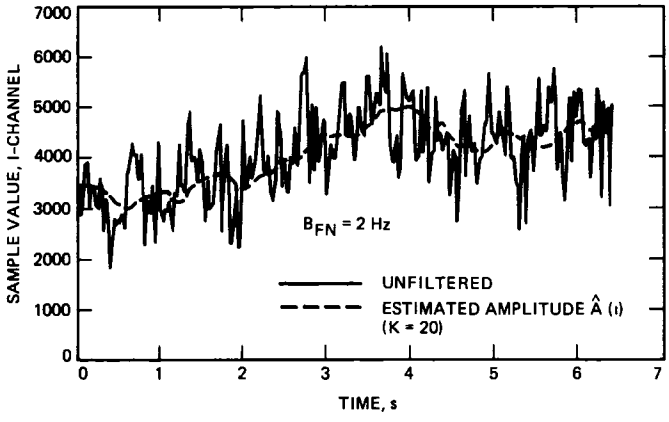

Fig. 1. Sample sequence of resampled observables. I-channel

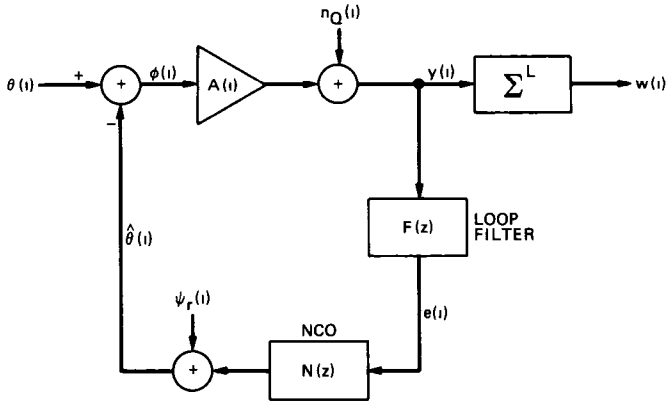

Fig. 3 Linear model of time-varying digital phase-locked loop

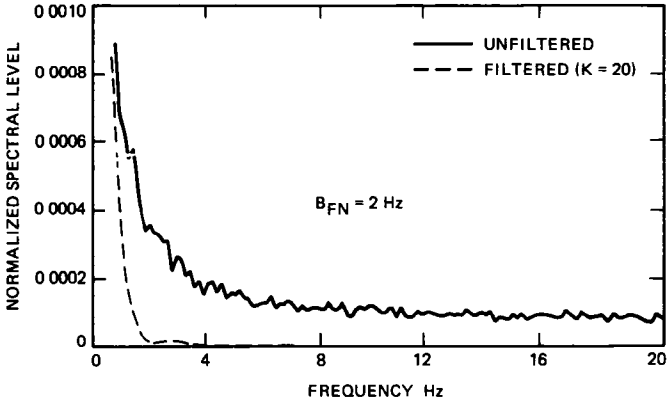

Fig. 2. Normalized spectral density estimates of amplitude fluctuations

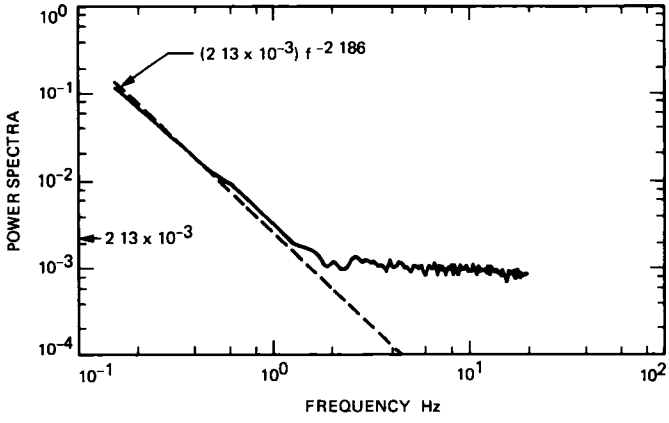

Fig 4 Estimated power spectral density of reconstructed observables

Appendix

Derivation of the Coefficients for the Inverse Filter, *P*(z)

The coefficients of Eq (12b) are derived

From equation (12) of [9],

$$G(z) = AKF(z)N(z)$$

$$= \frac{\frac{r}{2}(z+1)\left[\frac{4B_LT}{r+1}(z-1)+\left(\frac{4B_LT}{r+1}\right)^2 z\right]}{(z-1)^2 z^2} \tag{A-1}$$

Let us assume that the variation in $A(t)$ is slow relative to the response time of the loop, which was the case in our experiment Thus, for short intervals we can use the approximation

$$A(t) \simeq AK$$

By Eq (12a),

$$P(z) = \frac{[1+G(z)]}{AK} \tag{A-2}$$

so

$$P(z) = \frac{\left[\frac{1-2z^{-1}+\left[\frac{r}{2}(d+d^2)+1\right]z^{-2}+\frac{r}{2}d^2 z^{-3}-\frac{r}{2}dz^{-4}}{1-2z^{-1}+z^{-2}}\right]}{AK} \tag{A-3}$$

where

$$d = \frac{4B_LT}{r+1}$$

Designating the input and output of $P(z)$ as $Y(z)$ and $V(z)$, respectively, we have

$$P(z) = \frac{V(z)}{Y(z)} \tag{A-4}$$

Then from (A-3) and (A-4),

$$V(z)\,[1-2z^{-1}+z^{-2}] = Y(z)\left[1-2z^{-1}+\left[\frac{r}{2}(d+d^2)+1\right]z^{-2}+\frac{r}{2}d^2 z^{-3}-\frac{r}{2}dz^{-4}\right] \tag{A-5}$$

Taking the inverse Z transform,

$$v(k)-2v(k-1)+v(k-2) = y(k)-2y(k-1)+\left[\frac{r}{2}(d+d^2)+1\right]y(k-2)+\frac{r}{2}d^2 y(k-3)-\frac{r}{2}dy(k-4) \tag{A-6}$$

Solving for $v(k)$ yields

$$v(k) = y(k)-2y(k-1)+\left[\frac{r}{2}(d+d^2)+1\right]y(k-2)-\frac{r}{2}d^2 y(k-3)-\frac{r}{2}dy(k-4)+2v(k-1)-v(k-2) \tag{A-7}$$

The coefficients of Eq (12a) can be obtained by inspection from Eq (A-7)

X-Band Resonant Ring Operation at 450 kW

D Hoppe and R Perez
Radio Frequency and Microwave Subsystems Section

This article documents the operation of the X-band (7 2-GHz) ring resonator at a power level of 450 kW, which represents the highest power level achieved in the resonator to date The ring resonator and the overall experimental setup are summarized The motivation for the present ring resonator experiment is described, and specific results are presented More general observations made while operating the ring at these power levels are described, and conclusions are drawn

I. Introduction

Resonant ring tests have been successfully conducted by the DSN at 7 2 GHz and 450 kW The component under test is a reduced-size square waveguide that is intended to simulate a critical area of a proposed 1-MW feedhorn In addition to these results, general observations made when operating the ring resonator at these power levels are summarized The experimental setup, including computer control for real-time frequency correction, is described in the following section

II. Description

The 7 2-GHz resonant ring (Fig 1) consists of an electrically continuous loop of copper waveguide (WR 125), 2 64 meters in mean circumference Two coupler sections are included in the loop a 13-dB (nominal) coupler for signal injection and a dual 58-dB (nominal) coupler used to sample the forward and reverse components of the traveling wave in the ring Two dual tuners form part of the feed path and allow optimization of the resonant ring operation for different parameters

As described in [1] and in JPL Publication TR-1526,[1] the signal source used to drive the resonant ring is a 7 19-GHz klystron transmitter with an output power range of 0 5 to 23 kW During steady-state operation of the resonant ring, essentially all of the input power from the transmitter source is dissipated due to resistive losses in the waveguide walls This dictates water cooling of the waveguide, achieved by soldered copper water jackets on each of the broad waveguide walls Separate cooling circuits are provided for the input waveguide and tuner assembly, as well as for the test piece section of the resonant ring

The resonant ring acts as a high-Q resonator ($Q \approx 5600$), with its resonant frequency determined by the electrical length of the waveguide loop Under steady-state conditions, a traveling wave is sustained in the ring of a magnitude a times the input power This factor a is the gain of the resonant ring and

[1] R B Kolbly, *X-Band Traveling Wave Resonator (TWR)*, JPL Publication TR-1526 (internal report), Jet Propulsion Laboratory, Pasadena, California, October 1973

is dependent upon the insertion loss of the waveguide loop that forms the ring That is, during optimum operation of the resonator, the input power is dissipated entirely in the resistive loss of the resonator

Figure 2 shows the experimental configuration used for the resonant ring testing The dual 58-dB power sampling couplers were calibrated using an HP 8510A network analyzer A previous publication on the resonant ring[1] describes the dual-power sampling coupler as having -60 dB coupling While this is valid for a measurement frequency of 8 5 GHz, it is erroneous to assume this value at 7 19 GHz This is of importance, because the ring is capable of resonance at many frequencies, including 8 5 GHz and 7 19 GHz The new calibration indicates a 2-dB or 58 percent error in any power levels computed using -60 dB of coupling at 7 19 GHz

The use of the dual power meter also enabled a direct display of the ratio between the forward and reverse power levels in the ring Because of thermal expansion due to the power dissipated in the waveguide walls, the physical length of the ring increased with increasing power levels, thus lowering the frequency (see Fig 3 [a] and [d]) This created a need for an automated frequency correction system in order to keep the system at the optimum resonant frequency for each power level A program was written to vary the source frequency in 25-kHz steps until the point of maximum resonant power was found As shown in Fig 3, a 10°C rise in cooling water temperature caused a drop in resonant frequency of 1 2 MHz as well as an increase in the Q of the ring

In order to operate the resonant ring in a repeatable fashion, a flowmeter was installed in each cooling circuit This also allowed visual inspection of the presence of coolant flow in any circuit Water flowing in the inner and outer waveguide wall cooling jackets was conducted in different directions in order to equalize the waveguide temperature over the resonator as much as possible

A port is provided at one of the elbows (of dimensions below cutoff frequency) in order to provide access for a fiber optic arc detector This allowed correlation of a transmitter shutdown with the existence of an arc in the resonant ring waveguide The coolant outlet temperature was monitored with a precision quartz thermometer

III. Experiment Description

The motivation for the restoration of the X-band resonant ring was the need for high-power testing capability during the development of a proposed 1-MW radar transmitter In particular, the resonator is required to test various sections of the proposed feedhorn (Fig 4) and associated hardware, including orthomode junctions

The tests described in this report are intended to simulate one of the four square waveguides that will feed the multimode feedhorn shown in Fig 5 Under normal operation, each of these guides transports 250 kW, and the output power of these four waveguides is then combined in a larger chamber and launched into the flared horn in a series of waveguide modes Theoretical analysis of the horn indicates that even though only 25 percent of the total power is present in each of these four square feeding waveguides, the largest electric field will occur in these guides This can be seen from the following formula, which expresses the maximum electric field (rms) as a function of waveguide dimensions, power level, and frequency for a pure TE_{10} rectangular waveguide mode

$$E_{max} = \left(\frac{2\eta P}{ab\tilde{\beta}}\right)^{1/2} \quad (1)$$

where

P = power level, W

a, b = waveguide dimensions, cm

η = 377 ohms

$\tilde{\beta} = [1 - (\lambda/2a)^2]^{1/2}$

From the equation, it can be seen that even though the power level goes up by a factor of 4 in the large chamber, this is more than compensated for by the increase in area $(a \times b) = a^2$, and decrease in $\tilde{\beta}$ The high electric fields in the feeding waveguides are present primarily because these guides operate close to cutoff $(\lambda \rightarrow 2a), \tilde{\beta} \rightarrow 0$

For the 1-MW horn, the following parameters are present for the four feeding waveguides $a = b = 0\ 8$ in , $P = 250$ kW, and $F = 8\ 51$ GHz ($\tilde{\beta} = 0\ 497$) From this and [1] we get $E_{max} = 9\ 6$ kV/cm For comparison, for the present radar transmitter, $P = 360$ kW, WR 125 waveguide, $E_{max} = 8$ kV/cm Thus, it is necessary to demonstrate the capability to operate waveguides at these high power levels, near cutoff, in order to have confidence in the 1-MW feedhorn design

Since only 7 2-GHz pump power is presently available for the resonant ring, the 0 8-in square part was scaled to 0 95 in square This maintains the same value for $\tilde{\beta}$, that is, the new section will run as close to cutoff as the original As a consequence of [1], more power is now needed to simulate the same electric field In particular

$$P_{new} = 250\ \text{kW} \left(\frac{0.95}{0.8}\right)^2 = 352.5\ \text{kW}$$

A two-section transformer from WR 125 to 0.95-in square waveguides was designed, and a test part consisting of two of these transformers and a straight section of 0.95-in square guide was electroformed. Two cross-sectional views of the test part are shown in Fig. 5. Measurements of the part indicated a return loss of greater than 30 dB over the operating range of the ring resonator. The following section describes the results of high-power tests made on this component, as well as general observations made when operating the resonator above 400 kW.

IV. General Operational Considerations

Prior to high-power operation of the resonant ring, the waveguide loop was disassembled and cleansed using a liquid copper cleanser. Smaller pieces were cleansed by immersion, and the couplers were cleansed by running moist patches through the waveguide. The flanges were then lapped to ensure flatness and a low resistance connection. A thin layer of silicone vacuum grease was then applied to the flanges to inhibit oxidation. The resonant ring was then reassembled, with attention given to flange alignment. It should be noted that this process was repeated whenever erratic operation accompanied by low gain was encountered. For the testing described in this article, cleaning was performed three times in a period of 28 days of operation (not consecutive). Examination of the waveguide tuners is also in order, especially under conditions of high reflected power into the transmitter along with very low gain. These events indicate a tuner failure, which results in the tuning element (less than 1/2 cubic inch of copper) dissipating power in the several kilowatt range.

During manual high-power operation of the resonant ring, care must be taken not to allow the power reflected to the transmitter to exceed the transmitter protective circuitry shutdown threshold. This is 500 W for the 20-kW, 7.19-GHz transmitter. Operation with less than 50 W of reflected power is much preferred, however, since any increase in input power to the ring will create a corresponding increase in reflected power. Normal operation under 50 W of reflected power usually allows enough time for frequency corrections after a power increase.

Tuning the resonant ring in stages was found to be advantageous. For example, if a power level goal of 300 kW is desired, tuning at 100 and 200 kW before final tuning at 300 kW allows for correction of ring parameters that change with temperature. The goals of tuning the resonant ring are twofold: (1) to minimize the standing wave ratio in the resonator (usually kept above 20 dB), and (2) to minimize reflected power to the transmitter after the first goal has been achieved. This form of tuning is performed in a careful manner, since both of these parameters are interrelated. Experience has shown that tuners A and B (see Fig. 3 [a]–[d]) are most effective in minimizing ring SWR, while tuners C and D have a more pronounced effect in controlling the power reflected to the transmitter.

It may be found that after a period of inactivity, or after cleaning, numerous shutdowns occur before a desired power level may be reliably maintained. This is most probably due to the vaporizing of small contaminant particles inside the waveguide. A dozen shutdowns before attainment of a high power level are common. An upward trend in power levels is indicative of normal ring self-cleaning. Scattered shutdowns normally occur as symptoms of a problem in the resonant ring. The greatest contributor to reliable resonant ring operation at high power levels is the absolute temperature of the coolant water. A flow rate as high as is practical in the waveguide walls is of paramount importance. It was observed that the rise in ambient temperature from morning to afternoon caused severely degraded operation in many instances. A cooling water flow of 4 gal/min on the main ring waveguide and 3 gal/min on the tuners allowed reliable operation at 450 kW, with an outlet water temperature of 39°C.

V. Experimental Results

After several weeks of experiments, a power level in excess of 400 kW was obtained regularly in the resonator. In particular, 400 kW was sustained for over 30 minutes.

Next, the 0.95-in square test section was inserted into the resonator. The part was cooled by flowing water over it externally at a rate of approximately 3 gal/min. Power levels of 400 kW and 450 kW were sustained for periods of 30 minutes, and a peak level of 463 kW was attained briefly. This level represents the upper limit on the ring power, determined by the available power from the 20-kW transmitter driving the resonator. The power level of 450 kW represents an electric field value of 10.8 kV/cm in the 0.95-in square section. This electric field level may be scaled to equivalent power levels in the 0.8-in square waveguide and WR 125 waveguide at 8.51 GHz using [1].

Using [1], 450 kW in 0.95-in square waveguide at 7.2 GHz represents 652 kW in WR 125 at 8.5 GHz, and 319 kW in 0.8-in square waveguide at 8.5 GHz, in terms of equivalent electric field.

The results of these tests demonstrate that there is at least a 1-dB margin in the four feeding waveguides of the 1-MW

horn under full power conditions During the resonator tests, the ratio of forward traveling ring power to reverse power was maintained at about 20 dB, so in effect a return loss of about 20 dB is accounted for in these tests When calculating the margins above, no sharp edges in the horn are accounted for When the test part was fabricated, all edges were given a 0 03-in radius except those connecting the WR 125 section to the 1 25-in by 0 770-in section, which is the first step in the transformer (see Fig 8) Without considering the effect of this sharp edge, field values of 9 44 kV/cm are present at this point Published data [2] indicate that electric field values near this edge may be nearly a factor of two greater than those calculated by [1], so the peak electric field in the test part probably occurs near this edge, not in the 0 95-in square section In any event, the 9 44-kV/cm value above is close to the 9 6-kV/cm field that will be present in the 1-MW horn, and the 0 8-in square section should support 250 kW, even with a single sharp edge present

VI. Conclusions

Resonant ring tests have been carried out on a reduced-size square waveguide This square waveguide section represents a scaled version of one of the critical areas in a proposed 1-MW feedhorn Tests confirm the capability of this section of the horn to withstand power levels in excess of 320 kW This represents a 1-dB margin over the required level of 250 kW Future investigations will include tests on an unscaled test part at 8 51 GHz, and should be able to give a margin of 2 6 dB In addition, the insulating properties of various gases such as SF6 and Freon nitrous oxide will be examined for possible implementation in the DSN 1-MW planetary radar at Goldstone

References

[1] W C Chen and R Hartop, "Improved Cooling Design for High-Power Waveguide System," *TDA Progress Report 42-63*, vol March–April 1981, Jet Propulsion Laboratory, Pasadena, California, pp 104–107, June 15, 1981

[2] S B Cohn, "Rounded Corners in Microwave High-Power Filters," *IRE Trans*, vol PGMITT-9, pp 389–397, September 1961

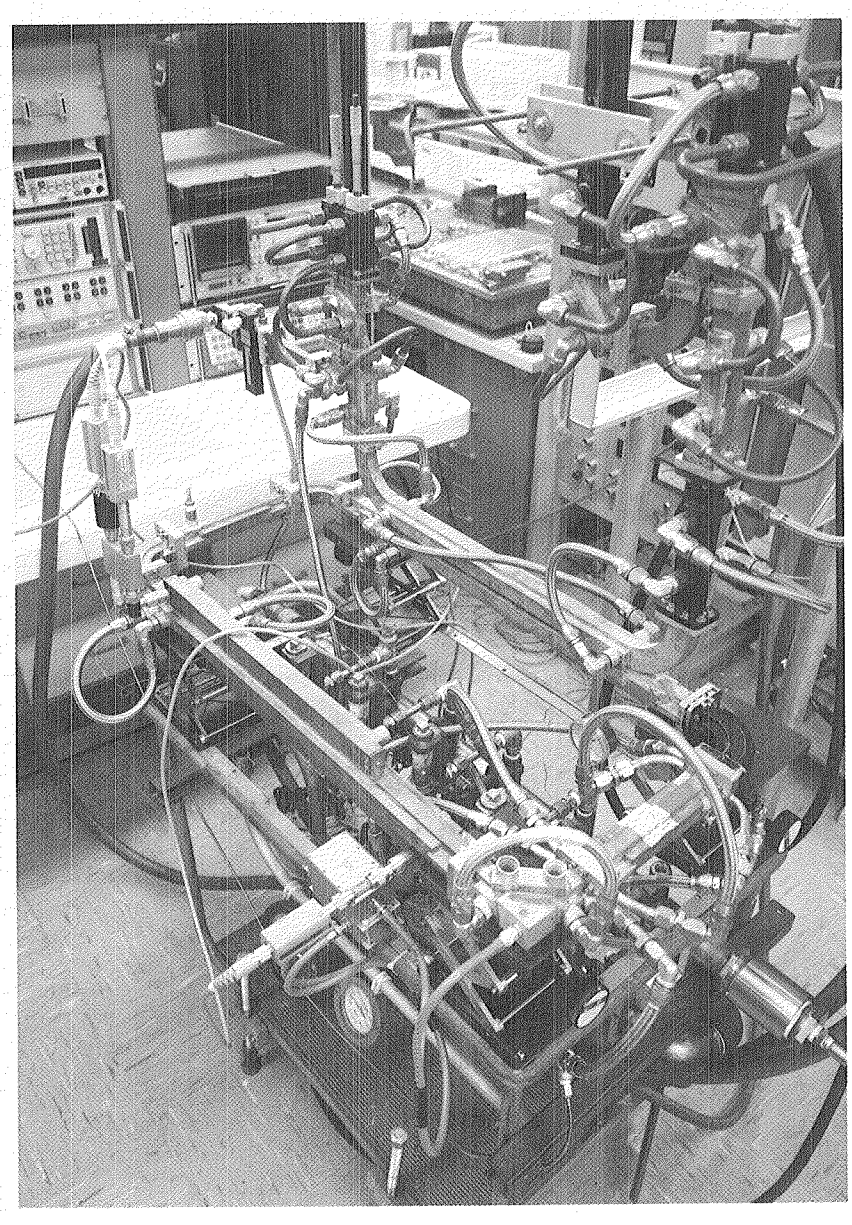

Fig. 1. The 7.2-GHz resonant ring

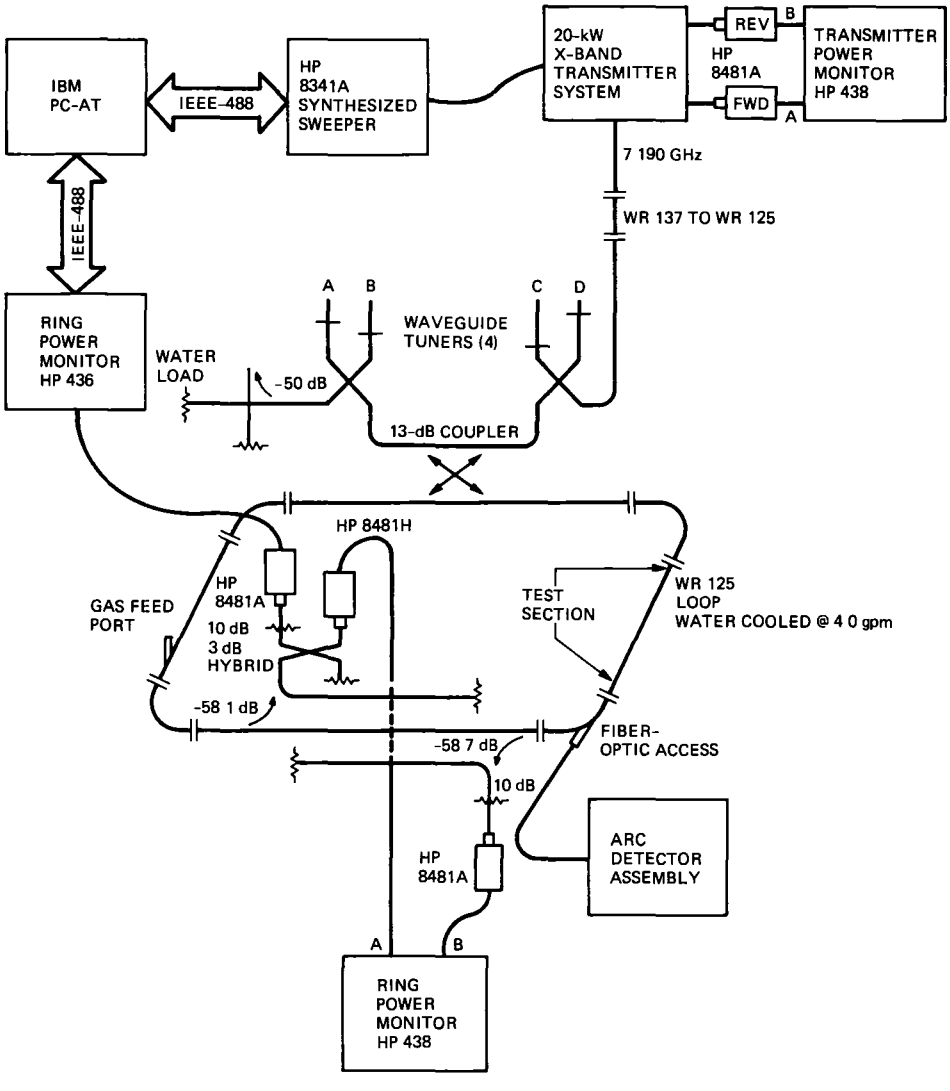

Fig 2 Experimental configuration used for resonant ring testing

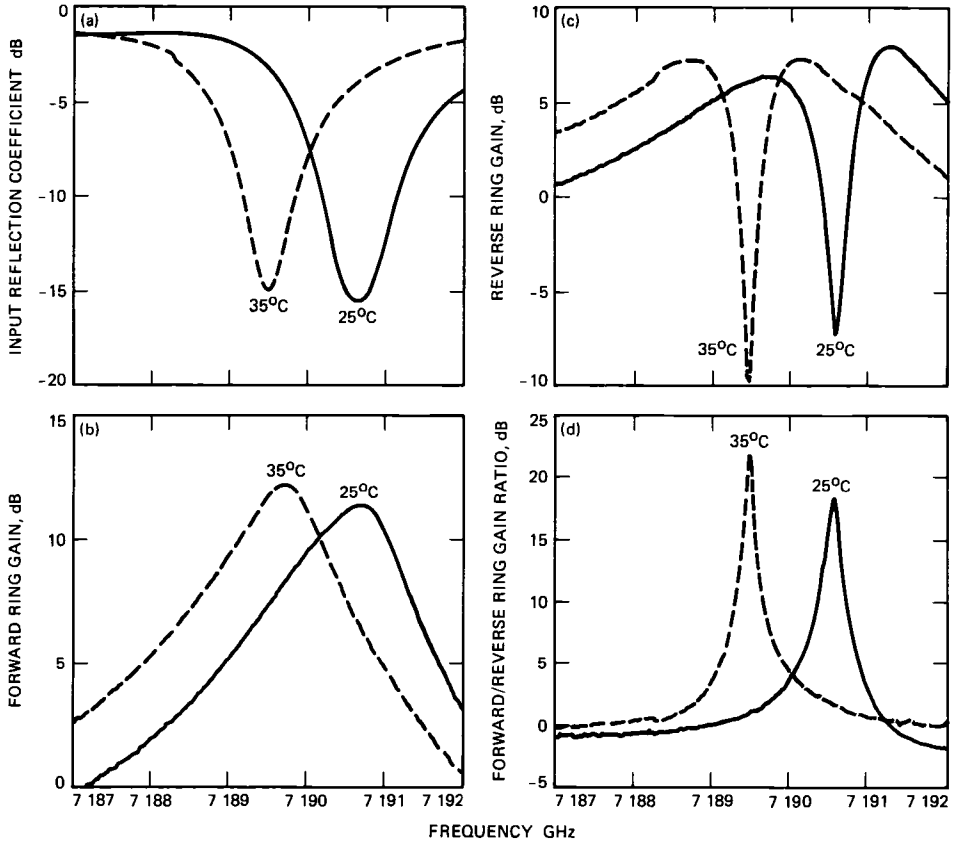

Fig 3 Resonant ring (a) input reflection, (b) forward gain, (c) reverse gain, and (d) forward/reverse gain ratio

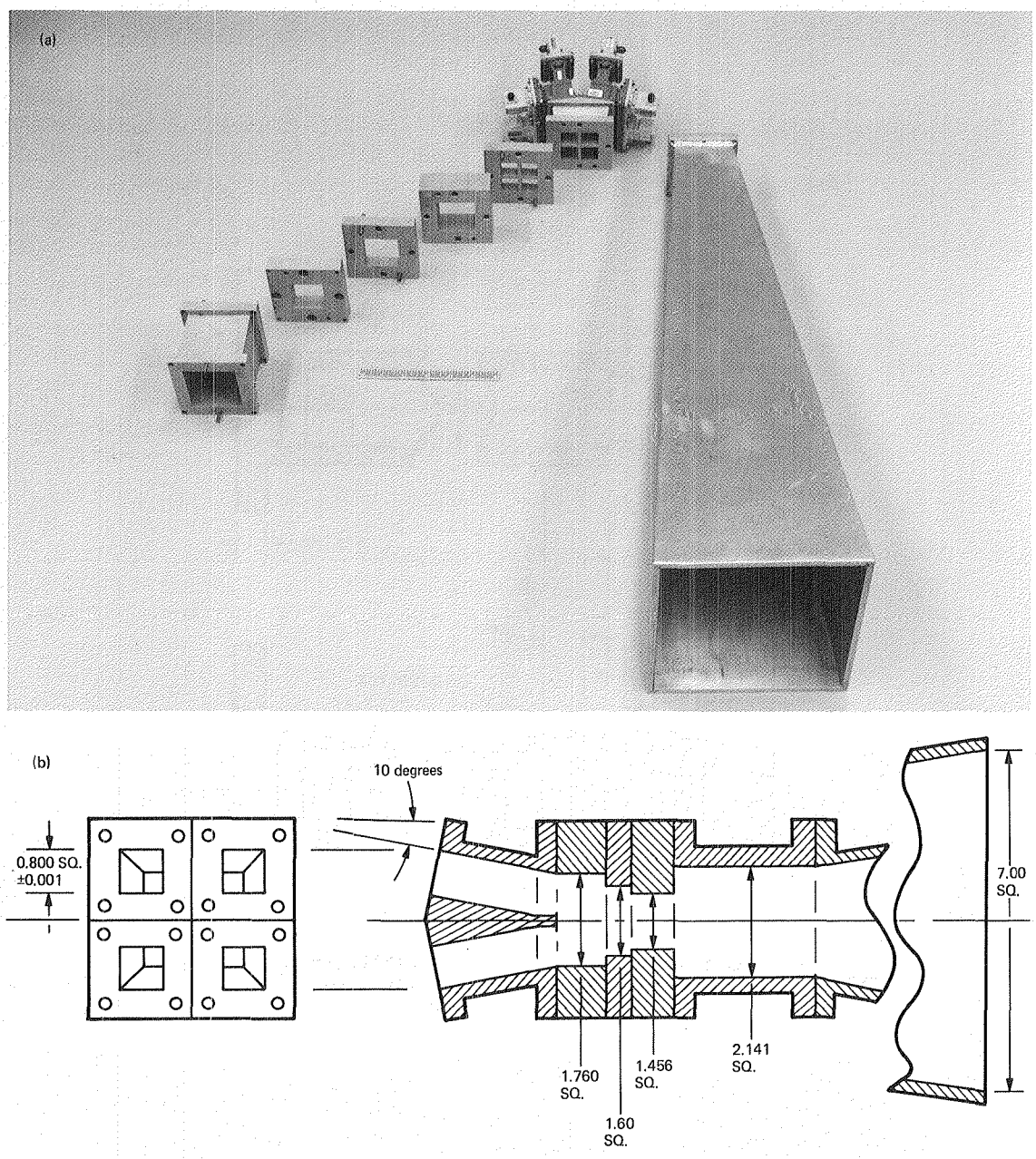

Fig. 4. The 1-MW feedhorn prototype: (a) full view; (b) detail of 1-MW feedhorn input section

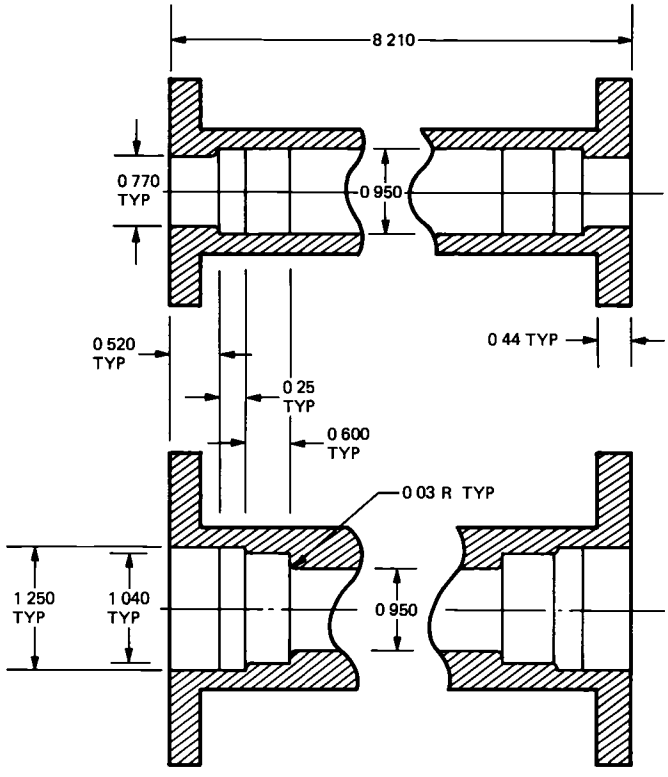

Fig 5 WR 125 to 0 95-in square to WR 125 transition

The Feasibility of the Disturbance Accommodating Controller for Precision Antenna Pointing

L L Gresham
NASA–ASEE Faculty Fellow, Summer 1987

F L Lansing and C N Guiar
Ground Antenna and Facilities Engineering Section

The objective of this study is to investigate the feasibility of a new pointing (position loop) controller for the NASA–JPL Deep Space Network antennas using the Disturbance Accommodating Control (DAC) theory A model that includes state dependent disturbances was developed, and an example demonstrating the noise estimator is presented as an initial phase in the controller design The goal is to improve pointing accuracy by the removal of the systematic errors caused by the antenna misalignment as well as sensor noise and random wind and thermal disturbances Preliminary simulation results show that the DAC technique is successful in both cancelling the imposed errors and maintaining an optimal control policy

I. Introduction

Large, precision antennas for millimeter and submillimeter wave astronomical listening require precision pointing capability in the face of a host of nonlinear and random disturbances Included in this category of noise sources are structural member deflections under wind, thermal and gravitational loading, bearing friction torques, and hysteresis as well as electrical, optical, and mechanical misalignments introduced by sensors, thermal deformations, and structure model imperfections Traditional approaches for compensating systematic disturbances rely on laboratory measurements and field data and employ open-loop (or feed-forward) compensation using static look-up tables to refine predicted target positions These techniques, although satisfactory in sub-X-band RF pointing, are marginal for the state-of-the-art telemetry requirements for the upcoming Voyager–Neptune flyby and beyond The augmentation of the deep space telemetry channel to provide Ka-band (32-GHz) capability to increase mission performance will require 1-mdeg pointing accuracy for feasible reception at distances greater than 20 AU The performance advantage between the current X-band and projected Ka-band is highly dependent on antenna pointing accuracy Successful deep space telecommunications will require the NASA–JPL 34-m and 70-m antenna pointing systems (see for example Fig 1) to exhibit pointing errors of 1 mdeg (rms) or better With current accuracy on the order of 5 to 10 mdeg, the antenna pointing loss at 32 GHz [1] as compared to loss at X-band (8 4 GHz) is magnified by the frequency squared The increased gain advantage of the Ka-band could easily be lost without comparable enhancement in the pointing accuracy, a performance requirement implicit to the higher gain antennas with narrower beamwidth

Antenna pointing–tracking errors are typically functions of static and dynamic factors Mechanical misalignment of sensors or inaccuracy in the predicts can be considered static

error sources, whereas dynamic factors would include wind, thermal and gravitational loading, etc The approach taken in this study is first to achieve a static error-free environment for precision pointing of the antenna The philosophy employed to achieve this goal is to treat the systematic misalignment errors, as well as the servocommands, as disturbances to the controlled system Hence, as an initial phase in the sequence of new controller design, this study addresses pointing-tracking in the presence of noise The research goal is intended to produce the end product controller, hence, further investigation is necessary to augment the controller to include dynamic errors caused by random thermal and wind disturbances

Antenna pointing improvements can be developed through a sequence of progressive controller modifications solely in the existing software routines Current algorithms can be enhanced to simultaneously provide servotracking and correction of the systematic errors as well as beam stabilization in the presence of random disturbance torques For a given antenna, servodrive, feed configuration, and surface distortion profile a computer software package could be developed to optimize the performance to achieve, adaptively, the maximum antenna gain for a prescribed direction vector with a "smart" controller

Typical antenna controllers consist of an analog rate loop and a position loop closed through a digital computer The control algorithms for the position control are either proportional-integral (PI) or state feedback control The PI control is accomplished by applying gains to the position error and the integral of position error The weighted sum of these signals is the commanded rate for the velocity loop Zero steady-state error to a ramp input is realized with the PI controller in this Type II system

The more sophisticated method utilizing state feedback allows specification of the eigenvalues of the closed position loop The initial disadvantage of the state feedback is the requirement that all the states of the system be available for the feedback control The technique of state estimation has circumvented this problem, providing the controller with an estimate value for each of the unmeasurable or uncertain state signals The feedback gains are selected to yield the designer's selected eigenvalues to achieve desired performance of the system This technique was incorporated in the upgrade of the 70-m antenna axis servos [2], [3] with the estimator gain vector selection based on system specifications, minimal estimator error, and insensitivity to encoder and digital-to-analog (D/A) quantizations

The unique controller enhancement proposed in this study suggests that, simultaneous with state estimation, another vector be estimated to represent the disturbance state which could then be used in determining a more complete control strategy The philosophy of the Disturbance Accommodating Controller (DAC) is based on the concept of state modeling of the disturbance vector as developed in [4] In the following section the basics of the DAC theory are discussed as applied to the antenna pointing problem A history of this DAC technique appears in [5]

II. Theoretical Background

The antenna pointing system can be modeled by a set of first-order linear differential equations

$$\left.\begin{aligned} \dot{x} &= \mathbf{A}x + \mathbf{B}u + \mathbf{F}w, \qquad x(0) = x_0 \\ y &= \mathbf{C}x \end{aligned}\right\} \tag{1}$$

where $x(t)$ is an $(n \times 1)$ state vector, $u(t)$ is an $(r \times 1)$ control effort vector, $y(t)$ is the $(m \times 1)$ output vector, and $w(t)$ is a $(p \times 1)$ collective disturbance vector representing the combined effects of all the uncontrolled forces/torques acting on the antenna For instance, $w(t)$ can be projected to include the effects of lateral winds, misalignments, etc It is assumed that $w(t)$ cannot be predicted or measured accurately The matrices **A**, **B**, **C**, and **F** represent the continuous-time transmission matrices for the respective signals

The state variable feedback is represented by the control law

$$u = -\mathbf{K}_x x \tag{2}$$

where $\mathbf{K}_x$ is a feedback gain matrix, not necessarily producing an optimum controller Two control cases will be analyzed further, the first assumes no disturbance **F** and the second case assumes that **F** exists

A. Assuming No Disturbances, F = 0

Substitution of Eq (2) into Eq (1) yields the closed-loop form with no disturbances,

$$\dot{x} = \mathbf{A}x - \mathbf{B}\mathbf{K}_x x = (\mathbf{A} - \mathbf{B}\mathbf{K}_x)x \tag{3}$$

The advantage of the state feedback is the ease by which the closed-loop eigenvalues of the system, obtained from Eq (3), are arbitrarily specified through the selection of the gain matrix $\mathbf{K}_x$ (also called the pole placement technique) However, the pole-placement method does not guarantee that the design is optimal On the other hand, if the optimal controller is designed, the quadratic performance technique, from

the theory of optimal control, provides the optimal steady-state solution to the minimum control effort and minimum transient deviation of the state from the origin problem, i e ,

$$u = -\mathbf{K}_g x \tag{4}$$

where the Kalman gain $\mathbf{K}_g = -\mathbf{R}^{-1}\mathbf{B}^T\mathbf{P}$ The term $\mathbf{P}$ is a symmetric positive semidefinite solution to the steady-state Riccati equation in the matrix form, that is,

$$\mathbf{A}^T\mathbf{P} + \mathbf{P}\mathbf{A} + \mathbf{Q} - \mathbf{P}\mathbf{B}\mathbf{R}^{-1}\mathbf{B}^T\mathbf{P} = 0 \tag{5}$$

The matrices $\mathbf{R}(>0)$ and $\mathbf{Q}(>0)$ are symmetric weighting matrices in the associated quadratic performance index for the continuous linear regulator, that is

$$J(t_0) = x(T)^T\mathbf{P}(T)x(T) + \int_{t_0}^{T} [x^T\mathbf{Q}(t)x + u^T\mathbf{R}(t)u]\, dt \tag{6}$$

Note that the control is a time-varying state feedback, even if $\mathbf{A}$, $\mathbf{B}$, $\mathbf{Q}$, and $\mathbf{R}$ are time-invariant, $K_g(t)$ varies with time

Implementation of state feedback requires knowledge of the entire state vector In practice, however, not all state variables are available for direct measurement Hence, a closed-loop *estimator* is utilized to predict the values of the unmeasurable state variables based on the measurements of the output and control variables The state estimator vector x' is described by

$$\dot{x}' = \mathbf{A}x' + \mathbf{B}u + \mathbf{K}_{0_x}(y - \mathbf{C}x'), \qquad x'(0) = x'_0$$

or

$$\dot{x}' = (\mathbf{A} - \mathbf{K}_{0_x}\mathbf{C})x' + \mathbf{B}u + \mathbf{K}_{0_x}y \tag{7}$$

where $\mathbf{K}_{0_x}$ is the estimator error gain matrix ($n \times m$), and the eigenvalues of $(\mathbf{A} - \mathbf{K}_{0_x}\mathbf{C})$ are commonly called the observer poles Recall that the system must exhibit complete observability in order to determine the state vector using the output and control variables

The inaccuracy, e, in the state dynamics incurred in using the full-order ($n \times 1$) estimate x' rather than the actual state x is given by subtracting Eq (7) from Eq (1) (with $F \equiv 0$), i e ,

$$\dot{e} \equiv \dot{x} - \dot{x}' = (\mathbf{A} - \mathbf{K}_{0_x}\mathbf{C})e \tag{8}$$

where $e = x - x'$ From Eq (8) it is apparent that the dynamic behavior of the error signal is determined by the observer poles If the matrix $(\mathbf{A} - \mathbf{K}_{0_x}\mathbf{C})$ is a stable matrix, the error vector converges to zero for any initial error $e(0)$

Since $\mathbf{A}$, $\mathbf{C}$ are fixed by the system, matrix $\mathbf{K}_{0_x}$ determines the estimator performance Again the pole-placement technique can position the estimator eigenvalues from Eq (8) for proper performance, that is, x' will converge to x regardless of the initial states $x(0)$ and $x'(0)$ Hence, the overall closed-loop noiseless system with full state estimator feedback can be expressed in the state variable notation as

$$\left[\begin{array}{c} x \\ \hline x' \end{array}\right] = \left[\begin{array}{c|c} \mathbf{A} & -\mathbf{B}\mathbf{K}_x \\ \hline \mathbf{K}_{0_x}\mathbf{C} & \mathbf{A} - \mathbf{B}\mathbf{K}_x - \mathbf{K}_{0_x}\mathbf{C} \end{array}\right] \left[\begin{array}{c} x \\ \hline x' \end{array}\right]$$

and

$$y = \left[\mathbf{C} \mid 0\right] \left[\begin{array}{c} x \\ \hline x' \end{array}\right] \tag{9}$$

Note that the dynamics of the closed-loop system depend on the eigenvalues of both the controller and the estimator However, the separation principle allows the independent design of the controller and the estimator gain matrices assuming the observer poles are chosen correctly

The optimal regulator described so far accommodates only initial conditions or impulse type disturbances and hence is incapable of tracking or handling typical noise inputs In the case of finite input disturbances, the control law of Eqs (2) through (9) cannot attain and maintain track, i e , $y(t) \neq y_c(t)$ where y_c is the commanded output

B. Case of $\mathbf{F} \neq 0$

Consider now the plant equations in the form of Eq (1) with $\mathbf{F} \neq 0$,

$$\dot{x} = \mathbf{A}x + \mathbf{B}u + \mathbf{F}w \tag{10}$$

where $\mathbf{F}$ is an ($n \times p$) matrix and $w(t)$ is a p-dimensional disturbance vector Let us formulate the optimal regulator problem in such a way that at the terminal time T, the resulting control law always brings the state $x(t)$ and the velocity $\dot{x}(t)$ back to the commanded state and velocity, $x_c(t)$ and $\dot{x}_c(t)$, respectively, in the presence of any finite constant disturbance $w(t) \equiv k$ With neither the noise nor the servocommand known a priori, treating $w(t)$ as either a deterministic input or a nondeterministic input with a known probability is impractical

since reliable information about the disturbance is not available The primary objective of the control is to manipulate $u(t)$ in Eq (10) so that the output $y(t)$ approaches and maintains the commanded value $y_c(t)$ promptly Hence, the problem is reduced to finding a control which minimizes the functional $J(u)$,

$$J(u) = \lim_{t \to T} \int_0^T [\langle x\, Q\, x \rangle + f(u, \dot{u}, \quad)]\, dt \qquad (11)$$

subject to the constraints imposed by Eq (10) where the vector disturbance $w(0) = 0$, and $w(t)$ is assumed to satisfy the linear differential equation

$$\alpha_\rho \frac{d^\rho w}{dt^\rho} + \alpha_{\rho-1} \frac{d^{\rho-1} w}{dt^{\rho-1}} + \quad + \alpha_1 \frac{dw}{dt} + \alpha_0 w = 0 \qquad (12)$$

where the α_i are known, real scalar constants

The class of admissible disturbances $w(t)$ defined in Eq (12) can be characterized as the set of scalar functions

$$w(t) = \mathbf{H} z(t) \qquad (13)$$

with $\mathbf{H}$ a real p X ρ matrix and where

$$\dot{z}(t) = \mathbf{D}z + \sigma(t) \qquad (14)$$

where z is a real ρ vector and $\mathbf{D}$ is real matrix (p X ρ) The $\sigma(t)$ in Eq (14) represents the uncertainty in the noise model This representation of $w(t)$, illustrated in Fig 2, shows that the optimal controller is designed by first building a duplicate model for the disturbance process typified by Eqs (13) and (14) This noise estimator is driven by the vector $\mathbf{C}x(t)$, as is the plant state estimator The noise estimate and the system state estimate are weighted and summed to yield the control law $u(t)$ As $t \to T$, $x(t)$ approaches the steady-state $x(t) = x_c(t)$ prior to any change in the state command

Mathematically the noise is not precisely known Hence, the $\sigma(t)$ represent completely unknown sequences of random-intensity, random-occurring, isolated delta functions Antenna experimental data have shown that the alignment uncertainty exhibits the less than noisy properties of a stochastic process, and thus, in this particular case, Eq (13) appears to be a reasonable model of the systematic disturbances

The control law is effectively divided into two parts, that is,

$$u = u_s + u_d \qquad (15)$$

where u_s is assigned the task of servoregulation, and the component u_d is responsible for counteracting both disturbances, $w(t)$ and the reference signal $y_c(t)$ in servotracking In the case of regulation, $y_c(t) \equiv 0$, the control u_d must be capable of satisfying the relation

$$\mathbf{B}(t)u_d(t) \equiv -\mathbf{F}(t)w(t) = -\mathbf{FH}z(t) \qquad (16)$$

for all admissible $w(t)$ in order to cancel out the disturbance $\mathbf{F}$ Johnson in [5] has shown that if the rank of $[\mathbf{B} \mid \mathbf{FH}]$ = rank of $[\mathbf{B}]$, then

$$-\mathbf{F}(t)\mathbf{H}(t) \equiv -\mathbf{B}(t)\mathbf{K}_z(t) \qquad (17)$$

for some gain matrix $\mathbf{K}_z(t)$ Failure of this condition means that some residual effect of $w(t)$ will always occur Assuming Eq (17) is satisfied, the counteraction torque, u_d, is

$$u_d(t) = -\mathbf{K}_z(t)z(t) \qquad (18)$$

and the regulation control, u_s, is chosen by the conventional means as

$$u_s(t) = -\mathbf{K}_x(t)x(t) \qquad (19)$$

The open-loop system augmented to include the noise state is described by

$$\left.\begin{aligned} \begin{bmatrix} \dot{x} \\ \hline z \end{bmatrix} &= \left[\begin{array}{c|c} \mathbf{A} & \mathbf{FH} \\ \hline 0 & \mathbf{D} \end{array}\right] \begin{bmatrix} x \\ \hline z \end{bmatrix} + \begin{bmatrix} \mathbf{B} \\ \hline 0 \end{bmatrix} u + \begin{bmatrix} 0 \\ \hline \sigma \end{bmatrix} \\ y &= [\mathbf{C} \mid 0] \begin{bmatrix} x \\ \hline z \end{bmatrix} \end{aligned}\right\} \qquad (20)$$

The exact closed-loop state and disturbance state vectors, assuming all states are available for measurement, are described by the differential equations

$$\begin{bmatrix} \dot{x} \\ \hline \dot{z} \end{bmatrix} = \left[\begin{array}{c|c} \mathbf{A} - \mathbf{BK}_x & \mathbf{FH} - \mathbf{BK}_z \\ \hline 0 & \mathbf{D} \end{array}\right] \begin{bmatrix} x \\ \hline z \end{bmatrix} + \begin{bmatrix} 0 \\ \hline \sigma(t) \end{bmatrix} \qquad (21)$$

Redefining the representation of Eq (20) so that the new state vector includes both system and disturbance states gives

$$\dot{\underline{x}} = \begin{bmatrix} \dot{x} \\ \hline \dot{z} \end{bmatrix} = \underline{\mathbf{A}}\,\underline{x} + \underline{\mathbf{B}}\,\underline{u} + \underline{\delta}$$

$$\underline{y} = \underline{\mathbf{C}}\,\underline{x} \tag{22}$$

Examination of Eq (21) reaffirms the criterion set forth in Eq (17) to eliminate the noise term in the system state equations However, an obvious problem arises how is it possible to access the actual disturbance state $z(t)$? Of course, $z(t)$ is not completely measurable, but it is possible to resort to estimator theory once again to observe and predict the noise state in an approach similar to that used in the plant state estimation Hence, an appropriate control is obtained by replacing the actual noise state in Eq (18) with the estimate of the noise state $z'(t)$, i e , where estimates of $z(t)$ and $x(t)$ can be obtained from $y(t)$ by on-line, real-time state reconstruction In general $\mathbf{K}_z(t)$ is shown to be not unique [4]

The actual closed-loop plant state $x(t)$, with the assumption that all states are available for measurement, and the disturbance state error variable $e_z(t)$ are described by the differential equations

$$\begin{bmatrix} \dot{x} \\ \hline \dot{e}_z \end{bmatrix} = \left[\begin{array}{c|c} \mathbf{A} - \mathbf{B}\mathbf{K}_x & \mathbf{FH} - \mathbf{B}\mathbf{K}_{0_z} \\ \hline 0 & \mathbf{D} + \mathbf{FH} \end{array}\right] \begin{bmatrix} x \\ \hline e_z \end{bmatrix} + \begin{bmatrix} 0 \\ \hline \sigma(t) \end{bmatrix} \tag{23}$$

where $e = z - z'$, with $\mathbf{K}_{0_z}$ the appropriate observer gain for the disturbance state estimator

Examination of Eq (23) reveals that if e_z is zero, the behavior of $x(t)$ is totally independent of the disturbance $w(t)$ Of course, the ideal case is rarely realized, however, $\mathbf{K}_{0_z}(t)$ is chosen so that $e_z(t) \to 0$ rapidly for all initial values of x_0, z_0, e_0 so that the closed-loop plant state $x(t)$ is essentially insensitive to external disturbances that can be generated by Eq (14)

Using the composite model of Eq (22), the corresponding augmented state estimator vector $x'(t)$ is described through observer theory as

$$\dot{\underline{x}}' = \underline{\mathbf{A}}\,\underline{x}' + \underline{\mathbf{B}}\,\underline{u} + \underline{\mathbf{K}}_0(\underline{y} - \underline{\mathbf{C}}\,\underline{x}')$$

or

$$\dot{\underline{x}}' = (\underline{\mathbf{A}} - \underline{\mathbf{K}}_0\underline{\mathbf{C}})\,\underline{x}' + \underline{\mathbf{B}}\,\underline{u} + \underline{\mathbf{K}}_0\underline{y} \tag{24}$$

where $\underline{\mathbf{K}}_0$, the composite estimator gain matrix, is chosen to force $\underline{x}'(t) \to \underline{x}(t)$ Using the same principle mentioned earlier in Eq (8), the eigenvalues of $(\underline{\mathbf{A}} - \underline{\mathbf{K}}_0\underline{\mathbf{C}})$ are chosen for the augmented system The practical control law for servoregulation in the face of noise becomes

$$\underline{u}(t) = -\underline{\mathbf{K}}_{\underline{x}}(t)\underline{x}'(t) = -\mathbf{K}_x(t)x'(t) - \mathbf{K}_z(t)z'(t) \tag{25}$$

where z', x' are the estimates of $z(t)$ and $x(t)$, respectively, obtained from $\underline{y}(t)$ by on-line, real-time state reconstruction, and $-\mathbf{K}_x(t)x'(t)$ is the control required to minimize a performance index if the disturbances were not present in Eq (10) In general $\mathbf{K}_z(t)$ is not unique, as shown in [4]

The system is reorganized now to include servotracking rather than just servoregulation Similarly the servocommand can be treated as a "disturbance" to the plant Recall that the primary control objective in the antenna pointing system is that of servotracking $y_c(t)$, where in general the command is related to the system variables $(x_1, \quad , x_n)$ by the equation

$$y_c(t) = \bar{C}(t)x(t) \tag{26}$$

In this case, the objective is to control the plant output $y(t)$ so that $\bar{C}$ is equal to $\mathbf{C}$ in Eq (1) The behavior of y_c is assumed expressible by the servocommand model

$$\left.\begin{aligned} y_c(t) &= \mathbf{G}(t)c(t) \\ \dot{c} &= \mathbf{E}(t)c(t) + \mu(t) \end{aligned}\right\} \tag{27}$$

where $\mathbf{G}(t)$, $\mathbf{E}(t)$ are determined beforehand by appropriate modeling procedures, and c represents the servocommand state vector The vector $\mu(t)$ represents the uncertain impulse sequences, similarly introduced in the disturbance model in the form of $\sigma(t)$ Note that in the case of set point regulation, y_c is essentially a constant, and hence $\mathbf{E}(t) \equiv 0$ and $\mathbf{G}(t)$ is the identity matrix with the assumption that the y_i are independent outputs In servotracking, the $y_c(t)$ are allowed to vary continuously with time and $\mathbf{E}(t)$ is chosen accordingly Exact servotracking cannot be realized unless the servocommand error $e = \mathbf{G}c - \mathbf{C}x$ is zero Hence, u_s must be chosen so that $(y_c \to y)$ rapidly approaches the null space of $\mathbf{C}$ for all initial conditions

Hence, the three individual plant, disturbance, and servocommand models can be combined into a single composite open-loop model

$$\dot{\underline{x}} = \begin{bmatrix} \dot{x} \\ \hline \dot{z} \\ \hline \dot{c} \end{bmatrix} = \underline{\mathbf{A}}\,x + \underline{\mathbf{B}}\,u + \underline{\delta} \tag{28}$$

where

$$\mathbf{A} = \left[\begin{array}{c|c|c} \mathbf{A} & \mathbf{FH} & 0 \\ \hline 0 & \mathbf{D} & 0 \\ \hline 0 & 0 & \mathbf{E} \end{array}\right], \quad \mathbf{B} = \left[\begin{array}{c} \mathbf{B} \\ \hline 0 \\ \hline 0 \end{array}\right], \quad \underline{\delta} = \left[\begin{array}{c} 0 \\ \hline \sigma(t) \\ \hline \mu(t) \end{array}\right]$$

$\underline{y} = \underline{\mathbf{C}}\,\underline{x}$ where $\underline{\mathbf{C}} = [\,\mathbf{C} \mid 0 \mid 0\,]$

Figure 2 illustrates the continuous-time system with the DAC installed The solution approach is as follows An appropriate generic control law for servotracking in the face of noise follows as

$$u = -\mathbf{N}(t)z'(t) - \mathbf{K}_x(t)x'(t) - \mathbf{K}_c(t)c'(t) \tag{29}$$

Utilizing the servocommand state estimator, the closed-loop plant can be described as

$$\dot{x} = (\mathbf{A} - \mathbf{B}\mathbf{K}_x)x + (-\mathbf{B}\mathbf{K}_z + \mathbf{FH})z' - \mathbf{B}\mathbf{K}_z c'$$

$$+ \mathbf{B}\,[\,-\mathbf{K}_z(z - z') - \mathbf{K}_x(x - x') - \mathbf{K}_c(c - c')\,] \tag{30}$$

With the appropriate choices of the gains, $\mathbf{K}_x$, $\mathbf{K}_z$, $\mathbf{K}_c$, the estimate errors will approach zero quickly and the noise terms in z should have no effect on $y(t)$

III. Mathematical Models for the Discrete-Time DAC

The continuous-time model of the disturbed dynamical system described in Eq (1) can be transformed into a discrete-time prototype for investigation of an analog plant controlled by a digital computer For simplicity, assume that the signal sampling time is coincident with the control effort application time In feedback controller designs, control decisions are determined in light of real-time data provided to the controller through sensors The term "sampled-data" denotes data provided to the controller which are updated only at specific isolated points in time Between these updates, the data provided to the controller typically are held constant Likewise, the control decisions are updated only at specific isolated times In between the decision updates, the control action $u(t)$ either remains constant or follows a prescribed interpolation rule The computer or digital controller is capable of processing only sampled-data and executing discrete-time control policies usually written as difference equations

An appropriate discrete-time representation of the system, disturbances, and servocommands, analogous to the continuous model, is required for the investigation Reference [6] derives the discrete composite state variable representation with the assumption that the noise is not state dependent, i e ,

$$\left[\begin{array}{c} x[(n+1)T] \\ \hline z[(n+1)T] \\ \hline c[(n+1)T] \end{array}\right] = \left[\begin{array}{c|c|c} A(nT) & FH(nT) & 0 \\ \hline 0 & D(nT) & 0 \\ \hline 0 & 0 & E(nT) \end{array}\right] \left[\begin{array}{c} x(nT) \\ \hline z(nT) \\ \hline c(nT) \end{array}\right]$$

$$+ \left[\begin{array}{c} B(nT) \\ \hline 0 \\ \hline 0 \end{array}\right] \underline{u}(nT) + \left[\begin{array}{c} \gamma(nT) \\ \hline \sigma(nT) \\ \hline \mu(nT) \end{array}\right]$$

$$y(nT) = [\,C(nT) \mid 0 \mid 0\,] \left[\begin{array}{c} x(nT) \\ \hline z(nT) \\ \hline c(nT) \end{array}\right] \tag{31}$$

where the discrete-time plant matrices are

$$A(nT) = \Phi_A\,[t_0 + (n+1)T, t_0 + nT\,]$$

$\triangleq$ plant state transition matrix in discrete time

$$B(nT) = \int_{t_0+nT}^{t_0+(n+1)T} \Phi_A\,[t_0 + (n+1)T, \tau]\,\mathbf{B}(\tau)\,d\tau$$

$$\gamma[(n+1)T] = \int_{t_0+nT}^{t_0+(n+1)T} \left[\Phi_A\,[t_0 + (n+1)T, \tau]\,\mathbf{F}(\tau)\mathbf{H}(\tau) \times \int_{t_0+nT}^{\tau} \Phi_D(\tau, \xi)\sigma(\xi)d\xi\right] d\tau$$

$$FH(nT) = \int_{t_0+nT}^{t_0+(n+1)T} \Phi_A\,[t_0 + (n+1)T, \tau]$$

$$\times\, \mathbf{F}(\tau)\mathbf{H}(\tau)\,\Phi_D(\tau, t_0 + nT)\,d\tau$$

and the discrete-time noise terms become

$$D(nT) = \Phi_D\left[[t_0 + (n+1)T, t_0 + nT]\right]$$

$\triangleq$ noise state transition matrix

$$\sigma(nT) = \int_{t_0+nT}^{t_0+(n+1)T} \Phi_D[t_0 + (n+1)T, \xi]\ \sigma(\xi)\, d\xi \tag{32}$$

In the time-invariant case, the matrices **A**, **B**, **C**, **F** are constant element matrices, and Eq (32) is simplified to

$$\left.\begin{aligned} A &= e^{\mathbf{A}T} \\ D &= e^{\mathbf{D}T} \\ B &= \int_0^T e^{\mathbf{A}(T-\tau)}\, \mathbf{B}\, d\tau \\ \gamma &= \int_0^T e^{\mathbf{A}(T-\tau)}\, \mathbf{FH} \\ &\quad \times \left[\int_0^\tau e^{\mathbf{D}(\tau-\xi)}\, \sigma(\xi + t_0 + nT)\, d\xi\right] d\tau \\ FH &= \int_0^T e^{\mathbf{A}(T-\tau)}\, FH\, e^{\mathbf{D}\tau}\, d\tau \\ \sigma &= \int_0^T e^{\mathbf{D}(T-\xi)}\, \sigma(\xi + t_0 + nT)\, d\xi \end{aligned}\right\} \tag{33}$$

Similarly, the discrete-time servotracking state model of Eq (27) can be represented in the form

$$\left.\begin{aligned} y_c(nT) &= G(nT)\, c(nT) \\ c[(n+1)T] &= E(nT)\, c(nT) + \mu(nT) \end{aligned}\right\} \tag{34}$$

where

$$\left.\begin{aligned} E(nT) &= \Phi_E[(n+1)T, nT] \\ &\triangleq \text{discrete transition matrix for the servocommand} \\ \mu(nT) &= \int_{t_0+nT}^{t_0(n+1)T} \\ &\quad \times \Phi_E[t_0 + (n+1)T, \xi]\ \mu(\xi) d\xi \end{aligned}\right\} \tag{35}$$

In the time-invariant case, Eq (35) is reduced to

$$\left.\begin{aligned} E(nT) &= e^{\mathbf{E}T} \\ \mu(nT) &= \int_0^T e^{\mathbf{E}(T-\xi)}\, \mu(\xi + t_0 + nT)\, d\xi \end{aligned}\right\} \tag{36}$$

The model may be generalized further to include various exceptional case studies [5] For example, the antenna systematic errors appear to be dependent on the particular azimuth/elevation position of the target, hence, the noise $w(t)$ can be made a function of the system orientation or of the state of the plant In this case the disturbance model can be augmented to include the state dependency by adding extra terms as follows

$$\left.\begin{aligned} w(nT) &= H(nT)z(nT) + L(nT)x(nT) \\ z[(n+1)T] &= D(nT)z(nT) + M(nT)x(nT) \\ &\quad + \sigma(nT) \end{aligned}\right\} \tag{37}$$

In this case it is necessary to derive the appropriate relationships from the continuous to discrete-time case in order to ascertain the mathematical meaning of the additional terms $L(nT)$ and $M(nT)$ in Eq. (37) These relations are given in Eq (38)

$$\left.\begin{aligned}\left[\begin{array}{c}x[(n+1)T]\\ \hline z[(n+1)T]\end{array}\right] &= \left[\begin{array}{c|c}A(nT) & FH(nT)\\ \hline M(nT) & D(nT)\end{array}\right]\left[\begin{array}{c}x(nT)\\ \hline z(nT)\end{array}\right]\\ &+\left[\begin{array}{c}B(nT)\\ \hline 0\end{array}\right]u(nT)\\ &+\left[\begin{array}{c}\gamma_1(nT)+\gamma_2(nT)\\ \hline \sigma(nT)\end{array}\right]\\ y(nT) &= [\,C(nT)\mid 0\,]\left[\begin{array}{c}x(nT)\\ \hline z(nT)\end{array}\right]\end{aligned}\right\} \quad (38)$$

where in the time-variant case,

$$\gamma_2[(n+1)T] = \int_0^T e^{\mathbf{A}(T-\tau)}\,\mathbf{FH} \times \left[\int_0^\tau e^{\mathbf{D}(\tau-\xi)}\,x(\xi+t_0+nT)\,d\xi\right] d\tau$$

and

$$M(nT) = \int_0^T e^{\mathbf{D}(T-t)}\,\mathbf{L}x(t+t_0+nT)\,d\tau$$

Construction of the on-line, real-time estimation of the three states—plant state $x(t)$, disturbance state $z(t)$, and the command state $c(t)$—requires the discrete-time state estimator given by

$$\left.\begin{aligned}\begin{bmatrix}x'[(n+1)T]\\ z'[(n+1)T]\\ c'[(n+1)T]\end{bmatrix} &= \begin{bmatrix}A(nT) & FH(nT) & 0\\ 0 & 0 & 0\\ 0 & 0 & E(nT)\end{bmatrix}\begin{bmatrix}x'(nT)\\ z'(nT)\\ c'(nT)\end{bmatrix}\\ &+\begin{bmatrix}B(nT)\\ 0\\ 0\end{bmatrix}\underline{u}(nT)+\begin{bmatrix}K_{0x}\\ K_{0z}\\ K_{0c}\end{bmatrix}\\ &\times\left\{\begin{bmatrix}C(nT) & 0 & 0\\ C(nT) & 0 & 0\\ 0 & 0 & 0\end{bmatrix}\begin{bmatrix}x(nT)\\ z(nT)\\ c(nT)\end{bmatrix}-\begin{bmatrix}y(nT)\\ y(nT)\\ y_c(nT)\end{bmatrix}\right\}\end{aligned}\right\} \quad (39)$$

where $\underline{u}(nT)$, $y(nT)$ and $y_c(nT)$ denote the inputs to the observer The matrices K_{0x}, K_{0z}, K_{0c} are arbitrary gain matrices that the DAC designer selects in accordance with the desired estimator response

In order to establish the dynamics of the estimators, consider the state errors e_x, e_z and e_c defined as

$$\left.\begin{aligned}e_x &= x(nT)-x'(nT)\\ e_z &= z(nT)-z'(nT)\\ e_c &= c(nT)-c'(nT)\end{aligned}\right\} \quad (40)$$

These error dynamics are described by the discrete equations derived from Eq (39), considering only first-order variations, as

$$\begin{bmatrix}e_x[(n+1)T]\\ e_z[(n+1)T]\\ e_c[(n+1)T]\end{bmatrix} = \begin{bmatrix}A+K_{0x}C & FH & 0\\ K_{0z}C & D & 0\\ 0 & D & E+K_{0c}G\end{bmatrix} \times \begin{bmatrix}e_x(nT)\\ e_z(nT)\\ e_c(nT)\end{bmatrix} + \begin{bmatrix}\gamma(nT)\\ \sigma(nT)\\ \mu(nT)\end{bmatrix} \quad (41)$$

In order to produce reliable estimates, the observer gain matrices (K_{0x}, K_{0z}, K_{0c}) are chosen so that the errors in Eq (40) decay toward zero rapidly between control updates Hence the homogenous solution of Eq (41) is made asymptotically stable to the errors equal to zero In general, Eq (41) is a time-varying set of difference equations The gains K_{0x}, K_{0z}, K_{0c} can be solved using the discrete Riccati equation from optimal control theory For the case of constant element matrices A, C, FH, D, the design of the estimator gain matrices can be accomplished by the conventional eigenvalue placement method Defining the error dynamics as a system with a characteristic matrix A_e

$$A_e = \begin{bmatrix} (A + K_{0x}) & FH & 0 \\ K_{0z}C & D & 0 \\ 0 & 0 & (E + K_{0c}G) \end{bmatrix} \quad (42)$$

the eigenvalues are positioned suitably (say, at zero) within the unit circle A block diagram of the composite observer is shown in Fig 4

IV. Determination of the Discrete-Time Control Function *u*

The determination of the control function u in the discrete-time case involves several steps

(1) The state estimators are weighted and summed to determine the control law, i e ,

$$u(nT) = f[x'(nT), c'(nT), z'(nT), nT] \quad (43)$$

(2) The control function is divided into two subtasks as mentioned previously,

$$u(nT) = u_s(nT) + u_d(nT) \quad (44)$$

where the component u_s is responsible for the servoregulation and the u_d effort is assigned the task of disturbance removal including servotracking Substitution of Eq (44) into Eq (27) yields the plant state relation

$$\begin{aligned} x((n+1)T) = {} & A(nT)x(nT) + B(nT)u_s(nT) \\ & + B(nT)u_d(nT) + FH(nT)z(nT) \\ & + \gamma(nT) \end{aligned} \quad (45)$$

Since the control effort in a discrete-time control problem is usually held constant between two consecutive sampling times, it is impossible generally to remove all the disturbance effects Likewise, the presence of the uncertainty sequence $\gamma(nT)$ also limits the idea of complete time cancellation of the noise Hence, the concept of "complete cancellation" means only that the noise effects $FHz(nT)$ are removed as they appear at isolated sample times, i e ,

$$B(nT)\,u_d(nT) + FH(nT)\;\; z(nT) + E(nT)\,c(nT) = 0 \quad (46)$$

The condition for existence of $u_d(nT)$ to satisfy Eq (46) is

$$[\,FH \mid A_e\,] = B[\,K_z \mid K_c\,]$$

Complete disturbance cancellation exists if, and only if,

$$FH(nT) = -B(nT)\,K_z(nT)$$

and

$$E(nT) = -B(nT)\,K_c(nT) \quad (47)$$

for some matrix $K_z(nT)$ and $K_c(nT)$ Assuming the conditions of Eq (47) are satisfied, the control $u_d(nT)$ can be chosen in a practical sense as

$$u_d(nT) = -K_z(nT)\,z'(nT) - K_c(nT)\,c'(nT) \quad (48)$$

where $z'(nT)$ is the noise state determined by on-line, real-time estimation of $z(nT)$ The enclosed loop error dynamics using e_z, e_c may be incorporated into the model as

$$\begin{aligned} x[(n+1)T] = {} & A(nT)\,x(nT) + B(nT)\,u_s(nT) \\ & - [B(nT)\,K_z(nT)]\;e_z(nT) \\ & - [B(nT)\,K_c(nT)]\;e_c(nT) + \gamma(nT) \end{aligned} \quad (49)$$

Hence, the noise effects have been reduced to the (BK_ze_z + BK_ce_c) term, which should decay rapidly toward zero, and, of course, the isolated uncertainty sequence $\gamma(nT)$ The servo-regulating control, $u_s(nT)$, can now be designed by conventional methods assuming the noise has been removed

A complete block diagram of the original continuous-time plant model, and the proposed DAC with full state discrete-time composite observer, is shown in Fig 4, with the control law

$$u_s = -K_x x'$$

and

$$u_d = -K_z z' - K_c c' \tag{50}$$

V. Summary of DAC Procedure

(1) The disturbance $w(t)$ is determined experimentally to ascertain distinguishing characteristics Suppose that $w(t)$ is noted to consist of an uncertain bias at times and in other intervals $w(t)$ exhibits uncertain ramp features Thus, the waveform of the disturbance has a general form

$$w(t) = k_1 + k_2 t \tag{51}$$

where k_1, k_2 are unknown constants which change value at unknown times

(2) With the description of $w(t)$, the designer determines the simplest differential equation model for this class of disturbances, that is, the lowest order differential equation for which Eq (51) is the general solution The corresponding DAC matrices H, D are determined from the general form given in Eqs (13) and (14) In observable canonical form the model becomes

$$w(t) = [\,1 \quad 0\,] \begin{bmatrix} z_1 \\ z_2 \end{bmatrix} \tag{52}$$

$$\begin{bmatrix} \dot{z}_1 \\ \dot{z}_2 \end{bmatrix} = \begin{bmatrix} -b_1 & 1 \\ -b_2 & 0 \end{bmatrix} \begin{bmatrix} z_1 \\ z_2 \end{bmatrix} + \begin{bmatrix} \sigma_1 \\ \sigma_2 \end{bmatrix} \tag{53}$$

where (b_1, b_2) are constants The characteristic polynomial of the disturbance model D is equated with the resulting characteristic polynomial attained from the Laplace transform of Eq (51), that is,

$$det\,[\lambda I - D] = \lambda^2 + b_2\lambda + b_1 = \lambda^2 \tag{54}$$

and in this example, b_1 and b_2 equate to zero

(3) The controller problem is separated into two subtasks,

$$u = u_s + u_d \tag{55}$$

such that u_s performs servoregulation and u_d is responsible for servotracking a command input and the disturbance removal Hence, the control effort u_s is chosen for regulation assuming no noise, typically,

$$u_s = -K_x x \tag{56}$$

The control law u_d has the form

$$u_d = -K_z z - K_c c \tag{57}$$

where K_z and K_c are chosen to ensure disturbance removal and tracking, respectively

(4) With available software tools, the equations can be incorporated into a single system simulation—see Eq (28)—and tested for various noise inputs and servocommands

VI. Test Model

A simplified test model for an antenna servomechanism is used to illustrate the DAC procedure (refer to Fig 3) The objective is to control the elevation of an antenna designed to track an RF signal The antenna and its drive mechanism have a moment of inertia J and damping B arising from bearing friction, aerodynamic friction, and the back emf of the dc-servodrive motor The equations of motion are

$$J\ddot{\theta} + B\dot{\theta} = T_c + T_d \tag{58}$$

where T_c is the net torque developed by the drive motor, and T_d represents the disturbance torques possibly due to wind, static misalignments, etc Substitution of the assumed coefficients in Eq (58) yields

$$\ddot{\theta} + 1\dot{\theta} + 6\theta = u + w \tag{59}$$

In this example, the coefficients for Eqs (58) and (59) were arbitrarily selected and may be unrealistic They were selected, however, to describe the effect of the new DAC controller The general shape of the servocommand angle $\theta_c(t)$ is assumed to be composed of step and ramp functions Hence, the servocommand $\theta_c(t)$ is modeled by y_c estimated using the commanded rate $\dot{\theta}_c(t)$, and the acceleration $\ddot{\theta}_c(t)$ For the purpose of maintaining a good tracking accuracy, it is reasonable to assume that the antenna drives are capable of following the peak velocity $\dot{\theta}_c(t)$ in the steady state with acceptable error Since the objective is to permit acceptable communication signal reception, the dependence of the signal amplitude on pointing error is a major concern The corresponding servocommand can be represented by the following state-space representation

$$\begin{aligned} \dot{c}(t) &= \mathbf{E}(t)\,c(t) + \mu(t) \\ y_c(t) &= \mathbf{G}(t)\,c(t) \end{aligned} \tag{60}$$

Similarly the disturbance $w(t)$ (assumed to be step and ramp torques in this example) can be modeled as suggested in Eq (54),

$$w(t) = \mathbf{H}z(t)$$
$$\dot{z}(t) = \mathbf{D}z(t) + \sigma(t) \tag{61}$$

Thus, the open-loop system can be represented in the form of Eq (28) where

$$\mathbf{A} = \begin{bmatrix} 0 & 1 \\ -6 & -1 \end{bmatrix}, \quad \mathbf{F} = \mathbf{B} = \begin{bmatrix} 0 \\ 1 \end{bmatrix}$$

$$\mathbf{D} = \mathbf{E} = \begin{bmatrix} 0 & 1 \\ 0 & 0 \end{bmatrix}, \quad \mathbf{G} = \mathbf{C} = [\,1 \quad 0\,]$$

$$\mathbf{H} = [\,1 \quad 0\,]$$

The state feedback gains have been chosen with K_x = [94, 19] to ensure the undisturbed system closed-loop poles at -10, -10 The estimator poles for the plant, noise, and servocommand states are selected in the usual manner using pole-placement techniques for approximately 3 to 5 times faster response than the combined plant and feedback controller A computer simulation of the closed-loop model in Eq (28), shown in Fig 5, is used to demonstrate the effectiveness of the DAC in disturbance rejection Figure 6(a) illustrates the controlled output variable $\theta(t)$ servotracking the command input $\theta_c(t)$ without the DAC The disturbance assumed in this example is plotted in Fig 6(b) with the controlled variable $y(t)$ Without control other than state feedback, the output is unable to distinguish the control input from the disturbance and tends to follow the noise signal rather than the servocommand

In Fig 7(a) and (b), the same example with the inclusion of the DAC demonstrates the effective servotracking of the command in the presence of the noise input Note that only a slight perturbation occurs in the controlled variable $y(t)$ at approximately 5 0 s just as the disturbance has occurred

The analogous discrete-time system has been simulated to demonstrate the degradation expected in tracking when the position-loop of the controller is implemented via a digital computer Figures 8 and 9 display the discrete-time system in a noisy environment both with and without the DAC incorporated in the loop, assuming a sampling time T = 0 1 second

VII. Conclusions

The feasibility of implementing a disturbance accommodating controller has been investigated as applied to an analog servodrive for positioning an RF antenna The DAC is designed for synthesizing and rejecting waveform-structured disturbances The form of the systematic pointing errors inherent in antenna tracking systems appears viable to this characterization of the disturbance as structured waveforms rather than the noise generated through random processes with statistical descriptors The waveform type of disturbances can be modeled according to a priori data by determination of the corresponding differential equation, and hence, the state representation of the waveform structured noise

In this study, simulation results show that the DAC is an appropriate technique for cancellation of the systematic errors, while simultaneously allowing an optimal control policy to regulate the system The ease with which the DAC is implemented along with the existing servo-control is another attribute of this technique Practical implementation issues such as model order, computation time, and storage requirements offer no expected challenges for microprocessor-based controllers Further study is necessary to incorporate the state-dependency issue in regard to systematic pointing errors expected in antenna position controllers

References

[1] M A Koerner, "Relative Performance of 8 5 GHz and 32 GHz Telemetry Links on the Basis of Total Data Return per Pass," *TDA Progress Report 42-87*, vol July–September 1986, Jet Propulsion Laboratory, Pasadena, California, pp 65–80, November 15, 1986

[2] J A Nickerson, "A New Linear Quadratic Optimal Controller for the 34-Meter High Efficiency Antenna Position Loop," *TDA Progress Report 42-90*, vol April–June 1987, Jet Propulsion Laboratory, Pasadena, California, pp 136–141, August 15, 1987

[3] R E Hill, "A Modern Control Theory Based Algorithm for Control of the NASA/JPL 70-Meter Antenna Axis Servos," *TDA Progress Report 42-91*, vol July–September 1987, Jet Propulsion Laboratory, Pasadena, California, pp 285–294, November 15, 1987

[4] C D Johnson, "Theory of Disturbance Accommodating Controllers," *Control and Dynamic Systems Advances in Theory and Application*, vol 12, New York Academic Press, chapter 7, pp 387–489, 1976

[5] C D Johnson, "Disturbance-Accommodating Control A History of Its Development," *Proc 15th Annual Meeting, Society of Engineering Science*, pp 331–347, December 1978

[6] C D Johnson, "A Discrete-Time Accommodating Control Theory," *Control and Dynamic Systems Advances in Theory and Application*, vol 18, New York Academic Press, chapter 6, pp 223–345, 1982

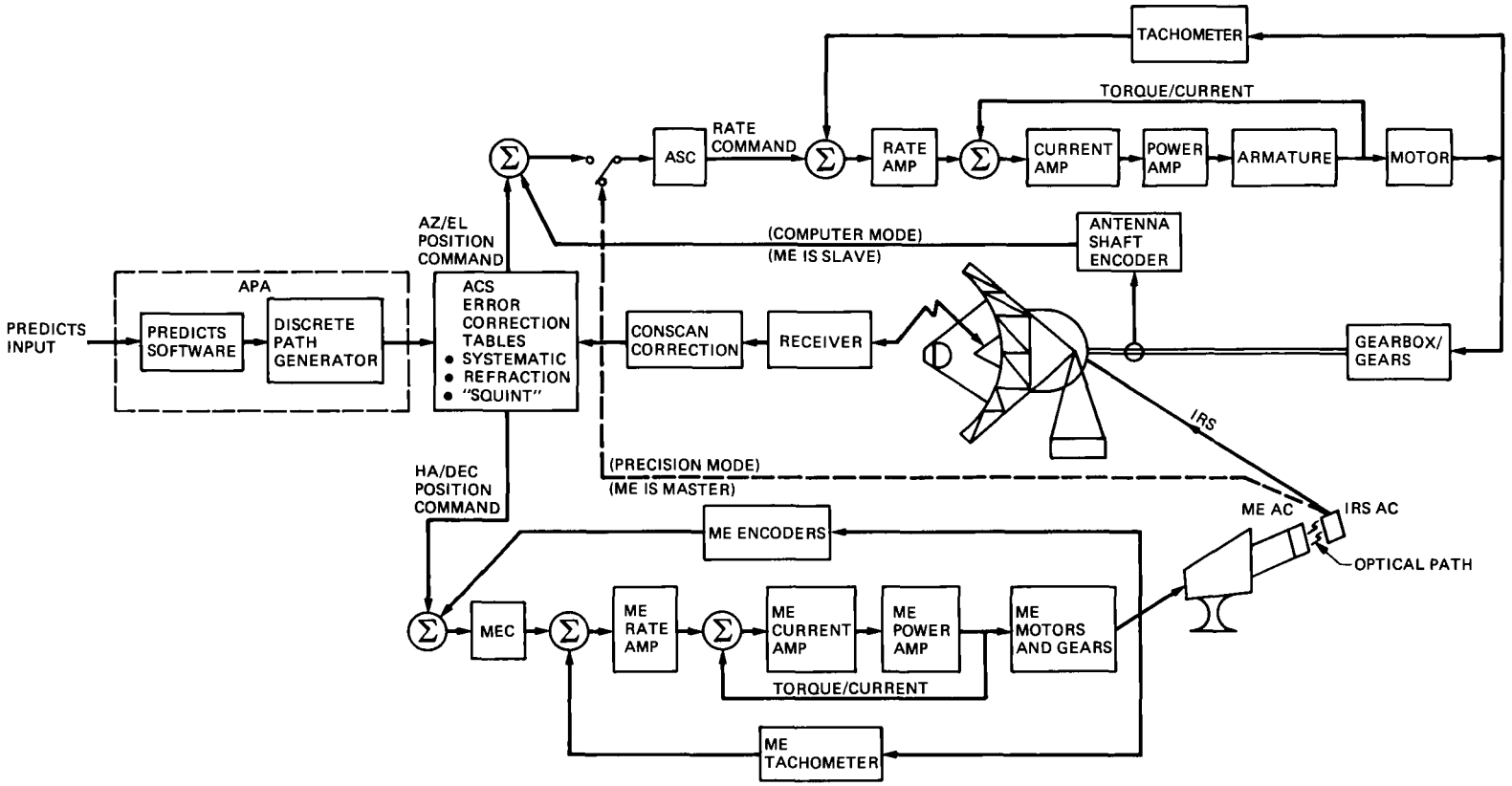

Fig 1 Overview of the 70-m antenna pointing system at JPL

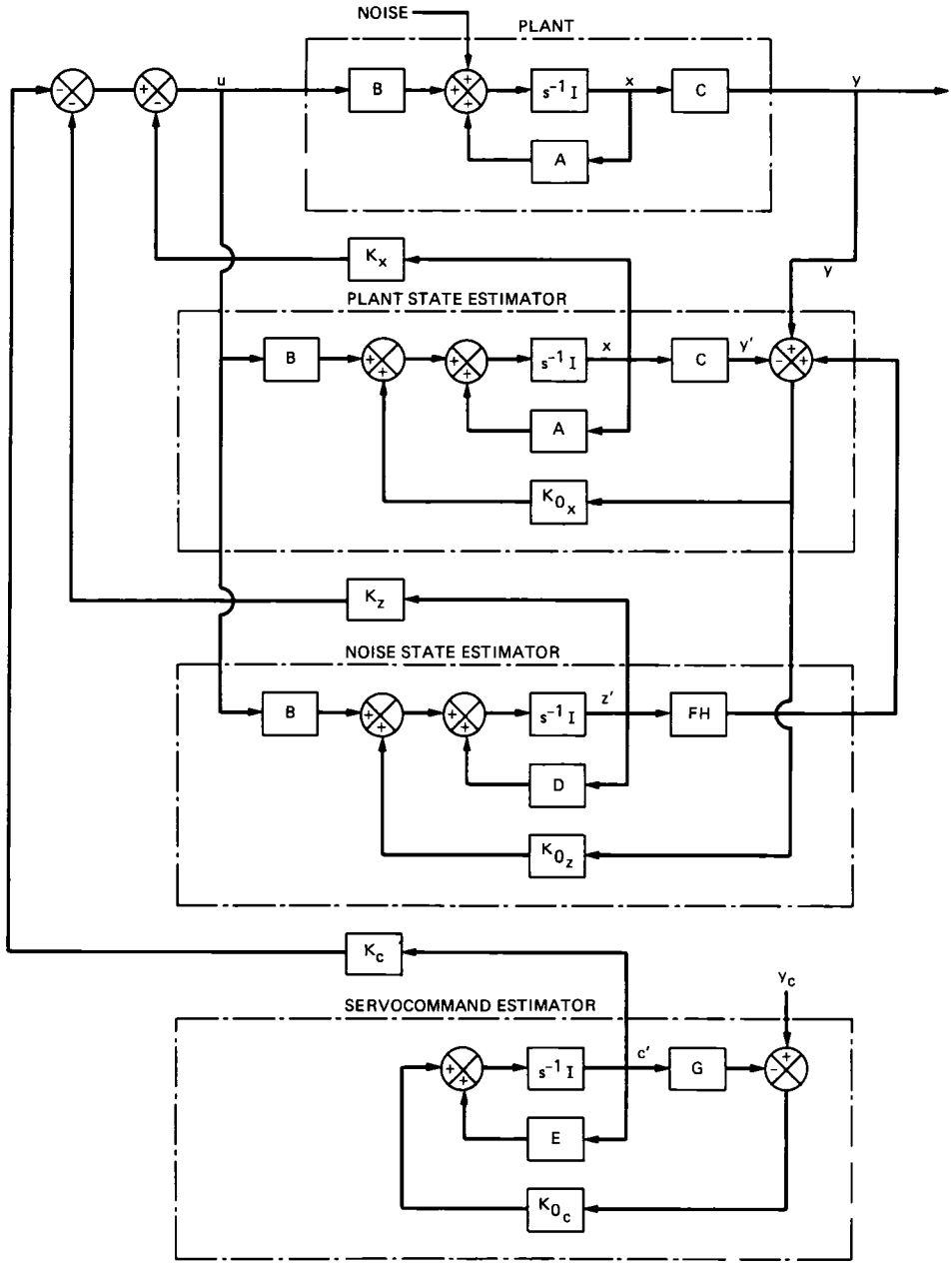

Fig 2. Functional diagram of the servotracker with the DAC installed

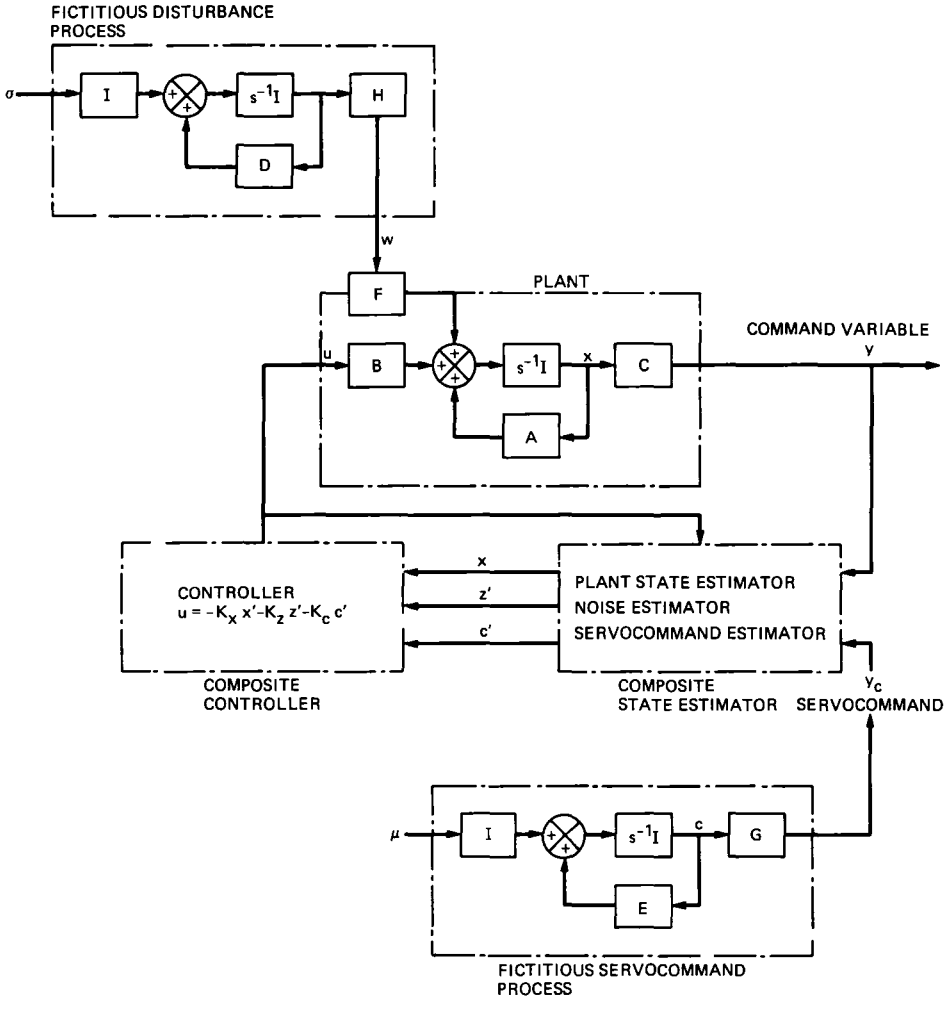

Fig. 3 Simplified block diagram of the plant and state feedback controller with composite estimator for servotracking

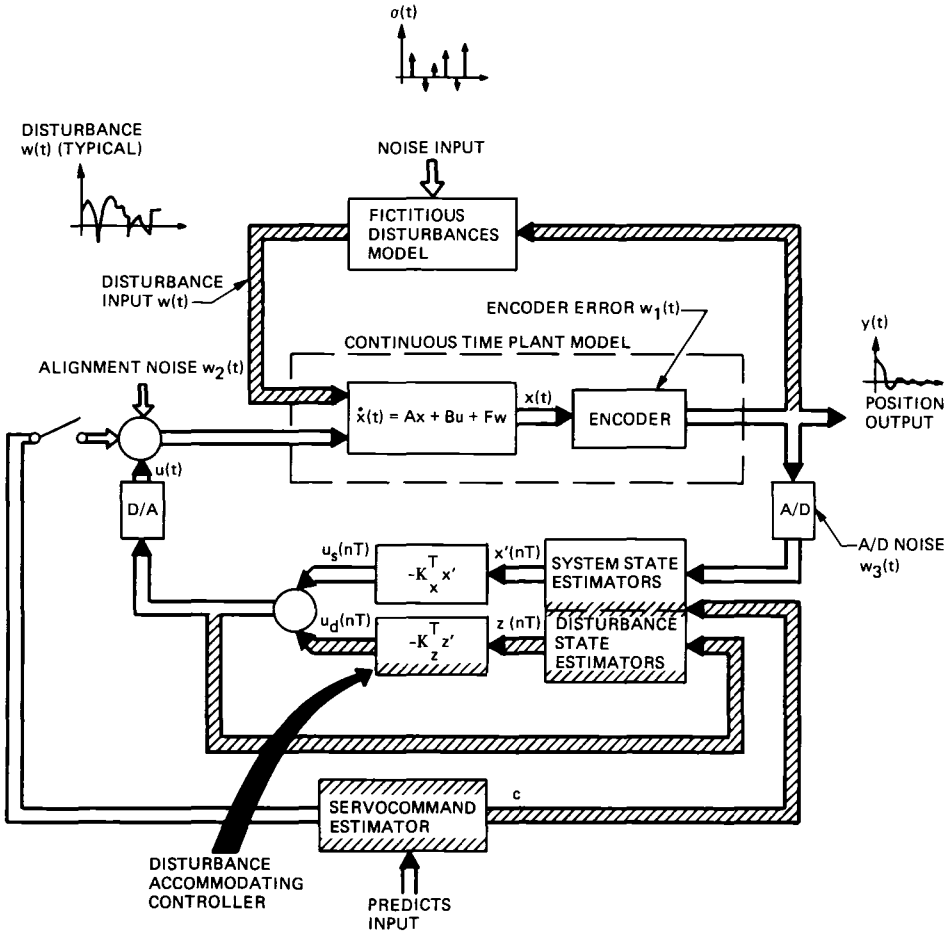

Fig 4. Configuration for the discrete-time disturbance accommodating controller (DAC) included in a digital servotracking system, slashes represent changes required to include the DAC in a typical state estimate feedback controller scheme

$$\begin{bmatrix} \dot{x}_1 \\ x_2 \\ x_1 \\ x'_2 \\ z_1 \\ z'_2 \\ c_1 \\ c_2 \\ \hline y_1 \end{bmatrix} = \left[\begin{array}{cccccccc} 0 & 1 & 0 & 0 & 0 & 0 & 0 & 0 \\ -6 & -1 & -94 & -19 & -1 & 0 & 100 & 20 \\ 19 & 0 & -19 & 1 & 0 & 0 & 0 & 0 \\ 164 & 0 & -264 & -20 & 0 & 0 & 100 & 20 \\ 500 & 0 & -500 & 0 & 0 & 1 & 0 & 0 \\ 625 & 0 & -625 & 0 & 0 & 0 & 0 & 0 \\ 0 & 0 & 0 & 0 & 0 & 0 & -10 & 1 \\ 0 & 0 & 0 & 0 & 0 & 0 & -25 & 0 \\ \hline 1 & 0 & 0 & 0 & 0 & 0 & 0 & 0 \end{array}\right] \begin{bmatrix} x_1 \\ x_2 \\ x_1 \\ x_2 \\ z'_1 \\ z'_2 \\ c_1 \\ c_2 \end{bmatrix} + \begin{bmatrix} 0 & 0 \\ 0 & 1 \\ 0 & 0 \\ 0 & 0 \\ 0 & 0 \\ 0 & 0 \\ 10 & 0 \\ 25 & 0 \\ \hline 0 & 0 \end{bmatrix} \begin{bmatrix} u \\ w \end{bmatrix}$$

Fig 5 Simulation model for the DAC servocommand example

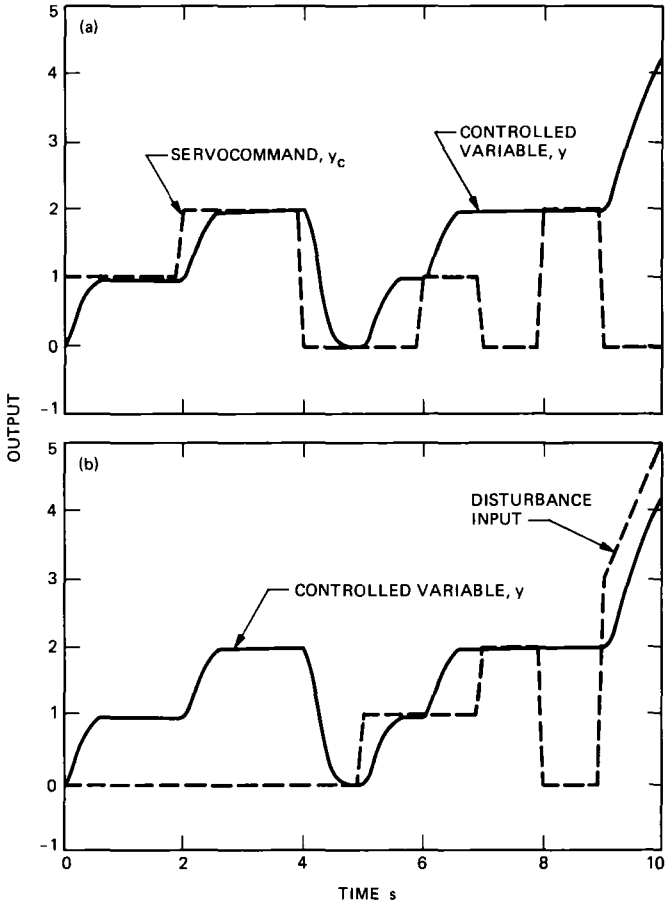

Fig 6 Servocommand response for the continuous-time example without the DAC installed. (a) servocommand and controlled variable; (b) disturbance input and the controlled variable $y(t)$

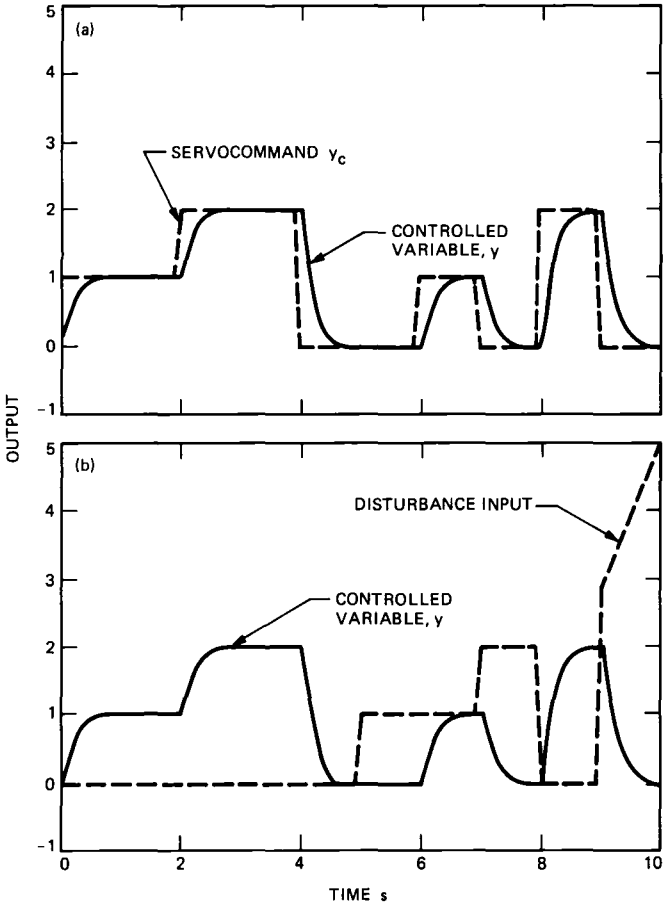

Fig 7 Servocommand response for the continuous-time example with the inclusion of the DAC. (a) servocommand and controlled variable; (b) disturbance input and the controlled variable $y(t)$

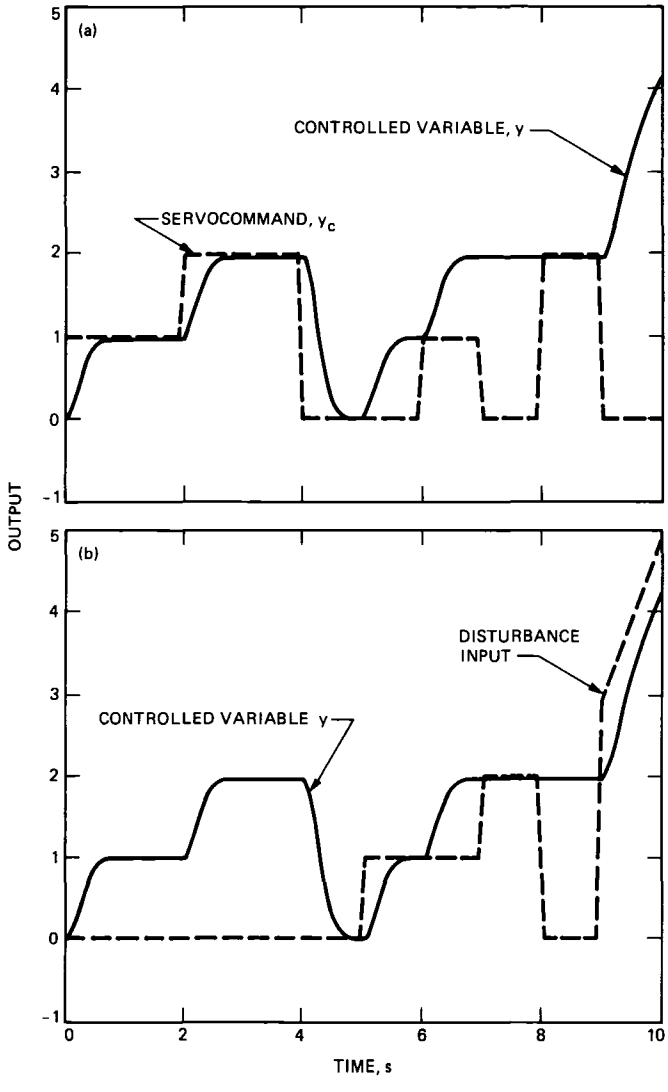

Fig. 8 Servocommand response for the discrete-time example without the DAC installed (a) servocommand input and controlled variable, (b) disturbance input and the controlled variable $y(t)$

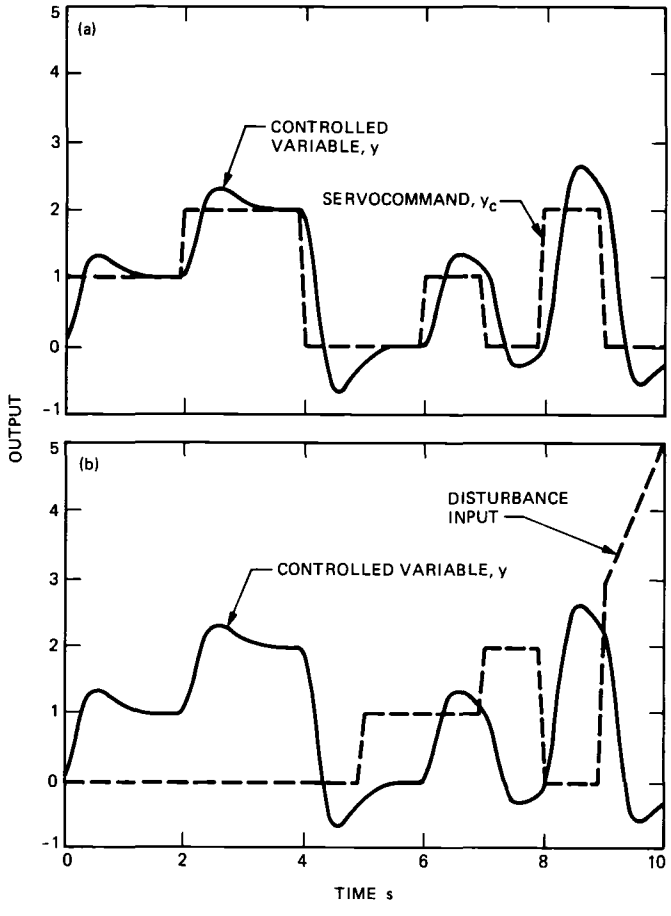

Fig. 9. Servocommand response for the discrete-time example with the DAC installed. (a) servocommand input and controlled variable; (b) disturbance input and the controlled variable $y(t)$

Digital Carrier Demodulation for the DSN Advanced Receiver

R Sadr and W J Hurd
Communications Systems Research Section

The digital in-phase and quadrature (I&Q) carrier demodulation for the Deep Space Network's Advanced Receiver is described and analyzed The system provides coherent demodulation for a variety of modulation formats including Binary Phase Shift Keying (BPSK), BPSK with carrier residual, Quadrature Phase Shift Keying (QPSK), Offset-QPSK (OQPSK), and Minimum Shift Keying (MSK) The article focuses on the theory and hardware design of the halfband filters which are the integral part of the demodulator The underlying theory of the filters is summarized, a breadboard hardware design is described, and a VLSI implementation is proposed which significantly decreases the hardware A second important problem analyzed is DC-offset in the demodulator This is a serious problem which translates into bias error in the residual carrier phase detector The dynamic range of the complex mixer is analyzed using a probabilistic approach. It is deduced that the resulting static phase error is less than 0 2 deg when the ratio of carrier power to noise power in the demodulator input bandwidth is -72 dB or higher Thus, the static phase error is negligible at a carrier power to noise spectral density of 0 dB-Hz for a 15-MHz bandwidth demodulator

I. Introduction

A new Advanced Receiver is presently under development for future implementation throughout the NASA Deep Space Network (DSN) The new receiving system will perform carrier and subcarrier demodulation, data detection, and Doppler extraction and will interface closely with the exciter, the ranging assembly, and the monitor and control subsystem This article is concerned only with the digital carrier demodulator We present the architecture and analysis of a digital demodulator for coherent carrier demodulation of the general class of amplitude and phase modulation Besides the current standard DSN modulation type of binary phase shift keying (BPSK) on subcarriers, with residual carrier [1], the demodulator is appropriate for Quadrature Phase Shift Keying (QPSK), Minimum Shift Keying (MSK), Staggered or Offset QPSK (OQPSK), and the standard DSN modulation but with fully suppressed carrier

The key characteristics of the demodulator are the passband width and ripple, the stopband width, attenuation, and ripple, and the DC-offset or bias introduced by the numerical accuracy effects The DC-offset is critical because it causes bias in measurement of the phase of residual carriers In this article, we specify the architecture of the demodulator, design

and analyze a practical implementation of the arm filters as halfband filters, and determine the numerical accuracy required to meet the DSN's needs

A. Previous Work

There are many references for a complete treatment of digital modulation techniques such as BPSK and QPSK [2], [3] The equivalency of staggered QPSK (OQPSK) and MSK is shown in [3], so-called serial MSK [3] is only equivalent to OQPSK when the input symbols at the transmitter are differentially encoded BPSK with carrier residual is described in [1], the architecture of the old version of the Advanced Receiver and tracking loops is discussed in [4] The effects of offset in sampling and the performance of the integrate-and-dump filter as a matched filter are discussed in [5] To reduce the loss incurred due to offset sampling, the weighted integrate-and-dump is proposed and analyzed in [6] References [7] and [8] provide extensive treatments of digital filter design The loss due to amplitude ripple within the passband of the anti-aliasing filter is discussed and analyzed in [9] Originally, Bellanger [10], [11] introduced the halfband filters for computation and storage reduction in multi-rate digital filtering applications, and he further analyzed the filter order, multiplication rate, and storage requirement of the halfband filters Reference [12] provides the hardware description and test results for the older version of the Advanced Receiver

B. Outline of Article

The receiver structure is described in Section II In Section III, the underlying theory of halfband filters is discussed In IIIB, a design example is given and the hardware architecture of a single board that has been fabricated and demonstrated in the laboratory is described A VLSI chip is outlined in IIIC that results in significant reduction in the chip count In Section IV, DC-offsets resulting in phase bias are analyzed, including the effects of numerical precision in the table for sine and cosine generation, and rounding A probabilistic approach is used Finally, in Section V, conclusions and some final observations are presented

II. Receiver Structure

A simplified block diagram of the receiver, showing portions of the receiver impacting demodulator design, is shown in Fig 1 The received signal from the S-, X- or K-band low noise amplifier is open-loop converted from radio frequency (RF) to intermediate frequency (IF) in highly stable wideband RF-to-IF downconverters, which now exist for S- and X-band The downconverter output goes into the IF strip In the IF strip, the carrier phase locked loop is closed by mixing the signal against the numerically controlled oscillator (NCO) output, resulting in a fixed second IF frequency This signal is filtered by an anti-aliasing bandpass filter, and down-converted to a final IF frequency The final IF signal is sampled by an A/D converter whose output goes to the digital demodulator The demodulator outputs digital in-phase and quadrature components to the baseband signal processor, which measures all statistics needed by the software algorithms and outputs detected telemetry symbols to the decoder(s)

The final IF frequency has been chosen to be 10 MHz in order to be compatible with existing DSN systems, such as the ranging system Thus, at the final IF output, the carrier is phase locked to 10 MHz The passband is approximately 10 ± 7 5 MHz, as limited by the anti-aliasing bandpass filters at the previous IF frequency

The demodulator block diagram is shown in Fig 2 The input is 8-bit digitized IF, with the carrier phase locked to 10 MHz The sampling rate is a fixed frequency near, but not exactly, 40 MHz A tentative value is 39 6 MHz The offset from 40 MHz is to minimize self-induced radio frequency interference (RFI) at the carrier frequency of 10 MHz The demodulator multiplies the input data by sine and cosine waveforms at 10 MHz, resulting in in-phase and quadrature baseband signals plus sum frequency terms The sum frequency terms are filtered out by lowpass "arm" filters

Throughout this article we denote the sampling period as T_s, the sampling rate as $f_s = 1/T_s$, the symbol period as T, the IF frequency as f_c, and the radian IF frequency as $\omega_c (= 2\pi f_c)$

The input samples are demodulated by the reference in-phase cos $(\omega_c nT_s + \hat{\phi}_c)$ and quadrature components sin $(\omega_c nT_s + \hat{\phi}_c)$, where $\hat{\phi}_c$ denotes the carrier phase reference These are generated from a look-up table Ideally, the multiplier output signals are filtered by a zonal lowpass filter, to filter out the double frequency images that result from the multiplication in the time domain of the signal by a sinusoid

The original spectrum, the mixer output spectrum and the desired filtered output spectrum are shown in Fig 3 Since the lowpass bandwidth after demodulation and filtering is only half the IF bandwidth, or 7 5 MHz, the sampling rate is reduced by a factor of two, resulting in the final spectrum in Fig 3 In this article, the application of halfband filters is considered for low-pass filtering of the demodulated signal This class of filters is a special case of lowpass Finite Impulse Response (FIR) filters which is particularly appropriate for removing mixer sum frequency terms and for use with a decimation factor of two

III. Halfband Filters

To meet the specification for a desired frequency response of a digital filter, it is desirable to minimize the order of the filter (denoted as N), thereby reducing the number of multiplication and addition operations required to implement the filter We have selected the halfband filters to eliminate the double frequency images that are produced by complex demodulation The following points are the main considerations that led us to select the halfband filters

(1) *Reduced hardware* Halfband filters require approximately half the number of multiplications and additions for a given N, when compared to an arbitrary linear phase digital filter This is because almost half of the N filter coefficients are zero

(2) *Equal passband and stopband width* Stopband width is the same as passband width This is ideal for eliminating sum frequency terms resulting in complex heterodyning, because the sum frequency terms to be eliminated have the same bandwidth as the difference frequency terms to be passed

(3) *Equal passband and stopband ripple* The ripple in the passband and the stopband is the same in peak deviation This results in approximately the same magnitude of signal-to-noise ratio loss due to passband ripple [9] and due to sum frequency noise aliased into the passband after decimation by two

(4) *Ease of implementation* When a decimation factor of two is employed, the processing rate is also reduced by a factor of two

For equiripple design of Finite Impulse Response (FIR) filters, it is necessary to specify a set of tolerance parameters in order to practically implement these filters The FIR design problem is then formulated as a Chebyshev approximation method [7], [8] These parameters, as shown in Fig 4, are

δ_p = ripple (deviation) in the passband from ideal response

δ_s = ripple (deviation) in the stopband from ideal response

$f_p = \omega_p/2$ = normalized passband edge frequency

$f_s = \omega_s/2$ = normalized stopband edge frequency

For the case when $\delta_p = \delta_s = \delta$ and $f_s = 0.5 - f_p$, then the resulting equiripple optimal solution to this approximation problem has the property that

$$H(e^{j\omega}) = 1 - H(e^{j(\pi-\omega)}) \tag{1}$$

that is, the frequency response of the optimal filter is odd-symmetric around $\omega = \pi/2$, and at $\omega = \pi/2$

$$H(e^{j\pi/2}) = 0.5 \tag{2}$$

It is shown in [8] that any symmetric FIR filter satisfying (1) has an impulse response of the form

$$h_k = \begin{cases} 1, & k = 0 \\ 0, & k = \pm 2, \pm 4, \pm 6, \end{cases} \tag{3}$$

Hence, all of the even coefficients are zero, except for $k = 0$ This reduces the complexity required to implement this class of filters Particularly when a decimation factor of 2 is used, the required number of multiplications is half of that needed for symmetrical FIR designs and one-fourth of that for arbitrary FIR designs The SNR loss due to amplitude ripple is studied in [9]

A. Halfband Architecture with Decimation Factor of 2

In this section, we outline a simplified architecture for an Nth (N-odd) order halfband FIR filter as shown in Fig 5(a) We denote the filter output as y_n, the input as x_n, and the filter coefficients as h_j For a FIR filter, the filter output y_n is

$$y_n = \sum_{j=-\left(\frac{N-1}{2}\right)}^{\left(\frac{N-1}{2}\right)} h_j x_{n-j} \tag{4}$$

The output of a halfband filter is found by invoking (3), and y_n can be expressed as

$$y_n = \sum_{\substack{j=-\left(\frac{N-1}{2}\right) \\ j \neq 0,\ j \text{ odd}}}^{j=\left(\frac{N-1}{2}\right)} h_j x_{n-j} + x_n \tag{5}$$

In this expression for y_n with even n (decimation factor of 2), the only term in the output that involves the even samples is the last term, which corresponds to the center tap of the filter Thus, it is possible to reduce the computation of y_n for even-n into a lower-order (half) filtering and an addition operation First, the input is demultiplexed into odd and even samples The odd samples are filtered using an $((N+1)/2)$-tap FIR filter The filter output is summed with the delayed even sample In Fig 5(b), the simplicity of this architecture is evident when comparing the original FIR structure to its equivalent model The length of the delay in the simplified model is

$(N + 1)/2 + \tau$, where τ is the pipeline delay through the FIR filter

Hardware realization uses an $(N + 1)/2$ order FIR filter, a shift register for the delayed even samples, and an adder for adding the delayed samples to the filter output This structure has the important additional advantage of operating the FIR filter at half the input frequency Thus slower components (multiply accumulators) than a general FIR filter can be used to implement this architecture, which directly impacts the cost Furthermore, it is also possible to take advantage of the symmetry of the FIR filter coefficients [7] to reduce the amount of computation by another factor of two

B. Halfband Filter Design

Some examples of halfband filters are shown in Table 1 These were obtained using the Remez exchange algorithm [7] In this article, we do not discuss the filter design package for this algorithm Our design package uses the standard linear phase filter design package in [7], which can be used to design a variety of types of FIR filters

In Table 1, the coefficients of three 15th order halfband filters are listed in the first 4 columns Only four coefficients need to be specified, since $h_{-k} = h_k$, $h_0 = 1$, and $h_k = 0$ for k-even The 5th column, f_p, is the upper band edge of the passband, expressed as a fraction of f_s The stopband starts at $0.5-f_p$ and the transition band is from f_p to $0.5-f_p$ The last column is the deviation of the filter from ideal

The frequency response of the 15th order filter corresponding to the first row of Table 1 is shown in Fig 6 For the filter of Fig 6, each coefficient is quantized to 9 bits of resolution, which is the coefficient accuracy of the FIR filter chip used in the DSN Advanced Receiver With the resolution of the figure, there is no increase in the stopband deviation relative to the −38 6 dB predicted in Table 1 This filter results in a $0.6 * 10^{-3}$ dB loss due to aliasing and the same amount due to passband ripple loss [9], thus, it results in a total loss of $1.2 * 10^{-3}$ dB

The halfband filter was built and tested using the architecture depicted in Fig 5(b) The FIR filter is implemented using an 8th order FIR filter chip, ZR-33891 (Zoran Corp), operating up to 25 MHz This chip supports 9-bit data and 9-bit coefficients, and it outputs 26 bits The block diagram of the realization is shown in Fig 7(a), and a photograph of the board is shown in Fig 7(b)

For proper alignment of the 26-bit output of the FIR chip and the full adder, it is clear from Eq (5) that the center tap corresponding to the delayed samples is "1," and therefore the output result of the FIR filter must be added starting at the 9th bit position

C. VLSI Chip for Halfband Filters

A custom VLSI chip is under development to reduce the chip count in the halfband filter from 33 chips to 2 chips The custom VLSI chip complements the ZORAN-33891 FIR chip This chip operates in a fully synchronous mode from an input clock with frequencies of up to 25 MHz The block diagram of the filter using this chip with the Zoran chip is shown in Fig 8 It is noted that the demultiplexer at the input of the filter is not included in the VLSI chip This is because of the demodulator design, wherein the odd and even samples are demultiplexed at the output into two paths to enable the use of slower (25 MHz) multipliers than would be required otherwise

A detailed specification of this VLSI chip is contained in the Appendix

IV. Dynamic Range and DC-Offset Analysis

A fundamental problem in the design of a digital mixer using finite precision arithmetic, especially fixed point arithmetic, is that a nonzero DC-offset (mean) is always present from quantization error, rounding, and truncation The DC-offset is very undesirable in the process of complex heterodyning, since it directly translates into static phase error for residual carrier systems

A. Maximum Allowable DC-Offset

In a residual carrier system the values of the Q-channel samples at the demodulator output are used to estimate the carrier phase When the signal-to-noise ratio is small, even a small DC-offset results in a large phase error To explicitly exhibit this fact, denote the carrier power as P_c, the noise power as N_0, the noise variance as σ^2, the bandwidth as B, and the DC-offset as β Then, for $P_c/N_0 = 0$ dB-Hz, the required threshold for the advanced receiver, and for $B = 15$ MHz, the carrier power signal to noise ratio is $P_c/\sigma^2 = P_c/(N_0 B) = -72$ dB The signal amplitude is given by $A = \sqrt{2P_c}$ The total power is dominated by noise, and its scaling is such that the 8-bit A/D converter saturates at 4σ Thus $\sigma = 2^5 = 32$, and A is 0 01, in units of the A/D output step size With slowly varying random phase, the expected value of the complex mixer output is $A * \sin(\phi) + \beta$ Approximating $A \sin(\phi) + \beta$ with $A\phi + \beta$, the average phase estimate is $\hat{\phi} = 1/A(A\phi + \beta)$ Therefore, the static phase error due to DC-offset is roughly β/A radians Hence, to keep the phase error under 0 1 radian, it is necessary to keep the dc offset under 0 001, or 90 dB below the total input power

B. Quantization and Scaling

To analyze the effect of quantization on the performance of the digital receiver, we consider the quantization and scaling model shown in Fig 9 and the A/D converter characteristic shown in Fig 10

1 Input quantization and scaling The input signal $r(t)$ passes through an AGC amplifier which controls the total power The A/D converter (sampler and quantizer) quantizes to 8 bits, covering the range -2^7 to $2^7 - 1$ in quantizer output units The nominal scaling is such that the total power at the quantizer output is 2^{10}, i e , saturation is at approximately 4σ

The FIR filter chip can accept only 9-bit inputs, which motivates the scaling at the multiplier output We discuss the scaling to obtain 9-bit outputs, although scaling down to 8 bits is also evaluated

The A/D output is multiplied by the in-phase and quadrature reference signals, which are stored in read only memory (ROM) These are stored as k-bit integers, $k = 12$ or 16 In either case, the amplitude is 2^{15}, i e , the k most significant bits of the 16-bit multiplier input are used The input signal from the A/D converter is scaled up by four at the input to the multiplier This scaling results in a maximum possible value at the multiplier output of 2^{17} times the signal input value, i e , a total maximum value of less than 2^{24}

The multiplier chip has a feature which allows rounding from the least significant 16 bits into the next bit This rounding feature is used, effectively scaling the level down by 2^{16} Thus the final output of the multiplier, after rounding, is in the range -2^8 to $2^8 - 1$, and is represented by $L = 9$ bits This forms the input to the FIR filter It is the DC-offset at this point in the system which dominates static phase error performance

2 Signal scaling The net effect of the above on signal level is to multiply the input Q-channel signal by $2 \sin(\omega_c n T_s + \hat{\theta})$ Expanding the sum and difference frequency terms of the multiplier output, the factor of 2 is cancelled The difference frequency term at the multiplier output has the same signal amplitude and the same noise power as the input process, i e , the Q-channel signal is $A \sin(\hat{\theta} - \theta)$ and the noise power in the low frequency process is σ^2

The approximate effect of the FIR filter is to pass all of the low frequency terms, amplified by the DC gain of the filter The DC gain of the filter, in amplitude is the sum of the coefficients, i e ,

$$\sum h_i$$

These coefficients can be expressed as 9-bit numbers, so the scaling is such that the center tap gain is 2^8, and the sum of h_i is approximately 2^9 Therefore, at the output of the FIR filter the signal is

$$2^9 A \sin(\hat{\theta} - \theta)$$

where A is the signal value at the A/D converter output, and the noise power is $2^{18}\sigma^2$ The input scaling has been chosen to saturate at 4σ with an 8-bit A/D converter (at low SNR) Preserving the same saturation level at the output clearly requires 17 bits The reason we also consider scaling the FIR filter input down by a factor of 2, to 8 bits, is so that only 16 bits would be required at the final output Another way to get a 16-bit output would be to round or truncate the least significant bit of the 17-bit output, but this would introduce DC offset

C. Sine and Cosine Table Accuracy

Demodulation is accomplished by multiplying the A/D converter output samples by cosine and sine tables These components are prestored in read only memory (ROM) and are quantized to k bits We specifically consider the case when $k = 12$ or 16 Besides having enough resolution in the sine and cosine tables it is important that the N-point tables be designed such that the sum over the N-points is very close to zero To satisfy this, consider the identity

$$\sum_{n=0}^{N-1} e^{j\omega_c n T_s} = \frac{1 - e^{j\omega_c N T_s}}{1 - e^{j\omega_c T_s}} \tag{6}$$

For this sum to be zero it is necessary that $\omega_c N T_s \cong 2\pi n$, for some integer n However, even if N satisfies this requirement, due to quantization (rounding in this case) to k-bits of each value in the ROM, this sum is never exactly zero

D. Evaluation of DC-Offset

To evaluate the DC-offset, we compute the sample mean at the output of the mixer The received signal is the sum of the transmitted signal plus Gaussian noise If we were to compute the sample mean by using Monte Carlo type simulation, the variance of the estimate would be $\sigma^2_{\text{out}} = \sigma^2/N$, where N is the number of independent noise samples To get a sufficiently accurate estimate we need $\sigma_{\text{out}} \ll 10^{-3}$, the required DC-offset For $\sigma_{\text{out}} = 10^{-4}$, it would be necessary to process $N = \sigma^2/\sigma^2_{\text{out}} = 2^{+10}/10^{-8} \cong 10^{11}$ samples This is clearly too many samples to process on a general purpose computer

However, it is possible to analytically derive the expression for the probability distribution function defined over the dynamic range of every stage of our system, since the number

of quantization intervals is small in our case The mean and the variance of the signal are then computed from the probability distribution

1 Probability distribution of the mixer output. In order to analyze the distribution of the dynamic range of the demodulated signal, we consider the received signal $r(t)$ in Fig 9 Define $\Omega = \{-M, -M+1, \quad, 0, 1, \quad, M-1\}$ where $2 * M$ denotes the number of quantization intervals at the output of A/D The probability space is (Ω, F, P), where F is the collection of all subsets of Ω In this section, we drive the first order discrete probability density function for $y_n = T(y(nT_s))$, where $T(\cdot)$ denotes the quantizer characteristic function shown in Fig 10 Here $\{y_n\}$ is a stationary discrete-time and discrete-valued stochastic process, generated by sampling and quantizing the continuous-time and continuous-valued stochastic process $y(t)$ for $t > 0$, i e , the discrete-time process $y(nT_s) \in \mathcal{R}_1$ (prior to quantization) is a Gaussian process in this case [2], [3], with mean m and variance σ^2

Let P_k denote the probability of the kth quantization interval, i e , $P_k = Pr(y(nT_s) \in A_k)$, for $k = -M, -M+1, \quad, 0, 1, \quad, M-1$, where $2 * M$ is the number of quantization levels Let

$$A_k = [k\Delta, (k+1)\Delta), \text{ for } -M < k < M-1$$

$$A_{-M} = [-\infty, -M\Delta), \text{ and } A_{M-1} = [M\Delta, +\infty)$$

Notice $\mathcal{R}_1 = \bigcup_{k=-M}^{M} A_k$ The probability of the received signal falling in the kth quantization interval is

$$P_k = Pr(y(t) \in A_k) = \int_{A_k} \frac{1}{\sqrt{2\pi}\sigma} e^{-\frac{(u-m)^2}{2\sigma^2}} du \qquad (7)$$

Let

$$erfc(x) = \int_{-\infty}^{x} \frac{1}{\sqrt{2\pi}} e^{-\frac{t^2}{2}} dt$$

Then

$$P_k = erfc\left(\frac{(k+1)\Delta - m}{\sigma}\right) - erfc\left(\frac{k\Delta - m}{\sigma}\right) \qquad (8)$$

The probability distribution of y_i is then $Pr(y_i = k) = P_k$ Figure 11(a) and (b) shows the input probability density and the cumulative probability distribution when the signal has zero mean and unit variance (= 2^{10} for 8-bit input data)

Next, we compute the probability distribution at the output of the multiplier, which multiplies the A/D output y_n by the value s_n, the output of the sine (or cosine) table, and then quantizes the product The output is denoted by $w_n = Q(s_n y_n)$, where $Q(\cdot)$ denotes the quantization function, at the multiplier output The quantizer $Q(\cdot)$ for fixed point arithmetic is truncation or rounding The function $Q(\cdot)$ depends on how the output product is rounded In our hardware implementation a standard 16-bit multiplier is used, which accepts two 16-bit inputs in two's complement and outputs a 31-bit product The product can be rounded only at one bit position, namely from the 15th bit into the 16th bit, where bits are labeled starting at zero for the least significant bit We scale the two input numbers such that $L = 8$ or 9 bits remain, because the filter which follows the multiplier can accept only 9 bits of input

The sequence s_n is quantized to k-bits Thus let

$$s_n \in \Omega' = \{-2^k + 1, \quad, 2^k - 1\}$$

and

$$w_n \in \Omega'' = \{-2^L + 1, \quad, 2^L - 1\}$$

Then $Pr(w_n = \alpha)$ may be expressed as

$$Pr(w_n = \alpha) = \sum_{\xi} Pr(Q(\xi y_i) = \alpha) Pr(S_n = \xi) \qquad (9)$$

since s_n 's and y_n 's are independent The sequence s_n is selected uniformly from an alphabet of size N, with k-bits of resolution, thus, $Pr(s_n = \xi) = 1/N$, and $Pr(Q(\xi y_n) = \alpha)$ is given by (8), for each $y_n = k$ and $\xi \in \Omega'$

Figure 12 shows the output densities for three cases Figure 12(a) and (b) is for the in-phase and quadrature components, respectively, for $L = 8$ and $k = 12$ Figure 12(c) is for the in-phase component, when $L = 8$ and $k = 16$ Figure 13 shows the input and output densities for a case of improper input scaling In particular the input signal level is higher by a factor of 4 in power, i e , the input power is 2^{12} The two spikes of the input probability distribution function are due to the improper scaling and consequent saturation

2 Results for computation of DC-offset In Table 2, the values of the induced DC-offset due to sine/cosine quantization (for $N = 99$, which is the number of points in the ROM table, and $\omega_c T_s = 1/3\,96$) and multiplier output quantization

are given This table lists the results for both the 12- and 16-bit sine and cosine tables, and with 9- and 8-bit quantized output These values were computed by calculating the mean of the probability distribution functions given in Eqs (8) and (9) Values in the table are in units at the output of the multiplier, scaled between 1 and −1, i e , scaled down by 2^8 from the integer representation

The first column is the resolution of the ROM table The second column is the number of bits at the output of the quantizer The last two columns give the resulting DC-offset at the output of the multiplier, corresponding to each arm This corresponds to the DC-offset bias in static phase error, for the sine table, and to error in measuring A, for the cosine table The gain of the system is such that the signal amplitude is the same at the multiplier output as the A/D converter output, i e , it is 0 01 integer units for P_c/N_0 = 0 dB-Hz Scaling the multiplier output to the range −1 to +1 reduces the signal amplitude by a factor of 2^8, to approximately $4 * 10^{-4}$ Referring to Table 2, the static phase error is small, i e , less than $4 * 10^{-5}$, for $k = 12$, $L = 8$ and for $k = 16$, $L = 9$, and is marginal for $k = 16$, $L = 8$

The DC-offset for the in-phase arm is not acceptable for $k = 12$, but is good for $k = 16$ For this reason we have elected to use the 16-bit resolution table, with 9-bit multiplier output resolution

3 Effects of FIR filter on static phase error In our hardware design each product $h_{i-n} w_i$ is computed and accumulated without any quantization Therefore, the mean value at the output of the filter is exactly equal to $\sum_{i=0}^{N-1} h_i$ times the mean value at the input The input mean is $A\phi + \beta$, where β is the DC-offset and the static phase error is β/A Since both β and A are multiplied by the same filter gain, there is no change in static phase error in the filter Some additional static phase error is introduced if the filter output is quantized in further processing

V. Conclusions

In this article we outlined the design and analysis of a digital complex demodulator to be used in applications that require high speed (up to a 50-MHz sample rate) and operate at very low SNR We found a cost-effective way to implement the digital low-pass filter required for this application A two chip solution with the architecture of a custom VLSI coprocessor chip was proposed The filter results in less than $1\,2 * 10^{-3}$ dB loss due to passband ripple and imperfect attenuation of the unwanted sum frequency terms at the output A comprehensive analysis of the dynamic range distribution was presented, using a probabilistic approach, and it was deduced that it is possible to attain a static phase error of less than 0 2 deg at the DSN advanced receiver threshold SNR of P_c/N_0 = 0 dB, with a 15-MHz bandwidth

References

[1] J H Yuen (ed), *Deep Space Telecommunications Systems Engineering*, JPL Publication 82-76 Jet Propulsion Laboratory, Pasadena, California, July 1982

[2] W C Lindsey and M K Simon, *Telecommunications Systems Engineering*, Englewood Cliffs, New Jersey Prentice-Hall, 1973

[3] R E Zeimer and R L Peterson, *Digital Communications and Spread Spectrum Systems*, New York Macmillan Publishing Co , 1985

[4] R Sfeir, S Aguirre, and W J Hurd, "Coherent Digital Demodulation of a Residual Carrier Signal Using IF Sampling," *TDA Progress Report 42-78*, vol April–June 1984, Jet Propulsion Laboratory, Pasadena, California, pp 135–142, August 15, 1984

[5] R Sadr and W J Hurd, "Detection of Signals by the Digital Integrate-and-Dump Filter With Offset Sampling," *TDA Progress Report 42-91*, vol July–September 1987, Jet Propulsion Laboratory, Pasadena, California, pp 158–173, November 15, 1987

[6] R Sadr, "Detection of Signals by Weighted Integrate-and-Dump Filter," *TDA Progress Report 42-91*, vol July–September 1987, Jet Propulsion Laboratory, Pasadena, California, pp 174–185, November 15, 1987

[7] A V Oppenheim and R W Schafer, *Digital Signal Processing*, Englewood Cliffs, New Jersey Prentice-Hall, 1975

[8] R E Crochiere and L R Rabiner, *Multirate Digital Signal Processing*, Englewood Cliffs, New Jersey Prentice-Hall, 1983

[9] R Sadr and W J Hurd, "Filter Distortion Effects on Telemetry Signal-to-Noise Ratio," *TDA Progress Report 42-88*, vol October–December 1986, Jet Propulsion Laboratory, Pasadena, California, pp 59–66, February 15, 1987

[10] M G Bellanger and G Bonnerot, "Interpolation, Extrapolation, and Reduction of Computation Speed in Digital Filters," *IEEE Trans ASSP*, vol 25, no 4, pp 231–235, August 1974

[11] M G Bellanger, "Computation Rate and Storage Estimation in Multirate Digital Filtering with Half-Band Filters," *IEEE Trans ASSP*, vol 25, no 4, pp 344–346, August 1977

[12] D H Brown and W J Hurd, "DSN Advanced Receiver Breadboard Description and Test Results," *TDA Progress Report 42-89*, vol January–March 1987, Jet Propulsion Laboratory, Pasadena, California, pp 48–66, May 15, 1987

Table 1 Examples of halfband filters with $N = 15$

Coefficients				Passband	DEV-dB
h_1	h_3	h_5	h_7	f_p	
0 312	−0 089	0 038	−0 017	0 187	−38 62
0 309	−0 081	0 029	−0 085	0 162	−51 25
0 312	−0 078	0 026	−0 006	0 150	−57 93

Table 2 Mean values (all numbers scaled to range ±1)

ROM resolution, k	Output resolution, L	Average, sine table	Average, cosine table	DC in-phase arm	DC quadrature arm
12	8	$2\,42 \times 10^{-4}$	$2\,86 \times 10^{-4}$	$4\,71 \times 10^{-4}$	$5\,48 \times 10^{-6}$
16	8	$1\,57 \times 10^{-5}$	$1\,36 \times 10^{-5}$	$-2\,98 \times 10^{-6}$	$-6\,15 \times 10^{-5}$
16	9	$1\,57 \times 10^{-5}$	$1\,36 \times 10^{-5}$	$-6\,55 \times 10^{-6}$	$-3\,57 \times 10^{-5}$

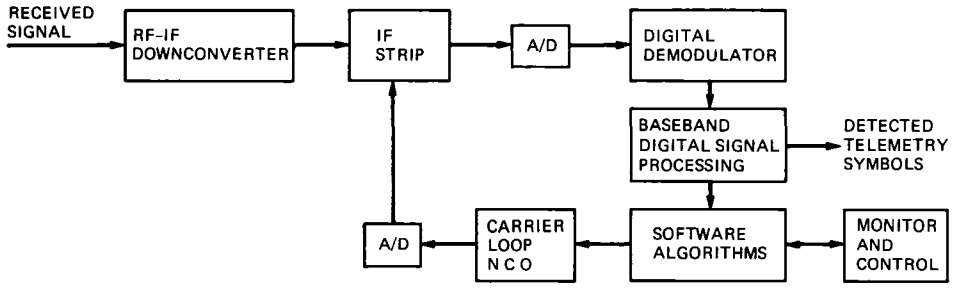

Fig. 1 Simplified architecture of advanced receiver

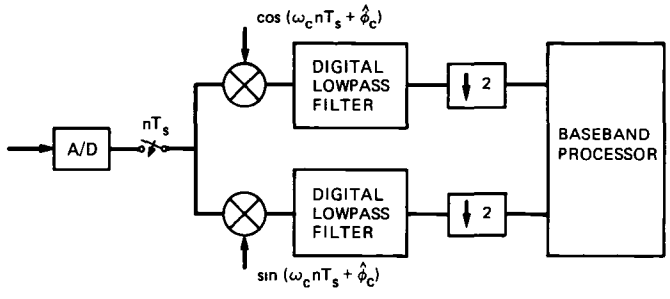

Fig 2 Complex demodulator

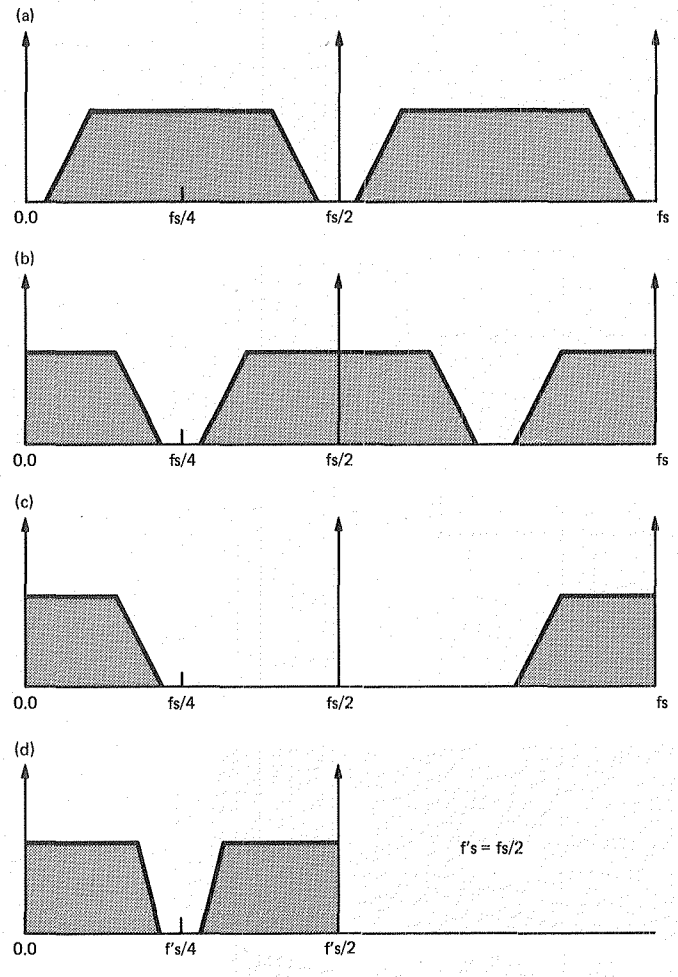

Fig. 3. Spectrum of signals: (a) A/D output; (b) mixer output; (c) filter output; and (d) decimated output

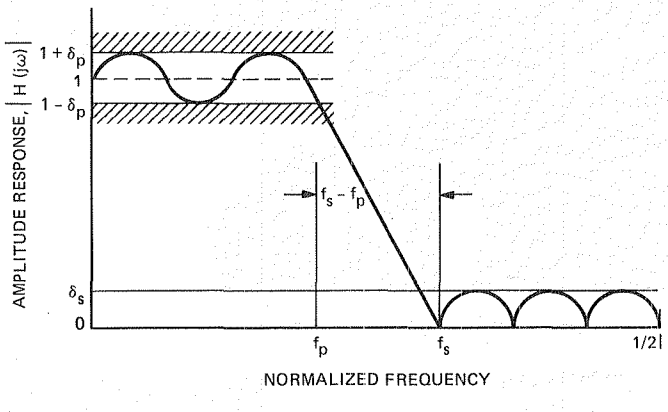

Fig. 4. Tolerance parameters for a practical FIR lowpass filter

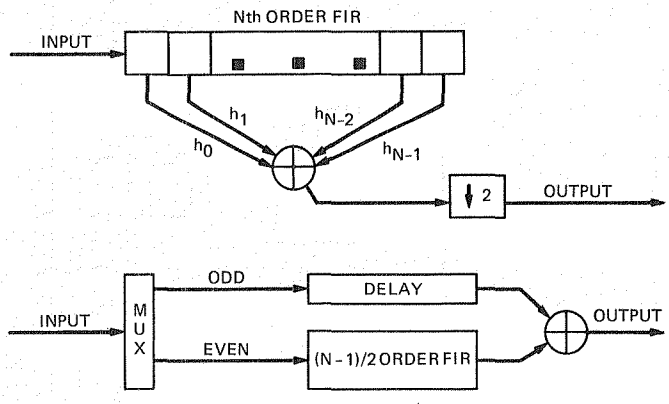

Fig. 5. FIR: (a) *N*th order FIR with decimation factor 2; (b) equivalent halfband model

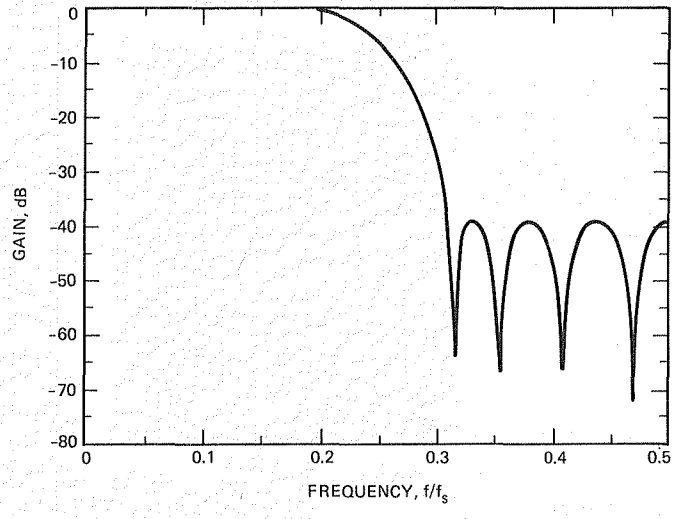

Fig. 6. Frequency response of a 15th order halfband filter

(a)

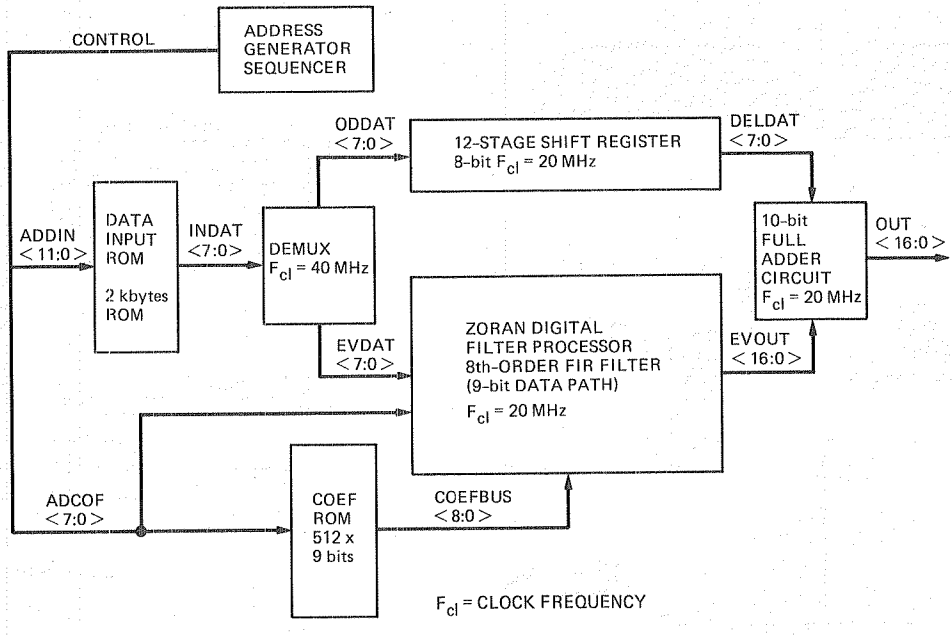

(b)

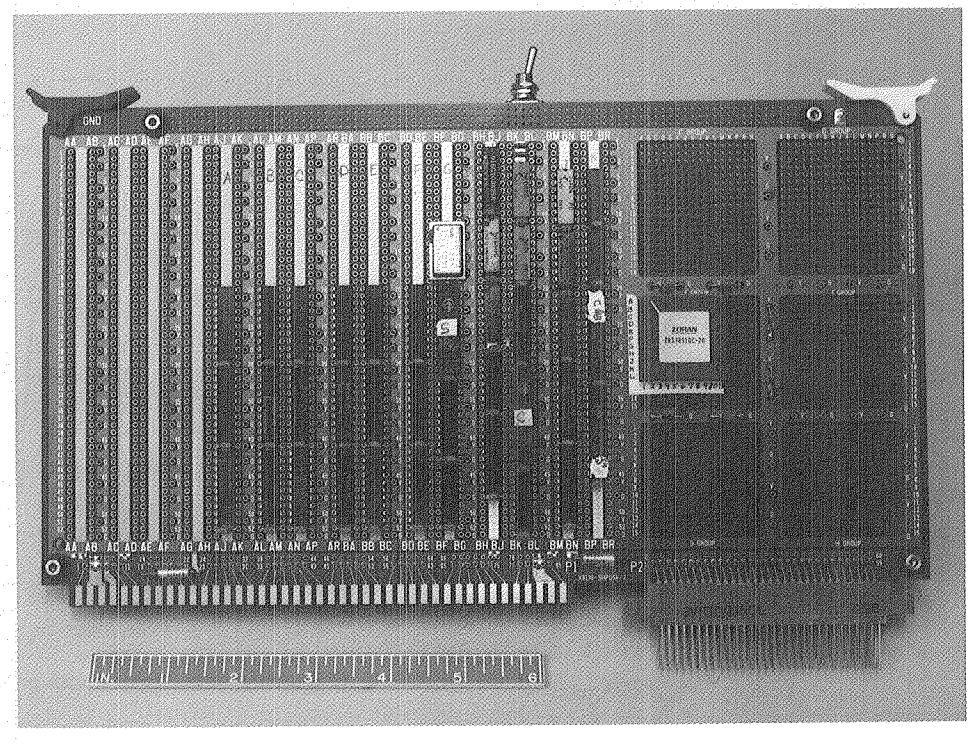

Fig. 7. Hardware realization of halfband filter: (a) block diagram; (b) breadboard

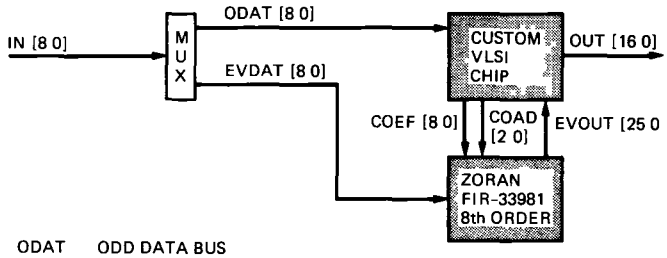

Fig 8 Custom VLSI coprocessor and ZORAN chip

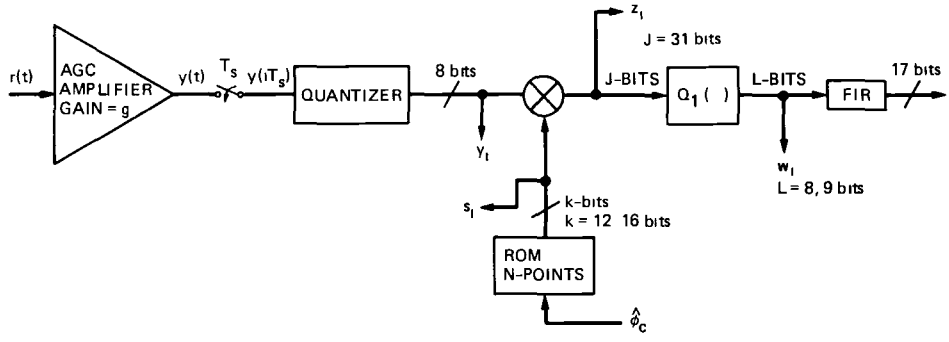

Fig. 9. Quantization model for analysis

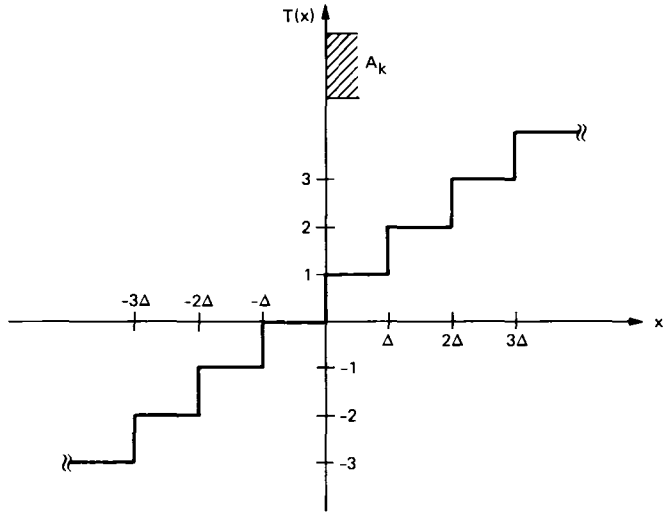

Fig. 10 A/D converter characteristic

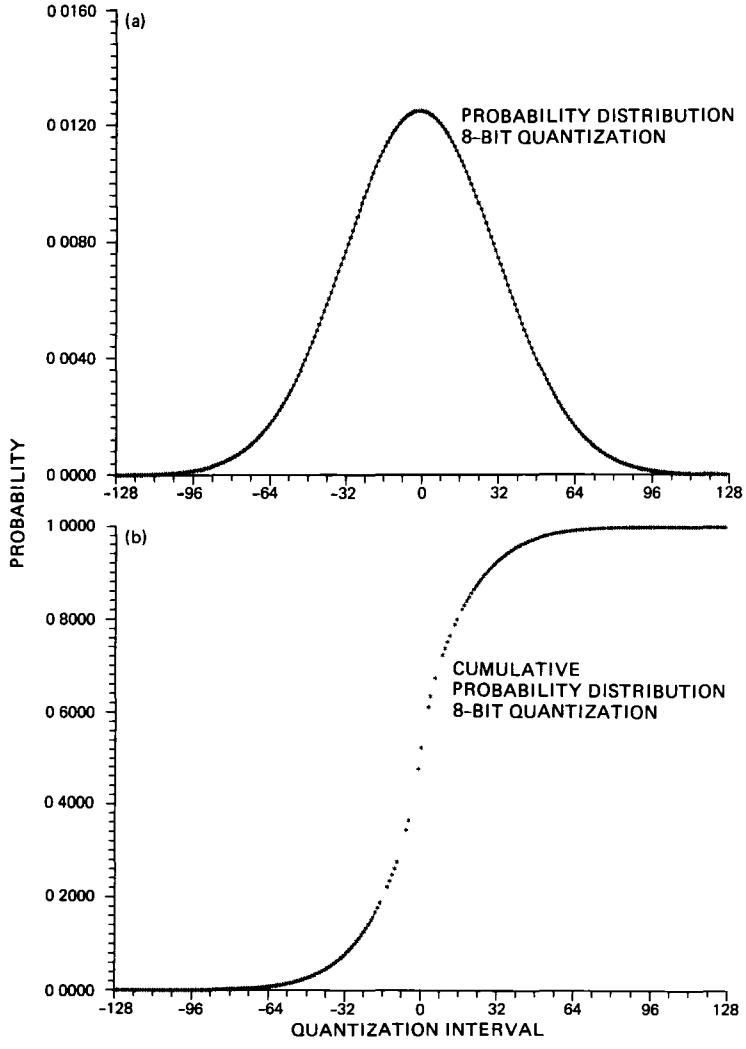

Fig 11 Probability functions for A/D converter output

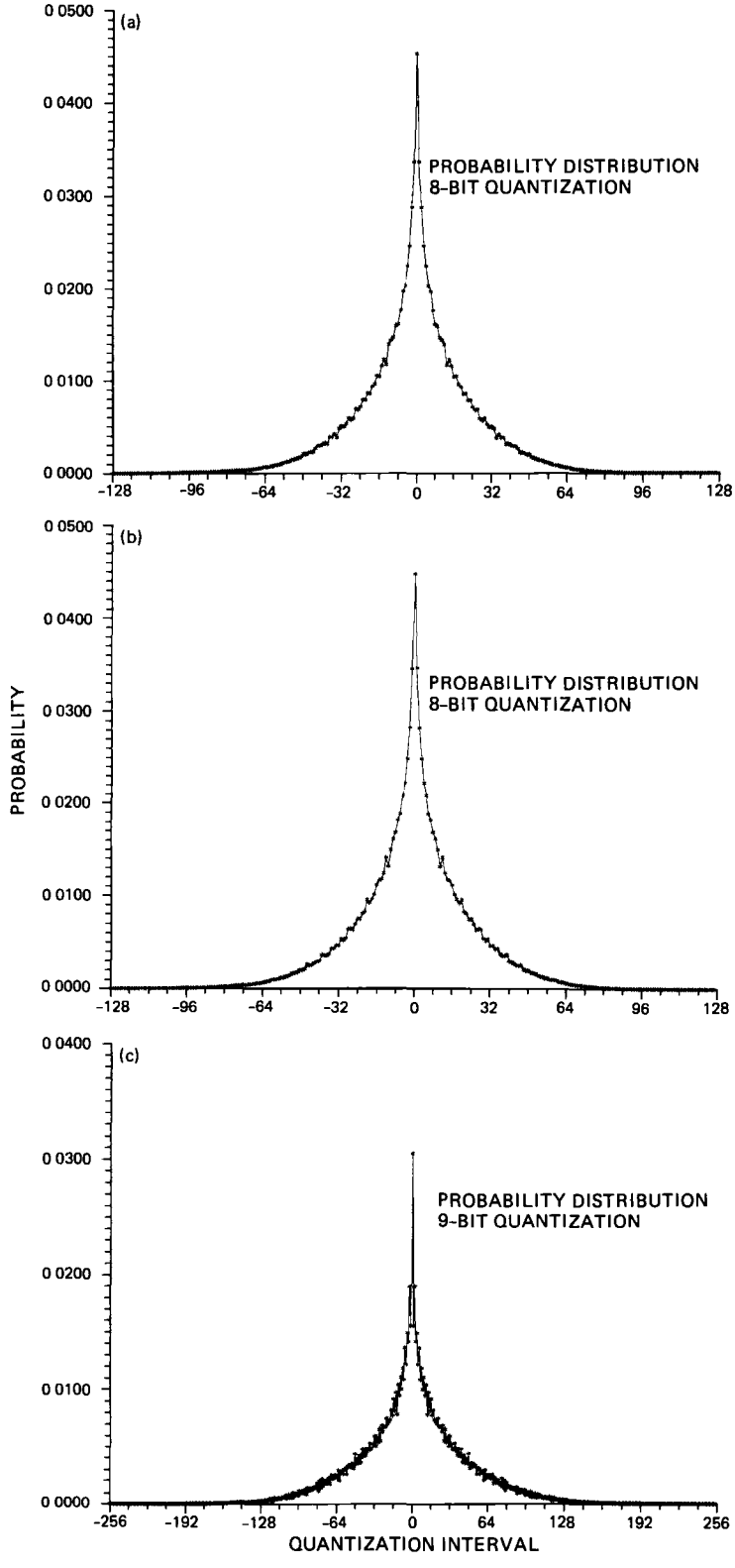

Fig 12 Probability densities at multiplier output for normal scaling (a) in-phase arm, (b) quadrature arm ($k = 12$, $L = 8$), and (c) in-phase arm ($k = 16$, $L = 9$)

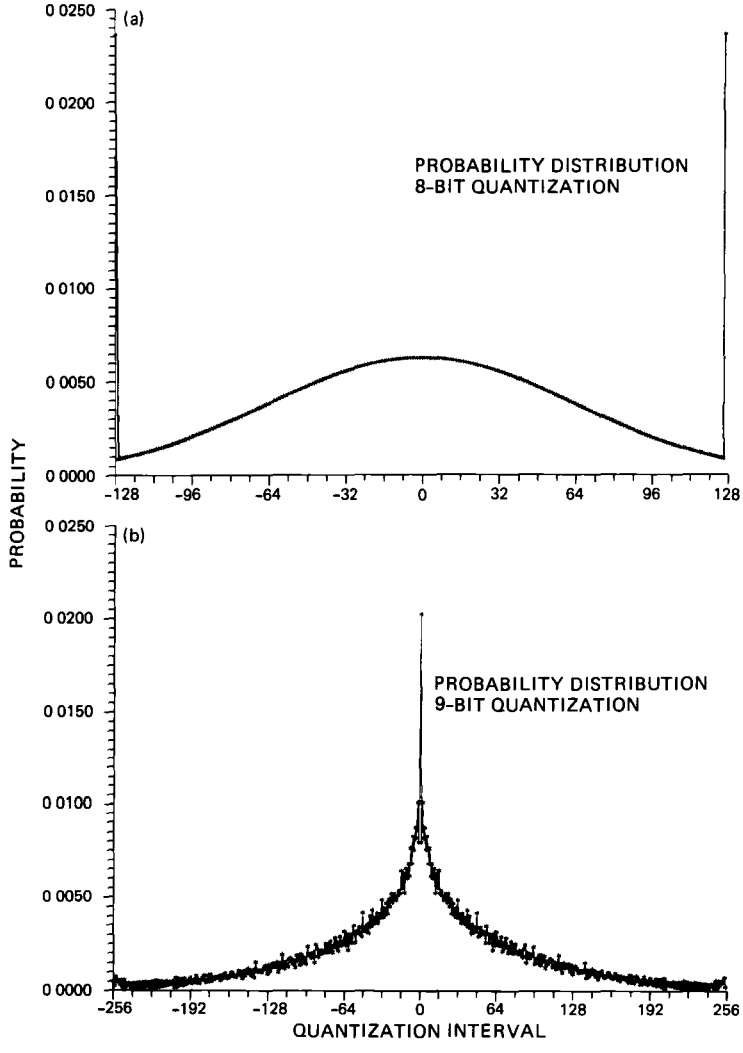

Fig 13 Probability densities at the A/D converter for signal scaled for input power of four times normal (a) input density (g = 1/2), (b) output density (k = 16, L = 9, g = 1/2)

Appendix
Chip Specification

In this appendix we outline the top-level specification of the design of a VLSI chip that complements the FIR chip, for a two chip solution of the halfband filter discussed in Section III The functional block diagram of this chip is shown in Fig A-1(a)

This chip operates in a fully synchronous mode from an input clock with frequencies up to 25 MHz The transfer of data from the input, through all subsequent stages within the pipeline, and to the output stage is performed on the rising edge of the input clock The 9-bit input data is delayed by a 12-stage shift register The delayed data ODATD is added to the input from the ZORAN chip As shown in Fig A-1(b), this chip contains an 8- by 9-bit-wide RAM that can be preloaded by the host In the normal mode of operation, 8 locations of the RAM are sequentially accessed, providing the coefficient stream to the ZORAN part

For host communication, during the initialization period, the input address strobe signal /AS (/ stands for active low) is asserted by the host to initiate a bus write cycle to the RAM The output data transfer acknowledge signal /DTACK, which is generated on-chip, is asserted when the input data is latched, so that the host may terminate the write cycle and thus negate /AS These two signals, and the input clock, are sufficient to provide both synchronous or asynchronous write cycles to the chip, depending on the type of host processor used to interface this chip

The 26-bit filtered data, EVOUT, is aligned with the 9-bit ODDAT as shown in Fig A-1(b) The least significant 7 bits are simply delayed by a pipeline delay to compensate for the delay introduced by the output stage Starting from the 9th bit (EVOUT-8), 9 bits are aligned to the input of the full adder, and the remaining bits are discarded because they are just sign extensions

The output of the 10-bit full adder, shown in Fig 11(b), is overflow protected at 17 bits, to prevent wrap-around when using the 2's complement number presentation A 17-bit output results

We have listed the pin list and the description of each signal Total pin count of this chip is 78 The timing specification of the signals and a detailed discussion of the operation of this chip are deferred to a later article

Table A-1. VLSI input/output definitions

Signal	Width	I/O	Name
CS	1	I	Chip Select
ODAT	9	I	Odd Data Bus
EVOUT	17	I	Filtered Even Data Bus
OUT	17	O	Output Data Bus
INH	9	I	Host Data Bus
/AS	1	I	Host Address Strobe
/DTACK	1	O	Data Transfer Acknowledge
INHA	3	I	Host Address Bus
COEF	9	O	Coefficient Data Bus
CLK	1	I	Input Clock
RESET	1	I	Reset Signal
VSS	4	X	+5 Volt Power Supply
GND	5	X	Ground Terminal

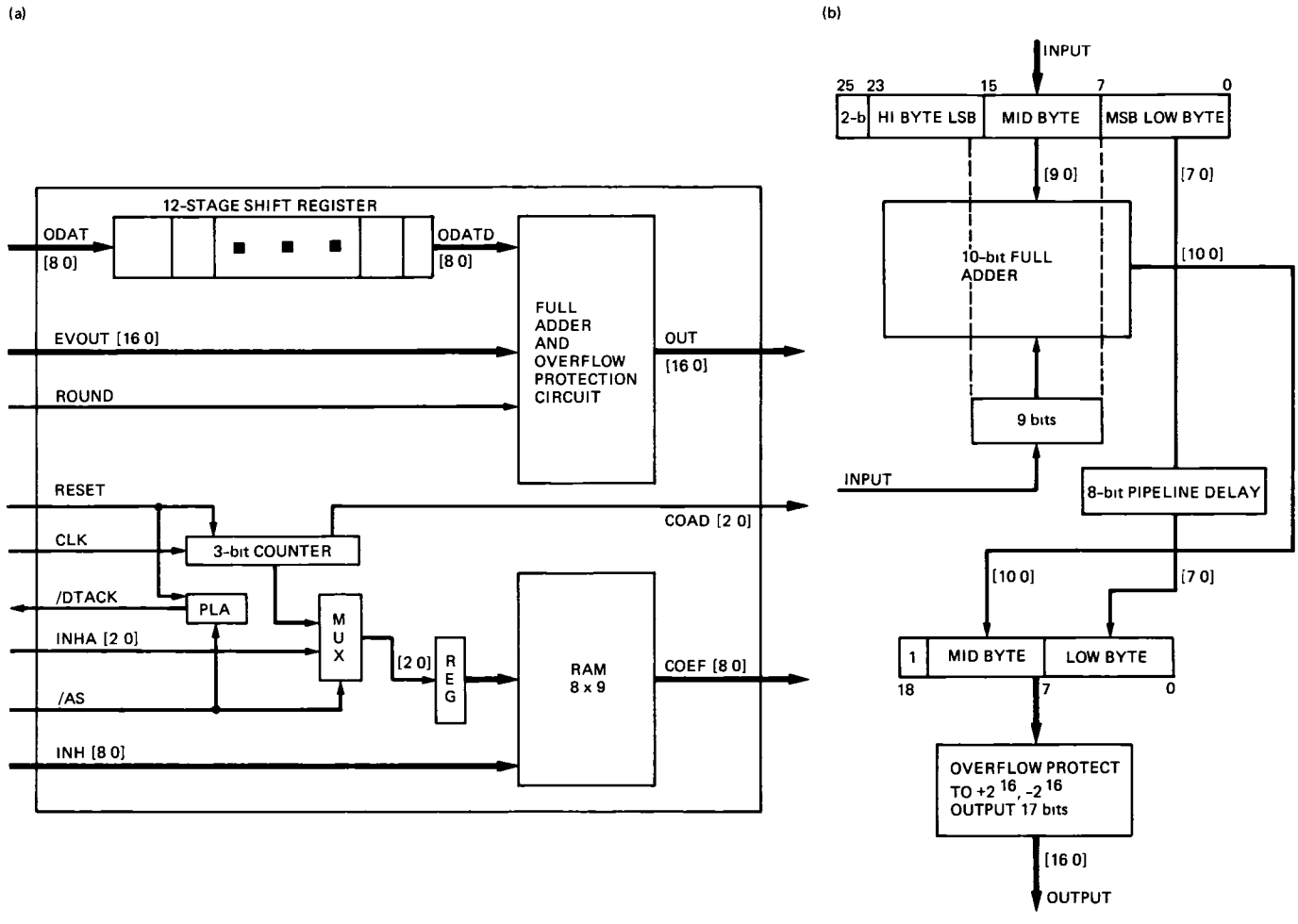

Fig A-1 Custom VLSI chip (a) functional block diagram, (b) full adder

Telemetry SNR Improvement Using the DSN Advanced Receiver With Results for Pioneer 10

W J Hurd, D H Brown,
V A Vilnrotter, and J D Wiggins
Communications Systems Research Section

A series of tracking tests was conducted in the spring of 1987 to demonstrate the reduced tracking threshold and the improved telemetry signal-to-noise-ratio performance of the DSN Advanced Receiver compared to current operational DSN systems The Pioneer 10 spacecraft, which is now out of the solar system, was tracked on four days The Advanced Receiver achieved an improvement in telemetry SNR of 1 to 1 5 dB over the operational system It was demonstrated that the spacecraft carrier signal is stable enough for tracking with a receiver carrier loop bandwidth of 0 5 Hz in the one-way mode and 0 1 Hz in the three-way mode, and that the Advanced Receiver is stable at 0 1 Hz This reduces tracking threshold by 10 to 15 dB compared to current receivers, which have minimum loop bandwidths of 1 to 3 Hz Thus, the Advanced Receiver will enable tracking of the Pioneer 10 spacecraft until its power source fails, circa 2000, which would not be possible with current DSN systems

I. Introduction

The digital Advanced Receiver (ARX) under development for the DSN can track signals that are 10 to 15 dB weaker than the threshold signal levels for current operational DSN receivers, as shown in Section V It can also improve the telemetry symbol signal-to-noise ratio (SSNR) by 1 to 1 5 dB compared to that achieved with current operational receivers used near their threshold signal levels This capability can enable the DSN to track the Pioneer 10 spacecraft until its power source fails, circa 2000, which would not be possible with current systems

To demonstrate this improved performance, a series of tests was conducted in the spring of 1987 using an existing breadboard of the ARX [1] The ARX tracked the Pioneer 10 spacecraft from the 64-m antenna at DSS 14, Goldstone, California This spacecraft was used because its carrier signal level is near the threshold for current DSN systems

The Advanced Receiver achieves its ability to track weak signals by using narrow bandwidth carrier-phase-locked loops obtained by optimizing the loop bandwidth for the specific conditions of carrier phase stability and carrier power to receiver noise spectral density This optimization was done in near-real time during the tests using a spectral estimation method previously described [2] The tracking threshold using the ARX is not limited by the stability of the receiver, as is the case for current operational receivers Instead, the thresh-

old is limited by the stability of the carrier signal received from the spacecraft Threshold improvements of 10 to 15 dB are thereby achieved

Besides using optimum carrier loop bandwidths, the Advanced Receiver reduces telemetry losses by realizing narrow bandwidth subcarrier and symbol tracking loops and by using sideband-aided carrier tracking to enhance carrier loop SNR without reducing loop bandwidth [1] In addition to the theoretical improvements the Advanced Receiver offers over operational systems, realization of all loops and of the symbol-detection-matched filters in one digital system virtually eliminates losses due to biases (dc offsets) and miscalibration

This article documents the improvements in telemetry symbol signal-to-noise ratio that were achieved during the Pioneer 10 tests The tests were conducted when the spacecraft was in both the one-way mode and the three-way mode In the one-way mode, there is no uplink signal from a ground station to the spacecraft, hence the spacecraft oscillator limits carrier phase stability In the three-way mode, the downlink carrier is phase locked to an uplink carrier transmitted from a ground station other than the receiving station Three-way tests were conducted with two different Sun–Earth probe (SEP) angles, both of which were small enough so that stability was limited by solar scintillation Carrier power levels were so weak that the Block IV DSN receiver operated from just above to just below the minimum acceptable margin of 8 5 dB, using the 3-Hz loop bandwidth

At all SNRs encountered, the Advanced Receiver achieved SSNRs 0 8 to 1 5 dB better than those of the operational DSN system, except when far-from-optimum loop bandwidths were used for experimental purposes, and except on one day This improvement is in agreement with theory At the weakest signal levels encountered, at low antenna elevation angles, the ARX had the ability to detect useful telemetry data, whereas the data detected by the standard equipment could not be decoded reliably

II. Test Description

The Pioneer 10 tracking tests were conducted on days 119, 121, 128, and 140 of 1987 using the 64-m antenna at DSS 14, Goldstone, California The station configuration is shown in Fig 1

The tests were conducted on a noninterference basis with standard Pioneer 10 tracking passes Data from the standard tracks were used to compare results The standard configuration for Pioneer 10 uses a Block IV receiver with a loop bandwidth of $2B_{LO}$ = 3 Hz The 1-Hz loop bandwidth available at 2 3 GHz (S-band) on the Block IV receiver was not used at any time during the tests The receiver output goes to a type A telemetry string consisting of a Subcarrier Demodulator Assembly (SDA), a Symbol Synchronizer Assembly (SSA), and a Telemetry Processor Assembly (TPA) computer Type B telemetry strings with Baseband Assembly (BBA) Demodulator Synchronizer Assemblies (DSAs) are not used for Pioneer 10 because of the low symbol rate, 64 symb/s The SSA and TPA calculate estimates of symbol signal-to-noise ratio (SSNR) using the moment method with unbiasing [3],[4] These estimates are displayed on the Central Monitor and Control terminal and can be logged and a hard copy obtained This hard copy was obtained on all days except the first day of tests The ARX used the unbiased split-symbol SSNR estimator [1],[5], which is statistically more accurate than the moment method The results of the two methods are directly comparable, since both are unbiased

The Advanced Receiver, as used in the Pioneer 10 tests, requires the spacecraft signal to be open-loop down-converted to an intermediate frequency (IF), with the carrier at 53 MHz ± 0 5 MHz This was done using the second Block IV receiver at the station, operated in the open loop mode An IF output of the Block IV receiver was used as the input to the ARX The ARX recorded its unbiased estimates of SSNR onto floppy disks, which were used in post-test processing to compare performance with that of the standard configuration The sequences of outputs of the ARX residual carrier phase detector were also logged on the disks Each day's pass was divided into several tests or cases The phase data from each test were processed in near-real time on a separate microprocessor to obtain power spectral densities of the phase processes and estimates of the optimum loop bandwidths The optimum loop bandwidth estimates were used to select parameters for the succeeding tests

III. Theoretical Performance

This section compares the theoretical performance of the ARX with that of the standard station configuration Performance is compared in terms of the theoretical loss in average telemetry symbol SNR due to phase error in the carrier, subcarrier, and symbol tracking loops Curves are presented for various carrier loop configurations for the ARX, taking into account the effects of phase noise from the Pioneer 10 oscillator This is the dominant instability in all of the tests when the spacecraft is in the one-way mode Similar results can be obtained for the three-way mode [2] For the three-way data in these tests, stability was limited by solar scintillation, but the stability was better than that of the Pioneer 10 oscillator

Figure 2 shows the theoretical loss in SSNR for the standard DSN system and for the ARX, for the one-way data, as

functions of input SSNR To establish a relationship between SSNR and the ratio of carrier power to noise density, note that the modulation index is 65 9 degrees, so the data power, P_d, is 7 dB more than the carrier power, P_c This, together with the symbol rate of 64 symb/s, results in a carrier-power-to-noise spectral density, P_c/N_0 (dB-Hz), which is 11 dB more than the SSNR The oscillator phase noise spectral density was modeled [2] using the measured phase data as $S(f) = S_1/f^3$ rad^2/Hz with $S(1)$ = 0 0012 rad^2/Hz (on each side of the carrier) The curves shown are the sum of the losses in the carrier, subcarrier, and symbol tracking loops

A. DSN System Losses

For the DSN system, oscillator noise was neglected, because the effect is negligible with the 3-Hz loop Carrier tracking loss was estimated as $-10 \log_{10} (1 - 1/\rho_L)$ (dB) [1] Theoretical radio loss ranged from 0 75 dB at an input SSNR of 3 to 1 2 dB at an SSNR of 0 dB At 3 dB, P_c/N_0 = 14 dB-Hz and the carrier margin in the 3-Hz loop is 8 2 dB, slightly below the recommended minimum margin of 8 5 dB In Fig 2, the loss curve for the DSN system is shown as a broken line for SNRs below this level, because cycle slipping occurs and the radio loss formula is not accurate

The SDA was operated in the narrow bandwidth mode Losses were obtained by interpolation to the symbol rate of 64 symb/s [2] Subcarrier losses ranged from 0 30 dB at an input SSNR of 3 dB to 0 36 dB at 0 dB

The SSA was operated in the medium range, narrow bandwidth mode The losses[3] range from 0 06 to 0 09 dB at SSNRs of 3 to 0 dB

B. Advanced Receiver Losses

Losses in the ARX arise from the carrier phase noise due to the Pioneer 10 oscillator as well as from the receiver noise Different carrier loop bandwidths were used, and sideband aiding was used in some cases In Fig 2, the residual-carrier-only cases and the sideband-aided cases are identified by RC and SA, respectively, followed by the carrier loop bandwidth in Hertz The subcarrier and symbol loop bandwidths were always 0 01 Hz

The receiver noise contribution to carrier (radio) loss is calculated as $-10 \log_{10} (1 - 1/\rho_L)$, where ρ_L is the loop SNR For residual carrier tracking, the loop SNR is $(P_c/N_0)/B_L$, where P_c/N_0 is the carrier-to-noise-density ratio and B_L is the loop bandwidth in Hertz Sideband aiding with optimum weighting increases the loop SNR by a factor of $1 + (P_d/P_c)S_L$, where S_L is the squaring loss factor, $1/(1 + 1/(2\,\text{SSNR}))$ At an SSNR of 3 dB, for example, the radio loss due to receiver noise is 0 17 dB with residual carrier tracking, and 0 03 dB with sideband aiding

The subcarrier loss is determined from the subcarrier loop SNR This is $\rho_{sc} = (P_d/N_0B_{sc})\,(2/\pi)^2 S_L$, where B_{sc} = 0 01 Hz is the subcarrier loop bandwidth The resulting loss is then approximately $4\,4(\rho_{sc})^{-1/2}$ dB Subcarrier loss is often significant because it decreases only as the square root of loop SNR, not as loop SNR This is why the loss is significant in the SDA In the ARX, the 0 01-Hz loop bandwidth is narrow enough to achieve loop SNRs of 35 to 32 dB Consequently, the loss was only 0 07 to 0 11 dB at SSNRs of 3 to 0 dB, respectively The ARX subcarrier loop thus improves SSNR by slightly over 0 2 dB compared to the SDA

The symbol synchronization loss is calculated similarly The loop is a transition tracking loop with a bandwidth of 0 01 Hz and a window width of W = 1/8 [6] For the Pioneer tests, the loop SNR varied from 36 to 34 dB, and the loss varied from under 0 02 to just over 0 02 dB

Figure 2 shows the losses for residual carrier loops with bandwidths of 0 25, 0 5, 0 7, and 1 0 Hz The 0 7-Hz loop is best at the lowest SSNRs, and the 1 0-Hz loop is best at the higher SSNRs This illustrates the optimization of carrier loop bandwidth The losses are much less than for the DSN system except for the 0 25-Hz bandwidth, which is much too narrow for the oscillator noise This bandwidth was used only so that its effect could be measured For the highest SSNR encountered, 3 dB, the ARX with a residual carrier 1 0-Hz loop has 0 76 dB less theoretical loss than the DSN system

When using sideband aiding, the best loop bandwidth is wider than that for a residual carrier loop This is because sideband aiding reduces the receiver noise component of phase error for a given bandwidth, and optimization results in a wider bandwidth to reduce the oscillator phase noise contribution The best bandwidth for the conditions encountered is approximately 1 3 Hz At an SSNR of 3 dB, sideband aiding reduces the loss by 0 15 dB relative to the 1 0-Hz residual carrier loop Total theoretical losses are only 0 19 dB

[1] ρ_L, the carrier loop SNR, was taken from Fig 1, Section TLM-20, of the *Deep Space Network/Flight Project Interface Design Handbook, Volume I Existing DSN Capabilities*, JPL Internal Document 810-5, Rev D, Jet Propulsion Laboratory, Pasadena, California

[2] As given in Fig 6 of Section TLM-30 (PC) (Rev A) of JPL Internal Document 810-5, Rev D, vol II, Jet Propulsion Laboratory, Pasadena, California

[3] Losses were obtained from Fig 18 of Section TLM-30 (PC) (Rev A) of JPL Internal Document 810-5, Rev D, vol II, Jet Propulsion Laboratory, Pasadena, California

for the best ARX configuration compared to 1 11 dB for the standard DSN system, an improvement of 0 92 dB

Although the theoretical improvement in SSNR due to sideband aiding was only 0 1 to 0 15 dB in the Pioneer 10 tests, it can be much more significant in some cases In the Pioneer tests, there was not much room for improvement over the residual carrier tracking loop This is because the carrier phase was stable enough that optimum bandwidth residual carrier loops yielded small losses This would not be the case at lower SNRs and the same phase stability For example, suppose the optimum residual carrier loop had a radio loss of 0 8 dB Sideband aiding could then reduce the loss typically by 0 6 dB, depending on modulation index and SSNR

IV. Results

The data collected on the four days of tracking indicate that the ARX provides an improvement in received symbol SNR of 0 8 to 1 5 dB under all signal conditions encountered In certain cases, the ARX was able to track and produce decodable telemetry when the Block IV was unable to do so

For each day, the recovered symbol SNR is plotted against time for the ARX and the standard station configuration in Figs 3 through 6 The ARX carrier tracking parameters were changed several times each day in order to provide a range of data for analysis Each set of parameters defined one test During each test, the sequence of outputs of the residual carrier phase detector was recorded onto a floppy disk After each test, while the next test was in progress, the phase data were processed on an auxiliary computer, obtaining power spectral density plots and estimates of the contributions to phase error variance of receiver noise and of phase process noise [2] The phase variance estimates were then used to estimate the optimum loop bandwidths for planning parameters of future tests

A case-by-case summary of ARX carrier loop parameters, the symbol SNRs obtained by the ARX and by the standard station, and the gain in SSNR achieved by the ARX is given in Table 1 The subcarrier and symbol loop bandwidths were fixed at 0 01 Hz, except for the first four cases on DOY 140, when they were 0 2 Hz The subcarrier frequency was 32 765 kHz The telemetry was received at 32 b/s, for a symbol rate of 64 symb/s

On each day, there is a general trend of decreasing SNR as a function of time due to the decrease in antenna elevation angle On DOYs 119 and 121, the spacecraft was transmitting in the one-way mode On DOYs 128 and 140, both the one-way and three-way modes were used, as indicated in Table 1 and in Figs 5 and 6

The following paragraphs discuss the operations, ARX configurations, and results on a day-by-day basis

A. DOY 119

The first day of Pioneer 10 tracking was DOY 119 Tracking was one way, and there was no a priori information available as to the stability of the spacecraft oscillator or the minimum carrier loop bandwidth which could be used The objectives of this day's tests were to determine the approximate optimum and minimum residual carrier loop bandwidths by tracking with loops of varying bandwidths, and to test sideband aiding

As on all days, the ARX logged its measurements of SSNR on floppy disks However, on this day only, the operations crew was not asked to log the SSA measurements of SSNR Instead, a partial log of SDA SSNR measurements was made manually from observing the Complex Monitor and Control (CMC) display Thus the comparison of SSNR results for DOY 119, Fig 3, is not as accurate as those for the succeeding days

Tests were run with a variety of configurations The first case was residual carrier tracking with a 1 0-Hz loop bandwidth, and the second case was the same bandwidth with sideband aiding Both achieved SSNRs approximately 0 9 dB better than the standard station While performing the spectral analysis, we ran the third case with a 0 25-Hz residual carrier loop Although able to track, the 0 25-Hz loop resulted in a 0 2-dB decrease in recovered SSNR compared with the standard station configuration The near-real-time analysis indicated a bandwidth of 0 7 to 0 9 Hz to be optimum, corroborating the poor performance of the 0 25-Hz loop This poor performance is attributable to the fact that the loop bandwidth is too narrow to track the phase process noise of the Pioneer 10 oscillator

Cases 4, 5, 8, and 9 used residual carrier loops of bandwidths of 0 7, 0 5, 1 0, and 1 0 Hz, respectively Cases 6 and 7 used 2 0- and 1 0-Hz sideband-aided loops All achieved SSNRs 0 7 to 1 3 dB better than the standard station

B. DOY 121

On this day, Fig 4, we repeated the activities of DOY 119 with emphasis on improving the recording of data The station personnel produced a hard copy of the station log of recovered SSNRs On this day, the improvement in SSNR with the Advanced Receiver was typically 0 3 dB The curves in Fig 4 are not completely distinguishable, thus, Table 1 should be used to compare results It is not known why the improvement was less on this day than on the other days For case 3, there

was no improvement relative to the standard station, because the loop bandwidth of 0 5 Hz was below optimum

Near-real-time analysis indicated that the best performance at low SNRs could be achieved with a 1 3-Hz sideband-aided loop, with a resulting loss of approximately 0 25 dB It was the intention to use this minimum loss configuration for the final, low-elevation-angle case to emphasize the improvement possible with the ARX Unfortunately, an error in operator control of the ARX resulted in the use of a 1 3-Hz residual carrier loop, which achieved an improvement relative to the standard station of approximately 0 3 dB

A series of acquisition tests was run between cases 4 and 5 Track was repeatedly interrupted, and all three loops were reacquired The fast carrier acquisition method was used, with a sampling rate of 64 samples per second, using 64-point FFTs and accumulating four successive FFT outputs noncoherently, i e , for four seconds The required carrier frequency prediction accuracy was ±32 Hz, as limited by the sampling rate The limitation of 64 samples per second was due to the particular software implementation, wherein the rate cannot exceed the symbol rate This limitation will be removed in the future Approximately ten reacquisitions were made, with various frequency errors up to ±25 Hz Symbol SNR was monitored every 20 seconds, the averaging and display update time, to determine lock All acquisitions were successful, with acquisition of all loops and good SSNR measurements occurring within one minute

C. DOY 127/128

This day afforded the first opportunity to track the spacecraft in the three-way mode It was anticipated that narrower loop bandwidths could be used than for the one-way mode, since the transmitted carrier reference would be a hydrogen maser rather than the spacecraft oscillator The results are shown in Fig 5

For the first half of the pass, cases 1 through 6, the spacecraft transmitted in the one-way mode Data collected here are consistent with earlier results The optimum bandwidth was 0 9 Hz, yielding total theoretical system losses under 0 5 dB Improvement over the standard station was 0 8 to 1 1 dB, except for case 3, for which the loop bandwidth was too wide and the improvement was only 0 6 dB

Transmission changed to the three-way mode at 0145, during case 7, and the receiver lost lock The SSNR estimates for this case should not be used for performance comparisons After acquiring the three-way transmissions, as expected, the resulting decrease in carrier phase noise allowed for tracking with narrower loop bandwidths Bandwidths of 0 5, 0 25, and 0 125 Hz were used, with a bandwidth of 0 3 Hz determined as optimum Performance improvements relative to the standard station were 1 0 to 1 3 dB

D. DOY 140

DOY 140 provided another chance to study the differences between one-way and three-way performance The first three cases were one-way transmissions, and the results again agreed with the previous data The analysis indicated an optimum bandwidth of 1 0 Hz for this day

Transmission changed to the three-way mode at 2320 The loop bandwidth was again varied, and the optimum bandwidth was determined to be 0 75 Hz At the time, this value was thought to be surprisingly large The analysis was repeated several times and yielded consistent results Further analysis conducted after the experiment resulted in the realization that on this day, the spacecraft was fairly close to the Sun Specifically, the Sun–Earth probe (SEP) angle was 12 degrees on DOY 140 and 24 degrees on DOY 128 When the SEP angle is small, the solar corona and solar winds affect the phase stability of the received carrier Even though a much more stable carrier phase was expected, the ARX was able to track and measure the noisy phase process so that the carrier loop bandwidth could be optimized in near-real time Performance improvements relative to the standard station were as much as 1 5 dB at low elevation angles

V. Threshold Improvement

Figure 7 illustrates the carrier threshold improvement which is achievable by loop bandwidth optimization The optimum carrier loop bandwidth (left-hand ordinate) for threshold tracking is shown as a function of phase process noise spectral density for oscillator phase noise and for solar scintillation-limited phase noise Optimum loop bandwidth is defined as the loop bandwidth which results in a phase error variance of 0 2 rad^2 at the lowest P_c/N_0 Optimization at this phase error variance was chosen because this is the variance for a phase-locked loop with no process noise and a loop SNR of 7 dB using linear theory Under these conditions, phase-locked loops slip cycles infrequently

The right-hand ordinate shows the minimum or threshold carrier power to receiver noise spectral density required for adequate telemetry performance The minimum P_c/N_0 for adequate margin was taken as the level which would achieve a 10-dB loop SNR This is slightly more conservative than the approximate loop SNR of 9 dB required to achieve the 0 2-rad^2 phase error variance at the point of optimization This conservative approach is taken because of the lack of experimental data under threshold conditions

The 1-Hz, 3-Hz, 10-Hz, and 30-Hz loop bandwidths of the DSN receivers are indicated along the left-hand axis of Fig 7 Note that the 1-Hz bandwidth is available only on the Block IV receivers and only at S-band, and that it is not routinely used because of phase instabilities, static phase errors due to Earth-rate Doppler rate, and operational difficulties in compensating for Doppler rate Note also that the DSN loops are specified in terms of $2B_{LO}$ at a "threshold" SNR, but that the actual one-sided loop bandwidth is approximately equal to the specified bandwidth for the range of loop SNRs of interest here Along the right-hand axis is indicated the range of P_c/N_0 that occurred in the Pioneer 10 tests The performance of the DSN 3-Hz loops degrades rapidly as P_c/N_0 decreases below 13 dB-Hz

Two phase-process-noise spectral shapes are considered in Fig 7 the $1/f^3$ shape characteristic of oscillator noise at low frequencies, and a $1/f^{8/3}$ shape assumed for phase noise induced by solar scintillation In the one-way mode, we observed a phase spectral density due to the Pioneer 10 oscillator of approximately -30 dBc/Hz, 1 Hz from the carrier As indicated, the loop bandwidth which optimizes tracking threshold is 0 5 Hz, and the minimum carrier SNR for adequate telemetry is 7 dB-Hz This is 6 2 dB lower than the 13 2 dB-Hz level required to have the minimum recommended carrier margin with a 3-Hz bandwidth DSN receiver loop (Although we tracked well with a 0 5-Hz loop during the tests, performance was better with a 1-Hz loop, because the carrier SNR was higher than the threshold SNR for the actual phase noise density)

In the three-way mode, we observed spectral levels due to solar scintillation of approximately -30 dB/Hz at an SEP of 12 degrees, and -40 dB/Hz at 24 degrees The corresponding threshold bandwidths are approximately 0 4 Hz and 0 08 Hz, and the threshold carrier SNRs are approximately 6 dB-Hz and -1 dB-Hz These thresholds are 7 dB and 14 dB lower than for the 3-Hz loops of the current DSN receivers This illustrates that threshold improvements of 10 to 15 dB over the current receivers are useful, and that they are achieved using the Advanced Receiver

Finally, it was noted that both the ARX residual carrier loops and the operational receivers resulted in radio losses of approximately 0 8 dB under the conditions defined here as threshold The ARX can usually reduce this loss to approximately 0 2 dB by using sideband aiding

VI. Conclusions

These Pioneer 10 tracking tests show that the Advanced Receiver achieves significant performance improvements over current operational DSN systems The threshold for acceptable carrier tracking is reduced by 10 to 15 dB, and the telemetry symbol SNR is improved by 1 to 1 5 dB when operating near threshold

During the tests, the input SSNRs varied from 3 dB when the DSS antenna was at high elevation angles to 0 dB at low elevation angles, and the corresponding carrier power to noise spectral densities varied from 14 to 11 dB-Hz The theoretical improvement in SSNR achieved by the ARX is 0 92 dB at an SSNR of 3 dB, when the ARX uses sideband aiding and a 1 3 Hz carrier loop bandwidth The theoretical improvement increases to approximately 1 3 dB at an SSNR of 0 dB

The experimental results confirmed the theory At high elevation angles and input SSNRs of 2 to 3 dB, the ARX performed from 0 7 to 1 1 dB better than the standard DSN system except when far-from-optimum loop bandwidths were deliberately used The improvement was 1 0 to 1 5 dB at SSNRs of approximately 1 dB

The improvement at low SSNRs is most important because decoding is unreliable below approximately 0 dB, at the symbol detector output For the last hour or so of each pass, the ARX achieved SSNRs above 0 dB, i e , decodable data, whereas the standard station obtained SSNRs below 0 dB

Finally, use of the Advanced Receiver can extend the tracking range for Pioneer 10 by 1 to 1 5 dB at the current telemetry rate of 32 b/s, compared to use of the Block IV receiver with a 3-Hz loop It can extend the tracking range by an additional 3 dB by reducing threshold, thereby enabling good carrier tracking when the total signal is so weak that the data rate is reduced to 16 b/s This can enable tracking until the spacecraft power source fails, near the turn of the century

References

[1] D H Brown and W J Hurd, "DSN Advanced Receiver Breadboard Description and Test Results," *TDA Progress Report 42-89*, vol January–March 1987, Jet Propulsion Laboratory, Pasadena, California, pp 48–66, May 15, 1987

[2] V A Vilnrotter, W J Hurd, and D H Brown, "Optimized Tracking Carriers With Phase Noise, Including Pioneer 10 Results," *TDA Progress Report 42-91*, vol July–September 1987, Jet Propulsion Laboratory, Pasadena, California, pp 141–157, November 15, 1987

[3] J W Layland, "On S/N Estimation," *Space Programs Summary 37-48 III*, Jet Propulsion Laboratory, Pasadena, California, pp 209–212, December 1967

[4] Q Vo, "Signal-to-Noise Ratio and Combiner Weight Estimation for Stream Combining," *TDA Progress Report 42-76*, vol October–December 1983, Jet Propulsion Laboratory, Pasadena, California, pp 86–98, February 15, 1984

[5] M K Simon and A Mileant, "SNR Estimation for the Baseband Assembly," *TDA Progress Report 42-85*, vol January–March 1986, pp 118–126, Jet Propulsion Laboratory, Pasadena, California, May 15, 1986

[6] W J Hurd and T O Anderson, "Digital Transition Tracking Synchronizer for Low SNR Coded Systems," *IEEE Transactions on Comm Theory*, vol COM-18, no 2, pp 141–147, April 1970

Table 1 Case-by-case results

DOY	Case	Name	Carrier loop		Way	Symbol SNR, dB		
			BL	RC/SA		ARX	STN	Gain
118	1	RC1HZ	1 0	RC	1	2 64	1 71	0 93
118	2	SA1HZ	1 0	SA	1	2 70	1 78	0 92
118	3	RCQHZ	0 25	RC	1	1 17	1 34	−0 17
118	4	RC700	0 7	RC	1	2 27	0 98	1 29
118	5	RC500	0 5	RC	1	1 83	1 09	0 74
118	6	SA2HZ	2 0	SA	1	1 79	0 51	1 28
118	7	SADEWT	1 0	SA	1	1 09	−0 22	1 31
118	8	RC1HZ2	1 0	RC	1	0 61	−0 61	1 22
118	9	RC1HZ3	1 0	RC	1	−0 02	−0 87	0 85
121	1	TRKTST1	1 0	RC	1	2 70	2 41	0 29
121	2	TRKTST2	1 0	SA	1	2 78	2 35	0 43
121	3	TRKTST3	0 5	RC	1	2 30	2 35	−0 05
121	4	TRKTST4	0 5	SA	1	2 30	1 97	0 33
121	5	PNSET(A)	1 3	RC	1	1 10	0 69	0 41
						0 64	0 28	0 36
						0.22	0 04	0 18
127	1	RC091271	0 9	RC	1	2 85	1 93	0 92
127	2	RC05128	0 5	RC	1	2 80	2 02	0 78
127	3	RC2127	2 0	RC	1	2 59	2 01	0 58
127	4	RC091272	0 9	RC	1	2 72	1 85	0 87
127	5	SA15127	1 5	SA	1	2 71	1 62	1 09
127	6	RC091283	0 9	RC	1	2 53	1 63	0 90
128	7	1WAY3WAY*	2 0	RC	1/3*	1 03*	1 38*	–
128	8	RC051282	0 5	RC	3	1 40	0 35	1 05
128	9	RC25128	0 25	RC	3	1 41	0 33	1 08
128	10	RC125128	0 125	RC	3	1 16	−0 11	1 27
128	11	RC251282	0 25	RC	3	0 30	−0 73	1 03
140	1	RC051401	0 5	RC	1	2 01	1 30	0 71
140	2	RC2140	2 0	RC	1	2 09	1 37	0 72
140	3	RC08140	0 8	RC	1	2 49	1 49	1 00
140	4	R01140	1 0	RC	3	1 97	0 78	1 19
140	5	RC75140	0 75	RC	3	1 87	0 78	1 09
140	6	RC051412	0 5	RC	3	1 56	0 62	0 94
141	7	RC25141	0 25	RC	3	1 16	−0 23	1 39
141	8	RC38141	0 37	RC	3	1 04	0 01	1 03
141	9	SA09141	0 9	SA	3	0 82	−0 70	1 52

*Lost lock when signal changed to three-way

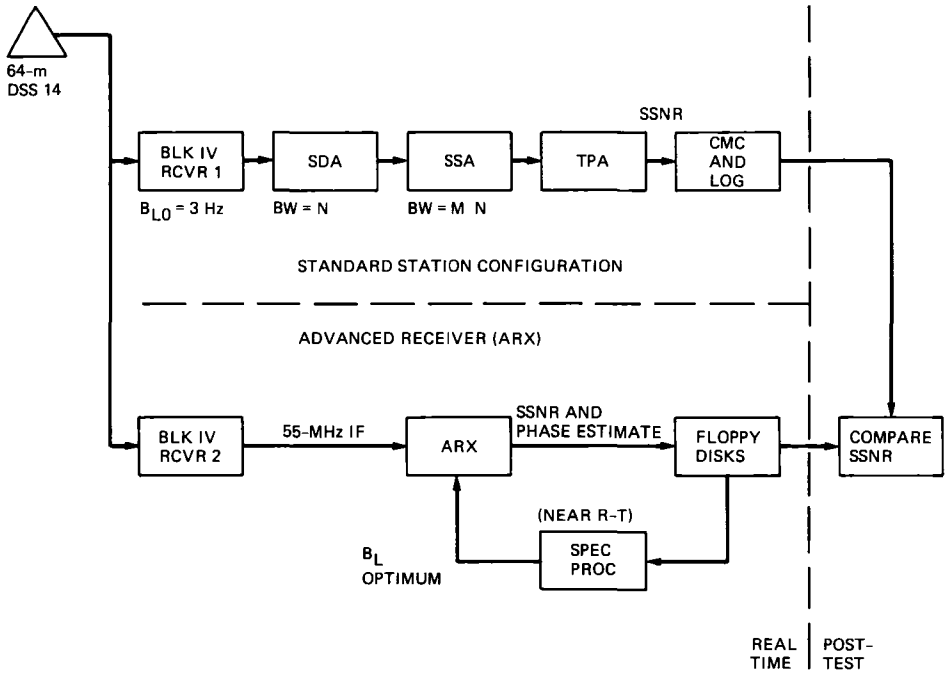

Fig 1 Test configuration

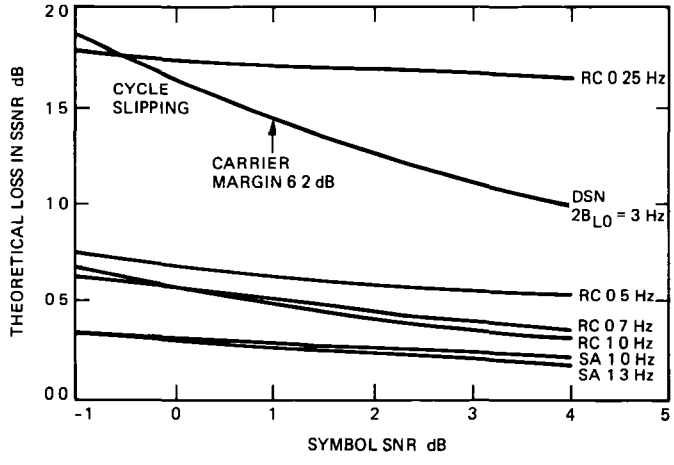

Fig 2 Theoretical losses for the DSN system and the advanced receiver for the Pioneer 10 oscillator one-way mode (RC = residual carrier, SA = sideband aided)

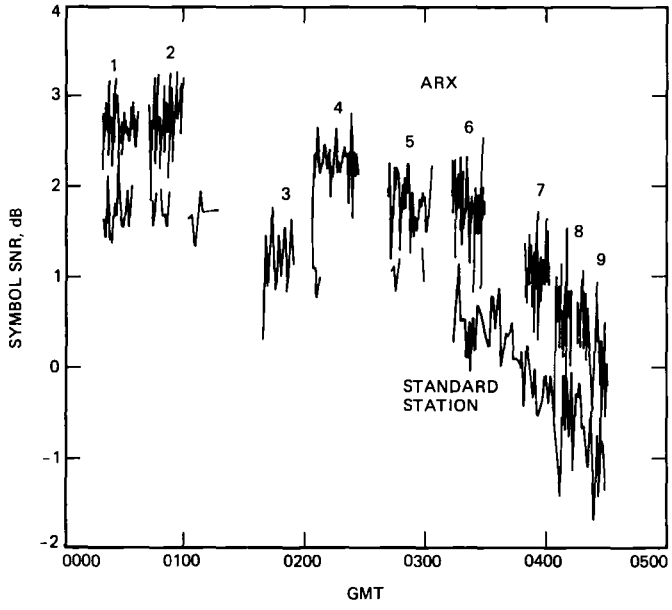

Fig 3 Symbol SNR versus time, DOY 119

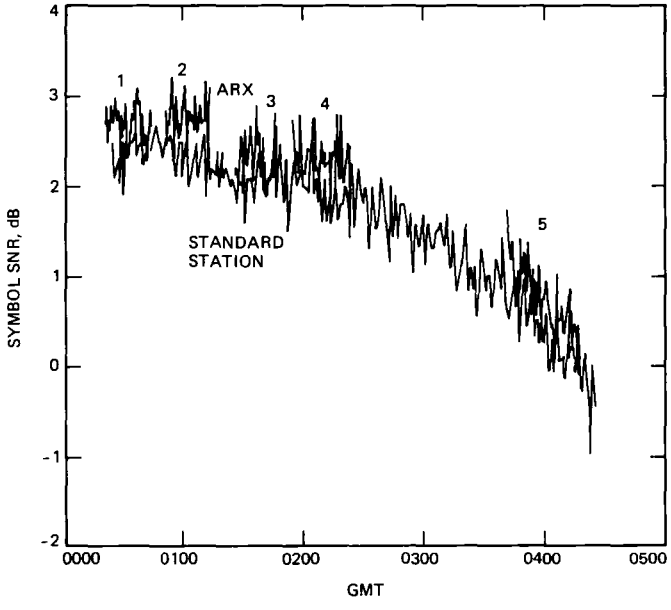

Fig 4 Symbol SNR versus time, DOY 121

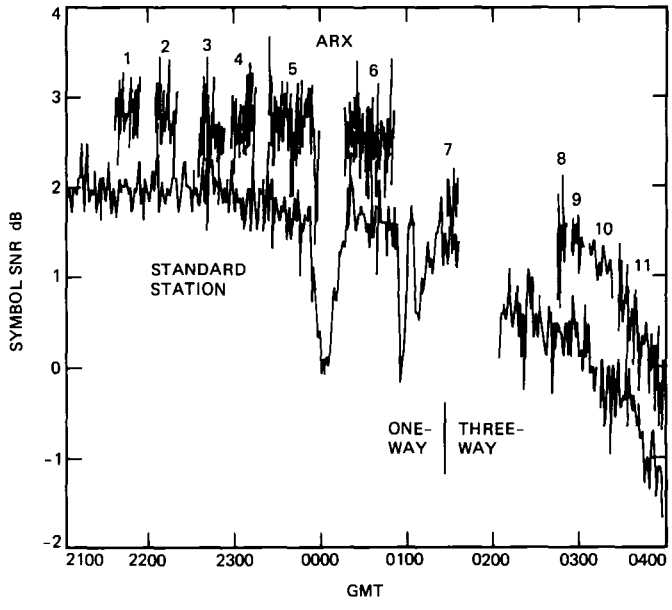

Fig 5 Symbol SNR versus time, DOY 128

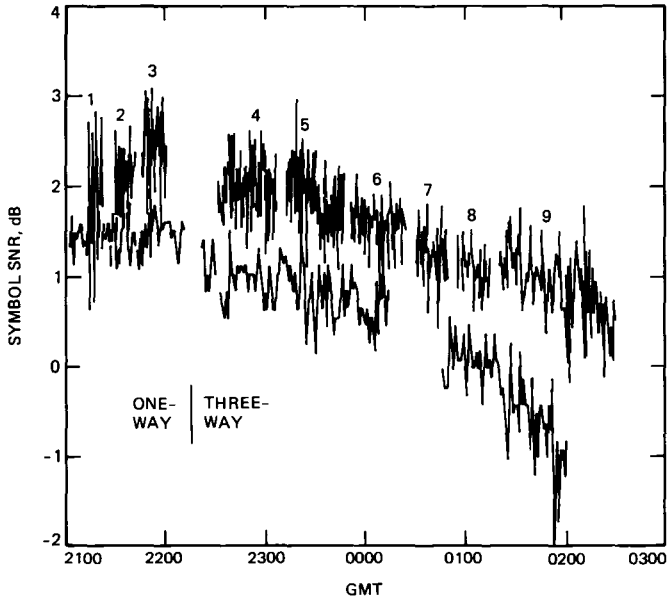

Fig 6 Symbol SNR versus time, DOY 140

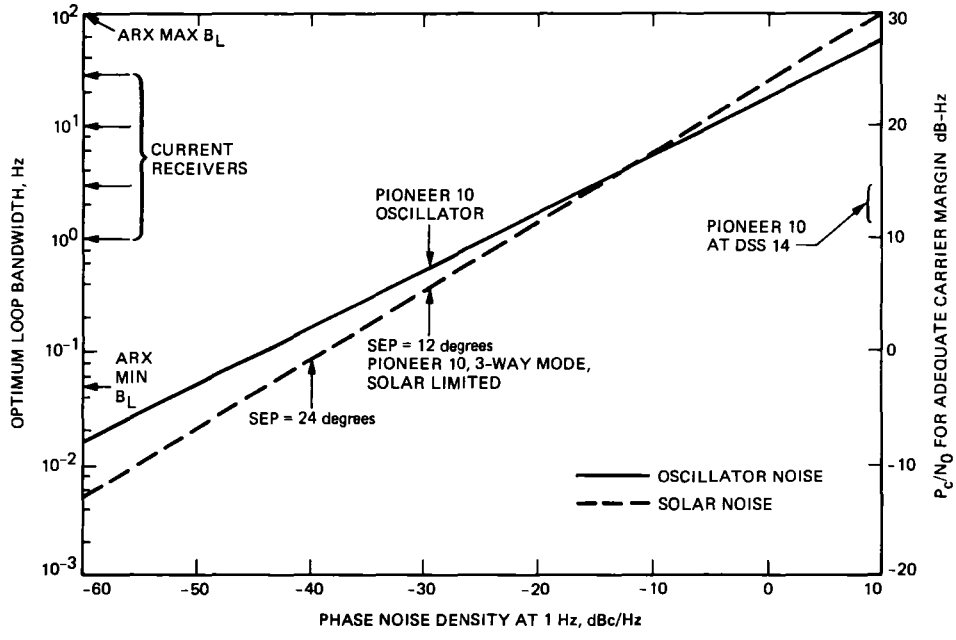

Fig 7 Carrier loop bandwidth to optimize threshold versus phase noise density

Advanced Receiver Tracking of Voyager 2 Near Solar Conjunction

D H Brown, W J Hurd, V A Vilnrotter, and J D Wiggins
Communications Systems Research Section

The Advanced Receiver (ARX) was used to track the Voyager 2 spacecraft at low Sun–Earth–probe (SEP) angles near solar conjunction in December of 1987 The received carrier signal exhibited strong fluctuations in both phase and amplitude The ARX used spectral estimation and mathematical modeling of the phase and receiver noise processes to set an optimum carrier tracking bandwidth This minimized the mean square phase error in tracking carrier phase and thus minimized the loss in the telemetry signal-to-noise ratio due to the carrier loop Recovered symbol SNRs and errors in decoded engineering data for the ARX are compared with those for the current Block III telemetry stream Optimum bandwidths are plotted against SEP angle Measurements of the power spectral density of the solar phase and amplitude fluctuations are also given

I. Introduction

It has long been known that strong solar corona effects can degrade the performance of telemetry systems In particular, the solar corona causes variation in the phase of the received carrier [1], [2] These effects are especially strong when the Sun–Earth–probe (SEP) angle is small For optimum coherent receiver performance, these carrier phase variations should be tracked by the receiver In a phase-locked loop receiver, this implies the use of a carrier loop bandwidth wide enough to track the phase variation Unfortunately, loop bandwidths cannot be made arbitrarily large because the loop signal-to-noise ratio decreases with increasing loop bandwidth This causes losses from phase jitter and cycle slipping at very low loop signal-to-noise ratios For a given thermal noise spectral density (N_0), phase process spectral density, and carrier power, there is an optimum bandwidth which minimizes the total energy in the phase error signal and hence minimizes losses [3]

The Voyager 2 spacecraft, currently en route to its encounter with Neptune in 1989, passed within a 0 56-degree SEP angle on day of year (DOY) 359, December 25, 1987 This provided an opportunity to study solar effects and to evaluate a method for optimizing carrier tracking loop bandwidths developed for use with the DSN Advanced Receiver (ARX) The ARX is a digital receiver which performs carrier demodulation, subcarrier demodulation, and symbol synchronization in one integrated unit [4] The optimization method was first used with the ARX during tracking experiments performed with the Pioneer 10 spacecraft in the spring of 1987 [5] In these experiments, the aim was to quantify the phase process associated with the Pioneer 10 spacecraft oscillator Since the Pioneer 10 signal level is nearing threshold, it is important that

it be tracked with the narrowest loop bandwidth possible During these tests, phase processes much stronger than expected were observed Investigation revealed this to be a solar effect, already significant for the weak Pioneer signal at an SEP angle of 11 8 degrees This suggested that the method for optimizing loop bandwidth in the face of the fixed phase process associated with the Pioneer spacecraft oscillator could be applied to the time varying process of solar phase scintillation

The ARX is well suited to this type of optimization Since it implements its tracking loop filters digitally, filter bandwidths can be set with great accuracy and flexibility Bandwidths available cover a range from approximately 0 05 to 100 Hz with better than 10 percent accuracy The tracking bandwidth can also be changed in real time without dropping carrier lock The measurement of the received carrier phase is facilitated by the fact that the ARX employs digital phase detection The ARX records a sequence of outputs from its digital phase detector onto a floppy disk An auxiliary computer then performs spectrum analysis on these records in near-real time and, from this, estimates the phase process spectral density and thermal noise level, and then the optimum tracking loop bandwidth In the future, the spectrum analysis and bandwidth optimization will be performed in the ARX in real time

The main goal of this experiment was to demonstrate the telemetry performance of the ARX with near-real-time bandwidth optimization and to compare it with the current receiver chain in the presence of strong solar corona effects Additionally, we hoped to gain a better understanding of solar corona effects and of the behavior of digital phase-locked loops in this type of environment

II. Experiment Description

The experiment involved tracking the Voyager 2 spacecraft at decreasing SEP angles with the ARX and the standard station configuration, and decoding and evaluating the two recovered telemetry streams The success criterion for the experiment was that the decoded data from the ARX data stream have a comparable number of errors or fewer errors than the standard station This allowed for a good relative performance measure, independent of SNR estimators which could be affected by amplitude variation

The ARX provides improved performance by using the near-real-time bandwidth optimization technique as described above As the system noise temperature and the magnitude of the phase process increase, the optimization algorithm computes new bandwidths and keeps the losses minimized Operationally in the DSN, using the Block III receiver, the strategy for dealing with the solar effects is to use a wide loop bandwidth to track the phase perturbations With low or highly variable signal levels, this approach can lead to losses from excessive carrier phase jitter It should be emphasized, however, that at very low SEP angles, the introduction of amplitude variation makes this a highly complex tracking environment For example, some instances may occur where the amplitude fading is so severe that no phase-locked loop could maintain lock In such a case, wide bandwidths may be more desirable in terms of reacquisition

A. Experiment Configuration

The experiment configuration used is shown in Fig 1 All tracks in this experiment were done on the 34-meter high efficiency antenna at Goldstone (DSS-15) The lower path in Fig 1 shows the standard station configuration The standard configuration uses a Block III receiver, a Subcarrier Demodulator Assembly (SDA), and a Symbol Synchronizer Assembly (SSA) The output of the SSA is a stream of soft-quantized symbols which is sent to a Maximum Likelihood Convolutional Decoder (MCD) The MCD outputs bits to a Telemetry Processor Assembly (TPA) which sends the data back to JPL via the ground communications facility (GCF) Backup tapes are also made at the station

At the minimum SEP angle, the Block III tracked with a nominal two-sided threshold bandwidth of 48 Hz, $2B_{L_0}$ Operating at +15 dB above threshold, this translates into an actual one-sided loop bandwidth of B_L = 70 Hz The SDA was configured with a medium loop bandwidth which is a nominal 0 375 Hz The SSA was configured for the medium range, narrow subrange, which at this symbol rate yields a loop bandwidth of 0 4 Hz

The ARX used an independent parallel channel shown as the upper branch in Fig 1 The VLBI downconverter mixes the low noise amplifier output against 8100 MHz At the nominal Voyager 2 carrier frequency of 8420 MHz, this centers the frequency band of interest at 320 MHz This is then mixed against 267 MHz to produce a carrier near 53 MHz, which is the center of the ARX tracking range The receiver tracks carrier, subcarrier, and symbol phases and produces soft symbols directly These are then passed to an MCD for decoding

ARX carrier tracking loop bandwidths are selected as indicated by the near-real-time optimization algorithm The subcarrier and symbol tracking loops in the ARX for all test cases used the following parameters Both subcarrier and symbol loop bandwidths were set to 0 1 Hz, and both used type III loops Initial acquisition was performed with 1 0-Hz type II loops These were then narrowed in two steps

B. Spectral Estimation and Bandwidth Optimization Method

Phase error spectra were obtained by performing Fourier analysis on the digital phase detector output The phase detector outputs, which are passed to the software for filtering, were recorded onto a floppy disk Each output file so generated contained M records of N points per record collected at a rate of r points per second The recording rate determines the total bandwidth of the transform The number of points determines the resolution of the transform

The output was processed on a Compaq 286 portable microcomputer Each record was Fourier transformed using the FFT algorithm Then the resulting spectra were averaged across the M records to provide a less noisy estimate of the received spectrum The averaged spectra were then processed with the "ad hoc" estimator as described in [3] This produced estimates of σ_n^2 and σ_p^2, which are estimates of the contribution of thermal noise and phase process, respectively, to total phase error variance Estimates of optimum bandwidth were produced from these variances and from knowledge of the tracking filter parameters These values were also used as seed values for a maximum likelihood estimator which produced more accurate estimates of the noise parameters in post-processing [6]

III. Results

The ARX tracked the Voyager 2 spacecraft from DSS-15 on DOYs 345, 348, 354, 355, 356, 357, and 358 of 1987 In this section, we present the performance comparison results in terms of recovered SSNR and errors in decoded engineering data Also presented is a record of the solar effects and their impact in terms of phase distortion, thermal noise temperature, and amplitude variation as a function of SEP angle These data are then tied together into a practical form in a plot of optimum carrier tracking bandwidth vs SEP angle

A. Recovered Symbol SNR

Figures 2 and 3 show the recovered symbol SNR for the two streams as a function of time for DOYs 357 and 358 For all previous days, the solar effects were not significant enough to degrade the recovered SSNR

By DOY 357 (Fig 2), with an SEP angle of 2 degrees, the solar effect is becoming significant in both carrier phase and amplitude (see Section IIIB) The SSNR measured by the standard station telemetry string is 3 to 4 dB less than that of the ARX and of its own measurement for DOY 345 The increase in system noise temperature for this day relative to DOY 345 was only two degrees One possible explanation for this discrepancy is that the varying amplitude has a strong biasing effect on the SSA SNR estimator The SSA uses the moment method of SNR estimation This produces a biased estimate which is then unbiased by the TPA The moment method uses the square of the mean symbol value, as opposed to the mean of the symbol value squared, to estimate the mean squared With a varying mean, the former approach will always yield a lower estimate of the mean squared than the latter and hence a lower estimate of SNR The split symbol SNR estimator used in the ARX computes the mean of the squared symbol value and hence always measures the true average SNR, even when it is time varying Since all data were decoded without error in both the ARX and standard telemetry streams, it is not known whether there actually was significant degradation in the standard string or whether there was merely inaccuracy in the SSA SNR estimator

This effect can be seen again for the SNR plots of DOY 358 (Fig 3) The SNR estimates for the standard station configuration are very low compared with the estimates for the ARX Based on the standard station estimate of P_c/N_0 and the knowledge of the modulation index and symbol rate, values in the range of 7 to 8 dB were expected The ARX estimates are in this range These are also consistent with the 2 4-dB increase in system noise temperature predicted

B. Comparison of Decoded Data

The only day on which significant error rates were expected was DOY 358 Unfortunately, on this day, a failure in the station air-conditioning system caused the data recording equipment to fail at the start of the pass and the entire station to be down for several hours Thus for a majority of the day there is no recorded telemetry Service was restored toward the end of the pass, in time to provide about 40 minutes of data for comparison

Due to the regular nature of the engineering data being transmitted at the time, it was easy to identify errors once the data were decoded The data were processed and analyzed by members of the Voyager project team As expected, data from DOY 357 were error-free for both receivers The data on DOY 358, however, indicated solar degradation effects on both data streams On ten spacecraft engineering channels, a total of 27 errors were found in the standard station receiver data and 24 were found in the ARX data How these errors relate to receiver performance is unclear Nine of these errors were concurrent errors, that is, both data streams produced errors for that data point These errors were probably the result of strong fades in the signal strength at those points In addition, each data point is made up of 8 bits which are derived from the symbol stream via the rate 1/2 decoder Thus we are not able to determine what the symbol error was at the output of either receiver based on the engineering data quality What can

be said is that the ARX performed at least as well as the current system in terms of recovered data

C. Solar Effects

In these experiments the ARX was shown to be an excellent tool for measuring solar effects The power spectral densities of both phase and amplitude fluctuations obey inverse power relations in certain regions around the carrier frequency of the form

$$S(f) \approx S_1 f^{-\alpha}$$

The exponent α for the case of solar scintillation at low SEP angles is typically 8/3 or less [2] The parameter S_1 is commonly interpreted as the value of the phase process power spectral density at 1 Hz For a given α, S_1 indicates the strength of the disturbance In this section we plot S_1, P_c/N_0, and optimum bandwidth as functions of SEP angle

1 S_1 **vs SEP** Much new work has been done recently in using the ARX to estimate solar scintillation parameters The data below were produced by using the "ad hoc" estimator introduced in [3] Although this method may have unmodeled error sources, it does produce reasonable values for use in estimating optimum carrier bandwidth, and was used in our field experiments Figure 4 shows a plot of S_1 vs SEP angle for angles from 0 86 to 4 6 degrees Note the sharp increase in S_1 under a 2-degree SEP angle

2 P_c/N_0 **vs SEP** Figure 5 shows a plot of P_c/N_0 vs SEP The values below 2 degrees are lower than expected, possibly due to amplitude fluctuations biasing the estimator as in the SNR estimator in the SSA The ARX estimates its received carrier power by averaging the in-phase channel samples and then squaring the average, which as mentioned before produces a value which is biased down This effect could have been avoided by averaging over shorter periods such that the amplitude was constant in that period

3 **Optimum bandwidth vs SEP** One of the important products of this work is that we now have a better idea of what loop bandwidth can be used when solar phase and amplitude scintillation are significant The plot of optimum bandwidth vs SEP as determined by the ARX is given in Fig 6 These values should apply for any phase-locked loop whose minimum loop bandwidth is limited by solar phase scintillation Specifically, this implies that the Block III could have tracked to within a 1-degree SEP angle with a two-sided loop bandwidth $2B_{L_0}$ = 12 Hz loop and increased the tracking margin by 6 dB

4 **Amplitude scintillation** The analysis of solar effects is significantly complicated by variation in amplitude The loop parameters, which affect the spectrum of the phase detector output, are not constant in this case Several approaches are being developed [6] to deal with these effects, including real-time adaptive techniques to modify the loop filter coefficients in response to changing signal levels To indicate the level of amplitude variation, Figs 7, 8, and 9 show raw in-phase channel samples as a function of time for DOYs 345, 356, and 358, which correspond to SEP angles of 11 degrees, 2 5 degrees, and 0 9 degree, respectively

On DOY 345, solar effects are negligible, and the fast variations in Fig 7 are due to errors in measuring carrier amplitude due to receiver noise Significant slow variations in carrier amplitude are evident in DOYs 356 and 358 These slow variations are due to solar scintillation On DOY 358, with an SEP angle of 0 9 degree, the estimate of carrier amplitude actually goes negative at times This appears to be due to very deep amplitude fades and the resulting cycle slipping in the carrier loop

IV. Conclusions

The Advanced Receiver was demonstrated successfully with the Voyager 2 spacecraft near solar conjunction Using much narrower bandwidths, the ARX demonstrated performance equal to or better than that of the current station configuration in terms of the quality of the decoded data By using near-real time bandwidth optimization, it was demonstrated that narrower bandwidths could be used at solar conjunction, thus increasing threshold by as much as 6 dB when solar phase scintillation dominates the received carrier phase process Comparison of recovered SNR is not applicable due to the inaccuracy of the standard station estimators in an amplitude fluctuating environment

References

[1] J W Armstrong, R Woo, and F B Estabrook, "Interplanetary Phase Scintillation and the Search for Very Low Frequency Gravitational Radiation," *Astrophysical Journal*, vol 230, p 570, June 1, 1979

[2] R Woo and J W Armstrong, "Spacecraft Radio Scattering Observations of the Power Spectrum of Electron Density Fluctuations in the Solar Wind," *Journal of Geophysical Research*, vol 84, no A12, pp 7288–7296, December 1, 1979

[3] V A Vilnrotter, W J Hurd, and D H Brown, "Optimized Tracking of RF Carriers With Phase Noise, Including Pioneer 10 Results," *TDA Progress Report 42-91*, vol July–September 1987, Jet Propulsion Laboratory, Pasadena, California, pp 141–157, November 15, 1987

[4] D H Brown and W J Hurd, "DSN Advanced Receiver Breadboard Description and Test Results," *TDA Progress Report 42-89*, vol January–March 1987, Jet Propulsion Laboratory, Pasadena, California, pp 48–66, May 15, 1987

[5] W J Hurd, D H Brown, V A Vilnrotter, and J D Wiggins, "Telemetry SNR Improvement Using the DSN Advanced Receiver, With Results for Pioneer 10," *TDA Progress Report 42-93*, vol January–March 1988, Jet Propulsion Laboratory, Pasadena, California, May 15, 1988 (this issue)

[6] V A Vilnrotter, D H Brown, and W J Hurd, "Spectral Estimation of Received Phase in the Presence of Amplitude Scintillation," *TDA Progress Report 42-93*, vol January–March 1988, Jet Propulsion Laboratory, Pasadena, California, May 15, 1988 (this issue)

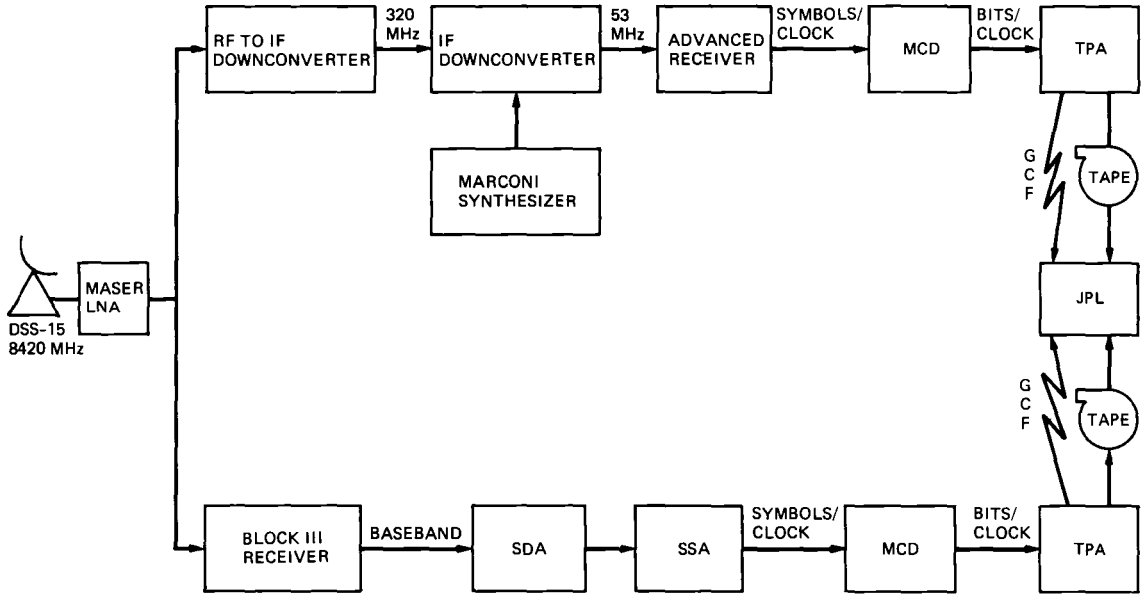

Fig. 1 Configuration for the solar conjunction experiment

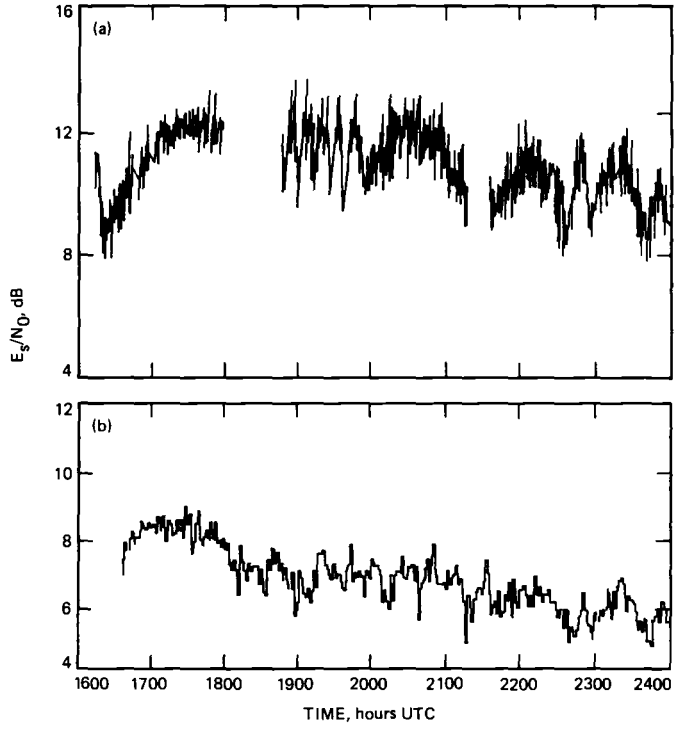

Fig 2 DOY 357 (a) ARX SSNR vs time, (b) station SSNR vs time

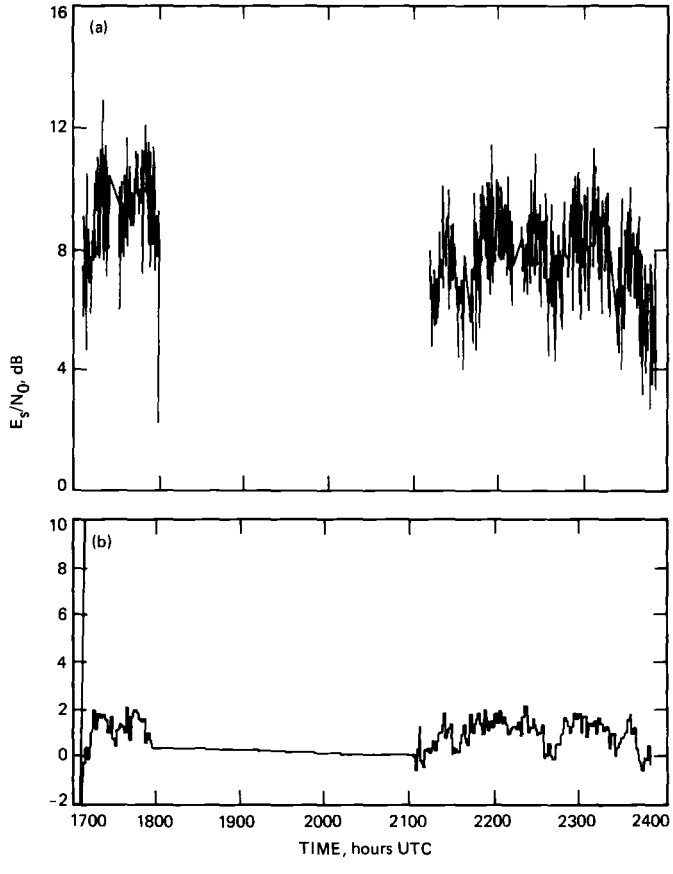

Fig 3 DOY 358 (a) ARX SSNR vs time, (b) station SSNR vs time

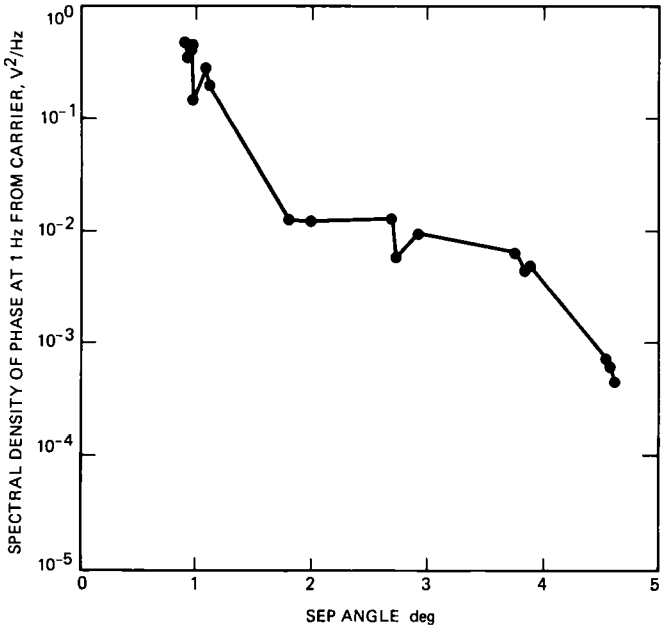

Fig 4 Spectral density vs SEP angle

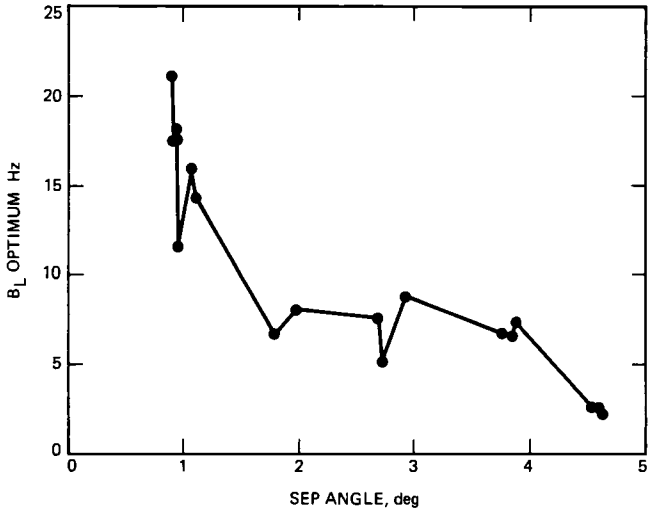

Fig 6 Optimum carrier loop bandwidth

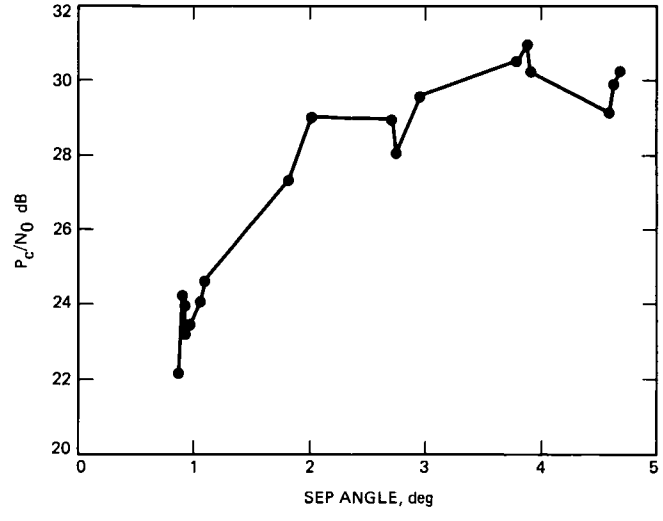

Fig 5 P_c/N_0 vs SEP angle

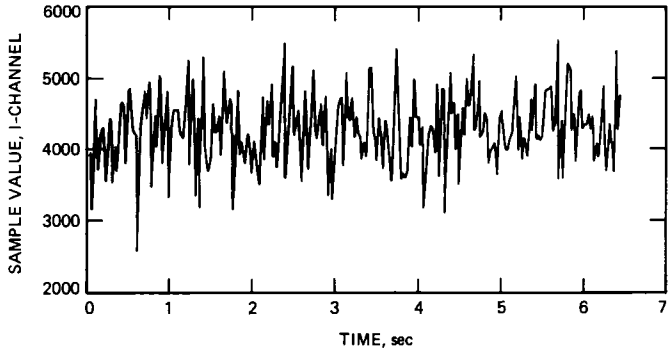

Fig 7 In-phase channel sample values vs time DOY 345

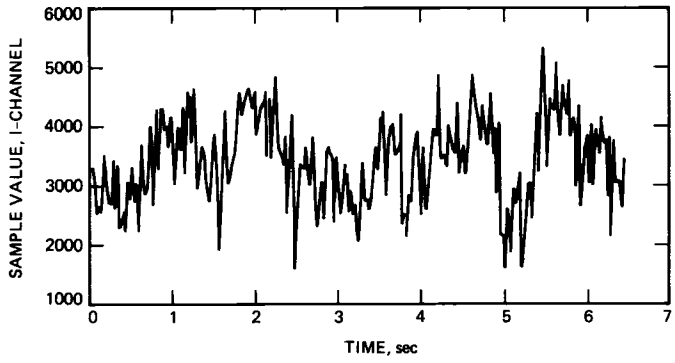

Fig 8 In-phase channel sample values vs. time DOY 356

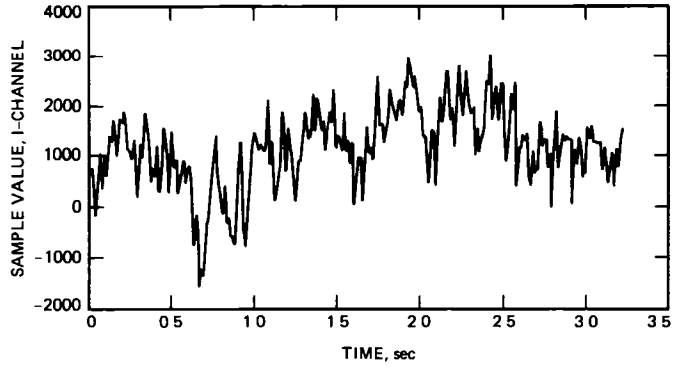

Fig. 9. In-phase channel sample values vs time DOY 358

A New Code for Galileo

S Dolinar
Communications Systems Research Section

Over the past six to eight years, an extensive research effort was conducted to investigate advanced coding techniques which promised to yield more coding gain than is available with current NASA standard codes The delay in Galileo's launch due to the temporary suspension of the shuttle program provided the Galileo project with an opportunity to evaluate the possibility of including some version of the advanced codes as a mission enhancement option A study was initiated last summer to determine if substantial coding gain was feasible for Galileo and, if so, to recommend a suitable experimental code for use as a switchable alternative to the current NASA-standard code The Galileo experimental code study resulted in the selection of a code with constraint length 15 and rate 1/4 The code parameters were chosen to optimize performance within cost and risk constraints consistent with retrofitting the new code into the existing Galileo system design and launch schedule The particular code was recommended after a very limited search among good codes with the chosen parameters It will theoretically yield about 1 5 dB enhancement under idealizing assumptions relative to the current NASA-standard code at Galileo's desired bit error rates This ideal predicted gain includes enough cushion to meet the project's target of at least 1 dB enhancement under real, non-ideal conditions

I. Introduction

After Galileo's launch was postponed by the suspension in the shuttle schedule, the Galileo telemetry link became the subject of extensive activity The new Galileo trajectory will result in reduced telemetry margins at encounter On the other hand, the delayed launch schedule affords an opportunity to seek countervailing enhancements Of the many possible enhancements, one of the easiest to implement is a change in the convolutional code

Convolutional codes have been used on deep space probes for many years A convolutional code is described by its constraint length K, its rate $r = 1/N$,[1] and N "connection vectors" of K bits each The encoder (which is the hardware necessary on the spacecraft) consists of a shift register of length K with N sets of taps This means that a new encoder is a fairly small change on the spacecraft because its complexity is only linear in K and N On the other hand, the decoder's complexity is roughly proportional to 2^K, so a change to a longer constraint length adds significantly to the problem of decoding on the ground

[1] In general, convolutional codes can have rational rates k/N, but rates $1/N$ are the simplest and the most interesting for the Galileo application

Over the past six to eight years, a great deal of research has been conducted in pursuit of advanced convolutional codes with rates $1/N, N \leqslant 6$, and constraint lengths $K \leqslant 15$ [1]–[5] These parameters were chosen so that decoders working at typical deep space data rates could be implemented with foreseeable technological advances

During the summer and fall of 1987, a search was conducted for an advanced convolutional code which could be used by Galileo as an experimental mission enhancement option Such a code is limited by the bandwidth of Galileo's radio modulator to rates $1/N$ with $N \leqslant 4$ A constraint length 15, rate 1/4 code which will allow more than 1 dB of gain over the current $K = 7$, $r = 1/2$ convolutional code was found This article describes the code search, the problems, and the result The experimental code has constraint length 15 and rate 1/4, and it is specified by its four connection vectors written in octal form as 46321, 51271, 63667, 70535 For symbol synchronization purposes, alternate output symbols produced by this code are to be inverted, as is the case with the current NASA-standard (7,1/2) code

An explanation of the connection vector notation and a detailed connection diagram for the Galileo experimental encoder are given in Section VII of this article The simulated performance of this code and a comparison with the performance of the current NASA-standard code are given in Sections V and VI

II. Background: An Extensive Previous Code Search Effort

Over the past six to eight years, the DSN undertook a research effort to study advanced coding techniques which promised to yield more coding gain than is available using current NASA-standard codes The goal for the research effort was approximately 2 dB of extra coding gain over present performance in typical deep space missions such as Voyager and Galileo This represents about half of the maximum possible theoretical gain between current performance and Shannon's ultimate limit on any code's performance The potential application ot the new codes would be deep space communications in the "far future "

The quest for 2 dB of coding gain took off in several directions from current codes The research focused on the same basic concatenation of a Reed–Solomon outer code with a convolutional inner code, but the code parameters were allowed to vary to levels not feasible when the present NASA standards were developed The research effort studied the effects of increasing the constraint length and decreasing the code rate of the convolutional code, and increasing the symbol size and optimizing the code rate of the Reed–Solomon code Due to a higher predicted payoff in performance versus complexity, a significant advance in convolutional code parameters was attempted, whereas the Reed–Solomon code parameters were varied only slightly from those of the present Reed–Solomon code used on Voyager and Galileo

The quest was declared a success when some codes were found which surpassed the 2-dB goal, with the best code improving performance by 2 11 dB To achieve this amount of gain, the convolutional code constraint length had to be increased to $K = 15$ and the code rate decreased to $r = 1/6$, with a 10-bit (1,023,959) Reed–Solomon code used as the outer code In addition, lengthy code searches were conducted using bounds, approximations, and simulations to search for good convolutional codes within any given code space The code space corresponding to any given constraint length K and code rate $r = 1/N$ contains an astronomical number of possible codes (2^{KN}) Therefore, intelligent search techniques had to be developed in order to locate a "best code" when only a tiny fraction of all possible codes could be evaluated explicitly Some of the work that went into this research is described in [1]–[4]

Table 1 shows the end result of the code search effort The performance of the best code found during the code search is listed along with four other significant benchmarks (1) uncoded performance, (2) the performance of the current NASA-standard (7,1/2) convolutional code by itself (unconcatenated), (3) the performance of the current NASA-standard convolutional code concatenated with the current Voyager/Galileo Reed–Solomon code, and (4) Shannon's limit on the performance of any code of arbitrary complexity All figures are for communication at a desired bit error rate of 10^{-6} over a Gaussian channel using BPSK signals Table 1 shows that the best code from the search comes within 2 01 dB of the Shannon limit In comparison, the current Voyager/Galileo concatenated code misses this ultimate limit by 4 12 dB, and the current convolutional code alone misses by 6 37 dB (at a 10^{-6} bit error rate) To complete the perspective, uncoded performance at a 10^{-6} bit error rate is 12 13 dB worse than the Shannon limit Thus, the best code discovered from the code search realizes just over half the maximum possible gain (measured in decibels) theoretically obtainable beyond the current concatenated code

III. Potential Application of Advanced Codes to Galileo

As a result of recent advances in VLSI technology that make long constraint length Viterbi decoders feasible, the use of advanced codes in deep space communications is no longer reserved for the "far future " The delay in Galileo's launch due to the temporary suspension of the shuttle program provided

the Galileo project with an opportunity to evaluate the possibility of including some version of the advanced codes as a mission enhancement option A study was begun last summer to determine if substantial coding gain was feasible for Galileo and, if so, to recommend a suitable experimental code to be available as a switchable alternative to the current NASA-standard Galileo code

IV. The Choice of Code Parameters for Galileo

The first thing that became apparent in the potential Galileo application was that the best code found during the original code search could not be directly applied to Galileo The bandwidth expansion necessary for a rate 1/6 convolutional code simply could not be accommodated in a Galileo retrofit In addition, there was a hard constraint on keeping the 8-bit (255,223) Reed–Solomon outer code Therefore, a new abbreviated code search was launched to investigate how much of the 2 11 dB of potential gain could be obtained within the Galileo constraints

The constraints imposed by Galileo were (1) an 8-bit (255,223) Reed–Solomon outer code, (2) a convolutional inner code with a rate no lower than 1/4 and preferably 1/2, and (3) a convolutional inner code with a constraint length small enough to guarantee that a practical Viterbi decoder could be built within the next few years Within these constraints, the objective was to pick the code parameters that would achieve the maximum coding gain at minimal cost and risk to the project

The earlier research had taken a giant leap forward to very advanced codes Galileo now needed an estimate of gains that could come from smaller leaps The initial phase of the code study for Galileo was to make rough estimates of the relative payoff for changing the code parameters unit by unit

The first step in this initial phase was to gather data from previous code search studies and form extrapolations to roughly estimate the variation of performance with each of the code parameters Approximate curves are shown in Fig 1 The points on these curves represent best codes found according to various sources [3]–[5] It is seen that an approximate gain of a little over 0 1 dB can be expected for each unit increase in K Another 0 6 to 0 9 dB can be expected for decreasing the code rate from 1/2 to 1/4, and about 0 2 to 0 3 dB for further decreasing the code rate from 1/4 to 1/6 The 10-bit Reed–Solomon outer code is worth about 0 25 dB relative to the 8-bit code Together, these components account for the 2 11-dB predicted gain of the $K = 15, r = 1/6$ convolutional code, 10-bit Reed–Solomon code concatenation versus the current NASA-standard $K = 7, r = 1/2$ convolutional code, 8-bit Reed–Solomon code concatenation

The second step in the initial phase was to evaluate the costs and risks to the Galileo project of selecting particular sets of code parameters The costs associated with varying each of the code parameters can be placed in three basic categories (1) effects on encoder complexity, (2) effects on decoder complexity, and (3) effects on other spacecraft and ground systems

Encoder complexity grows only modestly with constraint length K and reciprocal code rate $N = 1/r$ The encoder needs a shift register of length K and N sets of taps (exclusive-OR gates) For good codes, the total number of taps is roughly proportional to N Technology was immediately available to build any encoder with $K \leqslant 15$ and $r \geqslant 1/6$, so encoder complexity was not a major driver in the selection of code parameters

In contrast, decoder complexity grows exponentially with constraint length K Memory and computational requirements for a Viterbi decoder increase as 2^K Viterbi decoders operating at 100 kbps are not currently available for values of K greater than about 10 However, 100-kbps decoders for $K = 13$ to 15 should be achievable within the next two years based on VLSI technology

Decoder complexity increases only modestly with reciprocal code rate N Decoder memory requirements are independent of N, and computational requirements increase only linearly with N Thus, decoder complexity was not a limiting factor in the choice of code rate

Even though decreasing the code rate has relatively minor effects on the encoder and decoder, it has significant effects on other spacecraft and ground systems, especially in a retrofitted system like the one proposed for Galileo, whose original system design was based on old assumptions about the best codes available The channel symbol rate increases linearly with reciprocal code rate N for a fixed information bit rate Therefore, bandwidth requirements increase linearly with N, the smallest suitable subcarrier frequency is proportional to N, and symbol clock speeds are proportional to N The symbol signal-to-noise ratio is less than the bit signal-to-noise ratio by 10 $\log_{10} N$ dB, and symbol tracking might be impaired

Increasing constraint length has no such side effects on other spacecraft and ground systems The costs of choosing a long constraint length code are confined to increased complexity in the encoder and decoder, primarily the decoder

The selection of code parameters for Galileo thus boiled down to the resolution of two major issues how much bandwidth expansion Galileo could tolerate and what constraint length would permit low-risk decoder development before Galileo's encounter at Jupiter To answer these questions, code performance evaluations were needed for the combinations of code parameters most acceptable (in terms of costs) in the Galileo application

The third and final step in the initial phase of the study was to perform new cursory code searches in the code spaces $K = 13$, 15 and $r = 1/2$, $1/4$ Figures 2 and 3 show some typical performance results from this very abbreviated study The data points plotted in Figs 2 and 3 represent simulated code performance under idealizing assumptions for a representative "best found code" for each combination of code parameters The idealizing assumptions are described in the next section At interesting levels of bit error rate (10^{-6} to 10^{-5} for concatenated coding and 5×10^{-3} for nonconcatenated coding), these curves indicate that 0 8 to 0 9 dB of performance gain is obtained by going from rate 1/2 to rate 1/4 and a little over 0 1 dB by going from constraint length 13 to constraint length 15 The project evaluated these predicted incremental performance gains relative to the costs and risks of selecting different constraint lengths and code rates

The constraint length issue was resolved in favor of going all the way to the maximum constraint length considered in the study, $K = 15$ Current strides in the development of the BIG Viterbi Decoder[2] for the DSN indicate that this assumption was realistic A prototype of a $K = 15$ Viterbi decoder should be completed by late 1990

The project's position on code rate was to stay with rate 1/2 if at all possible, because this would confine changes on the spacecraft to the new encoder (plus a switch for invoking the experimental code option) However, given the large payoff in coding gain for going from rate 1/2 to 1/4, the required spacecraft modifications were evaluated for rates down to 1/4 Code rates lower than 1/4 could not be considered, because Galileo's Radio Frequency Subsystem could not tolerate more than a doubling of the subcarrier frequency Eventually, the decision was made to select a code with rate 1/4, because this was the only alternative that would guarantee a worthwhile performance gain of at least 1 dB This choice of code rate means that the spacecraft needs not only an optional experimental encoder but also a mechanism for doubling the subcarrier frequency and symbol clock rate whenever the optional encoder is invoked Appropriate modifications to Galileo's Telemetry Modulation Unit were approved by the project in order to support the experimental rate 1/4 code

With the code parameters selected at $K = 15$, $r = 1/4$, approximately 1 5 dB of theoretical relative coding gain was the goal Some portion of the theoretical gain will undoubtedly be whittled away due to such things as extra radio loss and the effects of non-ideal interleaving A practical target was set for at least 1 dB of real net gain from the experimental code

V. The Abbreviated Code Search for Galileo

The original code search investigated thousands of codes with constraint lengths 13, 14, 15 and code rates 1/4, 1/5, 1/6 Randomly selected codes were subjected to a quick initial evaluation based on free distance calculations and transfer function bounds on the error probability Full Viterbi decoder simulations were then performed for just a handful of best candidates from the initial evaluation

The best code found during the original study was a constraint length 15, rate 1/6 code with connection vectors 46321, 51271, 63667, 70535, 73277, 76513 The original work only cursorily examined codes with the particular combination of parameters $K = 15$, $r = 1/4$, and thus a new code search was needed to recommend an experimental code for Galileo

Due to the short time constraints on inputs to the project's decision to implement an experimental code, the Galileo code search could not be as thorough as the search conducted during the original work A decision was made to focus on (15, 1/4) codes whose four connection vectors are subsets of the six connection vectors of the best (15,1/6) code found during the original study The rationale for this choice is the inverse of the "good codes generate good codes" notion [1] that guided much of the original work All 15 of these "subset codes" were given a preliminary evaluation using free distance calculations and transfer function bound techniques A few non-subset codes were also tested, but none performed better than the best of the subset codes

All codes were tested over a very narrow range of bit-energy to noise-spectral-density ratio (E_b/N_0) between 0 3 dB and 0 5 dB[3] This range of E_b/N_0 was selected to approximately satisfy Galileo's dual bit error rate requirements of

[2]Work on this decoder will be reported in subsequent issues

[3]All values quoted for E_b/N_0 in this report refer to the bit-energy to noise-spectral-density ratio for the convolutional code alone For concatenated coding, this is equivalent to treating all of the Reed–Solomon code's symbols as information symbols

5×10^{-3} for the convolutional code alone, and 10^{-5} for the convolutional code concatenated with Galileo's (255,223) 8-bit Reed–Solomon code All error performance comparisons were based on ideal assumptions, and they do not include allowances for real-system degradations due to radio loss, finite quantization of decoder inputs, or non-ideal interleaving of Reed–Solomon symbols

The specific idealizing assumptions used for all the Galileo-directed Viterbi decoder simulations were (1) essentially no quantization of metrics (precision limited only by the 64-bit floating point precision of the computer), (2) 128-bit memory path truncation length, and (3) ideal interleaving of Reed–Solomon symbols Metric quantization is actually 3 bits for the current NASA-standard (7,1/2) MCD (Maximum-likelihood Convolutional Decoder), and it was assumed to be 4 bits for most of the original code search work For the current study, it was felt that simulating an ideal soft-decision Viterbi decoder (i e , no quantization of metrics) would produce a fairer comparison of relative code performance, because there was no time to optimize the choice of quantization levels for any tested code Memory path truncation length is infinite for an ideal Viterbi decoder and 64 bits for the current NASA-standard (7,1/2) MCD A rough rule of thumb developed for the smaller constraint length codes is that the truncation length should be about 5 times the constraint length [6] in order for the decoder to approach ideal performance This factor of 5 may have to be increased somewhat for the low signal-to-noise ratios typical of a concatenated system A 128-bit truncation length was judged adequate to cover constraint lengths through $K = 15$ Galileo's 8-bit Reed–Solomon symbols are interleaved to a depth of only two symbols, and this is grossly insufficient for removing intersymbol dependencies Average lengths of error bursts from (15,1/4) decoders are approximately 30 bits at Galileo's required performance levels However, without a good model for estimating Reed–Solomon code performance in the face of intersymbol dependencies, the fairest approach to evaluating relative code performance was to compare all codes on the basis of an ideal interleaving assumption

The results of the preliminary evaluations of the 15 subset codes are shown in Table 2 The codes are listed in order of predicted merit at $E_b/N_0 = 0.5$ dB, based on an approximate error probability lower bound derived from a transfer function expansion [4] The table also shows the free distance for each code, a parameter which determines code performance at extremely low error probabilities or high values of E_b/N_0 Somewhat surprisingly, at the low E_b/N_0 required for Galileo, some of the poorest subset codes under the maximum free distance criterion are some of the best codes under the transfer function bound criterion (and vice versa) Unfortunately, neither criterion provides a definitive indicator of relative code performance in this range of E_b/N_0

Four of the subset codes were selected for further testing via full simulation of the Viterbi decoder The four selected codes included both of the top-ranked codes under the two criteria discussed above The Viterbi decoder simulation would provide a definitive comparison of code performance if it could run long enough Its major shortcoming is the inordinate amount of computer time required for each simulation Decoding 200,000 bits for one (15,1/4) code at one value of E_b/N_0 consumes about 60 hours of CPU time on a Sun 3/260 computer

The results of the full simulation tests of the four candidate subset codes are shown in Table 3 The table also lists full simulation results for two non-subset codes One of these was suggested in an earlier study [3] as a perturbation of the subset code with maximum free distance, and the other is derived from a good (13,1/4) code

The codes in Table 3 were tested at the low end of the desired range in E_b/N_0 (0.3 dB) in order to maximize the number of error samples for a valid statistical comparison For comparison purposes, all codes were subjected to the same extremely long sequence of 800,000 noise samples

Table 3 lists both the simulated bit error rate and the simulated symbol error rate for 8-bit Reed–Solomon symbols The symbol error rate is the predominant factor that determines the performance of each candidate convolutional code when concatenated with Galileo's Reed–Solomon outer code Symbol error rates of 2.1×10^{-2} to 2.5×10^{-2} correspond to concatenated code bit error rates of 10^{-6} to 10^{-5}, under the assumption of ideal interleaving of Reed–Solomon symbols

Each estimate of bit error rate or symbol error rate in Table 3 was based on 200,000 decoded bits Due to the propensity of convolutional decoder errors to occur in long bursts, each (15,1/4) code simulated at 0.3 dB only produced slightly more than 100 independent error bursts The corresponding 1σ accuracy in the bit error rate and the symbol error rate estimates is about 10 to 15 percent

The two subset codes that were top-ranked according to one of the two criteria for preliminary code evaluation produced more simulated bit errors and more simulated symbol

[4] D Divsalar and S Dolinar, "All $K = 15$, $r = 1/4$ Codes Derived From the Best $K = 15$, $r = 1/6$ Code," JPL IOM 331-87 2-324 (internal document), Jet Propulsion Laboratory, Pasadena, California, July 27, 1987

errors than the two tested subset codes that were not top-ranked on either preliminary scale The performance of the latter two codes could not be distinguished with any degree of statistical significance, the code with the higher free distance (d_{free} = 35) was nominated for the original experimental encoder breadboard design and is the code ultimately selected for implementation on Galileo The two non-subset codes listed in Table 2 did not fare as well as the two best subset codes Approximately a dozen additional non-subset codes suggested from various sources were partially simulated, but these simulations were aborted long before the decoding of 200,000 bits when it became apparent that their performance was inferior to that of the recommended code

A programming glitch was discovered in the random number generator which was used for the results in Table 3 It is not known whether the inadvertently programmed random number generator has desirable statistical properties Two of the codes listed in Table 3 were retested with a properly reprogrammed random number generator These two codes were the recommended code for Galileo and the code with the largest free distance The results of the tests with the new random number generator are shown in Table 4 The table shows simulation results at E_b/N_0 = 0 3 dB and 0 5 dB for both codes, and at E_b/N_0 = 0 1 dB and 0 7 dB for the recommended code only The error rate estimates are based on 200,000 decoded bits for E_b/N_0 = 0 3 dB and 0 5 dB, 100,000 bits for E_b/N_0 = 0 1 dB, and 400,000 bits for E_b/N_0 = 0 7 dB The corresponding 1σ accuracy in the error rate estimates is about 10 to 15 percent for E_b/N_0 = 0 1 dB and 0 3 dB, and 15 to 20 percent for E_b/N_0 = 0 5 dB and 0 7 dB

The recommended code won all comparative simulation tests for bit error rate performance with both random number generators, though many differences were not statistically significant individually It won all but two symbol error rate comparisons, losing by statistically insignificant margins to one code in Table 3 and a different code at one value of E_b/N_0 in Table 4 Bit error rate comparisons were weighted more heavily than symbol error rate comparisons, due to Galileo project emphasis on improving non-concatenated performance, and due to the dubious validity of the ideal interleaving assumption that was necessary to directly link convolutional code symbol error rates with concatenated code bit error rates All in all, the recommended code seems to be a solid though not absolutely optimum code that will function well in its intended application on Galileo

VI. Comparison With the Current NASA Standard (7,1/2) Code

Table 4 also lists simulation test results obtained with the reprogrammed random number generator for the current NASA-standard (7,1/2) convolutional code at values of E_b/N_0 ranging from 1 05 dB to 2 55 dB These error rate estimates are based on the same idealizing assumptions used for simulating the (15,1/4) codes, and they are several tenths of a decibel more optimistic than actual MCD (Maximum-likelihood Convolutional Decoder) performance The table shows that at Galileo's desired bit error rate of 5×10^{-3} or symbol error rate of $2\,5 \times 10^{-2}$, the recommended (15,1/4) code offers about 1 5 dB of improvement over the NASA-standard (7,1/2) code under the same ideal circumstances for both codes

VII. Galileo Experimental Code Specification

The recommended experimental code for Galileo has constraint length 15 (memory length 14) and rate 1/4 The connection vectors for the four output symbols per input information bit are represented in octal form as 46321, 51271, 63667, 70535 Equivalently, in binary form these are 100110011010001, 101001010111001, 110011110110111, 111000101011101 Each of the four output binary code symbols per input information bit is obtained as a modulo-2 sum of the current information bit and a subset of the 14 previous information bits corresponding to the positions of the 1's in the appropriate connection vector The leftmost connection vector bit indicates a connection to the current information bit, and each succeeding bit indicates a connection or non-connection to the next most recent information bit

A connection diagram for the Galileo code is shown in Fig 4 In addition to the basic code connections, this diagram also indicates that the first and third output symbols should be inverted The alternate symbol inversion has no effect on code performance and is included solely to aid symbol synchronization by ensuring that the encoder will not produce long runs of 0's or 1's in response to constant input Alternate symbol inversion avoids arbitrarily long runs of all 0's or all 1's in response to constant input as long as the parity of successive connection vectors does not alternate odd-even-odd-even [7] Since the experimental code has three connection vectors with odd parity and one with even parity, the parity cannot alternate odd-even-odd-even, and the ordering of the output symbols is inconsequential

VIII. Postscript: An Issue of Code Transparency

Shortly after the choice of experimental code for Galileo, the question of code transparency arose with respect to the selected code The present NASA-standard (7,1/2) convolutional code has a useful property that makes it transparent to inversion of input data bits A binary code is transparent to

input inversion if complementing every bit in the input data stream causes every symbol in the output encoded symbol stream to be complemented as well A necessary and sufficient condition for the transparency of a rate $1/N$ convolutional code is that all N of its connection vectors have odd parity

The code transparency feature is useful because a maximum-likelihood decoder encountering an accidentally inverted, transparently coded symbol stream will decode the exact complement of the maximum-likelihood data stream, and the true maximum-likelihood data bits can be easily recovered by removal of an overall binary ambiguity In contrast, an accidentally inverted symbol stream encoded by a non-transparent code will produce decoded output from which the true maximum-likelihood data bits cannot be directly recovered

Galileo's biphase modulated symbol stream possesses an inherent sign ambiguity that must be resolved at some point If the symbols are encoded by a non-transparent code, ambiguity removal must precede decoding Transparently coded symbols, on the other hand, may be decoded either before or after the ambiguity is resolved

Code transparency was not a constraining criterion during either the original extensive code search or the limited Galileo-directed search reported here Transparent codes are the exception rather than the rule For example, only one-sixteenth of all (15,1/4) convolutional codes are transparent As a result, not many tested long constraint length codes happen to be transparent Not one of the (15,1/4) codes evaluated during the Galileo-directed search is transparent In particular, the recommended experimental code choice for Galileo is not transparent

A transparent code was constructed by making a tiny modification to the recommended experimental code The motivation for this particular modification was a potential small performance advantage suggested by certain symmetry considerations as applied to the first three bits and last three bits of the recommended code's connection vectors The transparent code differs from the recommended code by just one bit in one of its four connection vectors The connection vectors for the transparent code are 46321, 51273, 63667, 70535

The transparent code has been subjected to simulation tests under the same ideal assumptions that applied to the other codes tested and reported above, using the reprogrammed random number generator only The simulation results for the transparent code are listed in Table 5 alongside the comparable results for the non-transparent recommended Galileo experimental code

The transparent code outperformed the recommended code at two of four tested values of E_b/N_0 if measured by simulated Reed–Solomon symbol error rate, or at one of four values of E_b/N_0 if measured by simulated bit error rate No other code previously tested had ever outscored the recommended code in more than one category However, all differences in simulated error rates for the two codes were statistically insignificant

Proper perspective for interpreting the simulation results can be obtained only by evaluating the raw estimated error rates with respect to the statistical uncertainties in the simulation predictions Figures 5 and 6 plot the simulated bit and symbol error rates for the transparent and non-transparent codes In these figures, the performance traces for both codes are plotted as wide swaths indicating $\pm 1\sigma$ uncertainty around the nominal error rate estimates listed in Table 5 Estimates of the statistical uncertainty of the simulation results are based on a geometric model for Viterbi decoder error bursts [5]

The plots in Figs 5 and 6 show no discernible performance difference between the transparent and non-transparent codes over the tested range of E_b/N_0 All of the small numerical differences in Table 5 pale in significance next to the statistical uncertainties inherent in the simulation Furthermore, even these small differences tend to cancel each other for these two codes Each code's performance swaths are intertwined both above and below the other's over the full tested range of E_b/N_0 The bottom-line conclusion to be drawn from Figs 5 and 6 is that the Galileo project's choice between the transparent and the non-transparent code had to be based on factors other than simulated code performance The decision of the Galileo project was that transparency was an insufficient reason to change the selected experimental code

IX. Summary

The Galileo experimental code search resulted in the code selection depicted in Fig 4 The code parameters were chosen to optimize performance within cost and risk constraints consistent with retrofitting the new code into the existing Galileo system design and launch schedule The particular code was recommended after a very limited search among good codes with the chosen parameters The recommended code is a solid though not absolutely optimum code that will function well in its intended application on Galileo It will theoretically yield about 1 5 dB of improvement under idealizing assumptions relative to the current NASA-standard code at Galileo's desired bit error rates This ideal predicted gain includes enough cushion to meet the target of at least 1 dB of enhancement under real, non-ideal conditions The (non-transparent) experimental code can be trivially modified to form a transparent code essentially equivalent in performance, but this modification was not approved for Galileo

References

[1] P J Lee, "New Short Constraint Length, Rate $1/N$ Convolutional Codes Which Minimize Required E_b/N_0 for Given Bit Error Rate," *TDA Progress Report 42-77*, January–March 1984, Jet Propulsion Laboratory, Pasadena, California, pp 41–56, May 1984

[2] P J Lee, "A Very Efficient Transfer Function Bounding Technique on Bit Error Rate for Viterbi Decoded, Rate $1/N$ Convolutional Codes," *TDA Progress Report 42-79*, July–September 1984, Jet Propulsion Laboratory, Pasadena, California, pp 114–123, November 1984

[3] J H Yuen and Q D Vo, "In Search of a 2-dB Coding Gain," *TDA Progress Report 42-83*, July–September 1985, Jet Propulsion Laboratory, Pasadena, California, pp 26–33, November 1985

[4] P J Lee, "Further Results on Rate $1/N$ Convolutional Code Constructions with Minimum Required SNR Criterion," *IEEE Transactions on Communications*, vol COM-34, no 4, pp 395–399, April 1986

[5] R L Miller, L J Deutsch, and S A Butman, *On the Error Statistics of Viterbi Decoding and the Performance of Concatenated Codes*, JPL Publication 81-9, Jet Propulsion Laboratory, Pasadena, California, September 1, 1981

[6] A J Viterbi and J K Omura, *Principles of Digital Communication and Coding*, New York McGraw-Hill, pp 258–259, 1979

[7] L D Baumert, R J McEliece, and H C A van Tilborg, "Symbol Synchronization in Convolutionally Coded Systems," *IEEE Transactions on Information Theory*, vol IT-25, no 3, pp 362–365, May 1979

Table 1 The quest for coding gain

Code	Required E_b/N_0 for 10^{-6} BER, dB	Coding non-optimality relative to Shannon limit, dB	Coding gain relative to current concatenated code, dB
Uncoded	10 54	12 13	–
Current convolutional (7,1/2)	4 78	6 37	–
Current concatenated (7,1/2) + 8-bit R–S	2 53	4 12	0 00
Code search best code (15,1/6) + 10-bit R–S	0 42	2 01	2 11
Shannon limit (unknown code of arbitrary complexity)	–1 59	0 00	4 12

Table 2 Preliminary evaluation of subset codes

Code connection vectors	d_{free}	Approximate BER bound at 0 5 dB
(51271, 70535, 73277, 76513)*	32	$4\,9 \times 10^{-4}$
51271, 63667, 70535, 76513	34	$5\,4 \times 10^{-4}$
(51271, 63667, 70535, 73277)*	34	$5\,4 \times 10^{-4}$
(46321, 51271, 63667, 70535)*	35	$5\,7 \times 10^{-4}$
46321, 51271, 63667, 76513	36	$6\,2 \times 10^{-4}$
46321, 63667, 70535, 73277	35	$6\,2 \times 10^{-4}$
46321, 51271, 70535, 76513	34	$6\,3 \times 10^{-4}$
46321, 51271, 70535, 73277	34	$6\,4 \times 10^{-4}$
51271, 63667, 73277, 76513	35	$6\,8 \times 10^{-4}$
46321, 51271, 73277, 76513	36	$7\,3 \times 10^{-4}$
63667, 70535, 73277, 76513	34	$7\,7 \times 10^{-4}$
46321, 63667, 70535, 76513	37	$7\,7 \times 10^{-4}$
46321, 63667, 73277, 76513	36	$8\,2 \times 10^{-4}$
46321, 70535, 73277, 76513	36	$8\,3 \times 10^{-4}$
(46321, 51271, 63667, 73277)*	38	$8\,6 \times 10^{-4}$

*Codes selected for full simulation

Table 3 Simulation results for candidate codes

Code connection vectors	d_{free}	Simulated bit error rate at 0 3 dB	Simulated symbol error rate at 0 3 dB
(46321, 51271, 63667, 70535)*†	35	$1\ 06 \times 10^{-2}$	$2\ 45 \times 10^{-2}$
(51271, 63667, 70535, 76513)*	34	$1\ 07 \times 10^{-2}$	$2\ 37 \times 10^{-2}$
(46321, 51271, 63667, 73277)*	38	$1\ 11 \times 10^{-2}$	$2\ 60 \times 10^{-2}$
46321, 51271, 63667, 73257	37	$1\ 12 \times 10^{-2}$	$2\ 64 \times 10^{-2}$
45177, 53365, 62313, 75655	35	$1\ 16 \times 10^{-2}$	$2\ 67 \times 10^{-2}$
(51271, 70535, 73277, 76513)*	32	$1\ 20 \times 10^{-2}$	$2\ 74 \times 10^{-2}$

*Subset codes from Table 2
†Recommended (15, 1/4) experimental code for Galileo

Table 4 Simulation results with reprogrammed random number generator

Code connection vectors	d_{free}	Simulated bit error rate	Simulated symbol error rate
(46321, 51271, 63667, 70535) †	35	$1\ 77 \times 10^{-2}$ @ 0 1 dB	$4\ 22 \times 10^{-2}$ @ 0 1 dB
		$9\ 5 \times 10^{-3}$ @ 0 3 dB	$2\ 24 \times 10^{-2}$ @ 0 3 dB
		$4\ 2 \times 10^{-3}$ @ 0 5 dB	$1\ 08 \times 10^{-2}$ @ 0 5 dB
		$2\ 2 \times 10^{-3}$ @ 0 7 dB	$5\ 1 \times 10^{-3}$ @ 0 7 dB
46321, 51271, 63667, 73277	38	$9\ 5 \times 10^{-3}$ @ 0 3 dB	$2\ 16 \times 10^{-2}$ @ 0 3 dB
		$4\ 9 \times 10^{-3}$ @ 0 5 dB	$1\ 16 \times 10^{-2}$ @ 0 5 dB
(171, 133)*	10	$3\ 68 \times 10^{-2}$ @ 1 05 dB	$8\ 53 \times 10^{-2}$ @ 1 05 dB
		$1\ 37 \times 10^{-2}$ @ 1 55 dB	$3\ 41 \times 10^{-2}$ @ 1 55 dB
		$1\ 11 \times 10^{-2}$ @ 1 65 dB	$2\ 77 \times 10^{-2}$ @ 1 65 dB
		$9\ 4 \times 10^{-3}$ @ 1 75 dB	$2\ 37 \times 10^{-2}$ @ 1 75 dB
		$7\ 6 \times 10^{-3}$ @ 1 85 dB	$1\ 91 \times 10^{-2}$ @ 1 85 dB
		$5\ 9 \times 10^{-3}$ @ 1 95 dB	$1\ 51 \times 10^{-2}$ @ 1 95 dB
		$4\ 4 \times 10^{-3}$ @ 2 05 dB	$1\ 14 \times 10^{-2}$ @ 2 05 dB
		$1\ 3 \times 10^{-3}$ @ 2 55 dB	$3\ 2 \times 10^{-3}$ @ 2 55 dB

*Current NASA standard (7,1/2) code
†Recommended (15,1/4) experimental code for Galileo

Table 5 Performance comparison of Galileo experimental code (non-transparent) and modified code (transparent)

Code connection vectors	d_{free}	Simulated bit error rate	Simulated symbol error rate
(46321, 51271, 63667, 70535)†	35	1.77×10^{-2} @ 0.1 dB	4.22×10^{-2} @ 0.1 dB
		9.5×10^{-3} @ 0.3 dB	2.24×10^{-2} @ 0.3 dB
		4.2×10^{-3} @ 0.5 dB	1.08×10^{-2} @ 0.5 dB
		2.2×10^{-3} @ 0.7 dB	5.1×10^{-3} @ 0.7 dB
(46321, 51273, 63667, 70535)*	36	1.87×10^{-2} @ 0.1 dB	4.45×10^{-2} @ 0.1 dB
		8.5×10^{-3} @ 0.3 dB	2.04×10^{-2} @ 0.3 dB
		4.6×10^{-3} @ 0.5 dB	1.07×10^{-2} @ 0.5 dB
		2.3×10^{-3} @ 0.7 dB	5.3×10^{-3} @ 0.7 dB

*Modified (15,1/4) code (transparent)
†Recommended (15,1/4) experimental code for Galileo (non-transparent)

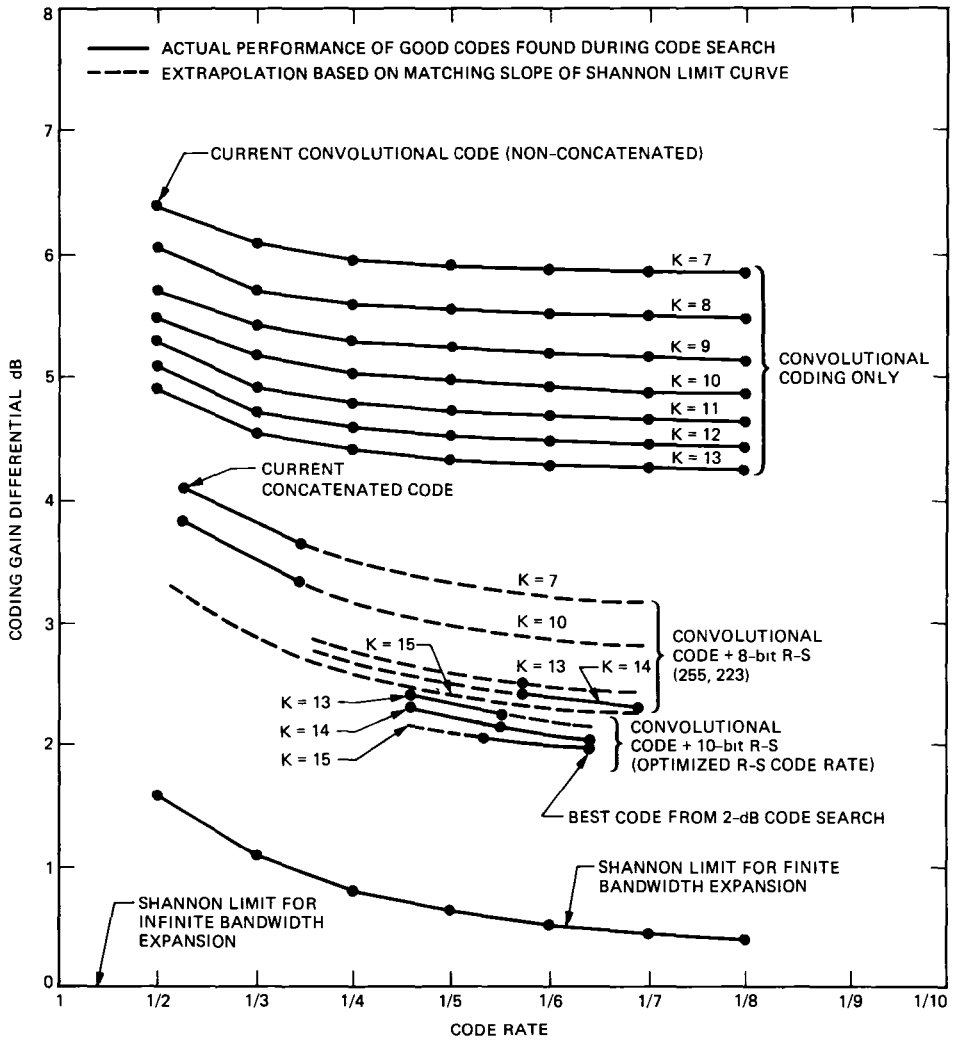

Fig 1 Coding gain differential relative to the Shannon limit for infinite bandwidth expansion at a bit error rate of 10^{-6}

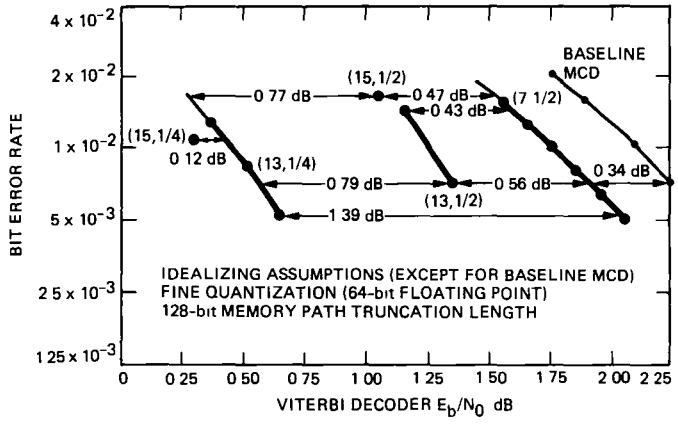

Fig 2 Best codes found during code parameter selection phase of study performance of convolutional codes alone (unconcatenated)

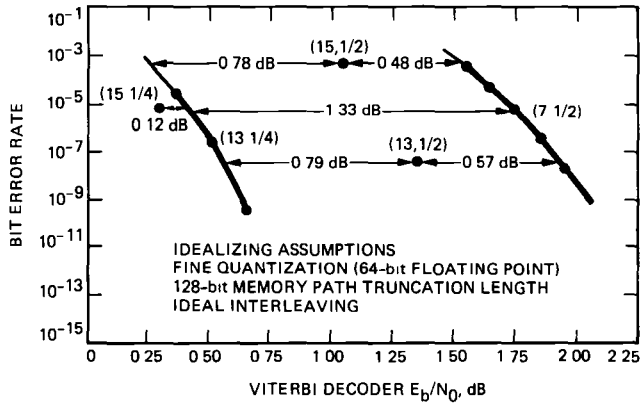

Fig 3 Best codes found during code parameter selection phase of study performance of convolutional codes concatenated with (255,223) Reed-Solomon code

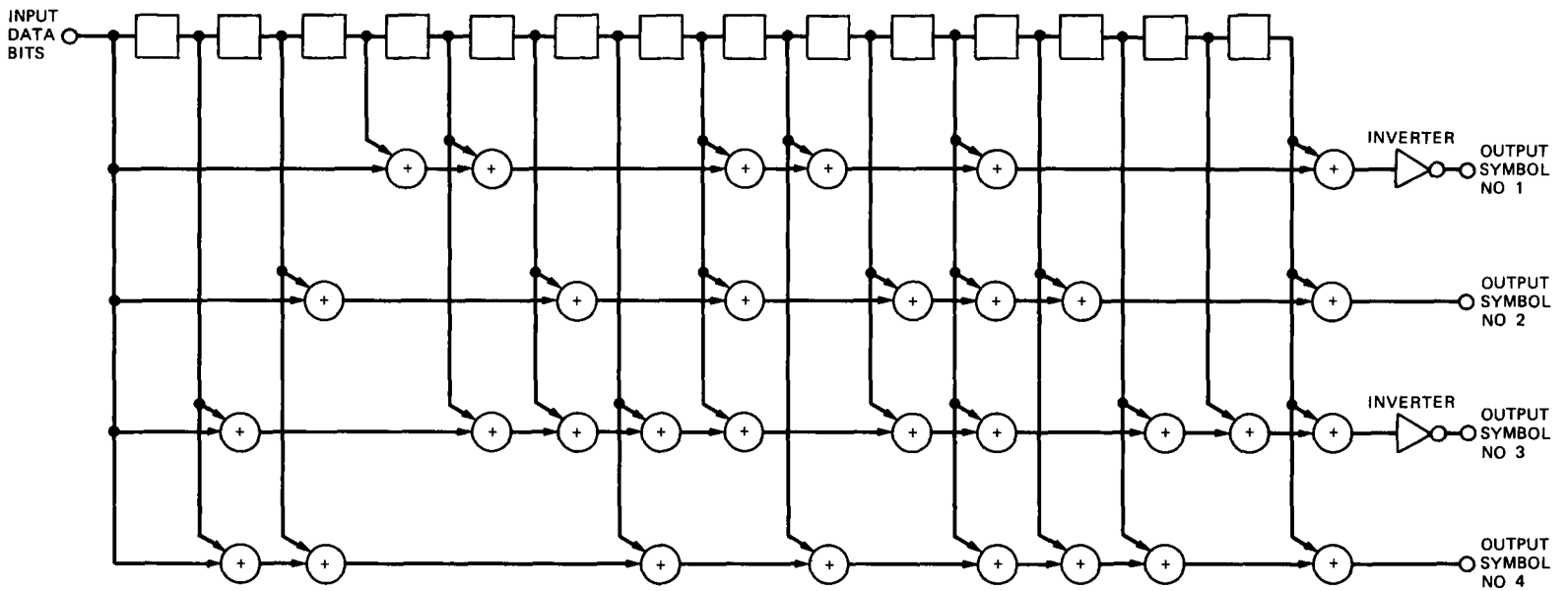

Fig 4 Encoder connection diagram for recommended Galileo experimental code

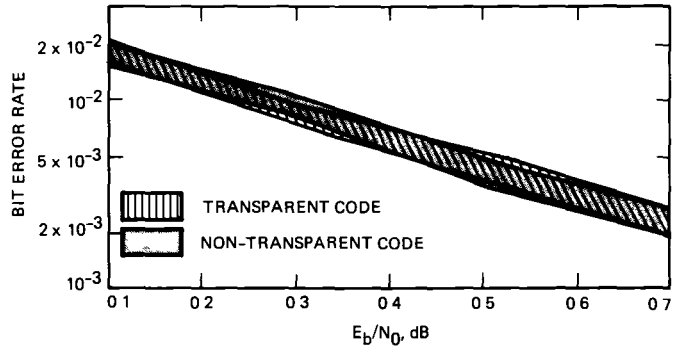

Fig 5 Simulated bit error rate for Galileo experimental code alternatives (± 1-sigma uncertainty swath indicated for both codes)

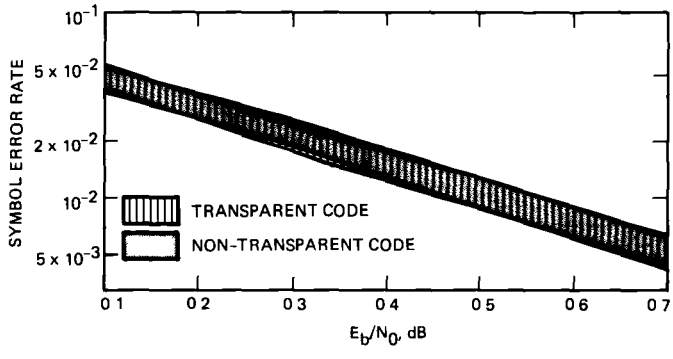

Fig 6 Simulated symbol error rate for Galileo experimental code alternatives (± 1-sigma uncertainty swath indicated for both codes)

Strawman Optical Reception Development Antenna (SORDA)

E L Kerr
Communications Systems Research Section

A strawman design of a ground-based station for receiving optical communications from deep space is presented This strawman will serve as a basis for further study and design refinement The recommendation to build rather than to use an existing facility is explained Parameters of the design have been selected to postulate a workable system, starting with a 10-m-diameter, hexagonally segmented, f/0 5 primary mirror The effects of variations of design parameters on performance and cost are discussed Some design formulas are included An electro-optical functional block diagram is presented and discussed Cost calculations are based on a previous cost model for the hardware or on typical construction costs per unit area for several types of facilities Other cost factors are included in the usual way for Construction of Facilities The ratio of high and low reasonable values was less than a factor of 2,with a best estimate of under $16,000,000

I. Strategy for Optical Reception Development

A long-range concept has been established for the development and deployment of optical communications for planetary use and beyond The concept is based on a number of assumptions, and although it has been modified occasionally as required by new constraints such as mission launch-date changes, its basic ingredients have remained very stable for several years Those key ingredients are (1) a ground-based optical reception development antenna by 1993, ready for the following item, (2) a mission-augmentation flight experiment package aboard Cassini, to be launched in 1995, (3) a spaceborne R&D optical reception station in conjunction with the space station by 1999, (4) a user spacecraft transceiver by 2000, and (5) an operational optical reception station in geosynchronous orbit by about 2015

Other optical communications development concepts are possible One could skip the ground-based optical reception development antenna and start directly with spaceborne optical reception However, it is believed that before major resources will be committed for a spaceborne facility, substantial confidence in the utility and performance of optical communications technology must be established Furthermore, it is believed that the spaceborne facilities will not be fully developed immediately but, like the current deep-space network, will continue to increase in capability long after they first become operational Thus, the ground-based antenna will be a key beginning point in the development of deep-space optical communication

Below, the strawman optical reception development antenna is introduced A rationale is outlined which favors build-

ing the antenna over renting time on existing astronomical facilities Various characteristics of a model facility that is adequate for the proposed experiments are then described Values of some parameters have been selected as a starting point for further discussion and research An electro-optical functional block diagram is presented and explained Preliminary estimated costs with high and low ranges are also presented on the basis of a combination of several different methods of costing

II. Introduction to the Strawman Optical Reception Development Antenna

A strawman optical reception development antenna based on the ground, together with the associated pedestal, observatory building, dome, sunshades, and signal processing, acquisition, tracking, and control systems, is postulated It will support development of tracking and data acquisition for deep-space probes as communications frequencies are raised to the visible region

Visible optical communication from deep space will initially be accomplished in spite of the disrupting effects of the Earth's atmosphere The optical phase of the received signal will be ignored Direct detection and photon counting will exploit the granularity of the optical signal to suppress noise The optical coherence will not be wasted, however, a narrow-band optical predetection filter will allow discrimination against solar interference

The optical reception antenna will be concerned primarily with photon collection Costs will be reduced by accepting considerable blur Coarse imaging of a portion of the received beam will permit acquisition and tracking of deep-space probes Imaging of natural bodies will be no better than adequate to verify sufficiently accurate coarse pointing of the antenna to a preselected portion of the sky Very fast[1] uncorrected primary optics will further sacrifice image quality for cost reduction by making the entire optical train fit within the sphere swept out by the motion of the primary collector The primary collector will consist of low-mass, rigidly mounted, hexagonal reflecting segments

[1] In optics, "fast" means that light passing through a lens converges to a focus in a distance that is short compared to the aperture diameter, and "slow" means the convergence distance is long The focal ratio or f number is the ratio of the focal length F to the aperture diameter D, so the larger the f number, the slower the lens and the slower the beam produced by the lens If the lens is used for photography, fast lenses allow rapid exposure of the film to the required density, and slow lenses make the exposure process slow

Daytime communication to within a small solar elongation angle will present sunshading and convective airflow problems not previously encountered by astronomical observatories The conventional pair of meridional external dome shutters will not be used Instead, an aperture plate running in meridional tracks and a pair of zonal shutters, above and below the plate, will limit the dome aperture to the same size as the telescope aperture (see Fig 1)

A solid cover will be selectable for mounting on the aperture plate to seal the dome against inclement weather, especially when high winds are expected When the antenna is in use, the aperture plate may carry a selected sunshade The sunshade will be rotated axially to prevent direct sunlight incidence on the primary mirror A sunshade will be selected according to the solar elongation angle from the deep-space probe in order to shade sufficiently without being unreasonably long, unduly reducing the field of view, or unnecessarily obstructing the aperture One sunshade will consist of a clear-aperture tube for use when the solar elongation angle is large Two other sunshades, containing internal vanes with coarse or fine spacing, will be used when the solar elongation angle is intermediate or small A control system will maintain alignment of the dome, aperture, sunshade, and telescope line of sight

The dome design philosophy and observatory site selection criteria will differ from those usually applied by astronomers Large seeing disturbances caused by the dome and sunshades, as well as by nighttime or daytime operation, will be tolerated along with considerable blur Altitude and exceptional seeing will likewise be traded for high visibility and easy logistics

III. Design Issues and Cost Drivers

A. The Decision to Build a New Facility or to Use an Existing Facility

A new facility should be built

Concerns expressed below preclude the use of an existing facility In summary, these are as follows (1) only a few facilities have telescopes large enough to demonstrate optical communication at significant data rates over representative large distances, (2) no existing facility has the sunshades required for daytime reception, nor could any facility accommodate an adequate sunshade within its dome, (3) existing facilities were not designed to cope with the added heating from daytime operation, nor would they cool rapidly enough to avoid degrading the performance expected by nighttime users, (4) conflicts with other users might be avoided by obtaining exclusive use, but exclusive use is not available on any telescope that is sufficiently large for a convincing demonstration, and (5)

short-term exclusive use of a large telescope might be obtainable for a crisis such as a flyby planetary encounter, but optical communications experiments are not being planned as crises

1 **Adequate diameter for a significant data rate** Demonstration of optical reception from Saturn at a data rate of 100 kbps is part of the current concept The minimum usable collector diameter is 10 meters, to provide something less than a 3-dB margin when receiving below the atmosphere under favorable weather conditions If time on an existing 10-m facility were unavailable for this demonstration, one could still receive 25 kbps from Saturn with a 5-m telescope like the one at Palomar, or 6 25 kbps with a 2 5-m telescope like the 100-inch Hooker telescope on Mt Wilson With any of these telescopes, there is always a short enough range somewhere on the way to Saturn within which 100-kbps optical communication is possible Nevertheless, it is important to demonstrate optical communication at a reasonable data rate all the way to Saturn in order to show the capability of coping with pointing problems and long loop delays

Accepting data rates from Saturn as small as 6 25 kbps or even 25 kbps would be a disappointment, since it would mean discarding all potential for mission augmentation if the optical communication works well Future missions are considering multispectral imagers and synthetic aperture radar science capabilities, sensors which generate enormous amounts of data The current plan is to show that optical communication can bring those data home

2 **The need for sunshades** A convincing demonstration requires daylight reception as well as nighttime reception, because many people do not understand that a telescope with good filtering can look through the blue sky The experiments must further demonstrate reception when the elongation of Saturn from the sun is relatively small, ideally as little as 3 degrees, in order to show capability comparable to that of radio

In order to receive communications at small solar elongations, the optical antenna or telescope must be sunshaded Direct sunlight on the primary mirror would produce intolerable scattering

No existing astronomical facility of the required size can accommodate a sunshade of the required length within its dome Astronomers do not use sunshades on the ends of their telescopes, they use the earth as a sunshade by observing at night Domes are very expensive, they are not usually built larger than the size needed to clear the telescope as it swings

Therefore, if an optical reception development facility is not constructed, one must obtain permission not only to rent time on an existing facility, but also to modify the facility One would need to add sunshade mounting tracks and interior shutters to the dome and provide for storage of the sunshades during inclement weather This modification of an existing facility would in itself be a large Construction of Facilities (C of F) project, but C of F money is rarely used to modify a rented facility A request for funds to do that would be discouraged from the start

3 **Thermal problems with existing facilities** Large astronomical facilities keep their domes closed during the daytime Opening them would cause heating of the interior and would set up turbulent convection currents These would blur the images, require opening up the field of view, and degrade the communication link performance by forcing acceptance of extra background light Most of the current analyses have made some allowance for such effects However, the convection currents would not die out until several nighttime viewing hours were lost One could not avoid schedule conflicts with other users by promising to use the telescope only during the day and to clear away all the equipment by nightfall The next day the astronomical users would complain that the seeing during their viewing time was spoiled because the telescope was still hot

Even worse, thermal shocks can distort the mirror The old large mirrors (e g , those on Mt Wilson and Mt Palomar) were made from Pyrex or even bottle glass Pyrex has a huge thermal expansion coefficient (for glasses), and bottle glass is worse It would take weeks for such mirrors to settle down after exposure to daytime temperatures if the dome were opened during the day If the facility did not have a modern, relatively thermally insensitive mirror, it would be difficult to obtain permission for daytime use at all Alternatively, one might have to retrofit the facility with a specially designed air-conditioning system

4 **Exclusive use requires accepting a small diameter** Conflicts with other users might be avoided, of course, by securing exclusive use of a facility Any attempt to obtain exclusive use of an existing facility with a 10-m-diameter telescope, however, appears to be hopeless If a small mirror size were accepted, it might be possible to negotiate exclusive use of some existing telescope facility (e g , the Hooker telescope) along with permission to mount sunshades on it

The sunshades would have to be built, retrofitted, and financed as special test fixtures to be discarded after the demonstrations One would still have to determine if the degradation of the imaging (and of the signal-to-background ratio) due to thermal cycling would be tolerable for optical communications demonstration purposes

The cost of following this procedure would be far less than that of the construction of a dedicated 10-m facility However, it would force us to accept a limited aperture and a low data rate from Saturn Additionally, the procedure would not provide a long-term development stepping stone for future optical reception systems

5 Scheduling problems for sharing a facility with adequate diameter The DSN could negotiate with any facility (including the new Keck 10-m telescope facility) to obtain viewing time for an event such as a flyby encounter Cassini, however, is not a flyby Some tests are also desirable on the way—say, between Jupiter and Saturn—but there would be no special time constraint to use as a crisis for negotiating purposes There would also be no crisis event once the probe was in orbit

Putting an experiment on an orbiter rather than on a flyby mission offers the advantage of flexibility in scheduling This advantage is much less valuable than a crisis when bargaining for viewing time, however Also, the managers of existing facilities will be reluctant to give time when they find out that the optical communications experimenters intend to modify the dome, temporarily disturb the viewing, and perhaps introduce an unknown, relatively long term thermal distortion into the optics

B. Telescope

1 Aperture diameter

The aperture diameter was chosen to be 10 m

In [1], it was shown that a 10-m telescope is at the knee of the curve of cost versus logarithmic communication growth, and it provides adequate optical channel capacity for many proposed mission requirements

2 Primary–secondary spacing

The primary–secondary spacing was chosen as half the primary diameter

Choosing the primary–secondary spacing at half the primary diameter fixes the primary f number close to $f/0.5$ Actually, if the central obstruction is one hexagon in a four-ring system, the primary f number may be $f/0.56$ Making the spacing any shorter would decrease the f number, worsen the uncorrected imaging unnecessarily, and worsen the departure of the paraboloidal figure from sphericity Lengthening the primary–secondary spacing would mean that the telescope could not swing within the sphere swept out by the primary diameter The common diameter of the observatory building and dome would then have to be increased at very substantial cost Whether the uncorrected image quality produced by such a fast primary beam will be sufficient for the derivation of adequate pointing, acquisition, and tracking information remains to be analyzed in detail

3 Post-secondary focal point

The post-secondary focal point was chosen as the primary mirror center

Just before the focus, a tertiary lens collimates the beam to a convenient diameter The optical train from there must fit behind the primary mirror within the sphere swept out by its radius for the cost reasons given above This and the secondary mirror diameter set the post-secondary f number

4 Primary mirror segmentation

Segmentation was chosen over a single-piece mirror

A 10-m-diameter single-piece mirror is too large and heavy to fabricate, coat, or swing in a telescope For glass mirrors, the thickness must be about one-sixth the diameter to maintain the polished optical figure If the specific gravity of the chosen glass were only 2 5, the mirror mass would be 327,000 kg, and the weight would be 360 tons

Segmentation was chosen over multiple mirrors

Multiple mirrors and multiple detectors would add detector noise without increasing the signal This could be serious at very low light levels when space probes are very far from earth

Multiple mirrors and a single detector may require extra light-collection mirrors, each with its own alignment requirements If energy collection were the sole issue, this would not be much worse than the alignment requirements of multiple segments However, some imaging capability is also necessary for the acquisition and tracking of the deep-space probe Image quality from a collection of mirrors may be much worse than that from a segmented mirror This trade must be reevaluated after the imaging requirements have been better determined

Segment substrates were chosen to be honeycomb rather than solid panels

A hexagonal glass substrate whose width w across the flats is 1 11 m, whose thickness is $w/6$, and whose density is 2500 kg/m^3 has a mass per unit area of 462 kg/m^2 Panels with similar stiffness and thermal stability, but using honeycomb core construction,[2] can be made with mass-to-unit-area ratios of less than 10 kg/m^2

[2] P N Swanson, *A Lightweight, Low-Cost Deployable Reflector (LDR)*, JPL Publication D-2283 (internal document), Jet Propulsion Laboratory, Pasadena, California, June 1985

Segment alignment was chosen to be manual rather than automated

It is assumed that gravitational distortion will not be problematic as the telescope is turned in different directions because of the low mass of the segments and because the truss rigidity need not be compromised by such space-flight requirements as low mass and deployability

Segmentation was chosen as hexagonal with four rings and 60 segments

The Keck telescope has three rings and 36 segments Segment width across the flats is calculated from the number of rings n and the overall aperture diameter D as $w = D/(2n + 1)$ For the 10-m Keck telescope w is 1 43 m, and for the SORDA w = 1 11 m

As the number of rings increases, the segment size, weight, and departure of a spherical segment figure from the overall paraboloidal figure all decrease Complexity, alignment problems, and residual alignment errors and their contribution to blur all increase as the number of rings increases The designers of the Keck telescope chose three rings rather than four in order to reduce the complexity of their active segment alignment system They feared that aligning 60 segments rather than 36 would represent a control problem too difficult to encounter on the first model Other users might profit from their experience, however, and use a larger number of rings in the future [2] With SORDA there is no control problem However, the alignment has been made more difficult by the use of four rings instead of three

The segment figure was chosen as paraboloidal rather than spherical

The departure of an $f/0\,5$ paraboloid from sphericity at the farthest points of a segment from the innermost ring amounts to about 1200 waves, or 0 6 mm This is far too much to correct by polishing, so paraboloidal segments were chosen at considerable increase in cost One spherical tool (the mold that forms the segment substrate) might cost $50,000, and it would serve for all 60 segments If the segments are to be paraboloidal, symmetry permits dividing the segment number by no more than 6 The SORDA design will require 10 tools, each of which might cost $250,000 because of their nonspherical shape Thus the tools for making a segmented paraboloidal mirror cost 50 times more than the tool for making multiple spherical mirrors mounted on a paraboloidal frame

Options to be studied also include using best-fitting spherical mirrors at each segment location, for which the tools would cost 10 times more than the one for making multiple spherical mirrors, or best-fitting spherical mirrors for each ring, for which the tools would cost four times as much

The outside diameter circle was chosen to be tangent to the corner hexagon's outer edges (see Fig 2)

Other options make the circle pass through the points of the midlateral hexagon neighbors (Fig 3), through the point of the midlateral hexagon (Fig 4), or through the outer end of the joint between the midlateral hexagon and its neighbor (Fig 5) The option chosen requires negligible trimming of any hexagon and provides the smallest width across the flats for a given diameter, at a cost of the loss of the unfilled irregular area at the edges Some of this area might be obstructed in any case by the tripod or hexapod that supports the secondary mirror

For an aperture of diameter D = 10 m, the segment width w across the flats for various options is

$$w = \begin{cases} 1\ 11\ \text{m} = D/9 & \text{tangent to the outer edge of the corner hexagon} \\ 1\ 20\ \text{m} = D\sqrt{39}/52 & \text{through the points of the midlateral hexagon neighbors} \\ 1\ 24\ \text{m} = D\sqrt{3}/14 & \text{through the point of the midlateral hexagon} \\ 1\ 32\ \text{m} = D\sqrt{129}/86 & \text{through the joints between the midlateral hexagon and its neighbors} \end{cases}$$

in order of increasing aperture filling and increasing number of trimmed hexagons The last option cuts all the outer ring hexagons substantially and completely fills the aperture

Increasing the segment width also increases the paraboloidal departure from sphericity at the extreme points This may increase costs depending on the method of forming and polishing tools for the panels The worst departure is at the outer points of the inner ring hexagons There the departure, as measured parallel to the telescope line of sight, is

$$2fD - \frac{19w^2}{48fD} - \sqrt{\left(2fD - \frac{19w^2}{48fD}\right)^2 - \frac{469w^4}{2304f^2D^2}}$$

where f is the focal ratio or f number For the four options mentioned above, with an $f/0\ 5$ primary mirror, the respective departures are 0 63 mm, 0 86 mm, 0 97 mm, and 1 26 mm

5 Primary mirror figure tolerance and surface quality

The root-mean-square figure tolerance and surface quality should be 2 μm

The use of low-mass honeycomb panels for low cost and mass reduction requires accepting a currently achievable figure tolerance and surface quality This means accepting considerable blur from this source as well as others, but the main purpose is just light collection A budget of blur, aberrations, diffraction, and seeing must be prepared and analyzed to determine how much disturbance from each source is tolerable

The most important cost driver after the diameter of the primary aperture is the amount of blur accepted for the telescope The major driver of blur is the surface quality of the primary mirror, when a rough reflector is accepted (It is assumed that the panels will remain in accurate alignment) The root-mean-square surface roughness σ accepted is about 4λ, with an estimated correlation distance $T_c = 0\ 25$ m, approximately one-fourth of the distance across the segments This would give a blur of $\theta = 9\ 33''$ (i e , all but $e^{-2} = 13\ 5$ percent of the light collected from a point source would be scattered into a cone of angle $\theta = 4\sqrt{2}\sigma/T_c$, according to [3]) Studies to date have shown that blur circles this size will not overly compromise the quality of deep-space communication links [1]

6 Secondary mirror diameter

The secondary mirror diameter was chosen to fit within one hexagon

This arrangement makes the primary beam as slow as possible, given the primary–secondary spacing, without requiring cut hexagons in the primary mirror The fractional area obstructed centrally is 1/61

C. Dome

1 Diameter

The dome diameter was chosen to be 12 m

The telescope primary diameter is 10 m Allowing 1 m on either side for clearance and wall thickness, the dome diameter is 12 m (39 ft) This size is within the upper range of commercially available standard sizes, at least for hemispherical domes However, if the lowest telescope elevation angle e_{min} to be used is less than 56 5 degrees, the dome required will exceed hemisphericity The fraction of a sphere required will be (156 5 degrees – e_{min})/180 degrees, or 0 87 for a telescope that can look horizontally

Alternatively, a much larger hemispherical dome could be used, with the telescope center mounted above the hemisphere center A 10-m-diameter telescope mounted 5 m above the center of a hemispherical dome, with 1 m of clearance above the telescope, would have an unobstructed horizontal view if the dome diameter were 22 m (72 ft) The observatory building cost would increase by a factor of $(22/12)^2 = 3\ 4$ The dome size would probably require custom fabrication

2 Thermal design

Special thermal requirements are imposed by operation at all hours

Astronomers do their observing at night using the Earth as a sunshade Domes are ordinarily kept closed during the day in order to prevent thermal shocks to monolithic mirrors that would not rethermalize for weeks The present requirements call for a dome and sunshades that will exclude direct sunlight on any part of the telescope, especially the primary mirror, but also on the mount and the back of the secondary mirror

3 Automatic dome positioning

The dome will be positioned automatically by the telescope pointing system

Automatic positioning of the dome relative to the telescope line of sight is desirable for reception of lengthy communications from the deep-space probe It is assumed that this positioning will be controlled by the same system that acquires and tracks the deep-space probe and points the telescope See Fig 6 for a block diagram of the systems

D. Sunshades

1 Location

The sunshade location was chosen to be external to the dome

Precise alignment between the sunshade and the telescope optics is not required The spacing between the primary and secondary mirrors, for example, is critical for focusing, but the sunshade may be made large enough to tolerate small parallel displacements of its optical axis from the telescope line of sight Small angular displacements will have no effect on the system performance as long as the sunshade has a clear aperture somewhat larger than the telescope aperture A sunshade with internal vanes would produce extra obstruction when displaced angularly, however

The dome is the most expensive ingredient in the observatory building, and its cost increases rapidly with diameter Mounting the sunshade externally rather than at the end of the telescope reduces the required observatory and dome diameter to the telescope swing diameter plus clearance

2 Strength

The dome will have to be stronger than usual to support sunshades

Telescope domes have to be strong to survive high winds at mountain sites An additional strength requirement, yet to be analyzed in detail, arises when a sunshade of considerable weight is to be positioned at various elevation angles for operation during moderate wind conditions A counterweight may be required, and the position or mass of the counterweight may require dynamic adjustment

Either the dome or the telescope structure must bear the weight of the sunshade One or the other will therefore require additional strength at extra cost Putting the sunshade on the dome rather than on the telescope increases the required precision of the automatic dome positioning The required precision is still not as stringent as that required for pointing the telescope

3 Aerodynamic design

The external sunshade will require redesign of dome aerodynamics

Good seeing—the maintenance of high image quality unperturbed by atmospheric turbulence—usually requires special dome design to ensure that airflow around the dome is as nearly laminar as possible The presence of one of several sunshades of varied internal vane configurations will alter the aerodynamics of the dome considerably and will present special design challenges

4 Length

The sunshade length was chosen to be 9 m

Making the external sunshade length equal to 3/2 of the dome radius R produces a structure that looks like a ball with a short protruding shaft (see Fig 1) This is not too unwieldy for pointing, given the wind loads to be borne during operation

5 Removable mounting

Sunshades will be removable

Table Mountain Observatory reports logging winds of 90 m/s (200 mi/h), and their domes survived An external sunshade would probably add too much wind load to a dome of reasonable strength, so the sunshades will be removed and stored safely when inclement weather is expected

6 Interchangeable mounting

Sunshades will be interchangeable

The sunshade limits the largest field of view of the telescope It should therefore be removable when it is not needed

The dome itself provides some sunshading If the aperture of the dome is a circle of the same diameter as the primary mirror, the dome radius is 6/5 of the primary mirror radius, and the primary mirror is situated in its swing sphere as far back as possible from the dome aperture, then direct sunlight will be excluded from the primary mirror as long as the angle between the telescope line of sight and the solar direction line is greater than 71 65 degrees The dome aperture circle and the primary mirror rim will lie in parallel planes separated by $\sqrt{R^2 - (D/2)^2} = 3\ 32$ m

Operation will often require looking closer to the Sun than 72 degrees Sunshades will be provided that will not unduly limit the telescope field of view An open tubular sunshade mounted on the dome aperture circle and extending from there by 3/2 of the dome radius, or 9 m, will exclude direct sunlight at a solar elongation angle from the deep-space probe of 39 07 degrees

The present Deep Space Network can communicate with a deep-space probe within about 1 degree of the Sun An open-tube sunshade to permit operation at that angle is too long Instead, a second sunshade will be provided, at the performance cost of the introduction of a small amount of additional obstruction and diffraction Eight equally spaced parallel-plate vanes extending from the end of a similar tube down to the dome radius (6 32 m) would permit looking to within 10 degrees of the rim of the Sun If the number of vanes is $n = 8$, the vane spacing is $D/(n + 1) = 1\ 11$ m

To look within 2 degrees of the rim of the Sun (solar elongation of 2 25 degrees), another sunshade would have 45 parallel plate vanes with a spacing of 22 cm This introduces considerably more obstruction than the other sunshade However, it will usually be needed only for tracking missions to the terrestrial inner planets, as the giant planets and Pluto spend little time at such small conjunction angles

E. Site Selection

The site will be chosen for high visibility and easy logistics rather than for good seeing

The signal attenuation of the clear atmosphere and the image-degrading effect of turbulence both decrease as elevation increases Elevation is not as important to optical reception as it is to astronomy, however, because there are ways to increase the signal strength, and because optical reception does not rely on clear images On the other hand, visibility (freedom of skies from cloud cover) is essential to this operation, and the site will be selected accordingly

Proximity to other Deep Space Network sites, which would simplify the logistics of maintenance and operation, is desirable but not mandatory

IV. Optical Functions, Signal Processing, and Control Systems

Figure 6 shows the electro-optical functional block diagram Between the blocks the laser beams are shown as broken lines, natural-light beams as thick solid lines, and electrical cables as thin solid lines

A. Optical Functions

The telescope primary and secondary and the beam-steering mirrors will be coated for high reflectivity in the extended visible region

Coating for high reflectivity at only the laser wavelength would increase the signal power while reducing background interference significantly Solar incidence and the need to provide some verification of correct pointing relative to the stars or planets prevent optimizing the reflectivity at the laser wavelength

If the primary mirror substrates were transparent and nonabsorbing (or absorbing but very stable thermally), it would be possible to coat the mirror segments to reflect the laser wavelength with high efficiency over a narrow spectral region of 10 or 20 nm The remaining natural light could be transmitted by the coating and substrate to a cooled, absorbing screen on the back of the primary mirror In this way it might be possible to avoid the need for sunshades However, the ability to see any natural objects in the sky (except the very brightest) would be lost This loss might not be inconvenient if the objects were to be viewed only occasionally for the purposes of checking calibration of the altitude and azimuth setting circles However, if a planet or guide star is to serve as a beacon for locating the spacecraft, then it has to be detectable

The tertiary collimator will be coated for broadband low reflectivity in the extended visible region

Once again, the antireflection coatings could be optimized only for the laser wavelength, but the transmission of natural light would suffer

Beam steering will be provided on two axes for both natural and laser light

Beam steering will first be used in acquiring the laser signal and centering it on the direct laser photodetector Once the signal is acquired, the beam-steering mirrors will provide fast reactions to remove pointing errors due to atmospheric disturbances and telescope vibrations

An optical filter with a tunable notch for the laser signal will separate laser light from natural light

The optical filter bandwidth will be as large as 1 nm or as small as 0 1 nm If it is very narrow it must be tunable to accommodate Doppler shifts of ±53 GHz (±0 05 nm) in the received signal from a distant spacecraft Very narrow bandwidths are usually achieved by combining in series a multilayer dielectric narrowband filter and an etalon These two elements may be separated The multilayer dielectric filter may be placed at an angle on a beamsplitter so the natural light (minus a narrow notch) can be sent one way through a focusing lens to a planet/star detector, while the narrowband light is filtered further by an etalon

A selectable power splitter will separate some of the laser signal for the acquisition and tracking system

About half the laser signal will be separated in the acquisition mode Later, once the signal is acquired, only about 5 to 10 percent of the laser light will be used for tracking The rest will be detected for communications A selectable power splitter is therefore required

The field stops will be adjustable for operating mode and conditions

During acquisition the field stops must be larger than they are during tracking Also, the direct laser photodetector field stop may be adjusted according to the amount of background present

B. Signal Processing

Once the signal is detected directly by the laser photodetector, it will receive very little immediate processing before being recorded and transmitted for signal processing at the telescope site The important information to be fed back to the systems controller immediately is just that the signal has been acquired

C. Control Systems

The operations processor receives commands to locate, acquire, and track spacecraft Localization is first achieved by prediction according to past tracking data and the epoch Pointing of the telescope and dome is done through appropriate controllers and is verified by detection of nearby stars and planets Once the acquirer/tracker reports acquisition of the spacecraft the operations processor follows it, receiving feedback from lines and sensors not shown on the diagram in Fig 6

V. Projected Costs

Preliminary estimates of Construction of Facilities costs for the strawman design are shown in Table 1, which shows best, low, and high estimates in order to provide a feeling for the error ranges involved The rationale for these items will now be explained line by line

The midpoint of construction year is the midpoint between the award and completion of the construction contract The earliest this could be is 1993 based on present cycles for approval of Construction of Facilities requests The latest pessimistic reasonable estimate is 1994, in order for the facility to be tested and available to support the proposed optical communications flight experiments on the Cassini mission

The annual inflation factor is used together with the midpoint of construction year to update projected costs for the telescope, sunshade, and dome as well as construction costs per unit area to the midpoint time of construction Costs also vary according to the contingency factor chosen and the percentage of total costs paid for architectural and engineering overseeing

The telescope, pedestal, and pointing and control system costs are then calculated according to [1], with inflation from 1985, contingency, and overseeing costs included Values in the cost estimate tables reflect the supposition that surface roughness is the major contributor to blur

Present sunshade cost, plus the cost of strengthening either the telescope pedestal or the dome to bear the sunshade weight and the cost of sunshade positioning controls, was coarsely estimated at $500,000 per meter of length in 1987 dollars When the sunshade is mounted on the telescope, the length was found by considering a single bounce within vanes spaced 2 cm apart when looking within 3 degrees of the Sun The present cost was then extended in the same way as the telescope cost

The location and mounting of the sunshade affect the common diameter of the observatory and dome From the diameter, costs are obtained in two different ways The observatory floor area is multiplied by a high cost of construction per unit area because of the reinforced concrete necessary and the foundation required for the pedestal The dome cost was obtained by scaling down the cost of the Keck telescope dome according to the same exponent factor, 2 6, as has been used for telescope diameter (This factor agrees well with off-the-shelf costs of domes up to 40 feet in diameter)

Costs for a modest-sized companion building were also included The area of the signal-processing building was doubled to account for the cost of the full plenum The site conditioning cost, the preliminary engineering report cost, and the final design cost were taken as percentages of the total cost, but the study and the environmental assessment were considered to be fixed costs The costs are based on certain models that include scaling studies of recently experienced costs, and typical costs of construction per unit area for various types of construction A subjective estimate was used only for the cost of one component (the sunshades), and this cost is less than ten percent of the total cost

VI. Conclusion

A workable model of a ground-based optical reception facility has been presented The facility is needed to support development of optical communication from deep-space probes No existing astronomical facility is available and suitable Reasonable choices of design parameters, design issues, cost drivers, and cost estimates with optimistic and pessimistic limits were included Several trade-study areas were identified which deserve further analysis These included the adequacy of uncorrected images for providing pointing, acquisition, and tracking information, the use of multiple mirrors instead of segmented mirrors, the use of segments with spherical instead of paraboloidal figures, the amount of blur to be accepted from mirrors with low surface quality, the location and configuration of the sunshade, dome aerodynamics and thermal design, and visibility and convenience at the site

References

[1] J R Lesh and D L Robinson, "A Cost-Performance Model for Ground-Based Optical Communications Receiving Telescopes," *TDA Progress Report 42-87*, vol July–September 1986, Jet Propulsion Laboratory, Pasadena, California, pp 56–64, November 15, 1986

[2] J Nelson, *The Design of the University of California Ten Meter Telescope*, University of California Draft UC TMT Report No 90, University of California at Berkeley, p 5-5, December 1984

[3] V A Vilnrotter, *Optical Receivers Using Rough Reflectors*, JPL Publication 85-25, Jet Propulsion Laboratory, Pasadena, California, pp 2-3–2-4, May 1, 1985

Table 1 Preliminary estimates of facility construction costs

Item	Approximate*		Low range†		High range††	
	Value	Cost	Value	Cost	Value	Cost
Midpoint of construction year	1993		1993		1994	
Annual inflation factor	4%		4%		6%	
Contingency factor	20%		15%		30%	
Architectural and engineering overseeing	2%		2%		2%	
Aperture diameter	10 m		10 m		10 m	
Blur circle or minimum field of view	9″		10″		8″	
Telescope, pedestal, pointing, control		$9,240,000		$8,020,000		$13,800,000
Primary *f*/number	*f*/0 5		*f*/0 5		*f*/0 5	
Primary focal length	5 m		5 m		5 m	
Sunshade length	9 m		9 m		1 3 m	
Sunshade, mount strength, positioning		$1,010,000		$960,000		$1,300,000
Sunshade 0 = on dome, 1 = on telescope end	0		0		1	
Swing radius of telescope	5 7 m		5 7 m		6 2 m	
Clearance swing to outside wall	1 m		1 m		1 5 m	
Observatory diameter	44 ft		44 ft		50 ft	
Observatory floor area	1521 ft^2		1521 ft^2		1963 ft^2	
Observatory building cost/unit area	$360/$ft^2$		$350/$ft^2$		$460/$ft^2$	
Observatory building cost up to dome		$550,000		$530,000		$900,000
Dome (2 6 power scaling from Keck)		$700,000		$680,000		$1,250,000
Signal processing building, full plenum	2500 ft^2		2500 ft^2		3000 ft^2	
Control room, facilities/utilities	750 ft^2		750 ft^2		1000 ft^2	
Construction cost/unit area	$230/$ft^2$		$220/$ft^2$		$290/$ft^2$	
Cost of companion building		$1,320,000		$1,270,000		$2,030,000
Site conditioning costs		$1,420,000		$1,270,000		$2,140,000
Total for construction of facilities		$14,240,000		$12,730,000		$21,420,000
Preliminary engineering report (PER)		$280,000		$250,000		$430,000
Design (final)		$850,000		$760,000		$1,290,000
Other study, environmental assessment		$200,000		$200,000		$200,000
Total cost		$15,570,000		$13,940,000		$23,340,000

*To be considered the best values between high and low ranges
†To be considered an optimistic reasonable estimate
††To be considered a pessimistic reasonable estimate

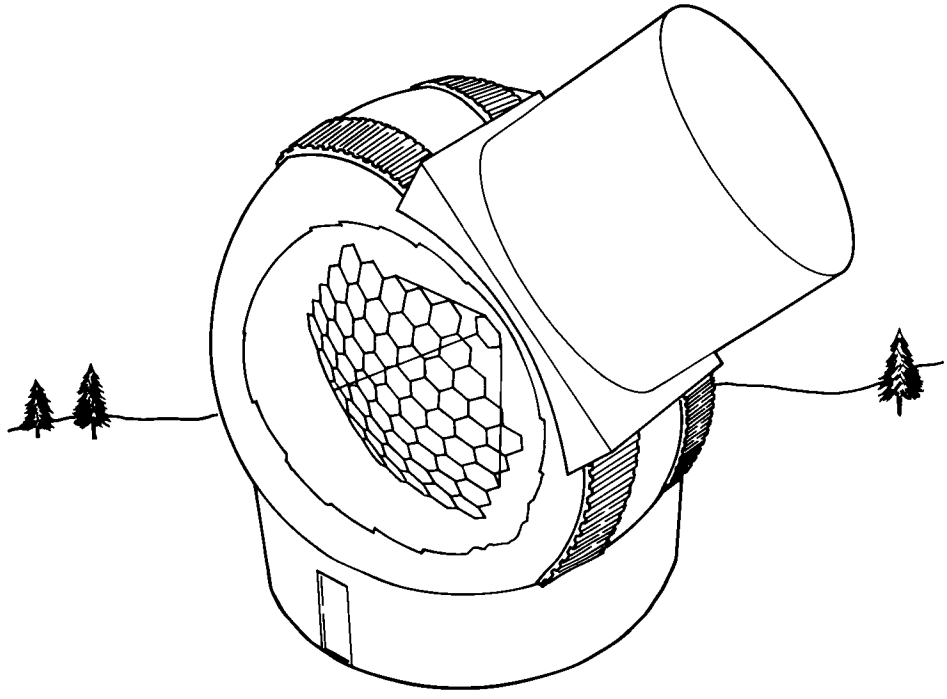

Fig. 1 Optical reception development antenna, observatory building, dome, and sunshades

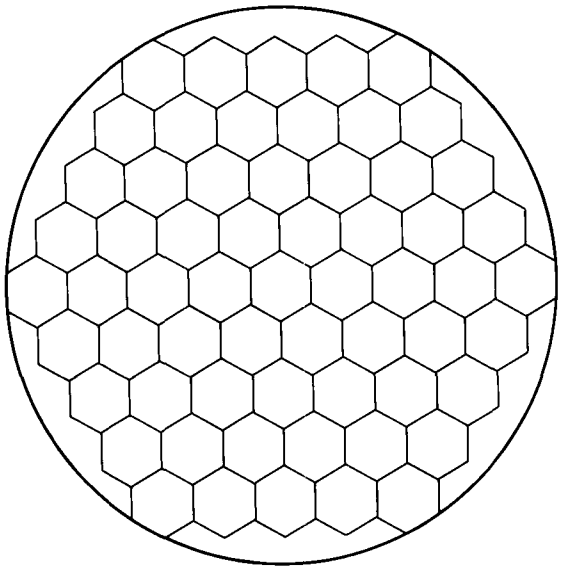

Fig 2. A four-ring hexagonal segmentation pattern with the outside diameter circle tangent to the corner hexagon outer edges

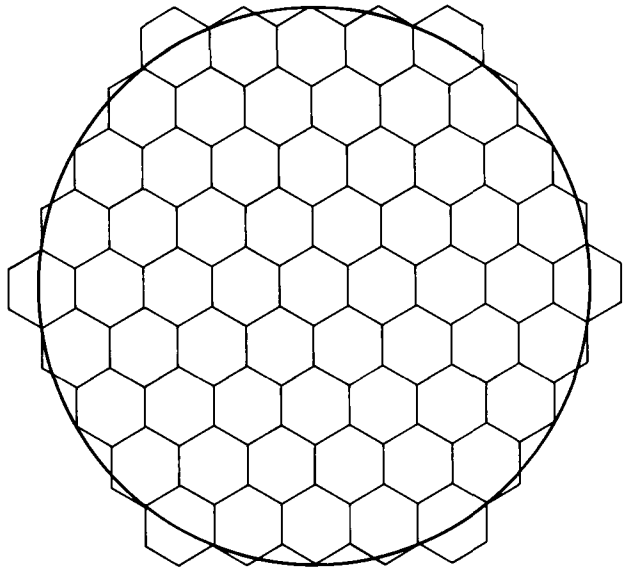

Fig 4 A four-ring hexagonal segmentation pattern with the outside diameter circle passing through the point of the midlateral hexagon

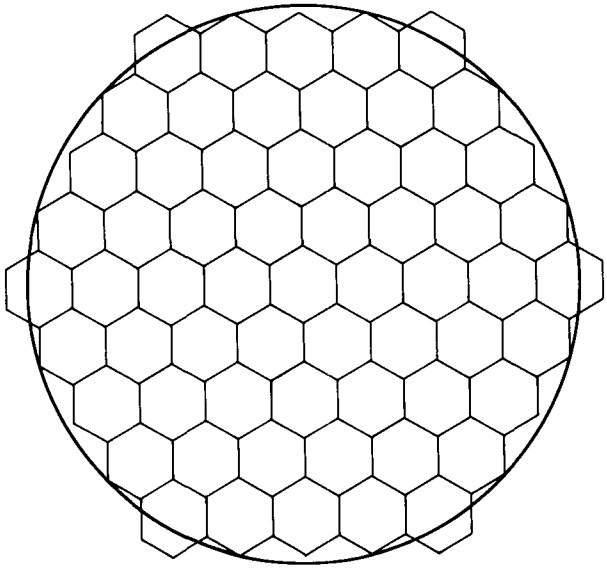

Fig 3 A four-ring hexagonal segmentation pattern with the outside diameter circle passing through the points of the midlateral hexagon neighbors

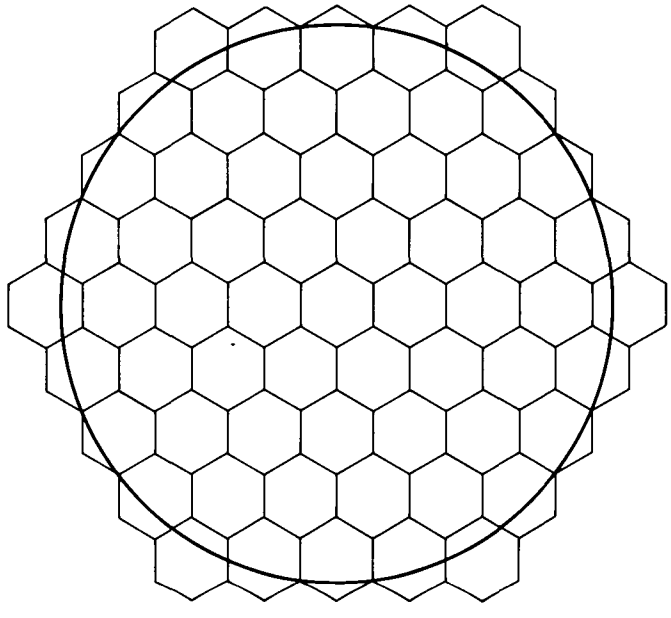

Fig 5 A four-ring hexagonal segmentation pattern with the outside diameter circle passing through the outer end of the joint between the midlateral hexagon and its neighbor

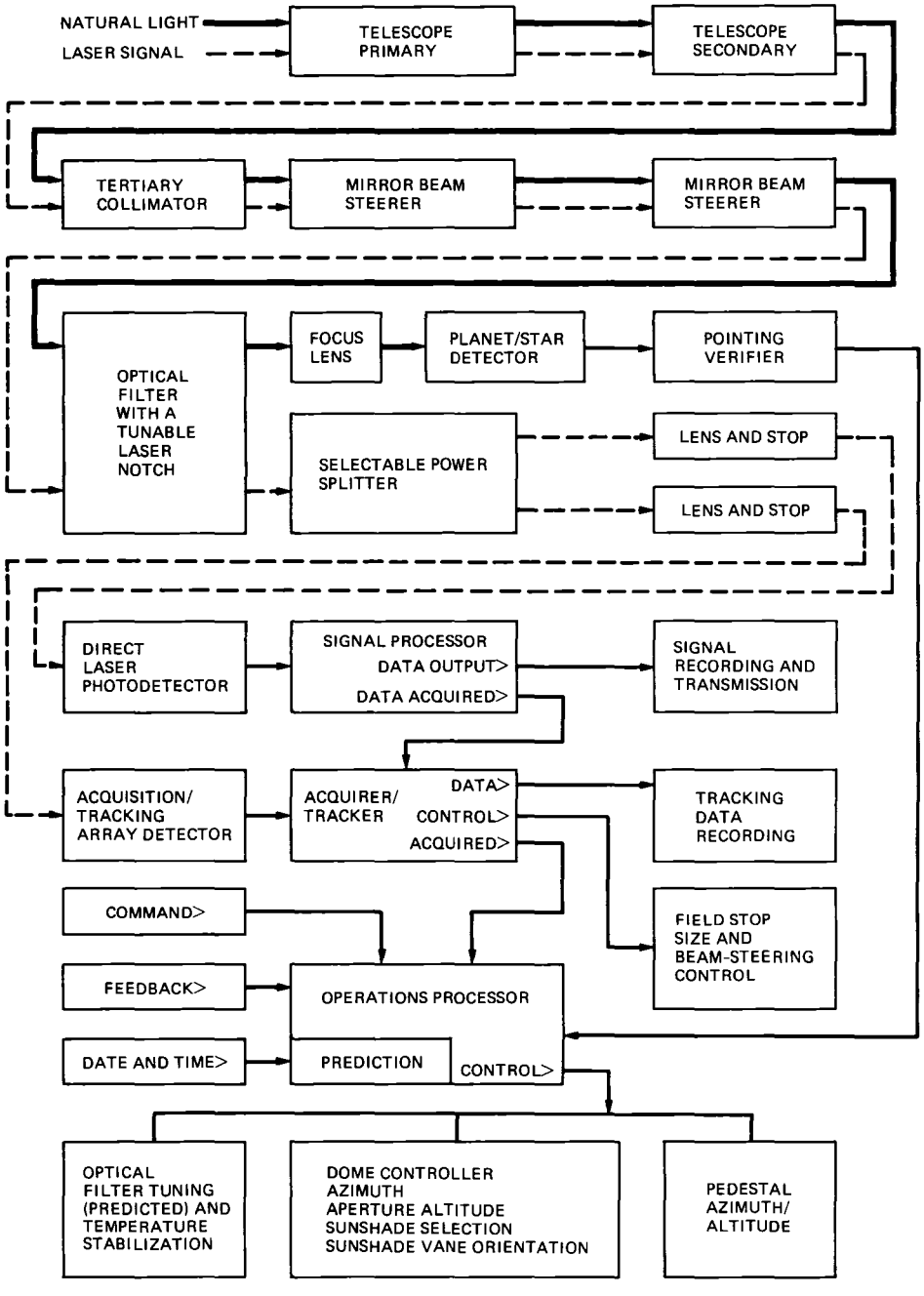

Fig. 6 An electro-optical functional block diagram of systems associated with the optical reception development antenna

Apparent Brightness of Stars and Lasers

B L Schumaker
Communications Systems Research Section

Foremost among issues affecting the potential use of astrometric techniques to locate and track laser-carrying spacecraft is the apparent brightness (detected energy or photon flux) of a laser relative to reference stars Broadband detectors offer improved sensitivity to stars (broadband "blackbody" sources), but not to lasers The important and fundamental step of calibrating laser and star brightnesses according to detector spectral sensitivity is carried out here for four representative kinds of broadband detectors, located above and below the atmosphere Stars are identified according to parameters traditionally used by astronomers temperature (spectral class, or color) and apparent brightness at visible wavelengths These are translated into an energy and photon flux for each kind of broadband detector and are then compared with the corresponding flux from a laser The comparisons are also given as "magnitude correction factors," i e , in astronomers' traditional units of 4 0 dB Astrometrists typically characterize the sensitivity of their instruments in terms of the precision with which they can make a relative measurement of position and the minimum brightness needed to achieve that precision (In an ideal instrument, limited only by $1/\sqrt{N}$ photon statistical fluctuations, these two descriptions would coincide) Given this information and the instrument's spectral sensitivity, one can use the calculations described in this report to infer the detectability of a laser and the precision with which it could be located and tracked Results show, for example, that while a star and a laser may have comparable brightnesses at visible wavelengths, to a broadband detector the star might appear brighter than the laser by anywhere from 2 to 17 dB, depending on the star's spectral class and the detector spectral sensitivity Since the limiting brightness quoted for a particular instrument is typically firm to within 4 0 dB (one magnitude), judging a laser's detectability by its visible brightness alone could lead to serious underestimation of the requirements on its effective radiated power The laser brightness corrections given here solve this problem

I. Introduction

The use of astrometric techniques to locate and track laser-carrying spacecraft is an intriguing and real possibility Measurement precision is influenced strongly by the number of reference stars in the field of view, which in turn depends on the sensitivity of the detector/telescope combination and the size of the field of view One way to improve sensitivity to stars and other broadband sources is to use broadband detectors Indeed, some of the most sensitive astrometric measurements made to date have used a CCD detector with a sensitivity range of at least 250 nm [1] On the other hand, use of a broadband detector will not increase the sensitivity to a laser or other narrowband source It is important, therefore,

to calibrate the relative brightness of lasers and potential reference stars according to the kinds of detectors used This article shows how to make careful comparisons of the flux that would be measured by prospective broadband detectors from stars (blackbody sources) and from lasers (monochromatic sources)

Three elements make up the definition of a star's or other celestial object's apparent brightness the quantity to be measured, the location of the measurement, and the wavelength range over which the measurement is made Astronomers traditionally take the measure of brightness to be received energy flux, or irradiance, and the measurement location to be the top of Earth's atmosphere The measurement wavelength range should, of course, be a particular detector's spectral sensitivity range Historically, to standardize descriptions, astronomers have used for this last element several different narrow spectral response functions, ranging from the ultraviolet through the visible Unfortunately, these narrowband characterizations are awkward and inappropriate indicators of the brightness that would be measured by broadband detectors from stars, as such they can lead to erroneous conclusions about the relative brightness of lasers (narrowband sources) and stars when both are viewed by broadband detectors

To make accurate comparisons between the brightness of lasers and stars, one therefore must translate from at least one of these narrowband brightness calibrations into the actual flux that would be measured by particular broadband detectors These translations depend on the spectral sensitivities of the detectors and on the spectral character of the source radiation—its effective temperature if it is blackbody, and its wavelength if it is monochromatic These translations are made in this article for apparent visual brightness (defined below) and four representative kinds of broadband detectors Next, the detected flux from a monochromatic laser (a function of laser power, transmit-aperture size, wavelength, and distance from receiver) is compared with that from stars of the same apparent visual brightness but of various temperatures, for the same four kinds of broadband detectors

Two pieces of information are needed to characterize the brightness of a star the star's temperature T or color (spectral class) and its apparent brightness (measured irradiance) in one of several standard narrow spectral regions, e g , the visible In this article, apparent visual brightness is chosen for the latter, it is defined as the irradiance measured at the top of Earth's atmosphere by a detector whose spectral sensitivity is described by the "visual response function" $V(\lambda)$ This narrow, sharply peaked function approximates the spectral response of the human eye Traditionally, astronomers describe apparent visual brightness in terms of "apparent visual magnitude" m_V, which is the visual irradiance normalized to a standard irradiance, in units of 4 0 dB (see Eq [5]) Hence the first part of this report translates from a star's temperature T and apparent visual magnitude m_V to the energy or photon flux that would be measured by a broadband detector with spectral sensitivity $D(\lambda)$ (see Eqs [12]–[15] and Table 3) Four representative kinds of detectors are considered, both above and below the atmosphere photomultiplier tubes (PMTs), charge-coupled devices (CCDs), avalanche photodiodes (APDs), and multianode microchannel arrays (MAMAs), detector sensitivities are described in the Appendix and in Fig 3(a) and (b)

A laser looking back at a detector can also be characterized by two quantities its wavelength λ_t and the irradiance it produces, $H_t \simeq P_t(\pi/4)(D_t/r\lambda_t)^2$, a function of the laser's power P_t, transmit-aperture diameter D_t, wavelength, and distance r from the detector Alternatively, it can be characterized by its wavelength and its apparent visual magnitude $m_V \equiv -2\,5 \log[10^{8\,5} V(\lambda_t)H_t]$ (see discussion in Section III and Eq [20]) The irradiance or photon flux measured by a detector with spectral sensitivity $D(\lambda)$ is just the product of $D(\lambda_t)$ and H_t or $(\lambda_t/hc)H_t$, respectively (h is Planck's constant and c is the speed of light) The flux measured by each of the four kinds of detectors described above is calculated in this report for a 1-W laser at Saturn with a 30-cm aperture, emitting at 0 532 micrometer (μ) (see Eqs [21]–[24] and Table 4) The results are easily scaled to lasers with different parameters at arbitrary distances

These quantitative comparisons of the measured flux from stars and lasers verify the predicted inadequacy of visual brightness (or any other narrowband measure of brightness) as an indicator of the relative brightness of lasers and stars viewed with broadband detectors A laser and a star might appear equally bright when viewed by the eye or other narrowband detector, but widen the spectral response of the detector and many additional photons will be detected from the star, whereas no additional photons will be detected from the laser Hence, to a broadband detector, the laser will appear dimmer than the star, how much dimmer depends on the temperature of the star and the spectral sensitivity of the detector For example, the G0, B0, and M0 rows of Table 5 indicate that with the broadband detectors considered here, a laser will appear between 4 and 8 dB (one and two magnitudes) dimmer than a solar-type (G0) star of the same apparent visual brightness, and as much as 16 dB (four magnitudes) dimmer than a very hot or very cold star of the same visual brightness (The Sun is a G2 star with an effective blackbody temperature of about 5770 K, see Table 1 [6])

Just how bright will a typical spacecraft laser appear? Consider a 1-W laser at Saturn, transmitting through a 30-cm aperture at 0 532 μ An observer above the atmosphere would

receive a photon flux of about $10^{5.5} \simeq 300{,}000\ m^{-2}s^{-1}$, and the laser would have an apparent visual magnitude $m_V \simeq 11.2$ (see Eqs [17] and [20]). On the ground the flux would be about 80 percent of this, equivalent to an effective $m'_V \simeq 11.5$. From Uranus, this laser would have $m_V \simeq 12.7$, and from Neptune $m_V \simeq 14.2$. A broadband detector such as a CCD or an APD might count as many as 50 percent of the incident laser photons, while a PMT or a MAMA would typically count only 10 percent. But from a solar-type star of this apparent visual magnitude, all these detectors would count many more photons, because the star is also emitting photons at wavelengths that lie outside the peak of the visual response function, but inside the response function of the detector. Table 5(b) compares the photon flux that would be measured by various detectors from a laser and from stars of 12 different temperatures, all of which have the same apparent visual magnitude m_V. It says, for example, that the UV-flooded CCD considered here would count approximately 7.3 dB (five times) more photons from a Sun-like (G0) star, and as much as 12.9 dB (≃20 times) more photons from a very hot (B0) star than it would from a laser, given that they all had the same apparent visual magnitude m_V. In astronomers' language (Table 5[d]), this says that a laser of $m_V \simeq 11$, say, would look to this CCD detector only as bright as a Sun-like star of $m_V \simeq 12.8$, or as bright as a very hot star of $m_V \simeq 14.2$.

These laser brightness "correction factors" are significant but not necessarily discouraging, for they still leave the laser sources envisioned for use on planetary spacecraft within the actual or expected capabilities of ground-based detectors and telescopes. (The situation is, of course, better for space-based detectors and telescopes.) For example, astrometrists at USNO in Flagstaff, using a 4-m ([1.6-arcminute]^2 field-of-view) reflector telescope with a CCD at its prime focus, claim a nightly precision of 10 milliarcseconds (mas), or 50 nrad, for relative position measurements on stars as dim as $m_V = 19$ [1]. Their CCD was less sensitive (typically only 15 percent effective quantum efficiency) and narrower spectrally (≃250 nm wide, centered at ≃575 nm) than the one considered here, so the corresponding laser brightness corrections would be less severe than those given here.

Gatewood et al. at the Allegheny Observatory in Pittsburgh, using a 30-in ([10-arcminute]^2 field-of-view) refractor, Ronchi ruling, and four PMTs, have demonstrated nightly precisions of 3 mas or better for solar-type stars of $m_V = 8$ or brighter [2], [3]. They used narrow-bandpass filters with their PMTs (50 nm wide, centered at 642.5 nm) in order to isolate the wavelengths nearest the minimum focus of the refractor's objective lens. Hence the laser brightness corrections (for a laser emitting near 642 nm) would again be smaller than those given here. Gatewood estimates that a 1-m or larger system like theirs, located where both seeing and visibility are better, could provide these precisions for stars down to $m_V = 14$, or improve them to tenths of milliarcseconds for $m_V = 8$ and brighter stars. He also estimates that a 1-m system in space could provide precisions of 0.1 microarcsecond.

Buffington at JPL's Table Mountain Observatory, using a 12-in (1.2-degree by 0.5-degree field of view) meridian-mount reflector with Ronchi grating and 12 PMTs, claims to be capable of nightly precisions of 4 mas for solar-type stars as faint as $m_V = 12$, and 15 mas for $m_V = 14$ stars [4]. Finally, for comparison, the European Space Agency's HIPPARCOS is expected to provide positions, parallaxes, and proper motions for 100,000 stars with $m_V = 10$ and brighter, with a precision of several milliarcseconds [4].

These examples of current astrometric capabilities give good reason to believe that lasers could be located and tracked successfully with existing or modestly improved astrometric technology and techniques.

II. Organization

This report is organized as follows. Section III reviews the definitions of astronomy's standard magnitude systems for describing source brightness. Although it has just been argued that these narrowband brightness measures are inappropriate for comparing lasers and stars, familiarity with them is essential, since all existing star catalogs and other sources of information about star locations and brightnesses use them. Section IV compares the visual irradiance and photon flux from stars with that which would be measured by broadband detectors. Section V does the same for monochromatic laser sources, with quantitative calculations restricted to the visible wavelength 0.532 μ, that of a frequency-doubled Nd:YAG laser. Section VI puts these calculations together to compare irradiance and photon flux from a laser with that from stars. Section VII summarizes the results and some of their implications.

Numerical results and support information are contained in figures and tables. The Appendix describes the spectral sensitivities assumed for the four kinds of detectors considered here, and for the spectral transmission of the atmosphere and the visual response function. These functions are graphed together in Fig. 3(a)–(c).

III. Review of Visual and Other Magnitude Systems

By convention, apparent brightness refers to the irradiance measured by an observer located at the top of Earth's atmosphere. Since stars radiate over a range of wavelengths broader than the sensitivity ranges of most detectors, it is customary

in astronomy to speak of apparent brightness in particular spectral regions, defined by certain standard spectral response functions Four major spectral response functions are used by astronomers (see Fig 1) the visual ("V") spans the wavelength range 500 nm to 600 nm and peaks at around 555 nm, the blue ("B") spans the range 400 nm to 500 nm and peaks at around 435 nm, the ultraviolet ("U") spans the range 300 nm to 400 nm and peaks at around 350 nm, and the photographic ("pg") closely resembles the blue response curve but peaks at 430 nm [5], [6] A fifth measure of brightness used by astronomers is the bolometric brightness ("b"), or total irradiance at all wavelengths This report compares apparent visual brightness, defined as the irradiance measured by a detector with spectral sensitivity $V(\lambda)$, with the brightness measured by various broadband detectors with spectral sensitivities $D(\lambda)$

The irradiance H_S measured by a detector with spectral sensitivity $S(\lambda)$ from a source that produces a spectral irradiance $H(\lambda)$ is

$$H_S \equiv \int S(\lambda)H(\lambda)d\lambda \tag{1}$$

A photon detector measures a flux

$$n_S \equiv \int S(\lambda)\left(\frac{\lambda}{hc}\right)H(\lambda)d\lambda \tag{2}$$

where $(hc)^{-1} = 10^{18\,7}$ J^{-1} μ^{-1} When $S(\lambda) = V(\lambda)$, these give the visual irradiance and photon flux, when $S(\lambda) = D(\lambda)$, they give the irradiance and photon flux measured by a detector with spectral sensitivity $D(\lambda)$ The total (bolometric) irradiance and photon flux correspond to $S(\lambda) = 1$

Associated with each of these systems is a reference value for the spectral irradiance at a special wavelength, typically that at which the spectral response function peaks For the visual response function, this wavelength is $\lambda_V \equiv 0\,55$ μ (Eq [10]) The brightness of a star, defined with respect to some spectral response function $S(\lambda)$, is traditionally described by giving the ratio of measured to reference spectral irradiance at these special wavelengths, in units of 4 0 dB, called "magnitudes" It is sufficiently accurate for most purposes to use reference values for the irradiance H_S, these are given below Thus, the irradiance from a source of apparent magnitude m_S is $10^{-0\,4m_S} \simeq (0\,4)^{m_S}$ times the irradiance from a source with $m_S = 0$

$$\frac{H_S(m_S)}{H_S(m_S = 0)} \equiv 10^{-0\,4m_S} \simeq (0\,4)^{m_S} \tag{3}$$

The more positive the magnitude, the dimmer the source The reference values $H_S(m_S = 0)$ for the standard spectral response functions described above are usually given in exponential form

$$H_S(m_S = 0) \equiv 10^{C_S}\ \text{W/m}^2 \tag{4a}$$

The constants C_S are [6]

$$C_V \simeq -8\,5$$

$$C_B \simeq -8\,19$$

$$C_U \simeq -8\,55$$

$$C_{pg} \equiv C_B - 0\,044 \simeq -8\,23$$

$$C_b \equiv C_V + \log\left[\frac{H_b(\odot)}{H_V(\odot)}\right] \simeq -7\,6 \tag{4b}$$

The constants for the U and B magnitude systems are derived from setting $m_B = m_V = m_U$ for the mean of six particular dwarf stars, all of spectral type A0 [7] The value for C_b comes from the stipulation that the Sun's apparent visual and bolometric magnitudes be equal, together with measurements of the solar bolometric and visual irradiances (1 35 kW/m^2 and 160 W/m^2, respectively) The visual irradiance from a source of apparent visual magnitude m_V is therefore

$$H_V(m_V) \equiv \int V(\lambda)H(\lambda,m_V)d\lambda = 10^{-0\,4m_V}\,10^{-8\,5}\ \text{W/m}^2 \tag{5}$$

where $H(\lambda, m_V)$ is the spectral irradiance ($H[\lambda]$ in the above discussion) produced by a source with apparent visual magnitude m_V Note that the visual irradiance from a source with $m_V = 0$ corresponds approximately to a flux of 10^{10} photons/m^2-s at wavelengths between 520 nm and 560 nm (see Eq [15a])

IV. Visual vs. Broadband-Detector Irradiance and Photon Flux From Stars

Although there is a one-to-one correspondence between a source's apparent visual magnitude m_V and the visual irradiance H_V it produces, there is no such correspondence between m_V and the general spectral irradiance $H(\lambda)$ produced by the source But knowledge of the latter is required to calculate the irradiance or photon flux that would be measured by a detector with spectral sensitivity $D(\lambda)$ Since stars radiate as blackbodies, the spectral irradiances they produce are proportional to the Planck distribution for a blackbody of temperature T

$$W(\lambda,T) = \frac{C_1}{\lambda^5(e^{C_2/\lambda T} - 1)}$$

$$C_1 \equiv 2\pi hc^2 = 10^{8\,57}\ \mu^4\text{-W/m}^2 \qquad (6)$$

$$C_2 \equiv \frac{hc}{k} = 10^{4\,16}\ \mu\text{-K}$$

where $k = 10^{-22\,86}$ J-K^{-1} Since the spectral irradiance is defined as that at the top of Earth's atmosphere, the proportionality factor for isotropically radiating blackbody sources is essentially independent of both wavelength and angle of incidence Hence for a star of blackbody temperature T, the spectral irradiances at different wavelengths scale as the ratios of the corresponding blackbody functions $W(\lambda,T)$

$$\frac{H(\lambda)}{H(\lambda')} = \frac{W(\lambda,T)}{W(\lambda',T)} \qquad (7)$$

The function $W(\lambda,T)$ varies little over the narrow region where $V(\lambda)$ is significant Hence the integral of $W(\lambda,T)$ weighted by $V(\lambda)$ can be approximated by the value of $W(\lambda,T)$ at λ_V

$$\int V(\lambda)W(\lambda,T)d\lambda \simeq W(\lambda_V,T)\int V(\lambda)\,d\lambda$$

$$\lambda_V \equiv 0\,55\,\mu \qquad (8)$$

This equality holds for blackbody temperatures from 2,800 K to 28,000 K, or star spectral classifications B through M (see Table 1) [6] The integral on the right is

$$\int V(\lambda)d\lambda \simeq 0\,089\,\mu \simeq 10^{-1\,05}\,\mu \qquad (9)$$

Using the definition (Eq [5]) of visual irradiance, one can now see that the spectral irradiance at the wavelength λ_V of a star of temperature T and apparent visual magnitude m_V is independent of T

$$H^{bb}(\lambda_V,m_V) = \frac{H_V(m_V)}{\int V(\lambda)\,\hat{W}_V(\lambda,T)d\lambda}$$

$$= 10^{-0\,4m_V}\,10^{-7\,45}\ \text{W/m}^2\text{-}\mu$$

$$\hat{W}_V(\lambda,T) \equiv \frac{W(\lambda,T)}{W(\lambda_V,T)} \qquad (10)$$

This is the relation used in practice to calibrate the visual magnitude system The spectral irradiance at any wavelength from a star of temperature T and apparent visual magnitude m_V is therefore

$$H^{bb}(\lambda,T,m_V) = H^{bb}(\lambda_V,m_V)\,\hat{W}_V(\lambda,T)$$

$$= 10^{-0\,4m_V}\,10^{-7\,45}\,\hat{W}_V(\lambda,T)\ \text{W/m}^2\text{-}\mu \qquad (11)$$

The normalized blackbody functions $\hat{W}_V(\lambda,T)$ for stars of spectral class B0 through M5, for wavelengths in the range 100 nm through 1200 nm, are plotted in Fig 2 and listed in Table 2

Given a star of temperature T and apparent visual magnitude m_V, and the spectral irradiance it produces as derived in Eq (11), the irradiance H_D that would be measured by a detector with spectral sensitivity $D(\lambda)$ is derived from Eq (1)

$$H_D^{bb}(T,m_V) \equiv \int D(\lambda)H^{bb}(\lambda,T,m_V)d\lambda$$

$$= 10^{-0\,4m_V}\,10^{-7\,45}$$

$$\times \int D(\lambda)\,\hat{W}_V(\lambda,T)d\lambda\ \text{W/m}^2 \qquad (12)$$

Here and in all other equations in this report, the integration range for λ is to be specified in units of micrometers This detected irradiance is now to be compared with the visual irradiance H_V (Eq [5]) from the same source Table 3(a) gives the logarithms of the ratios

$$\frac{H_D^{bb}(T,m_V)}{H_V(m_V)} = 10^{1\,05}\int D(\lambda)\,\hat{W}_V(\lambda,T)d\lambda \qquad (13)$$

for stars of 12 different spectral classes and the nine spectral response functions described in Appendix A The detected irradiance $H_D(T,m_V)$ from a star of temperature T and apparent visual magnitude m_V is easily recovered from Table 3(a), with the help of Eq (5)

It can be argued that in reality, most kinds of detectors that have reasonable sensitivities at visible wavelengths do not measure energy flux (irradiance), but rather measure photon flux For a nearly monochromatic source of radiation the two are proportional But for blackbody radiation viewed with a broadband detector, energy flux can be appreciably different

from photon flux For true photon detectors, the relevant quantity for describing apparent brightness is the photon flux n_D measured by a detector with spectral sensitivity $D(\lambda)$, defined in Eq (2) From Eq (11) for the spectral irradiance of a star, the detected photon flux n_D from a blackbody of temperature T and apparent visual magnitude m_V is

$$n_D^{bb}(T, m_V) = 10^{-0.4 m_V}\, 10^{10.99} \times \int D(\lambda)\left(\frac{\lambda}{\lambda_V}\right)\hat{W}_V(\lambda, T)\, d\lambda \quad \mathrm{m^{-2}s^{-1}} \tag{14}$$

($[\lambda_V/hc] = 10^{18.44}\mathrm{J}^{-1}$) The visual photon flux from a source of apparent visual magnitude m'_V is

$$n_V(m'_V) \simeq 10^{-0.4 m'_V}\, 10^{9.94} \quad \mathrm{m^{-2}s^{-1}} \tag{15a}$$

(The approximation sign refers to the assumption that all photons arrive with wavelength $\lambda_V \equiv 0.55\ \mu$, at which $V(\lambda)$ is maximum) Hence the ratio of detected to visual photon flux from a star of apparent visual magnitude m_V is

$$\frac{n_D^{bb}(T, m_V)}{n_V(m_V)} = 10^{1.05} \int D(\lambda)\left(\frac{\lambda}{\lambda_V}\right)\hat{W}_V(\lambda, T)\, d\lambda \tag{15b}$$

The logarithms of these ratios are listed in Table 3(b) Note that the ratios of detected to visual irradiance or photon flux from a star (Eqs [13] and [15]) need not be greater than one That is, even though a broadband detector is sensitive to photons of many different wavelengths, its efficiency is typically much poorer than that of the eye at visible wavelengths

The numbers in Table 3(a) and (b) need only be multiplied by −2 5 to give the brightness correction in magnitudes between visual and detected irradiance or photon flux This has been done in Table 3(c) and (d) When the magnitude correction is negative, the detector measures a greater flux than does the eye from a given star These magnitude corrections are similar in definition to astronomers' "bolometric correction' $BC(T)$ The latter is the ratio of total irradiance to visual irradiance, in units of magnitudes

$$BC(T) \equiv m_b - m_V = -2.5 \log\left[10^{-0.9}\frac{H_b^{bb}(T, m_V)}{H_V(m_V)}\right] = -2.5\left(0.15 + \log \int \hat{W}_V(\lambda, T)\, d\lambda\right) \tag{16a}$$

Here the bolometric irradiance is defined by

$$H_b^{bb}(T, m_V) \equiv \int H^{bb}(\lambda, T, m_V)\, d\lambda = 10^{-0.4 m_V}\, 10^{-7.45} \int \hat{W}_V(\lambda, T)\, d\lambda \quad \mathrm{W/m^2} \tag{16b}$$

and the additive constant arises because of the difference in reference values for calibration of the visual and bolometric magnitude systems (Eq [4]) Note that the bolometric correction is always negative, because a star's total irradiance is always greater than its irradiance at visible wavelengths For reference, the bolometric corrections for stars of the 12 spectral types considered in this report are included in Table 1

V. Visual vs. Broadband-Detector Irradiance and Photon Flux From Lasers

Calculations similar to those just made for stars can be made for monochromatic sources A laser at a distance r from the top of Earth's atmosphere, transmitting a power P_t at wavelength λ_t through a telescope of area $A_t = (\pi/4)(D_t^2)$, produces an irradiance

$$H_t = \frac{P_t}{r^2\Omega_t} = \frac{P_t A_t}{r^2\lambda_t^2} = P_t\frac{\pi}{4}\left(\frac{D_t}{r\lambda_t}\right)^2 = 10^{-12.96} F_0 \quad \mathrm{W/m^2} \tag{17a}$$

where the dimensionless scale factor F_0 is

$$F_0 \equiv \frac{\left(\frac{P_t}{1\mathrm{W}}\right)\left(\frac{D_t}{30\ \mathrm{cm}}\right)^2}{\left(\frac{r}{10\mathrm{AU}}\right)^2\left(\frac{\lambda_t}{0.532\ \mu}\right)^2} \tag{17b}$$

Since 0 532 μ is a wavelength of special interest, it is denoted henceforth by λ_s

$$\lambda_s \equiv 0.532\ \mu \tag{17c}$$

The spectral irradiance produced by the laser is

$$H_t(\lambda) = H_t\,\delta(\lambda - \lambda_t) \tag{18}$$

The visual irradiance $H_V^{mc}(\lambda_t, m_V)$ from a monochromatic (mc) laser emitting at wavelength λ_t follows from Eq (5)

$$H_V^{mc}(\lambda_t, m_V) = V(\lambda_t) H_t = 10^{-12\,96} F_0 V(\lambda_t) \text{ W/m}^2$$

$$= 10^{-12\,98} F_0 \left[\frac{V(\lambda_t)}{0\,95}\right] \text{W/m}^2$$

$$\equiv 10^{-0\,4 m_V}\, 10^{-8\,5} \text{ W/m}^2 \tag{19}$$

where $V(\lambda_s) \simeq 0\,95$ The scale factor F_0 and apparent visual magnitude m_V of a laser are thus related by

$$m_V = 11\,15 - 2\,5 \log [F_0 V(\lambda_t)]$$

$$= 11\,2 - 2\,5 \log \left[\frac{F_0 V(\lambda_t)}{0\,95}\right] \tag{20}$$

The detected irradiance H_D from a laser of apparent visual magnitude m_V (or scale factor F_0) emitting at wavelength λ_t is

$$H_D^{mc}(\lambda_t, m_V) = \int D(\lambda) H_t(\lambda) d\lambda = D(\lambda_t) H_t$$

$$= 10^{-12\,96} D(\lambda_t) F_0 \text{ W/m}^2$$

$$= 10^{-0\,4 m_V}\, 10^{-8\,5} \left(\frac{D(\lambda_t)}{V(\lambda_t)}\right) \text{ W/m}^2 \tag{21}$$

The ratio of detected to visual irradiance is therefore

$$\frac{H_D^{mc}(\lambda_t, m_V)}{H_V^{mc}(\lambda_t, m_V)} = \frac{D(\lambda_t)}{V(\lambda_t)} \tag{22}$$

The logarithms of these ratios are given in Table 4(a) for $\lambda_t = \lambda_s$ and the usual nine spectral response functions The detected irradiance $H_D^{mc}(\lambda_t, m_V)$ from a monochromatic source with apparent visual magnitude m_V (or scale factor F_0) emitting at wavelength λ_s is easily recovered from Table 4(a) and Eq (21)

The irradiance (Eq 17[a]) from a monochromatic source implies a photon flux

$$n_t = \left(\frac{\lambda_t}{hc}\right) H_t = 10^{5\,47} \left(\frac{\lambda_t}{\lambda_s}\right) F_0 \text{ m}^{-2}\text{s}^{-1}$$

$$\simeq 300{,}000 \left(\frac{\lambda_t}{\lambda_s}\right) F_0 \text{ m}^{-2}\text{s}^{-1} \tag{23}$$

The visual photon flux is

$$n_V^{mc}(\lambda_t, m_V) = V(\lambda_t) n_t = 10^{5\,45} \left(\frac{\lambda_t}{\lambda_s}\right) F_0 \left[\frac{V(\lambda_t)}{0\,95}\right] \text{ m}^{-2}\text{s}^{-1}$$

$$= 10^{-0\,4 m_V}\, 10^{9\,93} \left(\frac{\lambda_t}{\lambda_s}\right) \text{ m}^{-2}\text{s}^{-1} \tag{24a}$$

(Eq [20]) The flux measured by a photon detector with spectral sensitivity $D(\lambda)$ is

$$n_D^{mc}(\lambda_t, m_V) = D(\lambda_t) n_t = \left[\frac{D(\lambda_t)}{V(\lambda_t)}\right] n_V^{mc}(\lambda_t, m_V) \tag{24b}$$

For $\lambda_t = \lambda_s$, it is obtained simply by multiplying Eq (24a) by the quantities whose logarithms are given in Table 4(a) Note that for monochromatic sources, the ratio of detected to visual irradiance or photon flux is typically less than one (the entries in Table 4[a] are negative), because most broadband detectors are less sensitive than the eye at visible wavelengths

As was done in the previous section for stars, the numbers in Table 4(a) can be multiplied by −2 5 to give the visual-to-detector brightness correction in magnitudes, this is done in Table 4(b) These corrections are positive, reflecting the poor sensitivity of broadband detectors at visible wavelengths compared to that of the eye

VI. Comparison of Star and Laser Brightnesses

It is now straightforward to compare the detected energy or photon flux from stars and lasers of the same (or different) apparent visual magnitudes The ratio of the measured irradiance from a monochromatic laser of apparent visual magnitude m_V (or scale factor F_0) emitting at wavelength λ_t to that from a blackbody of temperature T and apparent visual magnitude m'_V is denoted here by $R(m_V - m'_V)$, a function of detector sensitivity $D(\lambda)$, laser wavelength λ_t, and star temperature T

$$\frac{H_D^{mc}(\lambda_t, m_V)}{H_D^{bb}(T, m'_V)} \equiv R(m_V - m'_V)$$

$$= 10^{-0.4(m_V - m'_V)} R(0)$$

$$= 10^{0.4 m'_V}\, 10^{-4.48}\, F_0\left[\frac{V(\lambda_t)}{0.95}\right] R(0) \tag{25a}$$

The ratio $R(0)$ is just the ratio of Eqs (22) and (13) above

$$R(0) = \frac{\left[\dfrac{D(\lambda_t)}{V(\lambda_t)}\right]}{10^{1.05} \int D(\lambda)\, \hat{W}_V(\lambda, T)\, d\lambda} \tag{25b}$$

Its logarithm for $\lambda_t = \lambda_s$, equal to the difference of the entries in Table 4(a) and Table 3(a), is tabulated in Table 5(a) for stars of 12 different temperatures and the nine different spectral response functions described in the Appendix

A similar ratio, $\bar{R}(m_V - m'_V)$, can be defined for photon flux

$$\frac{n_D^{mc}(\lambda_t, m_V)}{n_D^{bb}(T, m'_V)} \equiv \bar{R}(m_V - m'_V)$$

$$= 10^{-0.4(m_V - m'_V)}\, \bar{R}(0)$$

$$= 10^{0.4 m'_V}\, 10^{-4.48}\, F_0\left[\frac{V(\lambda_t)}{0.95}\right] \bar{R}(0) \tag{26a}$$

The ratio $\bar{R}(0)$ is just the ratio of Eqs (24) and (14)

$$\bar{R}(0) \equiv \frac{n_D^{mc}(\lambda_t, m_V)}{n_D^{bb}(T, m_V)} = \frac{\left(\dfrac{\lambda_t}{\lambda_V}\right)\left[\dfrac{D(\lambda_t)}{V(\lambda_t)}\right]}{10^{1.05} \displaystyle\int D(\lambda)\left(\frac{\lambda}{\lambda_V}\right) \hat{W}_V(\lambda, T)\, d\lambda} \tag{26b}$$

Its logarithm for $\lambda_t = \lambda_s$, equal to the difference of the entries in Table 4(a) and Table 3(b) minus 0.01 = log (λ_s/λ_V), is tabulated in Table 5(b) Note that, as expected, the ratios $R(0)$ and $\bar{R}(0)$ are always less than one, i e , the entries in Table 5(a) and (b) are all negative

The logarithms of the ratios $R(0)$ and $\bar{R}(0)$ listed in Table 5(a) and (b) need only be multiplied by −2 5 to give the brightness difference in magnitudes, as measured by a given broadband detector, between a laser (emitting at 0 532 μ) and a star of identical apparent visual magnitude These positive "monochromatic magnitude corrections" are given in Table 5(c) and (d) For example, Table 5(d) shows that if a CCD looks at a laser and a very hot (B0) star of identical m_V, the laser will appear approximately 3 2 magnitudes (≃13 dB) dimmer than the star, for solar-type (G0) stars, the difference is only about 1 8 magnitudes (7 dB)

VII. Summary and Concluding Remarks

This article has shown how to make precise quantitative comparisons of the flux measured by certain broadband detectors from stars and lasers Results show that for a given detector, the difference in measured flux from a star and a laser of similar apparent visual brightness depends strongly on the spectral class of the star The difference is greatest for stars much hotter or colder than our Sun, since most of their radiation is outside the visible region of the spectrum The difference is smallest, but by no means negligible, for stars of spectral classes A through K, or temperatures between 4000 K and 10,000 K These comprise the majority of known stars (see Table 6[a] and [b]) [6] In particular, results showed that a laser will appear dimmer than a Sun-like G0 star of equal apparent visual brightness by the following factors for the detectors considered approximately 6 dB for the PMT, 7 dB for the CCD, 8 dB for the APD, and 6 dB for the MAMA Ground-based observation did not change these numbers significantly for the CCD, and changed them by less than 1 dB for the others (see Table 5[a] - [d])

For the astrometrist with a broadband detector trying to locate the position of a laser-carrying spacecraft, these results have the following implications First, hot and cold stars that are as much as 1 5 magnitudes (6 dB) fainter in the visible than Sun-like stars may appear just as bright and be just as good reference stars as the visibly brighter Sun-like stars (refer to Table 3[a]-[d]) Second, the expected apparent brightness of the laser must be calculated for a particular detector in the manner described in this article, its visual brightness can give a seriously exaggerated estimate of its would-be measured brightness relative to stars of the same apparent visual brightness, by anywhere from 2 to 17 dB (Table 5[a]-[d])

References

[1] D G Monet and C C Dahn, "CCD Astrometry I Preliminary Results From the KPNO 4-m/CCD Parallax Program," *Astron J* , vol 88, pp 1489–1507, October 1983

[2] G Gatewood et al , "A Preliminary Look at Astrometric Accuracy as a Function of Photon Counts," *Astron J* , vol 90, pp 2397–2398, November 1985

[3] G Gatewood, "The Multichannel Astrometric Photometer and Atmospheric Limitations in the Measurement of Relative Positions," *Astron J* , vol 94, pp 213–224, July 1987

[4] A Buffington, "A Photometric Astrometric Telescope Using a Ronchi Ruling," submitted to *Review of Scientific Instruments*, 1987

[5] H L Johnson, "Photometric Systems," in *Basic Astronomical Data Stars and Stellar Systems III*, K A Strand (ed), Chicago University of Chicago Press, pp 204–229, 1963

[6] C W Allen, *Astrophysical Quantities*, London Wm Clowes and Sons, Ltd , pp 197–207, 1976

[7] K R Lang, *Astrophysical Formulae*, New York Springer-Verlag, pp 558–565, 1974

[8] J G Timothy, "Multianode Microchannel Array Detector Systems Performance Characteristics," *Optical Engineering*, vol 24, pp 1066–1071, 1985

Table 1 Star spectral classes, temperatures, and bolometric corrections

Spectral type	Temperature, K	$BC(T)$
B0	28,000	−2 80
B5	15,500	−1 50
A0	9,900	−0 40
A5	8,500	−0 12
F0	7,400	−0 06
F5	6,600	0 0
G0	6,000	−0 03
G5	5,500	−0 07
K0	4,900	−0 20
K5	4,100	−0 60
M0	3,500	−1 20
M5	2,800	−2 30

Table 2 Normalized blackbody functions $\hat{W}_V(\lambda, T)$

(Eqs [6] and [10] of text)

$$\hat{W}_V(\lambda, T) \equiv \frac{W(\lambda, T)}{W(\lambda_V, T)} = \frac{\left(\frac{\lambda_V}{\lambda}\right)^5 (e^{C_2/\lambda_V T} - 1)}{e^{C_2/\lambda T} - 1}$$

$$C_2 \equiv \frac{hc}{k} = 10^{4\,16}\,\mu - K, \qquad \lambda_V \equiv 0\,55\,\mu$$

λ	Star type											
	B0	B5	A0	A5	F0	F5	G0	G5	K0	K5	M0	M5
0 1	45 19	2 00	0 03	0 00	0 00	0 00	0 00	0 00	0 00	0 00	0 00	0 00
0 2	20 07	6 68	1 41	0 67	0 31	0 15	0 08	0 04	0 01	0 00	0 00	0 00
0 3	7 03	4 32	2 13	1 51	1 05	0 74	0 53	0 39	0 24	0 10	0 04	0 01
0 4	2 91	2 36	1 74	1 50	1 27	1 09	0 95	0 82	0 66	0 45	0 30	0 15
0 5	1 39	1 32	1 22	1 17	1 12	1 08	1 04	1 00	0 94	0 85	0 77	0 64
0 6	0 74	0 77	0 83	0 85	0 88	0 91	0 94	0 97	1 02	1 11	1 22	1 43
0 7	0 43	0 48	0 56	0 61	0 67	0 72	0 78	0 85	0 96	1 20	1 51	2 26
0 8	0 26	0 31	0 39	0 44	0 50	0 56	0 63	0 71	0 84	1 16	1 62	2 91
0 9	0 17	0 21	0 28	0 32	0 37	0 43	0 50	0 58	0 71	1 06	1 61	3 32
1 0	0 12	0 15	0 20	0 24	0 28	0 34	0 39	0 46	0 59	0 93	1 51	3 48
1 1	0 08	0 10	0 15	0 18	0 22	0 26	0 31	0 37	0 49	0 81	1 37	3 47
1 2	0 06	0 08	0 11	0 14	0 17	0 21	0 25	0 30	0 40	0 69	1 23	3 34

Table 3(a). Ratios of detected to visual irradiance for stars

(Eq [13] in text)

$$\log\left[\frac{H_D^{bb}(T,m_V)}{H_V(m_V)}\right] \equiv \log\left(10^{1\,05}\int D(\lambda)\,\hat{W}_V(\lambda,T)d\lambda\right)$$

Star type	Detector type								
	PMT	CCD	APD	MAMA	atm + PMT	atm + CCD	atm + APD	atm + MAMA	atm + vis
B0	0 21	1 48	0 32	0 48	−0 10	0 47	0 23	−0 14	−0 10
B5	0 10	0 99	0 32	0 29	−0 18	0 43	0 24	−0 23	−0 10
A0	−0 05	0 68	0 35	0 05	−0 29	0 38	0 27	−0 35	−0 10
A5	−0 11	0 60	0 36	−0 05	−0 34	0 37	0 29	−0 40	−0 10
F0	−0 17	0 54	0 38	−0 15	−0 38	0 36	0 31	−0 45	−0 10
F5	−0 23	0 51	0 40	−0 23	−0 42	0 36	0 34	−0 50	−0 10
G0	−0 27	0 49	0 42	−0 30	−0 46	0 36	0 36	−0 54	−0 10
G5	−0 32	0 48	0 45	−0 36	−0 49	0 37	0 39	−0 58	−0 10
K0	−0 37	0 48	0 49	−0 44	−0 53	0 39	0 43	−0 64	−0 10
K5	−0 44	0 52	0 58	−0 55	−0 58	0 44	0 53	−0 72	−0 09
M0	−0 50	0 59	0 68	−0 65	−0 61	0 52	0 63	−0 79	−0 09
M5	−0 53	0 76	0 89	−0 76	−0 62	0 71	0 85	−0 87	−0 07

Table 3(b) Ratios of detected to visual photon flux for stars

(Eq [15b] in text)

$$\log\left[n_D^{bb}\frac{(T,m_V)}{n_V(m_V)}\right] \equiv \log\left(10^{1\,05}\int D(\lambda)\left(\frac{\lambda}{\lambda_V}\right)\hat{W}_V(\lambda,T)d\lambda\right)$$

Star type	Detector type								
	PMT	CCD	APD	MAMA	atm + PMT	atm + CCD	atm + APD	atm + MAMA	atm + vis
B0	0 06	1 06	0 35	0 25	−0 22	0 42	0 27	−0 27	0 30
B5	−0 04	0 75	0 37	0 08	−0 29	0 40	0 30	−0 35	0 30
A0	−0 17	0 58	0 41	−0 13	−0 38	0 38	0 34	−0 45	0 30
A5	−0 22	0 54	0 43	−0 21	−0 42	0 38	0 37	−0 50	0 30
F0	−0 27	0 51	0 46	−0 29	−0 46	0 38	0 40	−0 55	0 30
F5	−0 32	0 51	0 49	−0 36	−0 49	0 40	0 43	−0 59	0 30
G0	−0 36	0 51	0 51	−0 42	−0 52	0 41	0 46	−0 63	0 30
G5	−0 39	0 51	0 55	−0 47	−0 54	0 43	0 49	−0 66	0 30
K0	−0 43	0 54	0 60	−0 53	−0 57	0 46	0 54	−0 71	0 31
K5	−0 48	0 60	0 70	−0 63	−0 60	0 54	0 65	−0 78	0 31
M0	−0 51	0 69	0 81	−0 70	−0 62	0 64	0 77	−0 83	0 32
M5	−0 52	0 90	1 04	−0 79	−0 60	0 86	1 00	−0 90	0 34

Table 3(c) Ratios of detected to visual irradiance for stars, in magnitudes

(Eq [13] in text)

$$-2.5 \log\left[H_D^{bb}\frac{(T,m_V)}{H_V(m_V)}\right] \equiv -2.5 \log\left(10^{1.05}\int D(\lambda)\,\hat{W}_V(\lambda,T)\,d\lambda\right)$$

Star type	Detector type								
	PMT	CCD	APD	MAMA	atm + PMT	atm + CCD	atm + APD	atm + MAMA	atm + vis
B0	−0.53	−3.69	−0.79	−1.19	0.25	−1.18	−0.57	0.35	0.24
B5	−0.25	−2.49	−0.81	−0.71	0.46	−1.07	−0.60	0.57	0.24
A0	0.11	−1.69	−0.86	−0.12	0.73	−0.96	−0.68	0.87	0.25
A5	0.27	−1.50	−0.90	0.13	0.84	−0.92	−0.72	1.00	0.25
F0	0.43	−1.36	−0.95	0.36	0.96	−0.90	−0.78	1.13	0.25
F5	0.57	−1.28	−1.00	0.58	1.06	−0.90	−0.84	1.25	0.25
G0	0.68	−1.23	−1.06	0.74	1.14	−0.90	−0.90	1.36	0.25
G5	0.79	−1.21	−1.12	0.89	1.22	−0.92	−0.97	1.46	0.25
K0	0.92	−1.21	−1.23	1.09	1.31	−0.97	−1.08	1.59	0.24
K5	1.11	−1.29	−1.44	1.39	1.45	−1.11	−1.31	1.80	0.23
M0	1.24	−1.46	−1.71	1.62	1.53	−1.31	−1.59	1.97	0.22
M5	1.32	−1.89	−2.22	1.89	1.55	−1.77	−2.12	2.19	0.18

Table 3(d) Ratios of detected to visual photon flux for stars, in magnitudes

(Eq [15b] in text)

$$-2.5 \log\left[n_D^{bb}\frac{(T,m_V)}{n_V(m_V)}\right] \equiv -2.5 \log\left(10^{1.05}\int D(\lambda)\left(\frac{\lambda}{\lambda_V}\right)\hat{W}_V(\lambda,T)\,d\lambda\right)$$

Star type	Detector type								
	PMT	CCD	APD	MAMA	atm + PMT	atm + CCD	atm + APD	atm + MAMA	atm + vis
B0	−0.15	−2.66	−0.88	−0.61	0.54	−1.05	−0.68	0.67	−0.75
B5	0.10	−1.88	−0.93	−0.19	0.73	−0.99	−0.74	0.87	−0.75
A0	0.42	−1.44	−1.02	0.32	0.95	−0.95	−0.85	1.14	−0.75
A5	0.55	−1.34	−1.08	0.53	1.05	−0.95	−0.92	1.25	−0.75
F0	0.68	−1.29	−1.14	0.73	1.14	−0.96	−0.99	1.37	−0.75
F5	0.79	−1.26	−1.21	0.90	1.22	−0.99	−1.07	1.48	−0.75
G0	0.89	−1.27	−1.29	1.04	1.29	−1.02	−1.15	1.57	−0.75
G5	0.97	−1.29	−1.36	1.16	1.35	−1.07	−1.23	1.65	−0.76
K0	1.07	−1.34	−1.49	1.33	1.42	−1.15	−1.36	1.77	−0.76
K5	1.20	−1.50	−1.74	1.57	1.50	−1.35	−1.62	1.94	−0.78
M0	1.28	−1.73	−2.03	1.76	1.54	−1.60	−1.92	2.08	−0.80
M5	1.29	−2.24	−2.59	1.98	1.51	−2.14	−2.49	2.25	−0.85

Table 4(a) Ratios of detected to visual irradiance and photon flux for lasers at $\lambda_s \equiv 0\,532\ \mu$

(Eqs [22] and [24] in text)

$$\log\left[\frac{H_D^{mc}(\lambda_s, m_V)}{H_V^{mc}(\lambda_s, m_V)}\right] = \log\left[\frac{n_D^{mc}(\lambda_s, m_V)}{n_V^{mv}(\lambda_s, m_V)}\right] = \log\left[\frac{D(\lambda_s)}{V(\lambda_s)}\right]$$

$$V(\lambda_s) \simeq 0\,952$$

Detector type	Ratio
PMT	−0 92
CCD	−0 22
APD	−0 32
MAMA	−1 00
atm + PMT	−1 02
atm + CCD	−0 32
atm + APD	−0 42
atm + MAMA	−1 09
atm + vis	−0 09

Table 4(b) Ratios of detected to visual irradiance and photon flux for lasers at $\lambda_s \equiv 0\,532\ \mu$, in magnitudes

(Eqs [22] and [24] in text)

$$-2\,5 \log\left[\frac{D(\lambda_s)}{V(\lambda_s)}\right]$$

$$V(\lambda_s) \simeq 0\,952$$

Detector type	Ratio
PMT	2 30
CCD	0 56
APD	0 80
MAMA	2 50
atm + PMT	2 54
atm + CCD	0 79
atm + APD	1 04
atm + MAMA	2 74
atm + vis	0 23

Table 5(a) Ratios $R(0)$ of detected irradiance from laser and stars of identical m_V

(Eq [25b] in text)

$$\log R(0) \equiv \log\left[\frac{H_D^{mc}(\lambda_s, m_V)}{H_D^{bb}(T, m_V)}\right]$$

$$= \log\left(\frac{\left[\frac{D(\lambda_s)}{V(\lambda_s)}\right]}{10^{1.05}\int D(\lambda)\,\hat{W}_V(\lambda, T)\,d\lambda}\right)$$

$$\lambda_s \equiv 0.532\,\mu, \qquad V(\lambda_s) = 0.952$$

Star type	Detector type								
	PMT	CCD	APD	MAMA	atm + PMT	atm + CCD	atm + APD	atm + MAMA	atm + vis
B0	−1.13	−1.70	−0.64	−1.48	−0.92	−0.79	−0.64	−0.96	0.001
B5	−1.02	−1.22	−0.65	−1.29	−0.83	−0.74	−0.66	−0.87	0.003
A0	−0.88	−0.90	−0.67	−1.05	−0.73	−0.70	−0.69	−0.75	0.005
A5	−0.81	−0.82	−0.68	−0.95	−0.68	−0.69	−0.70	−0.69	0.005
F0	−0.75	−0.77	−0.70	−0.86	−0.63	−0.68	−0.73	−0.64	0.005
F5	−0.69	−0.73	−0.72	−0.77	−0.59	−0.68	−0.75	−0.59	0.005
G0	−0.65	−0.72	−0.75	−0.71	−0.56	−0.68	−0.78	−0.55	0.005
G5	−0.61	−0.71	−0.77	−0.65	−0.53	−0.69	−0.80	−0.51	0.004
K0	−0.55	−0.71	−0.81	−0.56	−0.49	−0.70	−0.85	−0.46	0.003
K5	−0.48	−0.74	−0.90	−0.45	−0.44	−0.76	−0.94	−0.37	−0.001
M0	−0.43	−0.81	−1.00	−0.35	−0.41	−0.84	−1.05	−0.30	−0.007
M5	−0.40	−0.98	−1.21	−0.25	−0.39	−1.02	−1.26	−0.22	−0.022

Table 5(b) Ratios $\bar{R}(0)$ of detected photon flux from laser and stars of identical m_V

(Eq [26b] in text)

$$\log \bar{R}(0) \equiv \log\left[\frac{n_D^{mc}(\lambda_s, m_V)}{n_D^{bb}(T, m_V)}\right]$$

$$= \log\left(\frac{\left(\frac{\lambda_s}{\lambda_V}\right)\left[\frac{D(\lambda_s)}{V(\lambda_s)}\right]}{10^{1\,05}\int D(\lambda)\left(\frac{\lambda}{\lambda_V}\right)\hat{W}_V(\lambda, T)d\lambda}\right)$$

$\lambda_s \equiv 0\,532\,\mu$, $\lambda_V \equiv 0\,55\,\mu$, $V(\lambda_s) = 0\,952$

Star type	Detector type								
	PMT	CCD	APD	MAMA	atm + PMT	atm + CCD	atm + APD	atm + MAMA	atm + vis
B0	−0 98	−1 29	−0 67	−1 25	−0 80	−0 74	−0 69	−0 83	−0 395
B5	−0 88	−0 98	−0 69	−1 08	−0 73	−0 71	−0 71	−0 75	−0 394
A0	−0 75	−0 80	−0 73	−0 87	−0 63	−0 70	−0 76	−0 64	−0 393
A5	−0 70	−0 76	−0 75	−0 79	−0 60	−0 70	−0 78	−0 59	−0 393
F0	−0 65	−0 74	−0 78	−0 71	−0 56	−0 70	−0 81	−0 55	−0 394
F5	−0 60	−0 73	−0 81	−0 64	−0 53	−0 71	−0 84	−0 50	−0 395
G0	−0 57	−0 73	−0 84	−0 59	−0 50	−0 73	−0 87	−0 48	−0 396
G5	−0 53	−0 74	−0 87	−0 54	−0 48	−0 74	−0 91	−0 43	−0 397
K0	−0 49	−0 76	−0 92	−0 47	−0 45	−0 78	−0 96	−0 39	−0 399
K5	−0 44	−0 82	−1 02	−0 37	−0 41	−0 86	−1 06	−0 32	−0 405
M0	−0 41	−0 92	−1 13	−0 30	−0 40	−0 96	−1 18	−0 26	−0 413
M5	−0 41	−1 12	−1 36	−0 21	−0 41	−1 17	−1 41	−0 19	−0 432

Table 5(c). Ratios $R(0)$ of detected irradiance from laser and stars of identical m_V, in magnitudes

(Eq [25b] in text)

$$-2.5 \log R(0) \equiv -2.5 \log \left[\frac{H_D^{mc}(\lambda_s, m_V)}{H_D^{bb}(T, m_V)} \right]$$

$$= -2.5 \log \left(\frac{\left[\frac{D(\lambda_s)}{V(\lambda_s)} \right]}{10^{1.05} \int D(\lambda) \hat{W}_V(\lambda, T) d\lambda} \right)$$

$$\lambda_s \equiv 0.532\,\mu, \qquad V(\lambda_s) = 0.952$$

Star type	Detector type								
	PMT	CCD	APD	MAMA	atm + PMT	atm + CCD	atm + APD	atm + MAMA	atm + vis
B0	2.84	4.24	1.59	3.69	2.29	1.97	1.61	2.39	−0.003
B5	2.56	3.04	1.61	3.21	2.08	1.86	1.64	2.17	−0.008
A0	2.19	2.25	1.67	2.62	1.81	1.75	1.71	1.87	−0.013
A5	2.03	2.05	1.71	2.37	1.69	1.71	1.76	1.74	−0.013
F0	1.87	1.92	1.75	2.14	1.58	1.69	1.82	1.60	−0.013
F5	1.74	1.83	1.81	1.93	1.48	1.69	1.88	1.48	−0.013
G0	1.62	1.79	1.86	1.76	1.39	1.70	1.94	1.38	−0.013
G5	1.52	1.76	1.93	1.61	1.32	1.71	2.01	1.28	−0.011
K0	1.38	1.76	2.03	1.41	1.22	1.76	2.12	1.14	−0.008
K5	1.19	1.85	2.25	1.12	1.09	1.90	2.35	0.94	0.002
M0	1.07	2.02	2.51	0.88	1.01	2.10	2.62	0.76	0.017
M5	0.99	2.45	3.02	0.61	0.98	2.56	3.15	0.55	0.054

Table 5(d) Ratios $\bar{R}(0)$ of detected photon flux from laser and stars of identical m_V, in magnitudes

(Eq [26b] in text)

$$-2.5 \log \bar{R}(0) \equiv -2.5 \log \left[\frac{n_D^{mc}(\lambda_s, m_V)}{n_D^{bb}(T, m_V)} \right]$$

$$= -2.5 \log \left(\frac{\left(\frac{\lambda_s}{\lambda_V}\right)\left[\frac{D(\lambda_s)}{V(\lambda_s)}\right]}{10^{1.05} \int D(\lambda) \left(\frac{\lambda}{\lambda_V}\right) \hat{W}_V(\lambda, T) d\lambda} \right)$$

$$\lambda_s \equiv 0.532\,\mu, \qquad \lambda_V \equiv 0.55\,\mu, \qquad V(\lambda_s) = 0.952$$

Star type	Detector type								
	PMT	CCD	APD	MAMA	atm + PMT	atm + CCD	atm + APD	atm + MAMA	atm + vis
B0	2.45	3.21	1.68	3.11	1.99	1.85	1.72	2.07	0.99
B5	2.20	2.44	1.73	2.69	1.81	1.78	1.78	1.87	0.98
A0	1.89	1.99	1.82	2.18	1.58	1.74	1.89	1.60	0.98
A5	1.75	1.90	1.88	1.97	1.49	1.74	1.95	1.48	0.98
F0	1.62	1.84	1.95	1.77	1.39	1.75	2.03	1.37	0.98
F5	1.51	1.82	2.02	1.61	1.31	1.78	2.11	1.26	0.99
G0	1.42	1.82	2.09	1.46	1.25	1.81	2.18	1.17	0.99
G5	1.33	1.84	2.17	1.34	1.19	1.86	2.27	1.08	0.99
K0	1.23	1.90	2.29	1.17	1.12	1.94	2.40	0.97	1.00
K5	1.10	2.06	2.54	0.93	1.03	2.14	2.66	0.80	1.01
M0	1.03	2.29	2.84	0.74	1.00	2.39	2.96	0.65	1.03
M5	1.02	2.80	3.39	0.53	1.03	2.93	3.53	0.48	1.08

Table 6(a) Star numbers (Ref [6], p 243)

N_{m_V} = number of stars per square degree brighter than visual magnitude m_V

$\log N_{m_V}$

m_V	Galactic latitude, degrees									mean 0 – 90
	0	±5	±10	±20	±30	±40	±50	±60	±90	
0 0		−3 9			−4 2			−4 3		−4 1
1 0		−3 3			−3 6			−3 7		−5 56
2 0		−2 7			−3 0			−3 1		−3 00
3 0		−2 14			−2 5			−2 6		−2 43
4 0	−1 55	−1 63	−1 68	−1 81	−1 96	−2 05	−2 10	−2 12	−2 20	−1 90
5 0	−1 08	−1 16	−1 23	−1 36	−1 49	−1 56	−1 60	−1 63	−1 69	−1 41
6 0	−0 60	−0 68	−0 75	−0 88	−1 00	−1 07	−1 12	−1 15	−1 20	−0 93
7 0	−0 16	−0 23	−0 30	−0 43	−0 54	−0 61	−0 66	−0 69	−0 74	−0 46
8 0	+0 29	+0 23	+0 15	+0 02	−0 08	−0 16	−0 21	−0 24	−0 30	+0 00
9 0	+0 78	+0 69	+0 61	+0 48	+0 38	+0 30	+0 25	+0 20	+0 14	+0 45
10 0	+1 25	+1 16	+1 08	+0 94	+0 82	+0 74	+0 68	+0 63	+0 55	+0 91
11 0	1 73	1 63	1 53	1 38	1 26	1 17	1 10	1 05	0 96	+1 34
12 0	2 18	2 07	1 93	1 80	1 67	1 57	1 49	1 42	1 33	+1 76
13 0	2 60	2 49	2 37	2 20	2 08	1 94	1 84	1 77	1 69	+2 17
14 0	3 02	2 91	2 78	2 60	2 44	2 28	2 18	2 09	2 01	+2 56
15 0	+3 42	+3 30	+3 18	+2 95	+2 78	+2 61	+2 50	+2 40	+2 27	+2 94
16 0	3 78	3 71	3 54	3 30	3 09	2 91	2 78	2 68	2 54	+3 29
17 0	4 13	4 08	3 90	3 60	3 37	3 19	3 05	2 94	2 78	+3 64
18 0	4 50	4 40	4 23	3 93	3 65	3 44	3 29	3 17	3 02	+3 95
19 0	4 8	4 7	4 6	4 2	3 9	3 7	3 5	3 4	3 2	+4 20
20 0	+5 0	+5 0	+4 9	+4 5	+4 1	+3 9	+3 7	+3 6	+3 4	+4 5
21 0	5 3	5 2	5 1	4 8	4 3	4 1	3 9	3 7	3 5	+4 7

Table 6(b) Relative numbers of stars in each spectral class (up to m_V = 8 5)

Class	B	A	F	G	K	M
% stars	10	22	19	14	31	3

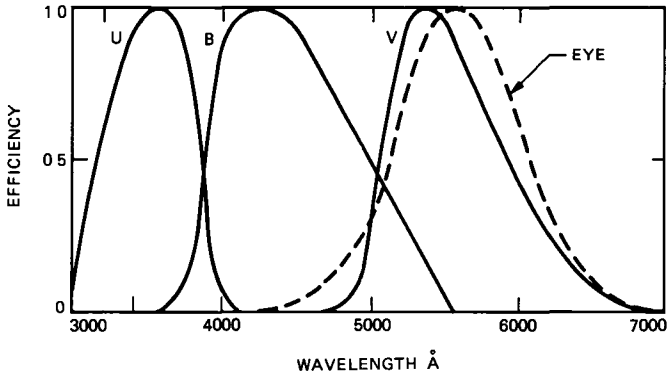

Fig 1 Sensitivity curves of the eye and of the UBV photometric system

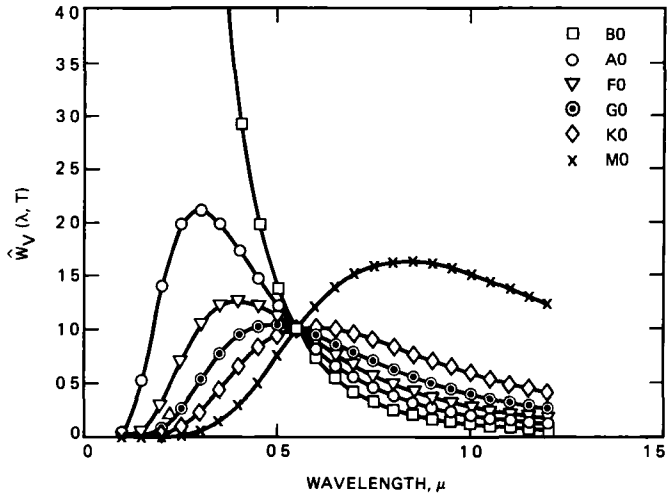

Fig 2 Normalized blackbody distributions

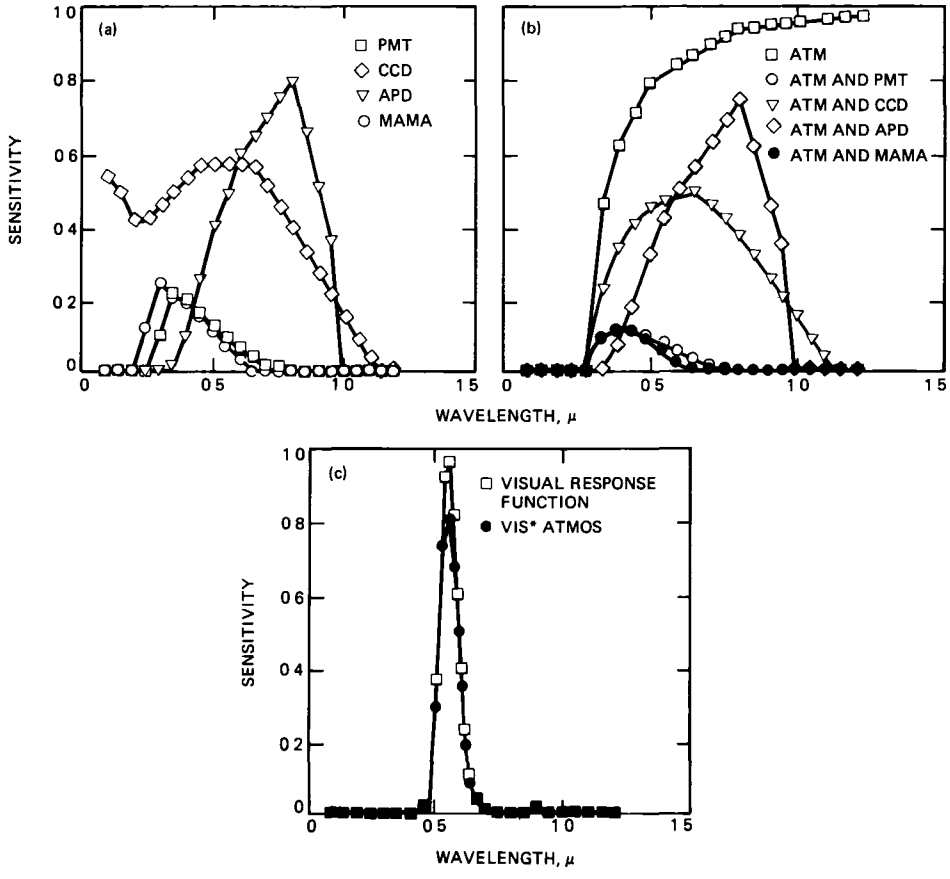

Fig 3 Spectral sensitivities by detector type (a,b), visual response function (c)

Appendix

Detector Spectral Quantum Efficiencies

The detector spectral sensitivities $D(\lambda)$ referred to throughout this report do not in practice represent only the spectral quantum efficiencies of the detectors They should also include the efficiency of the receiving optics as well as an atmospheric transmission function for detectors beneath the atmosphere In these calculations the receiving-optics efficiency has been ignored, since it is highly system-dependent and typically is designed to be approximately constant over the range of the detector's spectral response Atmospheric transmission is included, however Therefore, nine different functions $D(\lambda)$ are considered The first four are the spectral quantum efficiencies of four representative kinds of detectors currently used or likely to be used for spacecraft applications—photomultiplier tubes, charge-coupled devices, avalanche photodiodes, and multianode microchannel array detectors [1] The next four are these efficiencies multiplied by the atmospheric transmission function defined in Allen [6] The last is a product of the atmospheric transmission and visual response functions, which gives a visual-brightness reference for ground-based observations The wavelength range chosen was 0 1 μ (a reasonable optics cutoff wavelength) through 1 2 μ (beyond which the sensitivity of most detectors is very poor) In all these functions, λ stands for wavelength in units of micrometers (μ) The functions are graphed together in Fig 3(a)–(c)

I. Photomultiplier Tube (PMT)

The spectral quantum efficiency of a Hammamatsu (S-20) PMT (R64a) is modeled approximately by the following series of linear functions

$2\ 13\lambda - 0\ 5325$	$(0\ 250 < \lambda < 0\ 350)$
$0\ 213$	$(0\ 350 < \lambda < 0\ 375)$
$-0\ 634\lambda + 0\ 4515$	$(0\ 375 < \lambda < 0\ 650)$
$-0\ 3065\lambda + 0\ 238$	$(0\ 650 < \lambda < 0\ 776)$

The quantum efficiency at $\lambda = 0\ 532\ \mu$ is 0 114

II. Charge-Coupled Device (CCD)

The spectral quantum efficiency of a Texas Instruments three-phase (UV-flooded) CCD (J Janesick, private communication) is modeled approximately by the following series of linear functions

$-0\ 8\lambda + 0\ 62$	$(0\ 10 < \lambda < 0\ 20)$
$0\ 42$	$(0\ 20 < \lambda < 0\ 25)$
$0\ 75\lambda + 0\ 23$	$(0\ 25 < \lambda < 0\ 45)$
$0\ 57$	$(0\ 45 < \lambda < 0\ 65)$
$-1\ 2\lambda + 1\ 35$	$(0\ 65 < \lambda < 1\ 12)$

The quantum efficiency at $\lambda = 0\ 532\ \mu$ is 0 57

III. Avalanche Photodiode (APD)

The spectral quantum efficiency of an RCA APD (30902S) is modeled approximately by the following series of linear functions

$1\ 8\lambda - 0\ 62$	$(0\ 35 < \lambda < 0\ 4)$
$3\ 0\lambda - 1\ 1$	$(0\ 40 < \lambda < 0\ 5)$
$1\ 7\lambda - 0\ 45$	$(0\ 50 < \lambda < 0\ 6)$
λ	$(0\ 60 < \lambda < 0\ 8)$
$-3\ 0\lambda + 3\ 2$	$(0\ 80 < \lambda < 1\ 0)$

The quantum efficiency at $\lambda = 0\ 532\ \mu$ is 0 454

IV. Multianode Microchannel Array (MAMA)

The spectral quantum efficiency of a MAMA device with a bi-alkali cathode [8] is modeled approximately by the following series of linear functions

$2\ 5\lambda - 0\ 5$	$(0\ 20 < \lambda < 0\ 3)$
$-\lambda + 0\ 55$	$(0\ 30 < \lambda < 0\ 35)$
$0\ 2$	$(0\ 35 < \lambda < 0\ 4)$
$-0\ 78\lambda + 0\ 51$	$(0\ 40 < \lambda < 0\ 66)$

The quantum efficiency at $\lambda = 0\ 532\ \mu$ is 0 095

V. Atmospheric Spectral Transmission Function

The spectral transmission function of Earth's atmosphere is modeled approximately by the following series of linear functions [6]

$10\ 5\lambda - 3\ 14$	$(0\ 30 < \lambda < 0\ 34)$
$3\ 33\lambda - 0\ 7$	$(0\ 34 < \lambda < 0\ 4)$
$1\ 6\lambda - 0\ 01$	$(0\ 40 < \lambda < 0\ 5)$
$0\ 5\lambda + 0\ 54$	$(0\ 50 < \lambda < 0\ 8)$
$0\ 08\lambda + 0\ 87$	$(0\ 80 < \lambda < 1\ 6)$
$1\ 0$	$(1\ 60 < \lambda)$

The transmission at $\lambda = 0\ 532\ \mu$ is 0 806

[1] Data on detector sensitivities were gathered by Jim Annis, a graduate student at the Institute of Astronomy in Hawaii, during his summer employment at JPL in 1987

Performance Analysis of a Noncoherently Combined Large Aperture Optical Heterodyne Receiver

C -C Chen
Communications Systems Research Section

The performance of a noncoherently combined, multiple-mirror heterodyne receiver is analyzed It is shown that in the absence of atmospheric turbulence, the performance of the noncoherently combined receiver is inferior to that of a monolithic, diffraction-limited receiver with equivalent aperture area However, when atmospheric turbulence is taken into consideration, the efficiency of a monolithic aperture heterodyne receiver is limited by the phase coherence length of the atmosphere and generally does not improve with increasing aperture size In contrast, the performance of a noncoherently combined system improves with an increasing number of receivers Consequently, given a fixed collecting area, the noncoherently combined system can offer superior performance The performance of the noncoherently combined heterodyne receiver is studied by analyzing the combining loss of the receiver SNR It is shown that, given the collecting area, the performance of the combined receiver is optimized when the diameter of each of the individual receivers is on the order of the phase coherence length r_0 of the atmospheric turbulence

I. Introduction

Optical heterodyne reception [1] provides an alternative to direct-detection schemes for free-space optical communication applications The ability to reject noncoherent background radiation has made the heterodyne system very attractive for applications where effective communication in the presence of strong background interference is required Furthermore, the use of frequency and phase modulation schemes can remove the peak power constraint that currently limits the application of higher-order direct-detection pulse-position modulation (PPM) schemes

The heterodyne receiver is more complicated than the direct-detection receiver Accurate wavefront matching between the incoming signal and the local oscillator (LO) is needed to ensure effective heterodyne reception Imperfect spatial mode matching can lead to destructive interference and, consequently, to degraded system performance For systems employing small receiver apertures, the required wavefront alignment accuracy can be achieved relatively easily because the wavefront distortions due to the receiving optics and the atmosphere are negligible For systems with large collecting apertures, such as those envisioned for deep-space reception, the difficulty in maintaining good optical surface quality across the input aperture can present a serious problem in achieving effective heterodyne reception The presence of atmospheric turbulence further complicates the problem Turbulence-induced beam wander and beam spreading can result in random fluctuations of the signal phase and ampli-

tude that are difficult to compensate for As a result, the performance of a large-aperture receiver generally does not improve with increasing collecting area

Alternatively, a large effective aperture can be achieved by combining the output signals from an array of smaller receivers These receivers can share a common support structure and tracking electronics to reduce construction cost Because each receiver is now smaller than the roughness scale of the incoming signal wavefront, the local-oscillator output can be accurately matched to the signal to achieve effective heterodyne reception Output signals from these receivers can then be combined electronically to improve the detection statistics Ideally, output signals from different apertures should be combined coherently to optimize the overall receiver performance In such a scheme, turbulence- and optics-induced phase shifts in the detected intermediate-frequency (IF) signals are first compensated electronically, and the outputs from these receivers are then added coherently Since correcting the IF phase distortion is similar to correcting the incoming phase front, a coherent combining system can offer performance comparable to that of a monolithic diffraction-limited receiver For systems with weak signal intensities, however, the low signal-to-noise ratio (SNR) and rapidly varying atmospheric conditions preclude the possibility of effective phase compensation The use of adaptive optics [2] in conjunction with an artificial guide star [3] can compensate for the atmospherically induced wavefront distortion However, such measures are costly and complicated An alternative is to noncoherently combine the outputs of several subaperture receivers In such a scheme, the detected IF signal of each individual heterodyne receiver is first noncoherently demodulated [4], and the outputs of these demodulators are then electronically combined

This article presents a simple analysis of a noncoherently combined heterodyne receiver A simple model for the output of the heterodyne receiver is first constructed The performance of a noncoherently combined optical heterodyne receiver is then analyzed It is shown that in the absence of atmospheric distortions, the performance of a noncoherently combined heterodyne receiver is worse than that of a single, monolithic-aperture heterodyne receiver of equivalent aperture size This is because the noncoherent demodulation process is more susceptible to noise when the signal power is weak Consequently, by subdividing the total collection area into a number of smaller receivers, the signal power collected by each receiver is smaller, thus leading to a degraded combiner performance When the atmospheric turbulence effect is taken into consideration, however, the performance of the monolithic-aperture receiver is limited by the phase coherence length of the atmosphere As a result, subdividing the aperture and noncoherently combining the subaperture outputs can actually lead to a significant improvement in performance A simple analysis shows that the combiner SNR is optimized when the diameter of the individual subaperture is on the order of the phase-coherence length of the atmosphere

II. Heterodyne Reception Technique

The structure of a simple dual-detector heterodyne receiver is shown in Fig 1 The incoming signal is first spatially mixed with a strong local oscillator The combined signal is then photodetected The mixing of the signal and LO generates an intermediate frequency term at each detector output which oscillates at the beat frequency ω_{IF} between the signal and LO The IF signal output of the dual-detector heterodyne receiver can be modeled as [1]

$$s_{IF} = \left(\frac{e\eta G}{h\nu}\right)\frac{1}{z_0}\int W_D(\mathbf{r})\vec{A}_S(\mathbf{r}) \times \vec{A}_{LO}(\mathbf{r})\cos\left[\omega_{IF}t + \phi_S(\mathbf{r}) - \phi_{LO}(\mathbf{r})\right]d\mathbf{r} + n(t) \tag{1}$$

where $(e\eta/h\nu)$ is the responsivity of the detector, G is the detector gain, z_0 is the impedance of the photodetector, $\vec{A}_S(\mathbf{r})$ and $\vec{A}_{LO}(\mathbf{r})$ are the amplitudes of the signal and LO electric fields, $\phi_S(\mathbf{r})$ and $\phi_{LO}(\mathbf{r})$ are the signal and LO phases, ω_{IF} is the IF frequency, and $n(t)$ is the additive noise at the detector output The function $W_D(\mathbf{r})$ in Eq (1) defines the area of the receiving aperture, i e ,

$$W_D(\mathbf{r}) = \begin{cases} 1 & \text{if } |\mathbf{r}| \leq \frac{D}{2} \\ 0 & \text{if } |\mathbf{r}| > \frac{D}{2} \end{cases} \tag{2}$$

In writing Eq (1), it was assumed that the mixing process took place at the receiver input aperture Alternatively, the heterodyne process can be described by the diffraction patterns of the signal and LO over the receiver focal plane These two descriptions are completely equivalent for systems employing perfect receiving optics For systems employing less-than-perfect optics, however, the description given by Eq (1) must be modified to include the optics-induced perturbations in the signal

The noise current $n(t)$ at the receiver output consists of the signal shot noise and the detector thermal noise In the limit of a strong LO, the shot noise term usually dominates the receiver thermal noise For all practical purposes, this LO shot noise can be modeled as an additive white Gaussian noise (AWGN) with power spectral density

$$N_s = \frac{e^2\eta G^2}{h\nu} P_{LO} = \left(\frac{e^2\eta G^2}{h\nu}\right)\frac{1}{2z_0}\int W_D(\mathbf{r})\,|\vec{A}_{LO}(\mathbf{r})|^2\,d\mathbf{r} \tag{3}$$

where P_{LO} is the LO power As a result, the optical heterodyne channel can often be modeled effectively as a Gaussian channel [1] Demodulation techniques for signals in the presence of white Gaussian noise have been studied extensively [4] In general, the IF signal can be demodulated either noncoherently or coherently Noncoherent demodulation is often accomplished with the use of an envelope detector shown in Fig 2 The output of the envelope detector can be written as

$$u = \sqrt{\frac{1}{2\sigma_N^2}\left[(A_c + n_c)^2 + (A_s + n_s)^2\right]} \tag{4a}$$

where

$$A_c = \left(\frac{e\eta G}{h\nu z_0}\right)\int W_D(\mathbf{r})\,\vec{A}_S(\mathbf{r}) \times \vec{A}_{LO}(\mathbf{r})\cos\left(\phi_S(\mathbf{r}) - \phi_{LO}(\mathbf{r})\right)d\mathbf{r} \tag{4b}$$

$$A_s = \left(\frac{e\eta G}{h\nu z_0}\right)\int W_D(\mathbf{r})\,\vec{A}_S(\mathbf{r}) \times \vec{A}_{LO}(\mathbf{r})\sin\left(\phi_S(\mathbf{r}) - \phi_{LO}(\mathbf{r})\right)d\mathbf{r} \tag{4c}$$

and n_c, n_s are the Gaussian quadrature noise components with zero mean and variance equal to $\sigma_N^2 = 2N_s/T_s$ The probability distribution of the detected envelope is known to be Rician distributed with density function [4]

$$p_1(u) = 2ue^{-(\beta+u^2)} I_0\left(2u\sqrt{\beta}\right) \tag{5}$$

where

$$\beta = \frac{A_c^2 + A_s^2}{2\sigma_N^2} = \left(\frac{e\eta P_S T_s}{h\nu}\right)\frac{1}{P_S P_{LO}\left(4z_0^2\right)}\iint W_D(\mathbf{r})W_D(\mathbf{r}') \times [\vec{A}_S(\mathbf{r}) \times \vec{A}_{LO}(\mathbf{r})]\,[\vec{A}_S(\mathbf{r}') \times \vec{A}_{LO}(\mathbf{r}')] \times \cos\left(\phi_S(\mathbf{r}) - \phi_{LO}(\mathbf{r}) - \phi_S(\mathbf{r}') + \phi_{LO}(\mathbf{r}')\right)d\mathbf{r}d\mathbf{r}' \equiv \eta_{het}\left(\frac{e\eta P_S T_s}{h\nu}\right) \tag{6}$$

The factor η_{het} in Eq (6) is known as the heterodyne efficiency of the receiver, and the quantity β is the signal-to-noise ratio of the envelope detector which can be interpreted as the number of signal photons incident on the receiver aperture multiplied by the heterodyne efficiency For systems with perfect spatial mode matching, the heterodyne efficiency is equal to 1 When the spatial modes are not properly matched, the contribution to the IF signal from different parts of the receiver aperture can interfere destructively and result in reduced heterodyne efficiency

In addition to the noncoherent demodulation scheme, the IF signal can also be coherently demodulated [4] In this scheme, a local reference carrier is synchronized to the IF carrier The received IF signal is then mixed with the reference carrier and the resulting baseband signal is matched-filter detected In the absence of time-varying perturbations in the signal amplitude and phase, the coherent demodulation scheme can result in superior receiver performance However, the coherent demodulator requires the generation of a local reference signal that is synchronized to the incoming IF carrier and is therefore more complicated Furthermore, because of the rapidly varying atmospheric condition and the weak signal power expected over a deep-space link, carrier phase tracking can be very difficult to accomplish The use of the noncoherent demodulation scheme eliminates the need to retrieve the IF signal phase and hence considerably simplifies the design of the receiver Consequently, only the noncoherently demodulated heterodyne receiver will be included in the present analysis

III. Noncoherently Combined Heterodyne Receiver

The performance of a single-aperture heterodyne receiver has been studied for free-space communication applications [5] In some cases, achievement of an effective communication link requires the use of a large effective receiving aperture However, the high cost of constructing a single monolithic-aperture heterodyne receiver with a large collecting area can be prohibitive because of the stringent demand on the quality of the optical surface Furthermore, high-bandwidth adaptive optics must be used to compensate for the atmospherically induced wavefront distortion if reception inside Earth's atmosphere is desired Such a measure can further increase the receiver cost Alternatively, the perform-

ance of the communications link can be improved by electronically combining the output currents from several spatially separated heterodyne receivers The block diagram of such a receiver is shown in Fig 3 For the analysis, it will be assumed that an array of identical receivers is used to detect the incoming signal These receivers can share a common support structure to reduce the construction cost

Because the individual receivers are identical, the output signals from these receivers can be assumed to be identically distributed Furthermore, the LO shot noise can be modeled as independently distributed In the limit where the number of receivers is large, the Central Limit Theorem can be used to model the combiner output as Gaussian distributed The error performance of this combined receiver can therefore be characterized by the combiner signal-to-noise ratio ρ_c which is given by

$$\rho_c = \frac{(E[s|\text{signal}] - E[s|\text{no signal}])^2}{\text{var}(s|\text{signal}) + \text{var}(s|\text{no signal})} \tag{7}$$

In Eq (7), $s \equiv \Sigma u_i$ is the sum of individual demodulator outputs, and $E[s|X]$ and $\text{var}(s|X)$ denote the conditional mean and variance of the variable s, subjected to the condition X, respectively For a binary Gaussian channel with SNR ρ_c, the bit error rate is [4]

$$BER = \frac{1}{2}\,\text{erfc}\left(\sqrt{\frac{\rho_c}{2}}\right) \tag{8}$$

Since the demodulator outputs $\{u_i\}$ are modeled as independent and identically distributed random variables, the mean and variance of s can be evaluated by summing the mean and variance of the individual demodulator outputs, and the combiner SNR can be simplified to

$$\rho_c = N \times \frac{(E[u|\text{signal}] - E[u|\text{no signal}])^2}{\text{var}(u|\text{signal}) + \text{var}(u|\text{no signal})} \tag{9}$$

where N is the number of combined subaperture receivers Equation (9) shows that for systems employing an array of identical heterodyne receivers, the performance improves with increasing number of receivers

By integrating with respect to the probability density function given in Eq (5), the first two moments of the noncoherent demodulator output can be written as

$$E[u] = \frac{\sqrt{\pi}}{2} e^{-\beta}\,{}_1F_1(3/2,1,\beta) \tag{10}$$

$$E[u^2] = (1+\beta) \tag{11}$$

The function ${}_1F_1(a,b,c)$ is the degenerate hypergeometric function The combiner SNR can then be evaluated by substituting the demodulator mean and variance calculated from Eqs (10) and (11) into Eq (9) For $\beta \ll 1$, the degenerate hypergeometric function in Eq (10) can be expanded in a power series

$$E[u] \approx \frac{\sqrt{\pi}}{2}\left[1 + \frac{\beta}{2} - \frac{\beta^2}{16}\right], \qquad \beta \ll 1 \tag{12a}$$

and the resulting combiner SNR is given by

$$\rho_c = N \times \frac{\frac{\pi}{4}\left[\frac{\beta}{2} - \frac{\beta^2}{16}\right]^2}{\left(1 - \frac{\pi}{4}\right)(2+\beta) - \frac{3\pi}{64}\beta^2}, \qquad \beta \ll 1 \tag{12b}$$

When $\beta \gg 1$, on the other hand, an approximation to the mean demodulator output can be found by Taylor expanding the square root in Eq (4a) and taking the expectation

$$E[u] \approx \sqrt{(1+\beta)}\left[1 - \frac{1+2\beta}{8(1+\beta)^2}\right], \qquad \beta \gg 1 \tag{13a}$$

The resulting combiner SNR is therefore

$$\rho_c \approx N \times \frac{\left[\sqrt{1+\beta}\left(1 - \frac{(1+2\beta)}{8(1+\beta)^2}\right) - \frac{\sqrt{\pi}}{2}\right]^2}{1 - \frac{\pi}{4} + \frac{1+2\beta}{4(1+\beta)}}, \qquad \beta \gg 1 \tag{13b}$$

Equations (12b) and (13b) show that for a system consisting of a fixed number of receivers, the performance can be improved by increasing the SNR of the individual receivers This can be accomplished by increasing the aperture of the individual receivers or by increasing the signal power For a fixed size of individual receiver apertures and incoming signal intensity, the combiner SNR increases linearly with the number of receivers N However, for a system with a fixed overall collecting area, subdividing the receiving area into several smaller receivers can result in a corresponding decrease of the individual receiver SNR Therefore, even though the combiner SNR depends explicitly on the number of receivers N, the

reduction in β with increasing N will actually lead to a reduction in the combiner SNR This fact is demonstrated in Fig 4 where the combining loss, which is the ratio of the combiner SNR to the SNR of a single monolithic aperture of equivalent size, is plotted against the number of receivers The figure was generated with no turbulence-induced degradation taken into account The parameter ρ_0 is the SNR of a monolithic receiver

Note that at small N, the combiner SNR decreases slowly with an increasing number of aperture segments When the amount of signal power received over each aperture decreases, however, the efficiency of the noncoherent demodulator decreases and the combining loss increases rapidly This is because of the nonlinear nature of the noncoherent demodulation process At very low signal powers, the noise contribution to the demodulator output is more significant and, as a result, the efficiency of the demodulator decreases with decreasing signal power In other words, given the overall receiving area, there is a penalty for subdividing the aperture and then noncoherently combining the demodulator outputs For a system with ρ_0 = 20 dB, the noncoherent combining loss when the aperture is subdivided into 1000 receivers is approximately 15 dB This combining loss decreases with increasing signal power It should be noted that this combining loss is due to the noncoherent demodulation process For systems employing coherent combining schemes, the combiner performance will depend only on the total collecting area, and thus will not degrade with an increasing number of receivers

IV. Atmospheric Turbulence Effect

The above analysis showed that, in the absence of atmospheric turbulence, the performance of a noncoherently combined optical heterodyne receiver is inferior to that of a monolithic-aperture system. In the presence of atmospheric turbulence, both the amplitude and phase of the incoming signal wavefront will be distorted Under the condition of weak turbulence, the log amplitude $\chi(\mathbf{r})$ and the phase $\phi(\mathbf{r})$ of the optical signal, after propagating through the atmosphere, can be modeled as stationary, Gaussian random processes [5] The autocorrelation of the amplitude and phase can be characterized by the atmospheric structure function $\mathcal{D}(\mathbf{r},\mathbf{r}')$ which can be written as

$$\begin{aligned}\mathcal{D}(\mathbf{r},\mathbf{r}') &= \mathcal{D}_{\chi}(\mathbf{r},\mathbf{r}') + \mathcal{D}_{\phi}(\mathbf{r},\mathbf{r}') \\ &= \langle |\chi(\mathbf{r}) - \chi(\mathbf{r}')|^2 \rangle + \langle |\phi(\mathbf{r}) - \phi(\mathbf{r}')|^2 \rangle\end{aligned} \tag{14}$$

The angle brackets in Eq (14) denote the ensemble average Tatarski [6] showed that, under the condition of weak turbulence, the structural function of the atmosphere can be characterized by its phase coherence length r_0 as

$$\mathcal{D}(\mathbf{r},\mathbf{r}') = 6.88(|\mathbf{r} - \mathbf{r}'|/r_0)^{5/3} \tag{15}$$

Under normal viewing conditions, r_0 is typically between 5 and 30 cm, and at a few outstanding sites, such as Mauna Kea, an r_0 in excess of 40 cm can occasionally be observed

The effect of turbulence on the performance of a heterodyne receiver is to reduce the heterodyne efficiency Since the atmospheric condition varies dynamically, the instantaneous IF signal amplitude and phase vary continuously If the integration time is much shorter than the characteristic time in which the atmospheric properties change significantly, however, it is reasonable to model the atmospheric turbulence as "frozen" over the integration period In this case the time dependence of the signal phase and amplitude can be ignored, and the receiver SNR can be described adequately using Eq (6) The expression for the SNR can be further simplified by noting that, under the condition of weak turbulence, the structural function $\mathcal{D}(\mathbf{r},\mathbf{r}')$ is dominated by the phase structural function $\mathcal{D}_{\phi}(\mathbf{r},\mathbf{r}')$ Over a sufficiently large aperture, the fluctuation in signal amplitude (scintillation) will be averaged so that its effect on the receiver SNR can be ignored Under these assumptions, the SNR of the noncoherent demodulator in Eq (6) can be written as

$$\beta = (\beta_0 A_R)\frac{1}{A_R^2}\iint W_D(\mathbf{r})W_D(\mathbf{r}')e^{\imath(\phi_s(\mathbf{r})-\phi_s(\mathbf{r}'))}\,d\mathbf{r}d\mathbf{r}' \tag{16}$$

where $\beta_0 = (\eta P_S T_s/h\nu A_R)$ is the number of signal photons received per unit area or, equivalently, the receiver SNR per unit area In writing Eq (16), it has been assumed that the LO can be approximated by a plane wave and that the amplitude fluctuation of the signal can be ignored

The statistical properties of the heterodyne SNR inside the atmosphere were first studied by Fried [7],[8] By taking the expectation of Eq (16) with respect to the signal phase and using the approximation that the signal phase is a zero-mean, Gaussian random process with structure function $\mathcal{D}_{\phi}(\mathbf{r},\mathbf{r}')$, Fried successfully calculated the average receiver SNR $\bar{\beta}$ in the presence of turbulence as [7]

$$\bar{\beta} = \beta_0 \frac{\pi r_0^2}{4}\psi(D/r_0) \tag{17}$$

where

$$\psi(x) = \frac{32x^2}{\pi}\int_0^1 \frac{u}{2}[\cos^{-1}u - u(1-u^2)^{1/2}]\, e^{-3.44x^{5/3}u^{5/3}}\, du \tag{18}$$

Figure 5 is a plot of the function $\psi(D/r_0)$ versus the diameter of the receiver aperture D/r_0. For $D/r_0 \ll 1$, the function $\psi(D/r_0)$ increases as the square of the aperture diameter. For $D/r_0 \gg 1$, the value of $\psi(D/r_0)$ approaches 1 asymptotically. Note that when $D = r_0$, the SNR is only 3 dB below what can be achieved with $D \to \infty$. As a result, a further increase in the aperture size will only result in a marginal increase in the receiver SNR, and very little can be gained by increasing the diameter of the receiver aperture beyond r_0.

Equation (17) shows that the limiting performance of a single monolithic-aperture heterodyne receiver inside the atmosphere is equivalent to that of a single aperture with diameter r_0 in the absence of turbulence. In addition to limiting the average SNR, the presence of atmospheric turbulence also induces a severe fluctuation in the detected SNR. By squaring the expression for β in Eq. (16) and taking the expectation with respect to the signal phase, the mean-square receiver SNR can be written as

$$\langle \beta^2 \rangle = \beta_0^2 \frac{1}{A_R^2}\int W_D(\mathbf{r}_1)W_D(\mathbf{r}_2)W_D(\mathbf{r}_3)W_D(\mathbf{r}_4) \times \langle e^{\,i\left(\phi_s(\mathbf{r}_1)-\phi_s(\mathbf{r}_2)+\phi_s(\mathbf{r}_3)-\phi_s(\mathbf{r}_4)\right)}\rangle \times d\mathbf{r}_1 d\mathbf{r}_2 d\mathbf{r}_3 d\mathbf{r}_4 \tag{19}$$

Equation (19) is very difficult to evaluate in a closed form. However, by applying Fried's approximation, a simple upper bound on the mean square SNR can be given by (Appendix A)

$$\langle \beta^2 \rangle \leqslant e^{0.461(D/r_0)^{5/3}} \beta_0^2 \left(\frac{\pi r_0}{4}\right)^2 \left(\frac{512}{\pi^3}\right) \times \left[\left(\frac{D}{r_0}\right)^4 \int K(w) w e^{-(D/r_0)^{5/3}w^2}\, dw\right] \tag{20a}$$

where

$$K(w) = \int_0^P dp \int_0^Q dq f\left(p + \tfrac{1}{2}w/D, q\right) f\left(p - \tfrac{1}{2}w/D, q\right)$$

$$P = 1 - w/2D$$

$$Q = [1 - (w/2D)^2]^{1/2}$$

$$f(x,y) = \cos^{-1}[(x^2+y^2)^{1/2}] - (x^2+y^2)^{1/2}[1-(x^2+y^2)]^{1/2} \tag{20b}$$

Equation (20a) can be evaluated numerically. The result, which is shown in Fig. 6, provides an upper bound for the mean square SNR fluctuation. Note that the upper bound diverges exponentially for $D/r_0 \geqslant 1$. Also shown in Fig. 6 are the results of a Monte Carlo simulation of the mean square SNR. In contrast to the diverging upper bound, the simulation data show that the mean square SNR actually converges at $D/r_0 \gg 1$. This convergence can be argued as follows: for $|\mathbf{r}_i - \mathbf{r}_j| \gg r_0$, the phase of the incoming signal at $\mathbf{r}_i$ and $\mathbf{r}_j$ will be completely uncorrelated so that the expectation of the exponent in Eq. (19) is negligible. By applying a simple geometrical argument, it can be reasoned that the integrand in Eq. (19) is negligible except when $\mathbf{r}_1 \approx \mathbf{r}_2$ and $\mathbf{r}_3 \approx \mathbf{r}_4$, or when $\mathbf{r}_1 \approx \mathbf{r}_3$ and $\mathbf{r}_2 \approx \mathbf{r}_4$. Consequently, only two of the four spatial integrals increase with increasing D, and the integral in Eq. (19) increases only as D^4. As a result, the mean square SNR converges as $D \to \infty$.

When the effect of turbulence is taken into account, the performance of the noncoherently combined heterodyne receiver depends on the actual probability distribution of β. Given $P_\beta(\beta)$, the probability distribution of β, the first two moments of the noncoherent demodulator can be calculated by averaging Eqs. (9) and (10) over the distribution of β as

$$E[u] = \int_0^\infty \frac{\sqrt{\pi}}{2} e^{-\beta}\, {}_1F_1(3/2,1,\beta) P_\beta(\beta)\, d\beta \tag{21a}$$

$$E[u^2] = \int_0^\infty (1+\beta) P_\beta(\beta)\, d\beta = 1 + \bar{\beta} \tag{21b}$$

A detailed description of the distribution of β is needed to evaluate these integrals. Unfortunately, due to the complexity of the expression shown in Eq. (16), the statistical properties for β are very difficult to characterize. However, when the variance of β is small, a simple approximation for the mean de-

modulator output can be found by expanding the conditional expectation of the demodulator output in a Taylor series (Appendix B)

$$E[u] \equiv \int_0^\infty \frac{\sqrt{\pi}}{2} e^{-\beta}\, {}_1F_1(3/2,1,\beta)\, P_\beta(\beta)\, d\beta$$

$$\approx \frac{\sqrt{\pi}}{2} e^{-\bar{\beta}}\, {}_1F_1(3/2,1,\bar{\beta}) - \frac{\sqrt{\pi}}{16} e^{-\bar{\beta}}\, {}_1F_1(3/2,3,\bar{\beta})\, \sigma_\beta^2 \tag{22a}$$

Because the second derivative of the conditional average of the demodulator output is always negative, it can also be shown that the average demodulator output is bounded from above by (Appendix B)

$$E[u] < \frac{\sqrt{\pi}}{2} e^{-\bar{\beta}}\, {}_1F_1(3/2,1,\bar{\beta}) \tag{22b}$$

For the analysis of noncoherently combined heterodyne receivers inside the atmosphere, it will be assumed that the individual receivers are spatially separated by a distance much greater than the phase coherence length r_0 of the atmosphere so that the output of these receivers can be modeled as independent and identically distributed Therefore, by substituting the expressions for the first two moments of the demodulator output from Eqs (21b) and (22b) into Eq (7), an estimate of the combiner SNR can be found for a noncoherently combined heterodyne receiver inside atmosphere Since Eq (22b) presents an upper bound for the mean demodulator output, it follows from Eq (7) that the combiner SNR derived is an upper bound for the actual combiner SNR Similarly, by substituting Eqs (21a) and (22a) into Eq (7), an approximation to the combiner SNR can be derived If we further substitute in the upper bound of the variance of β given in Eq (20), the resulting combiner SNR will be an approximate lower bound of the actual combiner performance

Given the expression for the combiner SNR, the performance of the combined receiver can be investigated Figure 7 is a plot of the combiner SNR versus the total receiving area for a noncoherently combined heterodyne receiver with several values of N, the number of receivers The incoming signal intensity β_0 and the atmospheric coherence length r_0 are fixed Also plotted in the figure is the SNR for a coherently combined heterodyne receiver with no turbulence This curve represents the best achievable performance for a heterodyne receiver at a given receiving area Note that when the total collecting area is small, the performance of the combined system degrades with an increase in the number of receivers This is because the efficiency of the noncoherent demodulation process degrades rapidly with decreasing signal power However, as the diameter of the receiver aperture increases beyond r_0, the SNR of the single-aperture receiver begins to saturate because of the atmospheric turbulence On the other hand, for systems employing a number of receivers, the combiner SNR continues to improve until the diameter of each receiver is greater than r_0 Therefore, for a system which requires a large collecting area, the performance can indeed be improved by combining the outputs from several receivers It should be noted, however, that despite the improvement in combiner performance with an increasing number of receivers, the performance of the noncoherently combined receiver is still far inferior to that of a coherently combined system In fact, for the given signal intensity assumed in Fig 7, the noncoherently combined receiver suffers more than 20 dB loss in the receiver SNR

It is interesting to evaluate the combining loss versus the number of receivers Plotted in Fig 8 is the combining loss of a noncoherently combined heterodyne receiver versus the number of receivers The total collecting aperture is fixed so that an increase in the number of receivers corresponds to a decrease in the diameter of the individual receiver apertures For systems employing a large number of small-aperture receivers, the loss due to noncoherent demodulation dominates so that the combining loss increases with an increasing number of receivers For systems using a small number of receivers, on the other hand, the SNR of each receiver is limited by the coherence length of the atmosphere, and hence the receiver performance improves with an increasing number of receivers Consequently, given the overall collecting area and the phase coherence length r_0, an optimal number of receivers can be found which maximizes the combiner SNR It should be noted, however, that Fig 8 was generated by fixing the total collection area of the combined receiver When the size of the individual receiver is fixed, it follows directly from Eq (7) that the performance of the combined receiver improves linearly with N It is also interesting to investigate the dependence of combining loss with different values of r_0, the phase coherence length Figure 9 is a plot of the combining loss versus the diameter of the individual aperture at different values of r_0 The total collecting area of the combined receiver is again assumed to be equivalent to that of a monolithic receiver with a 10-meter diameter It is seen that the performance of the combined receiver is optimized when the diameter of the individual receiver D is approximately equal to the phase coherence length r_0 The combining loss increases rapidly when the size of the individual aperture becomes much larger than r_0

V. Conclusions

Combining outputs from a number of small-aperture heterodyne receivers can significantly reduce the cost of constructing a receiver with a large collecting area In principle, output signals from these small-aperture receivers can be combined

to improve the detection statistics Compared to systems employing a single, diffraction-limited aperture, however, the noncoherently combined receiver suffers from the combining loss due to the noncoherent demodulation process This combining loss increases rapidly with an increasing number of aperture segments The loss due to noncoherent combining is worse for systems with weak incoming signals For systems with a large number of segments ($N \approx 100$), the combining loss is on the order of 15–25 dB for systems with an effective single-aperture SNR of 10–20 dB The combining loss is smaller for systems with higher signal powers

When the atmospheric turbulence is taken into consideration, however, the performance of a monolithic-aperture heterodyne receiver is limited by the size of the phase-coherence cell of the atmosphere As a result, increasing the size of a monolithic aperture will not result in a corresponding improvement in system performance For such a system, the noncoherently combined receiver can provide a significant improvement in system performance The analysis showed that, given the size of the overall collecting aperture, the performance of the receiver is optimized when the diameter of the individual subaperture is equal to the phase coherence length of the atmosphere r_0 Increasing the size of the individual aperture beyond r_0 can result in a saturation of individual SNR On the other hand, reducing the subaperture to a size smaller than r_0 will increase the combining loss and hence degrade the system performance

It should be noted that for large N, the combining loss of the noncoherently combined heterodyne receiver is due primarily to the inefficiency in the noncoherent demodulation process It was assumed throughout this article that the coherent combining is ineffective due to the weak signal power and the rapidly varying atmospheric condition For systems in which this assumption can be relaxed, the coherent combining scheme can be used to improve receiver performance significantly One such system is the large-aperture heterodyne receiver in space Although the alignment errors between individual receivers can induce random phase shifts between the detector outputs, these phase errors are fixed and can therefore be accurately measured and properly compensated in the absence of rapidly varying atmospheric conditions Another scheme is to use the adaptive optic technique to correct for the atmospherically induced wavefront distortion The required high signal power can be provided through the use of natural or artificial guide stars [3] Receiver performance comparable to that of a monolithic, diffraction-limited receiver can be obtained, at least in principle, with the use of a coherent signal combining scheme

Acknowledgments

The author acknowledges Dr James R Lesh for his helpful discussions, and Mr Moe Zaw Win for carrying out the computer simulation

References

[1] R Gagliardi and S Karp, *Optical Communications*, New York Wiley, 1975

[2] J W Hardy, "Active Optics A New Technology for the Control of Light," *Proc IEEE*, vol 66, no 6, pp 651–697, June 1978

[3] L A Thompson and C S Gardner, "Experiment on Laser Guide Star at Mauna Kea Observatory for Adaptive Imaging in Astronomy," *Nature*, vol 328, no 6127, pp 229–231, July 16, 1987

[4] W Lindsey and M K Simon, *Telecommunication Systems Engineering*, Englewood Cliffs, New Jersey Prentice-Hall, 1973

[5] J E Kaufmann and L L Jeromin, "Optical Heterodyne Intersatellite Links Using Semiconductor Lasers," presented at the IEEE GLOBECOM'84, Atlanta, Georgia, November 27–29, 1984

[6] V I Tatarski, *Wave Propagation in a Turbulent Medium*, New York McGraw-Hill, 1961

[7] D L Fried, "Optical Heterodyne Detection of an Atmospherically Distorted Signal Wave Front," *Proc IEEE*, vol 55, no 1, pp 57–67, January 1967

[8] D L Fried, "Atmospheric Modulation Noise in an Optical Heterodyne Receiver," *IEEE J Quantum Electron* , vol QE-3, no 6, pp 213–221, 1967

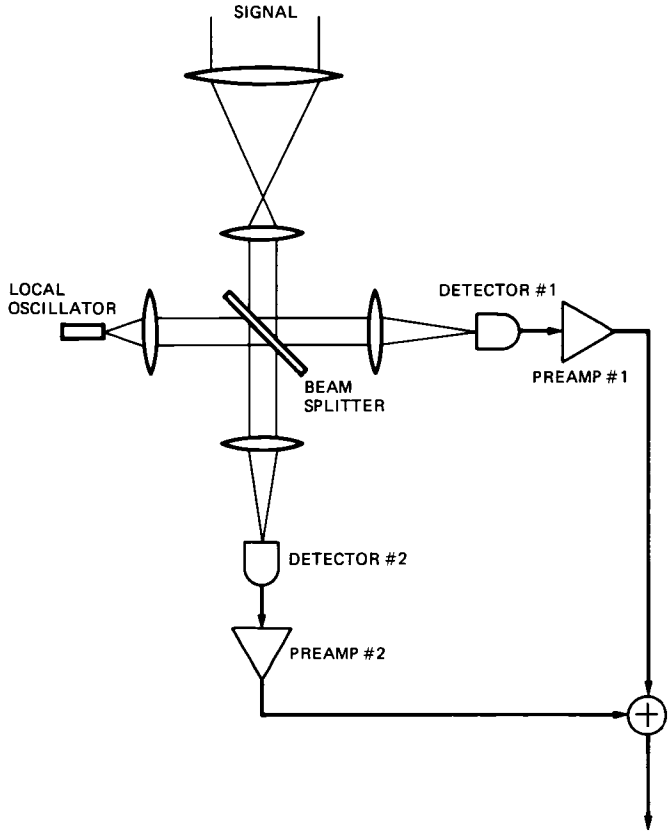

Fig 1. Block diagram of a dual-detector heterodyne receiver

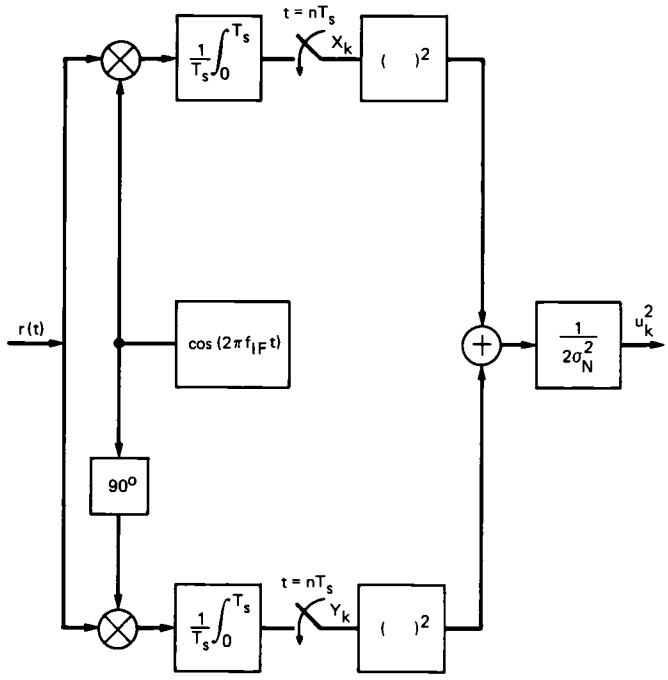

Fig 2 Structure of a noncoherent envelope demodulator

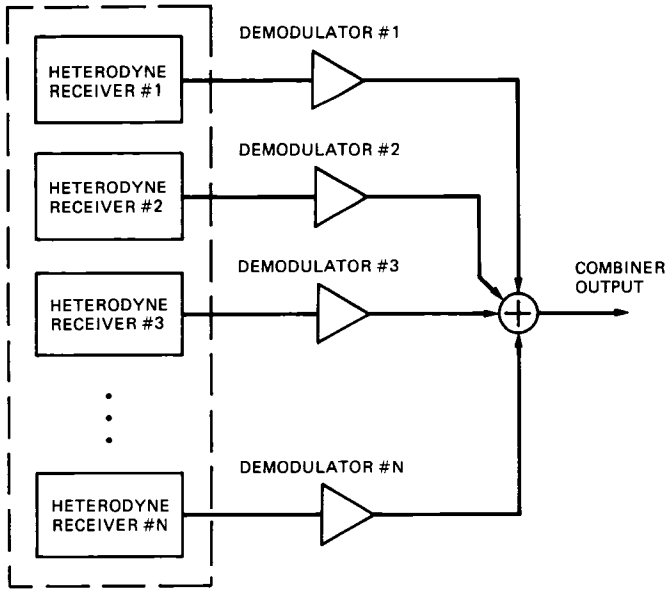

Fig. 3 Block diagram of a noncoherently combined heterodyne receiver

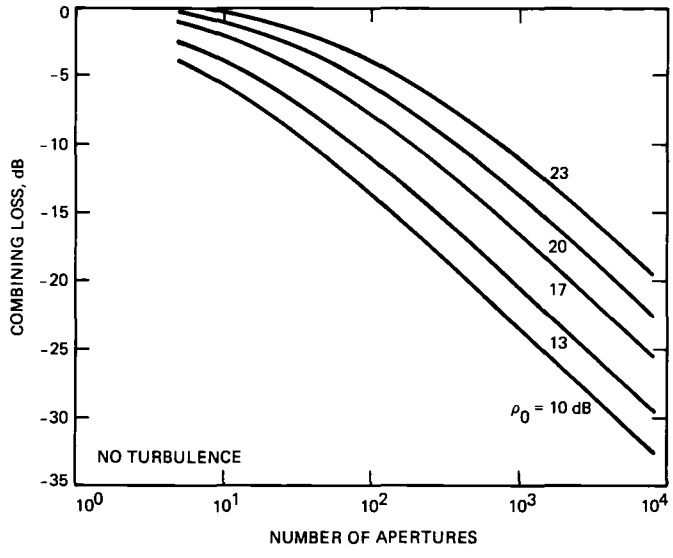

Fig 4 Combining loss of a noncoherently combined heterodyne receiver with a fixed overall aperture size

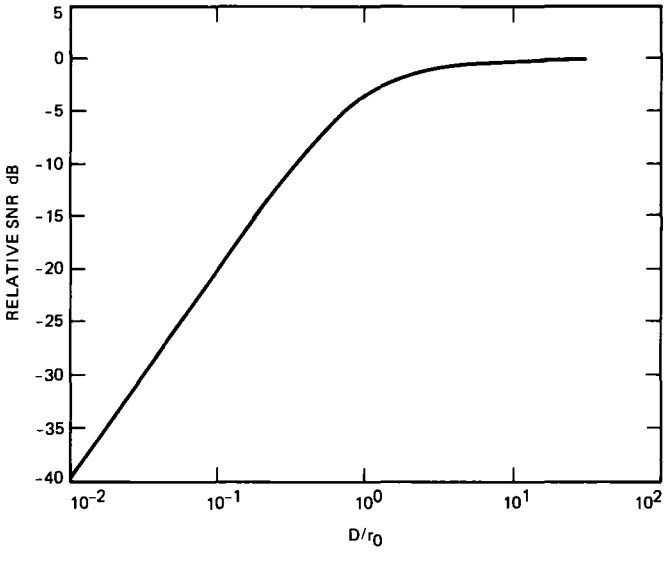

Fig 5 The value of $\psi(D/r_0)$ versus the diameter of the aperture D/r_0

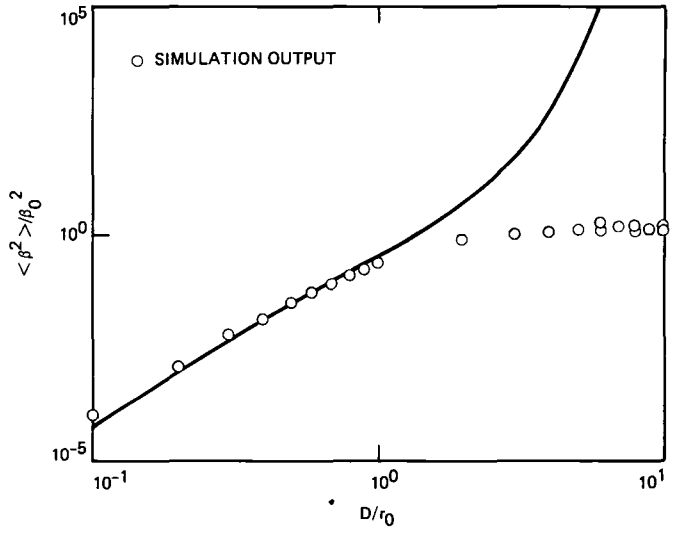

Fig 6 Mean square value of the demodulator SNR $<\beta^2>$ versus the diameter of the receiver aperture Also plotted are the mean square values calculated from the Monte Carlo simulations

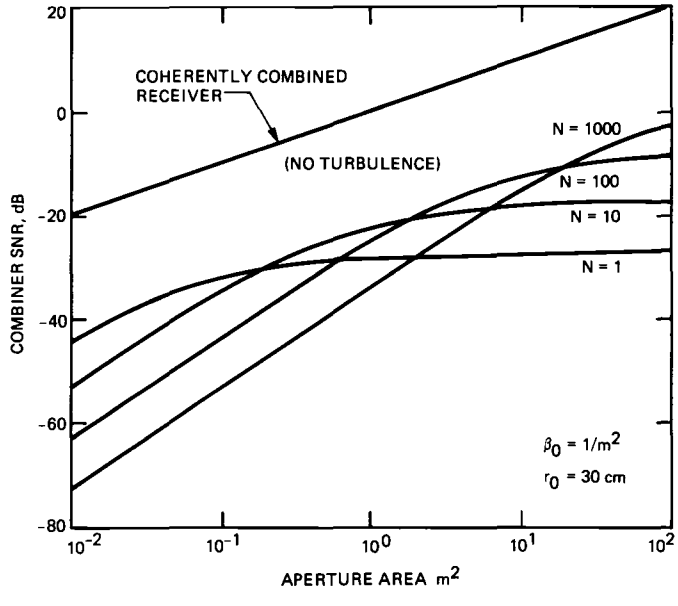

Fig 7 Combiner SNR versus the total area of the collecting aperture for several values of *N*, the number of receivers Also plotted is the SNR of a coherently combined receiver of equivalent aperture area

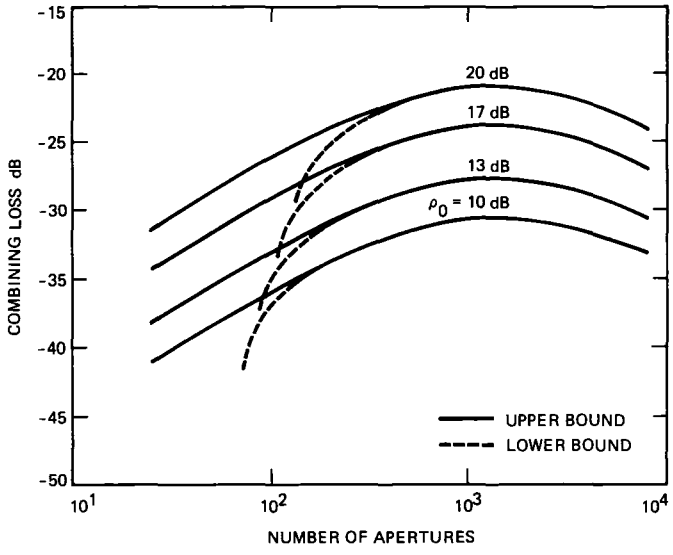

Fig. 8. Combining loss of a noncoherently combined heterodyne receiver with the saturation effect of the atmosphere taken into account The total collecting area of the receiver is equivalent to a 10-m-diameter monolithic aperture, and the atmospheric coherence length r_0 is 30 cm

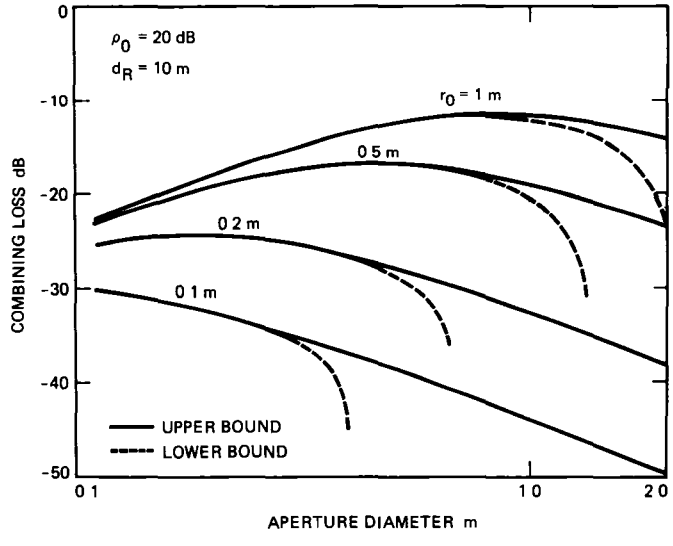

Fig. 9. Combining loss versus the diameter of the individual aperture for a system with an equivalent aperture diameter of 10 meters

Appendix A

Derivation of the Mean Square Receiver SNR

Given the expression of β in Eq (16), the mean square SNR, $\langle \beta^2 \rangle$, can be written as

$$\langle \beta^2 \rangle = \beta_0^2 \frac{1}{A_R^2} \int W_D(\mathbf{r}_1) \quad W_D(\mathbf{r}_4)$$

$$\times \langle e^{\imath(\phi_S(\mathbf{r}_1)-\phi_S(\mathbf{r}_2)+\phi_S(\mathbf{r}_3)-\phi_S(\mathbf{r}_4))} \rangle$$

$$\times d\mathbf{r}_1 d\mathbf{r}_2 d\mathbf{r}_3 d\mathbf{r}_4 \tag{A-1}$$

The expectation over $\phi_S(\mathbf{r}_1)$ can be evaluated by using the assumption that $\Phi_S(\mathbf{r}_1,\mathbf{r}_2,\mathbf{r}_3,\mathbf{r}_4) = \phi_S(\mathbf{r}_1) - \phi_S(\mathbf{r}_2) + \phi_S(\mathbf{r}_3) - \phi_S(\mathbf{r}_4)$ is a zero-mean Gaussian random variable The resulting expectation value of the exponential is given by

$$\langle e^{\imath\Phi_S(\mathbf{r}_1,\mathbf{r}_2,\mathbf{r}_3,\mathbf{r}_4)} \rangle = e^{-\sigma_\Phi^2/2} \tag{A-2}$$

where σ_Φ^2 is the variance of $\Phi_S(\mathbf{r}_1,\mathbf{r}_2,\mathbf{r}_3,\mathbf{r}_4)$ Equation (A-2) can be further simplified by realizing that

$$(a-b+c-d)^2 = (a-b)^2 + (a-d)^2 + (b-c)^2 + (c-d)^2 - (a-c)^2 - (b-d)^2 \tag{A-3}$$

and that the expectation of the phase-difference square is simply the phase structural function, i e , $\mathscr{D}_\phi(\mathbf{r}_1 - \mathbf{r}_2) = \langle |\phi_S(\mathbf{r}_1) - \phi_S(\mathbf{r}_2)|^2 \rangle$ By substituting Eq (A-2) into Eq (A-1), the mean-square SNR can be written as

$$\langle \beta^2 \rangle = \beta_0^2 \frac{1}{A_R^2} \int W_D(\mathbf{r}_1) W_D(\mathbf{r}_2) W_D(\mathbf{r}_3) W_D(\mathbf{r}_4)\, e^{\left\{1/2[-\mathscr{D}_\phi(|\mathbf{r}_1-\mathbf{r}_2|)-\mathscr{D}_\phi(|\mathbf{r}_3-\mathbf{r}_4|)]\right\}}$$

$$\times e^{\left\{1/2[-\mathscr{D}_\phi(|\mathbf{r}_1-\mathbf{r}_4|)-\mathscr{D}_\phi(|\mathbf{r}_2-\mathbf{r}_3|)+\mathscr{D}_\phi(|\mathbf{r}_1-\mathbf{r}_3|)+\mathscr{D}_\phi(|\mathbf{r}_2-\mathbf{r}_4|)]\right\}} d\mathbf{r}_1 d\mathbf{r}_2 d\mathbf{r}_3 d\mathbf{r}_4$$

$$= \beta_0^2 \left(\frac{16D^4}{\pi^2}\right) \int W_1(\mathbf{u}_1) W_1(\mathbf{u}_2) W_1(\mathbf{u}_3) W_1(\mathbf{u}_4)\, e^{3.44(D/r_0)^{5/3}[-|\mathbf{u}_1-\mathbf{u}_2|^{5/3}-|\mathbf{u}_3-\mathbf{u}_4|^{5/3}]}$$

$$\times e^{3.44(D/r_0)^{5/3}[-|\mathbf{u}_1-\mathbf{u}_4|^{5/3}-|\mathbf{u}_2-\mathbf{u}_3|^{5/3}+|\mathbf{u}_1-\mathbf{u}_3|^{5/3}+|\mathbf{u}_2-\mathbf{u}_4|^{5/3}]} d\mathbf{u}_1 d\mathbf{u}_2 d\mathbf{u}_3 d\mathbf{u}_4 \tag{A-4}$$

where we have carried out the substitution of variables, $\mathbf{r}_i = D\mathbf{u}_i$, and applied the 5/3 power law of the phase structural function to factor out the term $(D/r_0)^{5/3}$

The mean square SNR given in Eq (A-4) is very difficult to evaluate numerically However, a simple upper bound of the integral can be obtained by using the fact that since $|\mathbf{u}_i| < 1/2$, $|\mathbf{u}_i - \mathbf{u}_j| = u_{ij} \leq 1$, and the 5/3 power of u_{ij} can be bounded from above and below by

$$u_{ij}^2 \leq u_{ij}^{5/3} \leq u_{ij}^2 + \left[\left(\frac{5}{6}\right)^5 - \left(\frac{5}{6}\right)^6\right] = u_{ij}^2 + 0.06698$$

$$0 \leq u \leq 1 \tag{A-5}$$

The bounds in Eq (A-5) are derived by solving for the maximum and minimum of the function $y(x) = x^{5/3} - x^2$ By substituting the upper bound into Eq (A-4) for terms with

positive exponents and the lower bound for terms with the negative exponent, a simple upper bound for the mean square SNR can be easily derived,

$$\langle \beta^2 \rangle \leqslant e^{0.461(D/r_0)^{5/3}} \beta_0^2 \left(\frac{\pi r_0^2}{4}\right)^2 \phi(D/r_0) \qquad \text{(A-6)}$$

where

$$\phi(D/r_0) = \frac{256}{\pi^4}\left(\frac{D}{r_0}\right)^4 \int W_1(\mathbf{u}_1) \quad W_1(\mathbf{u}_4) \times e^{[-(D/r_0)^{5/3}|\mathbf{u}_1-\mathbf{u}_2+\mathbf{u}_3-\mathbf{u}_4|^2]} \, d\mathbf{u}_1 d\mathbf{u}_2 d\mathbf{u}_3 d\mathbf{u}_4 \qquad \text{(A-7)}$$

Since the integral involves only a single variable of the form $\mathbf{w} = |\mathbf{u}_1 - \mathbf{u}_2 + \mathbf{u}_3 - \mathbf{u}_4|^2$, the 4-fold integral in Eq (A-7) can be collapsed into a single one-dimensional integral of the form [7]

$$\int W_1(\mathbf{u}_1) \quad W_1(\mathbf{u}_4) e^{-t^{5/3}|\mathbf{u}_1-\mathbf{u}_2+\mathbf{u}_3-\mathbf{u}_4|^2} \, d\mathbf{u}_1 \quad d\mathbf{u}_4 = 2\pi \int K(w) w e^{-t^{5/3}w^2} \, dw \qquad \text{(A-8)}$$

where

$$K(w) = \int_0^P dp \int_0^Q dq f\left(p + \tfrac{1}{2}w/D, q\right) f\left(p - \tfrac{1}{2}w/D, q\right)$$

$$P = 1 - w/2D$$

$$Q = [1 - (w/2D)^2]^{1/2}$$

$$f(x,y) = \cos^{-1}[(x^2+y^2)^{1/2}] - (x^2+y^2)^{1/2}[1-(x^2+y^2)]^{1/2} \qquad \text{(A-9)}$$

Appendix B
Derivation of Eq. (22)

Given the probability distribution of β, $P_\beta(\beta)$, the expectation value of the noncoherent demodulator output is given by

$$E[u] \equiv \int_0^\infty f(\beta) P_\beta(\beta)\, d\beta \tag{B-1}$$

where $f(\beta) = E[u|\beta] = (\sqrt{\pi}/2)e^{-\beta}{}_1F_1(3/2,1,\beta)$ is the conditional expectation of u The integral in Eq (B-1) depends on the distribution of β and hence is in general difficult to evaluate However, when the distribution of β is sufficiently narrow, we can expand $f(\beta)$ around the mean SNR $\bar{\beta}$ as

$$f(\beta) \approx f(\bar{\beta}) + f'(\bar{\beta})(\beta - \bar{\beta}) + \frac{f''(\bar{\beta})}{2}(\beta - \bar{\beta})^2 + \tag{B-2}$$

The derivatives of the function $f(\beta)$ can be evaluated by taking the derivatives of the degenerated hypergeometric function, and applying the recurrence relations

$$\frac{df(\beta)}{d\beta} = \frac{d}{d\beta}\left(\frac{\sqrt{\pi}}{2} e^{-\beta}{}_1F_1(3/2,1,\beta)\right)$$

$$= \frac{\sqrt{\pi}}{4} e^{-\beta}{}_1F_1(3/2,2,\beta) \geq 0 \tag{B-3}$$

$$\frac{d^2f(\beta)}{d\beta^2} = -\frac{\sqrt{\pi}}{8} e^{-\beta}{}_1F_1(3/2,3,\beta) \leq 0 \tag{B-4}$$

By substituting the Taylor expansion in Eq (B-2) into Eq (B-1), the expectation value can be written as

$$E[u] \approx \int_0^\infty \left(f(\bar{\beta}) + f'(\bar{\beta})(\beta - \bar{\beta}) + \frac{f''(\bar{\beta})}{2}(\beta - \bar{\beta})^2\right) P_\beta(\beta)\, d\beta$$

$$= f(\bar{\beta}) + \frac{f''(\bar{\beta})}{2}\sigma_\beta^2 \tag{B-5}$$

where the first order term vanishes because of the fact that

$$\beta = \int_0^\infty \beta P_\beta(\beta)\, d\beta \tag{B-6}$$

To show that $f(\bar{\beta})$ is an upper bound of Eq (B-1), note that since the second derivative of $f(\beta)$ is less than zero for all β, the function $f(\beta)$ is always less than the linear term $g(\beta) = f(\bar{\beta}) + f'(\bar{\beta})(\beta - \bar{\beta})$ Consequently, $f(\bar{\beta})$, which is derived by substituting $g(\beta)$ for $f(\beta)$ in Eq (B-1), is always greater than the actual expectation value

Effect of Detector Dead Time on the Performance of Optical Direct-Detection Communication Links

C -C Chen
Communications Systems Research Section

Avalanche photodiodes (APDs) operating in the Geiger mode can provide a significantly improved single-photon detection sensitivity over conventional photodiodes However, the quenching circuit required to remove the excess charge carriers after each photon event can introduce an undesirable dead time into the detection process The effect of this detector dead time on the performance of a binary pulse-position-modulated (PPM) channel is studied by analyzing the error probability It is shown that, when background noise is negligible, the performance of the detector with dead time is similar to that of a quantum-limited receiver For systems with increasing background intensities, the error rate of the receiver starts to degrade rapidly with increasing dead time The power penalty due to detector dead time is also evaluated and shown to depend critically on background intensity as well as dead time Given the expected background strength in an optical channel, therefore, a constraint must be placed on the bandwidth of the receiver to limit the amount of power penalty due to detector dead time

I. Introduction

The single-photon detection sensitivity of avalanche photodiodes (APDs) can be improved significantly by operating the APDs in the Geiger mode [1] In contrast to conventional photodetectors that are susceptible to circuit noise, the extremely high gain of the Geiger-mode APD allows single-photon events to be detected effectively For deep-space communications where the energy efficiency is critical, the use of the Geiger-mode APD will allow the implementation of near-quantum-limited optical communication links

To operate the APD in the Geiger mode, the APD is first cooled to reduce the number of thermally excited charge carriers The APD is then reverse-biased beyond its breakdown voltage A single photon event will then initiate an avalanche of charge carriers and generate a detectable signal Because of the strong reverse bias, however, the APD must be quenched after each photon event to remove the excess charge carriers and stop the avalanche This quenching process introduces an undesirable dead time into the detection process Photons that arrive after the initial photon event and before the end of the quenching process will therefore not be detected The presence of detector dead time can also perturb the count statistics of the photodetector Compared to a conventional detector for which the detection process can be modeled as a Poisson arrival process, the number of detectable photon events of a Geiger mode APD over a fixed interval is limited by its dead time The distortion of count statistics can result in a higher bit error rate for optical communication channels Conse-

quently, a higher signal power is required to maintain the given error performance In this article, the effect of detector dead time on the performance of an optical PPM system is analyzed It is shown that in the presence of detector dead time, a higher signal power is required to maintain channel performance This power penalty is then numerically evaluated for several different signal and background strengths

II. Photocount Statistics

In the absence of the detector dead time, the detection of photon events can be modeled as a Poisson arrival process for which the probability of detecting k events over a time period $[0, T_s)$ is given by

$$p(k) = \frac{(\lambda T_s)^k}{k!} e^{-\lambda T_s}$$

where the constant λ is the average rate of arrival for photons The photocount rate λ can be related to the intensity of the optical signal by

$$\lambda = \frac{\eta P_s}{h\nu}$$

where η is the quantum efficiency of the detector, P_s is the intensity of the incident optical signal, h is Planck's constant, and ν is the frequency of the optical signal

When the detector dead time is considered, the actual count statistics of the receiver can be very different from the photon arrival statistics This difference is illustrated in Fig 1 The photons that arrive after the initial photon event and before the end of the quenching process will not be detected In the presence of the detector dead time, the detection statistics are no longer Poisson distributed In fact, for a detector with dead time Δ, the maximum observable count over a period of $[0, T_s)$ is $k_{max} = \lfloor T_s/\Delta \rfloor + 1$ where $\lfloor x \rfloor$ denotes the largest integer that is smaller than x Furthermore, since the detector dead time can overlap two adjacent time slots, the count statistics over a given time slot will also depend on the received optical intensity over the previous time slot For a receiver with dead time Δ, the probability of detecting k photon events where $k \leqslant k_{max} - 2$ is given by (Appendix)

$$p(k) = e^{-\delta K_0 - (1-k\delta)K_1} \times \left\{ \frac{K_1(1-k\delta)^k}{k!} + \sum_{\ell=0}^{k-1} \frac{K_1^\ell}{\ell!} \left[(1-k\delta)^\ell - \left(1-(k-1)\delta\right)^\ell e^{-\delta K_1} \right] \right.$$

$$+ \sum_{\ell=0}^{k} \frac{K_0 K_1^k}{\ell!(K_0+K_1)^{k-\ell+1}} \times \left[\left(1-(k+1)\delta\right)^\ell e^{\delta(K_0+K_1)} - (1-k\delta)^\ell \right]$$

$$+ \sum_{\ell=0}^{k-1} \sum_{m=0}^{\ell} \frac{K_0 K_1^\ell}{m!(K_0+K_1)^{\ell-m+1}} \times \left[\left(1-(k+1)\delta\right)^m e^{\delta(K_0+K_1)} - (1-k\delta)^m (1+e^{\delta K_0}) + \left(1-(k-1)\delta\right)^m e^{-\delta K_1} \right] \left. \right\}$$

where $\delta = \Delta/T_s$ is the normalized dead time and K_0, K_1 are the average number of incident photons over the previous and the present time slots, respectively The probability of observing $k_{max} - 1$ and k_{max} events can also be calculated

$$p(k \mid k = k_{max} - 1) = 1 - e^{(1-(k+1)\delta)K_0} + \frac{K_0 K_1^k}{(K_0+K_1)^{k+1}} e^{(1-(k+1)\delta)K_0} + e^{-\delta K_0 - (1-k\delta)K_1} \left\{ \frac{K_1^k (1-k\delta)^k}{k!} + \sum_{\ell=0}^{k-1} \frac{K_1^\ell}{\ell!} \left[(1-k\delta)^\ell - \left(1-(k-1)\delta\right)^\ell e^{-\delta K_1} \right] \right.$$

$$+ \sum_{\ell=0}^{k-1} \frac{K_0 K_1^\ell}{(K_0+K_1)^{\ell+1}} e^{(1-k\delta)(K_0+K_1)} + \sum_{\ell=0}^{k-1} \sum_{m=0}^{\ell} \frac{K_0 K_1^\ell}{m!(K_0+K_1)^{\ell-m+1}} \times \left[\left(1-(k-1)\delta\right)^m e^{-\delta K_1} \right.$$

$$- (1 - k\delta)^m (1 + e^{\delta K_0})\Big] - \sum_{\ell=0}^{n} \frac{K_0 K_1^k}{\ell!(K_0 + K_1)^{k-\ell+1}} (1 - k\delta)^\ell \Bigg\}$$

$$p(k \mid k = k_{\max}) = e^{(1-k\delta)K_0} - e^{-\delta K_0 - (1-(k-1)\delta)K_1} \times \sum_{\ell=0}^{k-1} \frac{K_1^\ell}{\ell!} \left(1 - (k-1)\delta\right)^\ell + e^{-\delta K_0 - (1-(k-1)\delta)K_1} \times \sum_{\ell=0}^{k-1} \sum_{m=0}^{\ell} \frac{K_0 K_1^\ell}{m!(K_0 + K_1)^{\ell-m+1}} \times \left(1 - (k-1)\delta\right)^m - e^{(1-k\delta)K_0} \sum_{\ell=0}^{k-1} \frac{K_0 K_1^\ell}{(K_0 + K_1)^{\ell+1}}$$

The probability distribution $p(k)$ is plotted in Fig 2 for different values of δ Note that for a receiver with no dead time, the photocount distribution is Poisson with mean K_1 In the presence of the detector dead time, the distribution is shifted towards the lower end Furthermore, the probability density is zero for $k > k_{\max}$

III. Performance Impact

The performance of optical channels under Poisson statistics has been investigated thoroughly in the literature [2], [3] It was shown that the pulse position modulation (PPM) channel offers superior performance over other modulation schemes In this scheme, each transmitted word is divided into M time slots, and the signal is encoded such that only one of these M slots contains the signal pulse Because the detector can be implemented by simply comparing the received photocounts over different slot periods and choosing the slot with the highest count, the PPM decoder is less sensitive to the fluctuation in background and signal strengths Furthermore, by compressing the signal power into a narrow time slot, a higher signal-to-noise ratio can be achieved and the overall system performance is improved

Given an ideal photon counting detector the probability of error for a binary optical PPM system can be written as [2]

$$PBE = \frac{1}{2}\left[1 + Q\left(\sqrt{2K_B},\ \sqrt{2(K_S + K_B)}\right) - Q\left(\sqrt{2(K_S + K_B)},\ \sqrt{2K_B}\right)\right]$$

where $K_S = \lambda_S T_s$, $K_B = \lambda_B T_s$ are the average number of signal and background photons received over the time slot, and $Q(\alpha, \beta)$ is the Marcum's Q function which is given by

$$Q(\alpha, \beta) = \int_\beta^\infty e^{-(\alpha^2 + x^2)/2} I_0(\alpha x)\, dx$$

where $I_0(x)$ is the modified Bessel function of order zero The above equation was derived by assuming that the photocount statistics of the receiver can be modeled as a Poisson arrival process In practice, the detectors used rarely achieve Poisson counting statistics Conventional PIN diodes and APDs, because of their low signal gain ($G = 1$ for PIN diodes, and $G \approx 100 - 300$ for APDs), are susceptible to the thermal noise that is in general not Poisson distributed When operating under low signal intensities, the low detection gain can result in a reduced single-photon detection efficiency and non-Poisson output statistics

The detection sensitivity can be improved by operating the avalanche photodiode in the Geiger mode [1] Because of the detector dead time associated with the Geiger mode of operation, however, the photocount statistics cannot be modeled as Poisson-distributed random variables Furthermore because of the finite duration of the detector dead time, the detection statistics for neighboring time slots become correlated The photocount statistics of a given time slot depend not only on the signal intensity, but also on the intensity received during the previous time slot In effect, the presence of the detector dead time introduces an intersymbol interference into the detection statistics

The actual error probability of the optical PPM channel under this intersymbol interference is difficult to analyze A simple estimate of the channel error rate, nevertheless, can be derived by assuming that the count statistics over different time slots are independent In this case the error probability of a binary PPM channel can be written as

$$PBE(K_0, K_1) = \frac{1}{2} \sum_{k=0}^{\infty} P(k \mid K_0) P(k \mid K_1) + \sum_{k=0}^{\infty} P(k \mid K_1) \sum_{\ell=k+1}^{\infty} P(\ell \mid K_0)$$

In the above equation, $P(k|K_0)$ and $P(k|K_1)$ denote the probability of receiving k counts in a slot where the average incident photons are K_0 and K_1, respectively The first term on the right-hand side of the PBE expression is the probability that both time slots receive equal counts, in which case a random choice was assigned at the decoder The second term on the right-hand side is simply the probability that the background time slot receives more photons than the signal time slot It should be remembered that the above PBE expression was derived by assuming that the receiver photocounts for adjacent time slots are uncorrelated The marginal count statistics for each time slot, however, still depend on the optical intensities received in the present and the previous time slots Using this approximation, the PBE of a binary PPM channel can be evaluated by averaging over different distributions of the transmitted sequences Plotted in Fig 3 is the probability of bit error for a binary PPM system assuming independent slot count statistics The PBE is evaluated by assuming that channel symbols are transmitted with equal probability It is seen from the figure that, at small values of δ, the effect of dead time on the channel PBE is almost negligible As the dead time increases, however, the channel error rate starts to increase For $\delta > 0\ 2$, the discrete quantization of the detector count statistics can result in an observable distortion of the PBE curves This fact can be seen from Fig 3 where, at $\delta \approx 1/3$ and $1/2$, the PBE curves display significant distortions due to quantization

It should be noted that the performance of the PPM receiver depends strongly on the background count statistics For channels with no background noise, the performance of the detector with dead time is identical to that of a quantum-limited receiver When background noise is present in the receiver, however, the performance of the receiver becomes very sensitive to the detector dead time Plotted in Fig 4 is the probability of bit error for a binary PPM channel at different values of the background intensity It is seen that, even for $K_B \approx 0\ 5$, the receiver performance is very sensitive to the detector dead time at $\delta > 0\ 1$

Finally, the increasing probability of bit error implies that higher signal power is needed to maintain the system performance in the presence of detector dead time The power penalty due to detector dead time can be defined as the ratio between the required signal power in the presence and in the absence of detector dead time This power penalty can be evaluated numerically Plotted in Fig 5 is the receiver power penalty versus dead time for a binary PPM channel at several values of the probability of bit error The background intensity is assumed to be $K_B = 1$ Note that the power penalty increases rapidly for $\delta > 0\ 1$ In particular, for PBE = 10^{-6}, the power penalty due to dead time is greater than 2 dB when $\delta > 0\ 1$ This implies that, in order to keep the power penalty due to detector dead time to within 2 dB, the system operating at PBE = 10^{-6} must have an effective detector bandwidth higher than $10/T_s$ Equivalently, the detector used in the receiver must be capable of counting photons at a rate higher than $10/T_s$ The required detector bandwidth is smaller for systems operating at lower bit error rates and weaker background intensities

The power penalty also depends strongly on the background intensity Shown in Fig 6 are the power penalty curves for a system operating at PBE = 10^{-3} and at different background levels Note that systems with higher background levels are more sensitive to the detector dead time Given the detector dead time, the power penalty is smaller for systems with weaker backgrounds In particular, for $\delta = 0\ 1$, the power penalty ranges from less than 0 1 dB for $K_B = 0\ 01$, to approximately 1 5 dB for $K_B = 2$

IV. Conclusions

The effect of detector dead time on the performance of an optical communication link was analyzed It was shown that, in the presence of a large detector dead time, the receiver photocount statistics are seriously distorted The distortion of photocount statistics can result in a degradation of the receiver performance for systems with nonzero background intensities As a result, higher signal power must be applied to maintain the performance of the optical channel This power penalty was shown to be a function of the desired BER, the detector dead time, and the background intensity When designing the optical channel using the Geiger mode APDs, therefore, sufficient power margin must be reserved to account for the losses due to detector dead time Similarly, given the power budget, the desired BER, and the expected background level, care must be taken to ensure that the detector employed has a sufficient bandwidth

References

[1] D Robinson and B Metscher, "Photon Detection With Cooled Avalanche Photodiodes," *Appl Phys Lett*, vol 51, pp 1493–1494, September 1987

[2] R Gagliardi and S Karp, "M-ary Poisson Detection and Optical Communications," *IEEE Trans Commun Tech*, vol CT-17, no 2, pp 208–216, April 1969

[3] R Gagliardi and S Karp, *Optical Communications*, New York Wiley, 1975

[4] D Snyder, *Random Point Processes*, New York Wiley, 1975

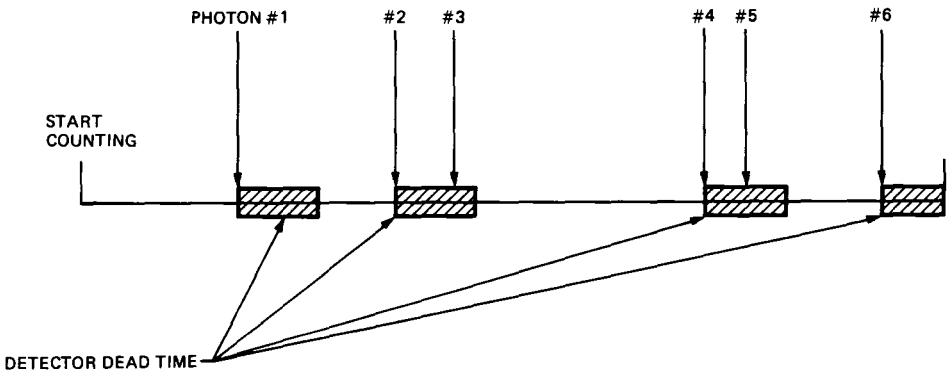

Fig 1. The count statistics for a detector with dead time can be very different from the photon arrival statistics

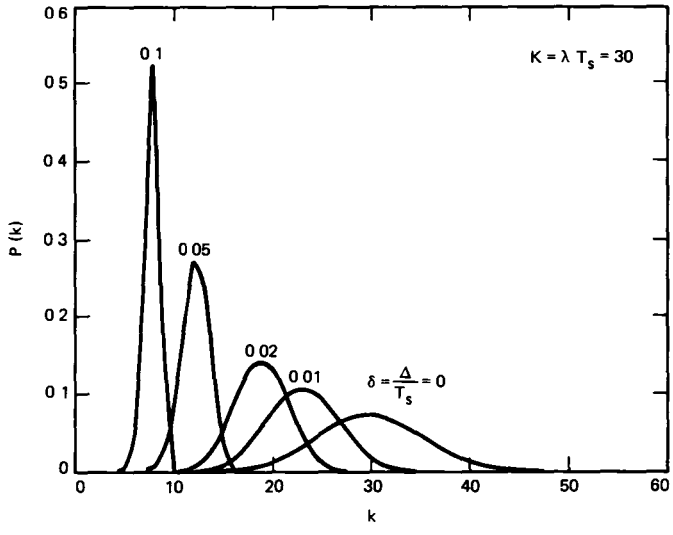

Fig 2 Probability distribution of detector photocounts at different values of detector dead time

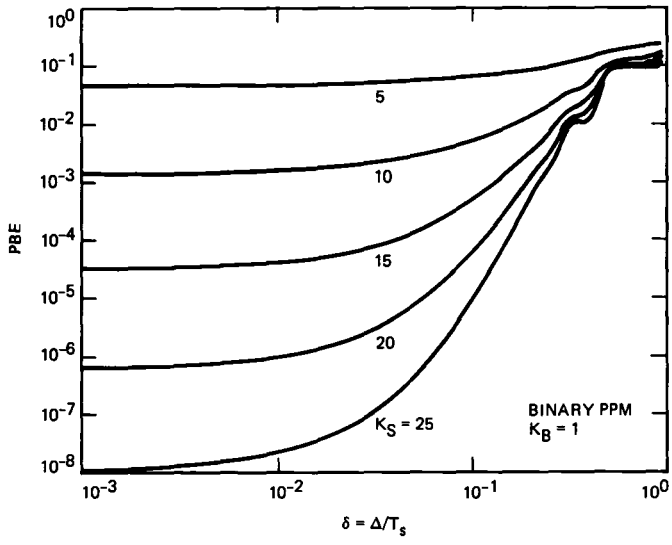

Fig. 3. Probability of bit error versus detector dead time for a binary PPM receiver with varying signal intensity

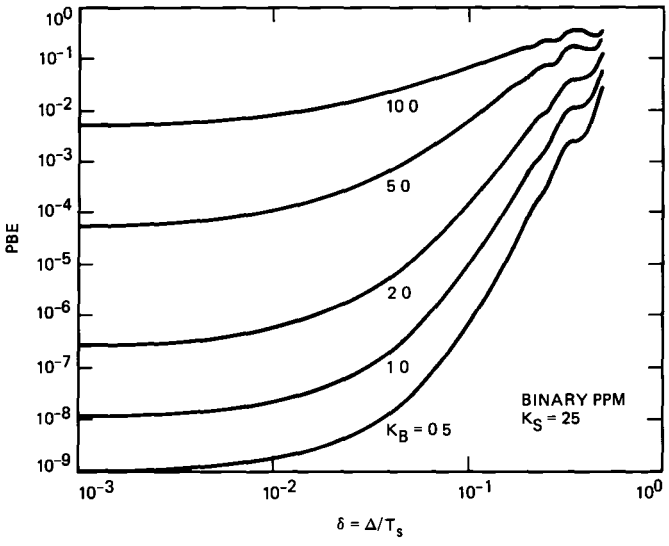

Fig. 4. Probability of bit error versus detector dead time for a binary PPM receiver with different background intensities

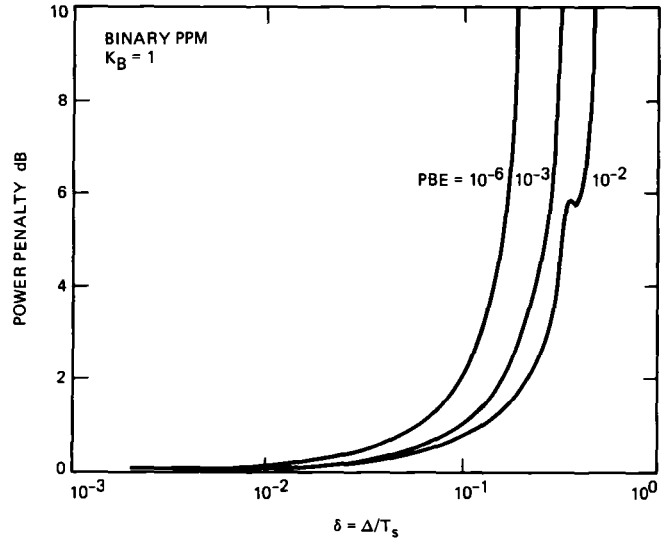

Fig 5 Power penalty due to detector dead time for a binary PPM receiver at different values of the probability of bit error

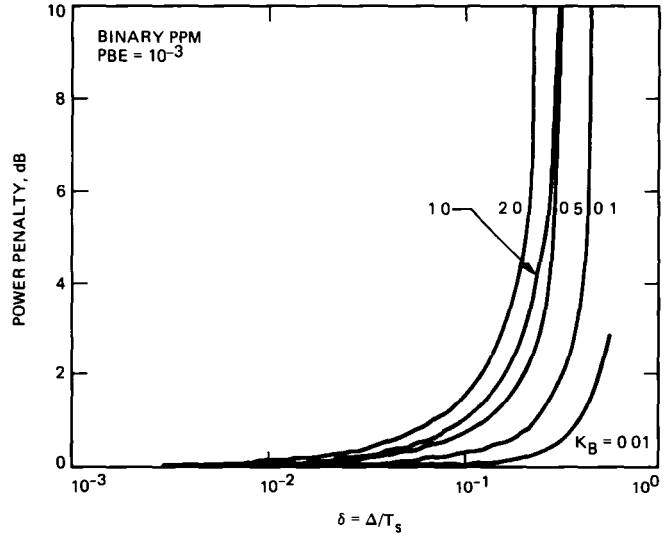

Fig 6 Power penalty due to detector dead time for a binary PPM receiver at different background intensities

Appendix

Evaluation of the Probability Distribution

The probability distribution for the count statistics can be divided into 4 different cases, depending on the time of arrival t_0 of the last detected photon before the start of the current counting period, and the time of arrival of the kth photon The probability density for each of the 4 conditions can be easily shown to be [4]

Case 1 $t_0 < -\Delta, t_k > T - \Delta$ $p(t_1, t_2, \quad , t_k)$

$$= \lambda_1^k \, e^{-\lambda_0 \Delta} \, e^{-\lambda_1 [t_k - (k-1)\Delta]} \, dt_1 \quad dt_k$$

Case 2 $t_0 < -\Delta, t_k < T - \Delta$ $p(t_0, t_1, \quad , t_k)$

$$= \lambda_1^k \, e^{-\lambda_0 \Delta} \, e^{-\lambda_1 (T - k\Delta)} dt_1 \quad dt_k$$

Case 3 $t_0 > -\Delta, t_k > T - \Delta$ $p(t_0, t_1, \quad , t_k)$

$$= \lambda_0 \lambda_1^k \, e^{\lambda_0 t_0} \, e^{-\lambda_1 (t_k - t_0 - k\Delta)} \, dt_0 \, dt_1 \quad dt_k$$

Case 4 $t_0 > -\Delta, t_k < T - \Delta$ $p(t_0, t_1, \quad , t_k)$

$$= \lambda_0 \lambda_1^k \, e^{\lambda_0 t_0} \, e^{-\lambda_1 [T - t_0 - (k+1)\Delta]} \, dt_0 \, dt_1 \quad dt_k$$

The probability of receiving k photons over the period $[0,T)$ is simply the integral of the probability density over the $k + 1$ dimensional region spanned by $(t_0, t_1, \quad , t_k)$ Depending on the number of photons k, the integral must be carried out over a different region

Case 1 $t_0 < -\Delta, t_k > T - \Delta$

Depending on the number of signal photons collected, the probability for this case is given by

$$k \leqslant k_{\max} - 1 \quad P(k) = \int_{t_1=0}^{t_2-\Delta} \int_{t_2=0}^{t_3-\Delta} \quad \int_{t_{k-1}=(k-2)\Delta}^{t_k-\Delta}$$

$$\times \int_{t_k=T-\Delta}^{T} p(t_1, \quad , t_k) \, dt_1 \, dt_2 \quad dt_k$$

$$k = k_{\max} \quad P(k) = \int_{t_1=0}^{t_2-\Delta} \int_{t_2=0}^{t_3-\Delta} \quad \int_{t_{k-1}=(k-2)\Delta}^{t_k-\Delta}$$

$$\times \int_{t_k=(k-1)\Delta}^{T} p(t_1, \quad , t_k) \, dt_1 \, dt_2 \quad dt_k$$

Case 2 $t_0 < -\Delta, t_k < T - \Delta$

$$k \leqslant k_{\max} - 1 \quad P(k) = \int_{t_1=0}^{t_2-\Delta} \int_{t_2=0}^{t_3-\Delta} \quad \int_{t_{k-1}=(k-2)\Delta}^{t_k-\Delta}$$

$$\times \int_{t_k=(k-1)\Delta}^{T-\Delta} p(t_1, \quad , t_k) \, dt_1 \, dt_2 \quad dt_k$$

$$= \frac{(T - k\Delta)^k \, \lambda_1^k}{k!} \, e^{-\lambda_1 (T - k\Delta)} \, e^{-\lambda_0 \Delta}$$

$k = k_{\max}$ Not admissible

Case 3 $t_0 > -\Delta, t_k > T - \Delta$

In this case the dead time resulting from the last photon that arrived before the start of the time slot will overlap into the current time period, and the resulting photocount probability must be averaged over the probability of arrival for the 0th photon

$$k \leqslant k_{\max} - 2 \quad P(k) = \int_{t_0=-\Delta}^{0} \int_{t_1=t_0+\Delta}^{t_2-\Delta} \quad \int_{t_{k-1}=t_0+(k-1)\Delta}^{t_k-\Delta}$$

$$\times \int_{t_k=T-\Delta}^{T} p(t_0, t_1, \quad , t_k) \, dt_0 \, dt_1 \quad dt_k$$

$$k = k_{\max} - 1 \quad P(k) = \int_{t_0=-\Delta}^{T-(k+1)\Delta} \int_{t_1=t_0+\Delta}^{t_2-\Delta} \quad \int_{t_{k-1}=t_0+(k-1)\Delta}^{t_k-\Delta}$$

$$\times \int_{t_k=T-\Delta}^{T} p(t_0, t_1, \quad , t_k)\, dt_0\, dt_1 \quad dt_k$$

$$+ \int_{t_0=T-(k+1)\Delta}^{0} \int_{t_1=t_0+\Delta}^{t_2-\Delta}$$

$$\times \int_{t_k=t_0+k\Delta}^{T} p(t_0, t_1, \quad , t_k)\, dt_0\, dt_1 \quad dt_k$$

$$k = k_{\max} \quad P(k) = \int_{t_0=-\Delta}^{T-k\Delta} \int_{t_1=t_0+\Delta}^{t_2-\Delta}$$

$$\times \int_{t_k=t_0+k\Delta}^{T} p(t_0, t_1, \quad , t_k)\, dt_0\, dt_1 \quad dt_k$$

Case 4 $t_0 > -\Delta,\ t_k < T - \Delta$

$$k \leqslant k_{\max} - 2 \quad P(k) = \int_{t_0=-\Delta}^{0} \int_{t_1=t_0+\Delta}^{t_2-\Delta} \quad \int_{t_{k-1}=t_0+(k-1)\Delta}^{t_k-\Delta}$$

$$\times \int_{t_k=t_0+k\Delta}^{T-\Delta} p(t_0, t_1, \quad , t_k)\, dt_0\, dt_1 \quad dt_k$$

$$k = k_{\max} - 1 \quad P(k) = \int_{t_0=-\Delta}^{T-(k+1)\Delta} \int_{t_1=t_0+\Delta}^{t_2-\Delta}$$

$$\times \int_{t_k=t_0+k\Delta}^{T-\Delta} p(t_0, t_1, \quad , t_k)\, dt_0\, dt_1 \quad dt_k$$

$k = k_{\max}$ Not admissible

Since the 4 cases stated above are mutually exclusive, the total probability of detecting k photons is the sum of the probabilities evaluated in all 4 cases By substituting the probability densities into the integrals, the probability for detecting k photons in the interval can be calculated

Efficient Multiplication Algorithms Over the Finite Fields $GF(q^m)$, Where $q = 3,5$

T K Truong, I S Hsu, and K M Cheung
Communications Systems Research Section

I S Reed
Department of Electrical Engineering
University of Southern California

Finite field multiplication is central to coding theory [1] For this application, there is a need for a multiplication algorithm which can be realized easily on VLSI chips In this article, a new algorithm is developed which is based on the Babylonian multiplication technique utilizing tables of squares This new algorithm is applied to the finite fields $GF(q^m)$, where $q = 3$ and 5 It is also shown that this new multiplier can be used to compute complex multiplications defined on the direct sum of two identical copies of such Galois fields

I. Introduction

Let $GF(q^m)$ be a finite field Also, let α be a primitive element in $GF(q^m)$ Then, $N = \{\alpha^0, \alpha^1, \alpha^2 \quad , \alpha^{m-1}\}$ is the standard basis set of the field $GF(q^m)$, and every fixed element $\alpha^j \in GF(q^m)$ can be uniquely expressed as $\alpha^j = b_0\alpha^0 + b_1\alpha^1 + \quad + b_{m-1}\alpha^{m-1}$, where $b_j \in GF(q)$ for $0 \leqslant j \leqslant m-1$ is an element in the ground field $GF(q)$ Thus, α^j can be represented as a coordinate vector of form $\alpha^j = [b_0, b_1 \quad , b_{m-1}]$ in the standard basis

The most straightforward method to perform a multiplication of two field elements in $GF(q^m)$ is the table lookup method To illustrate this procedure, let $\beta = [b_0, b_1 \quad , b_{m-1}]$ and $\gamma = [c_0, c_1, \quad , c_{m-1}]$ be two elements of the field $GF(q^m)$ in a standard basis representation Further, let a "log" table be used to find the exponents i and j of $\beta = \alpha^i$ and $\gamma = \alpha^j$ This is accomplished by using elements β and γ as addresses to locate the logarithms i and j of β and γ, respectively After the addition $k = i + j \bmod (q^m - 1)$ of these exponents, an "antilog" table is used to find the coordinate vector representation for α^k in a standard basis The element k serves as the address of the field element in the antilog table

It is reported [2, page 71] that the Babylonians and Egyptians were the first to use tables of squares to efficiently realize a multiplication over the field of integers In this article, it is shown that such an algorithm can be used to realize a multiplication over the finite fields, $GF(3^m)$ or $GF(5^m)$ The operations needed to realize this multiplier are only two squares and three additions of elements in $GF(q^m)$ where $q = 3$ and 5 The square of any element in the field can be obtained by the table lookup method The advantage of this new multiplier is that

it does not need the antilog procedure required in the conventional table lookup method Also in this new method, the antilog procedure in the conventional method is replaced by three additions in $GF(q^m)$

It is well known [3] that a conventional coding system depends crucially on the fast multiplier in the finite fields $GF(q^m)$ Therefore, the fast multiplication over $GF(q^m)$ for $q = 3$ and 5 can be used for deep space communications in a concatenated coding system In a coding system, the input sequence is a string of binary digits In order to use multiplication over $GF(q^m)$ where $q = 3$ and 5, one first needs to convert an input binary sequence to a trinary or quinary sequence, and inversely to reconvert the output trinary or quinary sequence back to a binary sequence Methods for realizing these radix conversions are given in [4, page 302]

It is shown next that the above new multiplier can be used to perform complex multiplications defined on both the extension field $GF(3^{2m})$ or on the direct sum of two copies of finite fields $GF(q^m)$, where $q = 3$, and 5 The complex multiplication defined on a direct sum can be performed by an efficient method as described in this article

II. Mathematical Preliminary

Before developing the Babylonian multiplication algorithm over the field $GF(q^m)$, we consider some properties of finite fields that are helpful to the following development First consider $GF(q^m)$ for $q \neq 2$ Also let $\gamma = \alpha^i \neq 0$ for $0 \leqslant i \leqslant q^m - 1$ be an element in $GF(q^m)$, where α is a primitive element in $GF(q^m)$

Definition If the polynomial $x^2 - \gamma = 0$ is solvable in $GF(q^m)$, then γ is called a quadratic residue in $GF(q^m)$, otherwise γ is known as a quadratic nonresidue in $GF(q^m)$

For $\gamma \neq 0$, let

$$\left(\frac{\gamma}{q^m}\right) = \gamma^{\frac{q^m-1}{2}} \tag{1}$$

It is seen in the next theorem that the symbol (γ/q^m) is a generalization of the Jacobi symbol to Galois fields [9] First it is not difficult to see that $(\gamma^{(q^m-1)/2}) = \pm 1$ Thus, from (1), $(\gamma/q^m) = \pm 1$, where "1" is the unit element of $GF(q^m)$ A more specific result is provided in the following theorem

Theorem 1 Let $q > 2$ If $(\gamma/q^m) = 1$, then γ is a quadratic residue in $GF(q^m)$ If $(\gamma/q^m) = -1$, then γ is a nonresidue in $GF(q^m)$

Proof See [5]

The following theorem is to be found in [5]

Theorem 2 Let $GF(q^m)$ be a finite field where $q > 2$ Then

$$\left(\frac{-1}{q^m}\right) = (-1)^{\frac{q^m-1}{2}} = \begin{cases} 1, \text{ for } q \equiv 1 \bmod 4 \\ 1, \text{ for } q \equiv 3 \bmod 4 \text{ and } m \equiv 0 \bmod 2 \\ 1, \text{ for } q \equiv 3 \bmod 4 \text{ and } m \equiv 1 \bmod 2 \end{cases} \tag{2}$$

Proof See Appendix

The following theorem is well known and a proof can be found in [5]

Theorem 3 Let $GF(q^m)$ be a finite field, where $q^m - 1 = q_1^{e_1} q_2^{e_2} \cdots q_r^{e_r}$, $(q_i, q_j) = 1$, for $i \neq j$ Then α is a primitive element in $GF(q^m)$ if and only if $\alpha^{(q^m-1)/q_i} \not\equiv 1 \bmod q$ for $1 \leqslant i \leqslant r$

III. Multiplication Over $GF(q^m)$ where $q = 3$ and 5

In this section, a fast method is developed to perform a multiplication on $GF(q^m)$ where $q = 3$ and 5 which uses tables of square roots This new technique, called the Babylonian multiplication algorithm over the field $GF(q^m)$ for two elements β and γ is obtained as follows

$$\delta = \beta\gamma = \sum_{i=0}^{m-1} d_i \alpha^{q^i} \equiv \frac{(\beta+\gamma)^2 + (\beta-\gamma)^2}{4} \bmod q \tag{3}$$

For $q = 3$, (3) becomes

$$\delta \equiv [(\beta+\gamma)^2 + (\beta-\gamma)^2] \bmod 3 \tag{4a}$$

For $q = 5$, (3) becomes

$$\delta \equiv -[(\beta+\gamma)^2 + (\beta-\gamma)^2] \bmod 5 \tag{4b}$$

It is easy to see that the operations needed to compute (4a) or (4b) require only two squares and three additions of elements in the field The square of any element needed in (4a) and (4b) is found by the table lookup method

IV. Complex Multiplication Over the Finite Field $GF(3^{2m})$, where m is odd

Consider $q = 3$ and m is odd, i e , $m = 2n + 1$ By Theorem 2, the negative unit element -1 is a quadratic nonresidue

in $GF(3^m)$, where $m = 2n + 1$ Thus, the polynomial $p(x) = x^2 + 1$ is irreducible in $GF(3^m)$ for $m \equiv 1 \bmod 2$ Hence a root, say $\imath$, of the quadratic polynomial equation,

$$p(x) = x^2 + 1 = 0 \tag{5}$$

exists and can be found in the extension field $GF(3^{2m})$ $GF(3^{2m})$ is composed of the set $GF(3^{2m}) = \{a + \imath b \mid a, b \in GF(3^m)\}$where $\imath$ is a root of (5), satisfying

$$\imath^2 \equiv -1 \bmod 3 \tag{6}$$

By the above, in order that $x^2 + 1 = 0$ not be solvable in $GF(3^m)$, it is necessary that $m = 2n + 1$ Thus, in $GF(3^{2m})$, the "imaginary" element $\imath$ in (5) plays a similar role over the finite field $GF(3^m)$ that $\sqrt{-1} = \imath$ plays over the field of rational numbers For example, suppose $a + \imath b$ and $c + \imath d$ are elements of $GF((3^m)^2)$ where $m \equiv 1 \bmod 2$ Then, by (5),

$$(a + \imath b) + (c + \imath d) = (a + c) + \imath(b + d) \tag{7}$$

and

$$(a + \imath b)(c + \imath d) = (ac - bd) + \imath(bc + ad) \tag{8}$$

These are the exact analogies of what one might expect if $a + \imath b$ and $c + \imath d$ were complex numbers The operations needed to compute (8) require only four multiplications and two additions in $GF(3^m)$

V. Complex Multiplication Defined Over the Direct Sum of Two Copies of $GF(q^m)$

Let $GF(q^m)$ be a finite field Further, let (-1) denote the negative of the real integer one and let $\imath$ be the solution of equation $x^2 = -1$ Finally, define the set $Z_{q^m}[\imath] = \{a + \imath b \mid a, b \in GF(q^m)\}$ of q^{2m} elements in such a manner that addition is given by $(a + \imath b) + (c + \imath d) = (a + c) + \imath(c + d)$ and multiplication is given by $(a + \imath b)(c + \imath d) = (ac - bd) + \imath(bc + ad)$, where $ac - bd$ and $bc + ad$ are elements in $GF(q^m)$

Theorem 4 If -1 is a quadratic residue in $GF(q^m)$, then the set $Z_{q^m}[\imath]$ is a commutative ring and is not a field

Proof It is not difficult to show that any arbitrary elements such as u, v, and w of $Z_{q^m}[\imath]$ satisfy the six postulates of a ring [6, page 1] Thus $Z_{q^m}[\imath]$ is a commutative ring

To prove that $Z_{q^m}[\imath]$ is not a finite field, it is necessary to show that its nonzero elements do not form a group under multiplication [7, page 126] To show this, assume there exists an inverse element w^{-1} of an arbitrary element $w = \alpha + \imath\beta \in Z_{q^m}[\imath]$ such that $ww^{-1} = 1$ Then,

$$w^{-1} = \frac{1}{\alpha + \imath\beta} = \frac{\alpha - \imath\beta}{\alpha^2\left(1 + \left(\frac{\beta}{\alpha}\right)^2\right)} \tag{9}$$

Since -1 is a quadratic residue in $GF(q^m)$, there exist two solutions $\pm s$ of $x^2 + 1 = 0$ in $GF(q^m)$ Let $w = \alpha + \imath\beta$ have the property that $s = \beta/\alpha$ Then the denominator of Eq (9) is equal to zero This implies that no inverse w^{-1} of w exists in $Z_{q^m}[\imath]$ Thus, $Z_{q^m}[\imath]$ is not a field

Now suppose that $\pm x$ are the solutions of $x^2 + 1 = 0$ in $GF(q^m)$ If $a + \imath b \in Z_{q^m}[\imath]$, then let ϕ be the mapping

$$\phi\ a + \imath b \rightarrow ((a + sb), (a - sb)) = (\gamma, \bar{\gamma}) \tag{10}$$

where $\gamma = (a + sb)$, $\bar{\gamma} = (a - sb)$ and $\gamma, \bar{\gamma} \in GF(q^m)$ With the same procedure that was used in the proof of Theorem 1 in [8], it can be shown that the mapping in (10) is an isomorphic mapping Also, it can be demonstrated that the set $S_{q^m} = \{(\alpha, \bar{\alpha}) \in GF(q^m)\}$is the direct sum of two copies of $GF(q^m)$, and that S_{q^m} is isomorphic to the ring $Z_{q^m}[\imath]$

The inverse mapping ϕ^{-1} which maps $(\alpha, \bar{\alpha}) \in S_{q^m}$ into $Z_{q^m}[\imath]$ is defined by

$$\phi^{-1}\ (\gamma, \bar{\gamma}) \rightarrow a + \imath b \tag{11}$$

To find a and b in (11), note that (10) implies

$$a + sb \equiv \gamma \bmod q \tag{12a}$$

$$a - sb \equiv \bar{\gamma} \bmod q \tag{12b}$$

Summing (12a) and (12b) yields

$$2a \equiv (\gamma + \bar{\gamma}) \bmod q \tag{12c}$$

Subtracting (12b) from (12a) yields

$$2sb \equiv (\gamma - \bar{\gamma}) \bmod q \tag{12d}$$

Since the quantities 2 and $2s$ are two nonzero elements in $GF(q^m)$, the inverse elements of these two elements exist in $GF(q^m)$ Thus,

$$a \equiv 2^{-1}\ (\gamma + \bar{\gamma}) \bmod q \tag{13a}$$

and

$$b \equiv (2s)^{-1}\ (\gamma - \bar{\gamma}) \bmod q \tag{13b}$$

Consider in the next section complex multiplications over the special finite rings $Z_{qm}[\imath]$, where $q = 3$ and 5

A. Complex Multiplication Over the Ring $Z_{3m}[\imath]$ Where m is Even

Consider the finite field $GF(3^m)$ where m is even, i e , $m = 2n$ By Theorem 2, one obtains $(-1/3^m) = 1$ Thus, -1 is a quadratic residue in $GF(3^m)$ Hence elements $\pm s$ exist in $GF(3^m)$ which are solutions of $p(x) = x^2 + 1 = 0$ To find these roots, note from (1) that

$$\left(\frac{-1}{3}\right) = (-1)^{\frac{(3-1)}{2}} = -1$$

Thus, -1 is a quadratic nonresidue modulo 3, and $x^2 + 1 = 0$ is not solvable in the ground field $GF(3)$ A root, say s, of the quadratic polynomial equation, $p(x) = x^2 + 1 = 0$ exists and can be found in the extension field $GF(3^m)$ To show this, let α be a primitive element in $GF(3^m)$, where $m \equiv 0 \bmod 2$ Then

$$\alpha^{3^m-1} \equiv 1 \bmod 3 \tag{14}$$

Since $4 \mid 3^m - 1$ for $m \equiv 0 \bmod 2$, Eq (14) becomes

$$\alpha^{\frac{3^m-1}{2}} = \left(\pm\alpha^{\frac{3^m-1}{4}}\right)^2 \equiv -1 \bmod 3 \tag{15}$$

or $s^2 + 1 = 0 \bmod 3$ where $s = \pm\alpha^{(3^m-1)/4} \epsilon GF(3^m)$ Evidently, $(s, -s)$ are the roots of the polynomial $p(x) = x^2 + 1 = 0$ over the Galois field $GF(3^m)$ where $m \equiv 0 \bmod 2$

Let $s = \pm\alpha^{(3^m-1)/4}$ Also let the set $Z_{3m}[\imath] = \{a + \imath b \mid a, b \epsilon GF(3^m)\}$ be a ring of 3^{2m} elements where $\imath^2 = -1$ Assume the mapping and its inverse mapping are defined by

$$\phi\ (a + \imath b) \rightarrow ((\alpha + sb), (\alpha - sb)) \tag{16a}$$

and

$$\phi^{-1}\ (\gamma, \bar{\gamma}) \rightarrow (\alpha + \imath b) \tag{16b}$$

where a and b are computed by

$$\alpha \equiv 2^{-1}(\gamma + \bar{\gamma}) \equiv 2(\gamma + \bar{\gamma}) \bmod 3 \tag{17a}$$

$$b \equiv (2s)^{-1}(\gamma - \bar{\gamma}) \bmod 3 \tag{17b}$$

Then, by Theorem 1 in [8] the ring $Z_{3m}[\imath]$ is isomorphic to the direct sum of two copies of $GF(3^m)$ which is defined by

$$S_{3m} = \{(\gamma, \bar{\gamma}) \mid \gamma, \bar{\gamma} \epsilon GF(3^m)\} \tag{18}$$

where $(\gamma, \bar{\gamma}) + (\beta, \bar{\beta}) = (\gamma + \beta, \bar{\gamma} + \bar{\beta})$ and $(\gamma, \bar{\gamma})(\beta, \bar{\beta}) = (\gamma\beta, \bar{\gamma}\bar{\beta})$

From (16) and (17), the arithmetic needed to compute the mapping ϕ and its inverse ϕ^{-1} require three multiplications, one multiplication by 2 and four additions in $GF(3^m)$ The operations needed to perform a complex multiplication in S_{3m} in (18) require only two multiplications in $GF(3^m)$

Example 1. Let $GF(3^2)$ be a finite field and α be a primitive element in $GF(3^2)$ Also let $A = \alpha^3 + \imath\alpha$ and $B = \alpha^4 + \imath\alpha^5$, where $\alpha^3, \alpha, \alpha^4, \alpha^8 \epsilon GF(3^2)$ Calculate the product of A and B by using a complex multiplication over the direct sum of two copies of $GF(3^2)$

Since $b(x) = x^2 + x + 2$ is a primitive irreducible polynomial over $GF(3)$, then the nonzero elements of $GF(3^2)$ are as follows α, $\alpha^2 = -\alpha - 2$, $\alpha^3 = -\alpha + 2$, $\alpha^4 = 2$, $\alpha^5 = 2\alpha$, $\alpha^6 = -2\alpha - 1$, $\alpha^7 = \alpha + 1$, and $\alpha^8 = 1$ From (15), $s = \pm\alpha^{(3^2-1)/4} = \pm\alpha^2$ are the solutions of $p(x) = x^2 + 1 = 0$, where $\pm\alpha^2 \epsilon GF(3^2)$ From (16a) and (16b), one obtains

$$A = \alpha^3 + \imath\alpha \rightarrow (\alpha^3 + \alpha^2\alpha, \alpha^3 - \alpha^2\alpha) = (\alpha^7, 0)$$

and

$$B = \alpha^4 + \imath\alpha^5 \rightarrow (\alpha^4 + \alpha^2\alpha^5, \alpha^4 - \alpha^2\alpha^5) = (\alpha, \alpha^2)$$

The multiplication over $Z_{3m}[\imath]$ is $(\alpha^7, 0)(\alpha, \alpha^2) = (1,0)$ From (17a) and (17b), one obtains $a \equiv 2(1 + 0) \bmod 3 = \alpha^4$ and $b \equiv (2\alpha^2)^{-1}(1 - 0) \bmod 3 = \alpha^2$ Hence $AB = a + \imath b = \alpha^4 + \imath\alpha^2$ This result can be verified readily by a direct computation

B. Complex Multiplication Over the Ring $Z_{5m}[\imath]$

Consider the finite field $GF(5^m)$ By Theorem 2, one obtains $(-1/5^m) = 1$ Thus, -1 is a quadratic residue in $GF(5^m)$ Hence elements $\pm s$ exist as the roots of $p(x) = x^2 + 1 = 0$ in $GF(5^m)$ To find the roots, it is not difficult to show that -1 is a quadratic residue modulo 5 and $x^2 + 1 = 0$ is solvable in the ground field $GF(5)$ Since $(\pm 2)^2 + 1 \equiv 0 \bmod 5$, then elements $s = \pm 2$ exist as the roots of $p(x) = x^2 + 1 = 0$ in $GF(5)$

Let the set $Z_{5m}[\imath] = \{a + \imath b \mid a, b \epsilon GF(5^m)\}$ be a ring of 5^{2m} elements, where $\imath^2 = -1$ Also let $s = \pm 2$ Assume the mapping and its inverse mapping are defined by

$$\Phi\ (\alpha + \imath b) \rightarrow ((a + 2b), (a - 2b)) = (\beta, \bar{\beta}) \tag{19a}$$

$$\Phi^{-1}\ (\beta, \bar{\beta}) \rightarrow (a + \imath b) \tag{19b}$$

where a and b are computed by

$$a \equiv 2^{-1}(\gamma - \bar{\gamma}) \equiv -2(\gamma + \bar{\gamma}) \bmod 5 \tag{20a}$$

and

$$b \equiv 2^2(\gamma - \bar{\gamma}) \bmod 5 \tag{20b}$$

Then the ring $Z_{5^m}[\imath]$ is isomorphic to the direct sum of two copies of $GF(5^m)$ which is defined by

$$S_{5^m} = \{(\gamma, \bar{\gamma}) | \gamma, \bar{\gamma} \in GF(5^m)\} \tag{21}$$

where $(\gamma, \bar{\gamma}) + (\beta, \bar{\beta}) = (\gamma + \beta, \bar{\gamma} + \bar{\beta})$ and $(\gamma, \bar{\gamma})(\beta, \bar{\beta}) = (\gamma\beta, \bar{\gamma}\bar{\beta})$

By (19) and (20), the arithmetic needed to compute the mapping Φ and its inverse Φ^{-1} requires three multiplications by powers of two and four additions in $GF(5^m)$ By (21), the arithmetic needed to compute a complex multiplication over S_{5^m} requires only two multiplications in $GF(5^m)$

Example 2 Let $GF(5^2)$ be a finite field and α be a primitive element in $GF(5^2)$ Also let $A = (\alpha^{12} + \imath\alpha)$ and $B = (\alpha^{10} + \imath\alpha^2)$, where α^{12}, α, α^{10}, and $\alpha^2 \in GF(5^2)$ Calculate the product of A and B by using a complex multiplication over the direct sum of two copies of $GF(5^2)$

Since $b(x) = x^2 + 2x + 3$ is a primitive irreducible polynomial over $GF(5)$, then the nonzero elements of $GF(5^2)$ are as follows α, $\alpha^2 = -2\alpha + 2$, $\alpha^3 = \alpha + 1$, $\alpha^4 = -\alpha + 2$, $\alpha^5 = -\alpha - 2$, $\alpha^6 = -2$, $\alpha^7 = -2\alpha$, $\alpha^8 = -\alpha + 1$, $\alpha^9 = 3\alpha - 2$, $\alpha^{10} = 2\alpha + 1$, $\alpha^{11} = 2\alpha - 1$, $\alpha^{12} = -1$, $\alpha^{13} = -\alpha$, $\alpha^{14} = 2\alpha - 2$, $\alpha^{15} = -\alpha - 1$, $\alpha^{16} = \alpha - 2$, $\alpha^{17} = \alpha + 2$, $\alpha^{18} = 2$, $\alpha^{19} = 2\alpha$, $\alpha^{20} = \alpha - 1$, $\alpha^{21} = -3\alpha + 2$, $\alpha^{22} = -2\alpha - 1$, $\alpha^{23} = -2\alpha + 1$, and $\alpha^{24} = 1$

In $GF(5^2)$, $s = \pm 2$ are the solutions of $x^2 + 1 = 0$ From (19a), one obtains

$$A = (\alpha^{12} + \imath\alpha) \rightarrow (\alpha^{12} + 2\alpha, \alpha^{12} - 2\alpha) = (\alpha^{11}, \alpha^{22})$$

and

$$B = (\alpha^{10} + \imath\alpha^2) \rightarrow (\alpha^{10} + 2\alpha^2, \alpha^{10} - 2\alpha^2) = (\alpha^7, \alpha^{17})$$

The multiplication over $Z_{5^2}[\imath]$ is

$$(\alpha^{11}, \alpha^{22})(\alpha^7, \alpha^{17}) = (\alpha^{18}, \alpha^{15})$$

From (20a) and (20b), one obtains

$$a \equiv -2(\alpha^{18} + \alpha^{15}) \bmod 5 = \alpha^{14}$$

and

$$b \equiv 2^2(\alpha^{18} - \alpha^{15}) \bmod 5 = \alpha^4$$

Hence $AB = a + \imath b = \alpha^{14} + \imath\alpha^4$ This result can be verified readily by a direct computation

VI. Implementation of Complex Multiplications

Let $GF(q^m)$ be a finite field $GF(q^m)$ can be generated by any irreducible polynomial of degree m over $GF(q)$ [3] However, for mathematical convenience it is more desirable to generate $GF(q^m)$ using a primitive irreducible polynomial

An algorithm to find a primitive irreducible polynomial of degree m over $GF(q)$ is given as follows

(1) Construct an irreducible polynomial $g(x)$ of degree m over $GF(q)$ via the method proposed in [3] The existence of such a polynomial is guaranteed, and there are

$$\frac{1}{m} \sum_{\imath=d, d|m} \mu(d) q^{\frac{m}{d}}$$

such polynomials, where $\mu(d)$ is the Moebius function

(2) Generate the field $GF(q^m)$ using $g(x)$

(3) Find a primitive element β in $GF(q^m)$ using Theorem 3

(4) Construct a primitive irreducible polynomial $b(x)$ via the following formula

$$b(x) = (x - \beta)(x - \beta^q) \quad (x - \beta^{q^{m-1}})$$

The primitive irreducible polynomial $b(x)$ so obtained can be used to generate the field $GF(q^m)$

Let the set $Z_{q^m}[\imath] = \{a + \imath b | a, b \in GF(q^m)\}$ be a set of q^{2m} elements where $\imath^2 = -1$ It is shown in the above sections that if $(-1/q^m) = -1$, $Z_{q^m}[\imath]$ is a field Also if $(-1/q^m) = +1$, $Z_{q^m}[\imath]$ is a ring Let $\gamma = a + \imath b$ and $\beta = c + \imath d$ be two elements in $Z_{q^m}[\imath]$ Let $\delta = x + \imath y$ denote the product of γ and β A complex multiplication of γ and β is defined to be $\delta = \gamma\beta = (a + \imath b)(c + \imath d) = x + \imath y$ where $x = ac - bd$ and $y = ad + bc$

It was shown in the above sections that complex multiplications over the ring $Z_{q^m}[\imath]$ can be more efficiently done in the transform domain $S_{q^m} = \{(\gamma, \bar{\gamma}) | \gamma, \bar{\gamma} \in GF(q^m)\}$ The flowchart of an algorithm for the multiplication over the ring

$Z_{qm}[\iota]$ is given in Fig 1 This algorithm has been verified by a software simulation

VII. Conclusion

In this article, the Babylonian multiplication algorithm using tables of squares is applied to special finite fields and complex rings The above new multiplication algorithm has been verified both by examples and simulation programs The computationally architectural designs for the Babylonian multiplication over the finite field or ring are both simple and regular and suitable for a VLSI realization Finally, this new multiplication algorithm can be applied to the development of coding systems based on the fields $GF(3^{2m})$ and $GF(5^{2m})$

References

[1] R Lidl and H Neiderreiter, *Finite Fields*, Reading, MA Addison-Wesley, 1983

[2] D Smeltzer, *Man and Numbers* New York Collier Books, 1962

[3] E R Berlekamp, *Algebraic Coding Theory*, New York McGraw-Hill Book Company, 1968

[4] D E Knuth, *The Art of Computer Programming*, vol 2, Reading, MA Addison-Wesley, 1976

[5] J P Wang, *Golomb's Conjecture in Finite Fields*, Master thesis Department of Mathematics, Beijing University, China, 1984

[6] N H McCoy, *Rings and Ideals*, Wisconsin George Banta Company, Inc , 1984

[7] I N Herstein, *Topics in Algebra*, Massachusetts Xerox College Publishing, 1975

[8] T K Truong, J J Chang, I S Hsu, D Y Pei, and I S Reed, "Techniques for Computing the Discrete Fourier Transform Using the Quadratic Residue Fermat Number Systems," *IEEE Trans on Computers*, vol C-35, no 11, pp 1008-1012, November 1986

[9] L K Hua, *Introduction to Number Theory*, Berlin, Heidelberg, and New York Springer-Verlag, 1982

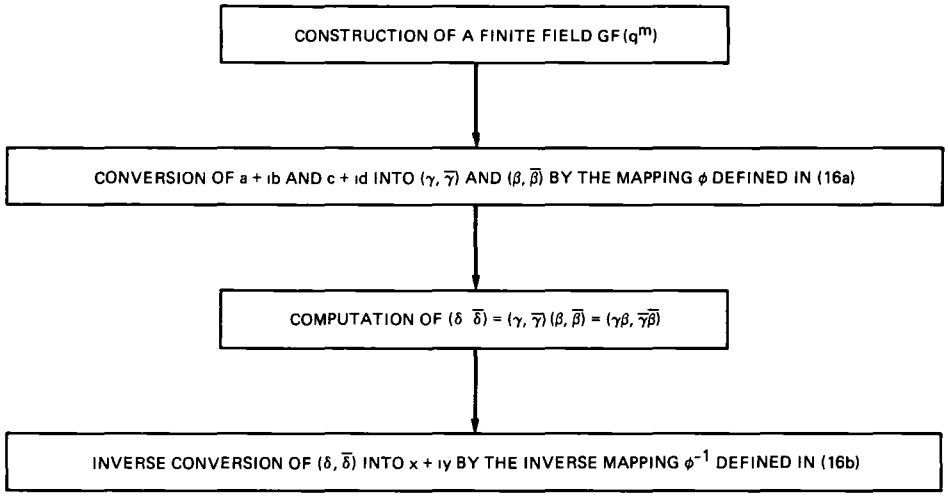

Fig. 1 A flowchart of implementing a complex multiplication over the ring $Z_{q^m}[i]$

Appendix
Proof of Theorem 2

First, one has

$$\frac{q^m - 1}{2} = \frac{(q-1)}{2}(q^{m-1} + q^{m-2} + \quad + q + 1)$$

$$\equiv \begin{cases} 0 \bmod 2 \text{ for } q \equiv 1 \bmod 4 \\ q^{m-1} + q^{m-2} + \quad + q + 1 \bmod 2 \\ \text{for } q \equiv 3 \bmod 4 \end{cases} \tag{A-1}$$

Thus, if $q \equiv 1 \bmod 4$, then (2) becomes

$$\left(\frac{-1}{q^m}\right) \equiv (-1)^{0 \bmod 2} = 1$$

If $q \equiv 3 \bmod 4$, then $q + 1 \equiv 0 \bmod 4$ Then (2) becomes

$$\frac{q^m - 1}{2} = q^{m-2}(q+1) + \quad + (q+1) \bmod 2,$$

for $m \equiv 0 \bmod 2$

and

$$\frac{q^m - 1}{2} = q^{m-2}(q+1) + \quad + q(q+1) + 1 \bmod 2,$$

for $m \equiv 1 \bmod 2$

From (3), one has

$$\left(\frac{-1}{q^m}\right) = (-1)^{\frac{q^m - 1}{2}} = \begin{cases} 1 \text{ for } q \equiv 3 \bmod 4 \text{ and } m \equiv 0 \bmod 2 \\ -1 \text{ for } q \equiv 3 \bmod 4 \text{ and } m \equiv 1 \bmod 2 \end{cases}$$

DSS 13 Microprocessor Antenna Controller

R M Gosline
Radio Frequency and Microwave Subsystems Section

This article describes a microprocessor-based antenna monitor and control system with multiple CPUs The system was developed as part of the unattended station project for DSS 13 and was enhanced for use by the SETI project The operational features, hardware, and software designs are described, and a discussion is provided of the major problems encountered

I. Introduction

The original work on the DSS 13 antenna controller was performed as part of the unattended station development [1] The objectives were twofold (1) to replace the existing antenna controller subsystem (consisting of a Modcomp II minicomputer and a custom-designed remote data collection unit) with standard microprocessor controllers similar to those of the other subsystems at DSS 13 through the use of modules recommended by the Computation and Control Module (CCM) committee, and (2) to generate new software using a high-level programming language and a top-down structured design Use of only commercially available modules simplified the requirements for documentation and sparing

Additional improvements were made to the system to support the SETI (Search for Extraterrestrial Intelligence) project The improvements consisted of two additional pointing modes for random curve fitting, control of a noise diode for the Noise-Adding Radiometer (NAR), and the capability to lock either servo axis in high speed

II. System Description

The DSS 13 26-meter antenna is an azimuth–elevation type with a hydraulic servo system Each axis has a high and low speed capability The maximum tracking rate in low speed is 0 2 degree/second in azimuth and 0 05 degree/second in elevation In high speed, the maximum rate is 2 degrees/second for each channel The encoder resolution is 20 binary bits, corresponding to 0 34 millidegree The antenna was constructed in 1958 at DSS 12 and was moved to its present location at DSS 13 in 1961 Thus it is old and rather fragile, requiring precise control of acceleration and deceleration The maximum values are shown in Table 1

Operation of the antenna in an unattended mode requires careful monitoring of many sensors to prevent damage to the system in the event of a failure Depending on the situation, an out-of-limit condition will cause one or more of the following actions

(1) An operator warning message

(2) Reduction of drive voltage

(3) STOP (controlled deceleration and brake activation) and shutdown of pumps and electronics

(4) Move to the stow position (zenith) and shutdown

A list of all analog sensors is shown in Table 2 All digital sensors are tabulated in Table 3 For data reporting purposes,

some angle values are treated as sensor data and are tabulated in Table 4

Unattended or remote control requires the use of high-level commands that are designated station-level commands The commands may be issued from the NOCC, the station controller, or the local console

A. Station-Level Commands

INIT	Turns on electronics and hydraulic pumps
CNF	Indicates the start of configuration or predict data The various types of configuration commands are shown in the next section
OFF	Performs a STOP, then shuts off hydraulics and electronics
OPR	Operates, moves antenna to follow predict data
STOW	Moves to the stow position and performs a STOP
STOP	Decelerates and applies brakes
STR	Requests status report (general health or selected data) The various types of status requests are shown in Subsection C
CLEAR	Resets lockout after a fault
HELP	Displays one of the help menus
CLOK	Synchronizes the APS clock to the station clock
CLDO	Clears direct offsets
CLPO	Clears position offsets
CLRO	Clears rate offsets
NDON	Turns noise diode on
NDOF	Turns noise diode off

B. CNF or Configuration Data Commands (All Preceded by CNF)

YEAR ⟨year⟩	The current year must be entered once after loading the program because the value is not available from the station clock
MODE ⟨IDLE, AZEL, SID, 3DAY, 3RAD, 3AZL⟩	Selects the desired tracking mode There are five tracking modes and an idle mode
IDLE	This mode bypasses any position update calculation holding the antenna at the current point The mode is used mainly for testing and maintenance
AZEL	The AZEL mode allows pointing to a given azimuth–elevation angle pair The purpose of this mode is to point to objects that are fixed relative to the local tangent plane (the collimation tower or synchronous satellites)
SID	A sidereal rate mode is used for tracking objects at sidereal rate from right ascension–declination coordinates This mode is used for objects such as radio stars
3DAY	This mode is used for tracking objects such as deep-space spacecraft or planets that are close to sidereal rate A second-order curve fit (parabolic) is generated from three sets of values of right ascension and declination for 0 hours GMT on 3 successive days
3RAD	This mode is similar to 3DAY but is more general in that a day–time parameter is specified for each point The time interval may range from 2 seconds to years Provision has been made to accept a fourth point which will cause points 2, 3 and 4 to shift to points 1, 2, and 3 at the original time of point 2 Thus, a continuous curve in right ascension–declination coordinates can be followed The fourth point, if used, must be sent in the time interval between the time of points 1 and 2 and must have a time greater than the time of point 3 Normally, the antenna tracks between points 1 and 2 but may continue beyond point 2 if a fourth point is not used
3AZL	This mode is identical to 3RAD except that the azimuth–elevation coordinate system is used
NAME ⟨reference name⟩	Allows the user to label a configuration set with a reference name
Xn ⟨az or ra angle⟩ [n = 1, 2, 3, 4]	Specifies an angle predict for azimuth or right ascension The value is interpreted according to the MODE Right ascension values may be formatted as decimal degrees or as hours, minutes, and seconds
Yn ⟨el or dec angle⟩	Specifies an angle predict for elevation or declination The value is interpreted according to the MODE Declination

	values may be formatted as decimal degrees or as degrees, minutes, and seconds
Tn ⟨day-time for Xn, Yn⟩	Time reference for 3RAD or 3AZL modes
WRAP ⟨L, R, C⟩	The mechanical range of movement in azimuth is extended 90 degrees beyond the normal 360 degrees of azimuth designated as center The counterclockwise extension is designated the left cable wrap and the clockwise extension is designated the right cable wrap A new track, defined by issuing an OPR command, normally starts in the center wrap regardless of the antenna's current position Tracking is allowed to continue into either the left or the right wrap This command allows an AZEL mode track to be started in left, right, or center cable wrap-up for maintenance and testing purposes
REFC ⟨ON, OFF⟩	Allows manual control of the refraction correction The default is on for right ascension-declination predicts and off for azimuth-elevation predicts
DFAZ ⟨az value⟩	Directs azimuth offset
DFEL ⟨el value⟩	Directs elevation offset
AEAZ ⟨az value⟩	Azimuth offset corrected for distortion The value entered is divided by the cosine of elevation and is not cleared by CLDO
AEEL ⟨el value⟩	Directs elevation offset This parameter results in the same offset as DFEL but is not cleared by CLDO
DFRA ⟨ra value⟩	Directs right ascension offset
DFDC ⟨dec value⟩	Directs declination offset
AZRT ⟨az rate⟩	Azimuth rate offset in degrees/second
ELRT ⟨el rate⟩	Elevation rate offset in degrees/second
TOFF ⟨day-time value⟩	Allows a time offset from the station clock for testing purposes
HSAZ ⟨T, F⟩	If true, this parameter causes the azimuth servo channel to remain in high speed If false, the normal speed selection logic is in effect
HSEL ⟨T, F⟩	If true, this parameter causes the elevation servo channel to remain in high speed If false, the normal speed selection logic is in effect

C. Status Request Commands (All Preceded by STR)

These commands will display the requested data on the operator display, printer, and station controller

(no parameter)	Reports general subsystem health and whether in local or remote control (selected by local function key)
CNF	Displays the entire current set of CNF parameters
ANA [⟨channel IDs⟩]	Displays the selected analog channel If no channel is specified, all analog channels are displayed The analog channels and channel IDs are shown in Table 2
DIG [⟨channel IDs⟩]	Displays the selected digital channel If no channel is specified, all digital channels are displayed The digital channels and channel IDs are shown in Table 3
ANG [⟨channel IDs⟩]	Displays the selected angle data value If no value is specified, all angle values are displayed The angle data channels and channel IDs are shown in Table 4
F	Displays all analog, digital, and angle values
TANG	Displays time-tagged (at the time of sampling) azimuth and elevation position readouts Normally, all data values are time-tagged when displayed This may be a second or two after the sample is actually read due to higher priority tasks

D. Maintenance Mode Commands

A set of low-level commands is available to assist station personnel in performing periodic maintenance or troubleshooting functions These commands bypass most automatic sequences and allow actuation of primitive control functions such as high-low pump selection brake actuation, pre-limit overrides, and application of direct drive voltages for the servo valves These commands are available only in the local control mode

III. Hardware

The system consists of two controllers as shown in Fig 1 The Data Collection Controller, located in the antenna pedes-

tal, collects analog and digital data from various sensors and reports this data to the main controller, located in the control room The main controller collects additional data from monitor points located in the control room The existing sensors and the data collection configuration were not altered to allow switching control between the Modcomp and the new controller during the debugging phase This allowed the station to perform its normal tracking schedule with minimal interference The Modcomp was removed upon the completion of integration of the new controller

The main controller's task is to provide operator interface, communication, display, local sensor interface, and the necessary logic and calculations for controlling the antenna to perform tracking and maintenance functions Communication with the station controller is through a star switch utilizing a JPL standard 15-line interface

The Data Collection Controller configuration is shown in Fig 2 It consists of a single board computer (8080 CPU) with 8 kbytes of on-board PROM and 4 kbytes of RAM The CPU drives a short-haul modem through a serial port and is interfaced to 24 digital channels through on-board parallel ports An external digital interface chassis uses commercial optical isolation modules to convert 24-Vdc antenna levels to TTL A 32-channel differential input multiplexer and an analog-to-digital converter provide interface to the analog channels All input lines are protected from lightning discharges by filters and varistor-type surge protectors A 64-kbyte RAM module, a floppy disk controller, a communication expansion module, and dual floppy disk drives allow development and testing of the software in the controller Both controllers utilize the Intel Multibus I After checkout, the program was burned into PROM and the development modules removed, leaving only the CPU and analog-to-digital converter cards in the Data Collection Controller

The main controller, configured as shown in Fig 3, utilizes two CPUs on the same Multibus CPU 1 provides interface to the angle encoders through its parallel ports and performs most of the tracking-related calculations CPU 2 provides interface to the star switch through its parallel ports and the serial data from the Data Collection Controller and modem through its serial port CPU 2 also performs the conversion of data to floating point and ASCII, performs the major part of the tasking logic, and initiates appropriate action in the event of a fault detection A video-keyboard display card (actually a third 8080 CPU) handles the screen display on a high-resolution monitor and operator interface The design allows near-real-time data to be displayed in the non-scrolling upper portion of the screen while scrolling information, alert messages, operator inputs, and specific data requests (via STR) are displayed in the lower portion Upper screen data that is not within expected limits or states is displayed in reverse video and flagged for possible monitor action The following screen displays and formats may be selected by single-stroke function keys

(1) Normal tracking operation

(2) Maintenance display

(3) Analog sensors (displayed in engineering units)

(4) Digital sensors

(5) Help menus (multilevel)

Another function key is used for the selection of local or remote control Sensor interface to the main controller is similar to that of the Data Collection Controller for monitor points originating or reported near the control room The addition of an input–output expansion module is necessary because the parallel ports of both CPUs are used by the star switch and angle readout interfaces Numerical computations are facilitated by three floating point processors dedicated to tracking computations, digital servo loop computations, and various data conversion tasks such as binary to floating point or ASCII A communications expansion module provides interface to a printer for data logging or program lists and an additional terminal to allow each CPU separate control for debugging purposes A digital-to-analog converter module provides the output drive voltages to operate the servo hydraulic system Two extra digital-to-analog channels are available for recording of test data such as offset overshoot As with the Data Collection Controller, all software was developed in the controller using a floppy disk controller and two disk drives

IV. Software

The software is written in Intel's PLM-80 language The program contains 10,209 lines of PLM-80 source code and 808 lines of assembly language for high-speed peripheral drivers for special input–output (floating point cards, 15-line software handshaking, and the binary angle position) The compiled program requires 51,523 bytes of program storage and 5948 bytes of data RAM For comparison, the Modcomp minicomputer program contained 2300 lines of FORTRAN and 4600 lines of assembly language, requiring 30k words of memory (a Modcomp word is 2 bytes)

Loading of the program is accomplished by reading a fully linked execution module from disk and operating the program from RAM Loading time is approximately 1 minute and is required only after a power failure

The top-level flowchart for the Data Collection Controller is shown in Fig 4 All of the flowcharts shown have been

condensed for illustration purposes, and some modules may represent a combination of several After an initialization module, the program enters an endless loop containing the routines REMDAT, which inputs data from the transducers, and REMSEND, which formats, adds a checksum, and sends the data over a serial link to the main controller A timer on the CPU board provides a 50-ms interrupt which is divided modulo 4, causing the main loop to be executed every 200 ms The serial line operates at 9600 baud The data is formatted in two 73 ASCII character blocks including a checksum, and sent continuously Unused channels are included in the fixed format to allow for expansion The data block can be displayed directly on a terminal if desired for verification

The main controller top-level software is shown in Fig 5 Both CPUs begin execution of the same code from the same memory location Each CPU has the ability to interrogate itself to find out which CPU it is and to jump to separate initialization routines From there, each enters a separate endless background loop except for the servicing of interrupts

The level 2 flowchart for CPU 1 is shown in Fig 6 The background modules perform the following functions

CHKSUM	Verifies that the program code has not changed
CHKSTAK	Generates a warning message if the stack is getting too large
HISTBUF	Snapshots data RAM for analysis in case of a failure

There are three interrupts used with CPU 1 Interrupts 3 and 4 are driven from the station clock at rates of 50 Hz and 1 Hz, respectively, and control all the time-dependent motion of the antenna for tracking Interrupt 2 is used to read a character of serial time from the station clock The station clock is read initially to establish time Thereafter, the antenna clock is incremented in the 1-Hz interrupt routine The 50-Hz routine counts each interrupt to ensure exact synchronization with the 1-Hz interrupt If the count is not correct or if the antenna time does not match station time, an error message is generated The count is also used modulo 5 to call the following modules every 100 ms

READOUTS	Inputs current position from the angle encoders
UPDATE	Updates the angle commands to the current time
SERVO	Updates the digital servo loop The loop equation was adapted from the MODCOMP program and is of the form Rn = K1 * Ro + K2 * Pe, where K1 and K2 are constants, Ro is previous rate command, and Pe is the position error The program uses eight sets of constants for all three combinations of azimuth–elevation, high–low speed, and type I or II servo If starting from rest, the servo is type I and switches to type II after 2 seconds The values of K1 and K2 were taken from the MODCOMP program and adjusted by observing the system response to step functions The final values are shown in Table 5
D2AOUT	Updates the current output drive voltage

After the interrupt 4 routine steps the clock, the following modules are called

ANAACTCNT	Decrements counters that control action on analog channels that exceed error limits until specified delays have expired
TIMERS	Decrements various state timers
CMPRATES	Computes the measured angle rates by differencing the position readouts

Depending on the tracking mode, one of the following modules is called to perform the appropriate calculation of the desired position for the next second

IDLE, AZEL, SID, 3DAY, 3RAD, 3AZL

Three more routines are called

CHKPRELIM	Checks the physical movement limits of the antenna and stops motion if the limits are about to be exceeded
REFC	Computes a refraction correction using the corrected Berman model The refraction correction automatically defaults to off in modes using azimuth–elevation inputs and turns on in modes using right ascension–declination coordinates The defaults may be overridden if desired
WINDAVG	Calculates the average wind based on the last 2 minutes If the average wind exceeds 45 mph or if a gust exceeds 55 mph, the antenna will automatically stow even if off or unattended

The CPU 2 level 2 software is shown in Fig 7 The background routines perform the following functions

SPEEDSELECT — Selects either high or low speed mode, depending on the angular distance to the desired point. An azimuth distance greater than 10 degrees or an elevation distance greater than 3 degrees will select high speed in that channel. If the channel is already tracking in low speed, the speed change algorithm will be performed to switch the channel to high speed. Similarly, an azimuth distance less than 10 degrees or an elevation distance less than 3 degrees will cause the speed change algorithm to switch to low speed. To prevent excessive overshoot when approaching a target in high speed, the maximum high speed rate is reduced to 0.5 degree/second if the distance to the target is less than 5 degrees.

CONVERT — Inputs the control room monitor channels and converts all channels (including those from the Data Collection Controller) to floating point and ASCII. Each sensor has a minimum and maximum value limit that may change depending on the current state. This module also checks sensor limits and writes data to the DATAOUT buffers. If monitor action is required due to a sensor out-of-limit condition, flags are set for the TASKREQ module.

MONACT — Performs the actual tasks selected by the logic in TASKREQ as a result of a monitor action.

TASKREQ — Selects the highest priority task and initiates required action. If it is a multiple-state task, the next state is initiated when ready.

TASKACT — Performs the actual tasks selected by the logic in TASKREQ as the result of a monitor alert, operator, or configuration input.

DATAOUT — Outputs data from the screen, star switch, or printer buffers.

Four interrupt routines handle the receipt of a character from the Data Collection Controller, a star switch message, an operator keyboard character, or a star switch message time out.

Five help menus are available at the local display, the station controller display or the remote display in the NOCC to provide the operator with assistance in remembering the commands available and their syntax. All operator and monitor events are logged on the printer as well as reported through the star switch for eventual recording on magnetic media. In addition, any sensor data may be selected for logging.

V. Discussion and Conclusions

Many lessons were learned configuring a maximum loaded 8080-based system with multiple processors. Difficulty was encountered in debugging problems relating to critical timing relationships between the CPUs. Available logic analyzers lacked the capability to trigger on combined events in each CPU and back-trace either the CPU or the bus.

The inability of the 8080 (and of most other CPUs, including 16-bit devices) to perform true bit operations greatly slows down the transfer of digital monitor and control data. The least addressable element is a byte. Therefore, changing a single bit in memory, an input–output port, or an interrupt mask requires reading the byte, changing the desired bit with a logical AND, OR, or XOR operation, and storing the byte. If more than one CPU or an interrupt routine attempts to alter a bit in the same byte, one of the changes may not be made. The Z80 CPU does allow bit operations and should be considered if one decides to use an 8-bit processor for monitor and control applications.

All software was developed in the controllers or in similar microprocessor computers. While this proved convenient from the standpoint of always having an editor or a compiler available, the time required for making changes in several modules, compiling, relinking, and listing was typically 4 hours. However, most of the debugging and patching was performed at the machine code level. One of the advantages of PLM is that the source statements are easily traceable and alterable at the machine code level. An extremely useful feature of the program was a built-in simulation of the servo loop and angle readouts. This allowed much of the debugging to be done at JPL rather than at the station.

Several undesirable features of the AMC-95/6011 floating point processors were encountered and should be given consideration when choosing components for future systems. Stack-oriented processors cannot be shared by multiple users (such as interrupt routines or other CPUs) if their state cannot be restored to the state at the time of an interrupt. The capability to save the processor stack and to restore it existed, but the status register could not be restored. It would also be useful in many applications to have access to the remainder following

a fixed point division for modulo operations Another annoying feature of the floating point processors was that if given operands were out of range, an unpredictable result was generated rather than a closest approximation In the refraction algorithm, for example, it is necessary to evaluate small powers of e If the argument is too close to zero, a very large result is obtained instead of unity In time critical control applications, where it is not possible to check the range of all operands before computation and it is too time consuming to execute floating point error handling routines, a closest approximation would be desirable It is unacceptable to simply report a range error and halt

The PLM compiler available for the 8080 does not support floating point directly Operands must be pushed onto the floating point processor stack, an operation code supplied, and the result taken off the stack and stored The execution time for getting numbers in and out of the stack is longer than some of the floating point operations themselves Using the floating point stack, some calculations can be chained to minimize this overhead, but clever manipulation of a stack is one of the tasks that one hopes to avoid by using a high-level language in the first place The PLM-86 compiler for the 8086 CPU using an on-board floating point processor avoids this and allows floating point operations to be written in algebraic form

While the objectives of this task have been achieved, it is clear that this represents a data point on the maximum capability of an 8-bit microprocessor-based system Limits of memory size, execution speed, module space, and general complexity were encountered All of these limits could be corrected by use of one of the more powerful 16-bit processors that have become available since the start of this project The software could be transferred with minor modifications to a 16-bit processor (8086) by converting from PLM-80 to PLM-86 This would provide execution time and memory space for inclusion of additional features such as CONSCAN, table of offsets, and library of frequently tracked sources

Reference

[1] R M Gosline, "DSS 13 Microprocessor Antenna Controller," *TDA Progress Report 42-77*, vol January–March 1984, Jet Propulsion Laboratory, Pasadena, California, pp 64–74 May 15, 1984

Table 1 Acceleration and deceleration limits

Variable	Low speed, deg/s/s	High speed, deg/s/s
Azimuth acceleration	0 005	0 045
Azimuth deceleration	0 016	0 075
Elevation acceleration	0 00125	0 04
Elevation deceleration	0 002	0 075

Table 2 Analog sensors

Identifier	Description	Units
A00	TACH AZ LOW SPEED 1	V
A01	TACH AZ HIGH SPEED 1	V
A02	TACH AZ LOW SPEED 3	V
A03	TACH AZ HIGH SPEED 3	V
A04	TACH EL LOW SPEED	V
A05	TACH EL HIGH SPEED	V
A06	PUMP 125HP LEFT	PSI
A07	PUMP 125HP RIGHT	PSI
A08	PUMP 75HP LEFT	PSI
A09	PUMP 75HP RIGHT	PSI
A10	RCVR AGC 1	V
A11	RCVR AGC 2	V
A12	RCVR NAR	V
A13	ATMOSPHERIC PRESSURE	mBR
A14	OUTSIDE TEMPERATURE	C
A15	RELATIVE HUMIDITY	%
A32	EL LS MOTR DIF PRESS	PSI
A33	EL HS MOTR DIF PRESS	PSI
A34	EL SYSTEM PRESS	PSI
A35	EL HS PRESS	PSI
A36	EL LS PRESS	PSI
A37	AZ HS MOTR DIF PRESS	PSI
A38	AZ LS MOTR DIF PRESS	PSI
A39	AZ HS SYSTEM PRESS	PSI
A40	AZ LS SYSTEM PRESS	PSI
A41	WIND SPEED SW TOWER	MPH
A42	WIND SPEED SE TOWER	MPH
A43	WIND AZ SW TOWER	DEG
A44	WIND AZ SE TOWER	DEG
A45	PUMP VOL 75HP LEFT	GPM
A46	PUMP VOL 75HP RIGHT	GPM
A47	PUMP VOL 125HP LEFT	GPM
A48	PUMP VOL 125HP RIGHT	GPM
A49	AZ LS ACCUM	PSI
A50	AZ HS ACCUM 1	PSI
A51	AZ HS ACCUM 2	PSI
A52	EL SYSTEM ACCUM 1	PSI
A53	EL SYSTEM ACCUM 2	PSI
A54	FLUID LEVEL	V
A55	LS CW CNTRBAL PRESS	PSI
A56	LS CCW CNTRBAL PRESS	PSI
A57	HS CCW CNTRBAL PRESS	PSI
A58	HS CW CNTRBAL PRESS	PSI
AWS	AVERAGE WIND SPEED	MPH

Table 3 Digital sensors

Identifier	Description	States	
D00	RIGHT WRAP UP	IN	OUT
D01	LEFT WRAP UP	IN	OUT
D02	AZ BRAKE 1	SET	REL
D03	AZ BRAKE 3	SET	REL
D04	EL BRAKE LEFT	SET	REL
D05	EL BRAKE RIGHT	SET	REL
D06	AZ SPEED	HIGH	LOW
D07	EL SPEED	HIGH	LOW
D08	DISABLE SWITCH	DISA	CLR
D09	PS 28VDC 1	ON	OFF
D10	PS 28VDC 2	ON	OFF
D11	AZ PRELIMIT	IN	OUT
D12	EL PRELIMIT	IN	OUT
D13	PS 28VDC ALL TIME	ON	OFF
D14	RCVR LOCK	IN	OUT
D15	REMOTE CONTROL IND	ON	OFF
D16	PUMP HP	125	75
D17	FINAL LIMIT BYPASS	SAFE	BAD
D32	PS 28VDC XDCR	ON	OFF
D33	H FLUID TEMP	SAFE	HIGH
D34	EL LUBE PRESS AND AC	ON	OFF
D35	PUMP 75HP START RLY	ON	OFF
D36	PUMP 125HP START RLY	ON	OFF
D37	PS 28VDC HYDROMECH	ON	OFF
D38	PS WIND TOWER	ON	OFF
D39	WRAP UP TENSION	SAFE	BAD

Table 4 Angle data

Identifier	Description
N00	AZ ANGLE POSITION
N01	EL ANGLE POSITION
N02	AZ ANGLE COMMAND
N03	EL ANGLE COMMAND
N04	AZ POSITION ERROR
N05	EL POSITION ERROR
N06	AZ RATE COMMAND
N07	EL RATE COMMAND
N08	AZ RATE ACTUAL
N09	EL RATE ACTUAL
N10	AZ TOTAL OFFSET
N11	EL TOTAL OFFSET
N12	HA TOTAL OFFSET
N13	DEC TOTAL OFFSET
N14	REFRACTION
N15	AZ DIRECT OFFSET
N16	EL DIRECT OFFSET
N17	HA DIRECT OFFSET
N18	DEC DIRECT OFFSET
N19	AZ AZ/EL OFFSET
N20	EL AZ/EL OFFSET
N21	AZ RATE OFFSET
N22	EL RATE OFFSET
N23	AZ ANGLE R/O DATA
N24	EL ANGLE R/O DATA

Table 5 Servo equation constants

Speed/type	Azimuth		Elevation	
	K1	K2	K1	K2
High speed – type I	0 600	0 200	0 650	0 300
High speed – type II	0 850	0 100	0 850	0 200
Low speed – type I	0 686	0 314	0 686	0 314
Low speed – type II	0 900	0 197	0 850	0 150

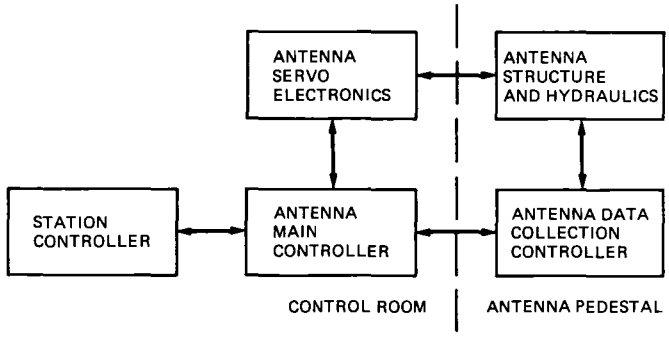

Fig 1 DSS 13 antenna controller functional block diagram

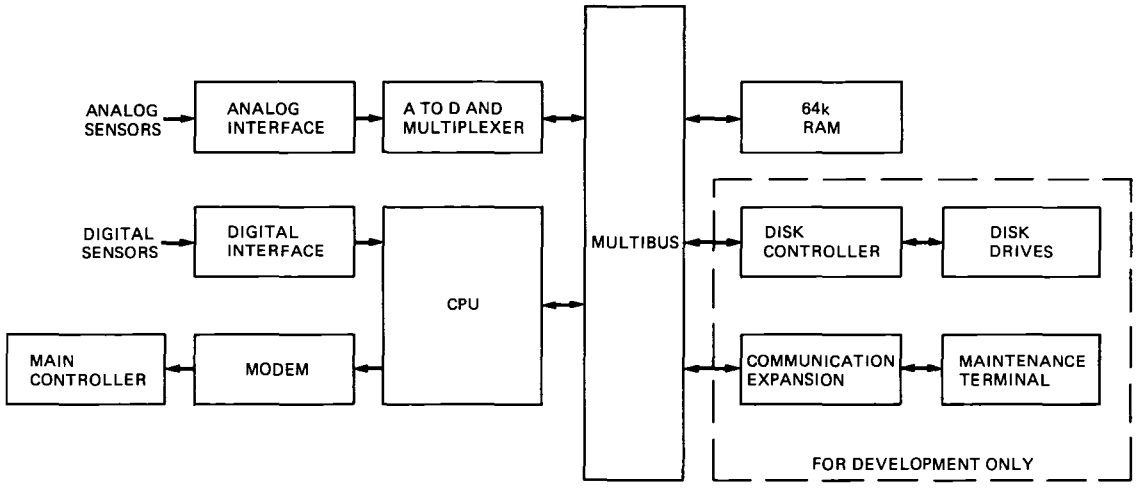

Fig 2 Data collection controller configuration

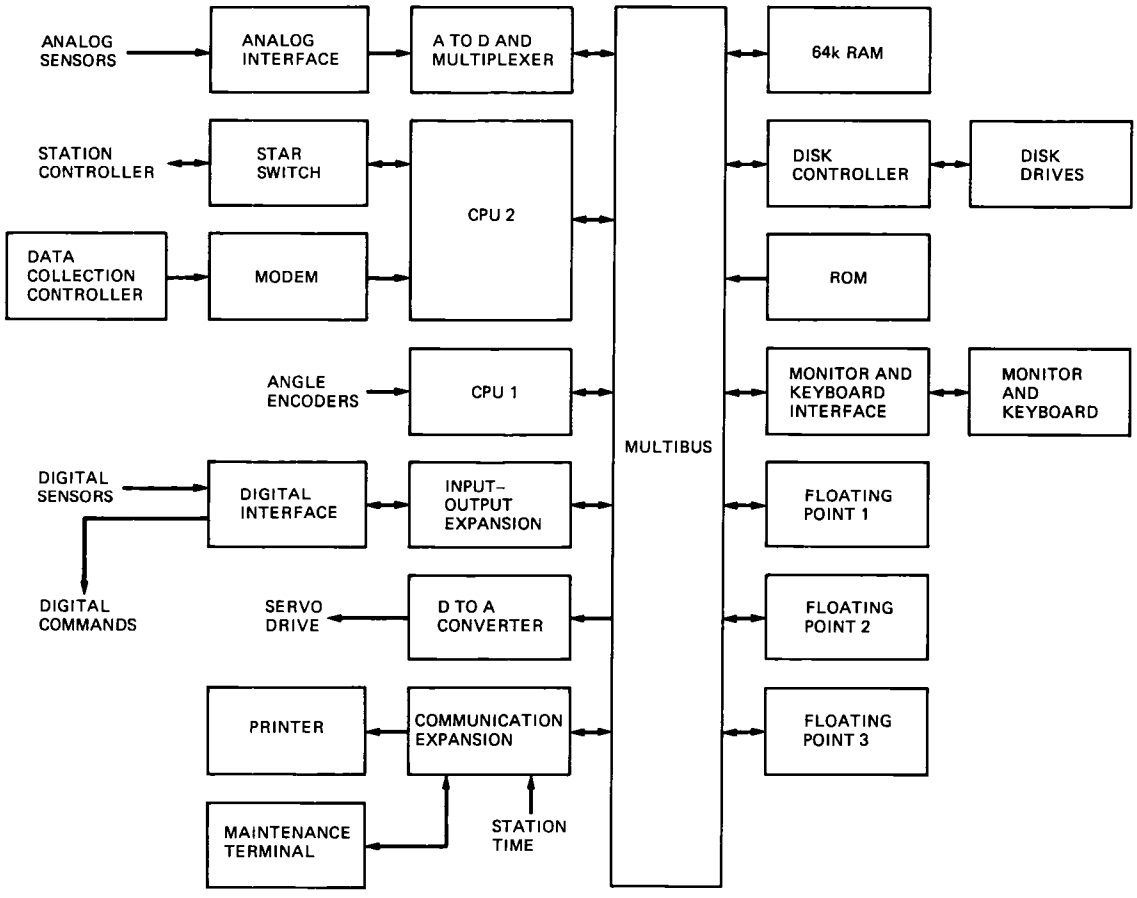

Fig 3 Main controller configuration

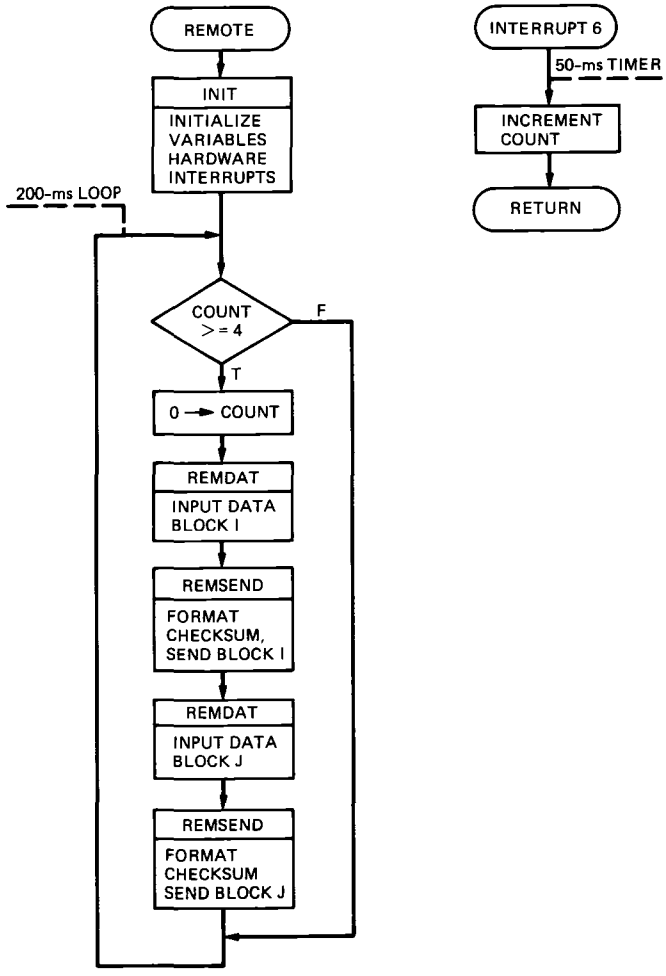

Fig 4 Data collection controller top-level software

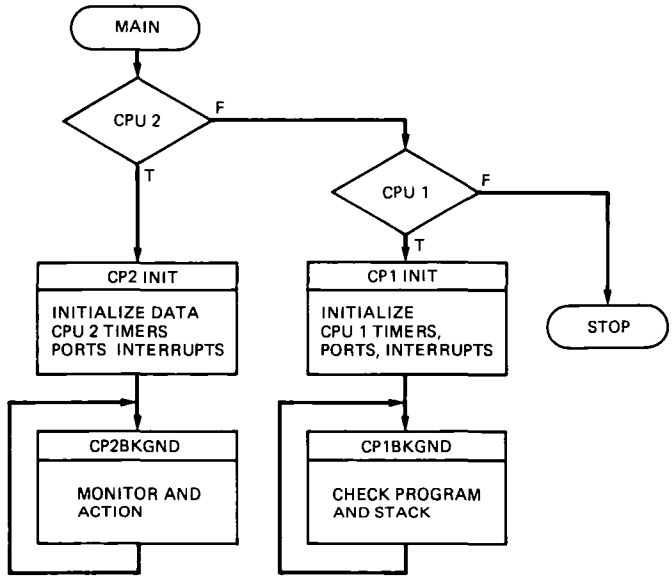

Fig 5 Main controller top-level software

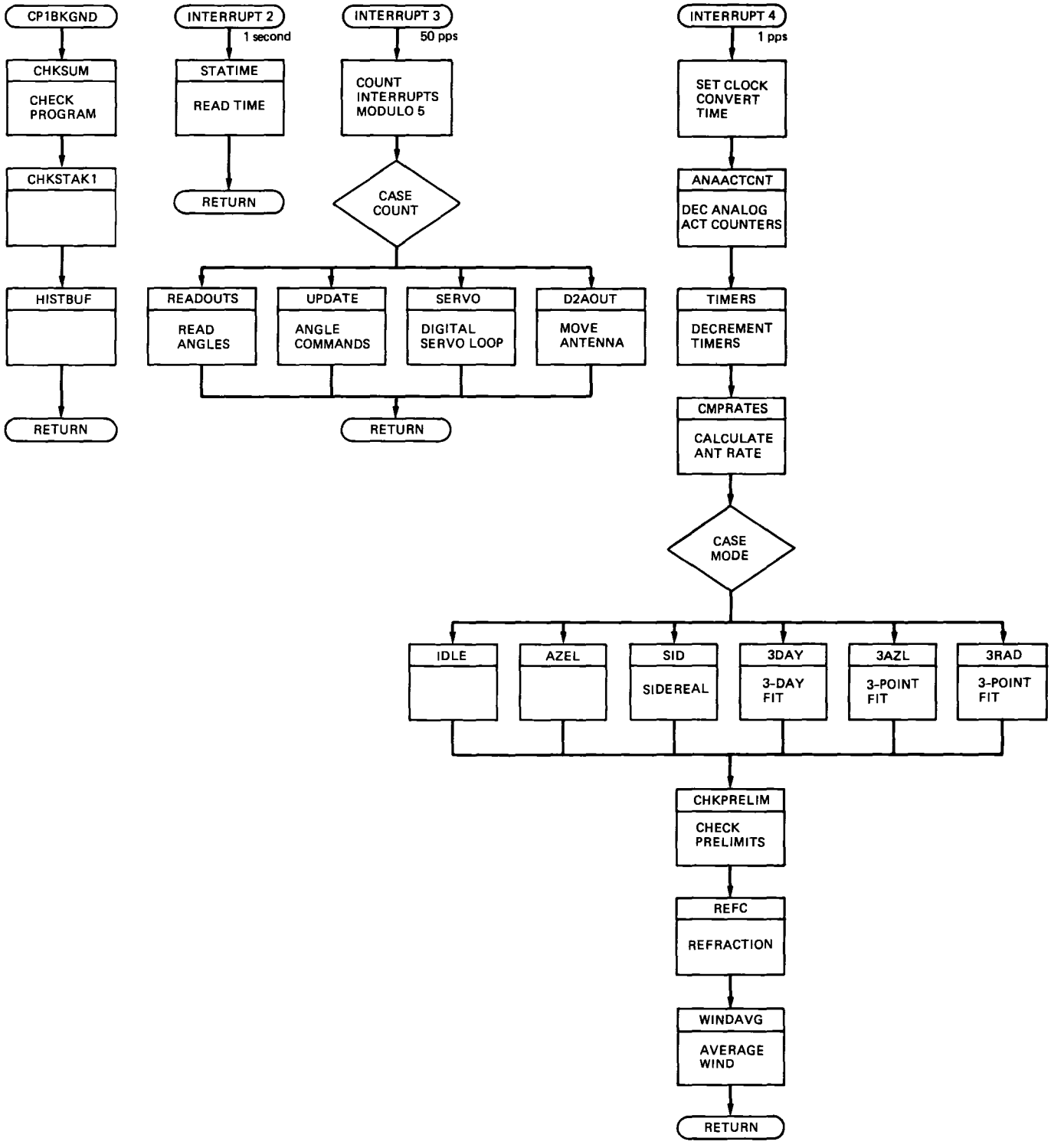

Fig 6 CPU 1 level 2 software

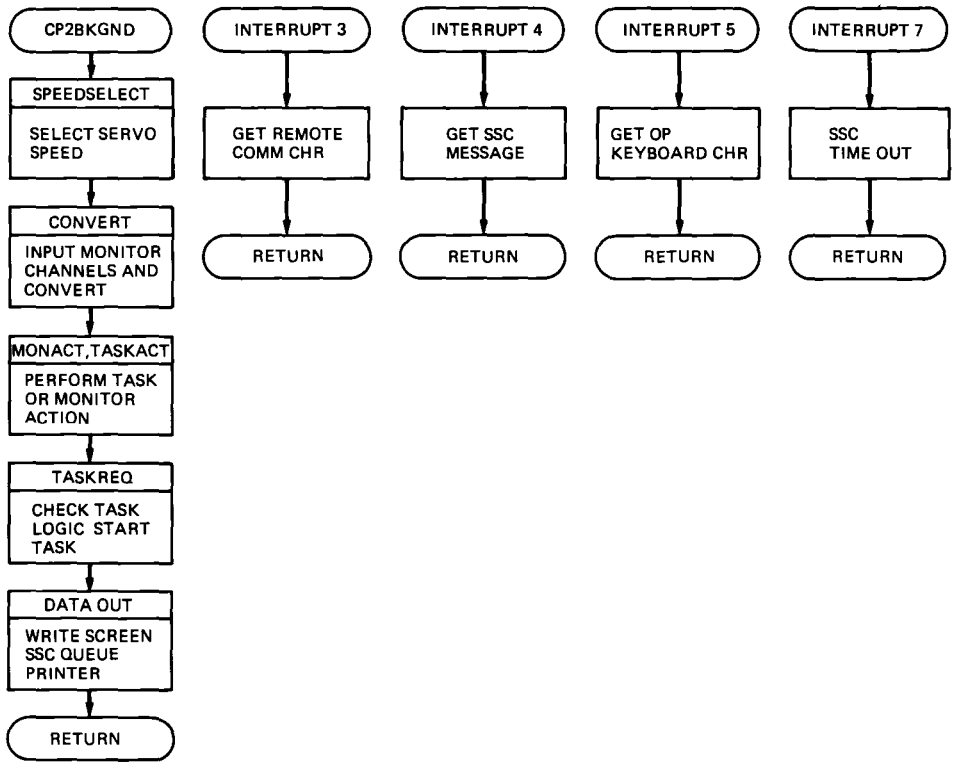

Fig 7 CPU 2 level 2 software

Heat Exchanger Demonstration Expert System

D G Bagby
Communications Systems Research Section

R A Cormier
Radio Frequency and Microwave Subsystems Section

This article describes a real-time expert system intended for detecting and diagnosing faults in a 20-kW microwave transmitter heat exchanger The expert system was developed on a LISP Machine, Incorporated (LMI), Lambda Plus computer using Process Intelligent Control (PICON) software The Heat Exchanger Expert System has been tested and debugged Future applications and extensions of the expert system to transmitters, masers, and antenna subassemblies are discussed

I. Introduction

An expert system is a computer program that embodies organized knowledge concerning some specific area of human expertise sufficient to perform as a skillful and cost-effective consultant [1] The goal of the Heat Exchanger Expert System Project was to write a program that achieved a high level of performance in diagnosing and troubleshooting heat exchanger problems in the Deep Space Network This article describes the results of that undertaking and discusses their implications for future DSN activities It was concluded that the project was successful and that the same techniques can be applied elsewhere in the DSN

With inadequate monitoring and control, problems can remain unidentified until serious damage has been done and can then take too long to fix Moreover, operations become more complex as functions are added to support new deep space missions Expert systems can enhance operator productivity by quickly identifying problems, diagnosing the causes of the problems, recommending appropriate solutions, and predicting impending problems that have not yet occurred The heat exchanger expert system is a harbinger of things to come

II. Heat Exchangers

The radio frequency power required to transmit navigation and command signals to distant spacecraft generates large amounts of heat which are dissipated by the transmitter heat exchanger Just as a water pump cools an automobile engine by circulating water through the engine and through a radiator, so too does the heat exchanger cool a transmitter by passing water through it to a cooling coil (see Fig 1)

When a heat exchanger fails to perform its cooling function properly, the entire transmitter becomes inoperable Many hours can be lost in finding the source of the problem, and many days may be required to repair it

In 1980, approximately 25 percent of all transmitter discrepancy reports arose from heat exchanger malfunctions This finding led to the installation of a new generation of heat exchangers for the DSN's low-power (20-kW) transmitters, which by 1987 had reduced the share of all transmitter discrepancy reports attributable to heat exchanger failures to 15 percent A typical example of heat exchanger failure occurred in Spain during the winter of 1986–87, when 70 mph winds and 20°F temperatures combined to freeze all three

coils The problem took 4 months to correct On another occasion, in 1988, a failed sensor on a California heat exchanger indicated a flow when there wasn't any The unsuspecting operator turned the transmitter on, and the resulting heat load burned up the klystron focus magnet, thereby deactivating the antenna for many weeks

Mishaps such as these and many others could have been prevented had a skilled engineer been available to constantly monitor all heat exchanger dials Such an arrangement is, of course, economically infeasible Failing this, the creation of an expert system with many of the capabilities of a skilled engineer seemed to be a worthwhile investment This was the motivation behind the heat exchanger expert system

III. The Expert System

The task was to test the feasibility of developing an expert system for maintaining a heat exchanger Since no active DSN heat exchangers were available, an old heat exchanger returned from the field to the Jet Propulsion Laboratory was used for testing purposes Sensors and a data collection device were added to the heat exchanger, and a computer was leased to process and analyze the data and to provide diagnostics

The first task was to determine which problems the heat exchanger expert system should address This involved a careful analysis of the problems that field personnel encountered, the amount of time they spent solving these problems, and the measures that they would consider helpful in performing their work The principal conclusions of this study were that the expert system should

(1) Isolate faults to the least replaceable unit

(2) Provide supervisors with equipment status and maintenance reports

(3) Furnish operators with alternatives if equipment is not operational

(4) Perform continuous on-line data acquisition and analysis

These conclusions constituted the design requirements for the expert system Each task is discussed below

A. Isolate Faults

The most difficult part of the job was to acquire from the expert the knowledge for solving heat exchanger problems and to translate that knowledge into a machine-readable data structure suitable for automated problem solving For every heat exchanger component, the expert was asked to identify all possible modes of failure, the symptoms or indicators of such failures, the sensor information necessary to isolate the failures, and the corrective actions required to remove them The expert's responses were then coded by a knowledge engineer into a set of "if-then" rules having the general form

IF ⟨situation⟩ THEN ⟨action⟩

where each rule corresponded to a piece of knowledge furnished by the expert A representative example of a rule is shown below

IF inlet resistivity <2 megohms and outlet resistivity >2 megohms,

THEN conclude that the main coolant loop is being contaminated

The final knowledge base of the Heat Exchanger Expert System contained over 300 such rules, organized as shown in Fig 2

B. Status Reports

In addition to isolating faults, the expert system had to provide the user with current status reports on all important heat exchanger components (e g , whether or not the heat exchanger was on, which pumps or fans were on, if pumps and fans were cycling properly, and whether or not the heat exchanger was operating under local control) Measurements such as these were essential for improving equipment availability and reducing operational costs Other important data for heat exchangers included equipment operating hours, momentary fault reports, past equipment failures, and repair records These data elements were provided automatically by the expert system

C. Furnish Alternatives

The expert system was also required to give the operator guidance about how best to proceed whenever the heat exchanger was "not operational " In that event, there were two possibilities either the heat exchanger was "available," which meant that it could still be used but that there were things wrong with it, or, alternatively, the heat exchanger was "not available," which meant that the heat exchanger could not be used under any circumstances The expert system had to be able to distinguish between these two situations and to issue appropriate instructions accordingly (see Fig 3)

The failure of the heat exchanger control connection due to pin corrosion is a type of failure which need not prevent transmitter operation, the heat exchanger can be operated locally independent of the transmitter This failure actually occurred at a DSN station, and the heat exchanger was subsequently

turned on locally Many other failures also allow normal operation provided appropriate action is taken In some cases, the heat exchanger may be operated in a limited capacity until repairs can be made Typical examples include fan failure (one cooling fan is usually adequate except on the warmest days when maximum uplink power is also required) and unstable coolant temperatures (stable coolant temperature is critical only for experiments requiring an extremely stable RF carrier, such as gravity wave searches) The expert system also provides a printed copy of this type of information to the operator whenever a problem occurs, thus improving equipment availability

D. On-Line Data Acquisition

It is not enough to know that a fault has occurred The user would also like to be able to predict when a fault is likely to occur so that preventive maintenance may be performed Continuous on-line data acquisition was incorporated into the expert system design to make such predictions possible A least squares regression line was applied to selected sensor values to direct the operator's attention to impending failures The expert system first alerts the operator to the presence of a potential problem, and then, by comparing those trends in on-line sensor values with certain prespecified parameters, the system predicts a time when those trends will become critical This mechanism mimics an attentive engineer and permits detection of wear-out and component degradation before actual failure Repairs can then be scheduled

An example of a slow failure that can be detected in a timely manner with on-line data monitoring is a slow coolant leak Such leaks often go undetected until the heat exchanger is turned off because the coolant has tripped the low-level sensor Another example is loss of cooling efficiency Cooling radiators collect dirt, bugs, and miscellaneous debris, all of which interfere with the cooling This problem is detected by on-line monitoring of the core air flow pressure Upward trends in pressure are evidence of fouling The monitoring of ambient air temperature can also be used to protect the coils from freezing When the temperature decreases below freezing, automatic turn-on of the circulating pumps provides protection if the cooling fans are not turned on (If the heat exchanger is turned on with the cooling fans operating, this will freeze the coils almost immediately)

When actual failures occur, the status of parameters just prior to the failure can provide information that reduces the time of isolating a fault because pertinent knowledge is localized, organized, and interpreted Quite often, once a failure has occurred, it is impossible to operate the equipment Short-circuited parts or failed interlock sensors are examples of faults that can be identified from data monitoring information of the operation just prior to failure

IV. Implementation

A. Inference Engine

In addition to the knowledge base of rules, a mechanism was needed for manipulating these rules to make logical deductions and diagnostics This mechanism, kept separate from the knowledge base, is essentially a mathematical theorem prover called an "inference engine " Its job was to derive conclusions about the status of the heat exchanger from current sensor values and the rules furnished by the expert system Thus, if the knowledge base contained the rule

IF A THEN B

and a sensor reported that A was true, the inference engine would deduce that B was also true Then the assertion that B was true might in turn trigger other rules having the form

IF B THEN C

and so on

Program execution consists of a continual sequence of such cycles that persists until either no rule executes or a halt is commanded At each cycle, all rules whose preconditions are satisfied by the contents of the working memory are determined If more than one rule is activated, one is selected by means of some suitable "conflict resolution" strategy All the actions associated with the selected rule are then performed, and the database is changed accordingly

Alternatively, if B is suspected to be the cause of a problem, then, armed with a rule of the form IF A THEN B, the inference engine may work backward and ask the sensor system to provide any confirming evidence about the existence of A

The most difficult thing about applying expert system techniques to a heat exchanger is that everything is time-dependent Consequently, all rules and variable values must be couched in terms of a particular point in time For example, the simple rule

IF A > B THEN C

becomes

IF A > B at time T THEN C at time T + 1

e g ,

IF tank level > (tank level as of 10 minutes ago),

THEN conclude tank level is rising

The tank level problem is one of the simplest examples Evaluating sequences of events over time with an expert system proved much more difficult As another example, for the expert system to ascertain whether or not two pumps were cycling properly, it had to have an internal model describing the last time a particular pump was on compared with the other pump This placed a significant demand on the inference engine, which not only had to compare events that occurred at different points in time but also, for purposes of isolating a fault that had transpired, had to recall past data or request confirming or disconfirming data from the data supplier—all in real time!

At the time of this study, there was only one commercially available inference engine possessing such capabilities the Process Intelligent Control, or PICON, produced by LISP Machine, Incorporated (LMI), of Cambridge, Massachusetts Accordingly, PICON was procured from LMI, together with its Lambda 2 Plus computer

B. Sensors

Before a single rule was developed, 81 sensors were placed on the heat exchanger For various reasons, not all of them could be used in the development of the rules Consequently, the rules were written for a subset of 57 sensors Of the 24 unused sensors, 3 failed, 4 did not provide any information due to equipment failure, 4 monitored parameters that were never actually used, 7 monitored transmitter heat load, which proved unusable, and 6 provided information available by other means The sensors that had been intended to capture the heat load could not be used because of the uncontrolled heat loss in the connecting pipes running between the heat exchanger and the transmitter This piping, exposed to rain, snow, wind, and sun, made heat balance calculations impractical Even test loads produced large standard errors

With the 57 sensors that were used, it was possible in some cases to identify a particular failed component, but in general fault isolation was confined to specifying the appropriate procedures and test equipment necessary to further isolate the fault to the defective part

C. Simulations

Simulation was chosen as the method for modeling the heat exchanger The entire expert system was divided into independent pieces and separately simulated sensor values Once confidence was achieved that the individual pieces were operating properly, they were joined together Finally, simulated sensor values were replaced with actual sensor values

There were a number of shortcomings with this approach It failed to account for sensor noise, signal timing, and unforeseen parameter variations The rule base that worked so well for simulated sensor values was often inadequate when applied to real sensors For example, the rule

IF reservoir level is decreasing,

THEN send "Differences in tank level indicate a leak" to the engineer

worked well in a simulated mode but misfired when confronted with fluctuations in the readings of the actual reservoir sensor, even when the actual reservoir level itself was constant The use of smoothing did not eliminate this problem, for noise was not the only factor that had to be considered (Fig 4) The reservoir level dropped whenever the pump was turned on This difference was traced to the expansion of the piping caused by the increased pressure of the coolant with the pump operating The effects of temperature, pressure, time delays for equipment to turn on and off, and sensor hysteresis were other considerations that were initially overlooked for the simulated data

D. User Interfaces

It is not enough for an expert system to simply come up with the right answer, that answer must also be presented to the operator in such a way that it can be understood Here, the LISP Machine contained icons, graphs, and displays that made every expert system operation clear Three different types of heat exchanger problems illustrate these capabilities a coolant flow interruption, a fan failure, and a leak in the main reservoir tank

1 **Coolant flow interruption** One way to create a flow interlock is to partially close the klystron collector flow valve of the transmitter Once flow falls, the expert system immediately detects a fault, and the words "Flow Interlock" appear on the console display (Fig 5) At the same time, the set of instructions listed in Fig 6 is sent to the operator via a printer The sequence of rules and sensor values leading up to that message can also be explicitly displayed

2 **Fan failure** To create a fan failure, one could open the fan circuit breaker When the circuit breaker opens, the expert system detects the source of the fault and notifies the operator with the message "Warning! Fans not operating properly " As before, the operator can call up detailed instructions and graphs to help pinpoint the source of the problem

3 **Reservoir leak** An illustration of the predictive capabilities of the expert system can be obtained by attaching the reservoir level transducer to a stochastic ramp function The regression line fitted to these reservoir level values and a pa-

rameter specifying the minimum safe reservoir level (20 gallons) then trigger the graph and warning message shown in Fig 7

IV. Tests

A test procedure was developed to verify the accuracy of the rule base and to measure its ability to provide operational information useful in the maintenance of the 20-kW transmitter heat exchanger Key features of the plan included a 72-hour soak test, an identification of various sensor failures, discovery of temperature and flow interlocks, the isolation of short-circuit faults, and the location of leaks The test procedure was applied to the expert system on two separate occasions in August of 1987 and in October of 1987 There was significant disagreement between the tester and the system engineer about which tests had passed and which had failed due to different interpretations of test specifications Figure 8 presents the more conservative results, i e , the stricter interpretation of the specifications As the diagram illustrates, the first series of tests yielded correct responses 54 percent of the time, while the second series of tests had a correct response rate of 70 percent The August tests were performed before the rule base had been debugged and before the heat exchanger was fully operational By October, the rule base had been debugged but the heat exchanger was still in need of repair All remaining errors were explainable and repairable

The tests results indicated that an operational heat exchanger expert system could be developed

V. Computer System Problems

The unexpected bankruptcy of LMI in April 1987 limited the amount of software and hardware support available during the entire development process Although the LISP Machine itself is now working properly, initially it had serious problems that would have been impossible to resolve without customer support from LMI These problems included a hard disk crash, a keyboard failure, and a problem within the terminal itself Numerous software crashes were traced to unsuitable environmental conditions such as nearby arc welding and high-power transmitter testing These disappeared with the introduction of a line conditioner

VI. Lessons Learned

The principal lesson learned from this project was that real-time expert systems are feasible in DSN applications The LMI Lambda computer and its PICON software were easy to work with and expedited the creation of the Heat Exchanger Expert System

More time spent initially on requirements and problem definition would pay off in an implementation Detailed test specifications would be written and agreed upon between testers and designers early in the design process This would be done after agreement was reached about the scope of the system and before the detailed design was begun This could eliminate discrepancies such as those found in the test results described above

More effort defining the types of sensors that are required to diagnose a problem would be useful Less effort spent trying to decide how best to use already available sensors is indicated The latter strategy produced many overly complex and cumbersome rules that could have been eliminated by the addition of a single sensor

A difficult aspect of developing a real-time expert system is establishing reliable connections with external devices and sensors An elaborate tailor-made C computer program was written just to effect communication between R-TIME, a proprietary real-time data interface, and the 57 heat exchanger sensors

Another problem encountered in this study was that sensors were not reliable, and additional sensors were needed to check the accuracy of other sensors The sensor data tended to be noisy, and many sensors failed to operate as expected Much time could have been saved had rules been added to the knowledge base to look for inconsistencies among collections of sensor values Simulations need to model the statistical characteristics of both the signals and the sensors

Real-time expert systems are difficult to build and to debug The systems can be fooled or misled by the execution sequence of data requests and rule firings This causes the expert system to generate erroneous messages, which greatly complicate the debugging process and validation of the knowledge base itself Extra time must be allowed for the debugging process

VII. Summary and Conclusions

This project developed and demonstrated an expert system that monitors and diagnoses transmitter heat exchanger failures in real time Sensors and data collection devices were added to a heat exchanger returned from the field An expert system was developed to collect and provide heat exchanger data and provide diagnostics All of this was accomplished in 8 months with the expenditure of 2 work-years of effort

The system will undergo further tests and refinement before it is made fully operational Eventually, the expert system

will be transferred to Goldstone, California, for testing by DSN operators If it is found that the expert system reduces transmitter downtime, then the same technology will be applied to other troublesome subsystems One likely candidate is the 70-meter antenna assembly, which now accounts for over half of all DSN downtime (54 8 percent) Other possibilities include the traveling-wave maser or the 20-kW CW microwave transmitter itself

Reference

[1] F Hayes-Roth, D A Waterman, and D B Lenat, *Building Expert Systems*, Reading, Massachusetts Addison-Wesley, 1983

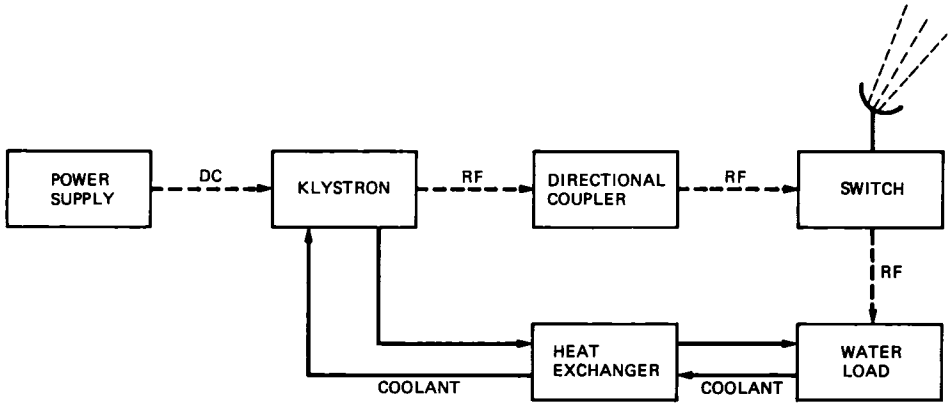

Fig 1 Block diagram of the 20-kW transmitter

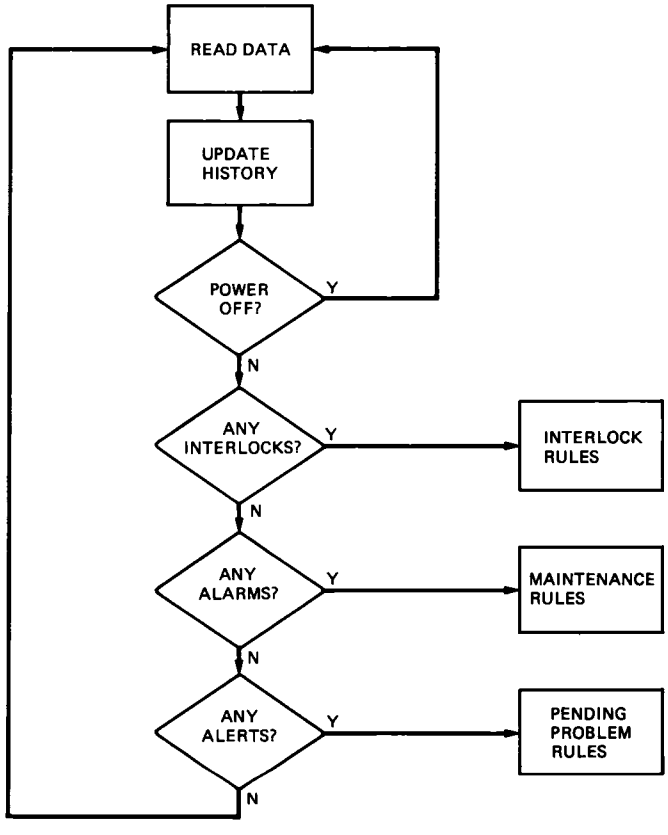

Fig 2 Expert system rule set structure

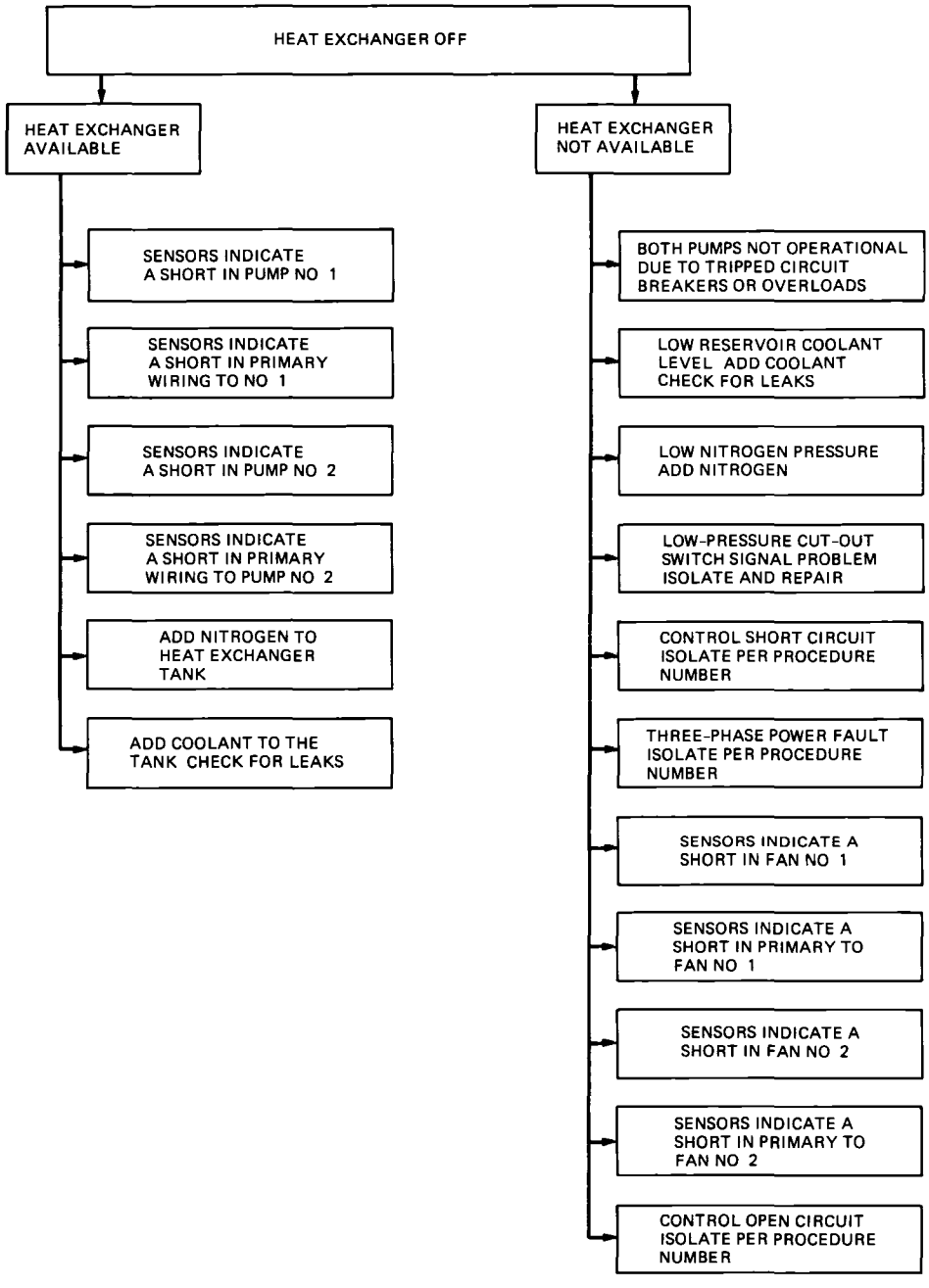

Fig 3 Heat exchanger "off" problem categories

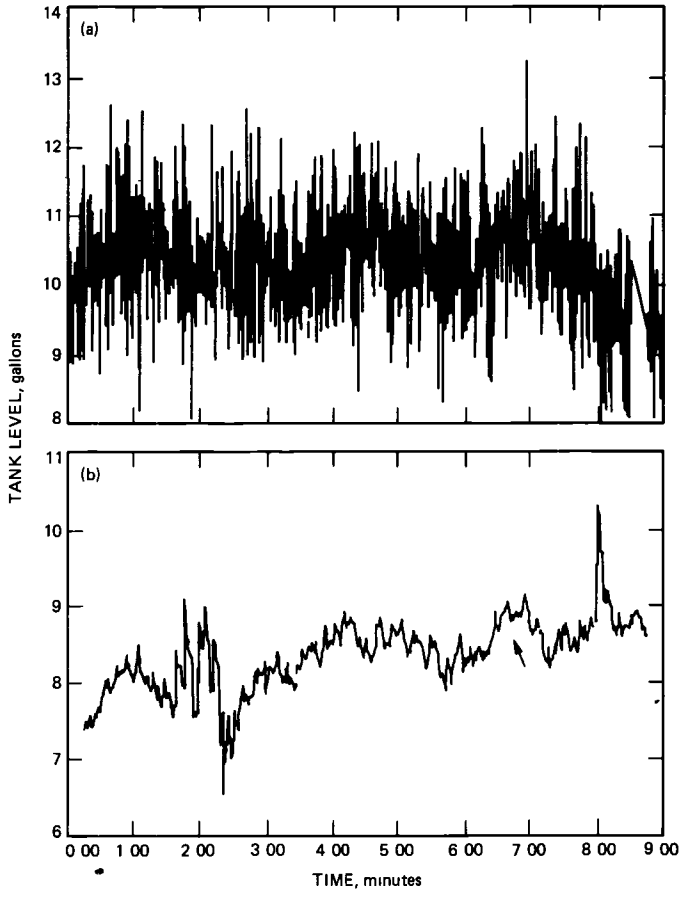

Fig 4 Comparison of (a) unsmoothed and (b) smoothed data

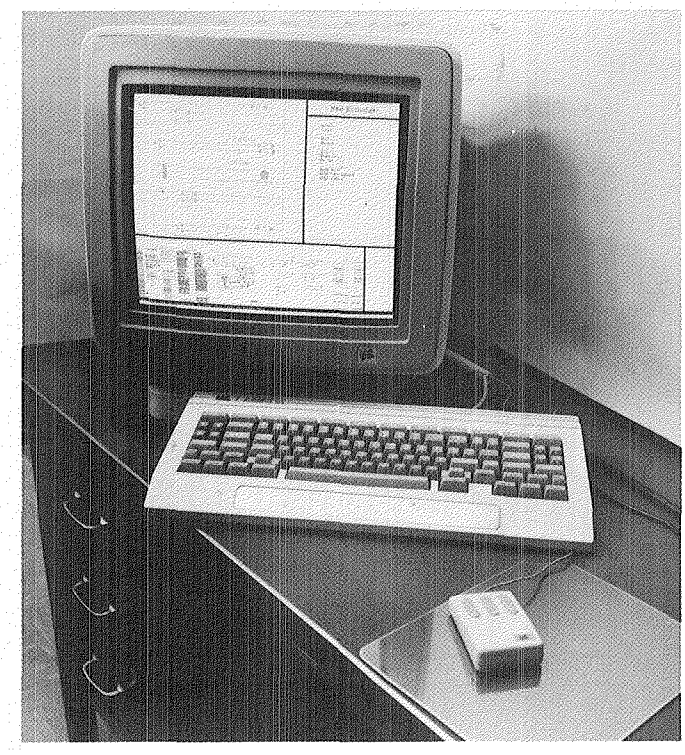

Fig. 5. Expert system console

```
**********************************************************************************
**********************************************************************************

                        PROCEDURE 2.1.1.4

     A flow interlock is indicated. Go to the power amplifier and to the
     heat exchanger and determine that:

     a) Heat exchanger input and output shutoff valves are fully open.

     b) Power amplifier input and output shutoff valves are fully open.

     c) All coolant circuit return valves are fully open.

     d) Adjust coolant inlet throttling valves for each cooling
        circuit to required flow, per manual TM 03202.


     If the above procedure has cleared the interlock then the
     problem was not a heat exchanger problem.

**********************************************************************************
**********************************************************************************
```

Fig. 6. Sample expert system printout

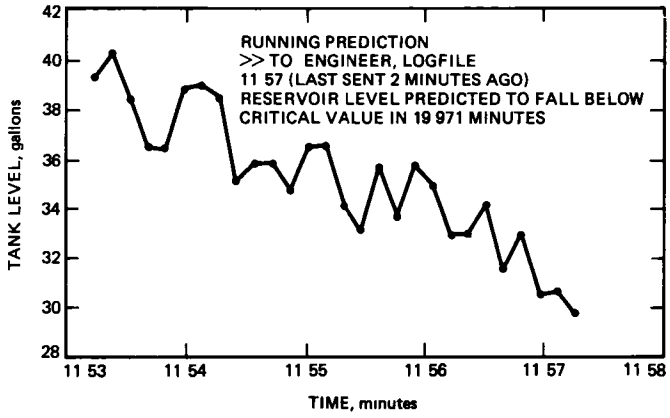

Fig 7 Sample expert system predictive analysis (heat exchanger reservoir level)

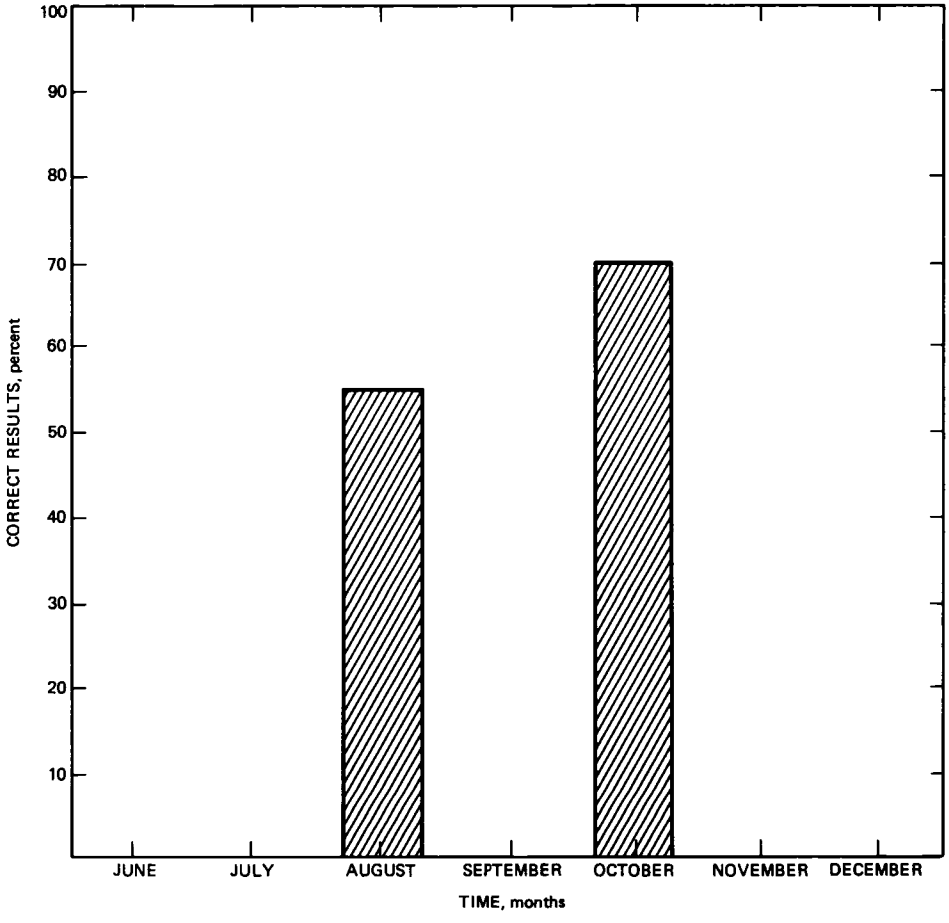

Fig. 8 Test results of the heat exchanger expert system

A Wideband, High-Resolution Spectrum Analyzer

M P Quirk
Institute for Defense Analyses, Princeton, New Jersey

H C Wilck, M F Garyantes, and M J Grimm
Communications Systems Research Section

This article describes a two-million-channel, 40-MHz-bandwidth, digital spectrum analyzer under development at the Jet Propulsion Laboratory The analyzer system will serve as a prototype processor for the sky survey portion of NASA's Search for Extraterrestrial Intelligence program and for other applications in the Deep Space Network The analyzer digitizes an analog input, performs a 2^{21}-point Discrete Fourier Transform, accumulates the output power, normalizes the output to remove frequency-dependent gain, and automates simple signal detection algorithms Due to its built-in frequency-domain processing functions and configuration flexibility, the analyzer is a very powerful tool for real-time signal analysis and detection

I. Introduction

A 2^{21} (2,097,152)-channel spectrum analyzer is being designed at JPL for real-time processing of signals with bandwidths of up to 40 MHz from the radio antennas of the DSN The spectrum analyzer will perform all functions from sampling the input waveform to detecting signals in the computed spectra Applications include radio-astronomy spectral analysis and continuum studies, high-resolution frequency analysis of wideband receiver systems in the DSN, radio-frequency interference (RFI) studies, and spacecraft telemetry acquisition and tracking The primary radio-astronomy application will be to serve as a prototype system for the sky survey analyzer for NASA's Search for Extraterrestrial Intelligence (SETI) program [3], in which the entire celestial sphere will be scanned in the microwave region for narrowband signals The final system to be used for the survey is planned to have a bandwidth of about 300 MHz and will consist of segments based on the prototype design [7]

The use of high-speed, commercially available CMOS VLSI components will allow millions of spectral points to be computed every second The real-time digital processing will be performed by a rack of special-purpose hardware modules configured as a pipe in which data flows from the input samplers through the Discrete Fourier Transform (DFT) to the frequency-domain processing modules The requirements of the SETI sky survey have guided the design of the frequency-domain modules The digital boards have parameters that can be programmed by a user to match specific signal processing and detection needs Interaction with users and with other devices is through the system controller, a workstation computer that controls and tests the hardware

The core of the analyzer is a matrix-style DFT pipe that can compute contiguous real-time transforms of up to two million points on a 40-MHz-bandwidth signal The analyzer performs a long $N = LM$-point DFT by considering the input

data as an $L \times M$ matrix, transforming the columns with L-long Fast Fourier Transforms (FFTs), multiplying the resultant matrix entries by complex rotation factors, and then transforming the rows with M-long FFTs (see Section IV) The input to the FFTs is a real sequence derived by mixing the Intermediate Frequency (IF) input to baseband and sampling at a rate equal to twice the IF bandwidth Real rather than complex sampling is used in order to eliminate the imaging caused by mismatches between the anti-aliasing filters on the real and imaginary legs of a complex mixer A $2N$-long real sequence is transformed using an N-long complex DFT by exploiting the symmetries in the spectrum The output spectra are unscrambled and then processed by special-purpose modules which can be programmed to perform signal detection algorithms For example, the Baseline module can be used to remove frequency-dependent system gain, to whiten the spectrum, or to suppress interfering signals The Output Processor can pick peaks and averages of groups of frequency powers for display or further processing

If desired, any board can perform a null operation and pass its input directly to its output This allows testing of the boards in isolation or in combination with other boards in the pipe, it also allows flexibility in the operation of the analyzer For example, by bypassing stages, transforms less than 2^{21} points can be performed, processing stages can be skipped, and the analyzer output can be taken from any section of the pipe

A special design feature is that the analyzer can process two separate input data streams in the pipe at the same time An "input switch" signal controls the selection between the two inputs, A and B, and labels each spectrum flowing down the pipe as type A or type B To accommodate two data streams, there are two power-accumulation memories, one for A spectra and one for B spectra This capability was built in so that the analyzer could cope with Dicke switching, in which the antenna beam alternates between a source of interest and a background source for calibration The addition of another IF stage would allow the analyzer to process any two input data streams, in particular, it may be desirable to process both the left-circular and right-circular polarizations of a radio-astronomy signal

The analyzer pipe has two output valves for the real-time data one for the spectrum imaging data and one for the output of the matched-filter detector The output processor works as a valve for the spectrum imaging data, extracting coarse-resolution or narrowband data for the graphics displays The other valve sends the workstation the frequency, bandwidth, and power of signals which pass a threshold test from the matched filter The output from both valves can be used for postprocessing

This spectrum analyzer is designed to be a flexible tool for real-time analysis at high data rates In response to a user's needs, the system can be reconfigured by software in milliseconds Configuration parameters which can be changed include the sampling rate, the length of the DFT, the accumulation frame lengths, the signal detection parameters, and the output processor controls

The next section is a more detailed discussion of the spectrum analyzer system and its operation Section III explains the synchronization and configuration controls Sections IV and V describe the design and operation of the 2^{21}-point transform, and Section VI describes the real-time frequency-domain processing modules and how they will be used for the SETI sky survey

II. The Spectrum Analyzer System

The spectrum analyzer is a pipeline architecture in which, after a start-up delay, all stages of the algorithm are executing concurrently [1] Figure 1 is a functional block diagram of the spectrum analyzer system The Intermediate Frequency (IF) Input Signal Conditioner mixes, filters, and samples the analog input at the desired sampling frequency The Input and Timing module collects sufficient data for a spectrum in one of the input buffers, selects the points for the first stages of the column transforms, and sends them to the Window module The Input and Timing module also generates the synchronization signals for the pipeline control The Window module multiplies the data by the coefficients of a window in order to suppress the sidelobes of the frequency response The spectrum of the windowed data is computed by the matrix FFT using two separate FFT modules, one for the rows and one for the columns

The 128-point column FFTs are 16-bit, fixed-point, radix-2 FFTs with two stages on a board Each FFT stage performs a radix-2 FFT butterfly operation and then implements the delay for the next stage The outputs from the column FFTs go into the matrix transpose memory, which selects the points for the row transforms Each point is multiplied by the appropriate complex rotation factor called a "twiddle" factor prior to entering the second FFT module The row FFTs are radix-4, floating-point FFTs with one stage per board Both FFT modules are fully pipelined [1] The matrix FFT was chosen because it allows small numbers of data points and twiddle factors to be resident on the FFT boards at the expense of performing the matrix transposes and twiddle factor multiplication In order to compute the transform of a $2N$-long real sequence using an N-point complex FFT, the even points are loaded into the real components and the odd points into the imaginary components of an N-long complex sequence The

transforms of the even and odd points are then formed from the symmetric and antisymmetric parts of the unscrambled transform, respectively, before the last radix-2 butterfly [2] This final operation is called the real-adjust

The FFT output data then go to the Power Accumulator which calculates the power of the complex spectrum samples and accumulates them on a frequency-by-frequency basis There are actually two independent accumulators so that two separate data streams can be accumulated The power spectra are then normalized using a predetermined baseline to remove frequency-dependent system gain The normalized spectra then go through a matched filter designed to detect narrow-band sources as they are swept by a moving antenna during the SETI sky survey The parameters of the filter can be adjusted based on noise statistics computed from the data spectra The spectral processing for the graphics displays is performed by the Output Processor which can select a band of frequency points or pick peaks and averages of groups of contiguous frequency points

The spectrum analyzer system is controlled by the microprocessor computer system whose primary function is data processing and graphics handling The system controller and postprocessor is a 68020-based Masscomp 5600 computer system with high-resolution graphics and sufficient storage and processing power to control and configure the spectrum analyzer and to perform additional data processing on the output spectra The computer system will generate graphics displays, archive data, provide antenna monitoring and control, and perform special-purpose processing Examples of special-purpose processing include signal identification, signal tracking, and removal of undesired interfering signals

The system controller also performs system tests and diagnostics It commands the Executive board to generate test synchronization signals and transmit and receive test vectors through the stimulus and response buffers The stimulus buffer contains 16 megabytes of read/write Masscomp-mapped memory—enough to hold 2^{21} complex floating-point samples Test input vectors generated by the microprocessor are written to the stimulus buffer at microprocessor speed and are then transferred to the Input and Timing module at the hardware processing speed The Executive board can cycle through the input data to generate periodic stimuli Output vectors return to the microprocessor via the response buffer, a ring buffer in which the last memory location is followed by the first one to form a continuous ring Data streams into the response-buffer memory until a programmed trigger condition is met After a trigger event, an additional specified number of data points are written, and then the data are available to be read After reading the data, the user resets a bit to arm the memory and the cycle repeats To check the system performance, output vectors can be compared to expected response vectors Since any module can be bypassed as the controller chooses, each module can be tested in isolation or with any combination of other modules The data buses in the system are configured so that any board can be supplied with its full data-width stimulus and have the full width response captured in the response buffer The widest data path consists of two complex numbers and two serial control lines Complex numbers are pairs of floating-point numbers (R,I), each 32 bits wide, thus the widest data path is 130 bits wide The floating-point representation is the IEEE 32-bit floating-point standard The serial control lines carry the synchronization pulses

III. Synchronization and Configuration Control

The operational flexibility of the spectrum analyzer arises from two sources The first source is the way the data flow is controlled using synchronization and framing signals, the second is the way parameters can be set to control the functions of the hardware modules The spectrum synchronization signals, explained below, include the start-of-spectrum indicator, valid spectrum indicators, the A/B indicator, and accumulation frame triggers The synchronization signals are generated by the Input and Timing module and sent down the processing pipe on two serial lines Each module delays the synchronization signals by an amount equal to its pipe delay before sending the signals to the next module in the pipe

The processing of a spectrum begins with data from one of the three 4-megabyte RAM buffers on the Input and Timing module The current buffer is read out by the delay commutator which outputs pairs of complex data samples which are to be combined in the first butterfly stage of the transform The start-of-spectrum indicator occurs every N complex samples, or every $N/2$ complex pairs Because of the periodicity of the delay commutator, the beginning of a new spectrum can occur only every N sample times Thus if the sampling rate is less than the 40-MHz processing rate and the next buffer is not full when the commutator is reset to start a new spectrum, N sample times must be skipped before the buffer can begin to be processed The first two time lines in Fig 2 show the write and read times for a 64-MHz real sampling rate Since the sampling rate is four-fifths the processing rate, after the start-up delay every fifth spectrum does not contain valid data, and a valid spectrum indicator does not appear in the third time line The processing pipe cannot be stopped to wait for the buffer to fill, the modules thus continue cycling through their processing, but the absence of the valid spectrum indicator prevents the data from being added into the accumulations or entered into the spectrum filter computations

Since two input channels can be in the pipe, there are two separate accumulator memories The A/B indicator identifies which accumulation each valid spectrum belongs to The lengths of the accumulations are controlled by the accumulation frame trigger which causes the current spectrum to be added into the appropriate accumulation, the next valid spectrum corresponding to that accumulation will then be deposited, not added, to the buffer The triggers for the A and B accumulations are controlled independently The bottom time line in Fig 2 shows the A frame trigger for accumulations of three spectra when all the spectra are type A The main use for the two separate channels is for Dicke switching In Dicke switching the antenna switches from looking at a source for K_1 spectra to looking at the background noise for K_2 spectra The spectrum analyzer controls the switch, discarding a specified number of spectra to allow synchronization with a pulsing signal or settling time for the Dicke switch For other applications, such as dual-polarization processing, the two accumulations allow the analyzer to process the inputs from two IF stages with maximum bandwidths of 20 MHz For dual-channel input the analyzer would alternate the spectra, thus the even-numbered spectra would belong to channel A and would be separate from the odd spectra which belonged to channel B

In order to generate the correct synchronization signals, the Input and Timing module has a group of control bytes which specify the number of spectra in the A and B accumulations, the number of invalid spectra between switching accumulations, and the base-two logarithm of the spectrum length There are also bits for a user-supplied sync code, for controlling the clock, and for forcing initialization of the analyzer The other modules also contain one or more control bytes to pass module parameters and control bits such as bypass and read switches Some of the controls allow multiple copies of one board design to be used for similar operations at different stages in the pipe For example, there are two copies of the multiplier board, one to perform the window multiply on the input data and one to do the twiddle-factor multiply between the row and column transforms The window is real, while the twiddle multiply is complex, thus one bit is used to select whether the board performs a real or a complex multiplication For complex multiplications, another bit selects whether or not the result should be divided by two To load the coefficient data onto the board, the operational/multibus switch is set to multibus mode, and the data words are transferred on the multibus

The fixed-point FFTs are computed using four copies of one board design, and the floating-point FFTs use seven copies of a floating-point design Each FFT board needs only one control byte to control which stage or stages of the FFT it computes The fixed-point FFT boards contain two stages of a radix-2 FFT, and the control byte contains the stage number, k, of the second stage, and two bypass bits, one for the first stage and one for the second If the first stage is not bypassed, its stage number is $k - 1$ Since the floating-point boards contain only one stage of a radix-4 FFT, the control byte contains only one bypass bit and the stage number Another function of the control bytes is to pass parameters unique to a board which program the operation of the board The frequency-domain boards have such parameters, and they are described in Section VI

All the boards have bypass switches which allow the input data to be passed directly to the output data lines The only board whose output is of a different form from its input is the floating-point converter which converts 16-bit fixed-point numbers to 32-bit floating-point numbers It therefore has two different bypass modes, one which passes 32-bit data to the output, and one which maps the 16-bit input data to the first 16 bits of the 32-bit output lines The bypass switches are all set independently and allow great flexibility in the use of the analyzer In test mode they allow every module to be tested independently or in combination with other modules in the pipe In operational mode they allow the spectrum analyzer to be customized to fit the user's application For example, FFTs shorter than the maximum length are implemented by skipping FFT stages using the bypass switches, the window stage can be skipped, and other processing stages can be skipped as desired

The control bytes are in the memory-address space of the workstation, thus, when a value is assigned to a control-byte location, a multibus transfer to the analyzer hardware is initiated This means that the system configuration can be altered in the length of time it takes to complete the multibus accesses Since the data computed with the new configuration propagate down the pipe, in general there will be a delay before the output contains valid spectra

IV. The Two-Million-Point DFT

The core of the spectrum analyzer is the two-million-point Matrix DFT which transforms the time-domain input signal into the frequency domain A real window can be applied to the DFT input to shape the frequency response The length of the transform, N, can be any power of two from $2^{17} = 131{,}072$ to $2^{21} = 2{,}097{,}152$

The windowed DFT of the input signal is

$$Y_i(k) = \frac{1}{N} \sum_{n=0}^{N-1} x_i(n) w(n) \exp\left(-j2\pi \frac{nk}{N}\right)$$

$$0 \leqslant k \leqslant N-1 \qquad (1)$$

where $\{x_i(n)\}$ is the input data and $\{w(n)\}$ are the window coefficients The subscript indexes successive spectra or, equivalently, segments of N samples Thus $x_i(n)$ refers to the $(iN + n)$th time sample

The spectrum computation is a Matrix FFT in which an $N = LM$-point DFT is computed using L- and M-point FFTs and a complex multiply stage The Matrix algorithm is derived in detail in [1] The central idea is that the N-long input sequence is decomposed into an L by M matrix such that

$$y_i(l,m) = y_i(Ml + m)$$

$$0 \leqslant l \leqslant L - 1,\ 0 \leqslant m \leqslant M - 1 \tag{2}$$

where $y_i(n) = x_i(n)w(n)$ for the ith spectrum The output transform sequence is recomposed by the mapping

$$Y_i(s,r) = Y_i(Lr + s)$$

$$0 \leqslant s \leqslant L - 1,\ 0 \leqslant r \leqslant M - 1 \tag{3}$$

Rewriting Eq (1) in terms of the matrix indices yields

$$Y_i(s,r) = \sum_{m=0}^{M-1} \sum_{l=0}^{L-1} y_i(l,m) \exp\left(-j2\pi \frac{(Ml + m)(Lr + s)}{ML}\right)$$

$$= \sum_{m=0}^{M-1} \exp\left(-j2\pi \frac{mr}{M}\right) \exp\left(-j2\pi \frac{ms}{ML}\right)$$

$$\times \sum_{l=0}^{L-1} y_i(l,m) \exp\left(-j2\pi \frac{ls}{L}\right) \tag{4}$$

The rightmost summation is a DFT of length L on the mth column The result will be called $q_i(s,m)$ The summation over m is an M-point DFT on the sth row of the matrix $\exp[(-j2\pi)(ms/LM)]q_i(s,m)$ The complex phasors $\exp[(-j2\pi)(ms/LM)]$ are called the twiddle factors

The advantage of the Matrix FFT method over a straight Decimation-in-Frequency (DIF) or Decimation-in-Time (DIT) FFT computation [1] is that by decomposing the N-point transform into short M- and L-point transforms, the long delay memories and twiddle-factor tables are not resident on the FFT boards but are concentrated into one large N-point matrix transpose buffer and one large twiddle-factor table

In the JPL spectrum analyzer the column transforms are computed via radix-2, DIF, fixed-point FFTs In a radix-2 algorithm the FFT is computed in $K = \log_2 L$ stages Each stage consists of a "butterfly" operation on $L/2$ pairs of complex points The butterfly operation

$$z_k(l) = \frac{z_{k-1}(l) + z_{k-1}(l + 2^{K-k})}{2}$$

$$0 \leqslant l \leqslant L - 1$$

$$z_k(l + 2^{K-k}) = \frac{\{z_{k-1}(l) - z_{k-1}(l + 2^{K-k})\} W_L^{l2^{k-1}}}{2}$$

$$1 \leqslant k \leqslant K \tag{5}$$

takes the sum and difference of the complex pairs and then multiplies the difference by the appropriate twiddle factor Dividing the results by two ensures that the maximum magnitude of the numbers does not increase by a factor of two at every stage At the kth stage, $1 \leqslant k \leqslant K$, the pairs for each butterfly operation are the results from the previous stage taken 2^{K-k} apart, $z_{k-1}(l)$ and $z_{k-1}(l + 2^{K-k})$, and the input to the first stage is the windowed data from the mth column, $z_0(l) = x_i(lM + m)$ $w(lM + m)$ The output from the last stage is $q_i(U(l)M + m) = z_K(l)$, where $U(l)$ is the bit reversal of l

The output from the fixed-point column transforms enters the matrix-transpose memory which unscrambles the columns and selects the data quadruples for the row FFTs Before the row transforms, the points are multiplied by the appropriate twiddle factor and converted from 16-bit, two's-complement, fixed point to IEEE 32-bit floating point The row transforms are radix-4, floating-point FFTs In the radix-4 algorithm the FFT is computed in $K = \log_4 M$ stages in which each stage implements a 4-point DFT followed by twiddle-factor multiplications

$$\begin{bmatrix} u_k(m) \\ u_k(m + 4^{K-k}) \\ u_k(m + 2 \times 4^{K-k}) \\ u_k(m + 3 \times 4^{K-k}) \end{bmatrix} = \begin{bmatrix} 1 & 1 & 1 & 1 \\ 1 & -j & -1 & j \\ 1 & -1 & 1 & -1 \\ 1 & j & -1 & -j \end{bmatrix} \begin{bmatrix} z_{k-1}(m) \\ z_{k-1}(m + 4^{K-k}) \\ z_{k-1}(m + 2 \times 4^{K-k}) \\ z_{k-1}(m + 3 \times 4^{K-k}) \end{bmatrix}$$

$$z_k(m) = u_k(m)$$

$$z_k(m + p \times 4^{K-k}) = u_k(m + p \times 4^{K-k}) W_M^{mp4^{k-1}}$$

$$1 \leqslant p \leqslant 3 \tag{6}$$

The input to the first stage consists of the twiddled points from the sth row, $z_0(m) = \exp[(-j2\pi)(ms/LM)]\, q_t(s,m)$ The output from the last stage is $Y_t(U_4(m)L + s) = z_K(m)$, where $U_4(m)$ is the 4-based digit reversal of m

Only two unique board designs are needed for the FFT computations one for the fixed-point, radix-2 transforms, and one for the floating-point, radix-4 transforms Although stage $k + 1$ in a radix-n FFT requires only $1/n$th the delay and coefficient memory of stage k, it is more economical to design, test, and maintain the boards if they are all exact replicas with the maximum memory requirements Figure 3 shows a block diagram of a fixed-point FFT stage On each board there are two FFT stages, each with an Arithmetic Unit (AU) to perform the complex butterfly, a PROM coefficient memory for the twiddle factors, and an SRAM delay memory with a cross-switch In addition, on each board there is a synchronization generator unit, a clock module, a local bus module, and a thermal protection module

The complex addition of Eq (5) is done as a 17-bit add with "OR rounding" carried out when the bit shift is done for the division by two The complex subtraction uses 16-bit subtracters which require the input data to have a magnitude less than 1/2 To avoid overflow conditions in the subtracters, the Input buffer is wired to ensure that the 8-bit data has a magnitude less than 1/2, and the window multiplication and FFT butterflies are designed not to increase the maximum magnitude Since the window coefficients have a maximum magnitude of one, the real window multiplication will have a resultant less than 1/2, and the divide-by-two in the FFT stages guarantees that the results maintain a maximum magnitude of 1/2 The twiddle-factor complex multiply is performed using Multiplier-Accumulators (MACs), dividing by two in the process The twiddle factors are stored in PROM memory as $\cos(\theta) - j \sin(\theta)$ There is a separate set of 128 sine/cosine pairs for each possible stage number, the appropriate set is read sequentially and repetitively Although each butterfly stage increases the maximum signal level by at most 1 bit, with 8-bit input samples and seven stages, the 16-bit arithmetic has sufficient dynamic range [4]

The output from the AU enters the cross-switch which changes the order of the data, choosing the correct data pairs for the next FFT stage The input pairs to the cross-switch at the kth stage are 2^{K-k} apart, the pairs' outputs to the next stage are 2^{K-k-1} apart This operation is carried out using a two-input, two-output multiplexer and a read-modify-write memory which outputs a location and then stores new data in the same location The memories act as 2^{K-k-1} delay memories, while the multiplexer either passes data straight through or switches the data paths The purpose of the sync code generator unit is to delay the sync code lines to match the data delay appropriate for the stage number The delay is calculated via a look-up table using the stage number as the address

Each floating-point board contains one stage of a radix-4 DIF FFT The AUs have eleven 50-nsec IEEE 32-bit floating-point adders and six 50-nsec IEEE 32-bit floating-point multipliers to perform the radix-4 butterflies The 32-kilobyte twiddle-factor memory is made up of 8k X 8 PROMs, and the cross-switch uses 8k X 8 static RAMs The output from the floating-point FFTs is digit reversed, and the final spectrum is formed in the Real-Adjust stage

V. The Real-Adjust Stage

A 40-MHz IF bandwidth can be sampled using a complex demodulator sampling at 40 million complex samples per second, or using a real demodulator sampling at 80 million real samples per second The N-point DFT of the complex sampled signal would have N independent complex points spaced 40 MHz/N apart For equivalent resolution, a $2N$-point transform would have to be computed on the real sampled signal Since the spectrum of the real signal is conjugate symmetric with $Y(2N - n) = Y^*(n)$, $0 \leqslant n \leqslant N$, only the first $N + 1$ points actually have to be computed The first $N + 1$ points of the $2N$-point transform of the real signal $y(m)$, $0 \leqslant m \leqslant 2N - 1$, can be computed using an N-point complex DFT by the following algorithm

$$z(n) = y(2n) + jy(2n + 1), \qquad 0 \leqslant n \leqslant N - 1 \tag{7}$$

Let Eq (7) be the input to an N-point transform Then the output $Z(k)$, $0 \leqslant k \leqslant N - 1$, is the sum of the transforms of the real sequence $y(2n)$ and the imaginary sequence $y(2n + 1)$, $0 \leqslant n \leqslant N - 1$ Since a real sequence has a conjugate symmetric spectrum and an imaginary sequence has a conjugate antisymmetric spectrum, the transforms of the even and odd points can be recovered from $Z(k)$ [2]

$$Y_E(k) = \frac{1}{2}\{Z(k) + Z^*(N - k)\}$$

$$Y_O(k) = \frac{-j}{2}\{Z(k) - Z^*(N - k)\}, \qquad 0 \leqslant k \leqslant N - 1 \tag{8}$$

where $Z(N) = Z(0)$ From the transforms of the even and odd points, the full transform is

$$Y(k) = \{Y_E(k) + Y_O(k)W_{2N}^{k}\}$$

$$Y(N-k) = \{Y_E^*(k) - Y_O^*(k)W_{2N}^{*k}\}, \qquad 0 \leqslant k \leqslant N \tag{9}$$

Note that this full real adjust would generate $N + 1$ complex numbers from the N complex inputs, yet the pipe can only accommodate N complex numbers To avoid this problem $Y(N)$ is not computed, since $Y(N)$ would not have been computed if complex demodulation had been used In Eqs (8) and (9), the point $Y(0)$ is computed only from $Z(0)$ and $Y(N/2)$ only from $Z(N/2)$ These two points are therefore handled together as the first data pair with the operation

$$Y(0) = \mathrm{Re}\{Z(0)\} + \mathrm{Im}\{Z(0)\}$$

$$Y(N/2) = Z^*(N/2) \tag{10}$$

VI. Frequency-Domain Processing Modules

The real-time, frequency-domain processing modules automate the detection of signals in the spectra and reduce the volume of output data These modules include the Power Accumulator, the Baseline module, the SETI Filter, and the Output Processor Since the spectrum analyzer under construction is a prototype design for a segment of the analyzer to be used in the sky survey portion of NASA's SETI program, these modules were designed to meet the requirements for detecting narrowband signals as an antenna scans the sky Essentially the goal of the survey is to search the entire celestial sphere in the microwave region from 1 to 10 GHz for signals as narrow as a few hertz The entire survey is expected to take about five years to complete and will use the radio telescopes of the DSN and other large antennas Since the survey involves an ambitious amount of data and processing, the spectrum analyzer is designed to perform the signal detection steps which must be applied to every spectral point in the pipe These steps include accumulating the power at each frequency, removing frequency-dependent system gain, and using a matched filter to detect stationary celestial sources scanned by the antenna beam Since the points which pass the matched-filter threshold test contain potentially interesting signals, they are sent to the workstation for postprocessing

The first frequency-processing module is the Power Accumulator which computes the power of each of the complex points output by the FFT and accumulates the power values in one of the channel-accumulation memories The length of the accumulation, L, can be from 1 to 2^{24} spectra The Baseline module then removes the frequency-dependent system gain from the accumulated spectrum by multiplying each channel by a precomputed inverse baseline value The baseline, $B(n)$, is computed by the workstation using spectra from an input noise source The baseline can be updated while the antenna is being repositioned between scans The accumulated, baselined output, $S_k(n)$, is

$$S_k(n) = \frac{1}{B(n)} \sum_{m=L(k-1)}^{Lk-1} |Y_m(n)|^2, \qquad k \geqslant 0 \tag{11}$$

The baselined spectra enter the SETI Filter module which is designed to detect narrowband signals and report the frequency, bandwidth, and accumulated power of these signals to the workstation The SETI Filter module contains a five-coefficient Finite Impulse Response (FIR) filter which takes a running average of each channel across successive accumulated spectra This spectrum filter can be a matched filter for any desired single-frequency time signature of duration less than or equal to five accumulation intervals The filter output

$$F_k(n) = \sum_{m=0}^{4} \alpha_{k,m}(n) S_{k-m}(n) \tag{12}$$

where the filter weights $\alpha_{k,m}(n)$, $0 \leqslant m \leqslant 4$ are equal to the desired time signature The filtered data then goes to the Threshold board which taps the data and locates regions with power above a computed frequency-dependent threshold The location, the number of frequency points in the region, and the total power in the region are computed and stored in an event memory which can be accessed by the workstation The Threshold board contains a bit mask which can be used to force frequency ranges known to be contaminated with RFI to be ignored

In order to allow for a varying noise temperature across the 40-MHz signal bandwidth, the spectrum is divided into a maximum of 128 subspectra, each with its own threshold and filter weights which depend on an estimate of the noise temperature in the subspectrum This estimate is proportional to the power in the Nth dimmest spectral bin, where N is a control parameter The filter weights are equal to their initial static values, or the initial values divided by the estimated noise temperature The threshold is equal either to an input constant θ, or to θ times the sum of the filter weights The Nth dimmest spectral bin for each subspectrum is determined with 24-bit accuracy by using a coarse-resolution histogram of the twelve most significant bits, determining the bin where the Nth dimmest power lies, fixing these twelve most significant bits, and then doing a histogram of the next twelve significant bits

The purpose of the matched filter is to integrate the power received at each frequency as the antenna beam sweeps across a source in order to use all the information from the source Figure 4 depicts a one-dimensional slice of the circularly symmetric expected response at a single frequency The combination of accumulating and then filtering results in a weighting function which is a step-like approximation to the bell-shaped response Combining five accumulations in this fashion as the antenna moves one Half-Power Beamwidth (HPBW) results in an SNR loss of 0 25 to 0 3 dB [5] Figure 5 depicts an oval antenna scan pattern with circles showing half-power beam areas The filtering implemented by the hardware integrates only along the direction of the antenna scan To approach uniform spatial sensitivity, the information from adjacent scans should be combined as well Adjacent scans are expected to be separated by one HPBW, as shown in Fig 5, thus, sources positioned at the edge between two scans would register in both scans, 3 dB lower than if the source were centered in one of the scans

In order to combine the data from adjacent scans optimally, all the spectral data generated between successive passes past a position would have to be stored, for a reasonable antenna scan pattern, this results in an unreasonable amount of data storage By sending only the spectral points which pass a threshold, the amount of data stored can be reduced to a fraction of the total with very little effect on the probability of missing a signal For example, setting the threshold to retain only 1 percent of the data reduces the probability of missing a narrowband signal by only one or two percent, but dramatically reduces the maximum required storage The combination of data from scan to scan is then done by software in the workstation

In addition to the matched-filter output, the workstation receives data from the Output Processor which controls the amount and form of the spectrum analyzer output to be used for spectrum displays The Output Processor has the ability to store both the peaks and averages of contiguous groups of spectral bins called "superbins" in a set of Multibus-mapped buffers The number of spectral bins per superbin is a programmable power of 2, and the first superbin may start at an arbitrary programmable location The output of this data reduction process goes into two double buffers, one for the peaks and one for the averages of each superbin The buffers can each contain a maximum of 1024 IEEE 32-bit floating-point numbers If the user-supplied parameters result in more than 1024 superbins, the extra bins are not calculated

VII. Conclusion

The wideband spectrum analyzer being developed is a powerful tool for real-time frequency-domain analysis of wide-bandwidth input signals By using the signal processing boards to average and threshold the spectra, the uninteresting data can be reduced and signals of potential interest, such as continuous-wave or narrowband signals, can be retained The system design principles were developed from experience with other large real-time systems, including a 20-MHz-bandwidth, 65,536-point spectrum analyzer completed in 1979 [6] and a real-time signal processing system for synthetic aperture radar containing four 20-MHz-wide, 16,384-point FFTs for performing convolutions One of the design goals was to make the hardware as flexible as possible within the constraints of the pipeline architecture while keeping the size down to one rack of equipment The sampling rate, the size of the transform, and the time-domain window are the only parameters needed to control the bandwidth and resolution of the output spectra Most of the programmable parameters control the real-time signal processing boards where flexibility is needed in order to allow specification of a wide range of signal detection algorithms The 40-MHz, 2^{21}-channel analyzer is a stand-alone system which is the prototype for an analyzer with a bandwidth of 300 MHz Some of the expected applications for both the 40-MHz and 300-MHz designs, in addition to the SETI sky survey, include radio astronomy spectral analysis and continuum observations, wideband, high-resolution frequency analysis of receiver systems in the DSN, detection of radio-frequency interference, and spacecraft telemetry acquisition and analysis

References

[1] L R Rabiner and B Gold, *Theory and Application of Digital Signal Processing*, Englewood Cliffs, New Jersey Prentice-Hall, Inc , pp 371–377 and 602–613, 1975

[2] J W Cooley, P A W Lewis, and P D Welch, "The Fast Fourier Transform Algorithm Programming Consideration in the Calculation of Sine, Cosine, and Laplace Transforms," *J Sound Vib* , vol 12, pp 315–337, July 1970

[3] E T Olsen, A Lokshin, and S Gulkis, "An Analysis of the Elements of an All Sky Survey," presented at IAU Symposium No 112, Boston, Massachusetts, June 1984

[4] E H Satorius, M J Grimm, G A Zimmerman, and H C Wilck, "Dynamic Range Constraints for Large Size, Hybrid Fixed/Floating Point FFTs," presented at the 20th Asilomar Conference on Signals, Systems, and Computers, Pacific Grove, California, November 10–12, 1986

[5] J Solomon, M P Quirk, E T Olsen, and W Lawton, "A Signal Detection Strategy for the SETI All Sky Survey," *TDA Progress Report 42-83*, vol July–September 1985, Jet Propulsion Laboratory, Pasadena, California, pp 191–208, November 15, 1985

[6] R F Emerson, "Biplex Pipelined FFT," *DSN Progress Report 42-34*, vol May–June 1976, Jet Propulsion Laboratory, Pasadena, California, pp 54–59, August 15, 1976

[7] G A Morris and H C Wilck, "JPL 2^{20} Channel 300 MHz Bandwidth Digital Spectrum Analyzer," presented at the IEEE International Conference on Acoustics, Speech, and Signal Processing, Tulsa, Oklahoma, 1978

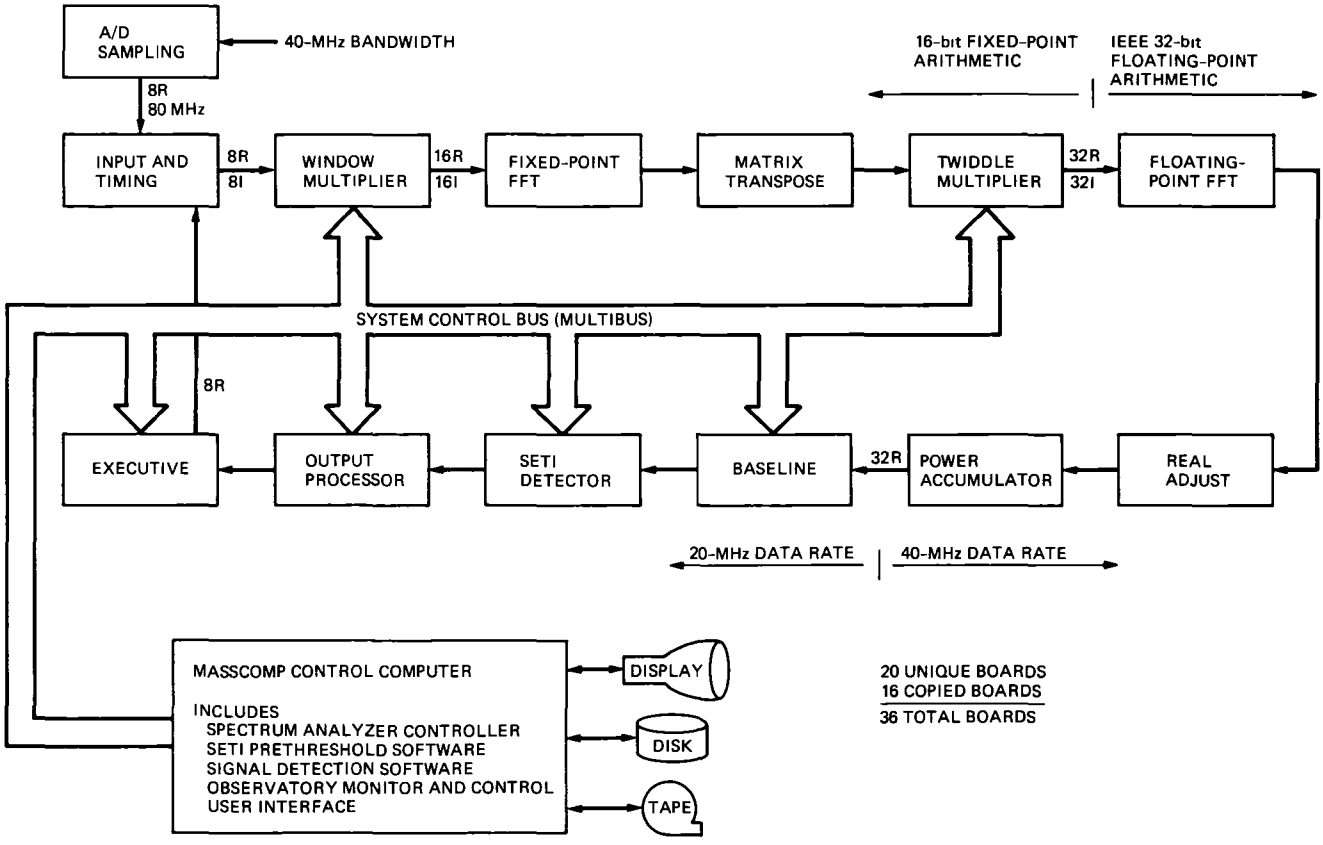

Fig 1 The DSN–SETI spectrum analyzer system

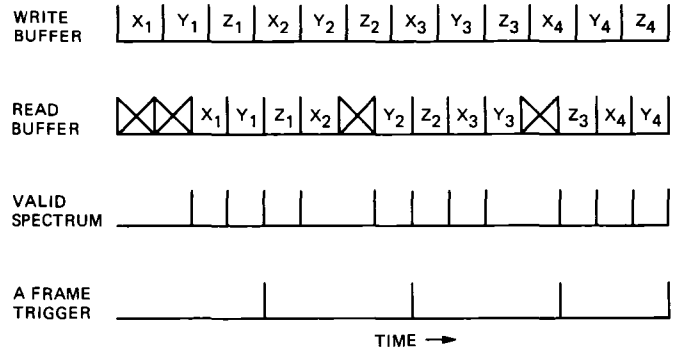

Fig 2 Input buffer write and read cycles, valid-spectrum indicator, and accumulation-frame trigger for a 32-MHz sampling rate with three accumulations per frame

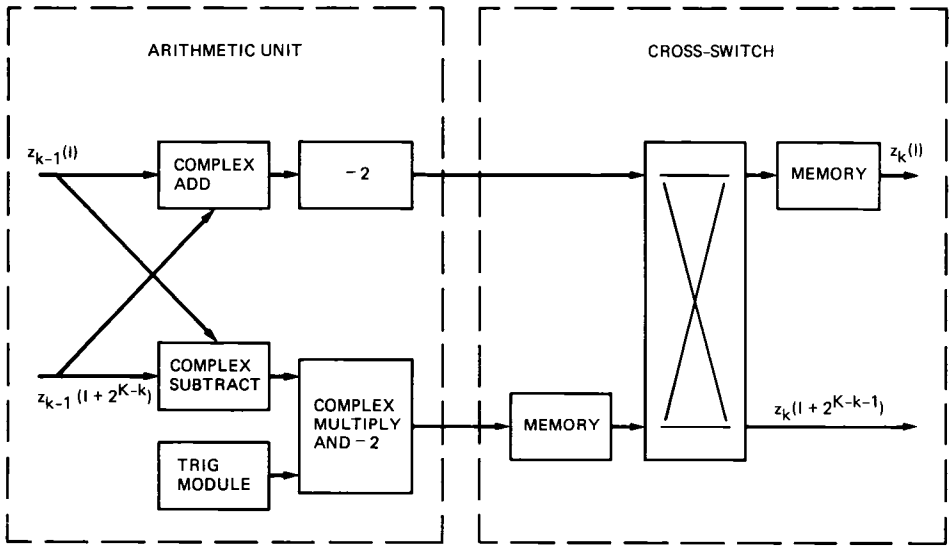

Fig 3 Block diagram for a radix-2 fixed-point FFT stage

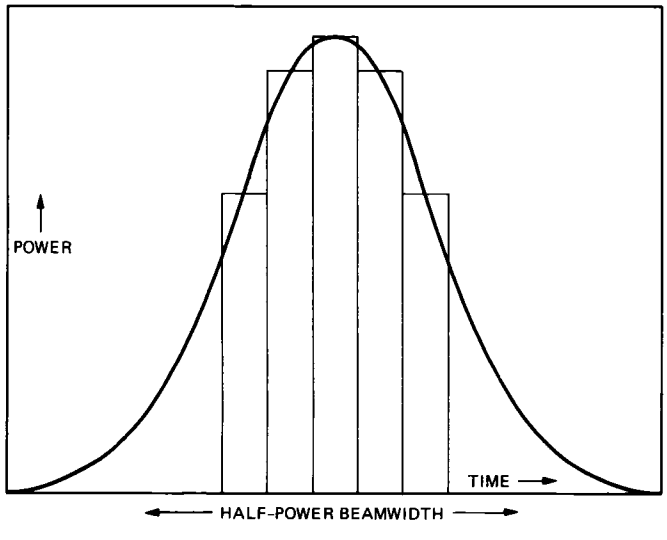

Fig 4 Response to a point source transiting the antenna beam Matched-filter values result in a staircase approximation to the response

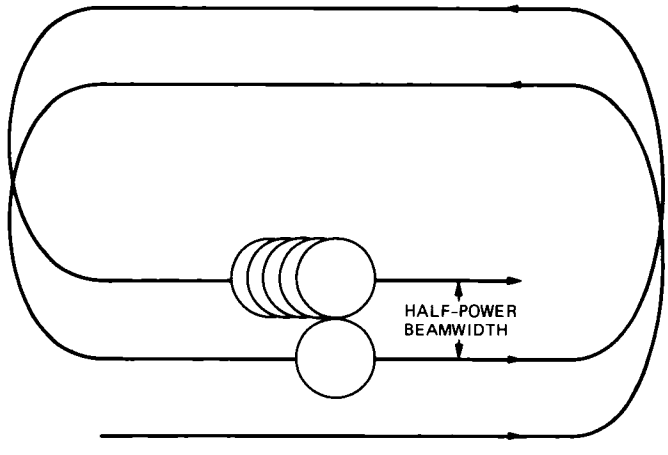

Fig 5 Oval antenna scan pattern Circles represent half-power beam areas

A 2.3-GHz Low-Noise Cryo-FET Amplifier

J Loreman
Radio Frequency and Microwave Subsystems Section

A cryogenically cooled, low-noise Field Effect Transistor (FET) amplifier assembly for use at 2 2 to 2 3 GHz has been developed for the DSN to meet the requirements of a Very Long Baseline Interferometry (VLBI) upgrade An amplifier assembly was developed at JPL that uses a commercial closed-cycle helium refrigerator (CCR) to cool a FET amplifier to an operating temperature of 15 K A cooled probe waveguide-to-coaxial transition similar to that used in the R&D Ultra-Low-Noise S-band Traveling Wave Maser (TWM) is used to minimize input line losses Typical performance includes an input flange equivalent noise contribution of 14 5 K, a gain slope of less than 0 05 dB/MHz across a bandwidth of 2 2 to 2 3 GHz, an input VSWR of 1 5 1 at 2 25 GHz, and an insertion gain of 45 ± 1 dB across the bandwidth of 2 2 to 2 3 GHz Three 2 3-GHz FET/CCR assemblies were delivered to the DSN in the spring of 1987

I. Introduction

A requirement for a broadband low-noise amplifier for 2 2 to 2 3 GHz was established as part of the VLBI upgrade The VLBI requirements did not demand the ultra-low-noise performance of a Traveling Wave Maser (TWM), and as reliability and bandwidth were priorities, the Radio Frequency and Microwave Subsystems Section (Section 333) proposed a design using a cryogenically cooled FET with a helium refrigerator (CCR) operating at 15 K Using this refrigerator rather than the 4 5-K refrigerators used by the TWMs increased reliability, and using the FET guaranteed that the required operational bandwidth was obtainable

The design requirements agreed upon between Section 333 and the VLBI project were an input flange equivalent noise contribution of 20 K maximum, a 1-dB bandwidth of 2 2 to 2 3 GHz, and an insertion gain of 45 dB Although no specification was given for phase delay versus frequency, it was to be measured for each amplifier assembly

II. Design

A. Refrigerator (CCR)

The overriding concern in the selection of the helium refrigerator was to improve the reliability of the FET/CCR over the existing maser helium refrigerators The main detractor in the reliability of the maser refrigerators is the need for a Joule–Thomson (J–T) expansion valve and the attendant helium gas heat exchangers to obtain the necessary 4 5-K operating temperature These refrigerators suffer occasional loss of capacity due to contamination in the helium, which solidifies in the heat exchangers or in the J–T valve There is also a reduction in refrigerator reserve capacity for 4-K operation, compared to 15-K operation, due to the heat load of these components Therefore, a significant increase in reliability is achieved simply by being able to select a refrigerator operating temperature of 15 K instead of 4 5 K The heat capacity of the 15-K CCR is 5 watts at 15 K, the calculated reserve heat capacity of the final design with the RF input and output lines, the amplifier, and all internal com-

ponents would be no less than 3 watts, compared to a typical reserve capacity of 400 to 700 milliwatts for a maser refrigerator with all the maser components installed The CCR vacuum housing and the internal configuration were based on the design used for the successful L-Band Venus Balloon Experiment FET/CCR The CTI, Inc , Model 350 helium refrigerator and compressor were incorporated into the design of the VLBI 2 3-GHz FET/CCR

There are several available helium refrigerators that are smaller than the CTI 350 However, even though a more compact design could be implemented, it was felt that reliability was enhanced with the greater heat capacity In addition, the expansion engine portion of the CTI 350 is essentially interchangeable with the expansion engine used by the maser CCRs and is supportable by the existing spares and maintenance capability in the DSN Figure 1 shows the CTI 350 CCR

B. Amplifier

At the time this project started, Section 333 was in the process of evaluating various commercially available coolable FET amplifiers and had demonstrated excellent noise performance and reliability with amplifiers made by Berkshire Incorporated The Berkshire commercial coolable FET amplifier used a Teflon circuit board substrate that has been very successful for cryogenic use, and has eliminated failures due to microstrip conductor separation and substrate breakage during thermal cycling In addition, Section 333 was evaluating High Electron Mobility Transistor (HEMT) devices being manufactured by General Electric and had successfully installed several of these HEMT devices into the first stage of amplifiers with a similar design This ensured the possibility of later upgrading to a HEMT first-stage device if these could be proven reliable for this project For these reasons, it was decided to incorporate the Berkshire FET amplifier into the design of the assembly Figure 2 shows the Berkshire amplifier mounted on the 15-K stage of the FET/CCR assembly (the vacuum jacket and radiation heat shields have been removed) Although the three amplifier assemblies were completed as FETs, the success of a 2 3-GHz HEMT/CCR installation at DSS-13 [1] demonstrates that these assemblies can be upgraded when desired to incorporate HEMT devices in the first stage As the gain of the cryogenically cooled FET amplifier is 34 to 37 dB, a room-temperature postamplifier and a variable attenuator were incorporated into the design to provide a nominal insertion gain of 45 dB The amplifier is protected from interfering signals above 3 3 GHz by a low-pass filter Figure 3 shows an RF schematic of the FET/CCR assembly

C. Waveguide-to-Coaxial Transition

To take advantage of the noise performance of the FET device and to eliminate the need for an input isolator, a broadband low-loss input line with good VSWR was required for the implementation of the VLBI 2 3-GHz FET/CCR In order to provide a substantial CCR heat capacity reserve, a design was required that also minimized heat transfer from the ambient temperature portion of the input line to the 15-K portion of the refrigerator A cryogenically cooled coaxial probe transmission line was first designed and implemented in 1973 for the 4 5-K, 2 3-GHz TWM/CCR [2] This input line was recently redesigned for 1 668 GHz and implemented in the DSN in a FET/CCR assembly used for the Venus Balloon Experiment [3] At an RF probe temperature of 4 5 K, the original input line contributed less than 0 1 K of the equivalent excess noise of the TWM noise temperature In the Venus Balloon FET/CCR, the input line contributed approximately 0 5 K equivalent noise temperature due to the increased RF probe physical temperature of 12 to 15 K The noise temperature contribution of the present 2 3-GHz cold probe input assembly is also estimated to be 0 5 K Figure 4 shows the final design of the 15-K, 2 3-GHz probe Figure 5 shows the assembled probe and waveguide transition

III. Performance

All performance goals were met with the 2 3-GHz FET/CCR the nominal cool-down time of the FET/CCR is 4 hours, the final stage operating temperature is 12 K, and the measured refrigerator reserve capacity exceeds 3 watts on all three FET/CCR assemblies Measurements of VSWR, gain, and phase delay were made on the prototype and deliverable FET/CCR assemblies with the Hewlett-Packard HP 8510 network analyzer Figure 6 shows plots of input VSWR, insertion gain, and phase versus frequency for a typical 2 3-GHz FET/CCR Noise temperature data were measured using a calibrated 2 3-GHz microwave horn at the zenith position and a section of microwave-absorbing material to obtain Y-factor power measurements between the "cold" sky and an ambient temperature load [4], [5] The absorber was placed over the horn aperture to provide the ambient temperature load The noise temperature instrumentation consisted of a 2 3-GHz horn connected to the input waveguide and the output of the FET/CCR assembly connected to a 2 3-GHz transistor amplifier with 23-dB gain, an isolator, a tunable 2 3-GHz filter with a bandpass of 10 MHz, a Hewlett-Packard 8484A power sensor, and an HP 436A digital power meter Figure 7 shows the schematic of the noise temperature measurement setup The equivalent input noise temperature of the FET/CCR assembly and the test amplifier may be calculated from the relationship

$$T_r = \frac{T_a - YT_h}{Y - 1}$$

where T_r is the equivalent input noise temperature of the FET/CCR system at the room-temperature input waveguide flange, in K, T_a is the physical temperature of the ambient

load, in K, T_h is the theoretical value of the sky background noise plus the noise contributed by the calibrated 2.3-GHz horn, and Y is the actual numerical ratio of the power ratio established by the measurement. Table 1 shows the measured values of equivalent input noise temperature for the three delivered FET/CCRs. The values have been corrected for the follow-on contribution of the measurement amplifier setup.

IV. Conclusions

All performance requirements for the 2.3-GHz FET/CCR system have been met, and the MTBF is expected to be 1 year. The completed 2.3-GHz FET/CCR assembly is shown in Fig. 8. Future plans include the incorporation of a HEMT device in the first stage of the Berkshire amplifier.

Acknowledgments

Thanks to Dean Norris for his work in matching the WR 430 waveguide and coaxial probe prototype, and for his assistance in the assembly of the FET/CCRs delivered to the DSN. Thanks to both Dean Norris and Leroy Tanida for assistance in the network analyzer measurements and in the noise temperature measurements.

References

[1] L. Tanida, "A 2.3-GHz Cryogenically Cooled HEMT Amplifier for DSS-13," *TDA Progress Report 42-91*, July–September 1987, Jet Propulsion Laboratory, Pasadena, California, pp. 94–101, November 15, 1987.

[2] R. Clauss and E. Wiebe, JPL Technical Report 32-1526, vol. XIX, February 15, 1974.

[3] D. Norris, "Low Noise Cryogenic Transmission Line," *TDA Progress Report 42-91*, July–September 1987, Jet Propulsion Laboratory, Pasadena, California, pp. 89–93, November 15, 1987.

[4] C. T. Stelzried, "Operating Noise-Temperature Calibrations of Low-Noise Receiving Systems," *Microwave J.*, vol. 14, no. 6, pp. 41–48, June 1971.

[5] C. T. Stelzried, *The Deep Space Network Noise Temperature Concepts, Measurements, and Performance*, JPL Publication 82-33, Jet Propulsion Laboratory, Pasadena, California, pp. 12-1–12-8, September 1982.

Table 1 Equivalent input noise contribution

FET/CCR	Noise contribution, K		
	2 2 GHz	2 25 GHz	2 3 GHz
No 1	14 0	14 4	16 3
No 2	17 6	16 9	17 5
No 3	10 7	12 1	11 0

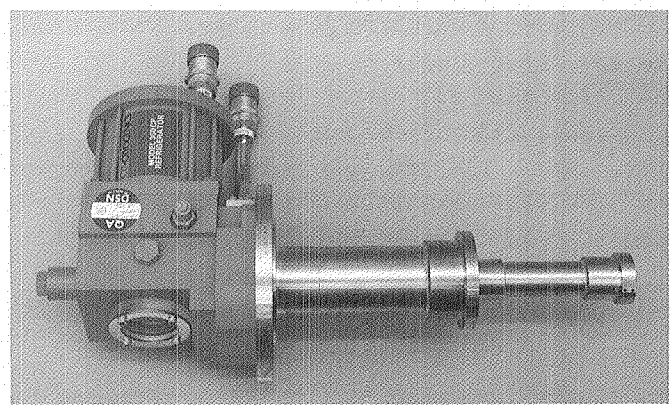

Fig. 1. CTI 350 refrigerator

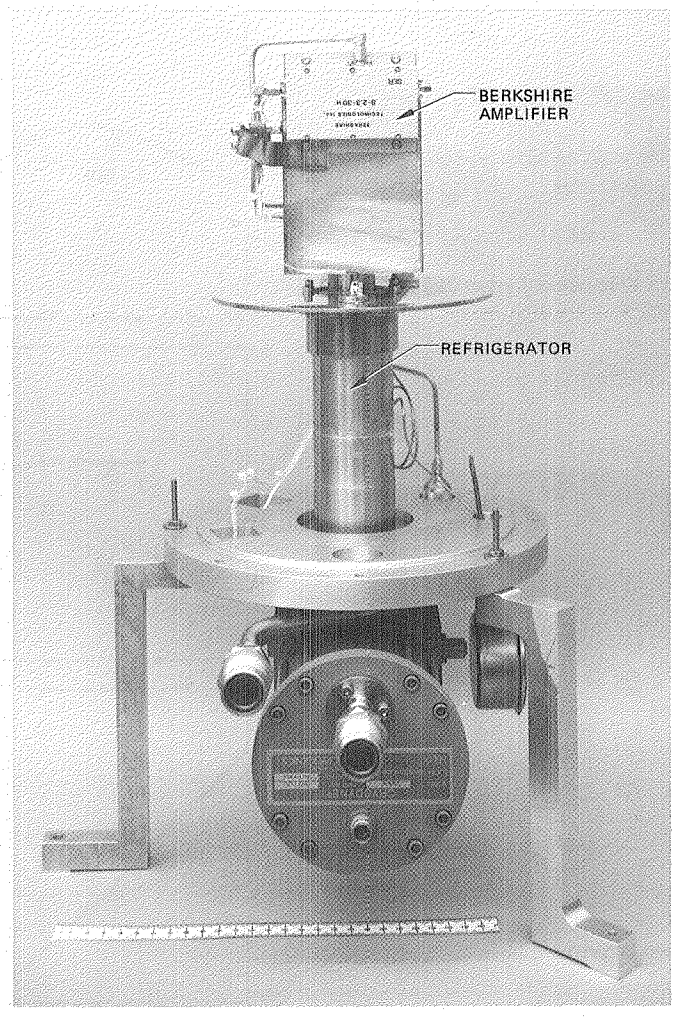

Fig. 2. Berkshire amplifier mounted on the 15-K station of the FET/CCR assembly (vacuum jacket and radiation heat shields removed)

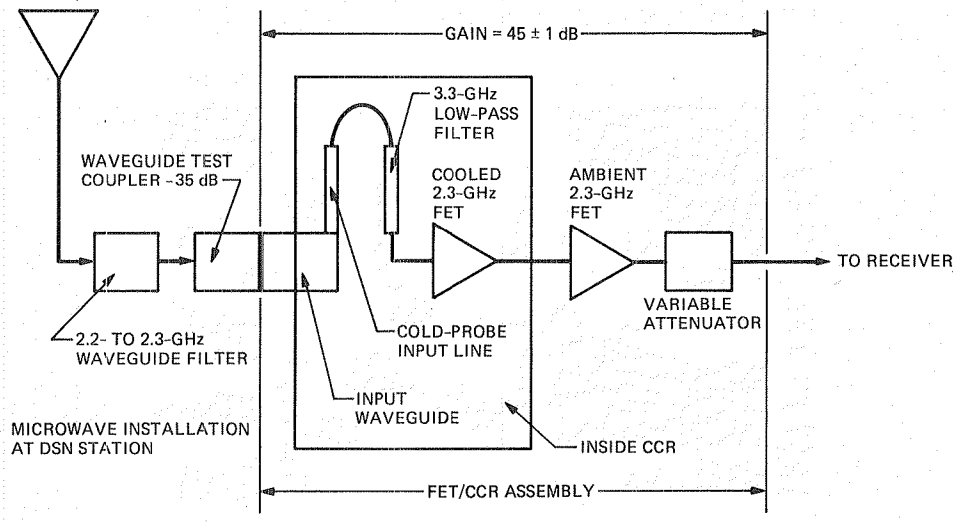

Fig. 3. RF schematic of the FET/CCR assembly

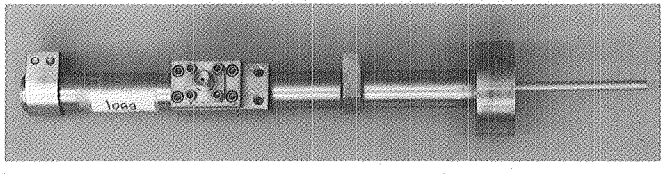

Fig. 4. Cryogenically cooled 2.3-GHz coaxial input line for use at 15 K

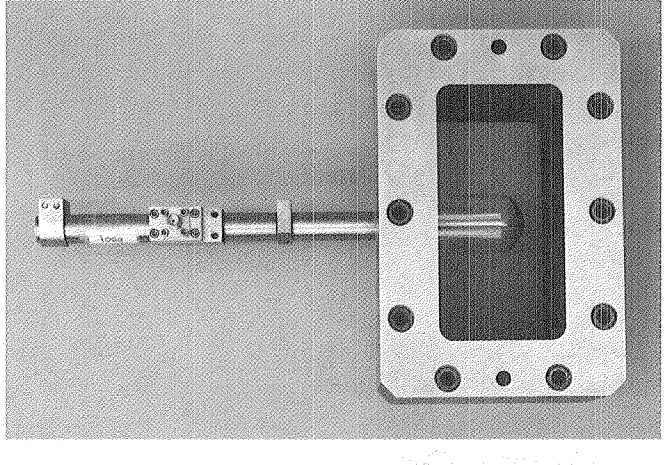

Fig. 5. Waveguide with coaxial probe installed

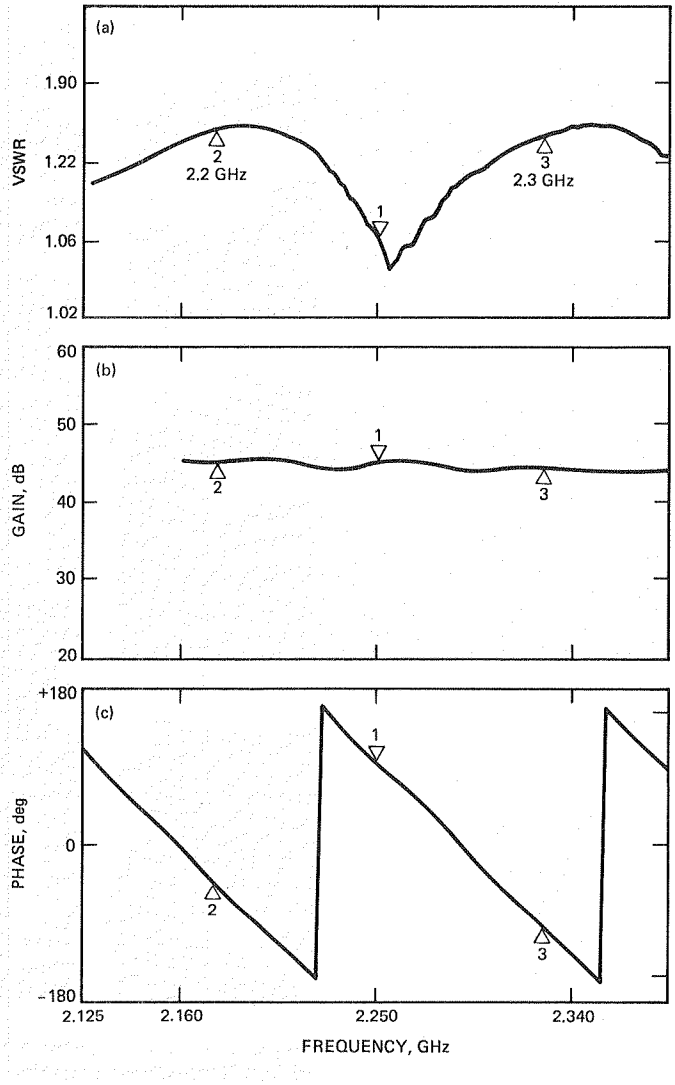

Fig. 6. Input VSWR, insertion gain, and phase versus frequency for a typical 2.3-GHz FET/CCR

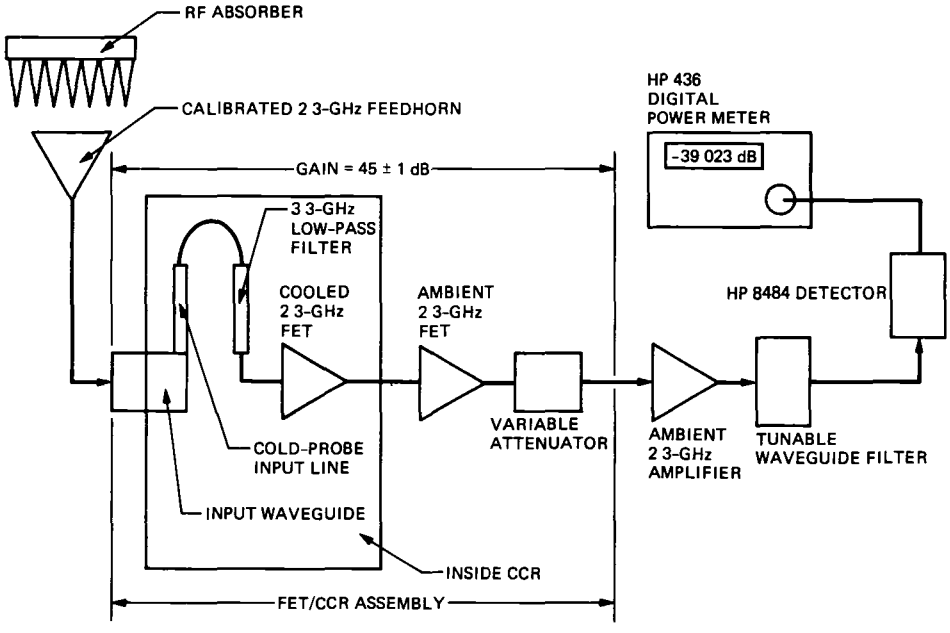

Fig 7 Noise temperature setup

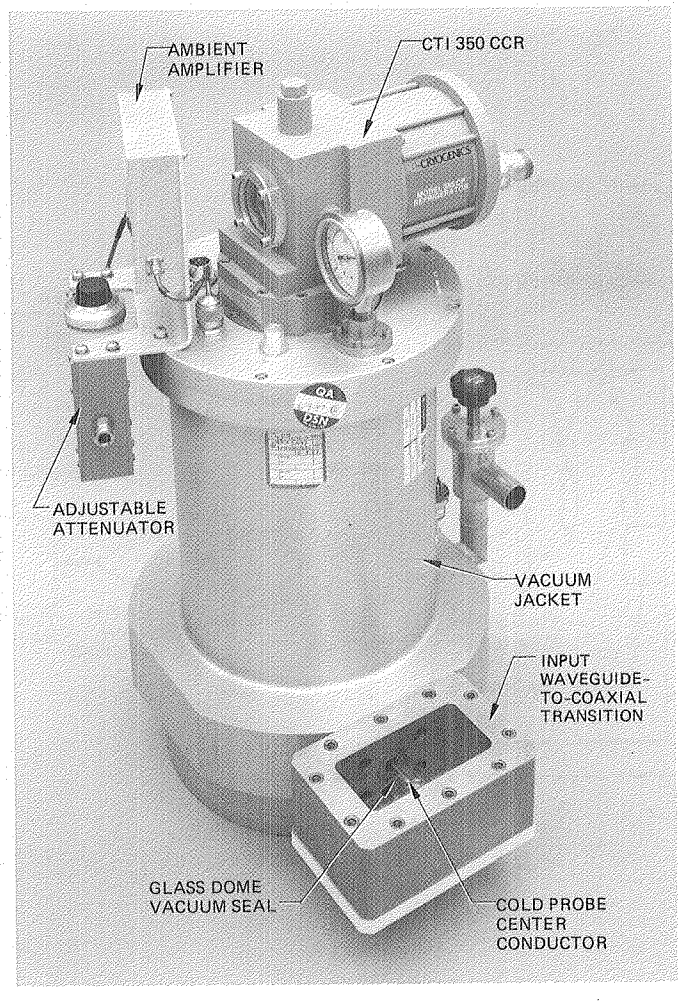

Fig. 8. The 2.3-GHz FET/CCR assembly

A Digitally Implemented Phase-Locked Loop Detection Scheme for Analysis of the Phase and Power Stability of a Calibration Tone

A C Densmore
Telecommunications Systems Section

A digital phase-locked loop (PLL) scheme is described which detects the phase and power of a high SNR calibration tone. The digital PLL is implemented in software directly from the description given in this article. It has been used to evaluate the stability of the Goldstone Deep Space Station open loop receivers for Radio Science. Included is a derivation of the Allan variance sensitivity of the PLL imposed by additive white Gaussian noise, a lower limit is placed on the carrier frequency.

I. Introduction

To facilitate the evaluation of the phase and gain stability of the DSN open loop receivers for Radio Science, a detection scheme was developed. Radio Science objectives accommodated include the study of the atmospheres and ionospheres of the planets and satellites by means of radio occultation of a signal sent from a spacecraft and received at Earth (at a Deep Space Station). The stability of the receivers directly affects the quality of the science return of the experiment.

The process of testing station stability supported by this detection scheme involves three stages. The first stage consists of running the test and digitally recording the calibration tone on tape. The tone is generated at 2.3 GHz or 8.4 GHz and is downconverted to an intermediate frequency inside the antenna, cabled to the Signal Processing Center, where it is further downconverted by the IF-to-video converter, and then sampled by an analog-to-digital converter and recorded on tape. The second stage in testing station stability is detection of the calibration tone frequency (phase) and power as functions of time from the voltage samples recorded on the tape, the detection is accomplished by computer software that directly implements the scheme presented in this article. The detected frequency and power are stored in a computer data file. The last stage involves postprocessing the detected data file to yield suitable statistical measures of the calibration tone stability. These measures include Allan variance [4] as a measure of frequency stability, phase variation plotted as a function of time, power spectral plots of the detected frequency and tone power, and simple plots of the detected frequency and tone power. The scheme presented in this article is an implementation of the second stage, detection of the frequency (phase) and power of the tone. This article does not discuss the details of the latter postprocessing stage, although the theoretical noise-limited Allan variance is derived.

The input signal intended for this detection scheme is assumed specifically to consist of a single tone centered in a narrow (relative to the sample rate) band of noise with a high signal-to-noise ratio. Recent DSN calibration tone tests have

provided a 40 to 50 dB-Hz SNR with a 100-Hz noise bandwidth which corresponds to a 20- to 30-dB signal-to-noise ratio These values are high enough to allow practical use of a noncoherent square-law power detector

In Sections III and IV, the linearized, continuous-time model of the detector is analyzed The continuous-time analysis of the discrete-time phase-locked loop (PLL) is justified by the assumption that the product of the PLL loop noise bandwidth and the sample period is much less than unity, i e , $PLLBW \cdot T \ll 1$ Section II discusses the block diagram and its digital implementation, from which the software is directly written, the software is the implementation of the PLL presented in this article and detects the phase and power information from the previously recorded calibration tone voltage samples The concluding Section V cites some of the results obtained using this scheme for DSN tests

II. Implementation

The heart of this detection scheme is a second order phase-locked loop In this section, the block diagram is presented and described

Figure 1 is the block diagram of the PLL detector The left-hand side of Fig 1 is a noncoherent tone-power detector used to normalize the amplitude of the input sinusoid, it is described in further detail in Section IV The upper right-hand corner of Fig 1 is the phase-locked loop circuit, it consists of a loop filter, a numerically controlled oscillator (NCO), a mixer, and a low-pass filter (LPF_1) The frequency of the NCO is directly proportional to its numerical input The mixer is used as a coherent phase detector, and the low-pass filter serves as a harmonic rejection filter by assisting the loop filter in attenuating the mixer second harmonic to afford greater choice of input carrier frequency, as explained in Section IIIC The PLL is described in further detail in Section III In order to detect that the loop is in lock, a lock detector is implemented, as shown in the lower right-hand corner of Fig 1 Assuming that the input sinusoid amplitude is properly normalized, the lock detector output takes the value unity in the phase-locked state If the loop is offset by a phase error ϕ, the lock detector output takes the value $\cos\phi$

The overall detector is implemented in software directly from the block diagram A bilinear s- to z-domain transformation is used to implement each function in discrete time given the corresponding s-domain transfer function

$$s = \left(\frac{2}{T}\right)\left(\frac{1 - z^{-1}}{1 + z^{-1}}\right) \tag{1}$$

where T is the sample period in seconds

This transform has the property that a single pole low-pass filter transformed to a discrete time recursive filter appears nearly as the same single pole filter at frequencies less than one-tenth the sampling rate and has a zero at half the sampling rate

Below are the bilinear transforms of the loop filter, the high-pass filter, and the low-pass filters Canonic form digital implementations for each are given in Fig 2

Loop filter

$$s\text{-domain} \quad F(s) = \frac{1 + as}{bs} \tag{2}$$

$$\text{bilinear transform} \quad F(z) = \frac{T + 2a}{2b} \; \frac{1 + z^{-1}\dfrac{T - 2a}{T + 2a}}{1 - z^{-1}} \tag{3}$$

High-pass filter

$$s\text{-domain} \quad H(s) = \frac{1}{1 + \dfrac{c}{s}} \tag{4}$$

$$\text{bilinear transform} \quad H(z) = \frac{2}{2 + cT} \; \frac{1 - z^{-1}}{1 - z^{-1}\dfrac{2 - cT}{2 + cT}} \tag{5}$$

Low-pass filter

$$s\text{-domain} \quad K(s) = \frac{1}{1 + \dfrac{s}{d}} \tag{6}$$

$$\text{bilinear transform} \quad K(z) = \frac{dT}{2 + dT} \; \frac{1 + z^{-1}}{1 - z^{-1}\dfrac{2 - dT}{2 + dT}} \tag{7}$$

III. Frequency Detection

Presented in this section is a detailed discussion of the choice of loop parameters and a discussion of the use of Allan variance as a measure of frequency stability A lower limit on the allowable input carrier frequency is derived by consideration of its effect on the Allan variance measure

A. Linear Loop Analysis

Consider the second order, baseband, linear PLL in the s-domain The PLL input is the radian phase $\theta(t)$, and the output is the detected radian frequency $\hat{\omega}(t)$ The forward gain path is the loop filter, $F(s) = (1 + as)/bs$, and the negative feedback path is an integrator, $G(s) = 1/s$ By Mason's rule, the closed loop transfer function [3] is given by

$$L(s) = \frac{F(s)G(s)}{1 + F(s)G(s)} = \frac{1 + as}{1 + as + bs^2} \tag{8}$$

The one-sided loop noise bandwidth is given by the following expression [1]

$$PLLBW = \frac{1}{2\pi}\int_0^{\infty} |L(j\omega)|^2 \, d\omega = \frac{a^2 + b}{4ab} \tag{9}$$

In order to evaluate the output of the PLL, the transfer function from input phase to output detected frequency is derived by Mason's rule

$$W(s) \doteq \frac{\hat{\omega}_{out}}{\theta_{in}}(s) = \frac{s(1 + as)}{1 + as + bs^2} \tag{10}$$

It is convenient to define the parameter $R \doteq a^2/b$ By manipulating Eq (9), the following relations are revealed

$$a = \frac{R + 1}{4(PLLBW)}, \qquad b = \frac{a^2}{R} \tag{11}$$

The system characteristic equation is

$$1 + \frac{1}{Q}\left(\frac{s}{\omega_n}\right) + \left(\frac{s}{\omega_n}\right)^2 \tag{12}$$

where

$$Q = \frac{1}{\sqrt{R}} \tag{13}$$

This reveals that R is the loop damping parameter Jaffee and Rechtin [2] specify optimum loop performance with $R = 2$ when the initial phase is unknown but uniformly distributed as a random variable Unless stated otherwise, R is assumed to equal 2 throughout the remainder of this article $R = 2$ makes the system slightly underdamped

B. Allan Variance

Allan variance is a statistical measure of the frequency stability of a signal It is a measure of fractional frequency fluctuations rather than absolute frequency fluctuations, a fluctuation of 1 Hz in a 10-GHz tone represents a lower Allan variance than the same 1-Hz fluctuation in a 10-MHz tone The sensitivity of the Allan variance measure is limited by the input noise, with too much noise the Allan variance measures only the noise The following defines the theoretical Allan variance in the case of detecting with the second order PLL the frequency of a pure tone with a high signal-to-noise ratio in a band of additive white Gaussian noise (AWGN)

A convenient estimate of Allan variance is given below as defined in Eq (4 22) of [4]

$$\sigma_y^2(\tau) = \frac{1}{2(M-1)}\sum_{i=1}^{M-1} [\bar{y}_{i+1}(\tau) - \bar{y}_i(\tau)]^2 \tag{14}$$

where

$$\bar{y}_i(\tau) = \frac{1}{\tau}\int_{(i-1)\tau}^{i\tau} \frac{\hat{\omega}(t)}{2\pi\nu_0}\, dt$$

where ν_0 is the nominal frequency of the calibration tone prior to any downconversion, $\sigma_y(\tau)$ is the RMS value of all the two-sample variances taken over the entire set of data A single two-sample variance is given by $[\bar{y}_{i+1}(\tau) - \bar{y}_i(\tau)]/\sqrt{2}$ The two-sample variance function, $p(t,\tau)$, is defined as the difference between two consecutive averages of a function, each taken over a period τ and normalized by $\sqrt{2}$

$$p(t,\tau) = \begin{cases} \dfrac{-1}{\tau\sqrt{2}}, & -\tau \leqslant t < 0 \\ \dfrac{1}{\tau\sqrt{2}}, & 0 \leqslant t < \tau \\ 0 & \text{otherwise} \end{cases} \tag{15}$$

The theoretical Allan variance of the fractional detected frequency at the output of the PLL is the statistical mean of the square of the convolution of the two-sample variance function $p(t,\tau)$, with the fractional detected frequency output of the PLL $\hat{f}(t)/\nu_0 = \hat{\omega}(t)/2\pi\nu_0$

$$\sigma_y^2(\tau) = E\left\{[(\hat{f}(t)/\nu_0) * p(t,\tau)]^2\right\} \tag{16}$$

$$\doteq \text{power in } (\hat{f}(t)/\nu_0) * p(t,\tau)$$

$$= \int_{-\infty}^{\infty} S(f)P(f,\tau)df \qquad (17)$$

where $P(f,\tau)$ = the power spectrum of the two-sample variance function [squared magnitude of the Fourier transform of $p(t,\tau)$]

$$P(f,\tau) = \frac{2\sin^4 \pi\tau f}{(\pi\tau f)^2} \qquad (18)$$

and $S(f)$ = the power spectrum of the detected fractional frequency due to AWGN about a pure tone input to the PLL

$$S(f) = S_\theta(f)\left|\frac{W(j2\pi f)}{2\pi\nu_0}\right|^2 \qquad (19)$$

where $S_\theta(f)$ = the phase power spectrum input to the PLL due to AWGN about a pure tone with high SNR

Narrowband, high SNR AWGN about a pure carrier represents a white phase noise power spectrum, $S_\theta(f)$, about the carrier with the same narrow band

$$S_\theta(f) = \frac{1}{2SNR}\ (\text{rad}^2/\text{Hz}), \qquad |f| < B_N/2 \qquad (20)$$

where B_N = input noise bandwidth By substitution,

$$\sigma_y^2(\tau) = \int_{-\infty}^{\infty} \frac{1}{8\pi^2\nu_0^2\, SNR}\left|\frac{j2\pi f(1+aj2\pi f)}{1+aj2\pi f - b4\pi^2 f^2}\right|^2 \times \frac{2\sin^4\pi\tau f}{(\pi\tau f)^2}\, df \qquad (21)$$

Numerical integration yields

$$\sigma_y^2(\tau) \Rightarrow \frac{3(PLLBW)}{4\pi^2\nu_0^2\, SNR\, \tau^2}, \qquad \tau(PLLBW) \gg 1 \qquad (22)$$

On a log-log plot of $\sigma_y(\tau)$ as a function of τ, the noise-limited Allan variance plotted for several detection loop bandwidths takes the shape of parallel lines each with a negative unity slope, this is shown in Fig 3 with $\nu_0^2\, SNR \approx 7.6 \times 10^{20}$ The individual plots are only shown for τ such that $\tau(PLLBW) > 1$, this is the only domain over which the SNR-limited Allan variance log-log plot has the negative unity slope By plotting only over this domain, any peculiar shape immediately draws attention to some phenomenon other than high SNR AWGN Note that the reduction of detection loop bandwidth to improve the Allan variance sensitivity further limits the minimum τ over which the Allan variance may be evaluated

C. Minimum Input Carrier Frequency

Consideration of the significance of the mixer sum product places a lower limit on the input carrier frequency for this detection scheme without acting as a detriment to the Allan variance frequency stability measurement This serves as a criterion for selecting the carrier frequency It is assumed that sampling does not disturb the two-to-one second- to first-carrier harmonic frequency relationship The criterion is that the Allan variance due to the harmonic term alone must be much less than the Allan variance due to the phase difference term alone

First let us consider the phase difference term The Allan variance was derived previously and is summarized below, but here absolute rather than fractional frequency variance is considered, so the ν_0^2 term is removed from Eq (22)

$$\sigma_y^2(\tau)\Big|_{\theta(t),\text{abs}} = \frac{3(PLLBW)}{4\pi^2 SNR\tau^2} \qquad (23)$$

Now consider the (absolute) Allan variance due to the second harmonic tone

$$\sigma_y^2(\tau)\Big|_{2f_0,\text{ abs}} = \int_{-\infty}^{\infty} S_2(f)P(f)\, df \qquad (24)$$

Recall that

$$P(f) = \frac{2\sin^4 \pi\tau f}{(\pi\tau f)^2} \qquad (25)$$

$S_2(f)$ is the power spectrum at the detector output due only to the second harmonic term Assuming zero loop gain at the second harmonic frequency, $S_2(f)$ is the product of the power spectrum of the second harmonic tone, the harmonic rejection filter response, and the loop filter response

$$S_2(f) = P\left[\frac{1}{2}\delta(f+2f_0) + \frac{1}{2}\delta(f-2f_0)\right]\left|LPF_1(j2\pi f)\right|^2\left|\frac{F(j2\pi f)}{2\pi}\right|^2 \qquad (26)$$

$P = 1/2$ is the power in the second harmonic tone at the output of the mixer Assuming the second harmonic is much higher than the corner frequencies of the filters, the follow-

ing approximations hold The corner frequency of the harmonic rejection filter is made equal to ten times the one-sided loop noise bandwidth so as to only negligibly affect the loop response

$$\left|LPF_1(j\,2\pi 2f_0)\right|^2 = \frac{1}{1+(2f_0/10\,PLLBW)^2} \Rightarrow \frac{25\,PLLBW^2}{f_0^2} \tag{27}$$

$$\left|\frac{F(j\,2\pi 2f_0)}{2\pi}\right|^2 \Rightarrow \left(\frac{2R\,PLLBW}{\pi(R+1)}\right)^2 \tag{28}$$

$$P(f) \Rightarrow \leqslant \frac{2}{(\pi\tau 2f_0)^2} \tag{29}$$

By substituting Eqs (26)–(29) into Eq (24) and comparing Eqs (23) and (24),

$$\sigma_y^2(\tau)\Big|_{2f_0} \ll \sigma_y^2(\tau)\Big|_{\theta(t)} \tag{30}$$

$$\frac{25\,PLLBW^4\,R^2}{\pi^4 f_0^4 (R+1)^2\tau^2} \ll \frac{3\,PLLBW}{4\pi^2 SNR\tau^2}$$

Solving for carrier frequency yields the following lower limit imposed by Allan variance detriment by the second carrier harmonic

$$f_0\Big|_{R=2} \gg SNR^{1/4} \times PLLBW^{3/4} \tag{31}$$

IV. Power Detection

The amplitude detector in Fig 1 consists of a square-law power detector preceded by a DC-blocking high-pass filter, and sinusoidal amplitude is estimated as the square root of twice the detected power $A \approx \sqrt{2(A^2/2+\sigma_N^2)}$ The perfectly smoothed square-law detected power is $A^2/2+\sigma_N^2$, but there is an uncertainty in the power detector output due to the finite smoothing of the post-detection filter, the purpose of this section is to specify the uncertainty

The signal input to the detector is assumed to have the form $A\cos\omega_C t + n(t)$, where $n(t) = \sqrt{2}n_c(t)\cos\omega_C t + \sqrt{2}n_s(t)\sin\omega_C t$ By narrowband noise theory, n_c and n_s are zero mean, uncorrelated, independent, low-pass, band-limited AWGN signals each with a two-sided bandwidth B_N and a two-sided power spectral density $N_0/2$ B_N is assumed to be much smaller than the sample rate

In [5] it is shown that the two-sided power spectrum at the output of the mixer is given by the following Equation (12-62) of [5] is rewritten below in the terms used in this article

$$S_{yy}(f) = (P+N_0B_N)^2\,\delta(f) + \begin{cases} 2PN_0, & 0<|f|\leqslant B_N/2 \\ 0 & \text{otherwise} \end{cases} + \begin{cases} N_0^2(B_N-|f|), & 0<|f|\leqslant B_N \\ 0 & \text{otherwise} \end{cases} \tag{32}$$

Second harmonic terms are neglected here with the assumption that the postdetection filter removes them, and $P = A^2/2$

Generally the postdetection low-pass filter noise bandwidth, $AGCBW$, is much smaller than the input noise bandwidth, i e , $AGCBW \ll B_N$ This allows the approximation, except for the impulse at the origin, that the power spectrum at the mixer output, $S_{yy}(f)$, is a constant equal to its value near DC In this case the total noise power at the output of the postdetection filter is given by the following expression

$$P_N \approx 2(2PN_0 + N_0^2B_N)AGCBW \tag{33}$$

The power in the desired signal is the DC component

$$P_S = (P+N_0B_N)^2 \tag{34}$$

The signal to total noise power ratio at the output of the square-law power detector is given by

$$SNR_{PD} = \frac{P_S}{P_N} = \frac{(SNR+B_N)^2}{2(2SNR+B_N)AGCBW} \tag{35}$$

where $SNR = P/N_0$ is the input signal to noise density power ratio Consider the normalized postdetection noise variance

$$\sigma^2 = \frac{1}{SNR_{PD}} \tag{36}$$

A simple definition of detection uncertainty (error bar) is given by

$$2\sigma\Big|_{dB} = 40 \log (1 + \sigma) \tag{37}$$

Substituting for σ yields the error bar for the power detection or tone power detection uncertainty

$$2\sigma\Big|_{dB} = 40 \log \left(1 + \sqrt{\frac{2(2SNR + B_N)AGCBW}{(SNR + B_N)^2}}\right) \tag{38}$$

V. Conclusion

The digital PLL detection scheme presented in this article has been used to evaluate the stability of the DSN open loop receivers as described in the introduction The results obtained have been very satisfactory The discoveries made using this scheme for calibration tone stability tests include the detection of a 200-millihertz frequency-modulated tone in an 8 4-GHz carrier and calibration tone frequency offsets on the order of microhertz This scheme has been used to evaluate tone generator–receiver system phase stability with a root Allan variance sensitivity of 10^{-17} at a 1000-second integration time The accuracy of this detection scheme depends only on the accuracy with which the software records individual parameters FORTRAN double precision variables are accurate up to 14 significant digits

The processing time required to detect from a three-hour digital recording the phase and power of each of two tones recorded simultaneously on separate channels at a 200-Hz sample rate, and to complete the differential and Allan variance postprocessing, was approximately eight hours using a FORTRAN 77 compiler on the PRIME 550 CPU in the JPL Radio Occultation Data Analysis (RODAN) facility

References

[1] G C Newton, L A Gould, and J F Kaiser, *Analytical Design of Linear Feedback Controls*, New York Wiley, 1957

[2] R M Jaffee and E Rechtin, "Design and Performance of Phase Locked Circuits Capable of Near-Optimum Performance Over a Wide Range of Input Signal and Noise Levels," *IRE Transactions on Information Theory*, vol IT-1, pp 66–76, March 1955

[3] R C Tausworthe, *Theory and Practical Design of Phase Locked Receivers*, vol I, JPL Technical Report 32-819, Jet Propulsion Laboratory, Pasadena, California, February 1966

[4] J Rutman, "Characterization of Phase and Frequency Instabilities in Precision Frequency Sources Fifteen Years of Progress," *Proc IEEE*, vol 66, no 9, pp 1048–1075, September 1978

[5] W B Davenport, Jr , *An Introduction to the Theory of Random Signals and Noise*, New York McGraw-Hill, pp 259–263, 1958

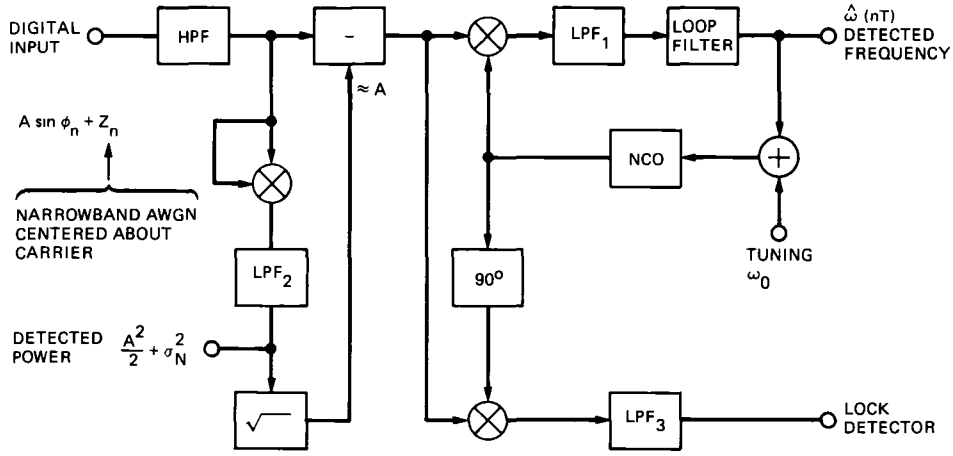

Fig. 1 Functional block diagram of PLL detector

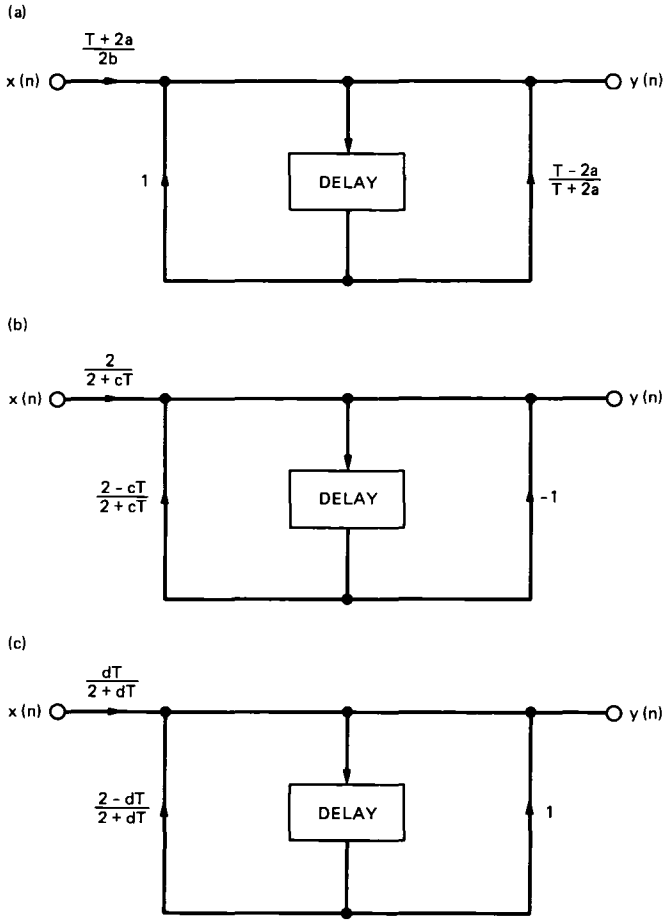

Fig 2 Canonic form digital implementations (a) loop filter, (b) high-pass filter, (c) low-pass filters

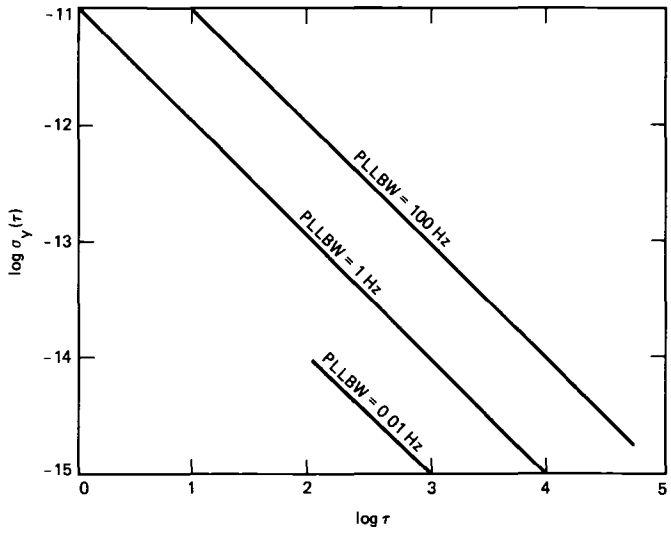

Fig 3 General SNR-limited Allan variance

An 8.4-GHz Dual Maser Front End for Parkes Reimplementation

D L Trowbridge, J R Loreman, and T J Brunzie
Radio Frequency and Microwave Subsystems Section
B Jenkins
Canberra Deep Space Communications Complex

An 8 4-GHz front-end system consisting of a feedhorn, a waveguide feed assembly, dual masers, and downconverters is being reimplemented at Parkes as part of the Parkes–Canberra Telemetry Array for the Voyager Neptune encounter The front-end system was originally assembled by the European Space Agency on the Parkes antenna for the Giotto project It was also used on a time-sharing basis by the DSN as part of the Parkes–Canberra Telemetry Array to enhance the data return from Voyager 2 at Uranus At the conclusion of these projects in 1986, the front-end system was dismantled, packed, and shipped to Europe Part of the system was then shipped to JPL on loan for reimplementation at Parkes for the Voyager Neptune encounter The system is being redesigned and refurbished for operation at Parkes Tasks include new microwave front-end control cabinets, a closed-cycle refrigeration data acquisition system, a new noise-adding radiometer system, a front-end controller assembly, and refurbishment of the dual 8 4-GHz traveling-wave masers (TWMs) and waveguide feed system

I. Introduction

The 8 4-GHz front-end system was installed on the Parkes antenna in 1985 It was originally assembled by the European Space Agency (ESA) for the Giotto project The RF package (Fig 1), containing a waveguide feed system, dual traveling-wave maser and closed-cycle refrigerator assemblies (TWM/CCRs or TWMs), and the TWM monitor and control instrumentation, was built by Airborne Instrument Laboratories (AIL) JPL provided the waveguide feed system, the TWM design based on the JPL Block IIA TWM [1], the TWM monitor and control instrumentation design, and technical consulting during the manufacturing and testing of the system As a result of an agreement between NASA/JPL and ESA, the front-end system was also used on a time-sharing basis by the DSN as part of the Parkes-Canberra Telemetry Array to enhance the data return from Voyager 2 at Uranus At the conclusion of these projects in 1986, the front-end system was dismantled, packed, and shipped to Europe Part of the system was then shipped to JPL on loan for reimplementation at Parkes for the Voyager Neptune encounter New developments to make the system operable at Parkes include new microwave front-end control cabinets, a closed-cycle refrigeration (CCR) data acquisition system, a new noise-adding radiometer (NAR) system, a front-end controller (FEC) assembly, and refurbishment of the dual 8 4-GHz traveling-wave masers (TWMs) and waveguide feed system

During the upcoming Voyager Neptune encounter, ESA will no longer be responsible for the maintenance and operation of the Parkes antenna front-end system As the decision

has been made not to replicate the ESA-designed monitor and control system (designed around an HP computer), a new system will be built around an Intel Multibus computer similar to the PCTA receiver/combining system Advantages of this approach include automated operation with the PCTA Parkes site, the availability of status information (and to some extent control) remotely at the Canberra site, and the ability to share common spares with PCTA equipment

In addition to the front-end monitor and control, a noise-adding radiometer (NAR) function will be added to the system Intended primarily to aid antenna pointing calibration procedures, the NAR will be capable of monitoring system temperature either pre-pass or during Voyager tracking

II. Parkes Front-End Description for the 1986 Uranus Encounter

The 1986 configuration consisted of the following

(1) Aerial cabin equipment, which included the feed and all microwave components, TWM low-noise amplifiers, downconverters, an upconverter, test signal switching, noise diode assemblies, and a monitor receiver

(2) Control room (pedestal) equipment, which included all monitoring and control for the front end

(3) A compressor room, which contained the helium compressors for the CCRs

The feedhorn assembly was located at the primary focus of the antenna and was connected to a rotatable polarizer and an orthomode transducer The system then provided two identical receive channels (for redundancy) using TWMs based on the JPL Block IIA TWMs and operating at 8425 MHz (nominal) with a 100-MHz bandwidth Downconversion to 325 MHz (nominal) was accomplished with two identical downconverters using fixed-frequency local oscillators at 8100 MHz phase-locked to the station 5-MHz timing Either of the 325-MHz downconverter outputs could be selected as the input to the short-loop telemetry receiver (not part of the front-end system)

A single monitor receiver with switchable input was provided for monitoring the masers The 8 4-GHz input signal to the monitor receiver was obtained from couplers located in each of the downconverters The local oscillator for the monitor receiver was also obtained from the downconverters, and hence the monitor receiver input switching selected both the 8 4-GHz input signal and the local oscillator as a pair Output was selected at 325 MHz (nominal)

The test signal injection system consisted of a programmable synthesizer operating at 425 MHz (nominal), an upconverter known as the X-band test generator, and a test signal switching and distribution network that allowed selection of different test signals to either maser input or output

The synthesizer output could be phase-modulated with high-rate data from an external source and was coherent with station timing Upconversion to 8425 MHz was accomplished with an 8000-MHz fixed-frequency local oscillator that was also coherent with station timing A wideband output for maser bandpass measurement and a narrowband output for telemetry testing were provided on the upconverter

The switching network consisted of a monitor/test signal/oscillator assembly and two TWM calibration assemblies based on JPL designs A test oscillator with no power supply was included but not used

The noise-adding radiometer consisted of a noise diode assembly and power supply for each maser, a square-law detector operating at 325 MHz from the monitor receiver, and a frequency counter The noise diode output power levels were continuously adjustable and could be modulated by an external source The noise output of each assembly was fed to the pre-maser coupler via a hybrid in the corresponding TWM calibration assembly Noise power was detected with a square-law detector, and the output frequency of the detector was coupled into a frequency counter that interfaced with the HP computer system

The highly automated front-end monitor and control (M&C) was based on a Hewlett-Packard system with bus extenders from the control room to the aerial cabin The HP system controlled the waveguide switches and polarizer and interfaced to both downconverters, the monitor receiver, and the upconverter to provide monitoring of 17 different failure alarms Another interface to the dual TWM control assembly was used to control the test injection switching and to monitor receiver functions The HP system was also used to monitor the CCRs via an analog interface This provided the ability to monitor the various CCR internal temperatures as well as gas flow, gas pressures, vac-ion (vacuum pump) current, and drive unit operation Maser tuning was performed manually using an HP power supply for magnet tuning and JPL-designed solid state pump control units located in the control room

The dual TWM control assembly was based on a standard DSN version but was modified to accept a TTL computer interface as part of the automation The control panel was located in the control room, and communication with the aerial cabin assemblies was provided by a two-way serial data link

Either manual or computer control was possible with this arrangement

Two multiconductor cables with 50 conductors each and 10 coaxial lines carried all M&C and RF signals through the wrap between the control room and the aerial cabin The system was designed to run from a primary power source of 240 Vac/50 Hz Step-down transformers were used to provide 220 and 115 volts where necessary

The antenna cabin hardware consisted of two full- and one half-size 19-inch relay racks and a welded aluminum frame supporting the dual maser package and associated equipment The frame and the maser package were transportable as a complete assembly and came with a trolley designed for that purpose Control room equipment was mounted in two 19-inch instrumentation racks with a desktop HP computer The helium compressors were freestanding in a room above the antenna azimuth bearing

III. Reimplementation for Parkes/Neptune

Reimplementation of the front end for the Voyager Neptune encounter required a substantial amount of redesign, procurement, and fabrication due to the absence of some key hardware components Specifically, all Hewlett-Packard commercial equipment had been removed from the system with the following consequences

(1) There was no way to control or read the position of the waveguide switches or polarizer (other than by hand)

(2) There was no way to monitor the health and status of the CCRs and compressors other than by personal inspection

(3) There was no way to monitor the health and status of the downconverters, monitor receiver, or upconverter other than by personal inspection

(4) There was no automation of system configuration or calibration

Some consideration was given to purchasing all the missing hardware and software needed for the system to be rebuilt and operated exactly as it was in 1986 However, this was abandoned due to financial and practical considerations

A number of fundamental constraints apply to the alternative approach taken, namely

(1) The equipment supplied by ESA is on loan to JPL and may not be modified without prior approval from ESA

(2) There are a limited number of cables available through the wrap on the Parkes antenna, so any new design should ideally use no more cables than were used in 1986 to do the same job

(3) The physical space for new equipment is limited and should not exceed that used in 1986, if possible

(4) Equipment weight in the aerial cabin needs to be minimized to avoid damage to the focus drive gear (The total weight in 1986 was considered excessive)

(5) There is no plenum air available in the aerial cabin or in the NASA trailer, however, a limited amount of room air conditioning will be available The usual constraints of operability, reliability, and maintainability also apply

IV. Parkes Front-End System for the Neptune Encounter

A. General Description

The RF configuration of the front end (Fig 2) will be virtually identical to that of the 1986 encounter, with the exception of pre/post-TWM signal coupling ports, provided for the Commonwealth Science Industrial Research Organization (CSIRO) of Australia, which operates and maintains the Parkes antenna The two new RF front-end control (RFFEC) cabinets (Fig 3) will be installed in the NASA trailer, requiring two new multiconductors between the antenna pedestal control room and the NASA trailer The two RFFEC cabinets are the maintenance point for tuning and adjusting the dual TWMs They contain the monitor receiver display (an HP 8590A spectrum analyzer), the 420-MHz (nominal) test signal source (an HP 8663A synthesizer signal generator), the front-end controller, a CRT terminal, the CCR data acquisition unit, and the TWM monitor and control equipment The aerial cabin racks A, B, and C (Fig 4) contain the balance of the front-end RF and TWM/CCR monitor and control equipment The antenna room racks contain equipment that must be relocated through additional cabling if they are not in close proximity to the TWM/CCRs or the waveguide feed system The total weight of the front-end equipment (including the RF package) that will be installed in the antenna room is 630 kilograms ±2 percent

The major changes being made to the front-end system will alter the way in which the system is monitored and controlled Reimplementation of the Parkes antenna front end will include a system for centralizing and automating the monitoring and control of the microwave electronics (Fig 5) This monitoring and control will be provided through the Parkes front-end controller (FEC) assembly, a multibus-based computer

mounted in one of the two front-end control cabinets (Fig 3) located in the Parkes NASA trailer The FEC will tie together individual pieces of equipment in the trailer that interface with hardware located in the antenna aerial cabin In addition to providing independent, stand-alone operation, the FEC will also interface directly to the PCTA communications controller for integrated operation with PCTA functions

The FEC assembly consists of a commercial multibus-type computer providing a card cage, a power supply, and an enclosure with slides The FEC chassis will contain four commercial computer boards an Intel 86/14 CPU with a floating-point arithmetic card, a D/A converter, and an IEEE-488 communications card, a RAM memory card, a ROM memory card, and an RS-232 serial communications card A power meter for the noise-adding radiometer will also be located within the FEC chassis and will consist of an A/D converter module and an additional custom multibus board, the NAR digital board Software for controlling the FEC will be designed from existing PCTA software modules, with additions and changes made where necessary for implementing specific tasks Spares for the FEC/NAR will be made at the assembly level

Control of the Parkes front end will follow the same philosophy that governs the PCTA operation during telemetry tracking will involve automated monitoring and control through the PCTA array controller, located at the Parkes site, remote monitoring and control by the CDSCC array controller will be possible through the intersite data link Pre- and post-pass maintenance (independent of the PCTA) will be provided locally through a CRT terminal located in the monitor receiver control cabinet A second CRT will be located on the third floor of the antenna pedestal dedicated for use during antenna pointing calibration All three terminals will be able to control equipment and alter the front-end configuration Selection of the controlling terminal will be made through a switch mounted on the front of the FEC chassis

The FEC will provide interfaces with the following front-end monitor and control instrumentation (Figs 6 and 7)

(1) IEEE-488 cabling from the Front-End Controller CPU to an HP quartz thermometer, the 420-MHz test signal synthesizer, the monitor receiver spectrum analyzer, an HP power meter, and (through an IEEE-488 extender to the aerial cabin) the noise diode relay switch controller, the test oscillator upconverter, an AC power controller for the waveguide switches, the monitor receiver, and each of the two downconverters

(2) Parallel TTL control lines from the front-end controller CPU to the dual TWM control panel

(3) RS-232 serial communication lines from the FEC serial ports to the following terminals

  (a) The PCTA communications controller

  (b) A local CRT terminal for monitor receiver system maintenance

  (c) A remote CRT terminal for NAR operation during antenna pointing calibration

  (d) The CCR data acquisition unit

(4) A 50-ohm coax from the PCTA receiver to the NAR A/D module in the FEC and from the FEC to the noise diode power assemblies in the aerial cabin

Tasks performed by the front-end controller will consist of

(1) Providing monitoring and control of the antenna waveguide switches and polarizer driver assembly This task includes monitoring of telltales showing the true mechanical position of the devices (not provided in 1986)

(2) Measuring system temperature using the Y-factor technique through automation of the waveguide switches, quartz thermometer, dual TWM control panel, and HP power meter This task includes automatic calibration (zeroing) of the HP power meter

(3) Performing NAR functions under remote control through automation of the noise diode assemblies and the NAR power meter This task includes the return of a time-varying analog signal, corresponding to measured system temperature, to the pedestal It also includes periodic calibration of the noise diodes

(4) Providing status updates and charting the performance history of the refrigerators and compressors as requested This task includes the generation of alarm messages on CCR out-of-limit conditions

(5) Monitoring of alarms from the downconverters, monitor receiver, and test signal upconverter These alarms include all power supplies, local oscillator power levels, timing, and phase-lock conditions

B. Detailed Functional Descriptions

1 Waveguide switching and polarizer control Monitoring and control of the two waveguide switches and polarizer will take place over the IEEE-488 using a remote HP 3488A switch control unit with plug-in HP 44471A relay modules for power control and an HP 44474A digital I/O module for telltale monitoring A new waveguide switch interface will be built to interface the switch controller to the existing cable har-

nesses and assemblies Manual control in the event of hardware failure will be possible from within the aerial cabin

2 **Y-factor system temperature measurement** Pre-pass system temperature measurement using the Y-factor technique will be fully automated by the front-end controller Coordinated operation will consist of

(1) Instructing the TWM controller assembly to remove all test signal sources from the receiver signal path

(2) Instructing the monitor receiver to select the appropriate signal path and positioning the waveguide switches to select the desired configuration (sky or ambient load)

(3) Calibrating the HP power meter by switching its input to an internal calibration signal

(4) Switching the meter to the monitor receiver and measuring the noise power levels

(5) Measuring the ambient load temperature using the quartz thermometer

(6) Calculating the system temperature and reporting the results to the operator

3 **Noise-adding radiometer** Noise-adding radiometers [2] operate by periodically injecting small, known quantities of noise into the antenna front end and then measuring the resulting increase in system noise power at the receiver For the Parkes reimplementation, this additive noise will be generated using a DSN noise diode assembly, the NAR power meter in the front-end controller will perform the noise power measurements During antenna pointing calibration operations, system temperature calculations will be carried out continually, with the FEC supplying a corresponding analog voltage to the pedestal via a D/A converter

Two noise diode assemblies will be supplied for the Parkes antenna, one for each of the two 8 4-GHz receive chains Each assembly consists of a noise diode oven and an associated power supply Each oven contains three diodes, providing noise temperatures of 0 25, 0 5, 1, 2, 4, 8, and 50 K, defined at the maser inputs The ovens are controlled through their power supply assemblies, each of which contains three independent power supplies, one for each diode Three relays per supply are used to select the amount of diode current (allowing three noise levels per diode), while a fourth TTL signal modulates the diode on and off (The diodes are not switched with the power supply relays)

Each power supply assembly is monitored and controlled through 21 digital I/O lines consisting of relay closures, telltale sensors, and diode modulation input Both assemblies will be operated through a remote HP 3488A switch control unit containing three HP 44474A digital I/O modules (16 channels per card), coaxial cable run directly from the FEC will supply the modulation control signals Since one HP controller will already be in place for operating the waveguide switches, common spares will exist for both the switch controllers and the digital I/O modules

At the other end of the receive chain, noise power measurements will be taken from the inputs of the Parkes telemetry receiver Each of the two 285- to 360-MHz RF signals will be split 3 dB in the signal select drawer and then fed directly to the power meter in the FEC The NAR power meter consists of a module comprising an analog-to-digital converter for sampling the noise inputs and a single Intel multibus stitchwire board under FEC control for accumulating individual power measurements, an averaged output is read over the bus by the 86/14 CPU Diode control, noise measurement, system temperature computation, and analog output programming are all handled by the CPU, with results included in FEC status displays

4 **CCR/compressor monitoring** The CCR/compressor monitor consists of three μMAC 5000 data acquisition assemblies and an IBM PC-XT data acquisition unit (DAU) [3] used for interfacing and data processing The DAU is located in one of the two front-end control cabinets (Fig 3) located in the Parkes trailer One μMAC will be located in the aerial cabin to monitor both CCRs (Fig 4), while the other two μMACs will be in the compressor room (Fig 8) to monitor one compressor each, data will be sent from the μMACs to the DAU at 1-minute intervals Communication between the μMACs and the DAU will be serial RS-232 and will use a coaxial cable daisy-chained to all devices An additional RS-232 port on the DAU will provide the interface to the FEC via an IBM PC serial communications card

The data acquisition unit will be located in one of the two Parkes front-end control cabinets and will be dedicated solely to CCR system monitor tasks The DAU will continuously display CCR and compressor parameters, updating the screen once a minute as data is received from the antenna These parameters will also be echoed to the FEC, and the most up-to-date values will be used to generate routine PCTA status displays

Monitored CCR/compressor parameters include

(1) CCR stage temperatures (4 5 K, 15 K, and 70 K)

(2) Reserve CCR heat capacity (percentage of normal)

(3) Helium pressures (supply, refrigeration return, JT return, tank, and oil stack differential)

(4) Joule–Thomson stage helium flow

(5) Motor phase currents (A, B, and C)

(6) Motor temperature

(7) Compressor temperatures (first and second stage)

(8) Vacuum pressure in the CCR vessel

In addition to the CCR/compressor parameter values, each record sent by the DAU to the FEC will be formatted with status flags indicating whether each value is within acceptable limits (All CCR/compressor alarm limits are to be entered at the DAU keyboard) Any out-of-limits conditions will cause the FEC to immediately send a PCTA-type alarm message (including an audible tone) to each FEC terminal

In order to keep track of performance history, the DAU will time-tag and log the CCR/compressor data to its hard disk every 15 minutes Given the capacity of the disk, an entire year's worth of data (96 records/day) can be recorded In addition to the long-term storage in the DAU, the front-end controller will keep track of the most recent 72 hours' worth of data transmitted to it (in 1-minute intervals) This performance history will be made available in two forms upon specifying a start date/time and a stop date/time, one or more parameters can be either displayed as a low-resolution graph (80 X 24 characters) or tabulated in columns Short-term history (up to 72 hours old) will have a maximum resolution of 1 minute, long-term history will have a 15-minute resolution Data records that are not found in the FEC short-term cache can be automatically requested from the DAU hard disk log, indexed by day of year, time of day, and CCR/compressor system number

5 Alarm monitoring The downconverters, monitor receiver, and test signal upconverter all have built-in alarms to indicate failures or performance degradation These alarms are detected by polling the equipment over the IEEE-488 and will be monitored by the front-end controller Alarm conditions will generate a PCTA-compatible alarm message and the condition of all monitored parameters will be included in routine FEC status displays

Alarms monitored include

(1) Downconverters

(a) DC power Detects if any power supply voltage drops by more than 15 percent

(b) Phase lock Detects if the 8 1-GHz local oscillator PLL is phase-locked

(c) Five-megahertz standard Detects low or missing 5-MHz references from the station FTS

(d) Low power Detects low local oscillator power

(e) Sum Detects if any of the above alarms are true

(2) Upconverter

(a) DC power Detects if any power supply voltage drops by more than 15 percent

(b) Phase lock Detects if the 8 1-GHz local oscillator PLL is phase-locked

(c) Five-megahertz standard Detects low or missing 5-MHz references from the station FTS

(d) Low power Detects low local oscillator power

(e) Sum Detects if any of the above alarms are true

(3) Monitor receiver

(a) DC power Detects if any power supply voltage drops by more than 15 percent

(b) Sum Detects if any of the above alarms are true

V. Dual TWM Refurbishment and Performance

The two TWM/CCRs were tested at JPL in the condition received from ESA One of the TWM/CCRs had a vacuum leak resulting from a damaged waveguide window, and both TWMs had shorted wires in their internal cable harnesses As a result, both TWMs were removed from the RF package and repaired prior to testing Test results of the TWM gain/bandwidth curves (Fig 9) indicated that both TWMs required adjustment of the gain/bandwidth shape in order to achieve the specified 100-MHz, 3-dB bandwidth The gain/bandwidth curves of the TWMs were adjusted to meet the Block IIA TWM specifications [1] by altering the magnetic field with a change in the length and/or thickness of the steel shims mounted on the top and bottom of the structure [4] The final gain/bandwidth curves achieved with both TWM 1 and TWM 2 are shown in Fig 10

The measured equivalent input noise temperature (referred to the room temperature input flange) is shown in Fig 11 for both TWMs The noise temperatures were determined by attaching a high-quality feedhorn to the waveguide input flange and then measuring the Y-factor obtained when alternately viewing the "cold" sky and an ambient termination microwave adsorber

Refurbishment of the TWM/CCRs consisted of the following

(1) Repairing CCR vacuum leaks

(2) Installing new internal wire harnesses and temperature sensor mounting brackets in both CCRs

(3) Adding an additional temperature sensor to the 15-K to 4 5-K heat exchanger on both CCRs to enable the CCR data acquisition system to monitor the percentage of CCR reserve cooling capacity

(4) Repairing and upgrading the solid-state pump source assembly Gunn oscillators and other waveguide components damaged by corrosion were replaced with new components, and new modulator/protect assemblies were installed to upgrade to the latest Block IIA requirements [5]

VI. Conclusion

A PCTA D/E-level design review for the Parkes front-end system was presented in November of 1987 The response indicated that the system with the new front-end controller, noise-adding radiometer, CCR data acquisition unit, system alarm monitoring, and refurbished RF front end will meet all station operation and maintenance requirements as well as the Voyager Neptune encounter project requirements

Acknowledgments

The Parkes front-end system refurbishment and reimplementation is the product of the Parkes front-end team members, including the authors, R Cardenas, L Fowler, J Kovatch, R Quinn, T Sweeney, R Zanteson, and all members of the Microwave Electronics Group under the supervision of S Petty Thanks are also due to L Hileman for his software contribution to this task

References

[1] D L Trowbridge, "Block IIA Traveling-Wave Maser," *TDA Progress Report 42-87*, vol July–September 1986, Jet Propulsion Laboratory, Pasadena, California, pp 158–164, November 15, 1986

[2] T J Brunzie, "A Noise-Adding Radiometer for the Parkes Antenna," *TDA Progress Report 42-92*, vol October–December 1987, Jet Propulsion Laboratory, Pasadena, California, pp 117–122, February 15, 1988

[3] L Fowler and M Britcliffe, "Traveling-Wave Maser Closed-Cycle Refrigerator Data Acquisition and Display System," *TDA Progress Report 42-91*, July–September 1987, Jet Propulsion Laboratory, Pasadena, California, pp 304–311, November 15, 1987

[4] D L Trowbridge, "X-Band, Low-Noise, Traveling-Wave Maser," *TDA Progress Report 42-60*, vol September–October 1980, Jet Propulsion Laboratory, Pasadena, California, pp 126–131, December 15, 1980

[5] R Cardenas, "The 8 4-GHz Low-Noise Maser Pump Source Assembly," *TDA Progress Report 42-91*, July–September 1987, Jet Propulsion Laboratory, Pasadena, California, pp 278–284, November 15, 1987

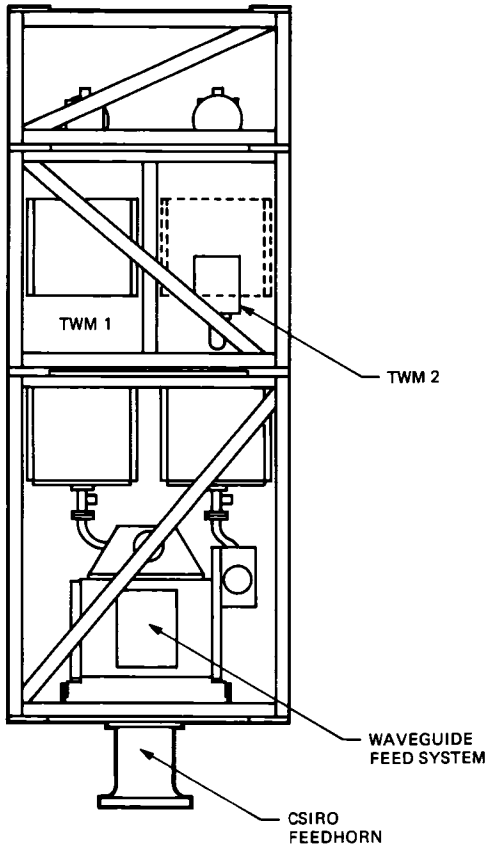

Fig 1 Parkes RF package

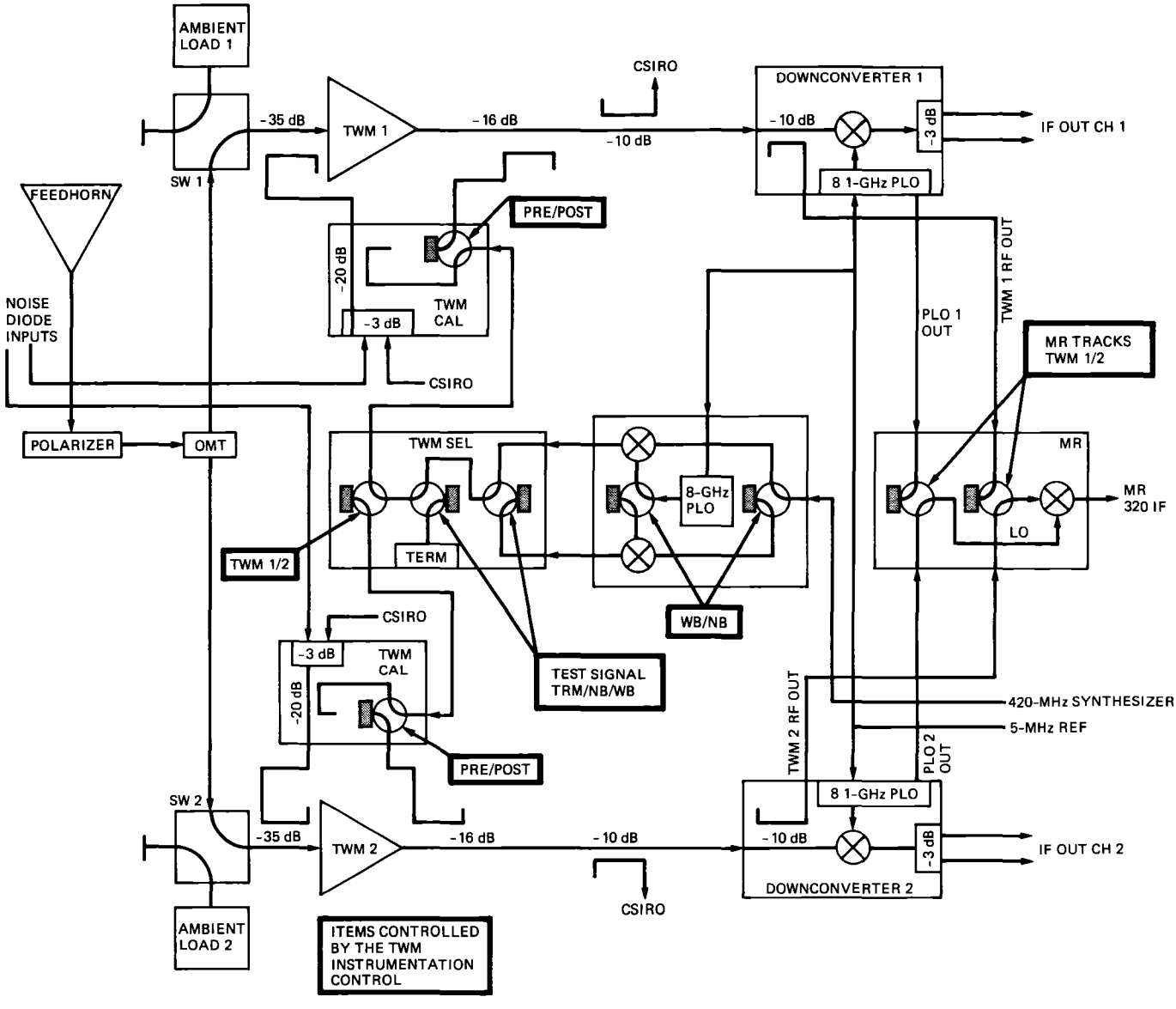

Fig 2. Parkes RF configuration

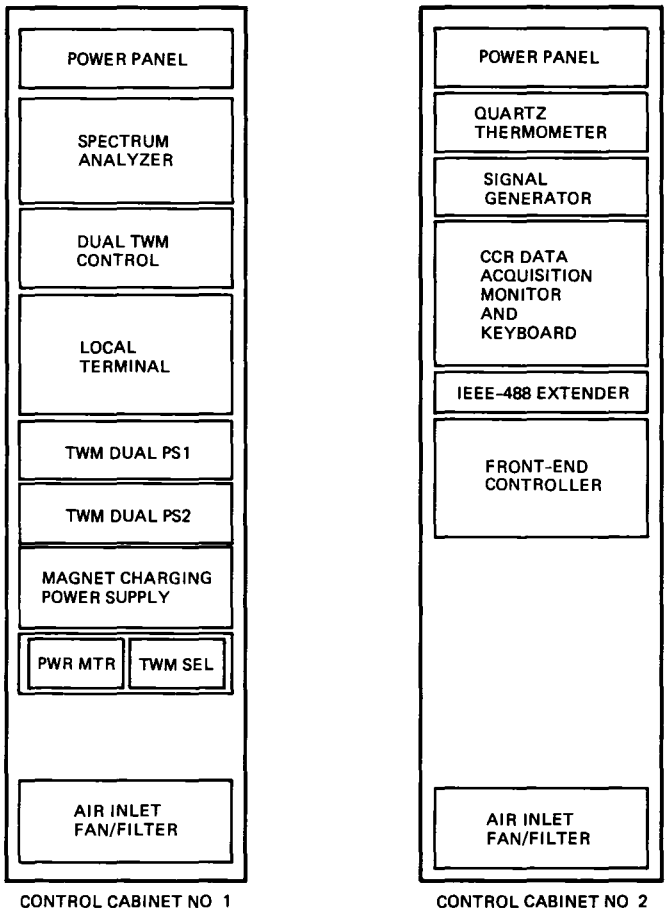

Fig 3 RF front-end control cabinets

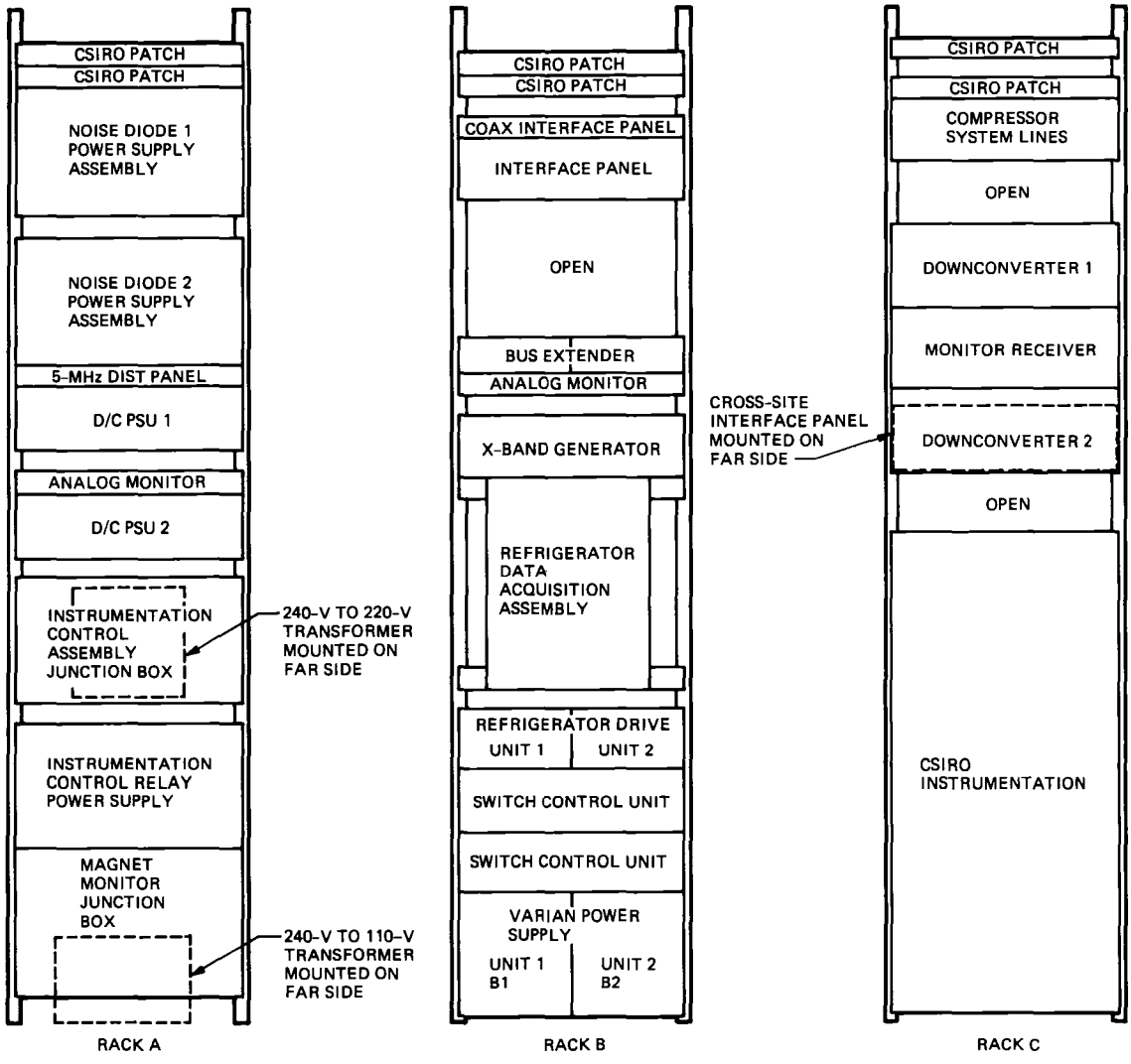

Fig 4 Aerial cabin racks for reimplementation at Parkes (rack A used by ESA)

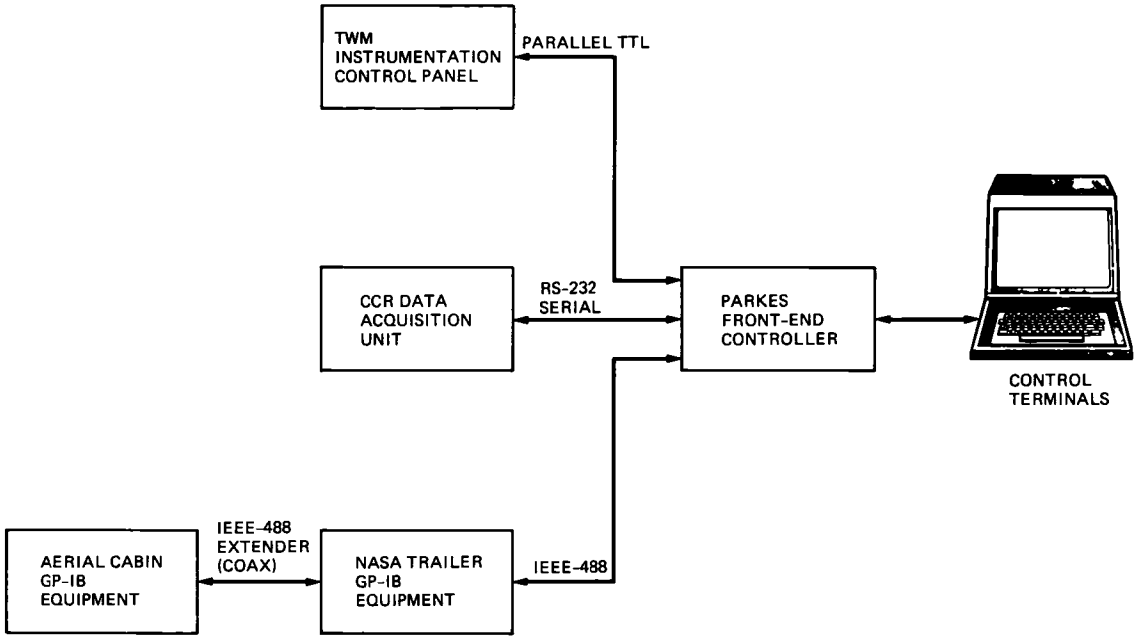

Fig. 5 Front-end monitoring and control block diagram

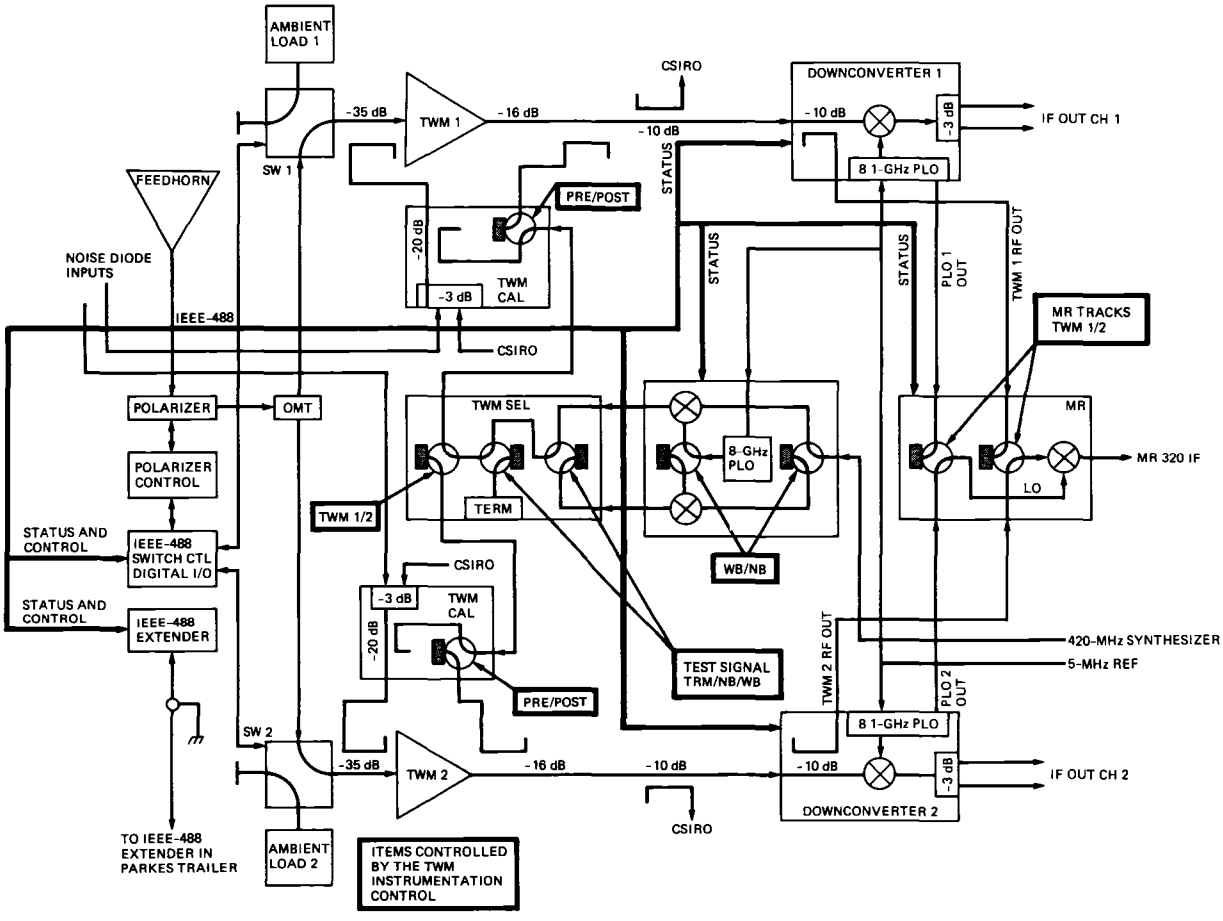

Fig 6 Control flow diagram antenna racks

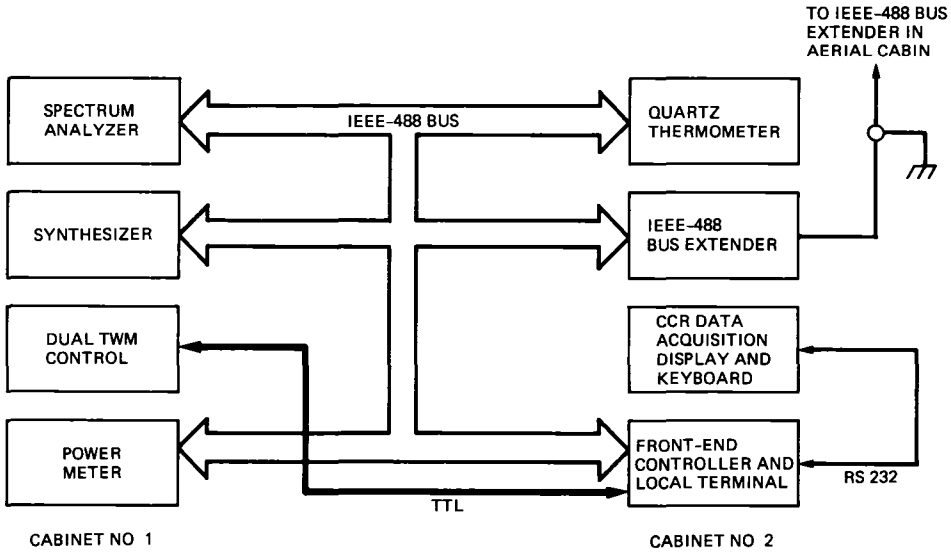

Fig 7 Control flow diagram control cabinets

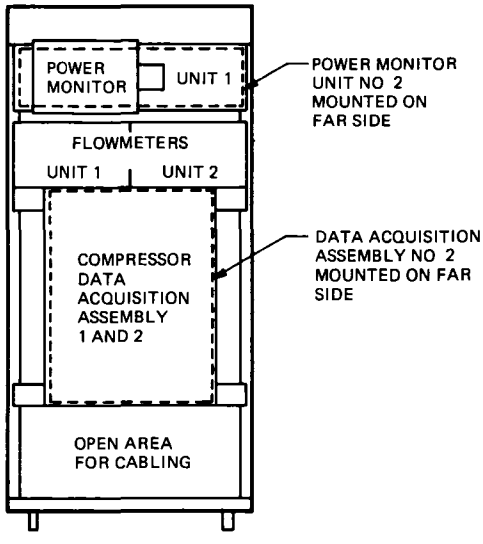

Fig 8 Compressor instrumentation half rack

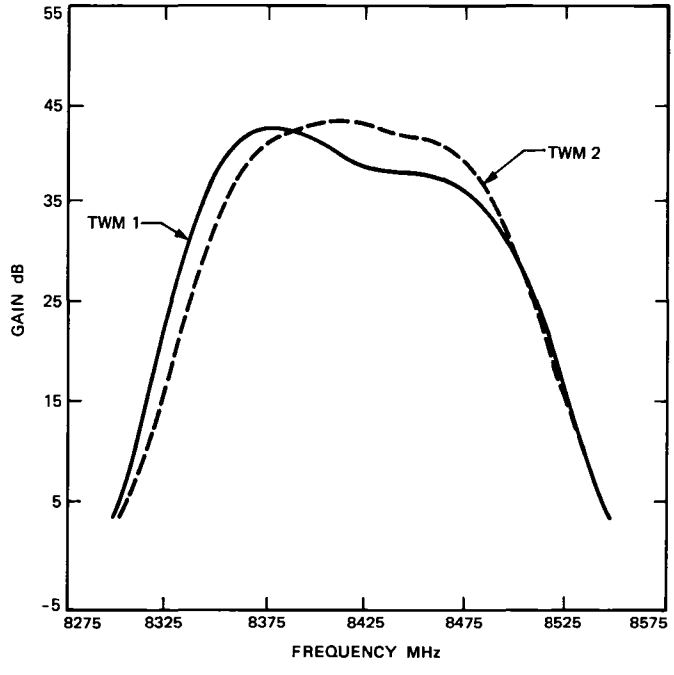

Fig 9 TWMs 1 and 2 gain/bandwidth curves prior to adjustment

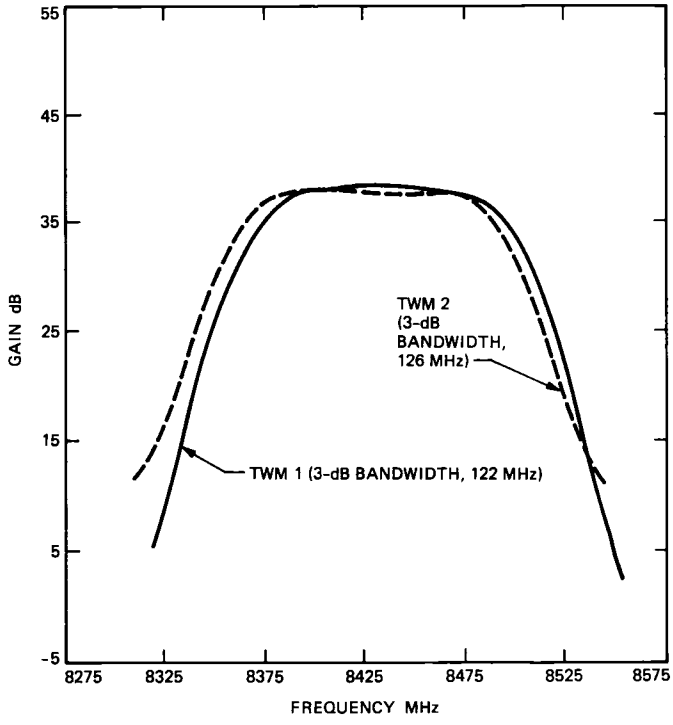

Fig 10 TWMs 1 and 2 gain/bandwidth curves after final adjustment

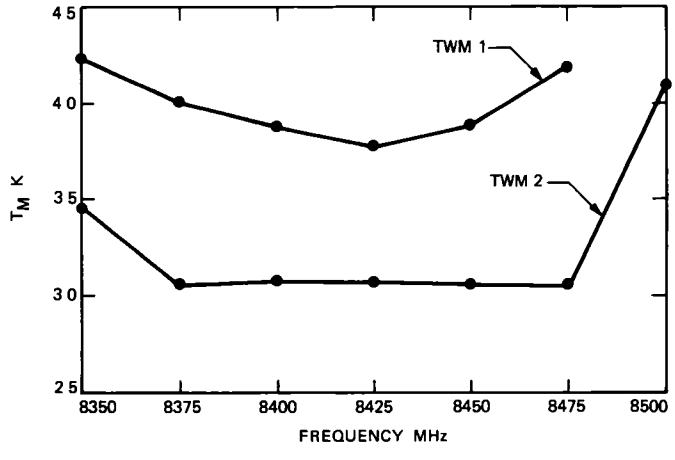

Fig 11 TWMs 1 and 2 equivalent input noise temperature

The Behavior of a Costas Loop in the Presence of Space Telemetry Signals

T M Nguyen
Telecommunications Systems Section

The telemetry modulation index, telemetry bit rate, subcarrier waveform, and subcarrier frequency are shown to be the key system parameters that contribute to the performance degradation of a Costas loop in the presence of space telemetry signals The effects of the Doppler in the loop are also investigated in this article The results of this study have been input to the Consultative Committee for Space Data Systems (CCSDS) for consideration in the future standard suppressed-carrier space telemetry system

I. Introduction

The Consultative Committee for Space Data Systems (CCSDS) has classified space telemetry signals into two categories Category A, non-deep space missions, and Category B, deep space missions Category A includes those missions having altitudes above the Earth less than 2×10^6 km, and Category B contains missions having altitudes above the Earth greater than 2×10^6 km For space telemetry signals, the CCSDS has recommended that a subcarrier be used with a residual carrier when transmitting at low bit rates and that PSK subcarrier modulation be used when a telemetry subcarrier is employed A square-wave subcarrier is recommended for Category B, and a sine-wave subcarrier for Category A [1]

Costas loop receivers with a residual carrier have been analyzed by M K Simon [2] This analysis has not considered the case where the signal utilizes PSK subcarrier modulation, and also has assumed that the loop phase error approaches zero at a high loop Signal-to-Noise Ratio (SNR) with the Doppler signal being compensated for

In this article, the performance degradation of the Costas loop in the presence of space telemetry signals is investigated This represents an extension of [2] to include PSK subcarrier modulation and the presence of Doppler in the input signal The assumption that the loop phase error approaches zero at a high loop SNR is removed in this analysis Only the linear approximation which is valid for small phase errors is assumed

II. Performance of the Costas Loop in the Presence of Deep Space Telemetry Signals

The deep space Category B telemetry signal recommended by the CCSDS can be presented mathematically by [1]

$$S(t) = \sqrt{2P} \cdot \sin(\omega_0 t + m \cdot d(t) \cdot P(t) + \theta(t)) \qquad (1)$$

where P is the total received power, ω_0 is the carrier radian frequency and $\theta(t)$ the corresponding Doppler signal to be estimated, m is the data modulation index with $d(t)$ the NRZ

binary valued data sequence, and $P(t)$ is the unit power square-wave subcarrier of frequency f_{sc}

The above signal is received in the presence of Additive White Gaussian Noise (AWGN), $n(t)$, with

$$n(t) = \sqrt{2}\,[N_c(t)\cos(\omega_0 t + \theta(t)) - N_s(t)\sin(\omega_0 t + \theta(t))]$$

where $N_s(t)$ and $N_c(t)$ are approximately statistically independent, stationary, white Gaussian noise processes with single-sided noise spectral density N_0 W/Hz, and single-sided bandwidth $B_H < (\omega_0/2\pi)$, and the Costas loop is used to track the received signal If $\phi_e(t)$ denotes the loop phase error, then from previous analysis of this type [2] (assuming $2\phi_e(t)$ is small enough so that the linearizing approximations are applicable, i e , $\sin(2\phi_e(t)) \approx 2\phi_e(t)$, $\cos(2\phi_e(t)) \approx 1$), we can show that

$$2\phi_e(t) = 2\phi_D(t) + 2\phi_M(t) + 2\phi_N(t) \tag{2}$$

where

$$\phi_D(t) = [1 - H(p)] \cdot \theta(t) \tag{3}$$

$$\phi_M(t) = \frac{P \cdot \sin(2m)}{2\gamma} \cdot H(p) \cdot M_f(t) \tag{4}$$

$$\phi_N(t) = \frac{H(p)}{2\gamma} \cdot N(t, 2\phi_e) \tag{5}$$

Note that the self-noise of data has been assumed to be small so that it can be ignored in the above equations

Here

$$H(s) = \text{closed-loop transfer function}$$

$$= \frac{\gamma K F(s)}{s + \gamma K F(s)} \tag{6}$$

where

K = (VCO gain) · (phase detector gain)

$F(s)$ = transfer function of loop filter

$$\gamma = P(\cos^2(m) - \alpha \cdot \sin^2(m)) \tag{7}$$

$$N(t, 2\phi_e) = \left[N_{fs}(t)^2 - N_{fc}(t)^2 + 2\sqrt{P}\left\{N_{fs}(t) \cdot \cos(m) - M_f(t) \cdot N_{fc}(t) \cdot \sin(m)\right\}\right] \cdot (2\phi_e) + \left[2 \cdot N_{fs}(t) \cdot N_{fc}(t) + 2\sqrt{P}\left\{N_{fc}(t) \cdot \cos(m) + M_f(t) \cdot N_{fs}(t) \cdot \sin(m)\right\}\right] \tag{8}$$

Here $M_f(t)$, $N_{fs}(t)$, $N_{fc}(t)$ are the equivalent low-pass arm filtered versions of $M(t)$, $N_s(t)$, $N_c(t)$, respectively Note that $M(t)$ is the PSK subcarrier modulated data signal which is given by

$$M(t) = d(t) \cdot P(t) \tag{9}$$

As an example, the relationship between $M(t)$ and the filtered version of $M_f(t)$ is given by

$$M_f(t) = G(p) \cdot M(t) \tag{10}$$

where $G(p)$ is the arm filter with p the Heaviside operator

In Eq (2) the loop phase error is expressed in terms of the loop phase error due to the Doppler signal ($\phi_D(t)$), loop phase error due to the modulation ($\phi_M(t)$), and phase error due to the noise ($\phi_N(t)$) The factor α in Eq (7) denotes the modulation distortion factor

$$\alpha = \int_{-\infty}^{\infty} S_M(f) \mid G(j2\pi f) \mid^2 \cdot df \tag{11}$$

Here $S_M(f)$ denotes the power spectral density of the data modulated subcarrier $M(t)$ It can be shown that for a square-wave subcarrier,

$$S_M(f) = \frac{4}{\pi^2} \sum_{\substack{k=1 \\ k \text{ odd}}}^{\infty} \frac{[S_d(f - kf_{sc}) + S_d(f + kf_{sc})]}{k^2} \tag{12}$$

where $S_d(f)$ is the power spectrum density of the equiprobable NRZ binary telemetry signal

Let us assume that the initial phase offset of the incoming signal from the phase of the free-running VCO, the data sequence, and the noise are independent Then, from Eq (2), the mean-squared tracking phase jitter can be shown to have the form

$$\sigma^2(\phi_e) = \sigma^2(\phi_D) + \sigma^2(\phi_M) + \sigma^2(\phi_N) \tag{13}$$

where $\sigma^2(\phi_D)$ is the mean-squared tracking phase jitter due to the Doppler signal, $\sigma^2(\phi_M)$ the phase jitter due to modulation produced by the residual carrier, and $\sigma^2(\phi_N)$ the jitter due to the noise Using [3] it is easy to show that, from Eq (2),

$$\sigma^2(\phi_D) = \frac{1}{2\pi}\int_{-\infty}^{\infty} |1 - H(j\omega)|^2 \cdot E\{|\theta(j\omega)|^2\} \cdot d\omega \tag{14}$$

$$\sigma^2(\phi_M) = \frac{[P\sin(2m)]^2}{(2\pi)[2\gamma]^2}\int_{-\infty}^{\infty} |H(j\omega)|^2 \cdot S_{Mf}(\omega) \cdot d\omega \tag{15}$$

$$\sigma^2(\phi_N) = \frac{1}{(2\pi)[2\gamma]^2}\int_{-\infty}^{\infty} |H(j\omega)|^2 \cdot S_N(\omega) \cdot d\omega \tag{16}$$

Here,

$E\{|\theta(j\omega)|^2\}$ = spectral density of the Doppler signal $\theta(t)$

$S_{Mf}(\omega)$ = spectral density of the data-modulated subcarrier $M(t)$ after low pass arm filtering = $S_M(\omega) \cdot |G(j2\pi f)|^2$

$S_N(\omega)$ = spectral density of the noise $N(t, 2\phi_e)$

Since the bandwidths of the process $M_f(t)$ and the noise $N(t, 2\phi_e)$ are very wide with respect to the loop bandwidth B_L, we can approximate Eqs (15) and (16), respectively, as follows

$$\sigma^2(\phi_M) \approx \frac{2[P\sin(2m)]^2}{[2\gamma]^2} \cdot B_L \cdot S_{Mf}(0) \tag{17}$$

$$\sigma^2(\phi_N) \approx \frac{2}{[2\gamma]^2} \cdot B_L \cdot S_N(0) \tag{18}$$

Here, we define the loop bandwidth B_L as

$$B_L = \frac{1}{2}\int_{-\infty}^{\infty} |H(j\omega)|^2 \cdot \frac{d\omega}{2\pi} \tag{19}$$

Since the CCSDS has recommended that the subcarrier frequency (f_{sc}) to bit rate (R_s) ratio be an integer [1], the power spectral density $S_{Mf}(\omega)$ of the data-modulated subcarrier $M(t)$ after low pass arm filtering is equal to zero at the origin (see Appendix A) Thus the mean-squared phase jitter due to the modulation is also equal to zero

If the spectrum of the loop phase error is very narrow compared to the noise component $N_c(t)$ after low pass filtering, so that it is constant relative to the noise components, then we can show that

$$S_N(0) = 2P \cdot N_0\left[4\sigma^2(\phi_e) + 1\right] \times \left[\frac{B'N_0}{P} + |G(0)|^2 \cos^2(m) + \beta \cdot \sin^2(m)\right] \tag{20}$$

where

$$B' = \frac{1}{2}\int_{-\infty}^{\infty} |G(j2\pi f)|^4 \cdot df \tag{21}$$

$$\beta = \int_{-\infty}^{\infty} S_M(f)\,|G(j2\pi f)|^4 \cdot df \tag{22}$$

From these results, the mean-squared tracking phase jitter can be shown, after some algebraic manipulations, to be

$$\sigma^2(\phi_e) = \frac{\sigma^2(\phi_D)}{\left[1 - \frac{4}{\rho_L} N(m,\alpha,\beta)\right]} + \frac{N(m,\alpha,\beta)}{\rho_L\left[1 - \frac{4}{\rho_L} N(m,\alpha,\beta)\right]} \tag{23}$$

where $N(m,\alpha,\beta)$ and ρ_L are given by

$$N(m,\alpha,\beta) = \frac{1}{(\cos^2(m) - \alpha \cdot \sin^2(m))} \times \left[\frac{1}{\delta'} + |G(0)|^2 \cos^2(m) + \beta \cdot \sin^2(m)\right] \tag{24}$$

$$\rho_L = \text{Loop Signal-to-Noise Ratio (SNR)} = \frac{P}{N_0 B_L} \tag{25}$$

δ' in Eq (24) is defined as

$$\delta' = \frac{P}{N_0 B'} \tag{26}$$

Since $\sigma^2(\phi_D)$ and $N(m,\alpha,\beta)$ are always greater than zero, then Eq (23) makes sense only when $(4/\rho_L) \cdot N(m,\alpha,\beta) < 1$

Thus, for $(4/\rho_L) \cdot N(m,\alpha,\beta) \ll 1$, Eq (23) can be approximated as

$$\sigma^2(\phi_e) \approx \sigma^2(\phi_D)\left[1+\frac{4}{\rho_L}\cdot N(m,\alpha,\beta)\right] + \frac{N(m,\alpha,\beta)}{\rho_L} + \frac{4}{(\rho_L)^2}\cdot N^2(m,\alpha,\beta) \tag{27}$$

The mean-squared tracking phase jitter described in Eq (27) shows how the Costas loop responds to the deep space telemetry signal The tracking phase jitter due to the Doppler appears as a high pass function, and the jitter due to noise appears as a low pass function Since the tracking phase jitter is inversely proportional to $[\cos^2(m) - \alpha \cdot \sin^2(m)]$, the loop will experience a serious degradation in tracking performance when the modulation index m of the data is near m_c (see [2], Eq (15))

$$m_c = \cot^{-1}(\sqrt{\alpha}) \tag{28}$$

At $m = \cot^{-1}(\sqrt{\alpha})$, the loop will drop lock at any loop SNR

If the Doppler signal can be compensated for and the loop SNR is very high, then Eq (28) can be written as

$$\sigma^2(\phi_e) \approx \frac{N(m,\alpha,\beta)}{\rho_L} \tag{29}$$

If the data does not utilize a square-wave subcarrier, then the result found in Eq (29) is similar to that found in [2] and [4] (with the ranging channel turned off)

III. Performance of the Costas Loop in the Presence of Non-Deep Space Telemetry

The signal format for non-deep space telemetry is the same as that for deep space except that a sine-wave subcarrier waveform is used in place of the square wave [1] Letting $M_1(t) = d(t) \cdot \sin(2\pi f_{sc} t)$, and assuming that the arm filters are built such that no spectral components greater than f_{sc} get into the error control signal in the loop, then following the above procedure we can show that the mean-squared tracking phase jitter for this case is (see Appendix B)

$$\sigma'^2(\phi'_e) = \sigma'^2(\phi_D)\left[1+\frac{4}{\rho_{1L}}\cdot N_1(m',\alpha_1,\beta_1)\right] + \frac{N_1(m'\,\alpha_1,\beta_1)}{\rho_{1L}} + \frac{4\cdot N_1^2(m',\alpha_1,\beta_1)}{(\rho_{1L})^2} \tag{30}$$

where $\sigma'^2(\phi'_D)$ is defined as in Eq (14), with $H(s)$ replaced by $H_1(s)$

$$H_1(s) = \frac{\gamma_1 \cdot K \cdot F(s)}{s + \gamma_1 \cdot K \cdot F(s)}$$

$$\gamma_1 = P[J_0^2(m') - 4\cdot\alpha_1 \cdot J_1^2(m')] \tag{31}$$

$$N_1(m',\alpha_1,\beta_1) = \frac{[(1/\delta') + 2|G(0)|^2 J_0^2(m') + 4\cdot\beta_1 \cdot J_1^2(m')]}{[J_0^2(m') - 4\cdot\alpha_1\cdot J_1^2(m')]} \tag{32}$$

where α_1 and β_1 are given by

$$\alpha_1 = \int_{-\infty}^{\infty} S_{M1}(f)\,|\,G(j2\pi f)\,|^2 \cdot df \tag{33}$$

$$\beta_1 = \int_{-\infty}^{\infty} S_{M1}(f)\,|\,G(j2\pi f)\,|^4 \cdot df \tag{34}$$

Here α_1 is the modulation distortion factor, and $S_{M1}(f)$ is the spectral density of $M_1(t)$ which is given by

$$S_{M1}(f) = S_d(f - f_{sc}) + S_d(f + f_{sc}) \tag{35}$$

Note that ρ_{1L} is defined the same as in Eq (25), with $H_1(s)$ in place of $H(s)$ for the computation of B_L If the jitter due to Doppler can be compensated for, and the loop SNR is high, then Eq (30) can be approximated as

$$\sigma'^2(\phi'_e) \approx \frac{N_1(m',\alpha_1,\beta_1)}{\rho_{1L}} \tag{36}$$

The loop will be degraded seriously in tracking performance when the modulation index m' is near the value m'_c, which will satisfy

$$[J_0(m'_c)/J_1(m'_c)]^2 = 4\cdot\alpha_1 \tag{37}$$

IV. Numerical Examples

It is shown that the Costas loop will be degraded seriously in tracking performance when the modulation index m (or m') is near the critical value, called m_c (or m_c'), which is given by Eqs (28) and (37) for deep space and non-deep space missions, respectively The loop will drop lock at any loop SNR when the modulation index satisfies these equations Therefore, it is crucial to understand the behavior of the modulation distortion factors α and α_1 as a function of data rate, subcarrier frequency, and arm filter noise bandwidth In this section we will evaluate these distortion factors and illustrate some numerical results for the single-pole Butterworth arm filter

The transfer function for the single-pole Butterworth filter is given by

$$|G(j2\pi f)|^2 = \frac{1}{1+(f/f_0)^2} \tag{38}$$

where f_0, the 3-dB bandwidth, is related to the two-sided noise bandwidth B_1 of the filter by

$$f_0 = \frac{B_1}{\pi} \tag{39}$$

Substituting Eqs (38) and (12) into Eq (11) and rearranging gives the modulation distortion factor α, for Category B, of the form

$$\alpha = \frac{8\cdot(f_0)^2}{\pi^2 T_s} \sum_{\substack{k=1\\ k\ \text{odd}}}^{\infty} \int_{-\infty}^{\infty} \frac{\sin^2(\pi T_s[f-kf_{sc}])}{k^2(f-kf_{sc})^2\,(f^2+f_0^2)}\cdot df \tag{40}$$

where $T_s = (1/R_s)$ is the symbol duration of the telemetry data sequence In uncoded binary systems, the bit duration equals the symbol duration Thus, the ratio of subcarrier frequency, f_{sc}, to bit rate, R_s for this case is

$$f_{sc}\cdot T_s = (f_{sc}/R_s) = n, \qquad n = 1,2,3, \tag{41}$$

Using contour integration and carrying out the necessary mathematics gives

$$\alpha = \frac{4}{\pi^2}\cdot\frac{B_1}{R_s}\sum_{\substack{k=1\\ k\ \text{odd}}}^{\infty} \times\left[a\left(n,k,\frac{B_1}{R_s}\right)\left\{b\left(n,k,\frac{B_1}{R_s}\right)\left[1-\exp\left(-\frac{2B_1}{R_s}\right)\right]+\frac{2B_1}{R_s}\right\}\right] \tag{42}$$

here $a(\ ,\ ,\ )$ and $b(\ ,\ ,\ )$ are given by

$$a(n,k,B_1/R_s) = \frac{1}{k^2\left[(nk\pi)^2+(B_1/R_s)^2\right]} \tag{43}$$

$$b(n,k,B_1/R_s) = \frac{(nk\pi)^2-(B_1/R_s)^2}{(nk\pi)^2+(B_1/R_s)^2} \tag{44}$$

The modulation distortion factor α_1 for Category A telemetry signals can be expressed in terms of $a(\ ,\ ,\ )$ and $b(\ ,\ ,\ )$ by evaluating Eq (33) For this case, it is found that

$$\alpha_1 = \frac{B_1}{R_s}\,a\left(n,1,\frac{B_1}{R_s}\right)\left\{b\left(n,1,\frac{B_1}{R_s}\right)\left[1-\exp\left(-2\frac{B_1}{R_s}\right)\right]+2\frac{B_1}{R_s}\right\} \tag{45}$$

The numerical results of Eqs (42) and (45) are plotted in Figs 1 and 2, respectively There, the modulation factors α and α_1 are plotted in decibels versus the ratio (B_1/R_s) for various values of n, the ratio of subcarrier frequency to bit rate Using these results for α and α_1 in Figs 1 and 2, the critical modulation index m_c versus the ratio (B_1/R_s) with n as a parameter can be plotted As an example, Fig 3 illustrates the critical modulation index m_c for Category B missions as a function of (B_1/R_s) Figures 1 and 2 show that the modulation distortion factors for both Categories A and B decrease as the subcarrier frequency to bit rate ratio, n, increases The physical meaning for this is that the degradation in tracking performance of the loop is less when we place the data further away from the carrier (at the expense of wider bandwidth) Furthermore, from these figures, we observe that for a given bit rate there exists an optimum noise bandwidth for the arm filters in the sense of minimizing the degradation in mean-squared tracking phase jitter It is also seen that the degradation in the modulation distortion factor for Category A is more than that of Category B for a given n and (B_1/R_s) Figure 3 shows that the critical modulation index m_c decreases as the noise bandwidth to bit rate ratio (B_1/R_s) increases Also, m_c is shown to

decrease as we place the data closer to the carrier frequency (decreasing in n) This means that the closer we place the data to the carrier, the more power the carrier requires to maintain a proper tracking performance

V. Conclusions

It has been shown that the Costas loop can be used to track space telemetry signals in the presence of Doppler This operation can increase mean-squared tracking jitter if there is a residual carrier, as was recommended for both Categories A (non-deep space) and B (deep space) telemetry signals The performance degradation of the loop can be optimized by choosing a proper subcarrier waveform, subcarrier frequency, bit rate, and arm filter noise bandwidth This article has numerically evaluated such degradation for single-pole Butterworth arm filters for both Categories A and B To completely understand the behavior of the Costas loop in the presence of space telemetry signals, the false lock performance still needs to be found

Acknowledgment

The author is indebted to Dr M K Simon for his valuable comments and helpful suggestions

References

[1] "Recommendations for Space Data System Standards Radio Frequency and Modulation Systems, Part 1 Earth Station and Spacecraft," CCSDS 401-B-1, Blue Book, Consultative Committee for Space Data Systems (CCSDS), January 1987

[2] M K Simon, "The Effects of the Residual Carrier on Costas Loop Performance as Applied to the Space Shuttle Orbiter S-Band Uplink," *IEEE Transactions on Communications*, vol COM-26, no 11, pp 1542–1548, November 1978

[3] A Papoulis, *Probability, Random Variables, and Stochastic Process*, New York McGraw-Hill, Chapter 10, 1960

[4] J K Holmes, *Coherent Spread Spectrum Systems*, New York John Wiley & Sons, Inc , 1982

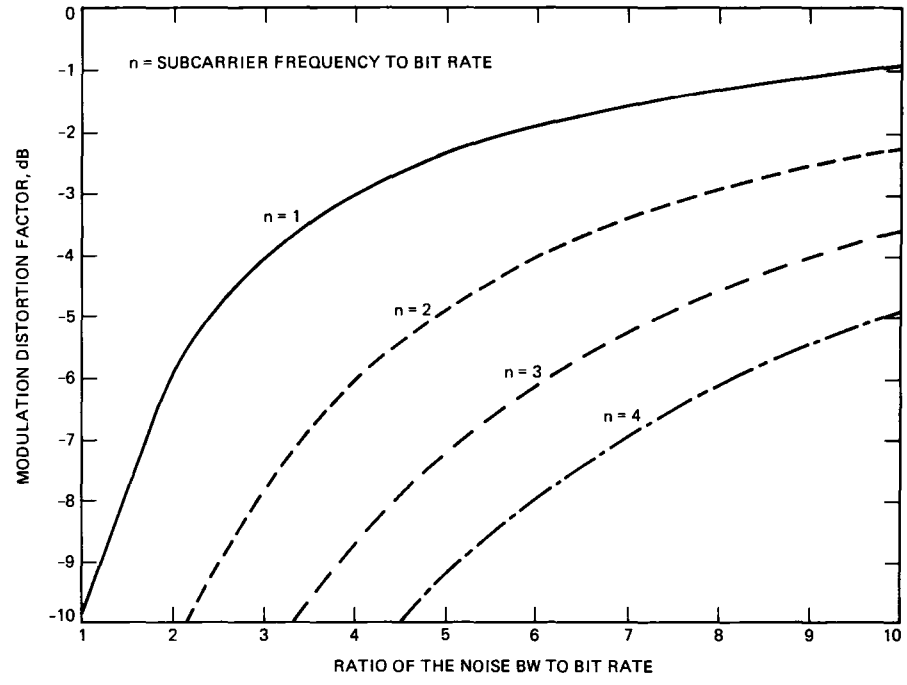

Fig 1 Modulation distortion factor vs (B_1/R_s), Category B

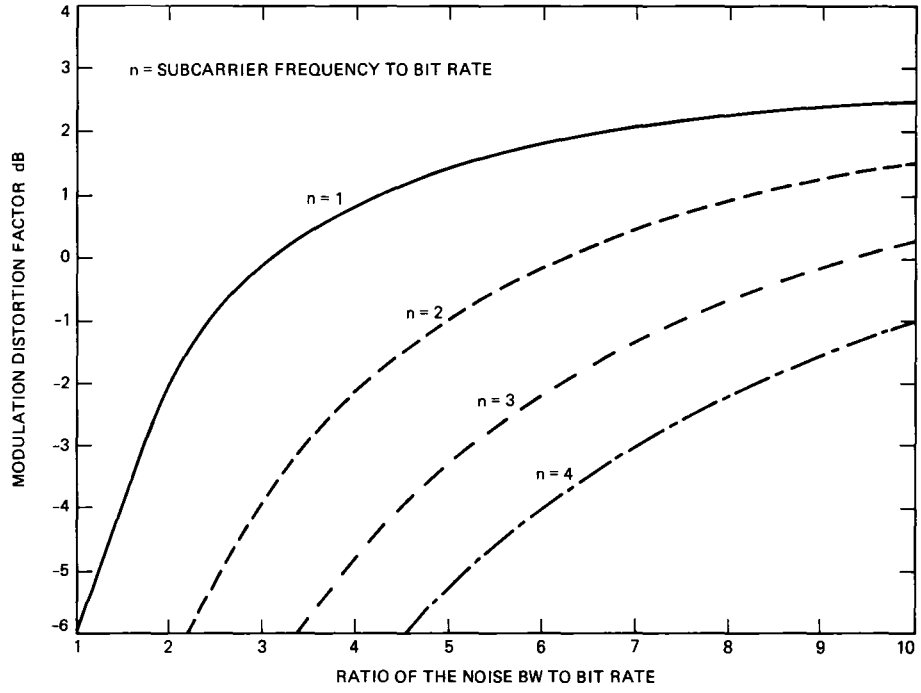

Fig 2 Modulation distortion factor vs (B_1/R_s), Category A

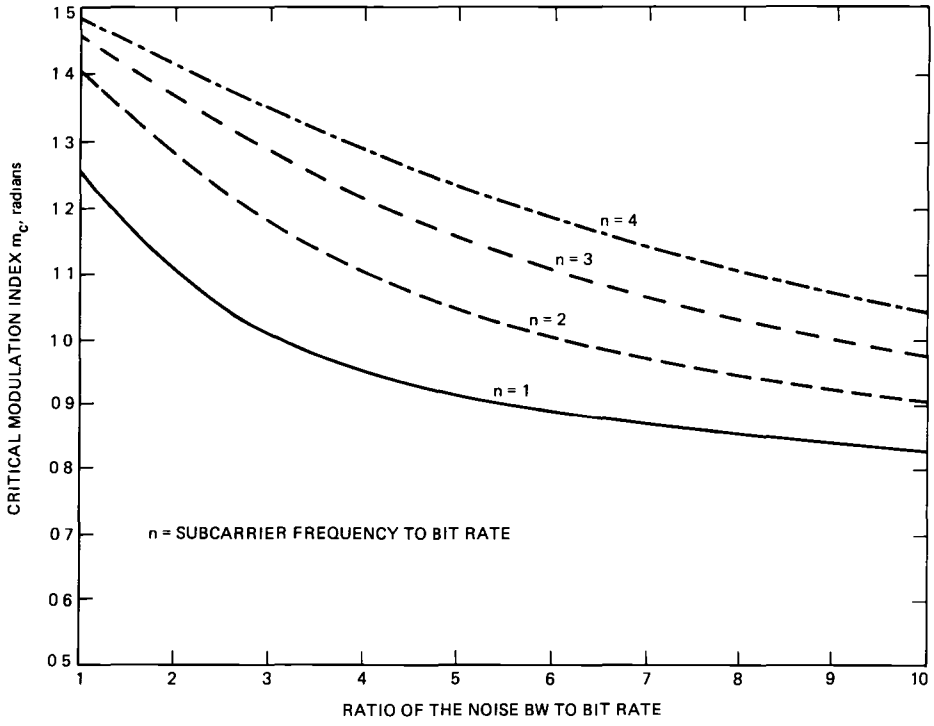

Fig. 3 Critical modulation index m_c vs (B_1/R_s), Category B

Appendix A

The power spectral density of the data-modulated subcarrier $M(t)$ after low-pass arm filtering is given by

$$S_{Mf}(\omega) = S_M(\omega) \cdot |G(j2\pi f)|^2 \qquad \text{(A-1)}$$

where $S_M(\omega)$ is given in Eq (12), and $G(\cdot)$ is the transfer function of the low pass arm filter

Since the CCSDS has recommended that the NRZ binary signal be used for $d(t)$, the power spectrum density $S_d(f)$ of the equiprobable NRZ binary signal is given by

$$S_d(f) = T_s \cdot [\sin(\pi f T_s)/(\pi f T_s)] \qquad \text{(A-2)}$$

The spectral density of the low pass arm filtered data-modulated subcarrier at the origin, for an NRZ binary signal, can be obtained by substituting Eq (A-2) into Eq (12), then substituting the result into Eq (A-1) and evaluating it at $\omega = 2\pi f = 0$ The result is given as follows

$$S_{Mf}(0) = \frac{8T_s}{\pi^2} \cdot \sum_{\substack{k=1 \\ k \text{ odd}}}^{\infty} \left[\frac{\sin(\pi T_s k f_{sc})}{(\pi T_s k f_{sc})} \right]^2 \cdot \left| \frac{G(0)}{k} \right|^2 \qquad \text{(A-3)}$$

From Eq (41), the product $(T_s f_{sc})$ always equals an integer Thus, Eq (A-3) becomes

$$S_{Mf}(0) = 0 \qquad \text{(A-4)}$$

Appendix B

From Eq (1), the non-deep space Category A signal can be written as

$$S'(t) = \sqrt{2P}\, J_0(m') \cdot \sin(\omega_0 t + \theta'(t)) + \sqrt{2P}\, J_1(m') \cdot d(t) \cdot \cos(\omega_0 t + \theta'(t)) \tag{B-1}$$

Here we have assumed that

$$20 \log_{10}(J_0(m')) \gg 20 \log_{10}(J_2(m'))$$

$$20 \log_{10}(J_1(m')) \gg 20 \log_{10}(J_3(m'))$$

If the Costas loop is used to track this signal in the presence of AWGN, then the loop phase estimate of $\theta'(t)$, $\hat{\theta}(t)$, can be shown to have the form

$$2\hat{\theta}'(t) = \frac{PKF(s)}{s}\left[[(J_0(m'))^2 - 4 \cdot \alpha_1 \cdot (J_1(m'))^2]\,(2\phi_e'(t)) + 4J_0(m') \cdot J_1(m') \cdot M_{1f}(t) + n_1(t, 2\phi_e')\right] \tag{B-2}$$

where

$$\phi_e'(t) = \theta'(t) - \hat{\theta}'(t) = \text{loop phase error} \tag{B-3}$$

$$n_1(t, 2\phi_e') = \left[N_{fs}(t)^2 - N_{fc}(t)^2 + 2\sqrt{P}\{N_{fs}(t) \cdot J_0(m') - 2M_{1f}(t) \cdot N_{fc}(t) \cdot J_1(m')\}\right] \cdot (2\phi_e') + \left[2 \cdot N_{fs}(t) \cdot N_{fc}(t) + 2\sqrt{P}\{N_{fc}(t) \cdot J_0(m') + 2M_{1f}(t) \cdot N_{fs}(t) \cdot J_1(m')\}\right] \tag{B-4}$$

$$M_{1f}(t) = G(p) \cdot M_1(t),\ M_1(t) = d(t) \cdot \sin(2\pi f_{sc} t) \tag{B-5}$$

It should be noted here that all the other parameters (which are not defined here) have been defined in the preceding sections, and that the previous assumptions (small loop phase error, small self-noise of the modulation) are used in deriving Eq (B-2)

Let

$$\gamma_1 = P[J_0^2(m') - 4 \cdot \alpha_1 \cdot J_1^2(m')] \tag{B-6}$$

where α_1 is the modulation distortion factor which was defined in Eq (33)

From Eq (B-3), Eq (B-2) can be rearranged as

$$2\phi_e'(t) = 2\phi_D'(t) + 2\phi_M'(t) + 2\phi_N'(t) \tag{B-7}$$

where

$$\phi_D'(t) = [1 - H_1(p)] \cdot \theta'(t) \tag{B-8}$$

$$\phi_M'(t) = \frac{2P \cdot J_0(m') \cdot J_1(M)}{\gamma_1} \cdot H_1(p) \cdot M_{1f}(t) \tag{B-9}$$

$$\phi_N'(t) = \frac{H_1(p)}{2\gamma_1} \cdot n_1(t, 2\phi_e') \tag{B-10}$$

where $H_1(s)$ is the closed-loop transfer function (for this particular case) which is defined in Eq (31)

Following the procedure in Section II, the mean-squared tracking phase jitter for non-deep space telemetry signals can be shown to take the form expressed in Eq (30)

DSN Very Long Baseline Interferometry System Mark IV-88

K M Liewer
TDA Engineering Office

This article presents a functional description of the Deep Space Network Very Long Baseline Interferometry system as it will exist at the end of 1988

I. Introduction

Very Long Baseline Interferometry (VLBI), in its simplest form, uses two radio telescopes to synthesize a radio telescope with an angular resolution equal to that of a telescope whose diameter equals the separation of the two telescopes The DSN makes use of this very high angular resolution to produce precision navigational data for spacecraft in deep space VLBI data is also used to produce source coordinates for radio reference sources and platform parameters, which include the relative antenna positions on the surface of the Earth and the instantaneous rotations of the Earth's surface relative to its mean position The VLBI system also supports a variety of astronomical and geodetic programs

II. VLBI Description

A schematic representation of a VLBI observation is shown in Fig 1 When the signals from the two antennas are correlated against each other, with a variable relative delay, the actual delay is given by the relative delay which maximizes the degree of correlation This time delay is the VLBI observable If the baseline vector is known, the angle of arrival of the radio waves and hence the source's angular position can be computed A priori knowledge of the observational parameters is, in general, not well enough known to unambiguously determine the absolute phase of the measured delay Measurements at several frequencies allow the group delay to be computed from the slope of phase versus frequency Measurements from the frequency channels with the smallest frequency separation have ambiguities which can be resolved from a priori knowledge The channels with wider frequency separation are used to progressively improve the precision of the delay determination This technique is called bandwidth synthesis For a complete description of VLBI, see [1]–[4]

VLBI accuracy is reduced by errors in knowledge of the baseline length and its orientation in relation to the instantaneous spin axis of the Earth, station clock drift, and unmodeled media delays In the case of navigation, these errors can be greatly reduced by observing a reference radio source that is angularly near a spacecraft Such an observational scenario is shown in Fig 2 By differencing the delay measured from the Extragalactic Radio Source (EGRS) observation with the delay measured from the observation of the spacecraft, one can determine the angular separation of the EGRS and the spacecraft in the direction perpendicular to the baseline The differencing process eliminates any errors that are common to both observations Reducing the angular and time separation of the observations increases the amount of commonality of the error sources and therefore reduces the common mode errors This procedure is called delta-differential one-way range (delta-DOR) It is analogous to differencing one-way ranging delays between two stations (DOR) and then differencing these ranges between two sources If delay measurements are made over some time interval, they can be differenced to pro-

duce a data type called delta-differential one-way doppler (delta-DOD) This gives an angular rate in the plane of the sky rather than an angular position and is analogous to doubly differenced doppler data The generic term for the differenced VLBI data is delta-VLBI

A penalty of using an EGRS as a reference is that angular positions and rates relative to the EGRS are produced rather than absolute positions and rates In order to make use of this data for navigation, the EGRS position must be accurately known from other measurements VLBI observations can determine relative station locations with an accuracy of 5 to 10 centimeters and source positions to an accuracy better than 30 nanoradians by repeated observations of many sources with varying observing geometries An ongoing program (Catalog Maintenance and Enhancement) in the DSN continues to improve the positional accuracy of a catalog of more than 100 EGRSs while adding sources for new projects when necessary

Another program supported by the DSN, called TEMPO (Time and Earth Motion Precision Observations), makes weekly VLBI observations that provide detailed knowledge of the short term fluctuations in the angular position of the Earth's crust relative to its mean position The quantities measured (platform parameters) are the variations in rotation/time (UT1 – UTC) and the variations in the position of the spin axis (polar motion) These platform parameters are used in the Orbit Determination Program for the reduction of delta-VLBI data as well as all other radiometric data types The TEMPO observations also produce information about the relative time offset and rate offset between the precision clocks at the DSCC and aid in maintaining clock synchronization and syntonization (relative frequency)

III. Key Characteristics

There are three distinct VLBI configurations currently implemented within the DSN This section will describe the key characteristics of the two new configurations and will conclude with a brief note about the third, which is being replaced by the other two

A. Narrow Channel Bandwidth (NCB) VLBI

NCB VLBI (also known as Block I VLBI) is used to produce most of the spacecraft navigation data (delta-VLBI data) and weekly EGRS measurements for determination of the platform parameters (TEMPO project) The name is derived from the use of relatively narrow bandwidth individual channels Table 1 shows the key parameters of the NCB configuration The sensitivity of the NCB VLBI system to both narrowband (spacecraft) and wideband (EGRS) signals is shown in Table 2

Because the recording rate is only 500 kbits/sec, the data can be recorded directly on a high capacity disk, and playback of the data can begin while the observations are still in progress This is important for those applications with tight time constraints on the delivery of the processed VLBI data

The VLBI observables are of little value until they are converted to angular positions and rates of a spacecraft or other source The achievable accuracy depends on this conversion and is also affected by external variables such as delays in the transmission media Figures 3 and 4 show estimated VLBI error budgets for spacecraft angular delay and rate measurements under typical conditions

The TEMPO project (also known as Clock Sync) observes from 16 to 20 EGRSs once a week on each DSN baseline (California to Spain and California to Australia) for a total of about 8000 seconds of data The Earth rotation parameters that are produced from this data are accurate to 30 cm (1 sigma) in each component The primary factors limiting the accuracy are the spanned bandwidth and SNR in the narrow channels

B. Wide Channel Bandwidth (WCB) VLBI

WCB VLBI is used primarily for producing the EGRS position catalog required for analysis of the delta-VLBI navigation data Because of the greater sensitivity and precision, relative to NCB, the WCB configuration is used for radio astronomy and geophysical studies associated with tectonic plate motion and deformation In some cases (e g , the Phobos Project), when it is necessary to use a very weak EGRS and the NCB sensitivity is too low, WCB VLBI can be used for delta-VLBI observations WCB VLBI is also known as Block II VLBI The WCB digital hardware at the station is the same as the Mark III hardware in use by the astronomical and geophysical communities The computer and software that control the hardware are different from those used by Mark III The data format produced by WCB VLBI is identical to the Mark III data

Key characteristics of the WCB configuration are shown in Table 1 The increased spanned bandwidth and data volume, due to increased channel bandwidth and simultaneous channel recording, give WCB VLBI much higher sensitivity than the NCB VLBI, as is shown in Table 2 For projects not requiring a fast turnaround time, the increased sensitivity of WCB VLBI allows the use of the 34-meter HEF subnet rather than the 70-meter subnet, which is usually required for NCB VLBI Because of the volume of data generated, it is not possible to transmit the data to the correlator electronically The need to mail tapes from the overseas stations limits the minimum time required to produce reduced data to 1 to 2 weeks

C. Block 0 VLBI

The first VLBI configuration implemented in the DSN was known as Block 0 It is identical to Mark II VLBI used at astronomical observatories around the world Like NCB and WCB VLBI, Block 0 can accept data from two frequency bands The IF that is used is centered at 50 MHz and comes from either Block IV or dedicated VLBI receivers It has up to 8 channels, each of which is 2 MHz wide, and with a maximum frequency separation of 40 MHz The channels are time multiplexed, and the data is recorded on standard videocassettes Although NCB VLBI is less sensitive than the Block 0, it can be automatically controlled by predicts, can play the data back electronically, and has better phase response This has led to the exclusive use of the NCB configuration for delta-VLBI and TEMPO activities The Block 0 configuration will be retained during testing of WCB VLBI but will not be used for taking operational data after 1989

IV. System Functional Description

In this section the VLBI system will be described in more detail In the first part of this section the Deep Space Communications Complex (DSCC) portion of the system will be presented, and in the second part the Network Operations Control Center (NOCC), JPL/CIT Correlator, and postcorrelation processing portions of the system will be described Figure 5 shows a block diagram of the VLBI system The flow of the actual VLBI data (processed RF signal) is shown with wide arrows, while control status, and calibration data flow is shown with small arrows

A. DSCC System

The VLBI system can use either the 34-m HEF or the 70-m antenna at each complex and can accept inputs from two frequency bands Currently only 2 3-GHz (S-band) and 8 4-GHz (X-band) signals can be received simultaneously Dual frequency observations allow corrections to be made for the effects of charged particles in the transmission media The 1 7-GHz (L-band) signal at the 70-m antenna, which is upconverted to S-band, can also be used Either left or right circular polarization may be used, however, the same polarization must be used by each of the antennas being employed Table 3 shows the details of the radio frequency signals which the VLBI system can process Because the phase of the RF signal is the end product of the VLBI system, the signal path is calibrated by injecting calibration tones into the RF feed prior to the low noise amplifiers Variations in the phase of these signals are applied as corrections to the observed radio source phase Operation of the Phase Calibration Generators (PCGs) is controlled by the Spectrum Processing Assembly (SPA) by means of messages sent to the Frequency and Timing Subsystem (FTS) controller

The RF signals are downconverted to a 300-MHz IF using phase stable local oscillators operating at the fixed frequencies of 2 0 (S-band) and 8 1 GHz (X-band) Signals at L-band are first upconverted to S-band using a 620-MHz local oscillator and then sent to the S-band downconverter

For NCB VLBI, an IF selector switch in the Signal Processing Center (SPC) sends the desired IF signals to a VLBI receiver (NVR) The receiver downconverts the IF signals to video frequency in up to twelve time-multiplexed channels The output of the receiver is then digitized and sampled, single sideband converted, and digitally filtered This digital processing occurs within the Data Channel Filter (DCF) Digital rather than analog processing is required in order to meet the phase ripple and out-of-band rejection specifications placed on the NCB VLBI configuration The bandpass of the filter can be set to one of four values After the bandpass filtering, the signal is passed to the Spectrum Processing Assembly for formatting and recording Under some conditions (e g , low Sun–Earth–probe angles), the phase of the RF signal may fluctuate enough during the minimum NCB channel multiplexing time that the correct RF cycle cannot be determined from data point to data point If only a single channel is being recorded in each frequency band, as is the case for delta-DOD, a band combiner can be used to eliminate the time multiplexing of the channels The band combiner simply sums the signals from two channels, and only the sum is recorded The individual signals can be recovered later, in the correlation process, although the system noise temperature is approximately doubled

For WCB VLBI, all of the IF signals are routed from the IF selector to the Data Acquisition Terminal (DAT), which is the processor and recording assembly for WCB VLBI Switching within the DAT selects the IF channels corresponding to the desired antenna and frequency band Fourteen video converters within the DAT produce filtered, clipped (one-bit digitized), single sideband downconverted video signals Both upper and lower sidebands are generated for a total of 28 2-MHz channels There are provisions for a range of filters within the video converters (see Table 1), but at this time only the 2-MHz bandpass filters are implemented All 28 channels can be recorded simultaneously or, if a smaller number is recorded, multiple recordings can be made on the same tape

The Digital Tone Extractor (DTE) monitors the phase calibration tones for phase drift and jitter Predicts loaded into the SPA contain standards and limits for the amplitude, drift, and jitter of the phase calibration tones The DTE output is used during precalibration at the station as part of a system co-

herence test and as a monitor during the remainder of the pass The SPA supplies the DTE with a model which is correlated with the video frequency signals from the DCF or the DAT to produce relative phase measurements

The Spectrum Processing Assembly (SPA) controls all parts of the SPC portion of the VLBI system through predicts and provides monitor data to the DSCC Monitor and Control (DMC) system The DMC provides the SPA with monitor data from the FTS, the Media Calibration Subsystem (DMD), and the Precision Power Monitor (PPM) Due to timing constraints, pointing angle information is sent directly to the SPA Monitor data from the VLBI assemblies (DAT, DCF, DTE, SPA), the receiver, and the subsystems just mentioned are reformatted by the SPA and sent via the Digital Communication Subsystem to the Network Operations Control Center (NOCC) The predicts (configuration and standard and limit information) which control and configure the DSCC VLBI system are sent from the NOCC to the SPA via the DMC The SPA has the ability to support separate WCB and NCB VLBI activities simultaneously Once the VLBI data is acquired it is sent electronically to the NOCC (in the case of NCB data), or tapes are mailed back to JPL (in the case of Block 0 or WCB data)

B. NOCC System

The NOCC contains the facilities for generating the required predicts, monitoring of VLBI operations in real time, correlating the VLBI data, and providing postcorrelation processing Figure 5 shows the subsystems within the NOCC

The NOCC Support Subsystem (NSS) provides antenna pointing predicts for VLBI activities, VLBI configuration parameters used at the DSCC, and the standards and limits used for monitoring system performance DSCC configuration and performance data is returned to the NOCC Radio Science/ VLBI real-time monitor (NRV) during a VLBI activity The displayed data are monitored by the Network Operations Control Team and Operations and Engineering Analysis for correct operation The NOCC VLBI Processor (NVP) receives the VLBI and monitor data directly from the Digital Communications Subsystem via wideband data lines and records it on disk The NVP consists of several independent computers, two hardware correlators, and disk storage capacity for approximately one week of VLBI data The NVP CPUs provide models and VLBI data to the correlators and receive the results of the correlation process which are phase as a function of time A complete description of the correlation process is contained in [2]-[4] Postcorrelation software in the NVP further edits the phase data, applies phase calibration corrections, compresses it to phase points at specified intervals, produces phase rate data, and sends the results to the DSN Navigation Subsystem (NAV) NAV reformats the processed VLBI data and forwards it to the appropriate project along with other radio metric data

The WCB VLBI videotapes are mailed to the JPL/CIT Block II correlator for processing This correlator handles much higher data rates than the NCB correlator and multiple simultaneous baselines Block 0 data is also processed on this correlator Once it is correlated, the data is brought to the NVP for postcorrelation processing This correlated data, after editing and calibration, is used as input to a parameter estimation program which produces station location and source position estimates This program is also used to process NCB VLBI data for TEMPO to produce corrections to Universal Time and the Earth's pole position The models used in the parameter estimation program are described in [5]

References

[1] A E E Rogers, "Very Long Baseline Interferometry With Large Effective Bandwidth for Phase-delay Measurements," *Radio Science*, vol 5, no 10, pp 1239–1248, October 1970

[2] J B Thomas, *An Analysis of Long Baseline Radio Interferometry*, JPL Technical Report 32-1526, vol VII, Jet Propulsion Laboratory, Pasadena, California, pp 37–50, February 15, 1972

[3] J B Thomas, *An Analysis of Long Baseline Radio Interferometry, Part II*, JPL Technical Report 32-1526, vol VIII, Jet Propulsion Laboratory, Pasadena, California, pp 29–38, April 15, 1972

[4] J B Thomas, *An Analysis of Long Baseline Radio Interferometry, Part III*, JPL Technical Report 32-1526, vol XVI, Jet Propulsion Laboratory, Pasadena, California, pp 47–64, June 15, 1973

[5] O J Sovers and J L Fanselow, *Observation Model and Parameter Partials for the JPL VLBI Parameter Estimation Software "MASTERFIT"-1987*, JPL Publication 83-89, Rev 3, Jet Propulsion Laboratory, Pasadena, California, December 1987

Table 1 Key system characteristics

Function	NCB system	WCB system
Number of simultaneous frequency bands	2	2
Spanned bandwidth	40 MHz (S) 100 MHz (X)	100 MHz (S) 400 MHz (X)
Number of channels	12	14
Channel multiplex time	0 2 sec (minimum)	N/A
Channel bandwidth	31 25, 62 5, 125, 250 kHz	2 0, 4 0 MHz*
Channel frequency resolution	10 Hz	10 kHz
Data rate (maximum)	500 kbit/sec	112 Mbit/sec
Recording media	High capacity disk or 9-track tape	Video tape
Storage capacity	2 Gbit/disk (2 disks), 0 9 Gbit/tape	100 Gbit/tape
Playback rate	120 kbit/sec	Tape shipment

*Expandable to include 0 125, 0 250, 0 5, and 1 0 MHz

Table 2 System sensitivity

Quantity	NCB system	WCB system
Minimum detectable EGRS flux* (5-minute integration)	0 15 jansky	0 005 jansky
Minimum detectable spacecraft signal* (1-second integration)	−168 dBm	−171 dBm

*Assuming two 70-meter antennas operating at an SNT of 30 K

Table 3. RF reception characteristics

Parameter	Antenna	
	34-meter HEF	70-meter
Frequency range, MHz		
L-band	N/A	1620–1685
S-band (HEMT)	2200–2305	N/A
S-band (maser)	N/A	2265–2305
X-band (HEMT)	8200–8600	N/A
X-band (maser)	8400–8500	8400–8500
System noise temperature, kelvins, zenith		
L-band		35
S-band (cryo-HEMT)	43	
S-band (maser)		15
X-band (cryo-HEMT)	50*	
X-band (maser)	21	21
Polarization		
L-band		LCP
S- and X-band	RCP or LCP	RCP or LCP

*Predicted value

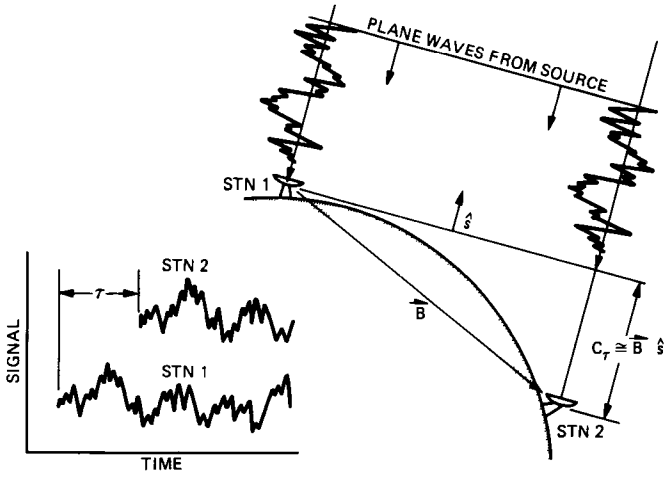

Fig 1 Schematic representation of a VLBI observation showing the measured delay, τ, which is given by the dot product of the baseline vector, B, and the unit vector to the source

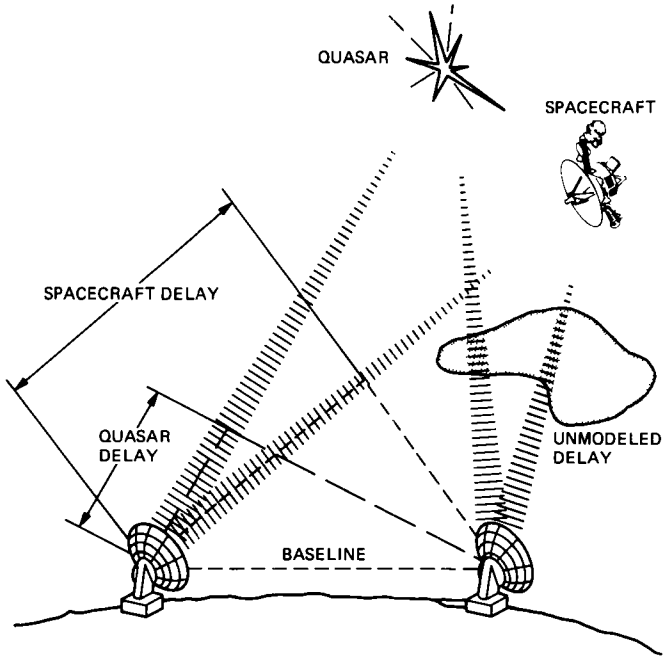

Fig 2 Schematic of a ΔVLBI observation Unmodeled media delays or baseline errors occur in the observation of both the Extragalactic Radio Source (EGRS) and the spacecraft These effects are greatly reduced by differencing the delay observations

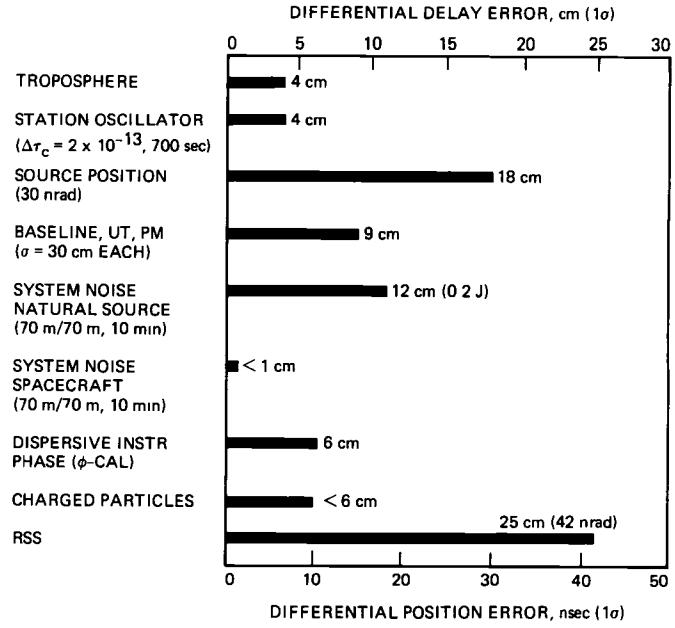

Fig 3 Delta-DOR angular position error budget for the Galileo Project A spacecraft-to-EGRS angular separation of 10 degrees, 600-second observations on each source, and 700 seconds between the EGRS and spacecraft observations are assumed

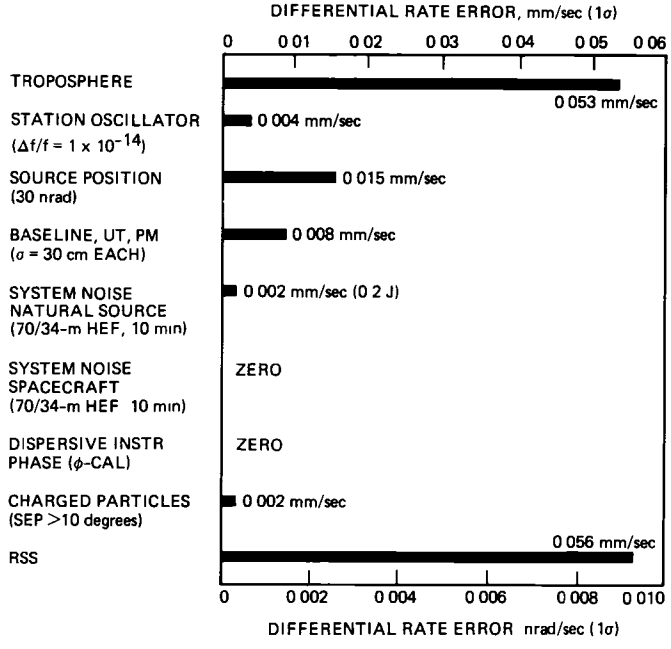

Fig 4 Delta-DOD angular rate error budget for the Magellan Project An average elevation angle of 15 degrees is assumed along with a Sun–Earth–probe (SEP) angle greater than 10 degrees, a spacecraft-to-EGRS separation of 10 degrees, and an integration time of 600 seconds The ΔDOD accuracy is dominated by unmodeled fluctuations in the troposphere

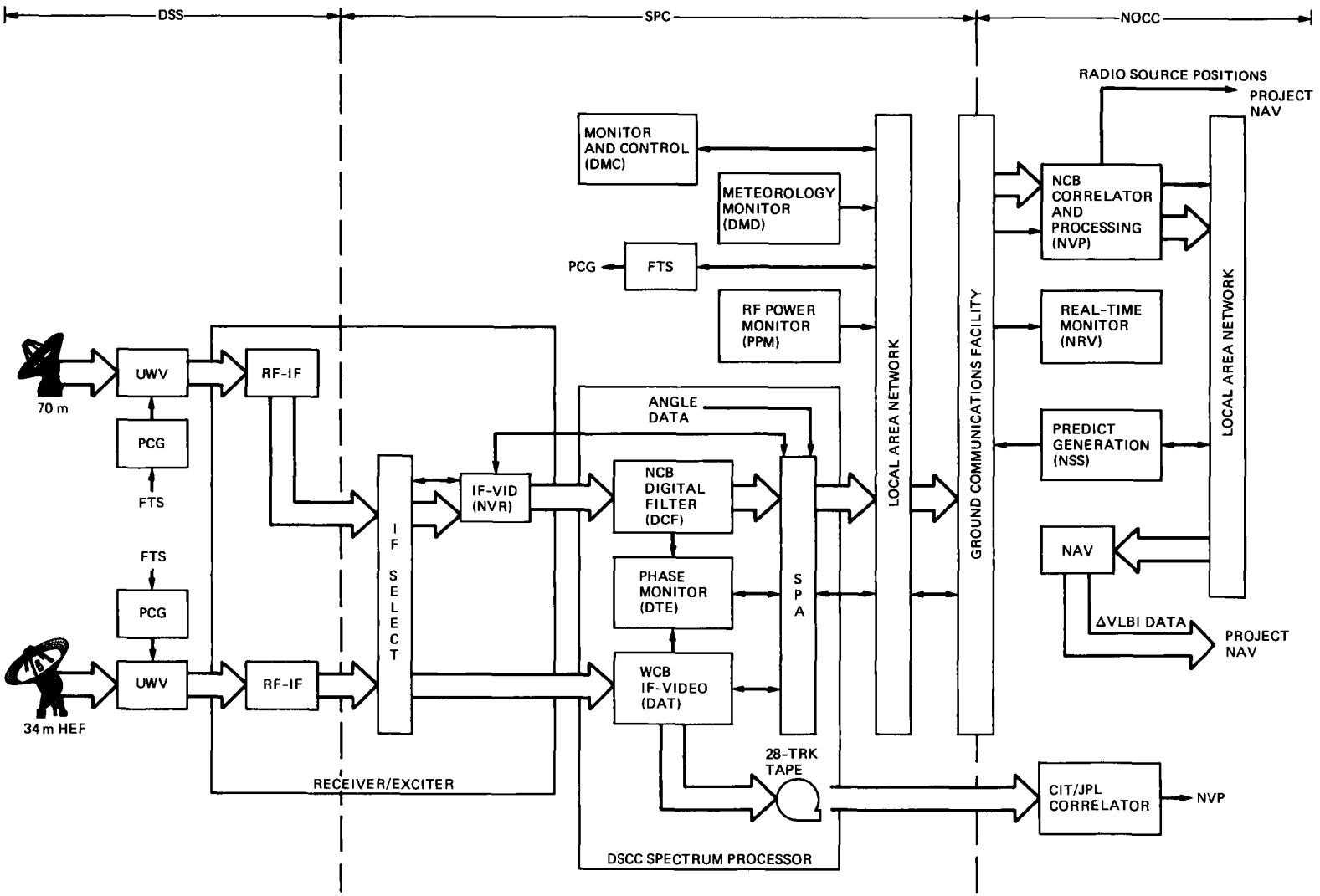

DAT	DATA ACQUISITION TERMINAL	NRV	NOCC RADIO SCIENCE/VLBI MONITOR
DCF	DATA CHANNEL FILTER	NSS	NOCC SUPPORT SUBSYSTEM
DMC	DSCC MONITOR AND CONTROL	NVP	NOCC VLBI PROCESSOR SUBSYSTEM
DMD	DSCC MEDIA CALIBRATION SUBSYSTEM	NVR	NCB VLBI RECEIVER
DSS	DEEP SPACE STATION	PCG	PHASE-CALIBRATION GENERATOR
DTE	DIGITAL TONE EXTRACTOR	PPM	PRECISION POWER MONITOR
FTS	FREQUENCY AND TIMING SUBSYSTEM	SPA	SPECTRUM PROCESSOR ASSEMBLY
NAV	NOCC NAVIGATION SUBSYSTEM	SPC	SIGNAL PROCESSING CENTER
NOCC	NETWORK OPERATIONS CONTROL CENTER	UWV	MICROWAVE SUBSYSTEM

PRIMARY DATA FLOW

CALIBRATION DATA AND CONTROL

Fig 5 VLBI system block diagram

X-Band Noise Temperature Near the Sun at a 34-Meter High Efficiency Antenna

T A Rebold and T K Peng
Telecommunications Systems Section

S D Slobin
Radio Frequency and Microwave Subsystems Section

X-band system noise temperature near the sun was measured at DSS 15, a 34-meter High Efficiency (HEF) antenna, in November 1987 Data was taken at angles off the center of the sun from 0 to 4 degrees At angles greater than 0 5 degree, the measured results agree with Voyager tracking data taken at Solar Conjunction in late December 1987 Within the solar disk, at angles lower than 0 27 degree, the temperature measured was lower than the prediction of a model by 30 percent, after adjusting for known receiver nonlinearities The discrepancy in this extreme case is probably caused by unknown nonlinearities in the receiver, uncertainties in the model, or both The measurement is nevertheless credible for practically all Sun–Earth–Probe angles of interest to deep space missions

I. Introduction

On November 26 and 27 of 1987, a test was performed at DSS 15 to determine the effect of solar radiation on the system noise temperature at low Sun–Earth–Probe (SEP) angles This test was prompted by the need to gather data in preparation for an advanced receiver test scheduled one month later during the Voyager solar conjunction, a low SEP angle event

Existing data on solar noise effects given in the *DSN/Flight Project Interface Design Handbook*[1] is insufficient on two counts First, data provided pertains only to the 64-m antenna and not to the newer High Efficiency (HEF) antenna at DSS 15 Second, this 64-m data does not identify the solar radiation level, which varies widely at X-band throughout the 11-year cycle of sunspot activity

Previous solar noise temperature measurements carried out at JPL include those at 2297 MHz measured at the DSS 14 64-m antenna [1] and at 20 7 GHz and 31 4 GHz, made with an early-model DSN water vapor radiometer [2] No such measurement at X-band has been performed Therefore, an additional factor motivating this measurement was to provide data necessary to characterize the HEF antenna performance in the design handbook

The measured data was compared with two additional sources of information The first source is a prediction from an

[1] *DSN/Flight Project Interface Design Handbook*, JPL Document 810-5 (internal report), vol 1, module TCI-40, Jet Propulsion Laboratory, Pasadena, California, 1983

analytical model of a large dish antenna taking into account the solar flux measurements for November 26 and 27 provided by the National Oceanic and Atmospheric Administration (NOAA) The second source is an independent noise temperature measurement obtained from DSS 43 and DSS 15 one month later during the Voyager solar conjunction This measurement was taken using the regular station Noise Adding Radiometer (NAR)

The report is divided into three major parts Section II describes the measurement and the data taken Section III describes an analytical model used to predict the system noise temperature when the antenna is pointing directly on the sun Finally, Sections IV and V conclude the report by comparing the measured data with the prediction and with the Voyager observations Error analysis for the measurement is presented in the Appendix

II. Measurement

A. Observation Strategy

A total of 5 hours over two days was allocated to the performance of the measurement at the station, allowing the sampling of about 100 points on two quadrants of the plane perpendicular to the boresight of the antenna Since the sun was anticipated to pass above the probe during the conjunction, the top two quadrants were chosen for the measurement The points were picked to lie on a Cartesian grid indexed by the sun's elevation and cross-elevation offsets from the probe

An existing contour map showing the gain distribution of DSS-13, a 26-meter antenna with a similar quadripod structure supporting the antenna subreflector, was used as a guide for the selection of data points This map showed that significantly higher sidelobes are generated by the antenna quadripod structure In order to investigate the effects of the quadripod structure on solar noise temperature increases, a large number of points were chosen to lie along these sidelobes, which form two diagonals crossing the origin at 45 and 135 degrees

At the station, the Antenna Pointing Assembly (APA) was given the coordinates of the sun for tracking in planetary mode, as well as a list of the desired sample points converted beforehand into elevation and azimuth offsets from the sun The sample points were compiled into a series of command macros and input into the APA by the station operator On both days the measurements were made in late afternoon, when the elevation of the sun varied from about 24 to 7 degrees Correspondingly, the antenna efficiency varied from about 64 percent to 61 percent due to gravity-induced structural deformations

B. Instrumentation

A block diagram of the station configuration and the instrumentation used to perform the test is shown in Fig 1 Data was recorded using a "quasar meter" being developed by the DSN Operations for use in VLBI applications The quasar meter consists of an HP 9816 computer recording power measurements from an HP 436A power meter, which is connected to the 300-MHz IF distribution of the open-loop receiver The station was receiving in X-band using the Block II maser The Y-factor machine connected to the Block III closed-loop receiver was used to provide pre-, post-, and in-track system temperature calibrations It also served as a real time monitor of the noise power received during the measurement

C. Measurement Procedures

Prior to tracking, station personnel performed a precalibration by recording ambient load and cold sky noise levels with the quasar meter and measuring the associated system temperatures with the standard DSN Y-factor method During tracking mode, data was recorded at a rate of one sample per second, while the antenna was pointed at the various elevation and cross-elevation offsets from the sun The typical dwell time at a given point was 2 5 minutes, except for occasional sweeps across the origin (sun) with dwell times at 20 seconds per point The ambient load was switched in periodically to ascertain proper functioning of the test configuration After tracking, a final postcalibration was performed

D. Data Analysis

Several steps were required to turn the raw power samples into system noise temperature measurements First, the average and standard deviation of the power samples acquired at each antenna offset were computed Second, the power measurements were converted into noise temperature using the pre- and post-calibrations The third step involves normalizing the temperatures to zenith by subtracting out the system noise temperature as a function of elevation angle (see Fig 2, which was the result of a separate measurement) The resulting temperatures indicate system noise level increases due to the presence of the sun at particular offsets from the antenna boresight This temperature will be referred to as the Solar Noise Temperature (T_{sn})

For very high noise temperatures, an additional step is taken to adjust for the effect of saturation in the receiving system To estimate the saturation effect, the gains and bandwidths of the amplifiers in Fig 1 are given in Fig 3 Gain compression occurs in the maser or in the RF/IF converter when the output power of either amplifier reaches its own saturation level Data on the Block IIA maser, which has the same saturation characteristics as the Block II maser used in this measure-

ment, indicates significant saturation above 2900 kelvins as seen in Table 1 (data provided by S Petty, Radio Frequency and Microwave Subsystems Section) Note that this data refers to the noise power at the input of the maser which was tuned to 45-dB gain Data on the RF/IF converter (provided by M Lambros of the same section) indicates a 1-dB compression level at 26 dBm and 0 1-dB compression at 16 dBm measured at the output of the converter, using a sinusoidal test signal

A quadratic curve fitted to the first three points of Table 1 was applied to the power measurements from the quasar meter in order to compensate for the maser compression The maximum adjustment was about 0 3 dB for power readings taken with the antenna pointed at the sun's center At this location, the adjusted T_{sn} reached its maximum of 8240 kelvins

This level of solar noise will not saturate the RF/IF converter according to the overall gain and bandwidth as shown in Fig 3 With a total gain of 85 dB from maser to converter and an effective bandwidth of 100 MHz, the output level from the RF/IF converter will reach only about 5 6 dBm at the maximum system noise temperature This is still about 10 dB lower than the 0 1-dB compression point of the converter (16 dBm)

However, there are uncertainties in the measurement of gain compression (about 0 1 dB), and the measured equipment was typical and not the actual equipment at DSS 15 Thus the error in the nonlinearity compensation applied to the power measurements could be as high as 10 percent in the positive direction due to the possibility of additional sources of compression Since it is more likely that there will only be more nonlinearity than what was measured and not less, the error in the negative direction should be less than 2 percent This assumption on the error in the nonlinearity compensation will be used in the error analysis in the appendix

Figures 4 and 5 show two quadrants of the antenna's field of view in the elevation versus cross-elevation coordinate system The locations where noise temperature was measured are indicated by black dots They are accompanied by the measured solar noise temperature T_{sn}

Figure 6 shows the entire data set condensed into a plot of solar noise temperature versus SEP angle The points are divided into two categories those that lie along the quadripod sidelobes at 45 and 135 degrees and those that do not As seen in the figure, for a given SEP angle the sun's influence on the system noise temperature is greater if it lies along a quadripod sidelobe This agrees well with antenna gain patterns showing higher sidelobes generated by the quadripod structure

E. Error Analysis

The noise temperature is determined from (1) the noise power measured with the power meter, and (2) the measured noise power and the noise temperature at both ambient load and zenith taken during calibration The accuracy of the noise temperature measurement reported here therefore depends on the accuracy of calibration and of the power meter Detailed analysis is given in the appendix The result is the following upper bound for the standard deviation of the measurement of the noise temperature increase due to the sun

for $T_{sn} \leqslant 2900$ kelvins,

$\sigma(T_{sn}) \leqslant 2\ 0 + 0\ 05\ T_{sn}$ kelvins

for $T_{sn} > 2900$ kelvins,

$\sigma(T_{sn}) \leqslant 2\ 0 + 0\ 15\ T_{sn}$ kelvins in the positive direction

$\leqslant 2\ 0 + 0\ 07\ T_{sn}$ kelvins in the negative direction

III. Predicted System Noise Temperature Increase Looking at the Center of the Sun

The expected increase in system noise temperature from a natural radio source is given as [3]

$$\Delta T = \frac{\eta S A}{2k} \tag{1}$$

where

η = 0 75 ± 0 05, antenna efficiency for the DSS 15 34-m antenna at 8420 MHz, looking at a source much larger than the beam solid angle It includes the effect of spillover, blockage, VSWR, dissipation, and surface imperfection but does not include beam-broadening factors such as illumination, phase, and cross-polarization

S = the flux density of the radio source, W/m^2-Hz

A = the physical area of the antenna, m^2

k = Boltzmann's constant (1 380622 X 10^{-23}), W/Hz-K

On the days of the measurements described here (November 26 and 27, 1987), the NOAA Space Environment Services Center[2] determined the total solar flux at 8800 MHz as measured at four locations over two days to be approximately

[2]U S Department of Commerce, National Oceanic and Atmospheric Administration, Environmental Research Laboratories, Space Environment Services Center, Boulder, Colorado

259 Solar Flux Units, or SFUs (1 SFU = 1×10^{-22} watts/m^2-Hz), with a total spread in the measurement of about 50 SFUs From comparisons of measurements made at a different time (February 3, 1988) at 4995 MHz and 8800 MHz, it was found that the solar flux varied with frequency approximately as

$$S \propto f^{1.2} \tag{2}$$

From this relationship, the flux at 8420 MHz (on November 26 and 27, 1987) is estimated to be

$$S = 246 \text{ SFUs}$$

The 1σ equivalent uncertainty of this estimate is about 5 percent, including the uncertainties of both steps

The flux received by a narrow beam antenna is proportional to the ratio of the solid angle of the antenna to the solid angle of the solar disk A number of corrections to this first-order approximation are discussed in [4] The solid angle of the main beam is given by

$$\Omega_M = K_p \theta^2 \tag{3}$$

where

θ = the half-power beamwidth of the antenna main beam, measured at 0 061 degree for DSS 15 from 12-deg to 60-deg elevation by W Wood (private communication), an uncertainty of 5 percent is estimated

K_p = a factor depending on pattern shape, estimated to be 1 03 ± 0 03 for nearly uniform illumination ([4], p 221)

The solid angle of the sun is

$$\Omega_{sun} = \frac{\pi}{4} D^2 \tag{4}$$

where D is the diameter of the solar disk, or 0 533 degree

Since the sun subtends an angle larger than the main beam, a correction to the main beam solid angle is made utilizing antenna pattern integrations made by T Y Otoshi (private communication) These calculations indicate that whereas 83.5 percent of the antenna power is in the main beam, 95 4 percent is within the solar disk This correction is 14 percent Therefore, the power within the solar disk is adjusted as follows

$$\Omega'_M = 1\ 14\ \Omega_M \tag{5}$$

The noise temperature increase for the sun (at a 24-degree elevation angle where the antenna efficiency is 0 64) is then estimated to be

$$\Delta T = \frac{\eta S A}{2K} \cdot \left(\frac{\Omega'_M}{\Omega_{sun}} \right)$$

$$= 11{,}890 \text{ kelvins} \tag{6}$$

Finally, this estimate is corrected to include the effect of limb brightening [4], which is an increase in temperature at the edge of the solar disk This increase is measured as a part of the total solar flux on the ground but is not observed by the main beam of the antenna, which is pointed to the center of the disk This factor is estimated to be 0 99 ± 0 01 The estimated X-band temperature is therefore

$$\Delta T = 11{,}770 \text{ kelvins}$$

The uncertainty of this estimate is about 15 percent, calculated as the root of the sum of the squares of the individual percentage errors given above

IV. Discussion

Figure 7 shows a comparison between the measured data and several data points taken during the Voyager solar conjunction at DSS 15 and DSS 43 using the standard DSN Noise Adding Radiometer These points, with SEP angles greater than 0 5 degree, are seen to fall above and below the measured curve and hence are consistent with the measurement in this region Therefore, the measurement can be used as a model for predicting the level of system temperature increase in this SEP range Since the temperature is directly proportional to the solar flux density as explained in Section III, a prediction can be obtained by scaling the measured temperatures The scale factor is simply the flux density at the time of interest divided by 246 SFUs, the flux density at 8 4 GHz during this measurement The flux density at any given time can be roughly estimated according to the solar cycle

The maximum measured noise temperature increase with the antenna pointing directly at the sun was about 8240 kelvins However, the model described in the previous section estimates the solar noise temperature based on recorded solar flux to be 11,770 kelvins with an uncertainty of about 15 percent Thus the measured temperature is 30 percent below the

prediction The exact cause of this difference is unknown One possibility is an unidentified nonlinearity in the receiver that has not been measured before Table 1 suggests that this nonlinearity, if it exists, would have a significant effect only at temperatures above 2933 kelvins Another possibility is error in the modeling

V. Conclusion

System noise temperature increases at X-band due to the sun were measured at DSS 15, a 34-m HEF antenna, using the station open-loop receiver The temperature was measured with an accuracy of about 5 percent up to 2900 kelvins Temperatures above 2900 kelvins were adjusted to compensate for known nonlinearity in the receiving system In this range the accuracy of the measurement is about 15 percent in the positive direction and 7 percent in the negative direction due to uncertainties in knowledge of the nonlinearity of the maser and the open-loop receiver

The measurement agrees well with Voyager tracking data taken during the solar conjunction at SEP angles greater than 0 5 degree It can be used as an experimental model for estimating system temperature increases for missions flying close to the sun, given a knowledge of the solar flux density at the desired time

For temperatures obtained with the antenna pointing directly at the sun, there is a difference of 30 percent between the measured value of 8240 kelvins and the predicted value of 11,770 kelvins The discrepancy in this extreme case is probably caused by unknown nonlinearities in the receiver, uncertainties in the model, or both

As a result of the investigation, it has become evident that there is much uncertainty in the knowledge of the noise temperature of the solar disk and no proven prediction at angles off the disk Further work is needed for the DSN to adequately characterize the noise temperature effects around the sun for the benefit of deep space missions

Acknowledgments

The authors are grateful to M Wert and R Caswell of DSN Operations for their help in implementing the procedure and the power meter R Owen and V Sutton were indispensable for their flawless operation of the antenna and equipment at Goldstone during the measurement Thanks are especially due to C Stelzried for providing helpful discussion in the preparation of this report

References

[1] D A Bathker and D W Brown, "Large Ground Antenna Performance with Solar Noise Jamming," *Proceedings of the IEEE*, pp 1949–1951 and 1966, December 1966

[2] M M Franco, S D Slobin, and C T Stelzried, "20 7 and 31 4 GHz Solar Disk Temperature Measurements," *TDA Progress Report 42-64*, vol May–June 1981, Jet Propulsion Laboratory, Pasadena, California, pp 140–159, August 15, 1981

[3] J A Turegano and M J Klein, "Calibration Radio Sources for Radio Astronomy Precision Flux Density Measurements at 8420 MHz," *Astronomy and Astrophysics*, vol 86, pp 46–49, 1980

[4] J D Kraus, *Radio Astronomy*, New York McGraw-Hill, 1966

[5] C T Stelzried, "Errors in Noise Temperature Measurement," *The Deep Space Network Noise Temperature Concepts, Measurements, and Performance*, JPL Publication 82-33, Jet Propulsion Laboratory, Pasadena, California, pp 25-1–25-3, September 15, 1982

Table 1 Saturation of the Block IIA X-band maser at high noise power (maser gain set at 45 dB)

Noise power at maser input, kelvins	Maser gain compression, dB
736	0
2933	0.1
36,931	1.0
92,767	2.0

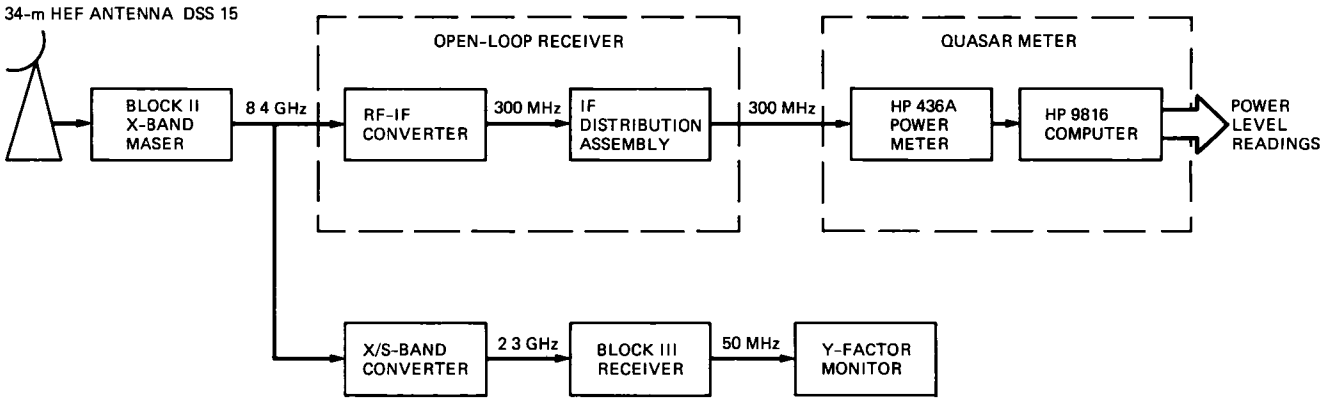

Fig. 1 Block diagram of the measurement system

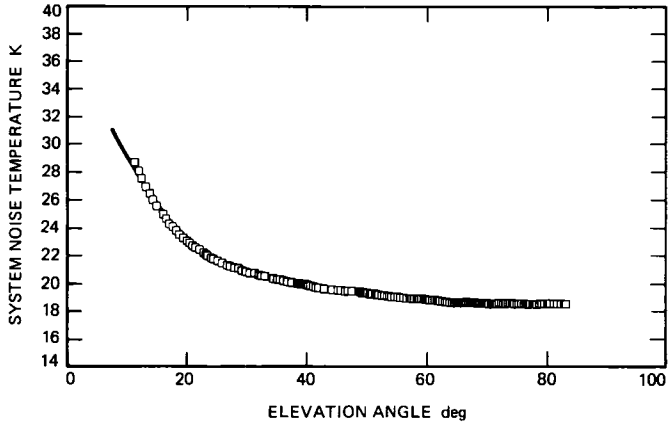

Fig 2 DSS-15 34-meter HEF X-band system noise temperature (with atmosphere), measured on January 12, 1988

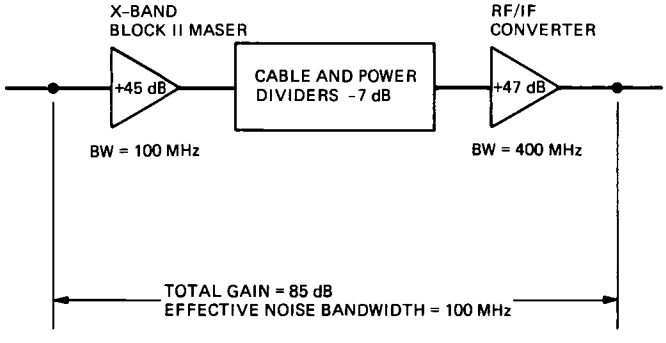

Fig 3 Receiver gains and bandwidths for saturation analysis

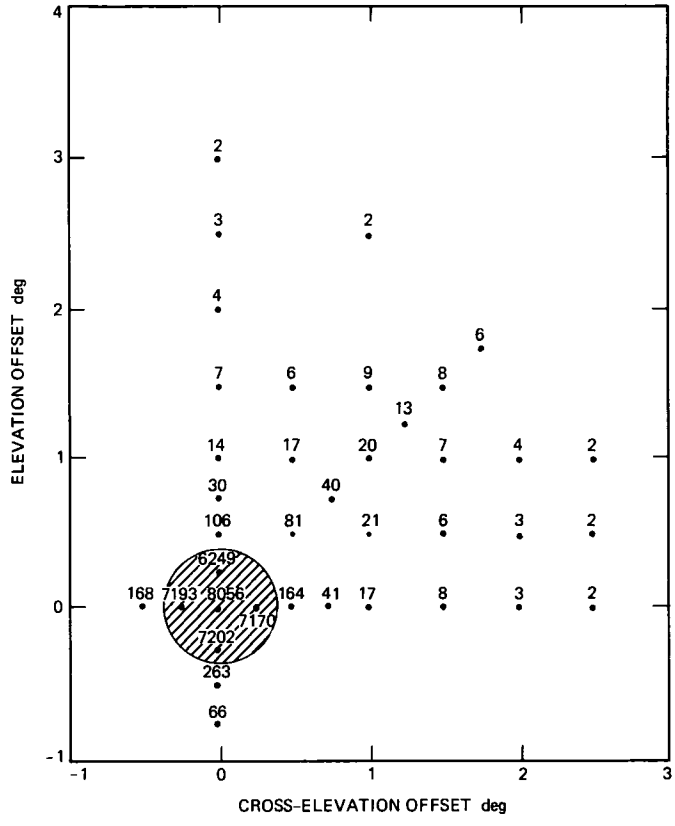

Fig 4. System temperature increase due to the sun at angular offsets from the antenna boresight, measured on November 26, 1987 Numbers within the circle are below prediction due to unaccounted receiver nonlinearity or model errors

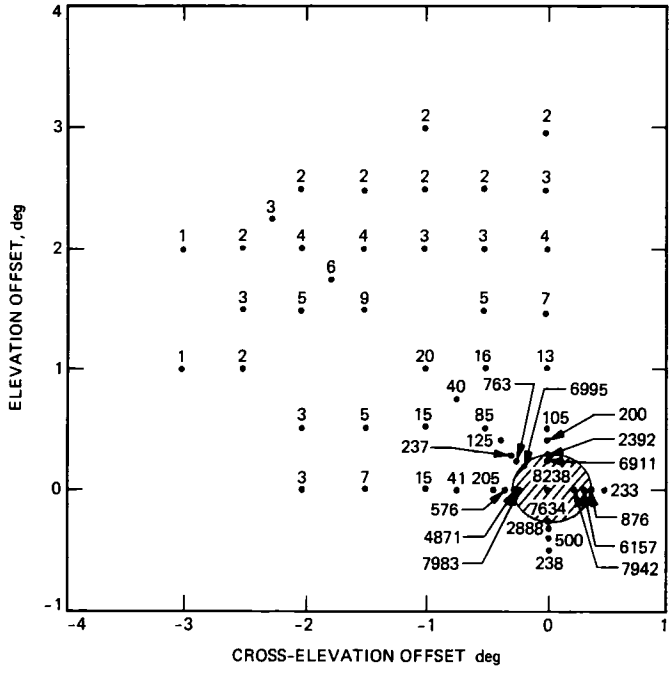

Fig. 5 System temperature increase due to the sun at angular offsets from the antenna boresight, measured on November 27, 1987 Numbers within the circle are below prediction due to unaccounted receiver nonlinearity or model errors

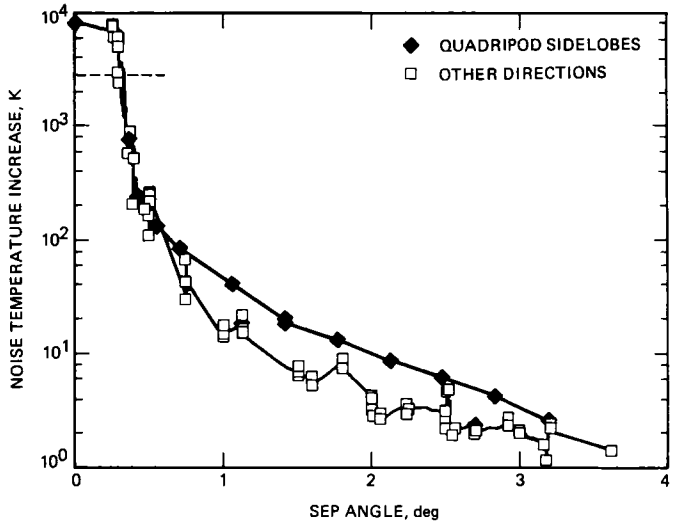

Fig 6 System temperature increases due to the sun at various SEP angles, showing larger temperature increases along quadripod sidelobes. Data points above the dotted line are below prediction due to unaccounted receiver nonlinearity or model errors.

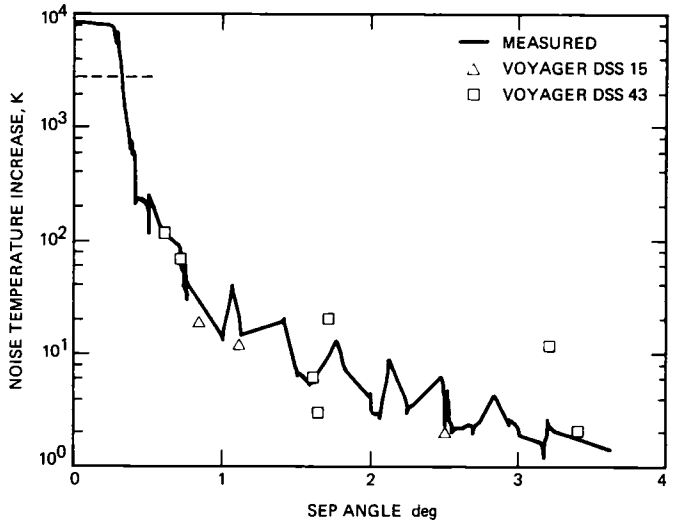

Fig. 7 Comparison of DSS-15 measured increase of system temperature with Voyager tracking data obtained at DSS 15 and DSS 43 during solar conjunction Data points above the dotted line are below prediction due to unaccounted receiver nonlinearity or model errors

Appendix

Calculating Error Bounds on Temperature Measurements

This appendix describes the method used to obtain estimates of error on the noise temperature measurements The measured noise temperature (T_m) in all cases is derived from the relation

$$T_m = (P_m - P_s)(T_a - T_s)/(P_a - P_s) + T_s \qquad \text{(A-1)}$$

where P_m is the measured power, P_s is the power reading at cold sky, T_s is the sky temperature (measured using the Y-factor method), P_a is the power reading at ambient, and T_a is the ambient temperature Note that P_s, T_s, P_a, and T_a were measured during calibration For temperatures above 736 kelvins the power, P_m, is compensated for the maser saturation prior to applying Eq (A-1)

Each parameter to the right of the equation is an average of many data points Uncertainties in these parameters contribute to the uncertainty of the noise temperature This is shown in the following equation obtained by taking differentials on both sides of Eq (A-1)

$$\begin{aligned}\delta T_m = {} & \delta P_m (T_a - T_s)/(P_a - P_s) \\ & - \delta P_s [(T_a - T_s)/(P_a - P_s) \\ & + (P_m - P_s)(T_a - T_s)/(P_a - P_s)^2] \\ & + \delta P_a (P_m - P_s)(T_a - T_s)/(P_a - P_s)^2 \\ & + \delta T_a (P_m - P_s)(P_a - P_s) \\ & + \delta T_s [1 - (P_m - P_s)/(P_a - P_s)] \end{aligned} \qquad \text{(A-2)}$$

Expressing $P_m - P_s$ in terms of $T_m - T_s$ according to Eq (A-1) and rearranging terms in Eq (A-2), we have the following equation

$$\begin{aligned}\delta T_m = {} & \delta T_s + (\delta P_m - \delta P_s)(T_a - T_s)/(P_a - P_s) \\ & + (T_m - T_s)[(\delta T_a - \delta T_s)/(T_a - T_s) \\ & - (\delta P_a - \delta P_s)/(P_a - P_s)] \end{aligned} \qquad \text{(A-3)}$$

The first term on the right is the error in calibrating the reference noise temperature The second term is the effect of error in the power meter reading when an actual measurement is taken Finally, the third term represents an error which is linearly increasing with the noise temperature measured The slope of the increase is determined by calibration errors

It can be shown that the standard deviation of the sum of several quantities is bounded from above by the sum of the standard deviations of the individual quantities We now use this inequality on Eq (A-3) to establish an upper bound on the temperature error

$$\begin{aligned}\sigma(T_m) \leqslant {} & \sigma(T_s) + \sigma(P_m - P_s)(T_a - T_s)/(P_a - P_s) \\ & + (T_m - T_s)[\sigma(T_a - T_s)/(T_a - T_s) \\ & - \sigma(P_a - P_s)/(P_a - P_s)] \end{aligned} \qquad \text{(A-4)}$$

An upper bound of the standard deviation of each term on the right hand side is estimated below [5]

$$\sigma(T_s) \leqslant 0\,7 \text{ kelvin}$$

$$\begin{aligned}\sigma(P_m - P_s) &\leqslant \sigma(P_m) + \sigma(P_s) \\ &\leqslant 0\,02P_m + 0\,02P_s\end{aligned}$$

The inequality above is based on the power meter specification and the observed noise in measured data, to an effective one-sigma uncertainty of 2 percent It can be rewritten as

$$\sigma(P_m - P_s) \leqslant 0\,02(P_m - P_s) + 0\,04P_s$$

Using this inequality and Eq (A-1) we obtain

$$\begin{aligned}\sigma(P_m - P_s)(T_a - T_s)/(P_a - P_s) &\leqslant 0\,02(T_m - T_s) \\ &\quad + 0\,04P_s(T_a - T_s)/(P_a - P_s) \\ &\leqslant 0\,02(T_m - T_s) + 0\,8\end{aligned}$$

The last inequality uses the approximate values of T_a (300 kelvins), T_s (19 kelvins), and the ratio of P_a to P_s of approximately 15

$$\begin{aligned}\sigma(T_a - T_s)/(T_a - T_s) &\leqslant [\sigma(T_a) + \sigma(T_s)]/(T_a - T_s) \\ &\leqslant 0\,004\end{aligned}$$

The last inequality uses the estimates $\sigma(T_a) \leq 0.4$ kelvin and $\sigma(T_s) \leq 0.7$ kelvin after Stelzried [5]

$$\sigma(P_a - P_s)/(P_a - P_s) \leq [\sigma(P_a) + \sigma(P_s)]/(P_a - P_s)$$

$$\leq [0.02P_a + 0.02P_s]/(P_a - P_s)$$

$$\leq 0.023$$

The last inequality uses the approximate ratio of P_a to P_s, 15, as before

Summarizing the above, we arrive at the following

$$\sigma(T_m) \leq 0.7 + 0.8 + (T_m - T_s)(0.02 + 0.004 + 0.023) \text{ kelvins}$$

With $T_s = 19$ kelvins, we have

$$\sigma(T_m) \leq 1.5 + 0.05(T_m - 19) \text{ kelvins}$$

This is a compact inequality showing the error in measured temperature as a function of the temperature However, the temperatures plotted in Figs 4–7 are actually the solar noise temperatures (T_{sn})

$$T_{sn} = T_m - T_{\text{elev}}$$

where T_{elev} is the system noise temperature as a function of elevation angle (shown in Fig 2) removed to normalize the measurements to solar effects only Assuming that no additional error enters from T_{elev}, we have

$$\sigma(T_{sn}) \leq 1.5 + 0.05(T_{sn} + T_{\text{elev}} - 19) \text{ kelvins}$$

At most, T_{elev} is about 30 kelvins This gives

$$\sigma(T_{sn}) \leq 2.0 + 0.05 T_{sn} \text{ kelvins}$$

One final consideration lies in the maser noise saturation for very high noise temperatures When the measured noise temperature is above 2900 kelvins, the nonlinearity of the Block II X-band maser is compensated This compensation could be off by a maximum of about 10 percent in the positive direction and 2 percent in the negative direction as mentioned in Section IIE These errors are added to the error when temperatures exceed 2900 kelvins In summary, the standard deviation of the error in the solar noise temperature is as follows

for $T_{sn} \leq 2900$ kelvins,

$\sigma(T_{sn}) \leq 2.0 + 0.05\ T_{sn}$

for $T_{sn} > 2900$ kelvins,

$\sigma(T_{sn}) \leq 2.0 + 0.15\ T_{sn}$ kelvins in the positive direction

$\leq 2.0 + 0.07\ T_{sn}$ kelvins in the negative direction

Baseband Assembly Analog-to-Digital Converter Board

I Doerksen and L Howard
Radio Frequency and Microwave Subsystems Section

This article reports on the design and development of an upgraded analog-to-digital converter board for the Baseband Assembly (BBA) of the Deep Space Communications Complex Telemetry Subsystem (DTM)

I. Introduction

The BBA combines and processes baseband signal inputs from up to eight Deep Space Network antennas tracking a single spacecraft The result is an improved symbol signal-to-noise ratio (SSNR) digital telemetry data output for the Telemetry Subsystem (DTM) [1]

The analog-to-digital converter board (ADB) is used by the Real-Time Combiner (RTC) and Demodulator Synchronizer Assembly (DSA) subsystems of the BBA The function of the ADB in both subsystems is to digitize an analog baseband telemetry signal for subsequent processing (see Fig 1)

II. Specifications

The ADB is designed to accommodate the mission-independent range of telemetry data rates, type of modulation, SNR, and signal level The major elements of the ADB are the automatic gain control (AGC) circuit and the analog-to-digital converter (ADC) For a description of the theory of operation of the AGC and ADC, see the Appendix

This ADB was designed to meet existing system specifications and to provide added operational capability of real-time, high resolution, AGC level and offset control The primary specifications are given in Table 1

III. Functional Description

The ADB consists of two identical signal conversion channels and a Multibus I computer interface (see Fig 2) The interface group provides the logic for standard Multibus I handshake control, board address detection, and on-board device selection Each analog-to-digital conversion channel consists of an input filter, a gain-controlled input amplifier, a signal amplifier (ADC driver), an automatic gain control circuit (AGC), and D/A converters for vernier gain and offset control

Vernier gain and offset in the AGC loop are under CPU control When the system software senses a need for adjustment of either offset or AGC level, the CPU loads the appropriate D/A with a new digital value to effect the necessary change

IV. Detailed Description

The control section of the board consists of logic for bus control, board and device address decoding, and data buffering Bus control logic provides standard Multibus I handshake functions for CPU-to-board data transfer On-board logic is isolated from the bus with tristate buffers to minimize contamination of analog signals by bus activity

The two dual D/A converters (DACs) are addressed by an external CPU Data written to the DACs cannot be read back Data written to a DAC represents a change in the vernier offset or AGC level The correctness of the new value can be determined by the system software

The analog input signal is attenuated by a 30-dB pad and filtered by a 7-pole, 7-MHz (50-ohm) low-pass Butterworth filter The filtered signal is coupled to a gain-controlled amplifier

The gain-controlled signal is capacitively coupled (DC isolated) to a high-speed operational amplifier which drives the analog-to-digital converter (ADC) The output of the ADC driver has a fixed offset of approximately −1 volt to center the signal in the midrange of the ADC The CPU-controlled vernier DC offset is summed with the data signal at the input to the amplifier to provide a more exact control of the offset adjustment

The ADC is a 20-megasample-per-second, full-parallel (flash) analog-to-digital converter capable of converting up to 7 MHz The ADC is configured for an 8-bit, false, two's-complement output A system clock is buffered on board to function as the ADC sampling clock

The AGC circuit consists of a half-wave rectifying power detector and an integrator The rectified signal is input to the integrating operational amplifier The output of the integrator drives the control input to the gain-controlled amplifier, closing the AGC loop The CPU-controlled vernier AGC level is summed with the feedback voltage at the input to the integrator Manual level control is possible by a hardware configuration of the board and manual level adjustment

V. Summary

Prototypes of the ADB were tested in a stand-alone configuration to validate the characteristics of data conversion and control functions The boards were subsequently installed in the Real-Time Combiner and Demodulator Synchronizer assemblies for system integration Integration consisted of control software development and system performance evaluation The results of testing, including system evaluation, showed that the prototypes met or exceeded all initial design criteria (see Fig 3 and Table 1)

Major considerations in the design of the ADB were reliability and ease of calibration Reliability was addressed by using mature technology, proven circuit design, and electronic components Manual preinstallation calibration consists of a single coarse offset adjustment per channel System calibration is completely under software control

The ADB uses current multilayer printed circuit board (PCB) technology The PCB was designed solely on an IBM-AT-based Futurenet CAE system The personal workstation approach to board design gave direct control of component layout and signal trace routing and eliminated time-consuming interaction with drafting/layout technicians The CAE-generated photo-plot and drill tape were directly used for fabrication

Reference

[1] C D Bartok, "Performance of the Real-Time Array Signal Combiner During Voyager Mission," *TDA Progress Report 42-63*, vol March–April 1981, pp 191–202, June 15, 1981

Table 1. Analog-to-digital converter board specifications

Parameter	Specification
Sample rate	20-MHz maximum
Resolution	8 bits
Digital output	8 bit, two's complement, TTL
Analog 3-dB bandwidth	500 Hz to 7 MHz
Input signal range	+24 to −24 dBm
CPU-controlled offset	
Range	0 2 volt
Resolution	0 2 volt/4096 = 0 049 millivolt
CPU-controlled AGC output level	
Tunable range	6 dB (0 2 volt to 0 8 volt for square wave)
Resolution	6 dB/4096 = 0 00146 dB (factor of 1 00033735)
Input impedance	50 ± 5 ohms

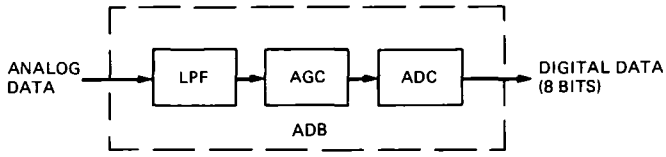

Fig 1. Analog-to-digital converter board simplified functional diagram

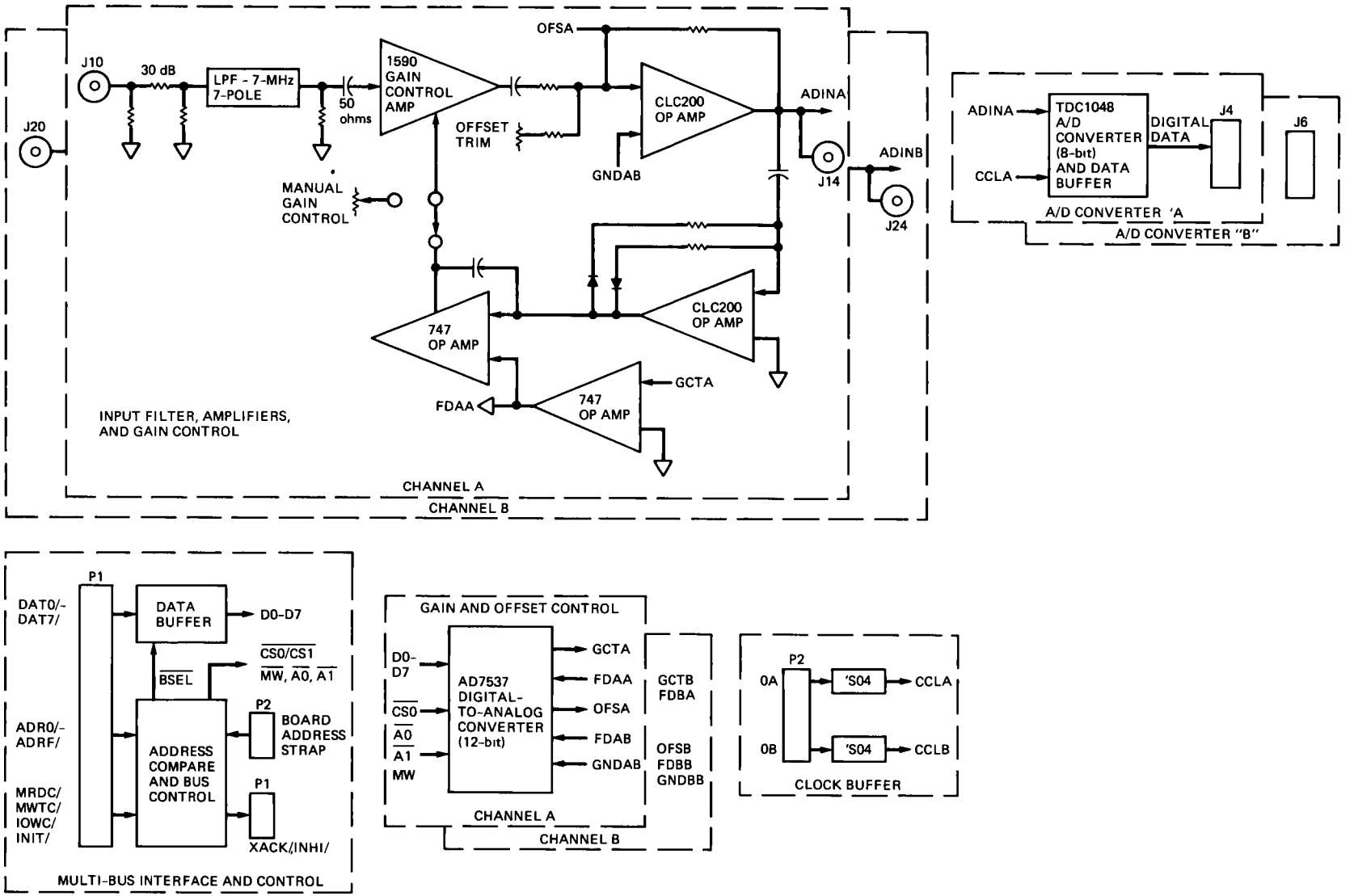

Fig. 2 Analog-to-digital converter board block diagram

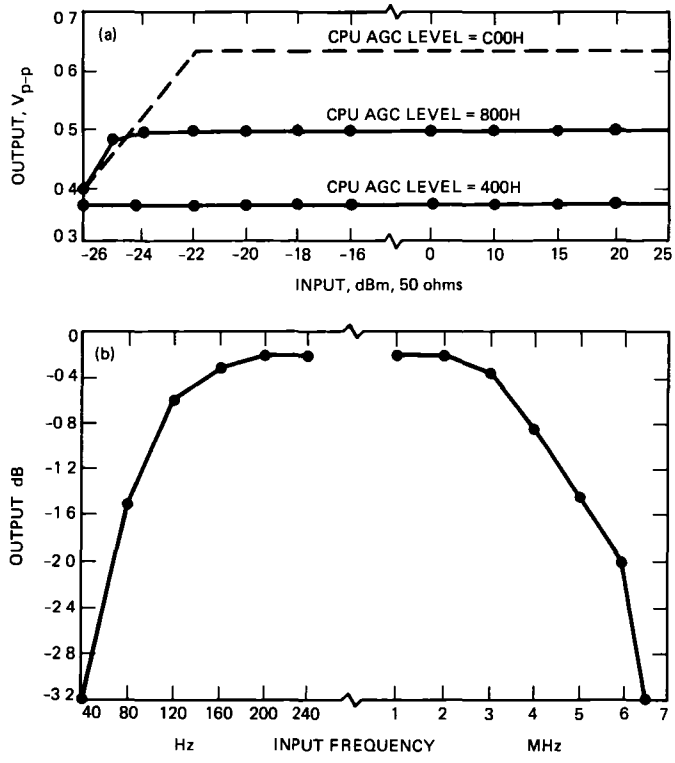

Fig 3 AGC (a) range and (b) frequency response

Appendix

AGC/ADC Description

The purpose of the automatic gain control (AGC) is to set the signal level so that it is properly scaled and centered in the range of the analog-to-digital converter

Signal-level detection is performed by a half-wave rectifier In order to accommodate the full range of symbol SNRs, the input/output levels were set as shown in Table A-1

I. ADC Characteristics

(8-bit, two's complement, 7-MHz BW, 20 msps)

The full ADC input range is ±128 = ±3 19σ units

The symbol SNR, R is related to the per-sample SNR, R_{rf}, by

$$R_{rf} = \frac{R \times r_{sy}}{2B} = \frac{S}{2N_0 B} = \frac{\mu_{rf}^2}{2\sigma_{rf}^2}$$

The linear rectifier output has an average value

$$V_{agc} = \frac{1}{2\sigma\sqrt{2\pi}} \int_0^\infty V e^{-1/2(V-\mu/\sigma)^2}\, dV + \frac{1}{2\sigma\sqrt{2\pi}} \times \int_0^\infty V e^{-1/2(V+\mu/\sigma)^2}\, dV$$

$$= \frac{\mu_{rf}}{2}\left[P\left(\sqrt{2R_{rf}}\right) - P\left(-\sqrt{2R_{rf}}\right) + \frac{e^{-R_{rf}}}{\sqrt{\pi R_{rf}}}\right]$$

$$= \frac{\mu_{rf}}{2}\left[P\left(\sqrt{2R_{rf}}\right) - P\left(-\sqrt{2R_{rf}}\right)\right] + \frac{\sigma_{rf}}{\sqrt{2\pi}} e^{-R_{rf}}$$

Thus, the mean sample voltage for any SNR is given by

$$\mu_{rf} = \frac{2V_{agc}}{\left[P\left(\sqrt{2R_{rf}}\right) - P\left(-\sqrt{2R_{rf}}\right) + \frac{e^{-R_{rf}}}{\sqrt{\pi R_{rf}}}\right]}$$

II. AGC Output Level

For a square-wave input without noise (pure signal), the AGC output is set to -1 V center, 0 5 V peak to peak In ADC units, this is

$$V_{agc} = \frac{\mu_{sq}}{2} = 16 \Rightarrow \mu_{sq} = 2V_{agc} = 32 = -1 \pm 0\,25\ \text{V}$$

For a noiseless sine wave, we denote the peak values by $\pm\mu_{sin}$ and

$$V_{agc} = 16 = \frac{\mu_{sin}}{\pi} \Rightarrow \mu_{sin} = \pi V_{agc} = 50\,3$$

$$= -1 \pm 0\,393 \text{ volts p-p}$$

For pure gaussian noise, we have for the average output of the half-wave rectifier

$$V_{agc} = 16 = \frac{1}{\sigma\sqrt{2\pi}} \int_0^\infty V e^{-V^2/2\sigma^2}\, dV = \frac{\sigma}{\sqrt{2\pi}}$$

or

$$\sigma = \sqrt{2\pi}\ V_{agc} = 40\ 1 \text{ (rms noise level)}$$

This corresponds to σ = rms noise voltage = 40 1/128 = 0 313 volt into 50-ohm noise power = $\sigma^2/50$ = 1 963 mW = 2 93 dBm

Table A-1 ADC input/output levels

Input level, V	Output code		
	Hex	Decimal	
−0 008	7FH	127	
−0 750	20H	32	μ_{sq}*
−0 096	D1H	1	
−1 004	00H	0	−1 V = center range
−1 012	FFH	−1	
−0 250	E0H	−32	μ_{sq}*
−2 000	80H	−128	

*$\pm \mu_{sq}$ = nominal levels for pure square-wave input
= −1 0 ± 0 25 V = ± 32 units (ADC)

Mark IV-85 Mission Support Planning and Future Mission Set

R J Amorose
TDA Mission Support and DSN Operations

The DSN is currently involved with supporting a group of mature deep space missions, none of which has been launched in the past ten years With great anticipation, the DSN is looking forward to the return of the Space Transportation System, which is scheduled to launch four deep space missions in 1989 through 1992 The DSN also supports earth orbiting spacecraft that are not compatible with the Tracking and Data Relay Satellite System (TDRSS)

I. Introduction

DSN Mission Support Planning is based on the total mission set and critical events listed in Figs 1, 2, 3, and 4 A group of older missions, including the Pioneers, the International Cometary Explorer, and the Voyagers, are being tracked daily by the deep space antennas located near Goldstone, California, Canberra, Australia, and Madrid, Spain While all of these missions have periods of important science return along with their normal interplanetary science data acquisition, the Voyager 2 spacecraft has one last significant planetary encounter

The Voyager Neptune encounter will be supported by the DSN from June through September of 1988, with the closest approach to Neptune on August 25, 1989 All three DSN Complexes plus the National Science Foundation's Very Large Array (VLA) in Socorro, New Mexico, the Parkes Radio Telescope in Parkes, Australia, and the Japanese Usuda station will be used for data collection during this encounter period The telecommunications link performance at the Neptune distance from earth requires the DSN to augment its capabilities in order to support the planned Voyager data rates (21 6-kbps maximum) Each of the DSN's 64-meter antennas has been upgraded to 70 meters The VLA has been equipped with X-band receive capability, the Parkes 64-meter antenna is being equipped with X-band receive capability and radio science ground support equipment, and the Usuda 64-meter antenna is being equipped with an S-band low-noise amplifier and radio science ground equipment

The VLA (27-antenna configuration) and the Goldstone 70-meter and 34-meter antennas will be arrayed to provide the project telemetry data, Parkes will be arrayed with the Canberra 70-meter and 34-meter antennas to provide the project telemetry data, and a non-real-time array of Parkes and the Canberra 70-meter antenna will provide X-band radio science data Usuda and the Canberra 70-meter antenna will provide S-band radio science data for a non-real-time array This multi-agency, multi-nation mission support plan has been several years in development and is currently in the implementation and test phase The DSN Operational Readiness date of March 7, 1989, will bring all these elements together (the

Parkes date is March 20) to support Voyager project pre-encounter test and training

II. Future Missions

The DSN is looking forward to five new deep space missions beginning with Magellan, which is scheduled to launch in April 1989 This will be followed closely by the previously mentioned Voyager encounter After a short break following the encounter, the DSN will begin supporting the Galileo mission, scheduled for launch in October 1989 While all of this NASA Deep Space Mission support is occurring, the DSN will be supporting the Soviet Phobos mission In conjunction with two orbiters and two lander spacecraft, the DSN 70-meter subnetwork will support the Phobos Mission for about 1 year after the first landing, scheduled for April 7, 1989 The second landing is scheduled for May 25, 1989 The fourth mission is the European Space Agency's Ulysses mission for which JPL provides the Mission Control function, and which is a NASA/ESA cooperative mission The launch is scheduled for October of 1990 Then, in August of 1992, the Mars Observer is scheduled for launch This will be the first all-X-band mission for the Deep Space Network

The DSN also has a 26-meter earth orbiter tracking subnetwork that supports non-TDRSS-compatible spacecraft This subnet is currently involved in supporting an extended mission set consisting of Nimbus-7, Dynamic Explorer-1, and Solar Maximum Mission

When the space shuttle returns to flight, the 26-meter subnetwork will provide prime support from Goldstone and emergency support from Canberra and Madrid

The major future work of this subnet will be the International Solar Terrestrial Program (ISTP) This multi-spacecraft program is scheduled for three launches in 1992 (Geotail, Wind, and Polar) and several more in 1995 (Soho and Cluster)

Additional work for the 26-meter subnetwork consists of providing, on a reimbursable basis, launch and drift orbit support of geosynchronous orbit spacecraft from Japan, France, and Germany (see Fig 3)

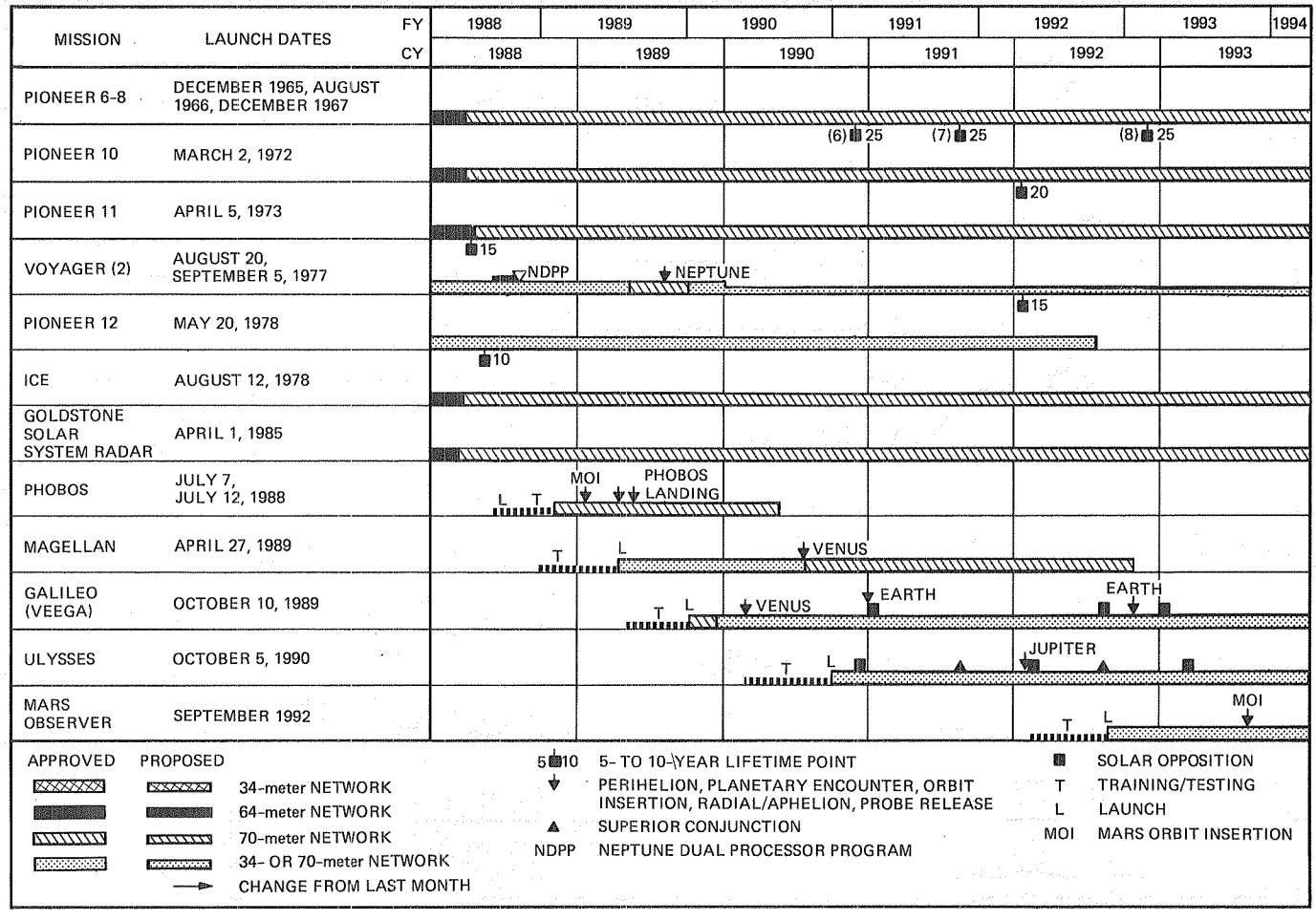

Fig. 1. Deep space missions

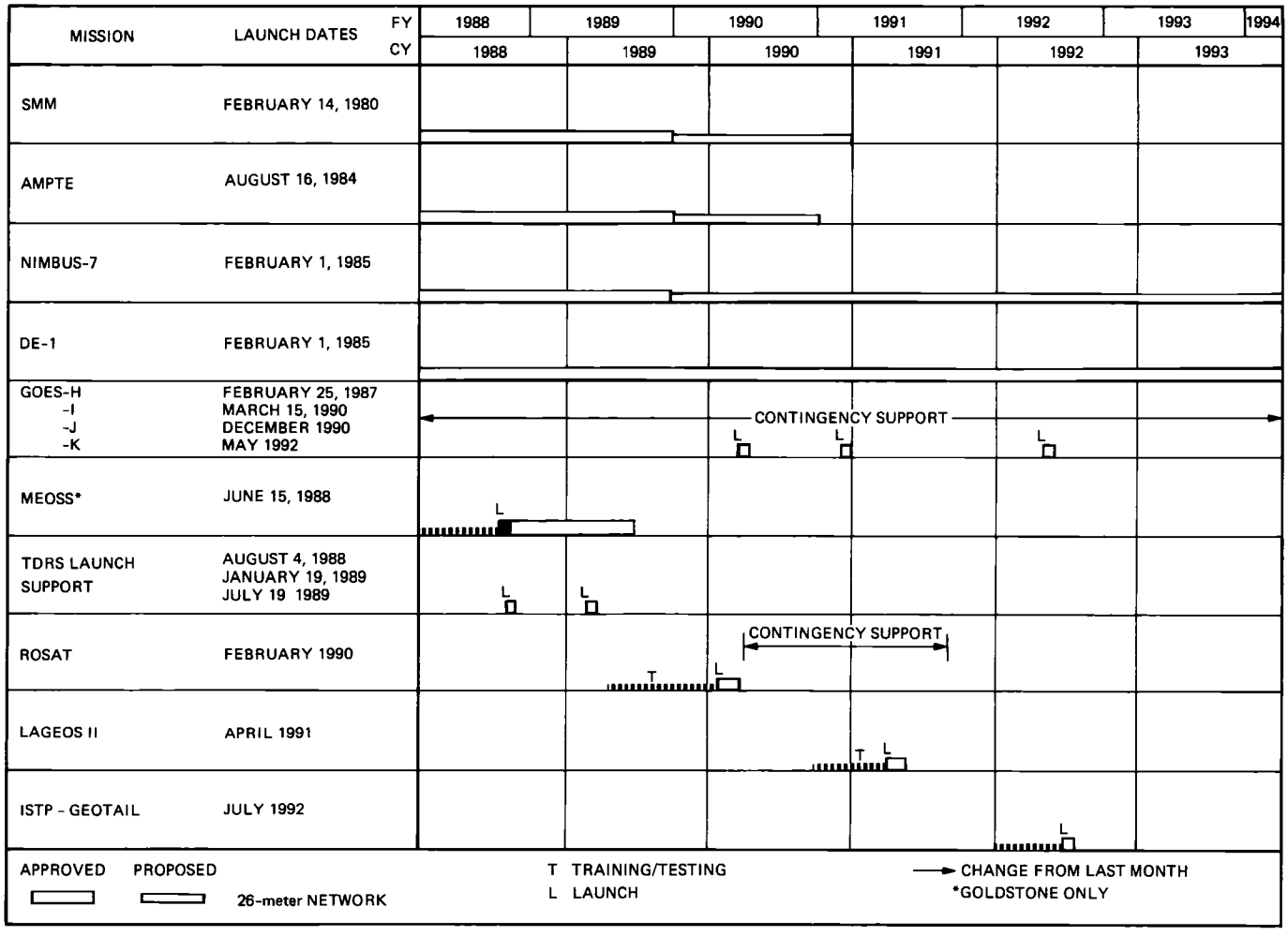

Fig 2 Earth orbiter missions

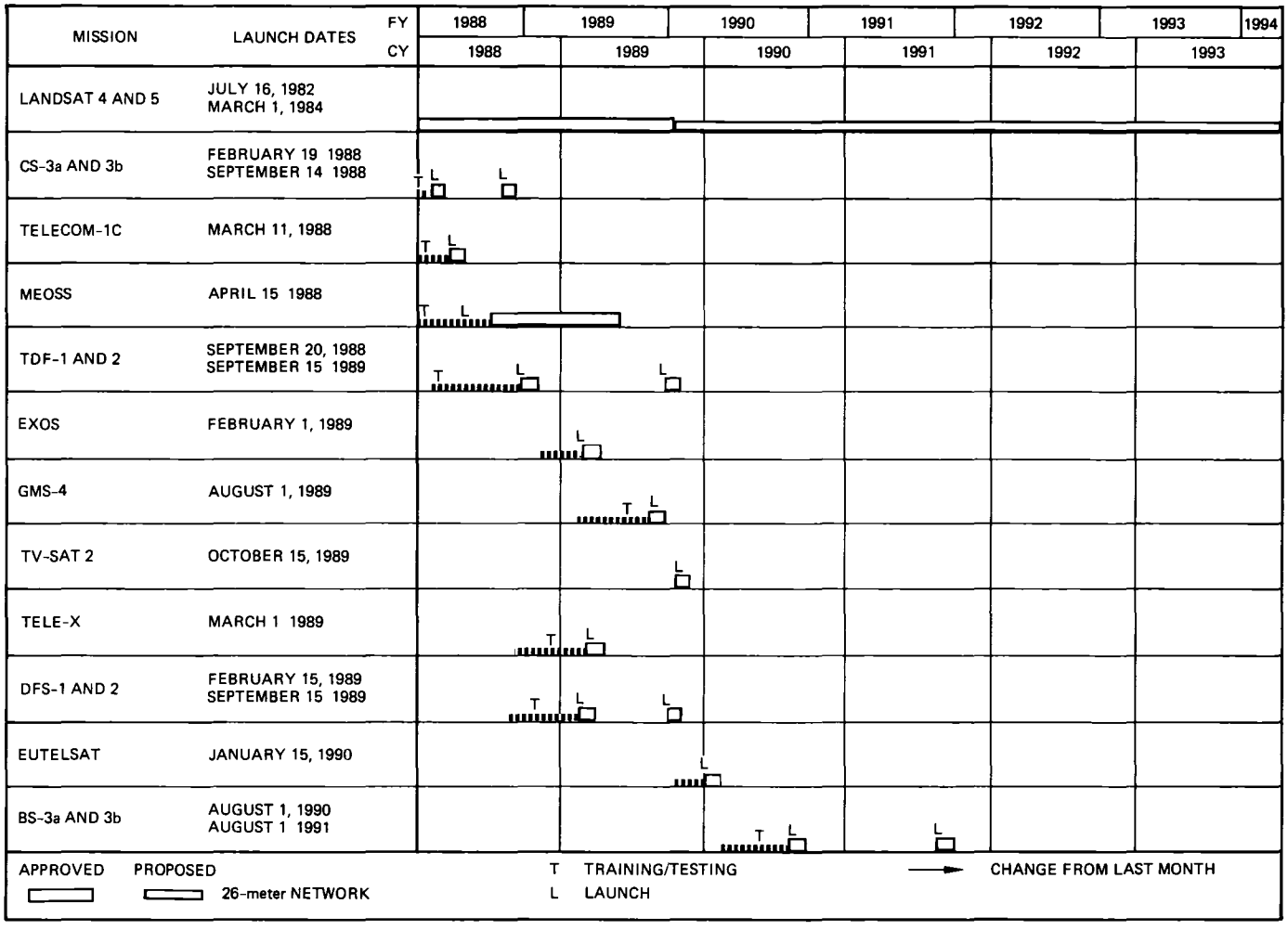

Fig 3 Reimbursable missions

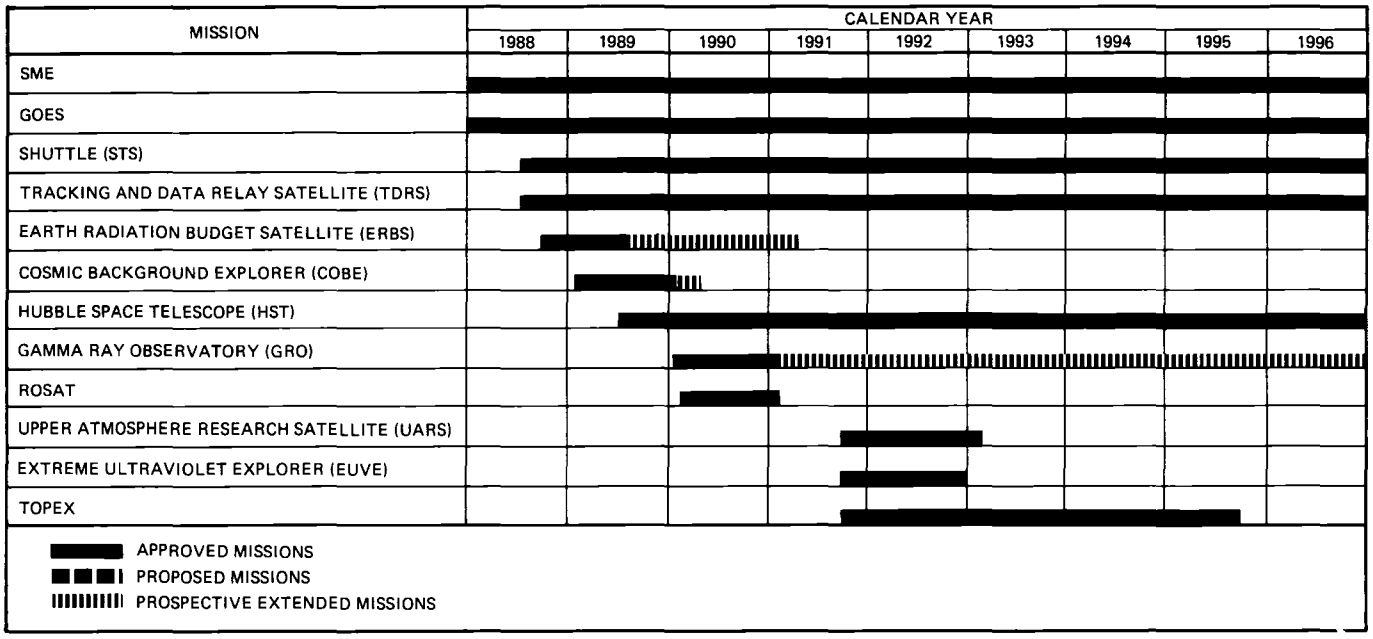

Fig 4 Emergency support missions

Determination of the Venus Flyby Orbits of the Soviet Vega Probes Using VLBI Techniques

J Ellis
Navigation Systems Section
T P McElrath
Federal Electric Corporation

In December 1984, the Soviet Union launched two identical Vega spacecraft with the dual objectives of exploring Venus and continuing to rendezvous with the comet Halley The two Vega spacecraft encountered Venus in mid-June 1985 and successfully deployed entry probes and wind-measuring balloons into the Venus atmosphere An objective of the Venus Balloon experiment was to measure the Venus winds using differential VLBI from the balloon and the flyby bus NASA's Deep Space 64-meter subnet was part of a 20-station worldwide network organized to collect data from the Vega probes and balloons

A critical element of this experiment was an accurate determination of the Venus relative flyby orbits of the Vega spacecraft during the 46-hour balloon lifetime Venus flyby solutions were independently determined by the Soviets using two-way range and doppler from Soviet stations and by JPL using one-way doppler and VLBI data collected from the DSN This article compares the Vega flyby solutions determined by the Soviets using a sparse two-way tracking strategy with JPL solutions using the DSN VLBI data to complement the Soviet data and with solutions using only the one-way data collected by the DSN

I. Introduction

In December 1984, the Soviet Union launched two identical Vega spacecraft with the dual objectives of exploring Venus and continuing to rendezvous with the comet Halley [1] The two Vega spacecraft encountered Venus in mid-June 1985 and successfully deployed entry probes and wind-measuring balloons into the Venus atmosphere Two weeks after the Venus encounter, maneuvers were executed to target the probes to a March 1986 comet encounter

Each spacecraft released an instrument-laden balloon which floated at an altitude of 54 km and traveled approximately one-third of the way around Venus during the 46-hour balloon lifetime An objective of this Venus Balloon experiment was to measure the Venus winds using differential VLBI (Very Long Baseline Interferometry) techniques The position and velocity of each balloon relative to the corresponding Vega bus were determined from simultaneous VLBI measurements from the balloon and the flyby bus A differenced spacecraft and balloon VLBI measurement was formed in which common

errors due to clock offsets, baseline errors, and media effects were canceled An independent estimate of the flyby trajectory relative to Venus was used to infer balloon position and velocity relative to a Venus-centered reference frame

The balloon experiment was a cooperative effort of the Soviet Union and France A worldwide radio interferometry network was organized by the French space agency, Centre National d'Études Spatiales (CNES), to continuously receive the signals broadcast by the Vega probes and the balloons This network included the 64-meter antennas in California, Spain, and Australia that are part of NASA's Deep Space Network

Since the accuracy of wind determination was directly related to the flyby accuracy, a critical element of the Venus Balloon experiment was an accurate determination of the Vega spacecraft orbits during the 46-hour balloon lifetime The goal was to determine the flyby position and velocity to a one-sigma accuracy of 15 km and 1 meter/sec

Both JPL and IKI (the USSR Space Research Institute) independently determined the Vega flyby orbits and exchanged radio metric data and trajectory information to arrive at a solution using combined Soviet and NASA data Soviet solutions were based on daily 10- to 20-minute passes of two-way doppler and range acquired during the Venus flyby phase JPL independently determined a solution using continuous passes of one-way doppler and delta VLBI data A combined solution was determined by JPL using the JPL delta VLBI and pseudo-geocentric range together with range rate information constructed from the Soviet radio metric data The Soviets independently determined a similar solution by combining the JPL VLBI data with the Soviet two-way data

This article compares the Vega Venus flyby solutions determined by IKI and JPL The sensitivity of the solutions to filter strategy, tracking data, and unmodeled error sources is discussed along with the merits of using VLBI data for planetary flyby navigation The application of VLBI data to the Halley encounter phase is described in [2]

II. Mission Characteristics

A. Encounter Conditions

Vega-1 was targeted to fly by Venus on June 11, at a closest approach distance of 45,200 km, and Vega-2 on June 15 at a distance of 30,500 km Two days prior to encounter, each spacecraft released the balloon/lander package and executed a Venus deflection maneuver The maneuver to target the spacecraft to the Halley encounter was executed 14 days after closest approach Although both encounters occurred within a 4-day period and closest approach was at the same time of day, the flyby geometries were sufficiently different to significantly influence the orbit determination accuracies The effect of approach geometry on orbit determination accuracy is discussed in Section V

B. Spacecraft Signal Characteristics

The Vega probes and balloons each carried a stable crystal oscillator which was used as a reference for transmitting an L-band signal at 1 668 GHz The L-band frequency was selected to be compatible with the reception capabilities of the international network of 20 radio observatories that were supporting the Venus Balloon experiment The Vega L-band signal consisted of either a pure carrier or two subcarrier tones separated by 6 5 MHz The two tones were transmitted for half-hour periods every two hours The DSN 64-meter stations were configured to receive the L-band signal broadcast by the Vega probes and balloons Continuous passes of one-way doppler were obtained from acquisition of the carrier signal VLBI data were formed by correlating the wideband tones received simultaneously at two widely separated DSN sites

In addition to the L-band capability, the probes also transmitted at a C-band frequency of approximately 6 GHz This frequency was used by the Soviets for two-way doppler and ranging

III. Radio Metric Tracking Data

During the Venus flyby phase, the Vega probes and balloons were tracked by the DSN 64-meter stations at Goldstone, Madrid, and Canberra and by two tracking sites in the Soviet Union Tracking activity was nearly continuous during the balloon lifetime phase Venus relative flyby orbits of the Vega probes were determined based on data collected during the 16-day maneuver-free phase This data span commenced two days before closest approach following the execution of the Venus deflection maneuver and terminated 14 days after encounter prior to the Halley target maneuver Table 1 summarizes the Soviet and DSN tracking data

The Soviet tracking strategy consisted of acquiring daily 10- to 20-minute passes of C-band two-way doppler and range with a 60-second sampling rate Data were acquired from two sites in the Soviet Union which were widely separated in longitude

During the same period, the DSN acquired L-band one-way data from the DSN 64-meter subnet Nearly continuous passes of one-way doppler were acquired by the DSN during the balloon lifetime from the 3 DSN sites DSN VLBI observations

were collected from the Goldstone–Madrid and Goldstone–Canberra baselines throughout the 14-day flyby phase The DSN data were calibrated for troposphere effects using a seasonal model Faraday rotation data were used to generate ionospheric calibrations for the VLBI observables At encounter, the Sun–Earth–probe angle was approximately 45 degrees

By alternately tracking the Vega spacecraft and an angularly nearby quasar whose location was known, a doubly differenced VLBI measurement was constructed called Delta Differential One Way Range (ΔDOR) Differencing the spacecraft and quasar VLBI measurements to form the ΔDOR observable cancels common errors due to clock synchronization, transmission media, and platform parameter uncertainty A typical VLBI observation sequence from each baseline consisted of quasar–spacecraft–quasar scans with a 7-minute scan for each source For the Venus flyby phase, all delta VLBI observations were formed with respect to the quasar P0202+14 which has a source strength greater than 1 Jansky The maximum spacecraft–quasar separation during the VLBI tracking phase was 16 degrees

IV. Flyby Orbit Determination Strategies

Planetary flyby navigation entails estimation of the probe's flight path relative to the target body When only ground-based radio metric data are available, the data must be a measure of the accelerations induced by the planet's gravitational field and must be of a sensitivity sufficient to measure changes in the flight path By fitting the observations to a model of the spacecraft dynamics, a planet relative orbit is determined

The Soviet approach to deep space navigation is fundamentally different from the approach used at JPL The Soviets depend on short 10- to 20-minute daily passes of range and doppler The orbit is determined by fitting the data over relatively long tracking arcs in which there has been sufficient change in the spacecraft geometry relative to the earth This procedure, because of its reliance on lengthy tracking arcs, requires an accurate model of the spacecraft dynamics and tends to be sensitive to any unmodeled non-gravitational effects In addition, the use of range data, especially for planetary encounter navigation, increases the sensitivity of the solutions to planetary ephemeris errors, station location errors, and ranging bias errors

JPL's approach to planetary encounter navigation typically relies on continuous 8- to 10-hour horizon-to-horizon passes of two-way doppler The diurnal signature inherent in a long continuous pass of doppler is a source of geocentric angle and angle rate information [3] Consequently, solutions can be determined using comparatively shorter tracking spans For planetary encounters, the ability of the nearly continuous doppler to sense the range rate changes induced by the planet's gravitational field establishes the planet relative spacecraft state The time of closest approach can be directly observed in the doppler residuals during the flyby

For flyby orbits, range data, because of their sensitivity to planetary ephemeris errors and station location errors, either are not used by JPL or are severely deweighted Consequently, one concern was that the Soviet Vega flyby solutions, with their dependence on range data, would be unduly sensitive to these error sources A Soviet solution using only two-way doppler was not feasible due to the short duration of the tracking passes

For the Vega missions, the only radio metric data available at JPL for independent orbit determination were data collected in a passive, listen-only mode This consisted of L-band one-way doppler and ΔDOR Nearly continuous passes of one-way doppler from 3 sites were acquired from the L-band carrier signal broadcast by the Vega probes For these data to be useful for orbit determination (i e , to determine the range rate from the doppler shift), the frequency characteristics of the on-board oscillator must be modeled Typically, it is assumed that the one-way doppler signal includes errors due to an unknown oscillator frequency bias and drift and is corrupted by oscillator instability and media effects

The ΔDOR observations, from the two nearly orthogonal baselines, directly determine the two angular components of position and velocity in a plane-of-sky (POS) frame, which is a plane perpendicular to the Earth–probe direction Information about the third component along the Earth–spacecraft direction can be determined from doppler tracking A continuous 8-hour pass of doppler will yield an estimate in which the geocentric radial component and the doppler bias and drift are highly correlated with the plane-of-sky position and velocity estimates The independent estimate of the POS components provided by the ΔDOR enables a determination of the remaining components via the doppler correlations [4] Consequently, use of the doppler data depended on the ability to model the frequency behavior of the Vega oscillator

Although both Vega oscillators were similar in design, the frequency characteristics of the one-way L-band signal were different The Vega-1 oscillator drifted at a rate of −0 5 Hz/day, and the Vega-2 drift rate ranged from 6 to 7 Hz/day Throughout the course of the continuous 46-hour tracking period, random jumps in the oscillator bias were observed which ranged from 0 1 Hz to 0 4 Hz A possible cause of the

discontinuities in frequency was on and off cycling of on-board instruments

V. Comparison of Solutions

Both JPL and IKI independently determined the Vega flyby orbits using a consistent and common set of assumptions to describe the spacecraft dynamics The solar radiation pressure constant was determined by the Soviets from two-way tracking data collected during the Earth–Venus phase Both agencies used the JPL DE118 planetary ephemeris JPL station locations and the location of the quasar (used to construct the ΔDOR observations) were expressed in a frame consistent with the DE118 planetary ephemeris The following three solutions were computed from the encounter data

(1) A Soviet solution based on the C-band two-way doppler and range The Soviet solution strategy consisted of estimating the position and velocity of the Vega probes using a Gaussian least squares estimator Data weights of 1 cm/sec and 500 meters were assumed for the two-way doppler and range Range bias errors were not treated in the estimation process

(2) A JPL solution using the L-band one-way doppler and ΔDOR data A batch sequential filter was used to estimate the spacecraft state, the one-way doppler bias and drift, and the quasar right ascension and declination Because of the random jumps in the transmitted L-band carrier frequency, the bias and drift for the on-board oscillator were modeled as a random walk process over the two-day balloon lifetime This assumed a batch size of two hours with an additive process noise of 1 Hz and 0 01 Hz/day for the doppler bias and drift The location of the quasar was estimated to account for an offset between the quasar catalog frame and the planetary FK-4 reference frame Data weights of 10 cm/sec (for a 60-second count time) and 1 meter were assumed for the one-way doppler and the ΔDOR

(3) A "combined" JPL–Soviet solution using the Soviet two-way data in combination with the JPL ΔDOR Since JPL did not have direct access to the Soviet two-way data, pseudo-geocentric range and range-rate observations were constructed from the IKI two-way solutions The Soviet tracking schedule (given in Table 1), along with information about the two-way range and doppler residuals with respect to these solutions, was used to construct the geocentric measurements Because of the problems inherent in modeling the one-way doppler, the combined solution did not include these data However, it was shown that inclusion of the one-way doppler had only a small effect on the combined solution and on its statistics The combined solution was based on using a simple least squares estimator to determine the spacecraft state, the quasar location, and a ranging bias The latter was included to model ranging bias errors inherent in the Soviet two-way range data The range and range rate were weighted at 500 meters and 1 cm/sec, respectively, and the ΔDOR at 1 meter

The three independent flyby solutions were evaluated by comparing the consistency of the estimates, their relative statistics, and the sensitivity of the solutions to unmodeled error sources and to filter strategy The quality of the fit to the observables, as given by the data residuals, was also used as a criterion A consider covariance was computed for each solution by JPL based on considering the effect of a correlated 12-by-12 Earth–Venus ephemeris covariance and the uncertainty of the JPL station locations No a priori information was available on the uncertainty of the Soviet station locations or on the ranging bias errors Table 2 summarizes the filter model and data weight assumptions

The consistency of the Vega solutions was compared using the combined solution as a reference The criteria for this comparison were the RSS differences in position and velocity during the 46-hour balloon lifetime Figures 1 and 3 display the RSS differences between the solutions Corresponding consider statistics for the three solutions are plotted in Figs 2 and 4

A. Vega-1 Solutions

A comparison of the Soviet solution and the combined solution for Vega-1 (Fig 1) shows that the addition of VLBI data to the Soviet two-way range and doppler solution changes this solution by less than 5 km and 3 cm/sec Expressing the components of this difference in solutions in a plane-of-sky frame shows that the difference is largely due to the components in the plane perpendicular to the Earth–Venus direction (i e , plane-of-sky components) The complementary information content of the two-way and ΔDOR data is illustrated by these solution differences For the combined solution, the radial component (i e , along the Earth–Venus line) is determined by the two-way data and the angular (plane-of-sky) components by the ΔDOR

The agreement between the two solutions is consistent with the consider statistics for the solutions given in Fig 2 During the 46-hour span, the maximum one-sigma position and velocity errors for the Soviet solutions were 12 km and 10 cm/sec For the combined solution, the maximum uncertainties were 4 km and 5 cm/sec Delta DOR residuals with respect to the combined solution had a one-sigma error of 0 27 meter, which translates into a 3 4-km error at Venus distance

The behavior of the position and velocity errors (Figs 2 and 4) as a function of time is characteristic of the error focusing effect due to the Venus flyby Position errors are at a minimum and velocity errors are at a maximum at closest approach Beyond periapsis, the position errors increase linearly to the end of the data arc due to a constant velocity error Unmodeled errors in the Earth–Venus ephemeris, which constituted the dominant consider error source, contributed an error of less than 8 km and 7 cm/sec to the Soviet solution The sensitivity to unmodeled ephemeris errors is reduced to less than 1 km and 1 cm/sec by combining the ΔDOR data with the two-way data Station location perturbations were found to be negligible

The JPL solution based on using one-way data differs from the combined solution by at most 14 km and 26 cm/sec, with the dominant component of this difference in the radial direction For the JPL solution, this component is determined by the one-way doppler By treating the bias and drift as a random walk process, the information content of the doppler data is degraded Maximum uncertainties for the JPL solution are 26 km at the end of the arc and 46 cm/sec at periapsis The increased uncertainty is due to the random characteristics of the one-way doppler bias and drift models The effect of ephemeris and station location errors is less than 1 km and 1 cm/sec

B. Vega-2 Solutions

Because of the difference in approach geometry, the behavior of solutions and the statistics for Vega-2 are considerably different from those for Vega-1 The key to understanding the effect of approach geometry is based on expressing the Venus relative orbital parameters in a plane-of-sky frame Table 3 lists the orbital parameters for the Vega-1 and -2 combined solutions In the POS frame, the inclination of the orbit plane for Vega-1 is 107 22 degrees and for Vega-2, 90 98 degrees Consequently, the Vega-2 orbit will appear as a disk viewed edge-on to an Earth-based observer The orientation of this orbit plane about the Earth–Venus line cannot be well determined from Earth-based range and doppler Essentially, the orbit can be rotated about this line and still yield the same range and doppler observations The orientation of this plane is explicitly determined from the angle and angle-rate information derived from the ΔDOR data Consequently, we can expect a significant improvement in the ill-conditioned doppler and range solution with the addition of VLBI data

The Soviet solution (Fig 3) differs from the combined solution by a maximum of 53 km and 61 cm/sec Components in the plane-of-sky direction account for a position difference of 53 km and a velocity difference of 59 cm/sec In the radial direction the maximum differences are 1 5 km and 18 cm/sec at periapsis The latter difference decreases to less than 1 cm/sec 4 hours after periapsis

The effect of the near singular approach geometry is manifested in the large position and velocity uncertainties (Fig 4) for the Soviet solution Maximum uncertainties are 48 km and 77 cm/sec, with the plane-of-sky components accounting for errors of 48 km and 75 cm/sec Of this total, Venus ephemeris uncertainty contributes an error of 40 km and 50 cm/sec, and measurement errors result in a 24 km and 48 cm/sec error When the ΔDOR data are included to form the combined solution, position and velocity uncertainties are reduced to 6 km and 32 cm/sec For this combined solution, the perturbation due to ephemeris errors is less than 1 km and 2 cm/sec The ΔDOR residuals with respect to the combined solution had a one sigma error of 0 24 meter which maps into a 2 4-km error at Venus at the time of encounter

A comparison of the JPL one-way solution and the combined solution shows a maximum difference of 16 km and 32 cm/sec, with the largest difference, 14 km and 28 cm/sec, in the radial direction The closer agreement between the JPL and the combined solutions reflects the significant contribution of the information content of the ΔDOR data Maximum position and velocity uncertainties for the JPL solution are 24 km and 54 cm/sec

C. Solution Sensitivity

1 **Ephemeris errors** The sensitivity of the range and doppler solutions to ephemeris is a function of the flyby geometry As the POS inclination approaches 90 degrees, the sensitivity to ephemeris errors increases However, the addition of ΔDOR significantly reduces the sensitivity of the solutions to ephemeris errors, independent of the approach geometry

2 **Range bias errors** Range bias estimates for the Soviet ranging data were obtained for both combined solutions The estimates for Vega-1 and Vega-2 were −0 33 km and 1 76 km, respectively In both cases, the uncertainties of the bias estimates were 1 8 km Estimating the range bias changed the combined Vega-1 solution by less than 1 km and 1 cm/sec The Vega-2 solution changed by 1 km and 20 cm/sec at periapsis and 4 km and 0 8 cm/sec at the end of 46 hours In both cases, the sensitivity to unmodeled ephemeris errors was reduced by estimation of the range bias An unmodeled 500-meter range bias error would have resulted in perturbations to the statistics of the Soviet Vega-1 and Vega-2 solutions of 4 km and 12 km

3 **Quasar locations** The location of the quasar was estimated to reduce the sensitivity of the solutions to the dominant ephemeris errors and to remove any bias in the ΔDOR

residuals due to frame tie errors Quasar location estimates derived from the two Vega solutions agreed to within 20 nanoradians in declination and 140 nanoradians in right ascension Uncertainties were 110 and 320 nanoradians, respectively

4 Delta DOR data span The sensitivity of the combined estimate to the VLBI data arc was evaluated by a comparison of solutions based on a subset of the ΔDOR data A Vega-1 solution was determined using only the ΔDOR data acquired from June 10–17, representing six of the ten available observations Delta DOR data from June 14–17, comprising ten of the fifteen observations, were used for a Vega-2 estimate A comparison of these solutions with the combined solutions using all the data showed a maximum difference of less than 1 5 km and 1 0 cm/sec The consistency of the solutions was further demonstrated by the residuals of the VLBI data not used for the solution No significant increase or trend was apparent in these pass-through residuals

VI. Conclusions

Results of this analysis demonstrate the value of VLBI data for planetary flyby navigation Solutions using the "sparse" Soviet two-way data combined with ΔDOR satisfied the accuracy goals of the Venus Balloon experiment By complementing the two-way data, the use of ΔDOR data improved the accuracy of the Vega solutions and reduced their sensitivity to errors in the ephemeris, which was the dominant error source The radial component of the solutions was determined by the two-way data and the plane-of-sky components by the ΔDOR Based on the consider statistics, accuracies of 4 km and 5 cm/sec were obtained for Vega-1 and 6 km and 32 cm/sec for Vega-2 In the case of the ill-conditioned two-way solution for Vega-2, the ΔDOR data were explicitly required to satisfy the accuracy goals

The results also demonstrate the feasibility of deep space navigation using listen-only or one-way data The accuracy of the Vega solutions using one-way data was limited by the need to model the behavior of the oscillator instabilities as a random walk process Even with these limitations, the one-way solutions differed from the "baseline" combined solutions by less than 14 km and 32 cm/sec and had a maximum uncertainty of 26 km and 55 cm/sec A Voyager quality ultrastable oscillator would have yielded solutions using only one-way data with accuracies comparable to the combined solutions

Acknowledgment

The authors wish to acknowledge the support provided by Dr C T Stelzried for guiding the successful implementation, planning, and operation of the Venus Balloon effort

References

[1] R Z Sagdeev, *et al*, "The Vega Venus Balloon Experiment," *Science*, vol 231, March 21, 1986

[2] J Ellis and T P McElrath, "Vega Pathfinder Navigation for Giotto Halley Encounter," *TDA Progress Report 42-87*, vol July–September 1986, Jet Propulsion Laboratory, Pasadena, California, November 15, 1986

[3] T W Hamilton and W G Melbourne, *Information Content of a Single Pass of Data From a Distant Spacecraft*, JPL Space Program Summary No 37-39, vol III, May 1966

[4] J Ellis, "Deep Space Navigation With Noncoherent Tracking Data," *TDA Progress Report 42-74*, vol April–June 1983, Jet Propulsion Laboratory, Pasadena, California, August 15, 1983

Table 1 Summary of Soviet and JPL tracking data

Data type	Vega 1	Vega 2
IKI 2-way data (daily 10-min passes)	June 9–14, 16–25	June 13–18, 20–29
JPL 1-way doppler (nearly continuous)	June 10, 08 40, to June 13, 07 30	June 14, 08 40, to June 17, 03 38
JPL ΔDOR		
Goldstone-Canberra baseline	June 10, 11, 17, 18, 24 (5 observations)	June 14, 15, 16 (2), 17, 20, 21, 28 (8 observations)
Goldstone-Madrid baseline	June 11, 12, 17, 18, 23 (5 observations)	June 14, 15, 16 (2), 17, 21, 27 (7 observations)

Table 2. Filter model assumptions

Variable	A priori standard deviation
Estimated parameters	
Spacecraft position	1×10^6 km
Spacecraft velocity	1 km/sec
Quasar right ascension	1×10^3 nanoradians
Quasar declination	1×10^3 nanoradians
Range bias	1×10^3 km
L-band one-way doppler bias	2×10^3 hertz
L-band one-way doppler drift	25 hertz/day
Process noise for stochastic parameters	
L-band one-way doppler bias	1 hertz
L-band one-way doppler drift	10^{-2} hertz/day
Consider parameters	
DSN station locations	
Spin radius	2 meters
Longitude	3 meters
Z-height	15 meters
Intercontinental baseline length	0 3 meter
Venus ephemeris	
Heliocentric position components	
Radial	1 km
Downtrack	30 km
Out-of-plane	8 km
Heliocentric velocity components	
Radial	1 mm/sec
Downtrack	0 1 mm/sec
Out-of-plane	4 mm/sec
Data weights	
C-band two-way doppler	1 cm/sec
C-band two-way range	500 meters
L-band one-way doppler	10 cm/sec
L-band ΔDOR	1 meter

Table 3 Venus relative orbital elements in plane-of-sky frame

Variable	Vega 1	Vega 2
Time (GMT)	June 11, 1985, 02 00	June 15, 1985, 02 00
Semi-major axis, km	−29521 75	−27461 66
Eccentricity	2 530010	2 111951
Inclination, degrees	107 2224	90 98203
Longitude of ascension node, degrees	84 24727	49 66605
Argument of periapsis, degrees	166 9286	166 4388
Mean anomaly, degrees	−10 69728	−16 22563

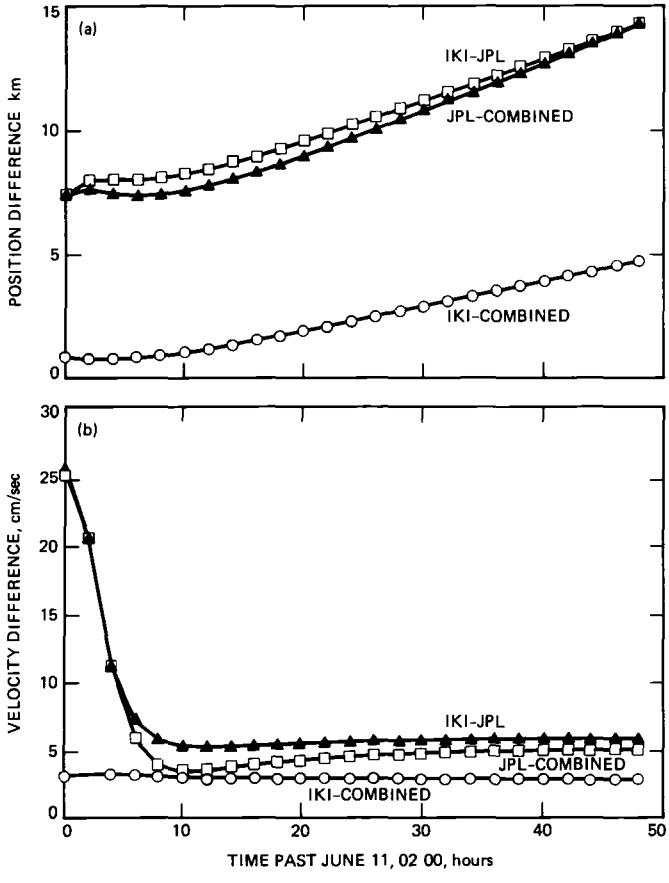

Fig 1 Vega 1 (a) position and (b) velocity differences

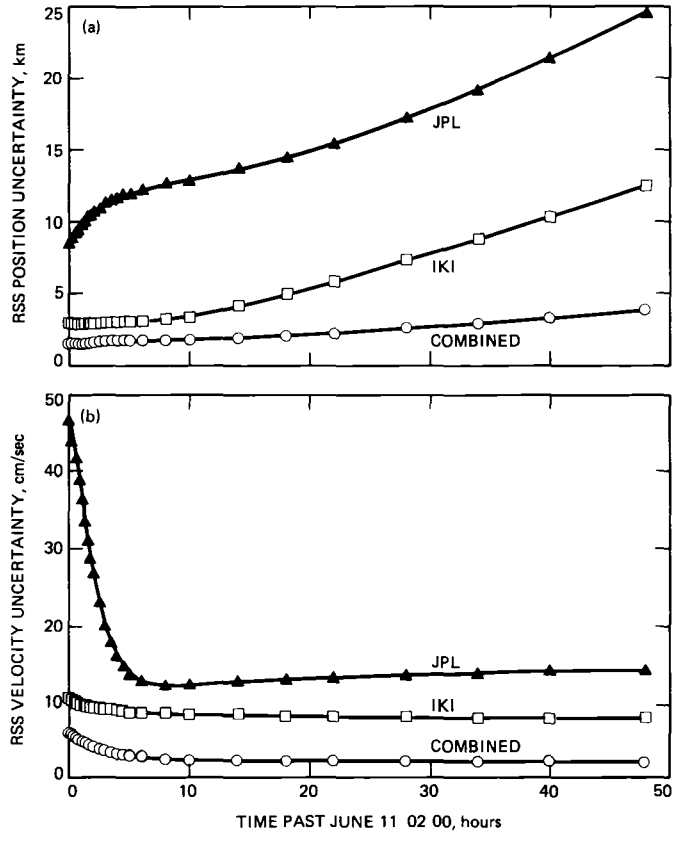

Fig. 2 Vega 1 RSS (a) position and (b) velocity uncertainties

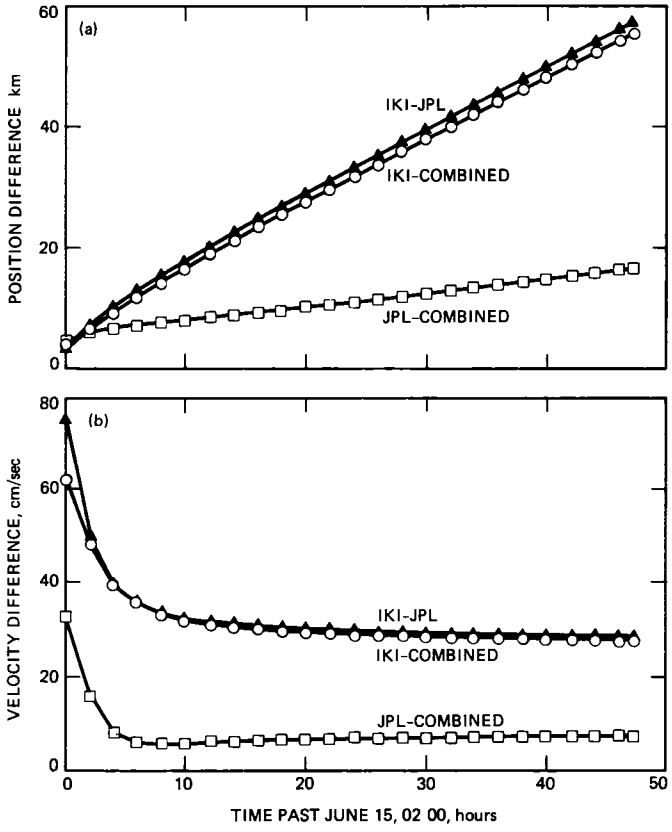

Fig 3 Vega 2 (a) position and (b) velocity differences

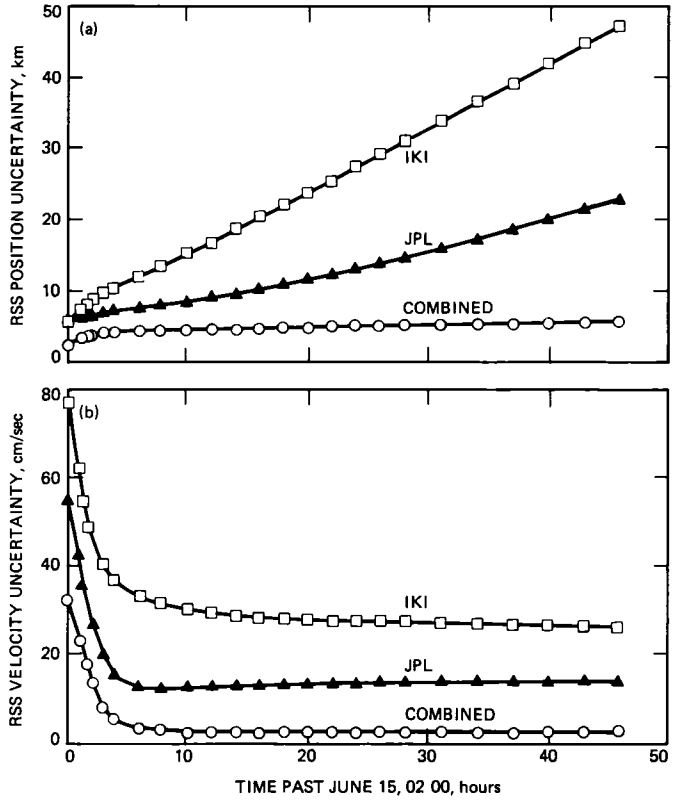

Fig 4 Vega 2 RSS (a) position and (b) velocity uncertainties

New CCIR Report on SETI

N F de Groot
TDA Technology Development Office

Since 1978, the reports and recommendations of the Comite Consultatif International des Radiocommunications (CCIR) have included a document describing SETI (the Search for Extraterrestrial Intelligence) in the context of radio frequency management. A new report to replace the old one has been adopted by a CCIR study group, both reports were written at JPL. Following introductory and background material, the text of the new report is given.

I. Introduction

The Comité Consultatif International des Radiocommunications, or CCIR (International Radio Consultative Committee), provides the technical rationale for the international treaty which governs the use of the radio frequency spectrum. Reports and recommendations of the CCIR are published at four-year intervals. Volume II, *Space Research and Radioastronomy* [1], has included a report dealing with SETI (the Search for Extraterrestrial Intelligence) since 1978. CCIR, a part of the International Telecommunication Union, includes a number of study groups. Study Group 2 deals with space research and radioastronomy and is responsible for the content of Volume II of the reports and recommendations.

For the November 1987 meeting of the CCIR Study Group 2, the United States proposed that a new report on SETI, written at JPL, be adopted as a replacement for the now obsolete 1978 document. The new report was adopted, and the text is given in Appendix A.

II. Background

The treaty mentioned above finds expression in the *Radio Regulations* [2], published by the International Telecommunication Union. With the exception of a few advisory statements that mention that SETI searches are being conducted, the *Radio Regulations* focus on the needs of other radio services for transmission bands and protection from interference. Considering the intense competition by government and commercial radio services for spectrum space in the microwave region of greatest interest to SETI, it is not surprising that there is no explicit regulatory protection for SETI searches.

SETI researchers would like to be able to listen at any frequency of interest without encountering man-made interference. Any man-made radio emission, authorized or not, intentional or not, is a potential impediment to a successful SETI search. Particularly because the range of interesting SETI frequencies is so very wide, regulatory protection from interference is simply not a practical expectation. Indeed,

listen-only allocations for radio astronomy and passive earth sensing activities are possible only because the needed frequency ranges are relatively narrow Transmissions in these bands are prohibited, and the allocations take into account the requirement to detect signals in known frequency ranges that are dictated by physical processes This is quite different from the SETI case where the needed frequencies are not known

Because regulatory protection cannot be obtained, another approach must be taken to achieve at least some cooperation that could assist SETI The approach taken by the United States has been to have a report in the CCIR literature that explains the SETI needs CCIR reports are formally adopted by the International Telecommunication Union and represent an international technical agreement with the report contents

The new CCIR SETI report, like its predecessor, was written at JPL, and survived an intensive review by technical peers, NASA, and a broad cross section of frequency management experts within the United States before being submitted by the Department of State to CCIR in Geneva

III. Text of the New Report

Appendix A presents the verbatim text of the new report Because the intended audience is familiar with CCIR documents, complete citations of referenced reports or other CCIR documents are not needed or given For a more general audience, it is perhaps helpful to provide the following citations

Reports 719 and 721, mentioned in Section 3 of Appendix A, may be found in the International Radio Consultative Committee's *Recommendations and Reports of the CCIR, 1986, Volume V Propagation in Non-Ionized Media* (Geneva International Telecommunication Union, 1986) Report 719-2 is entitled "Attenuation by Atmospheric Gases", Report 721-1 is called "Attenuation by Hydrometeors, in Particular Precipitation, and Other Atmospheric Particles "

Document 2/60, mentioned in Section 4 1 of Appendix A, is a Draft New Report, *Method of Calculating Attenuation, Noise Temperature, and Telecommunication Link Performance for the Selection of Preferred Frequency Bands* This report, written at JPL and submitted by the United States to the CCIR, was approved by Study Group 2 during its interim meeting in Geneva from November 16 to December 4, 1987 Report 700, mentioned in Section 7 of Appendix A, may be found in the International Radio Consultative Committee's *Recommendations and Reports of the CCIR* (Geneva, International Telecommunication Union, 1986)

The subtitle of the report shown in Appendix A includes a reference to Question 17/2 CCIR work is guided by formally adopted statements that describe the considerations which lead to a decided set of needed studies These statements are called questions The current version of Question 17/2 was adopted in 1982, and the text may be found in Appendix B

The SETI report shown in Appendix A is considered a draft because, although adopted by Study Group 2 at its interim meeting in Geneva last year, it has not yet been adopted by the entire CCIR meeting in Plenary Assembly That will occur in 1989 or 1990 One must be patient in CCIR work

Acknowledgment

The author would like to particularly acknowledge the assistance of Dr Michael J Klein of JPL and Dr Jill Tarter of NASA Ames Research Center, experts in the SETI field Without their technical suggestions and critique, the author, who is not a SETI expert, would have been unable to prepare the successful report which was approved by the CCIR

References

[1] International Radio Consultative Committee, *Recommendations and Reports of the CCIR, 1986, Volume II Space Research and Radioastronomy*, Geneva International Telecommunication Union, 1986

[2] *Radio Regulations*, Geneva International Telecommunication Union, 1985

Appendix A

(Note The following text was approved by CCIR Study Group 2 at its Interim Meeting, Geneva, 23 November - 4 December, 1987)

RADIOCOMMUNICATION ASPECTS OF SYSTEMS TO SEARCH FOR EXTRA-TERRESTRIAL INTELLIGENCE (SETI)

(Question 17/2)

1 Introduction

Many scientists believe that life may be common in our galaxy and that it could have developed into advanced forms that possess a telecommunication capability similar or superior to ours We do not know the frequencies, modulations, polarizations and locations of transmitting stations used by extra-terrestrial civilizations, if they exist To discover signals from these stations, it is necessary to make an extensive search of the radio frequency spectrum, in all directions from Earth The conduct of such a systematic search with great sensitivity has become feasible in recent years

The possibility of receiving radio signals from extra-terrestrial intelligent life was first pointed out in 1959 [Cocconi and Morrison, 1959] The first search in the microwave region was carried out in 1960 [Drake, 1960] Since then at least 47 searches have been conducted by 8 countries, utilizing 24 observatories [Tarter, 1985] These efforts have not detected evidence of signals from extra-terrestrial beings The searches, however, covered only a tiny fraction of the frequencies, modulation schemes, and directions that are considered reasonable choices from the point of view of a comprehensive search, and at sensitivities that may not have been adequate

Additional comprehensive searches are being planned and implemented

2 Search considerations

Assuming that signals from extra-terrestrial beings are reaching the Earth, our ability to detect them depends upon

a the flux density of the signals arriving at Earth,

b the collecting area of our antenna, and its illumination efficiency,

c the sensitivity of our receiver,

d our ability to point our antenna in the correct direction,

e and our ability to distinguish the received signal from natural noise and from the man made electromagnetic environment

The flux density of an extra-terrestrial signal depends on the transmitted e i r p and the characteristics of the path of propagation

3 Signal power flux density [1]

The flux density of the signal to be detected is unknown Because of the very great distances that are necessarily involved, the flux density may be very low, and detection would therefore be limited by the sensitivity of the receiving system

For a receiving system on the surface of the Earth, the attenuation of the atmosphere reduces the strength of the unknown signal The attenuation is a function of frequency and weather condition [Reports 719, 721]

For a receiving system located outside the atmosphere of the Earth, for example, on the Moon, the attenuation of the atmosphere is avoided and the possibility of signal detection is correspondingly improved

Fig 1 presents curves of signal power flux density as a function of e i r p for several assumed distances, not including the attenuation of the atmosphere

4 Receiving system sensitivity

For a given antenna gain, the sensitivity of the receiving system to be used for SETI search is determined by its system noise temperature, the resolution bandwidth chosen for the search and by the integration time

4 1 System noise temperature

System noise temperature is determined by the characteristics of the equipment plus the sky noise temperature seen by the receiving antenna For receiving equipment with a very low noise temperature, e g , less than 30 K, sky noise can be a fundamental limitation to system sensitivity at some frequencies

For a receiving system outside the atmosphere of the Earth, the sky noise is determined by the cosmic background noise (3 K) plus radio noise emissions from our galaxy The total sky noise temperature is less than 7 K between approximately 1 and 100 GHz, and this range is called the free-space microwave window

Sky noise as seen from the surface of the Earth during clear weather, with an atmospheric water vapor density of 7 5 gm/m^3, 90 deg elevation angle, is less than 7 K between approximately 1 and 15 GHz [Document 2/60] In the 15 to 100 GHz range, the sky noise contributed by the atmosphere rises appreciably, primarily due to H_2O and O_2, thereby reducing the probability of detecting extra-terrestrial signals that may be present

As limited by sky noise temperature and its effect on receiver sensitivity, the frequency range over which maximum sensitivity may be realized is much reduced for a station located on the surface of the Earth, as compared to one located outside the atmosphere

---

[1] In the context of this report, the term "power flux density" refers to power per unit area This meaning is consistent with definitions and usage of the International Telecommunication Union Some readers may use the term in a different way

4 2 Signal integration time

By integrating the signal-plus-noise power over a period of time, the signal to noise ratio for a continuously present signal may be improved by approximately (bandwidth x integration time)$^{0.5}$ Integration is one of several effective modes for signal detection The time of integration is limited by two factors signal frequency stability, and the observation time available on desired antenna systems

4 2 1 Frequency stability

The frequency of the arriving signal will include a Doppler shift that depends on the relative velocity between the transmitter (at the time of transmission) and the receiver This shift may change with time as a result of relative acceleration of the transmitter and receiver The signal to noise ratio improvement that results from integration depends upon the ability to track the Doppler shifted signal The improvement in signal to noise ratio resulting from non-coherent integration may be reduced as a result of imperfect signal frequency tracking

4 2 2 Available search time

The total time it will take to search the volume of space in which there might be extra-terrestrial intelligent life depends on the signal integration time per channel, the number of antenna pointing directions, and the range of frequencies to be included If the time available for use of particular search antennas is limited the integration time for each channel and for each pointing direction is correspondingly limited Under these circumstances the search sensitivity is constrained by the time available for the planned search

4 3 Minimum detectable signal power

For a signal that remains within the detection bandwidth during the integration time, the minimum detectable signal power of the search receiver, assuming a signal-to-noise ratio of 1, is given by [NASA 1973]

$$P_{min} = 10 \quad LOG \left[kTB \quad \frac{1 + (1 + B \quad tau)^{0.5}}{B \quad tau} \right] \qquad dBW$$

where

k = Boltzmann's constant

T = Temperature (K)

B = detection bandwidth (Hz)

tau = integration time (sec)

Fig 2 shows P_{min} as a function of integration time for several bandwidths Points A and B in the Figure identify P_{min} for two candidate search receivers with the characteristics listed in the legend

Fig 3 illustrates the relationship between the received power flux density for the conditions assumed in Figure 1, and the search sensitivity of two candidate receiving systems The dashed horizontal line represents the sensitivity of a system using a 34m diameter antenna with 50% efficiency, 30 K noise temperature, 10 Hz bandwidth, and 2 sec integration time The solid line represents the sensitivity of a system using a 300m diameter antenna with 50% efficiency, 30 K noise temperature, 1 Hz bandwidth, and 1000 sec integration time Combinations of e i r p and distance that result in detectable flux densities are those that lie above the respective sensitivity lines for the hypothetical systems

When detection bandwidth is not limited by signal frequency drift, the most sensitive receiver is obtained by use of a detection bandwidth which matches the spectral width of the received signal The problem is that this bandwidth is not known in advance An associated problem is that, for a single receiver, reducing the detection bandwidth correspondingly increases the time needed to search a particular frequency range, unless a large number of narrow detection channels can be used simultaneously For example, to search the range from 1 to 2 GHz with a single channel receiver having a bandwidth of 1 Hz and an integration time of 10 sec would require 317 years It is for this reason that comprehensive searches utilize receivers that are able to simultaneously examine millions of spectral channels, each having a narrow detection bandwidth

5 Antenna pointing direction

Antennas with high gain (large collecting area) are desirable in order to increase search sensitivity and correspondingly enhance the probability of detection The associated difficulty is that an increase in gain results in a decrease in beamwidth, with a corresponding increase in the number of pointing directions needed to search a given fraction of the sky For a given integration time, an increase in pointing directions results in an increase in total search time

Antenna pointing strategies and the selection of integration time and other system parameters are important elements of the design of a SETI search

6 Signal identification and interference rejection

A principal problem facing the discovery of extra-terrestrial signals from another intelligence is the successful determination that the detected signal is not the result of noise, natural or man-made

The probability that the amplitude of random noise will exceed a given value is well understood A noise peak that exceeds a given threshold value will be detected and is called a false alarm The threshold value determines the false alarm rate, and this rate may be calculated for the case of Gaussian white noise Raising the threshold in order to reduce the false alarm rate reduces the receiver sensitivity

With the exception of natural astrophysical emissions or an extra-terrestrial signal, signals received by a search station will be man-made It is therefore necessary that the search station have the ability to classify these signals and reject them as candidates for possible further observation and analysis The rejection may be based on a-priori knowledge of signals in the environment of the search station, or be based on measurements made by the station The success of excluding these interfering signals from the data base used for further detailed analysis is a major component in the feasibility of a successful search

The increasing use of the radio frequency spectrum as time passes suggests that SETI searches should be conducted as soon as possible in order to minimize the problem of radio frequency interference It should be noted that, from the point of view of SETI, all man-made radio emissions, authorized or not, represent potential radio frequency interference

The rapidly growing use of the geostationary satellite orbit will increasingly preclude the possibility of searching a zone of the sky above the equator of the Earth within the frequency ranges used by satellite transmitters The size of the zone is determined by the number of geostationary satellites and their e i r p

7 Candidate bands to be searched

Keeping in mind that the frequency and other characteristics of extra-terrestrial signals are unknown, it is nevertheless necessary to decide the bands of frequencies with which a search should begin For search stations on the surface of the Earth, maximum sensitivity is limited by the noise temperature and attenuation of the atmosphere, as described earlier Additionally, a number of particular bands have been postulated as likely candidates for search on the basis of physical principles

A detailed discussion of the rationale for selecting particular frequencies as candidates for early or intensive search is beyond the scope of this report Report 700-1, Geneva 1986, presents some of the rationale for certain frequencies A common aspect of proposals for particular search frequencies is that they lie near spectral lines of natural radiation, e g , atomic hydrogen (1420 MHz), the hydroxyl radical (1612, 1665, 1667, and 1720 MHz), formaldehyde (4830 MHz), and the ground state spectral line of the lightest artificial atom, positronium (203 385 GHz) The assumption is that extra-terrestrial beings may elect to transmit on frequencies near to these emission lines, or perhaps some multiple of them, with the idea that other civilizations would be aware and would listen accordingly

Several bands allocated to the radioastronomy service are protected from man-made emissions, and there are similar bands for passive sensing Because of their protection from interference, these bands are also candidates for use in connection with SETI searches

There are many points of view concerning the frequencies that may be used for extra-terrestrial communication It must be remembered that we have no reliable a-priori knowledge about the character or existence of signals we are attempting to receive It is for this reason that comprehensive searches over wide frequency ranges and in all directions from Earth are proposed

8 Conclusion

The possibility of detecting radio signals from other civilizations in our galaxy, if they exist, is strongly dependent upon a quiet radio environment at sites where searches for these signals are conducted Although it is true that modern technology will allow some discrimination against man-made signals, it is also true that the use of the radio spectrum for a wide variety of telecommunication services and functions is rapidly increasing the need for such discrimination As time passes, the probability of successful detection is correspondingly reduced

It is therefore important that the requirements for the search for extra-terrestrial signals be kept in mind, and that cooperation be encouraged to the maximum degree possible to protect search sites from interference

REFERENCES

COCCONI, G , and MORRISON, P [1959] *Searching for Interstellar Communications,* Nature, 184, 884

DRAKE, F D [1960] Sky and Telescope 39, 140

National Aeronautics and Space Administration, *Project Cyclops,* Ames Research Center, Moffett Field, California, USA, Report CR 114445, Revised Edition, July 1973, 243 pp

TARTER, J [1985] SETI Observations Worldwide, *The Search for Extra-terrestrial Life Recent Developments,* pp 271-290 ed M D Papagiannis, D Reidel Publishing Co

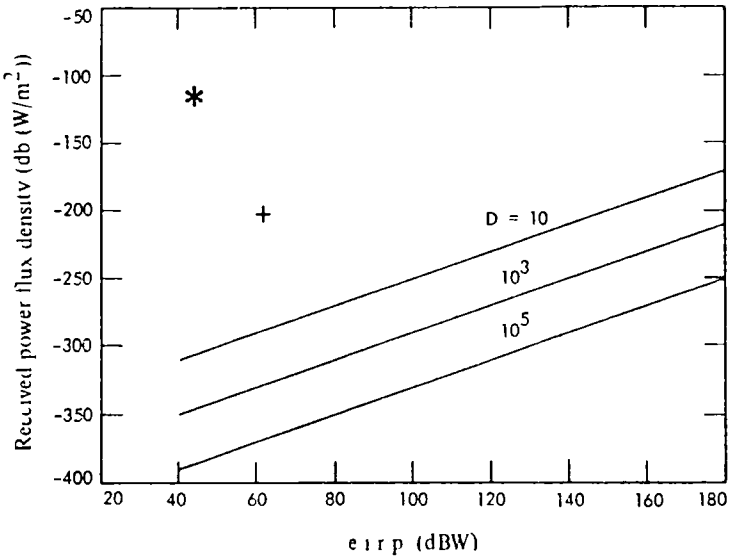

Figure 1 – *Received power flux density versus e i r p*

D Distance light years (1 light year = 9.46 x 10^{15} m)
* From geostationary satellite
+ From Voyager spacecraft at Neptune

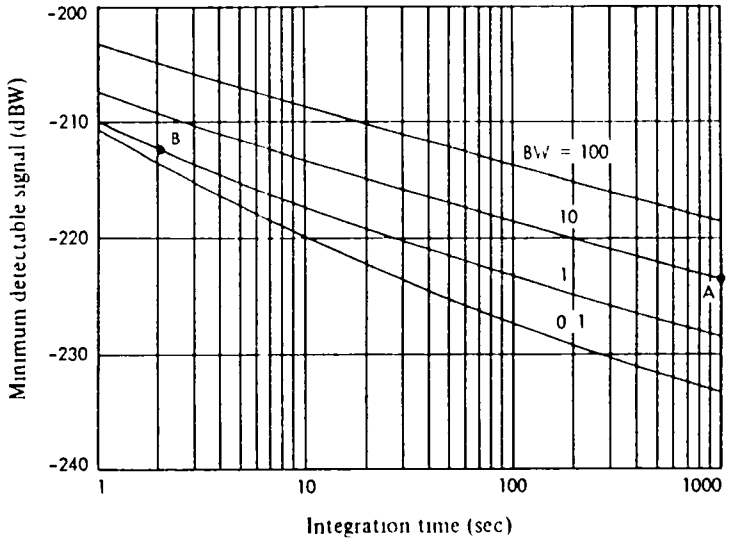

FIGURE 2 – *Minimum detectable signal power*

30 K system noise temperature BW Bandwidth (Hz)
Candidate system A BW = 10 Hz integration time = 2 sec
B BW = 1 Hz integration time = 1000 sec

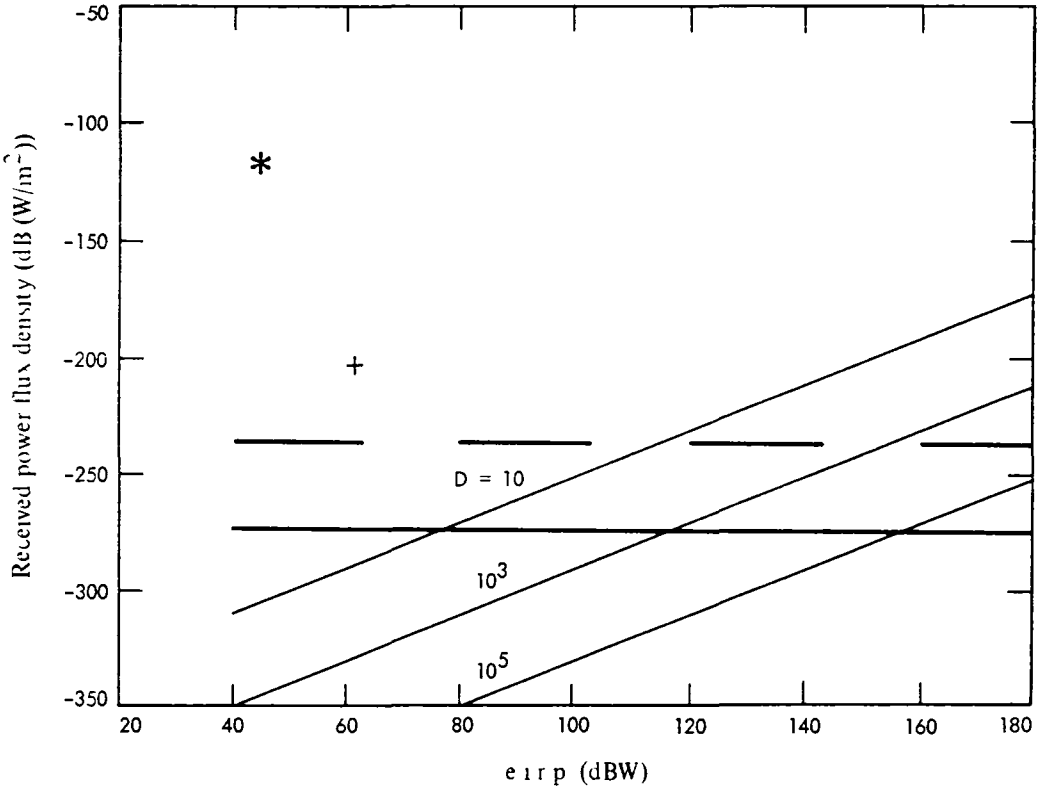

FIGURE 3 – *Signal detection capability*

Sensitivity — — — System A using 34m antenna (see text
——— System B using 300m antenna and Fig 2)
D Distance, light years (1 light year = 9 46 x 10^{15} m)
* Satellite in geostationary orbit
+ Voyager spacecraft at Neptune

Appendix B

(Note The text of CCIR Question 17-1/2 is given below)

QUESTION 17-1/2

RADIOCOMMUNICATION REQUIREMENTS FOR SYSTEMS TO SEARCH FOR EXTRA-TERRESTRIAL INTELLIGENCE

(1976-1982)

The CCIR,

CONSIDERING

(a) that many scientists believe intelligent life to be common in our galaxy,

(b) that electromagnetic waves are presently the only practical means of detecting the existence of intelligent extra-terrestrial life,

(c) that it is believed to be technically possible to receive radio signals from extra-terrestrial civilizations,

(d) that, although it is not possible to know the characteristics nor to predict the time or duration of these signals in advance, it is reasonable to believe that artificial signals will be recognizable,

(e) that, while an artificial signal of extra-terrestrial origin may be transmitted at any frequency, it is technologically impractical to search the entire radio spectrum, but the band searched should be sufficiently wide to make detection of a signal reasonably probable,

(f) that technological and natural factors which are dependent on frequency determine our ability to receive weak radio signals,

(g) that the search for radio signals from extra-terrestrial civilizations will use increasingly sensitive systems which could receive harmful interference from very weak man-made signals,

(h) that it is necessary to share with other services the bands in which the search is conducted,

(j) that available technology will allow a search for these signals from the Earth, from earth orbit, and, eventually, from the Moon, and to minimize interference, certain locations on Earth and ion space may be preferred,

UNANIMOUSLY DECIDES that the following questions should be studied

1 what are the probable characteristics of radio signals which might be broadcast by extra-terrestrial civilizations and the technical characteristics and requirements of a system to search for them,

2 what are the preferred frequency bands to be searched and the criteria from which they are determined,

3 what protection is necessary for receiving systems conducting a search for artificial radio signals of extra-terrestrial origin,

4 what criteria will make the operation of a search system feasible in shared, adjacent and harmonically related bands of other services,

5 what is the optimum search method,

6 what are the preferred locations, on Earth and in space, for a search system?

Note See Report 700

An Electronically Tuned, Stable 8415-MHz Dielectric Resonator FET Oscillator for Space Applications

M Lakshminarayana
Spacecraft Telecommunications Equipment Section

A voltage-controlled 8415-MHz FET oscillator stabilized by a dielectric resonator is described The oscillator provides a linear electronic tuning range of over 3 2 MHz with a flat power output equal to +1 8 dBm (27°C nominal), a single-sideband noise to carrier ratio of -68 dBc/Hz at 1 kHz off carrier, and a frequency temperature coefficient of 0 54 part per million/°C over a -24°C to 75°C range The oscillator withstood 150 krads (Si) of gamma radiation with no significant performance degradation The overall performance of the FET oscillator is in many ways far superior to that of an equivalent bipolar oscillator for space applications

I. Introduction

An 8415-MHz FET oscillator was developed for application as a phase-locked oscillator in a transponder for a spacecraft-based system, the NASA standard X-band transponder The advantages of this system were reduced size and complexity due to the elimination of multiplier chains, excellent frequency stability, electronic tunability over a large bandwidth, simplicity of temperature compensation, and low power consumption

This article describes a high stability voltage-controlled FET oscillator that includes an amplifier connected in a feedback loop with a temperature-stabilized dielectric resonator The oscillator configuration [1]-[4] and design were optimized to meet the design goals A detailed comparison of FET oscillator performance against that of a bipolar oscillator is given [5], [6] This technology development was successfully transferred to a telecommunications equipment contractor A summary of this technology transfer effort is given in Section V

II. FET Oscillator Design and Performance

The block diagram of the FET dielectric resonator oscillator (FET DRO) [1]-[3] is illustrated in Fig 1 A photograph of this oscillator is shown in Fig 2 The oscillator consists of a single-stage FET (Mitsubishi MGF 1402) amplifier of 11 6 dB gain, a 10-dB coupler, and a dielectric resonator on a 1 65-mm quartz spacer in the amplifier drain-to-gate shunt feedback loop The dielectric resonator is made of barium tetratitanate of dielectric constant k = 38 6, and its unloaded Q is equal to 4800 at 8400 MHz The resonator has a temperature coefficient of +3 5 ppm/°C One part of the coupler supplies the output signal, while the other supplies the signal to the feedback loop The insertion loss of the feedback loop, including the resonator and the coupler, is about 7 8 dB The loop has an excess gain of 3 8 dB A hyperabrupt silicon tuning varactor (Metallics MMD830-P55) at the end of a quarter-wavelength open stub is used to tune the circuit The resonator coupling and open-stub line lengths are adjusted to provide an electronic tuning of 3 4 MHz The measured loaded Q (Q_L) is

approximately equal to 2700 Further reduction in the loaded Q will increase the tuning range but will degrade the phase noise of the oscillator The circuit is etched on a 0 635-mm alumina substrate that is solder attached to a plated titanium base plate of a thickness equal to 0 89 mm. The circuit is enclosed in a rectangular box as shown in Fig 2 The dimensions of the box are 51 8 X 40 4 X 26 9 mm and can be reduced to 38 1 X 38 1 X 20 3 mm The FET DRO is mechanically tuned between 8412 MHz and 8490 MHz with a metal disc tuner over the dielectric resonator, and can be set within ±2 kHz

The electronic tuning characteristics of the FET DRO are illustrated in Fig 3 The electronic tuning range at any temperature setting within the designed temperature range from -20°C to +75°C is greater than 3 2 MHz (measurements were made at -24°C, 0°C, +27°C, +52°C, and +75°C) The varactor bias (frequency control voltage, V_{FC}) voltage range is from 0 to +15 V The selected value for the nominal frequency control voltage was equal to 8 V The tuning is quasi-linear, and its deviation from the best straight line fit over the 3 2-MHz tuning range is within ±14 percent The nominal power output at room temperature (27°C) is +1 8 dBm, with a maximum power variation of ±0 3 dB over the tuning range

The FET DRO was tested for the temperature dependence of oscillator frequency and power The results, as shown in Fig 4, indicate less than a 1-MHz peak-to-peak frequency drift and less than a +2 1 ppm/°C peak-to-peak temperature coefficient over the measured temperature range The average temperature coefficient over the temperature range is less than +0 54 ppm/°C The peak-to-peak power variation over the temperature range is less than 0 9 dB, and the total peak-to-peak power variation over the temperature range, including 0 5 dB maximum power variation over the 3 2-MHz tuning range, is less than 1 5 dB The single-sideband (SSB) phase noise density levels measured at different temperature settings and at different tuning bias levels [4] were found to be within the range of -66 to -69 dBc/Hz at a 1-kHz offset from the carrier These results meet the specified design requirements (Table 2) for application in a spacecraft transponder

III. Bipolar (BJT) Oscillator Design and Performance

The purpose of this design study was to compare the performance of the bipolar dielectric resonator oscillator against that of the FET oscillator for a spacecraft transponder application The bipolar dielectric resonator oscillator (bipolar DRO) [5], [6] is designed as a negative resistance oscillator The basic breadboard oscillator layout and component locations on an alumina substrate are shown in Fig 5 The NPN bipolar transistor (NE64587) used for this application is packaged in a common collector configuration to facilitate heat transfer from the transistor chip to the heat sink by solder attachment of the transistor package directly to the heat sink The stabilizing dielectric resonator is the same as that used in the FET oscillator circuit The dielectric resonator mounted to a 1 65-mm quartz spacer is coupled to the base microstrip line by placing it at about one-quarter wavelength away from the transistor base terminal The positioning of this dielectric resonator is critical as it determines the cavity-loaded Q, electronic tuning range, phase noise, and power output characteristics Electronic tuning of the bipolar DRO oscillator is accomplished by means of simple bias tuning, to vary the transistor base–collector capacitance The transistor biasing network is illustrated in Fig 6

The electronic tuning characteristics shown in Fig 7 were obtained by adjusting the dielectric resonator position to provide about 3 5 MHz of linear electronic tuning (125 kHz/V) over the frequency control base voltage (V_{FC}) range of -20 V to +8 V The electronic tuning deviation from the best straight line fit over this 3 5-MHz tuning range is less than ±3 percent The measured loaded Q is approximately equal to 600 Output power variation over the electronic tuning range was less than 0 8 dB The power output is equal to -3 8 dBm at V_{FC} = 0 V and at a temperature of 25°C The measured SSB phase noise is less than -70 dBc/Hz at a 1-kHz offset from the carrier in a 1-Hz bandwidth at any temperature setting (-25°C to to +72°C) and electronic tuning bias level The measured temperature performance of the bipolar oscillator with a temperature-compensated (T_{cf} = +3 5 ppm/°C) dielectric resonator is illustrated in Fig 8 The frequency temperature stability is better than -2 4 ppm/°C over -25°C to +72°C However, the power output of the oscillator varied by about 6 dB over the full temperature range, which can be flattened by employing buffer amplifiers The main reason the bipolar DRO was not pursued further for a spacecraft transponder application was its large power consumption (750 mW vs 90 mW for a FET) However, the bipolar DRO is ideally suited for applications where low phase noise design is most important

IV. Performance Comparison of FET and Bipolar Oscillators

In this section, a comparison of the FET DRO and the bipolar DRO for similar output frequency (8400- to 8500-MHz) and electronic tuning bandwidth (3-MHz) requirements is presented Oscillator circuit configurations and devices are compared in Table 1 Both of these circuits use a stabilizing dielectric resonator The bipolar DRO is a low Q (Q_L = 600) negative resistance oscillator, whereas the FET DRO is a high Q (Q_L = 2700) shunt feedback oscillator In the case of the bipolar DRO, it was necessary to lower the Q_L to 600 to ob-

tain the required 3 2-MHz linear electronic tuning, which in effect increased the phase noise However, the measured phase noise of the bipolar DRO is about 5 dB lower than that of the FET DRO This is a direct consequence of a lower $1/f$ noise corner frequency [1] for the bipolar device [5] The $1/f$ noise corner frequency for the bipolar transistor [5] is approximately equal to 6 3 kHz, whereas that for the FET device [7] is 700 kHz The bipolar oscillator is bias tuned by tuning the transistor collector-base junction capacitance The FET DRO is tuned by applying voltage across a silicon tuning diode whose shunting capacitance is electromagnetically coupled into the resonator fields

A complete list of the X-band (8415-MHz) DRO design goals attempted, along with the results achieved by the bipolar and FET oscillators, is compiled in Table 2 The goals for the mechanical frequency setting (8400 to 8500 MHz ±5 kHz), electronic frequency tuning range (3 MHz), tuning linearity (±15 percent), and frequency pulling (<100 kHz for 1 5 1 VSWR load) have all been met or exceeded The frequency temperature stability goal is <2 ppm/°C The dielectric resonator used in these oscillators has a temperature coefficient of +3 5 ppm/°C The measured average values of frequency temperature stability over the -20°C to +75°C range for FET and bipolar oscillators are 0 54 ppm/°C and -2 4 ppm/°C, respectively Further temperature compensation is necessary for the bipolar oscillator Nonharmonic spurious signals are less than -60 dBc for both oscillators All spurious signals are less than -77 dBc for the FET oscillator The bipolar oscillator has a second harmonic level of -16 dBc at its output and can be reduced to the goal requirement of less than -40 dBc by a buffer amplifier and a filter The bipolar oscillator generates a power level equal to -3 8 dBm at its emitter output It requires a buffer amplifier to increase its power output to the 0-dBm goal requirement level and to flatten the power variation to the ±1-dB goal over the tuning bandwidth and temperature ranges The FET oscillator meets the power output and power flatness requirements without a buffer amplifier, thus saving the additional power consumption and volume that would be required by the amplifying circuits

These oscillators were exposed to cobalt-60 gamma radiation at a level of 150 krads (Si), and the effects of radiation on the oscillators were studied The overall results for these oscillators indicate insignificant change in the measured parameters such as frequency, power, phase noise, bias current, and tuning characteristics

The four main trade-off concerns between these oscillators are (1) power consumption, (2) phase noise, (3) linear tuning bandwidth, and (4) power flatness The bipolar oscillator requires a maximum of 750 mW of dc power and operates at an efficiency of about 0 07 percent The FET oscillator has better efficiency (1 5 percent) and requires less than 90 mW of dc power (88 percent lower than the bipolar DRO) over the required 3-MHz electronic tuning range The single-sideband (SSB) phase noise that can be achieved for bipolar and FET oscillators is between -69 and -75 dBc/Hz and -66 to -69 dBc/Hz at 1 kHz from the carrier, respectively. Lower SSB phase noise values are possible by reducing the electronic tuning range For a given tuning bandwidth the bipolar DRO provides lower (by 5 dB or more) phase noise characteristics than the FET DRO

V. Summary of the Dielectric Resonator Oscillator (DRO) Technology Transfer Effort

The DRO technology discussed in the previous sections was transferred to the NASA X-band (8415-MHz) transponder contractor for implementation into the transponder design receiver local oscillator phase-locked loop (7459 MHz) and the exciter downlink oscillator phase-locked loop (8415 MHz) The contractor-fabricated engineering model local oscillator FET DRO (7459 MHz) is shown in Fig 9 The circuit is etched on a 0 635-mm-thick alumina substrate that is solder attached to a plated molybdenum base plate of a thickness equal to 0 635 mm The circuit is enclosed in a rectangular (aluminum) box of dimensions 30 5 X 38 1 X 13 7 mm The selected FET for this application is a high gain (12-dB) FET (Mitsubishi MGF 1402) with a low $1/f$ noise corner frequency (700 kHz) [7] The circuit is designed as a series-feedback negative resistance oscillator [1], [3] The length of the 37-ohm shorted stub attached to the FET source lead and the length of the 37-ohm transmission line between the drain lead and the 50-ohm output line are optimized for a maximum reflection coefficient (at 7459 MHz) at the gate The gate is conjugately matched with the equivalent resonant circuit model of the dielectric resonator coupled to the 50-ohm line attached to the gate The position and the spacing of the dielectric resonator relative to the gate transmission line are adjusted for the conjugate match with a zero-degree phase shift at the dielectric resonator reference plane at the operating frequency The dielectric resonator mounted on a 2 5-mm-high quartz spacer is electromagnetically coupled to the gate line at a distance of 5 4 mm from the gate (see Fig 9) The circuit is tuned by a hyperabrupt silicon tuning diode (Alpha DKV6550C-304-001) attached to a quarter-wavelength 50-ohm open stub line The open stub is electromagnetically coupled to the dielectric resonator The circuit layout also consists of a 50-ohm quarter-wavelength trap at 6 GHz with a 100-ohm series resistance attached to the drain circuit to suppress spurious oscillations at around 6 GHz

The adhesive used between the dielectric resonator and the quartz spacer, as well as between the spacer and the alumina, is

Ablebond 293-1 Five adhesive materials were evaluated for their dielectric constant, outgassing, peel strength, and cure cycle The adhesive trade-off summary is tabulated in Table 3 Of these, two adhesive materials—Ablebond 293-1, with a high peel strength equal to 3 88 kg, and Solithane 113-300, with a low peel strength equal to 0 68 kg—were further evaluated by measuring in a test fixture the temperature-induced shift in the resonant frequency of the adhesive-mounted dielectric resonator of temperature coefficient 0 ppm/°C The shift in the resonant frequency of the resonator over the qualification temperature range of -20°C to +75°C for Solithane 113-300 adhesive was 910 kHz, while that for Ablebond 293-1 was 630 kHz The performance of the adhesive Ablebond 293-1 is clearly superior in terms of its high peel strength and low temperature-induced frequency drift Ablebond 293-1 was the adhesive selected for the engineering model FET DRO

The electrical frequency tuning vs temperature performance characteristics of the 7459-MHz FET DRO (Fig 9) are shown in Fig 10 A bias tuning range of 6 5 V (nominal) ±6 V provided a tuning capability of ±1 8 MHz minimum over the hardware qualification temperature range of -20°C to +75°C, with a tuning linearity of less than ±10 percent The oscillator results show an overall frequency temperature slope of +3 7 ppm/°C This frequency drift can be further compensated by using a dielectric resonator of a thermal coefficient approximately equal to -3 7 ppm/°C The RF power output variations with tuning voltage and temperature are shown in Fig 11 The nominal RF power output level at a +6 5-V tuning voltage and at 25°C is +4 23 dBm The maximum power variation from the nominal power level is ±0 5 dB over the tuning voltage and qualification temperature ranges The measured single sideband phase noise at a 1-kHz offset from the carrier was less than -60 dBc/Hz The output of the oscillator has a second harmonic signal level of -25 dBc and a nonharmonic spurious signal level of -2 dBc at 11,896 MHz These spurious signals require further filtering to satisfy the requirements of -40 dBc for harmonic signals and -65 dBc for nonharmonic spurious signals

VI. Conclusions

The FET DRO is more efficient and consumes considerably less dc power than the bipolar DRO Measured SSB phase noise data confirm that the bipolar's performance is clearly superior to that of the FET oscillator, being about 5 dB lower in phase noise for frequency offsets of 100 Hz to 1 kHz from the carrier For space applications, the FET DRO is preferred to the bipolar DRO because of its lower dc power consumption, better thermal frequency stability, linear electronic tunability, and higher RF output power capability The technology transfer to industry was satisfactorily accomplished

This article summarized the performance characteristics and demonstrated the feasibility of X-band (8415-MHz) dielectric resonator oscillators for space communication applications Trade-offs between FET and bipolar oscillators have been identified and characterized

Acknowledgments

Acknowledgment is given to the contributions of D E Lebach and A W Kermode during the course of this work

References

[1] M. Camiade, A Bert, J Graffeuil, and G Pataut, "Low Noise Design of Dielectric Resonator FET Oscillators," in *Proceedings of the 13th European Microwave Conference*, pp 297–302, 1983

[2] O Ishihara, T Mori, M Sawano, and M Nakatani, "A Highly Stabilized GaAs FET Oscillator Using a Dielectric Resonator Feedback Circuit in 9–14 GHz," *IEEE Trans Microwave Theory and Tech* , vol MTT-28, pp 817–824, August 1980

[3] A P S Khanna et al., "Microwave Oscillator Analysis," *IEEE Trans Microwave Theory and Tech* , vol MTT-29, pp 606–607, June 1981

[4] D B Leeson, "A Simple Model of Feedback Oscillator Noise Spectrum," *Proc IEEE*, vol 54, pp 329–330, February 1966

[5] M R Lakshminarayana, "A Low Noise Dielectric Resonator Stabilized X-Band Bipolar Oscillator," presented at the IEEE-sponsored Seventh Biennial University/ Government/Industry Microelectronics Symposium, Rochester, New York, June 9–11, 1987

[6] M R Lakshminarayana, "Electronically Tuned Microwave Oscillator," NASA Technical Brief, vol II, no 7, item no 160, pp 28–29, July–August 1987

[7] A N Riddle and R J Trew, "Low Frequency Noise Measurements of GaAs FETs," in *Proc of 1986 IEEE MTT-S International Microwave Symposium Digest*, pp 79–82, June 1986

Table 1. Active device and dielectric resonator oscillator circuit comparisons

Parameter	FET DRO	Bipolar DRO
Nominal frequency	8415 MHz	8415 MHz
Active device	MGF 1402-01 Gate length = 0 8 μm Gate width = 400 μm	NEC 64587
Circuit configuration	Shunt feedback	Negative resistance
$1/f$ noise corner frequency (f_c)	>700 kHz	6 3 kHz
Device noise figure	2 5 dB	5 2 dB
Resonator type	Transtech D8512 (+3 5 ppm/°C) barium tetratitanate Q_0 = 4800 at 8400 MHz	Transtech D8512 (+3 5 ppm/°C) barium tetratitanate Q_0 = 4800 at 8400 MHz
Spacer	Quartz, spacer 1 65 mm	Quartz, spacer 1 65 mm
Cavity Q_L	2700 mm	600 mm
Tuning device	Hyper-abrupt silicon diode MMD 830-P55	Bipolar transistor base–collector junction capacitance is bias tuned
Mechanical dimensions	51 8 X 40 4 X 26 9 mm	47 X 31 8 X 24 1 mm

Table 2. Comparison of FET and bipolar dielectric resonator oscillators

Parameter	Specifications	Measured performance	
		FET DRO	Bipolar DRO
Mechanical tunability	8400–8500 MHz ±5 kHz	8412–8490 MHz ±2 kHz	8387–8601 MHz ±2 kHz
Electrical tunability	±1 6 MHz about f_0	±1 70 MHz (linear)	±1 75 MHz (linear)
Frequency tuning linearity	±15% to BSL	±14%	±3%
Output power*	0 ± 1 dBm −20°C to +75°C	+1 5 to +2 4 dBm	+0 8 to −4 7 dBm
Power flatness vs tuning*	±0 5 dB	±0 3 dB	±0 5 dB
Power flatness vs temperature*	±0 5 dB −20°C to +75°C	±0 5 dB	±3 dB
Total output power variation over both temperature range and maximum tuning range*	±1 dB −20°C to +70°C	±0 75 dB	±4 5 dB†
Frequency stability vs temperature	2 ppm/°C between −20 and +75°C	+0 54 ppm/°C (average)	−2 4 ppm/°C
SSB phase noise at 1 kHz from carrier	−60 dBc/Hz	−66 to −69 dBc/Hz	−69 to −75 dBc/Hz
Harmonics	−40 dBc	−77 dBc	−16 dBc
Nonharmonic spurious	−65 dBc	−77 dBc	−68 dBc
Frequency pulling	100 kHz for 1 5 1 VSWR all phase load	<26 kHz	11 kHz
Frequency pushing ±1% supply voltage variation (gate and/or drain voltage)	<100 kHz	<25 kHz	<17 kHz
Frequency control terminal impedance	>2 kohms	1500 kohms	15 24 kohms
Power consumption*	<200 mW	90 mW	750 mW
Operating voltage	<±28 V	+4 and −2 V	−14 V ± 1%
Tuning voltage*	<±15 V	0 to −15 V	−15 to +8 V
Output impedance	50 ± 5 ohms	50 ± 5 ohms	50 ± 5 ohms
Efficiency*	>0 5%	1 5%	0 07%
Cold and hot turn-on at any temperature	OK	OK	OK
Radiation immunity*	150 krads (Si)	No performance degradation	No performance degradation

*Goals
†Unbuffered output

Table 3 Dielectric resonator oscillator adhesive trade-off summary

Material	Dielectric constant	Outgassing	Peel strength, kg		Cure	Form
			Unetched	Etched		
Epon 838/V125	2 95–3 85 @ 1 MHz, 25°C (estimated)	0 51–1 65% TML* 0 12–0 77% VCM† (est range)	1 61	0 57	24 hours at 21°C or 2 hours at 66°C	Premixed frozen in syringe (epoxy)
Scotchweld 2216 Gary	5 51 @ 1 kHz, 24°C	0 82% TML 0 06% VCM	1 75	0 68	24–48 hours at 25°C or 2 hours at 66°C	2-part mix at 25°C (epoxy)
Solithane 113-300	3 4 @ 10 MHz, 27°C	0 50% TML 0 02% VCM (estimated)	0 68	1 34	48 hours at 25°C or 3 hours at 66°C	Premixed frozen in syringe (urethane)
Sigma Plastronics #1 typ II 1 1 ratio	2 7 @ 8000 MHz, 25°C	0 64% TML 0 01% VCM	1 11	1 59	8–10 hours at 25°C or 3 hours at 66°C	2-part mix at 25°C (epoxy)
Ablebond 293-1	3 6–4 0 @ 1 kHz, 25°C	1 32% TML 0 08% VCM	3 88	3 31	24 hours at 60°C or 4 hours at 75°C	Premixed frozen in syringe (epoxy)

*TML = total mass loss
†VCM = volatile condensable material

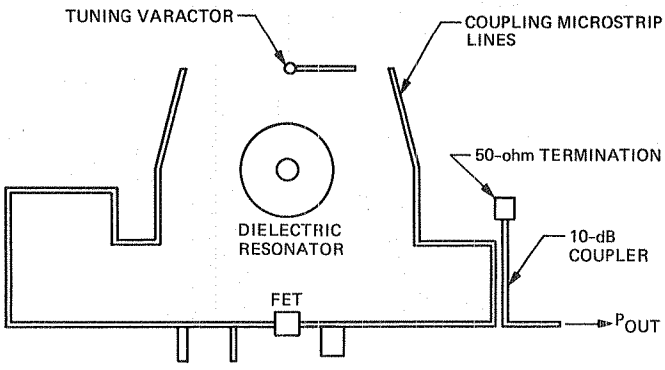

Fig. 1. Block diagram of the FET dielectric resonator oscillator

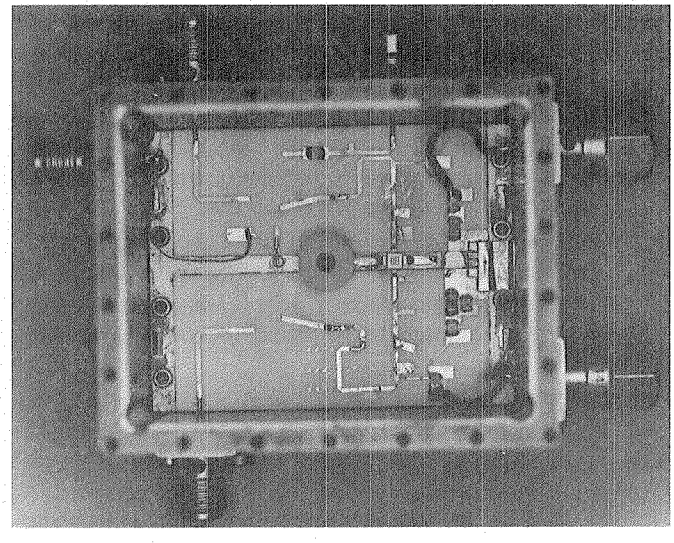

Fig. 2. FET dielectric resonator oscillator assembly

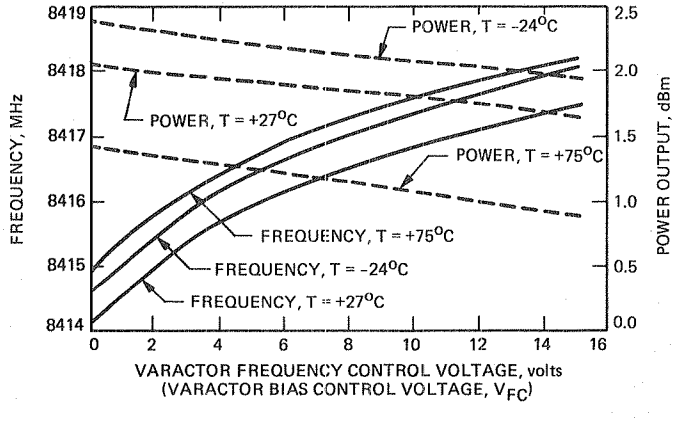

Fig. 3. FET DRO electronic tuning characteristics

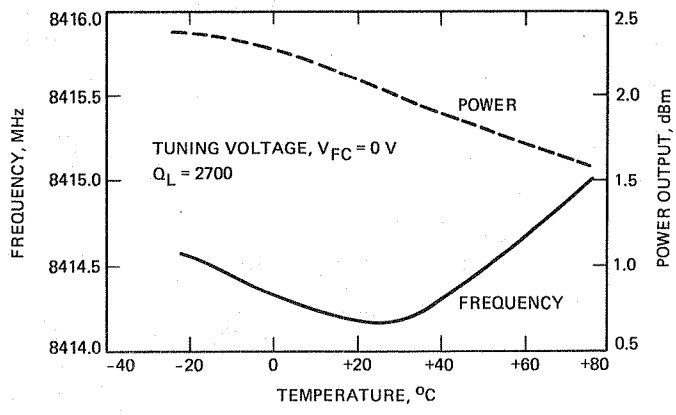

Fig. 4. FET DRO temperature performance characteristics

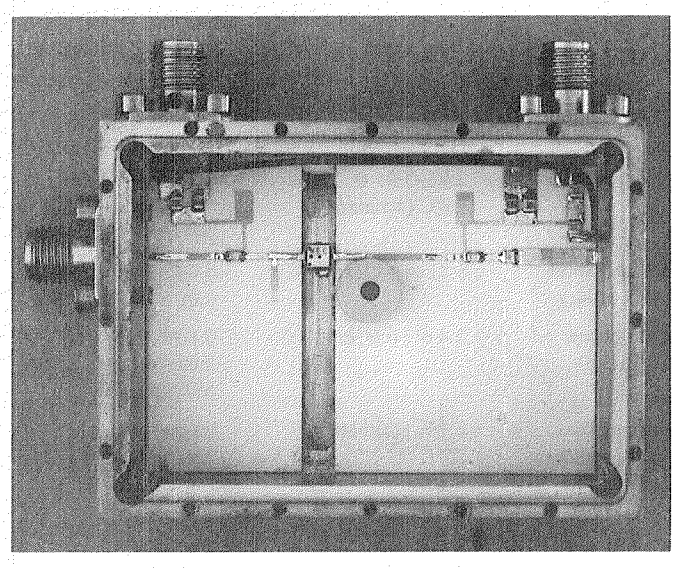

Fig. 5. Bipolar dielectric resonator oscillator assembly

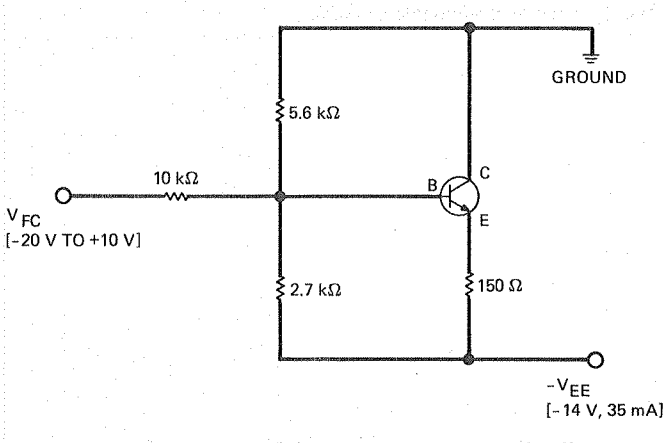

Fig. 6. Bipolar transistor DC biasing circuit for linear electronic tuning

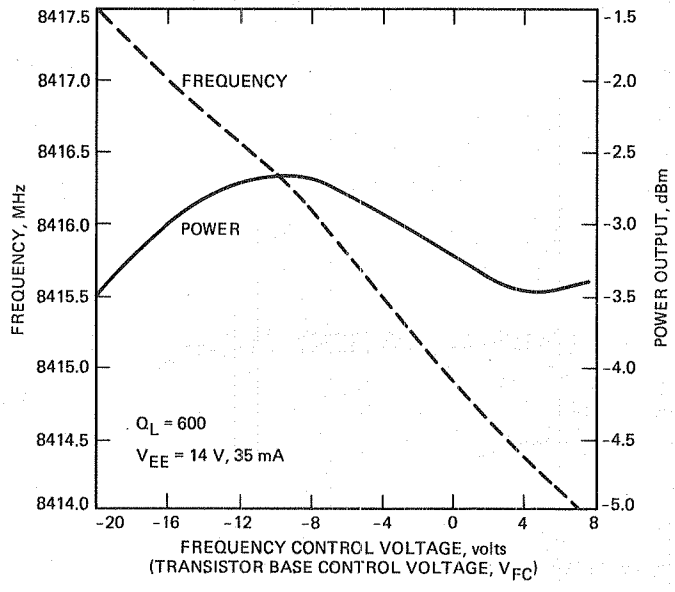

Fig. 7. Bipolar DRO electronic tuning characteristics

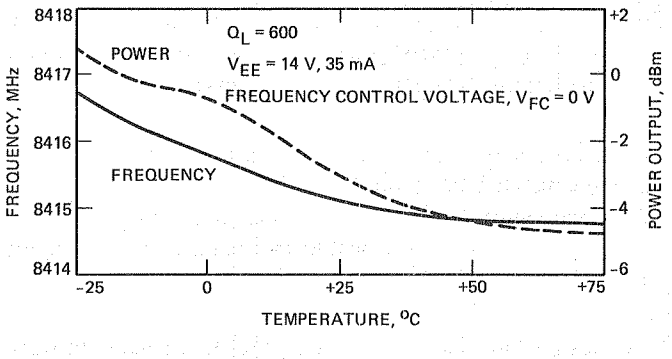

Fig. 8. Bipolar DRO temperature performance characteristics

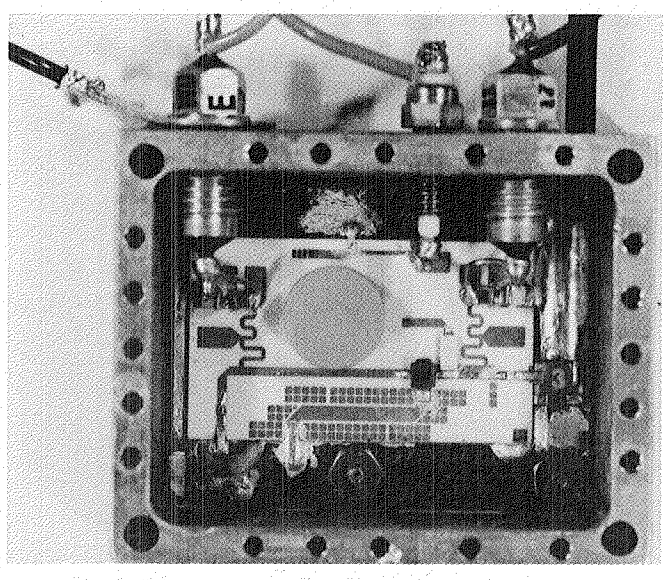

Fig. 9. The 7459-MHz local oscillator FET DRO assembly

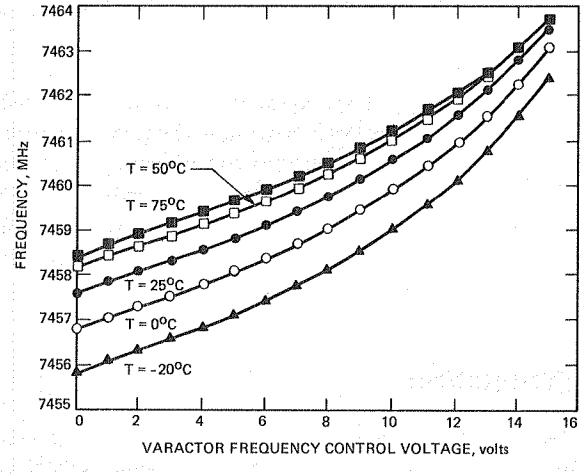

Fig. 10. The 7459-MHz local oscillator FET DRO electronic tuning characteristics

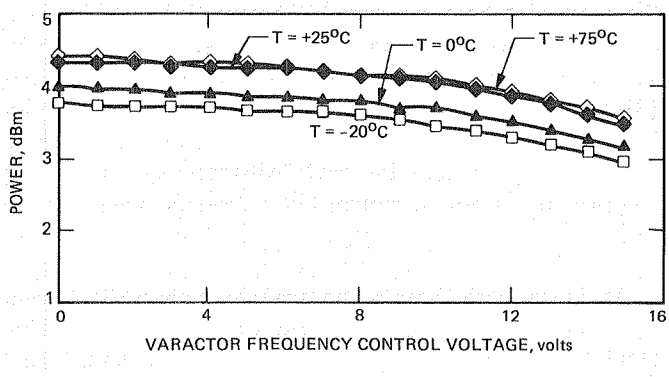

Fig. 11. The 7459-MHz local oscillator FET DRO output power vs. tuning voltage and temperature

Goldstone Solar System Radar Performance Analysis

E Satorius and S Brokl
Communications Systems Research Section

A simulator has been developed which models the digital baseband data paths of the planetary radar receiver system as configured in the ranging mode The simulator is useful for quantifying the effects of digital quantization errors on radar receiver sensitivity and for predicting receiver performance In this article, a performance analysis of the radar receiver is presented using system parameters that correspond to those for the upcoming Mars observations Thus, the results provide an assessment of anticipated data quality for these observations

I. Introduction

Development of the high speed data acquisition ranging system for the Goldstone Solar System Radar (GSSR) has been reported in a series of articles over the past several years [1]–[4] For range-Doppler mapping applications, the system utilizes a binary phase-coded (BPC) transmitted waveform and the received echoes are complex basebanded, sampled, and demodulated with a replica of the transmitted BPC waveform The system is composed of high speed digital front end filters [4] and complex demodulators [3] The demodulator output is transferred to the system computer (VAX 11/780 with FPS-5000 array processor) for data reduction, e g , generating range-Doppler maps A system block diagram is presented in Fig 1

As shown, both in-phase and quadrature channels are sampled (nominally at 40 MHz in the current system) and are input to pre- and post-baud integrating filters The pre-baud filter integrates 5 input samples per output data sample, and the post-baud filter integrates N_{baud} input samples per output data sample (N_{baud} is a user-specified input parameter) The function of these integrating filters is to decimate the data by a factor of $5N_{baud}$, thereby reducing the throughput rate into the demodulators (correlators/accumulators)

The data paths out of the A/D converters are 8 bits wide but are expanded to 16 bits after the pre-baud integrators A further expansion to 32 bits occurs after multiplication by the scaling constant so that the post-baud integration is carried out with 32-bit integer arithmetic

Following post-baud integration, the 32-bit data are truncated to the N_{bits} most significant bits (N_{bits} is nominally 4 but is treated as an input parameter for our performance analysis calculations) Finally, the truncated data are correlated and accumulated to produce a stream of correlation data which are output to the system computer

Actually, the above block diagram corresponds to just one of the complex data acquisition channels Multiple complex

channels are frequently used, e g , in interferometry mapping of Venus Thus, the performance analysis presented in this article is limited to monostatic, single polarization measurements which utilize only a single complex channel Nevertheless, these results are indicative of trends in multi-channel system performance as a function of the various input system parameters

II. System Overview

The basic function of the system (prior to the computer) is to correlate the received echoes with a replica of the transmitted BPC waveform

$$\phi(\tau) = \int_0^T x(t)\, BPC(t+\tau)\, dt$$

where $x(t)$ is the received complex data, $BPC(t)$ denotes the BPC waveform which is a periodic binary pseudo-noise (PN) sequence generated by a linear shift register, and T is the period of the BPC waveform

$$T = \Delta T N_{\text{code}}$$

where N_{code} denotes the PN code period and ΔT denotes the duration of a single code element (baud) The complex input, $x(t)$, is composed of the received (basebanded) signal plus system noise

$$x(t) = s(t) + n(t)$$

In our systems analysis, we model the received signal as a Doppler-shifted and scaled version of the transmitted BPC waveform

$$s(t) = ABPC(t)\, e^{j\phi} e^{j\Delta\omega t}$$

where the Doppler offset, $\Delta\omega$, is an input parameter

In correlating the input data with the transmitted BPC waveform, the digital system hardware computes a maximum of 256 correlation lags (range bins) $\phi(k\Delta T/N_{os})$, $0 \leqslant k \leqslant 255$, where N_{os} represents the number of computed lags per code baud ($N_{os}\Delta T$ also represents the time interval between data samples in the correlator, note that N_{os} can be controlled by the appropriate choice of N_{baud}) As discussed in [3], the correlation lags are computed sequentially using a pipeline architecture After the maximum number of lags (<256) is computed, a new set of correlation lags is computed, thereby generating the two-dimensional array of data.

$$c(i,k) \equiv \phi_i \frac{k\Delta T}{N_{os}}, \qquad 0 \leqslant k \leqslant 255$$

$$i \equiv \text{lag set index} = 0, 1, 2,$$

In computing the correlation data, lagged products are summed over the entire length of the code However, this sum is broken down into partial sums of 256 terms corresponding to the maximum register length of the correlators For PN codes which exceed the register length of the correlators, i e , when $N_{os}N_{\text{code}} > 256$ (recall that the data samples in the correlators are separated in time by $\Delta T/N_{os}$ seconds, *not* ΔT seconds), sequential lag sets are accumulated

$$A(i,k) = \sum_{j=1}^{N_{acc}} c(N_{acc}\, i + j, k)$$

where the number of accumulations, N_{acc}, is chosen such that $256\ N_{acc}$ approximately spans the period of the code, i e , $256\ N_{acc} \approx N_{os}\, N_{\text{code}}$ In this case, the accumulated correlation lag data, $A(i,k)$, is input to the system computer For short PN codes such that $N_{os}\, N_{\text{code}} < 256$, N_{acc} is set to 1

The system computer calculates the range-Doppler map data, $RD(n,m)$, by Fourier transforming the lag set data in conjunction with power combining, i e ,

$$RD(n,m) = \sum_{j=1}^{N_{sa}} |Y_i(n,m)|^2, \qquad 0 \leqslant m \leqslant 255$$

$$-N_{\text{bins}}/2 \leqslant n \leqslant N_{\text{bins}}/2$$

where N_{sa} is the number of spectra accumulated, N_{bins} is the number of Doppler bins, and $Y_i(n,m)$ represents the Fourier transformed correlation data

$$Y_i(n,m) = \sum_{k=-N_{\text{bins}}/2}^{N_{\text{bins}}/2} A(k + iN_{\text{bins}}, m)\, e^{-2\pi jkn/N_{\text{bins}}}$$

The performance of the system can be conveniently expressed in terms of the output signal-to-noise ratio, SNR_o, which is defined by

$$SNR_o \equiv \frac{\langle R\rangle_{S+N} - \langle R\rangle_N}{\sqrt{\left\{\langle (R - \langle R\rangle_N)^2\rangle_N\right\}}}$$

where $\langle\cdot\rangle_N$ denotes the average background noise level and $\langle\cdot\rangle_{S+N}$ denotes the average signal-plus-noise level The ratio $PG = SNR_o/SNR_{in}$ is the system processing gain where SNR_{in} denotes the input signal-to-noise ratio (in the front-end low-pass filter bandwidth) The theoretical system processing gain, ignoring quantization and sampling effects, is the product of the coherent and incoherent processing gains

$$PG = 2BTN_{bins}\sqrt{N_{sa}}$$

where B is the bandwidth of the front-end low-pass filters The factor $2BTN_{bins}$ represents the coherent processing gain and $\sqrt{N_{sa}}$ is the incoherent gain realized by the power combining [5] In the next section, we present the results of computer simulations of the digital acquisition system which can be compared directly with the above theoretical results for system processing gain

III. Simulation Results

In evaluating system performance, we have developed a computer simulation test bed which models the digital high-speed data acquisition system depicted in Fig 1 The simulator program, written in FORTRAN 77, is portable and has been run with minimal modifications on both the Communications Systems Research Section (Section 331) Radar VAX 11/780 computer (without making use of the FPS 5000 array processor) and Cydrome's new Cydra computer (currently on loan to Section 331) The run times for the Cydra are all approximately 7 times faster than the 11/780 run times, and thus the results presented in this section were obtained with the Cydra computer

The simulation input parameters, corresponding to the upcoming S-band monostatic BPC Mars experiment, include (1) the system (A/D) sample rate (set at 40 MHz), (2) the bandwidth, B, of the front-end low-pass filters which are modeled as 6th-order digital Butterworth filters (B is set at 6 MHz), (3) the total number of Doppler bins, N_{bins} (set at N_{bins} = 128), (4) the number of spectral power accumulations, N_{sa} (set at either N_{sa} = 1 or 50), (5) the number of accumulations, N_{acc}, used in computing the correlation lags (set at 1), (6) the total number of correlation lags computed per set (255), (7) the number of samples integrated in the post-baud filters (N_{baud} = 24), (8) the number of bits, N_{bits}, used in computing the correlation lags (N_{bits} = 4 will be used in the Mars experiment, but we have also used N_{bits} = 8 in our performance analysis), (9) the PN code baud, ΔT (set at 6 μsec), (10) the signal Doppler offset frequency, $\Delta\omega$ (set at $\Delta\omega$ = 0 Hz), (11) the PN code period, N_{code} (set at N_{code} = 127), (12) the input RMS system noise level (which was set at 1/3 of the full scale A/D voltage), (13) the DC bias offset of the A/D converters (nominally set at 0 but varied in the simulation experiments to measure the impact on system performance), and (14) the input signal-to-noise ratio, SNR_{in} (which was set at either -30 dB or -55 dB to model the range of expected input SNRs for the S-band BPC Mars observations) The above values for the system clock rate, the PN code baud, and the number of post-baud integration samples correspond to N_{os} = 2 computed correlation lags per code baud

The output from each simulation experiment is a sample range-Doppler map, $RD(n,m)$, as defined above in Section 2, consisting of 2560 data points (128 Doppler bins X 20 range bins) Given this map, sample values for SNR_o are computed and compared against the theoretical limit

$$SNR_o = SNR_{in}\, 2BTN_{bins}\sqrt{N_{sa}}$$

The first set of simulation experiments consisted of high input SNR tests (SNR_{in} = -30 dB), all corresponding to one power accumulation (N_{sa} = 1) For these cases and using the input parameters as specified above, the theoretical limit on system output SNR is given by

$$SNR_o = SNR_{in}\, 2BTN_{bins} \approx 30\ 7\ \text{dB}$$

The average sample output SNRs from the simulation experiments corresponding to different noise realizations and using both N_{bits} = 4 and 8 are tabulated in Table 1 As is seen, the current system (with N_{bits} = 4) is within 1 5 dB of theoretical performance Increasing the correlator input data paths to 8 bits improves system performance by approximately 1 dB

The second set of tests was conducted to assess the impact of a DC bias offset at the A/D converters on system performance All of these tests were again run at the high input SNR level (SNR_{in} = -30 dB) with N_{sa} = 1 and N_{bits} = 4 and 8 The results of these experiments are presented in Figs 2 and 3 As is seen, at least in terms of output SNR, the system is remarkably robust to A/D bias offsets For N_{bits} = 4 (Fig 2), the sample output SNR varies by only approximately 2 dB up to DC bias offset levels of 0 1, above which system performance degrades dramatically This bias level (0 1) corresponds to 10 percent of the A/D full scale input level or, equivalently, to approximately 13 quantization levels of the A/D converters For N_{bits} = 8 (Fig 3), output SNR again drops dramatically at a DC bias offset in excess of 0 1, but the variation in output SNR below this offset level is less than that for N_{bits} = 4

The final set of system tests consisted of low-input SNR tests (SNR_{in} = -55 dB) corresponding to both 1 power accumu-

lation and 50 power accumulations For these cases, the theoretical limits on system output SNR are given by

$$SNR_o = SNR_{in}\, 2BTN_{bins} \approx 5\ 7\ \text{dB}\ (N_{sa} = 1)$$

and

$$SNR_o = SNR_{in}\, 2BTN_{bins}\sqrt{50} \approx 14\ 2\ \text{dB}\ (N_{sa} = 50)$$

Slices of the range-Doppler output maps evaluated at the maximum signal bin and spanning a total of ±16 Doppler bins are plotted in Fig 4 for both N_{sa} = 1 and 50 As is seen, the signal peak is clearly detectable for N_{sa} = 50 For N_{sa} = 1, the signal is visible but cannot be unambiguously detected (a number of noise peaks exceeded the signal peak over the entire 2560-point range-Doppler map computed for this case) The computed output SNR for these cases were $SNR_o \approx 6\ 3$ dB (N_{sa} = 1) and $SNR_o \approx 12\ 6$ dB (N_{sa} = 50) The former case is anomalous due to the high level of system noise (relative to the signal level) The latter case, corresponding to 50 power averages, is within 1 6 dB of theoretical performance which corresponds closely to the results presented in Table 1 for the high SNR case

IV. Conclusions

The simulation results presented here suggest that system performance should be within approximately 1 5 dB of theoretical over the nominal range of system operating parameters which will be utilized in the upcoming Mars BPC experiments Furthermore, the incorporation of 8-bit input data to the correlators will only increase performance by approximately 1 dB Finally, the system appears to be robust against A/D bias offsets at least for the short code bauds used in the Mars BPC experiments (The impact of DC bias offset will be more severe as the code baud increases due to the increased post-baud integration required)

It should be noted that although these simulations do take into account the finite digital precision effects inherent in this system, other effects such as A/D nonlinearities will further limit system performance over what has been predicted by this performance analysis

References

[1] L Deutsch, R Jurgens, and S Brokl, "The Goldstone R/D High Speed Data Acquisition System," *TDA Progress Report 42-77*, vol January–March 1984, Jet Propulsion Laboratory, Pasadena, California, pp 87–96, May 15, 1984

[2] S Brokl, "Polynomial Driven Time Base and PN Generator," *TDA Progress Report 42-75*, vol July–September 1983, Jet Propulsion Laboratory, Pasadena, California, pp 84–90, November 15, 1983

[3] S Brokl, "Demodulator and Accumulator for the High-Speed Data Acquisition System," *TDA Progress Report 42-77*, vol January–March 1984, Jet Propulsion Laboratory, Pasadena, California, pp 97–103, May 15, 1984

[4] K Farazian and R Jurgens, "Programmable Digital Baud Integrators for the Radar High-Speed Data Acquisition System," *TDA Progress Report 42-79*, vol July–September 1984, Jet Propulsion Laboratory, Pasadena, California, pp 142–151, November 15, 1984

[5] H Van Trees, *Detection, Estimation, and Modulation Theory, Part I*, New York Wiley Press, 1968

Table 1. High input SNR test results

SNR_o simulation experiments, dB		SNR_o theoretical limit, dB
$N_{bits} = 4$	$N_{bits} = 9$	
29 3	30 4	30 7

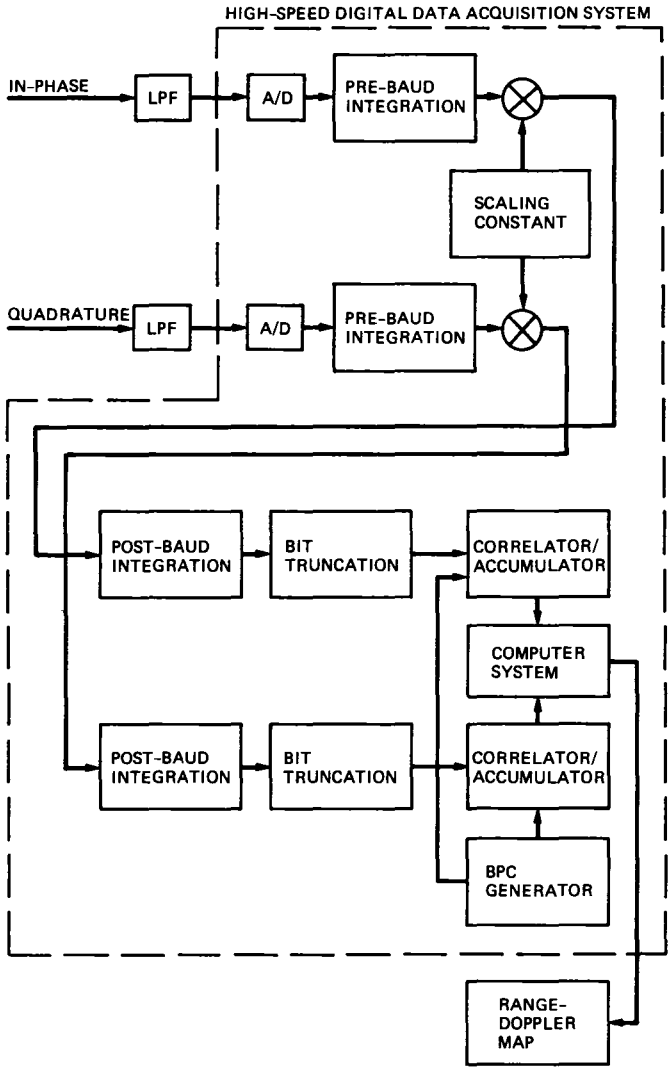

Fig 1 System block diagram

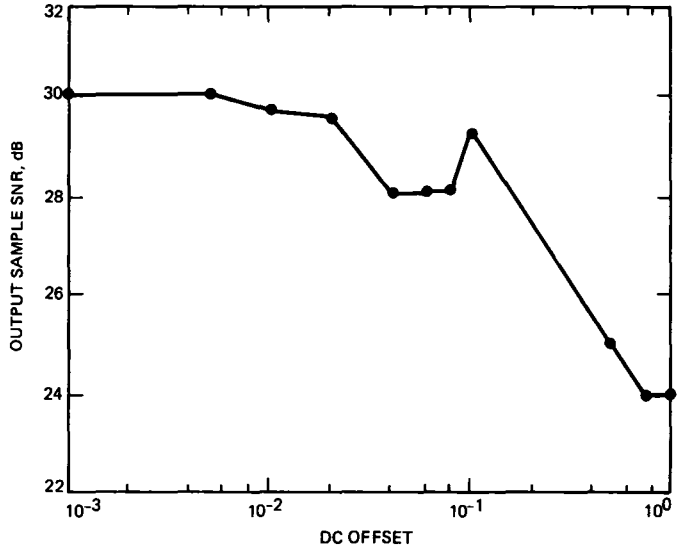

Fig. 2 System output SNR for $N_{bits} = 4$

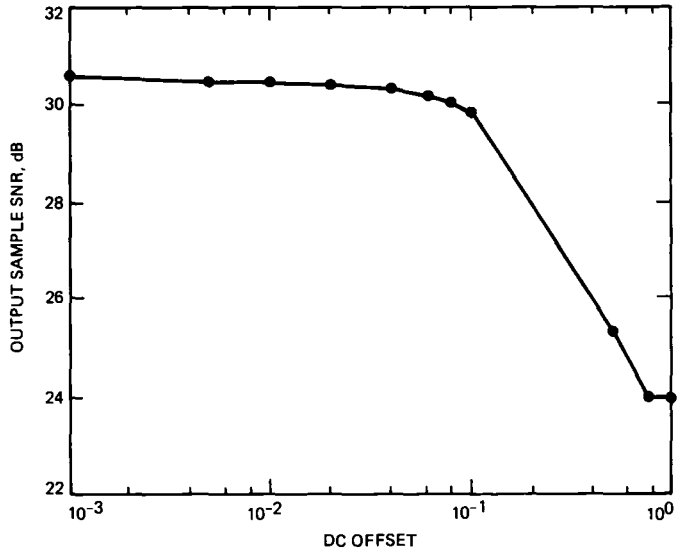

Fig 3 System output SNR for $N_{bits} = 8$

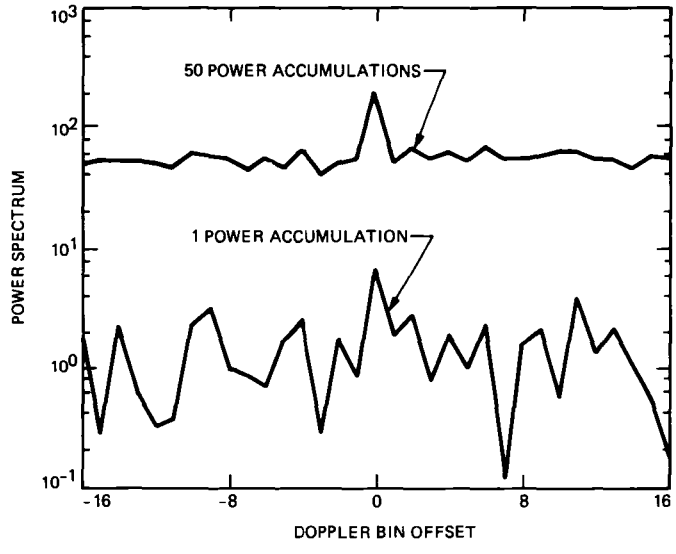

Fig 4 Output range-Doppler data for $SNR_{in} = -55$ dB

DSS 14 Antenna Calibrations for GSSR/VLA Saturn Radar Experiments

C N Guiar
Ground Antennas and Facilities Engineering Section

R L Riggs
TDA Engineering

R Stevens
Office of Telecommunications and Data Acquisition

M Wert
TDA Mission Support and DSN Operations

DSS 14 pointing and gain were calibrated to support X-band bi-static radar observations of Saturn's rings The observations used the Goldstone Solar System Radar and the National Radio Astronomy Observatory Very Large Array in Socorro, New Mexico

The pointing calibrations were based on conscan offset data collected during Voyager 1 and 2 support passes The conscan data show angle-of-arrival sensing with no bias and 0 3-mdeg 1-σ error Using the calibrations, demonstrated blind pointing performance on Saturn was <3-mdeg 1-σ error

Meteorological observations at the site were used to reduce elevation errors caused by atmospheric refraction The techniques used corrected about one-third of the error– poorer than expected performance

I. Introduction

This article describes the calibration of the beam pointing and the gain of the DSS 14 64-m antenna in preparation for a series of X-band (8 5-GHz) radar observations of the rings of Saturn For the radar observations, DSS 14 illuminated the planet rings, and the VLA in Socorro, New Mexico, received the echo The VLA used antennas that had been recently outfitted for X-band reception in preparation for support of the Voyager 2 Neptune encounter

The plan for the work was developed in late March, 1987, the work was performed at DSS 14 during April and the first

three weeks of May Radar observations of Saturn's rings were conducted May 23 through May 31

The performance goals were ambitious $\leqslant$2-mdeg 3-σ beam pointing error, $\leqslant$3-dB 3-σ absolute gain error

A secondary objective of the work was to develop and demonstrate improved techniques for application to calibration of the DSN antennas for spacecraft mission support

II. Summary

This report describes the calibration techniques used and presents the results obtained

A. Techniques Used

The basic technique used for the pointing calibrations was to collect conscan data on a non-interference basis during Voyager 1 and 2 support passes Also, beam scans were made of Saturn's thermal radiation Then, the pointing calibrations obtained from the Voyager conscan tracks and the Saturn scans which used the "XRO" antenna feed cone were translated to the radar "XKR" feed cone

To meet the elevation pointing accuracy objectives, an improved technique was required to correct for atmospheric refraction The current technique is to calculate refraction bending based on average site meteorological conditions—referred to as default parameters The approach used here was to make meteorological measurements at the site during a pass, and from them provide corrections to the values calculated for the default parameters

Also, we aspired to develop some empirical data on wind induced pointing errors from the instrumented conscan tracks On all tracks providing good conscan data the wind was, alas, benign, no useful data were obtained

We used the measurement techniques developed by the 70-m Upgrade Project to determine the radar system receive configuration antenna efficiency

B. Results Obtained

The pointing capability was demonstrated during the radar observations by short scans of the blackbody emission of Saturn using the radar receive mode feed Saturn is a poor target for the purpose (approximately 6-mdeg disc diameter, approximately 1 1-K source temperature), but it was the best available technique for direct validation of the beam pointing

Saturn scans were normally made twice in each radar pass during the period day-of-year (DOY) 145 through 164 That period included the Saturn rings and succeeding Titan moon observations Averaging the results gave a worst beam pointing error of 5 9 mdeg and a mean error of 2 7 mdeg The resulting 1-way degradation from pointing errors was 0 32 dB maximum, 0 09 dB mean Clearly we did not meet the 2-mdeg 3-σ pointing error calibration goal However, the degradation in quality of the radar observations resulting from DSS 14's pointing errors was evidently small

In the time available, it was not possible to provide a sensitive receiving capability on the radar transmit mode feed, so its pointing could not be demonstrated, only inferred

The effort to demonstrate better correction for atmospheric refraction was partially successful Use of concurrent meteorological data reduced the average elevation errors during a pass by perhaps 30 percent—we expected much greater error reduction

One set of antenna efficiency vs elevation angle data was obtained for the radar receive mode The results show a peak aperture efficiency of 46 7 percent at 42 degrees elevation Lacking suitable coupling to the receiver, the measurement could not be accomplished for the radar transmit mode

III. The DSS 14 Pointing System

A. Introduction

The techniques used for making and applying the antenna calibrations involve the operational pointing system and various off-line data collection and analysis tools This section describes the basic pointing system An end-to-end antenna pointing system block diagram is shown in Fig 1, a glossary of abbreviations is given in Table 1

B. Pointing by Predicts

The antenna is pointed based on target angle vs time predictions prepared at the JPL NSS and transmitted to the Complex SPC prior to a tracking support pass The predicts are computed from spacecraft or other celestial body ephemerides They are in the form of topocentric direction cosines, and for spacecraft tracks they are supplied at ten minute intervals In principle, the errors inherent in the predicts are completely negligible

Before the tracking pass, the complex CMC Operator sends the antenna predicts to the APA The APA transforms the direction cosines of the predicts to Az–El coordinates The LMC Operator sends the Az–El predict points and an antenna pointing Systematic Error Correction Table (SETBL) from the APA computer disk to the antenna mounted ACS microcom-

puter The ACS interpolates the predicts and provides angle position signals to which the antenna is slaved via either the MEC (for the Master Equatorial Precision mode) or the ASC (for the Computer Control backup mode) The Precision mode was used for all of our work

Also, the antenna can be pointed from predicts aided by a scanning mode that senses, and corrects to, the true direction-of-arrival of the radio signal That mode is conscan (for conical scanning), it can sense and correct errors as large as the half-power beamwidth of the antenna

C. Pointing by Conscan Aided Predicts

Conscan works in the following way The APA generates a circular scan pattern for the antenna and sends it to the ACS The ACS adds the scan pattern to the corrected pointing predicts Software in the REC computes and sends received signal levels to the APA via the SPC LAN

The correlation of the scan position of the antenna, as reported by the ACS, with the received signal level variations allows the APA to compute corrections to the scan pattern center The APA sends the corrections to the ACS Thus, within the capability of the closed-loop control system, the scan center is pointed precisely to the apparent direction-of-arrival of the spacecraft signal

As will be discussed in the following section, the offsets between the signal direction-of-arrival as computed by conscan, and the direction defined by the corrected pointing predicts, provided the source for most of our calibration data

IV. Conscan Offset Data Collection, Reduction, and Analysis

A. Introduction

During the period for making the pointing calibrations, DSS 14 was heavily loaded with spacecraft mission support It was necessary that our data collection be a non-interfering by-product of that support Conscan is the normal operational antenna mode for spacecraft support at X-band We used non-intrusive data capture programs to collect conscan offset data from the channel between the APA and the ACS

The basic approach in using the spacecraft conscan offset data is to presume that the predicts are correct and that conscan correctly senses the direction of the signal Then, any systematic offsets are attributed to systematic pointing errors of the antenna beam

Because conscan offsets were the basic source of calibration data, we did some analyses to characterize their quality That work is presented in Appendix A

B. Conscan Data Collection and Processing

1 **Background** Voyager 2 and Saturn are nearby in the sky—separated by about an hour in right ascension and 2 deg in declination Therefore, Voyager 2 data were directly applicable to the Saturn pointing calibrations, Voyager 1, which reaches 65 deg elevation at DSS 14, provided data to stabilize the calculation of the antenna systematic error parameters

During the period DOY 086 to 142, conscan offset data were collected on 21 Voyager passes—all but a few of the scheduled support passes Those few passes were designated by the Voyager Project as involving critical support

Preliminary conscan data were obtained from DOY 086 to 099, various problems with the pointing system were experienced from DOY 104 to 118, and the data obtained during that period were of little use From DOY 120 to 139 good data were obtained from two Voyager 1 and three Voyager 2 passes, and from one pass observing Saturn's thermal radiation Those data were the basis for the antenna Systematic Error Table (SETBL) developed for the Saturn radar observations

Figure 2 shows the mean offsets of the raw conscan data from the Voyager tracks during the period DOY 086 to 142 The period of faulty pointing system performance is evident

2 **Techniques used** Figure 3 illustrates the sequence of steps used to collect the conscan data and to develop the antenna pointing error model and SETBL The steps are described in the following paragraphs The software programs involved are developmental, not in the operational DSN library

The CAPTURE program accesses the antenna information transmitted between the APA and the ACS via a monitor port on the APA modem patch panel Time tagged azimuth and elevation angles and azimuth and elevation conscan offsets are logged to a file and displayed on the monitor and line printer The data collection is not in-line, it is accomplished without interference during mission support tracking

The PLOTSCAN and CONPLOT programs provide plots of the conscan offset data PLOTSCAN plots cross-elevation, elevation, and beam pointing offsets versus azimuth angle CONPLOT plots azimuth, elevation, and cross-elevation offsets versus time

The plots allow immediate assessment of the conscan offset data quality Bad or suspicious data can be easily identified for file editing prior to using the record for calibration purposes

Statistical analysis of the conscan data file is provided by ANA-CON The mean and standard deviation (σ) of the azimuth, elevation, cross-elevation, and beam pointing offsets are calculated Also, signal losses in decibels from the beam offsets are determined, and offsets exceeding 3σ are identified

The edited conscan data file is input to READCON READCON outputs an offset file in a format suitable to input to CONCORR for computing refraction correction, and to input to PHO9 for computing the parameters of the antenna pointing systematic error model The techniques used for computing refraction correction, and the results obtained, are discussed in detail in Appendix B

The PHO9 program works best with 50 to 100 input points A typical conscan offset raw data file from an 8-hour Voyager track has about 300 points Also, data from tracks on several days normally are used to compute a set of model parameters To reduce the size of a conscan offset data input file for PHO9

(1) All data from periods when conscan is not functioning stably are edited out, as previously discussed,

(2) Selected sections of tracks from different days are used,

(3) To further reduce the file size, every other sample of a record is deleted That process provides less smoothing of the conscan offset data (estimated 1σ of 0 3 mdeg with all data points vs 0 5 mdeg with deletions)–it was used for simplicity in preparing the file

V. Techniques for Development of Systematic Error Correction Tables

A. Introduction

The pointing error modeling approach used in the DSN is based on expected physical behavior of the antenna It was developed by optical and radio astronomers, it has been successfully applied to major radio astronomy facilities [1]

The complete pointing error model for an antenna is a sum of separate error functions Table 2 shows the individual error sources and the elevation and cross-elevation error functions used to develop the complete model systematic error correction table The functions in Table 2 apply for the "precision" mode which uses the Master Equatorial as the pointing reference

B. Techniques Used

The observational data are used by the PHO9 error model program to generate or refine an antenna systematic pointing error model PHO9 determines the "P" constants in the individual error functions of Table 2

PHO9 reads the edited conscan offset data file It then sums the offsets from the a priori error model–the systematic error correction model used during the track–with the conscan offsets, resulting in the total offsets due to systematic errors Finally, PHO9 uses a linear least squares fitting routine to compute the "P" parameters of the new systematic error model

Programs are available that provide display of the systematic error model and its parameters PLOT'MDL plots the systematic error model versus hour angle for a specified declination PRMDLANL prints the model "P" parameters and the quality of their determination by the PHO9 fitting TABLES tabulates azimuth and elevation offsets of a systematic error model at 5-degree increments of azimuth vs elevation

Finally, the SECPHO program takes a set of model parameters and calculates a Systematic Error Correction Table (SETBL) The output of SECPHO is a suitably formatted file that is loaded into the ACS via the APA using a VT-100 simulator program The last step provides the SETBL for operational use

VI. Final Development of Systematic Error Correction Table for Use in GSSR/VLA Saturn Radar Experiment

A. Introduction

Conscan offset data from five Voyager passes late in the period (DOY 120, 125, 126, 127, and 136) appeared good They were the basis of our final SETBL The statistics of the error data for these days are given in Table 3

B. Process of SETBL Development

A SETBL was developed using the data from the passes on DOY 120, 125, 126, and 127 The SETBL table used during each of those tracks was M4X31N, its "P" parameters are given in Table 4 The data from each of the four cited days were edited by the methods described in the previous section and merged into one file The SETBL calculated from that file was M4X31B, its "P" parameters are also given in Table 4

SETBL M4X31B was used during the track on DOY 136 with results as shown in Table 3 Then, the data from DOY 136 were edited and merged with the data file used to generate SETBL M4X31B, and that revised file was used to generate the set of "P" parameters M4X31C (cf Table 4)

On DOY 139, the blackbody (thermal radiation) from Saturn was scanned using SETBL M4X31C The results are shown in Fig 4—the mean cross-elevation offset is −1 1 mdeg, the mean elevation offset is +4 0 mdeg

We reviewed the recent results from Voyager passes and the Saturn track and decided to accept the −1 1 and +4 0 mdeg mean offsets These offsets were added to the P1 and P7 terms, respectively, to form the "P" parameter set M4X31C(REV) (cf Table 4) M4X31C(REV) was our final version of the systematic error correction for the antenna using the "XRO" Cassegrain cone

The SETBLs were based on Voyager conscan and Saturn offset data using the "XRO" Cassegrain cone However, the "XKR" Cassegrain cone is used for radar measurements The antenna beam using the "XRO" cone is slightly offset from the beam using the "XKR" cone—the offset must be accounted for in applying the pointing calibrations to the radar The correction is made by adjusting the beam collimation error parameters

$$P1(XKR) = P1(XRO) + 0\ 0105\ (deg)$$

$$P7(XKR) = P7(XRO) + 0\ 0045\ (deg)$$

The above corrections are based on previous measurements at DSS 14 by D Girdner

VII. Beam Pointing Measurements During Period of Radar Observations

Beam pointing was checked regularly during the period of the radar observations using beam scans of Saturn's blackbody radiation Usually we made one check at the beginning and one check at the end of each radar track With the aid of a simple program on a PC, it took about 10–15 minutes to complete a set of scans and estimate the beam error indicated by the data

These measurements used the Noise Adding Radiometer (NAR) and the Square Law Detector Assembly (SQLD) in the GSSR equipment room in the pedestal The microwave system and the receiver front end were as configured for the radar track

The results from the beam pointing checks from Saturn scans are shown in Figs 5 (antenna temperature from Saturn's radiation), 6 (cross-elevation error), and 7 (elevation error) The data shown were taken during the period of the radar observations of Saturn's rings, and during a subsequent period of radar observations of Saturn's moon, Titan

From the average cross-elevation and elevation errors of the preceding figures, we calculate the average beam errors (Fig 8), and from those, estimate the one-way loss from pointing errors The loss results are shown in Fig 9 The worst loss on a day is 0 32 dB, the mean and median losses for the 12 days are 0 09 dB and 0 05 dB, respectively We expect those results are representative of the pointing performance during the actual radar observations

VIII. Antenna Efficiency Measurements of the Radar (XKR) Feed Cone

Our original intention was to calibrate the antenna with both the transmit and receive radar feeds We were unable to provide a satisfactory receiving configuration for the transmit feed, and therefore did not accomplish its calibrations

Antenna efficiency measurements were taken of the radar receive feed at the radar operating frequency, 8,495 MHz The measurements were made on DOY 134 The experimental procedures used were those recently developed for the efficiency measurements of the large antennas before and after their upgrade from 64 m to 70 m [1] Figure 10 is a functional block diagram of the equipment used

The results of the efficiency measurements are shown in Fig 11 The curve is a mean square quadratic fit to the circled data points The maximum efficiency was 46 7 percent at 42 degrees elevation

IX. Conclusions

(1) Conscan offset data were collected and analyzed on a noninterference basis during Voyager support passes Using that data and a few hours of noisy Saturn beam scan data, blind pointing of 2 to 3 mdeg mean beam error was provided That beam error results in <0 1 dB mean one-way degradation for the radar

[1] K Bartos, et al , "Antenna Gain Calibration Procedure," JPL D-3794 (internal publication), Jet Propulsion Laboratory, Pasadena, California, November 15, 1986

(2) When the system is functioning normally, conscan points the antenna in the direction of the received signal with essentially no bias and about 0 3 mdeg standard deviation (see Appendix A) That is very high quality pointing calibration data

The operational conscan system needs an improved protocol for setting and demonstrating its closed loop parameters

(3) The improvement in elevation pointing accuracy from use of concurrent surface atmospheric measurements for the refraction correction was less than expected (see Appendix B) The results we obtained were really not suitable for the precision pointing and calibration of 70-m apertures at X and Ka bands

The techniques involved must be improved in the future

(4) A configuration to allow direct measurement of the pointing and gain of the radar transmitter feed must be provided

Reference

[1] R Stevens, R L Riggs, and B Wood, "Pointing Calibration of the MKIVA DSN Antennas for Voyager 2 Uranus Encounter Operations Support," *TDA Progress Report 42-87*, vol July-September 1986, Jet Propulsion Laboratory, Pasadena, California, pp 206-239, November 15, 1986

Table 1 Glossary of abbreviations for text and figures

ACM	Antenna control and monitor
ACS	Antenna control subassembly
APA	Antenna pointing assembly
ARA	Area routing assembly
ASC	Antenna servo controller
CMC	Central monitor and control (console)
FEA	Front end area
IRS	Intermediate reference structure
LAN	Local area network
LMC	Link monitor and control (console)
MDA	Metric data assembly
MEA	Master equatorial assembly
MEC	Master equatorial controller
MMA	Meteorological monitoring assembly
NAR	Noise adding radiometer
NASCOM	NASA communications
ND	Noise diode
NSS	Network support subsystem
PC	Personal computer (IBM compatible)
REC	Receiver-exciter controller
SETBL	Systematic error table
SPC	Signal processing center
TWM	Traveling-wave maser

Table 2 Systematic pointing error model for 64-m antenna (precision mode)

Error	Cross-elevation model	Elevation model	Cross-declination model	Declination model
Cross-elevation collimation	P1	–	–	–
Elevation collimation	–	P7	–	–
Gravity flexure	–	P8cos (el)	–	–
Hour angle declination orthogonality	–	–	-P11sin (dec)	–
Hour angle axis alignment	–	–	P12sin (h angle) sin (dec)	P12cos (h angle)
Hour angle axis alignment	–	–	-P13cos (h angle) sin (dec)	P13sin (h angle)
Declination encoder bias	–	–	–	P16
Hour angle encoder bias	–	–	P21cos (dec)	–

Table 3 Conscan error statistics for DOYs 120, 125, 126, 127, and 136

DOY	SETBL	Cross-elevation		Elevation		Number of points
		Average	σ	Average	σ	
120	4X31N	−0 3	1 1	1 1	1 9	102
125	4X31N	−1 4	1 1	−2 5	0 8	33
126	4X31N	2 5	0 7	0 5	0 8	27
127	4X31N	−2 1	0 7	1 3	1 1	45
136	4X31B	−2 6	0 7	0 6	1 1	16

Table 4 Systematic error correction table parameters (degrees)

Parameter number	M4X31N	M4X31B	M4X31C	M4X31C (REV)
1	−0 00389	−0 00031	−0 00349	−0 00459
7	0 02018	0 02756	0 02555	0 02955
8	−0 03179	−0 03806	−0 03782	−0 03782
11	0 00647	0 00000	0 00000	0 00000
12	0 00000	−0 00213	0 00079	0 00079
13	0 00000	−0 00357	−0 00067	−0 00067
16	0 00126	0 00121	0 00064	0 00064
21	−0 00664	−0 00743	−0 00564	−0 00564

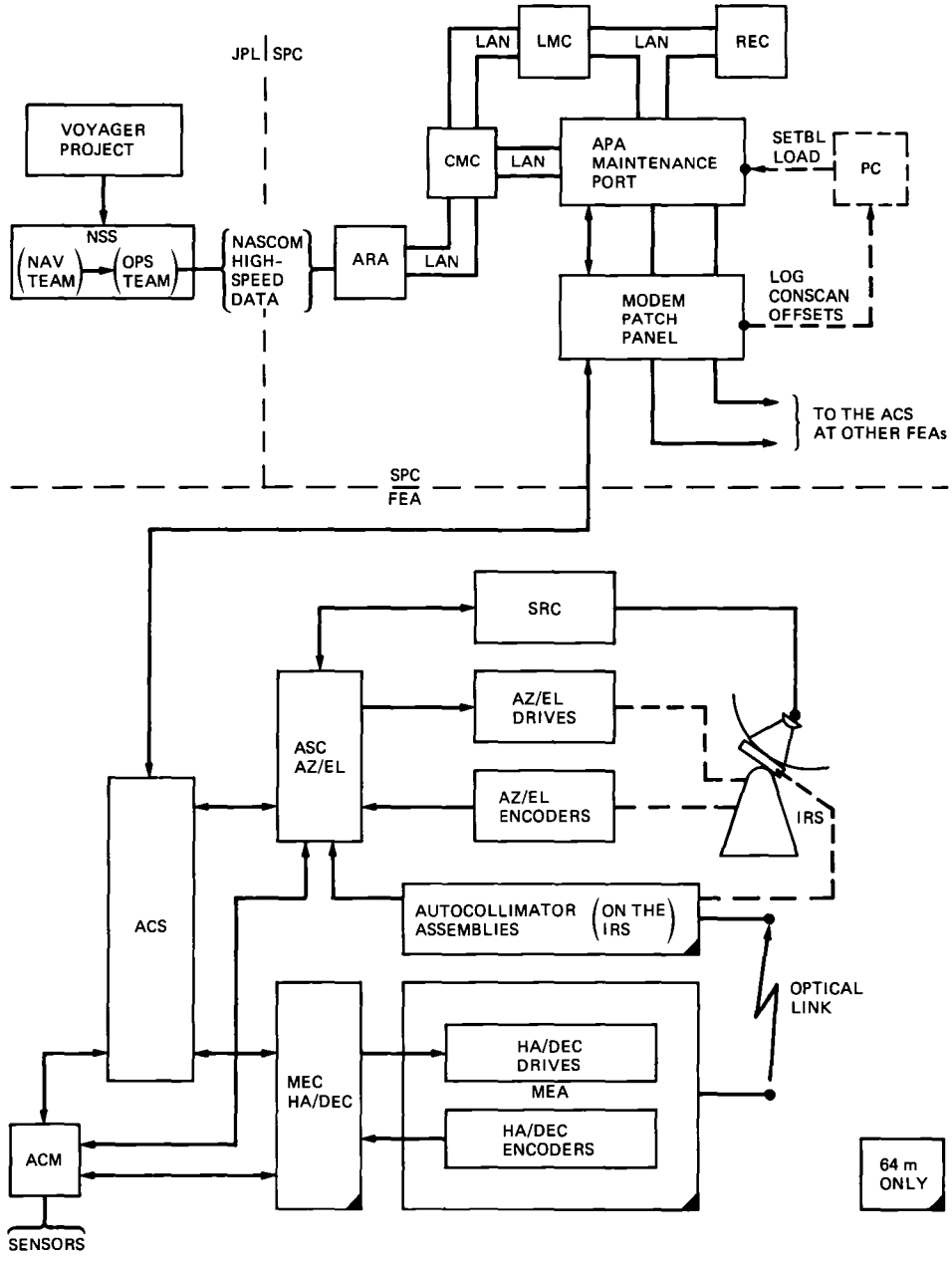

Fig 1 DSS 14 end-to-end antenna pointing system

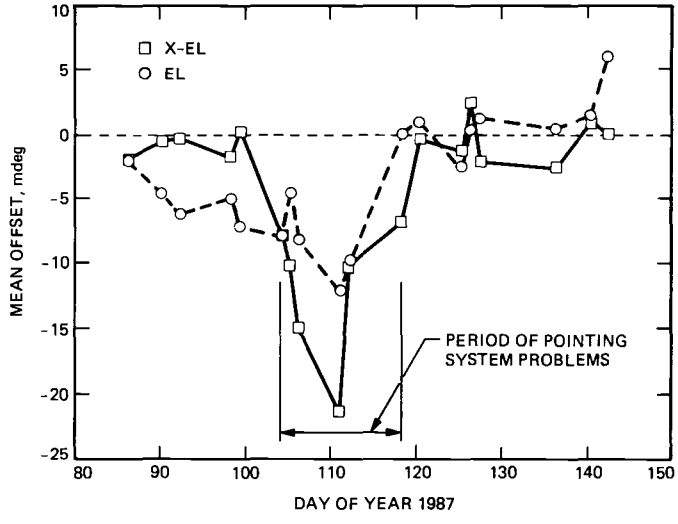

Fig 2 Conscan offsets from Voyager tracks

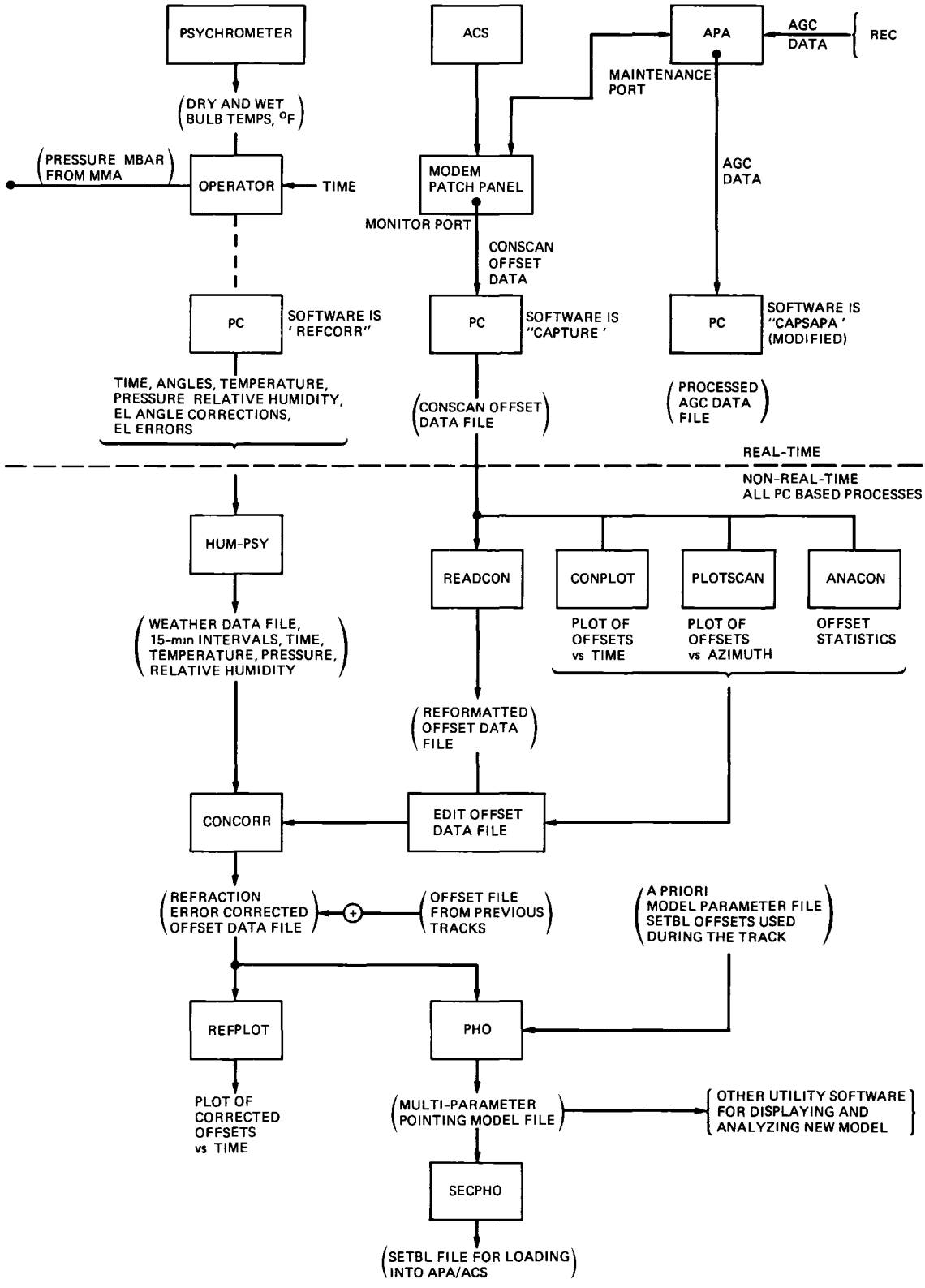

Fig 3 Block diagram of conscan data acquisition and data processing

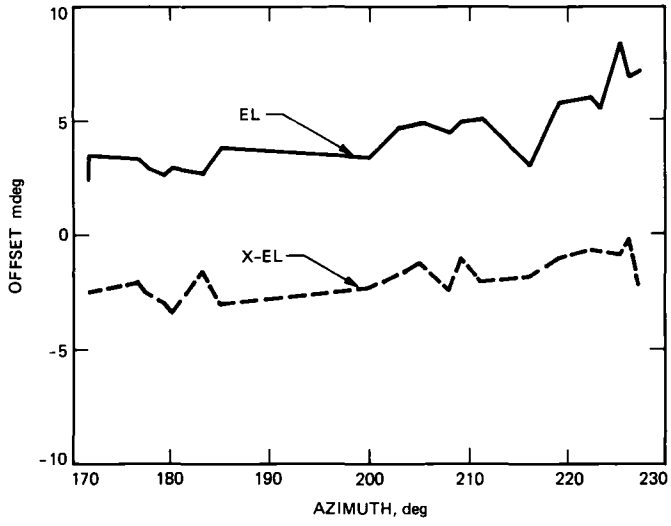

Fig. 4 Cross-elevation and elevation from Saturn blackbody scans on DOY 139

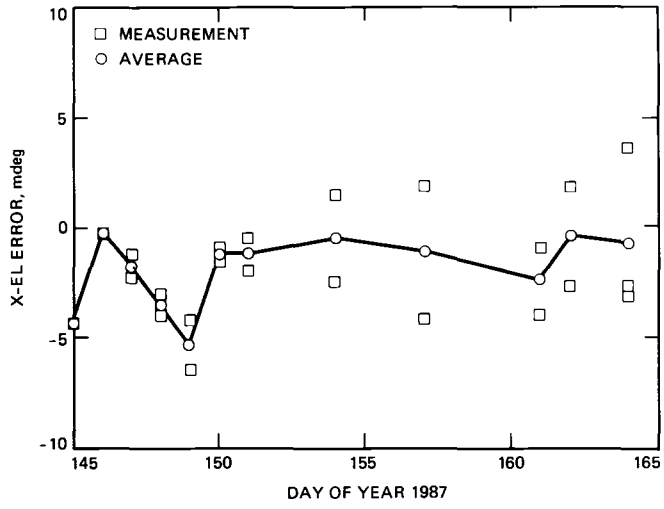

Fig 6 Cross-elevation errors from Saturn scans

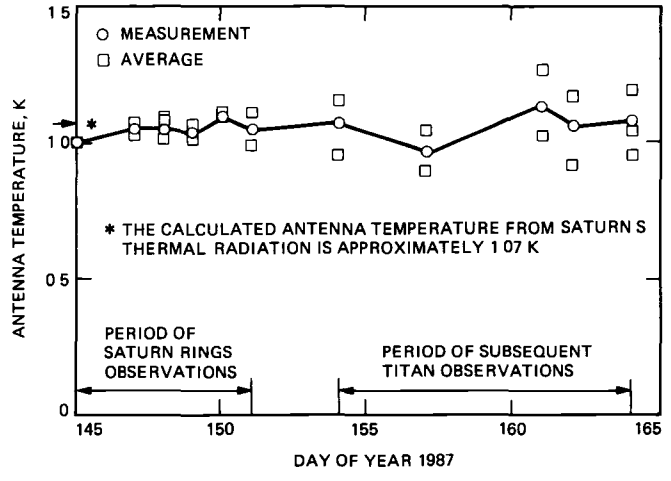

Fig 5 Antenna temperature from Saturn blackbody radiation observations

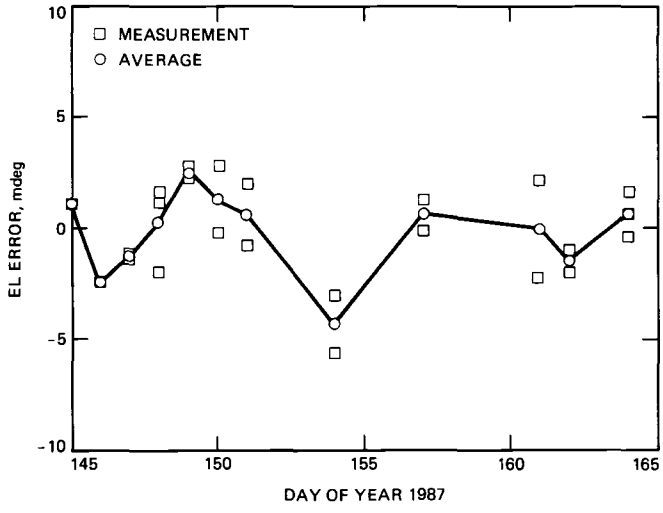

Fig 7 Elevation errors from Saturn scans

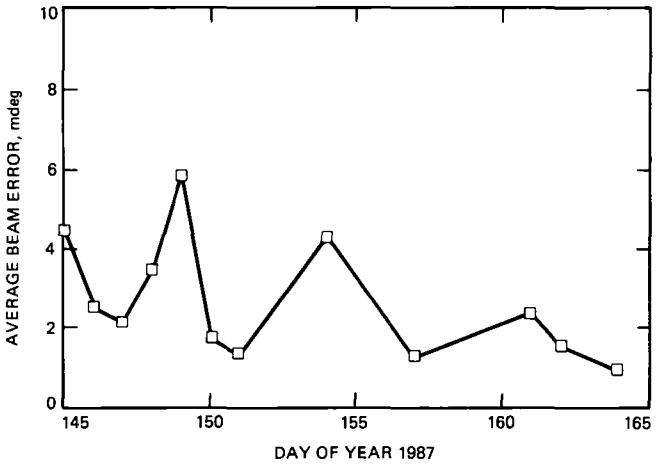

Fig 8 Average beam pointing errors from Saturn scans

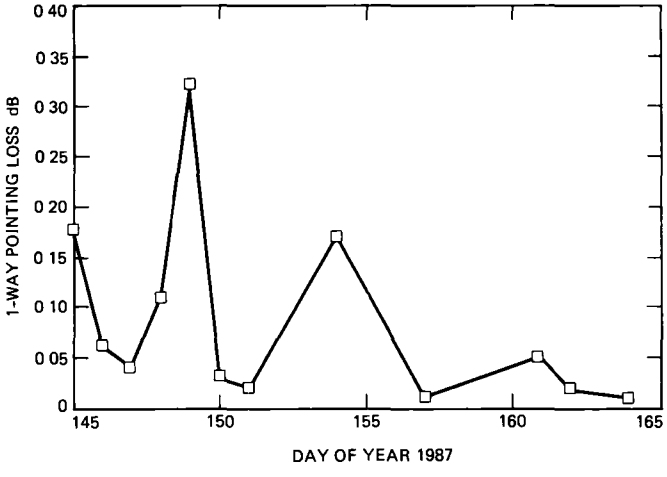

Fig 9 Average pointing loss calculated from Saturn scans

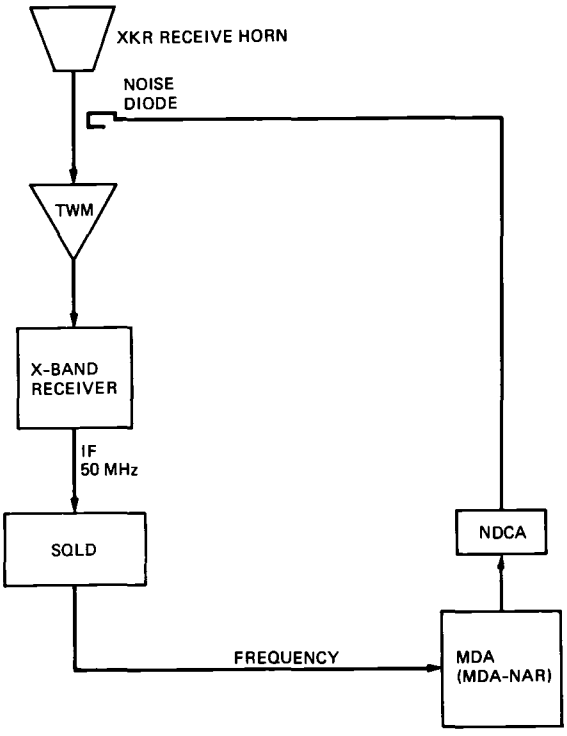

TWM = TRAVELLING WAVE MASER
SQLD = SQUARE LAW DETECTOR
MDA = METRIC DATA ASSEMBLY
NDCA = NOISE DIODE CONTROL ASSEMBLY
IF = INTERMEDIATE FREQUENCY

Fig 10 Functional block diagram of antenna efficiency measurement equipment

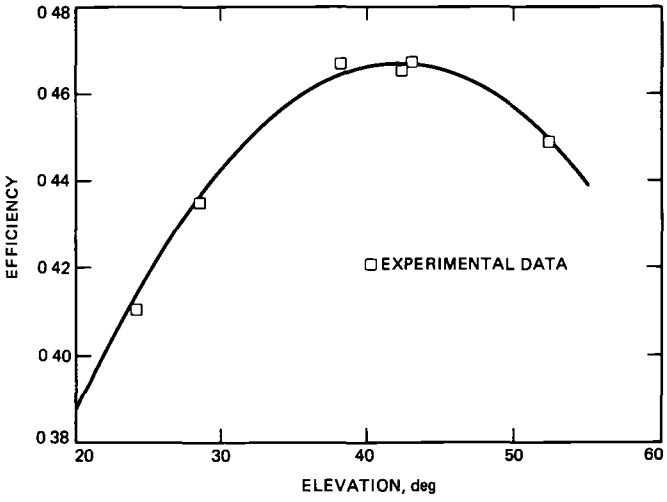

Fig 11 Antenna efficiency of XKR cone receive feed

Appendix A

Experimental Investigation of Conscan Performance

I. Introduction

Conscan offset data from spacecraft tracking were used to determine the systematic errors in antenna pointing We have done analyses to assess some of the quality parameters of the data

Conscan performance is affected by signal level variations that are not due to ground antenna pointing (e g , changes in ground system gain, changes in spacecraft antenna pointing and radiated carrier power) To characterize those effects empirically, we examined the conscan performance during a high activity Voyager pass that included changes in the telemetry modulation index and changes in spacecraft attitude limit cycle amplitude

Also, we examined the detailed signal level variations and related angular offsets during conscan acquisition and tracking We obtained estimates of response and smoothing time, pointing jitter, and pointing bias for the conscan system

The instrumentation and data analysis techniques used and the results obtained are reviewed in this Appendix However, before proceeding, we review some basics of the conscan system

II. A Primer on Conscan Technical Performance

The source document for this discussion is [A-1]

When the conscan axis is offset from the exact direction of arrival of the signal, amplitude modulation of the receiver output at the scan frequency results For small offsets, the offset between the conscan axis and the direction of signal arrival is a constant multiplier of the modulation amplitude in decibels The constant is determined by the scan radius and the antenna half-power beamwidth (3 0 mdeg and 36 mdeg, respectively, at DSS 14), it is approximately 9 0 mdeg/dB (peak-to-peak)

In the MKIVA implementation of conscan[1] the magnitude and orientation of the angular offset are calculated by cross-correlation of the signal modulation with the scanning waveform The calculation is made for each scan cycle by a Fast Fourier Transform The calculation must have an appropriate scale factor, "A," to faithfully convert the modulation in decibels to equivalent angular offset in millidegrees—"A" embodies the antenna beam's mdeg/dB noted above, and the gain and scan period integration time of the correlation calculation "A" can be determined experimentally by observing the correlator output while conscanning on a target with a fixed and known offset

We define [A × offset (1)] as the correlator output from the scan with the conscan axis having offset (1) The conscan system forms the subsequent offsets to be sent to the antenna as

$$\text{offset}(2) = \text{offset}(1) - h \times A \times \text{offset}(1)$$

or

$$\text{offset}(2) = \text{offset}(1) \times (1 - h \times A)$$

and so forth

The parameter "h" is a gain selected such that $0 < (1 - h \times A) < 1$

Rewiite the above relation as

$$\text{offset}(2) / \text{offset}(1) = (1 - h \times A)$$

which illustrates that conscan reduces each subsequent offset by the factor $(1 - h \times A)$, the nth offset is given by

$$\text{offset}(n) / \text{offset}(1) = (1 - h \times A) \wedge (n - 1) \qquad \text{(A-1)}$$

A useful measure of the closed loop dynamic response of conscan is the time, τ, to reduce an initial offset by 1/e If N is the number of P second scans—following the initial scan—required for the reduction, then

$$\text{offset}(N + 1) / \text{offset}(1) = 1/e = (1 - h \times A) \wedge (N)$$

$$N = -1 / \log (1 - h \times A)$$

and

$$\tau = N \times P \qquad \text{(A-2)}$$

in seconds

[1] J R Smith, "Conscan," unpublished notes, Jet Propulsion Laboratory, Pasadena, California, October 23, 1984

For example, a (1 – h × A) of 0 95 gives N = 19 5 scans, which for a 32-second scan period gives τ = 624 seconds, or 10 4 minutes An initial offset is reduced by factors 0 36 (1/e) after one τ, 0 14 after two τ, 0 05 after three τ, for practical purposes, an acquisition or reacquisition is complete after two to three τ seconds

The effects on conscan data quality from noise on the signal level are a complicated matter Some aspects of the matter are treated in detail in [A-1], for present purposes we take one basic result the random angular jitter from a single scan is reduced by the square root of N for continuous closed loop conscan tracking

III. Conscan Performance During a High Activity Voyager Pass

The CAPSAPA program, developed by D Kiewicz, logs time tagged carrier signal level data from the APA maintenance port on a noninterference basis during a pass We used CAPSAPA to collect and display signal level data from several Voyager passes

Figure A-1 shows smoothed signal level vs time for the DOY 086 Voyager 2 pass There were several spacecraft mode change events during the pass The spacecraft events, including attitude limit cycle changes, link 1-way/2-way changes, and modulation index changes, are annotated in the figure

Figure A-2 shows conscan offsets recorded during the DOY 086 pass The spacecraft events and the conscan on/off periods are annotated in this figure, also

Examination of Figs A-1 and A-2 shows

(1) The spacecraft attitude limit cycling does not significantly affect the conscan performance (refer especially to the period 1030 to 1140 GMT)—that is as expected, considering that the spacecraft period is 15 to 30 minutes, whereas the conscan period is 32 seconds,

(2) A significant change in signal level that occurs within a conscan period will result in a significant transient in the conscan offsets (refer to the spacecraft mod index change at 1630 GMT),

(3) When conscan is turned off prior to a significant spacecraft event, and the conscan offsets are retained, pointing will continue quite smoothly when conscan is turned back on (refer to the mod index change event at 1220 GMT, and the receiver O/L event at 1555 GMT, compare that with the receiver O/L event at 1155 GMT when the conscan offsets were zeroed out before turning conscan back on),

(4) Conscan system acquisition or settling time during the pass is 15–20 minutes (refer to the initial acquisition at 1020 GMT, and the transients at 1155 and 1630 GMT in Fig A-2) Also, the peak-to-peak deviation about a smoothed version of the offsets in both axes is indicated as approximately 1 mdeg (see Fig A-2) This performance is generally representative of that observed on the Voyager passes that did not have known system problems

During the initial phase of conscan data collection we analyzed several Voyager passes in the way discussed above We soon concluded that it was not necessary to collect signal level data in order to do reliable editing of the conscan offset files for use in determining systematic pointing errors The required editing—elimination of conscan transient periods, and of conscan off or malfunctioning periods—could be done by examination of the conscan offset raw data plots, plus station logs and spacecraft event schedules

However, we continued collection of signal level data, the data were used to help characterize conscan system performance That work is presented in the next section

IV. Performance of Conscan in Normal Acquisition and Tracking

A. Analysis of Conscan Acquisitions

Figure A-3 shows the scan modulated receiver output during the first conscan acquisition of Voyager 2 on DOY 086 The data are 5-second samples of the received signal level as logged by CAPSAPA Spectral analysis of the noisy data shows that the regular variation is the 32-second conscan period

The amplitude of the scan modulation decays as the acquisition proceeds The estimated envelope of the modulation is sketched in the figure—it is about 0 28 dB at the start and about 0 16 dB after twelve scans From that sample we estimate (1 – h × A) = 0 95, and τ = 10 4 minutes using Eqs (A-1) and (A-2) from Section II Examination of the recorded conscan angular offsets for the same period shows consistent behavior about 2 4 mdeg decaying to 1 6 mdeg, which when converted by the 9 mdeg/dB agrees with the modulation dBs

Figure A-4 shows a similar signal level plot during a conscan reacquisition of Voyager 1 on DOY 118 From these data we estimate (1 – h × A) = 0 88, and τ = 4 3 minutes Again the recorded conscan offsets were found to be consistent with the behavior of the signal level modulation

The closed loop response is quite different for the two tracks discussed above—no doubt a result of different con-

scan parameter settings Unfortunately, we did not keep careful records of the parameters in use, nor did we perform pre-pass tests to experimentally determine the constants "h" and "A " Therefore, we cannot say whether or not the conscan dynamic performance was as it should have been

In a later section (V B), we outline proper calibrations of the conscan system to qualify its performance In hindsight, we should have performed such calibrations at intervals during the conscan offset data collection work

B. Analysis of Conscan Tracking

The CAPSAPA program can be used to make an estimate of the amplitude of the scan period sine wave found in a scan period length of the signal level record CAPSAPA can then calculate the beam error (BE) corresponding to the sine wave amplitude (using the 9 mdeg/dB) and display and store the estimates for each scan cycle The total beam error angular offset as derived from each scan period is resolved into two orthogonal components, BE1 and BE2, relative to the signal level record (The CAPSAPA estimation is analogous to the cross-correlation calculation performed each scan cycle by the conscan system It provides an independent assessment of the functioning of the conscan system)

Figure A-5 is a plot of angular errors calculated by CAPSAPA as described above for 1,983 individual scan cycles The data are from Voyager 1 and 2 passes of DOYs 118, 125, 127, 132, and 136

Some statistics of the data in Fig A-5 are

	BE1	BE2
Mean	–0 00 mdeg	–0 02 mdeg
σ	1 13 mdeg	1 27 mdeg

The most significant characteristic of the data is that the means are essentially zero, as they should be if conscan is operating properly without biases The cause of the non-circular pattern of the data in Fig A-5 is not yet understood

The total beam error should be approximately Rayleigh distributed The probability function of BE for the data of Fig A-5 is shown in Fig A-6, it has a standard deviation of 1 7 mdeg For example, to show the similarity, a Rayleigh distribution function, fit by inspection to the BE data, is also plotted, it has a standard deviation of 1 4 mdeg

The cumulative probability functions for the BE data and the example Rayleigh distribution are shown in Fig A-7

Recall from the earlier discussion in Section II that the jitter on a single scan is reduced by the square root of N, the number of scans during the period of one closed loop time constant, τ Thus, to relate the statistics of the single scan errors developed above to the actual conscan offset jitter observed, we must estimate N From the records of ten passes we found an average value for τ of about 11 minutes For a scan period of 32 seconds, the average N is 20, giving root N of 4 5 Thus, assuming Rayleigh distribution properties, we should see a standard deviation on BE of the conscan offset data of 1 7/4 5 = 0 4 mdeg

Inspection of the complete conscan offset data records from two typical passes, one quiet, one noisy, showed peak-to-peak jitter in each axis of about 1 0 mdeg There are about 100 independent samples in each conscan error record, so we estimate error standard deviation as the (peak-to-peak)/5 That gives 0 2 mdeg per axis, or a Rayleigh distributed BE with 0 3 mdeg standard deviation

The angle jitter as calculated from the signal level modulation (0 4 mdeg) and that observed from the actual conscan offsets (0 3 mdeg) agree reasonably

V. Observations on Conscan Performance

A. Quality of Offset Data for Antenna Pointing Calibrations

From the discussion presented, we conclude the following

(1) All periods of transient or anomalous conscan performance can be identified and must be deleted from an offset file before it is used as pointing calibration data

(2) A properly prepared conscan offset file provides true angle of arrival of the signal to about 0 3 mdeg BE standard deviation The biases appear to be completely negligible

B. Calibrations of the Conscan System

There are some straightforward calibrations that should be performed on the conscan system to ensure that its performance is proper and understood The frequency of performing the calibrations needs to be determined by experience with the stability of the system–certainly they should be a part of preparing for antenna pointing calibration work, and for operations requiring guaranteed high performance of the conscan system

We only describe the concept of the calibrations The actual procedures for their accomplishment need to be worked out by DSN system engineering and operating personnel

(1) *Open loop determination of system gain constants* With the conscan loop open, set in a known offset (e g ,

10 mdeg for the 64-m at X-band) in one axis and measure the value of the constant "A", repeat in the other axis. Similarly, determine the product h × A, "h" should be set to provide a desired closed loop time constant as determined by (1 - h × A)

(2) *Open loop determination of axis cross-coupling* Perform as in (1) but observe the offset signal in the orthogonal axis Repeat with the other axis The conscan phase delay should be adjusted so that the angular cross-coupling is <5 percent

(3) *Observation of closed loop behavior–"snap-on-tests"* Set in a 10 mdeg offset in one axis and then close the conscan loop Observe the decay of the offset It should have a time constant within 10 percent of that expected from the value of (1 - h × A) Repeat with offsets in the opposite direction, and for the other axis

During the snap-ons, observe the activity of the orthogonal axis It is expected to display some cross-cross coupling even though the static setting is correct

(4) *Validation that the conscan axis and the beam maximum coincide* Establish stable conscan tracking on a spacecraft providing a steady signal level Turn off conscan (leave offsets in), and perform beam scans ±10 mdeg in each axis

C. Other Investigations Identified

(1) To understand and demonstrate the dynamic behavior of the MKIVA conscan system, an appropriate computer simulation model should be developed The model would be run for the envelope of values of the (1 - h × A), scan period and width, and receiver time constant parameters, in the presence of noise

(2) To develop the optimum conscan closed loop time constant settings for various support needs, e g , rapid acquisition, or very low jitter tracking, a series of snap-on tests with various settings of the operating parameters should be performed and analyzed at the stations

The simulation results would be used to guide the development of the tests at the stations, and to verify or interpret the test results

References

[A-1] J E Ohlson and M S Reid, *Conical-Scan Tracking With the 64-m-diameter Antenna at Goldstone*, Technical Report 32-1605, Jet Propulsion Laboratory, Pasadena, California, October 1, 1976

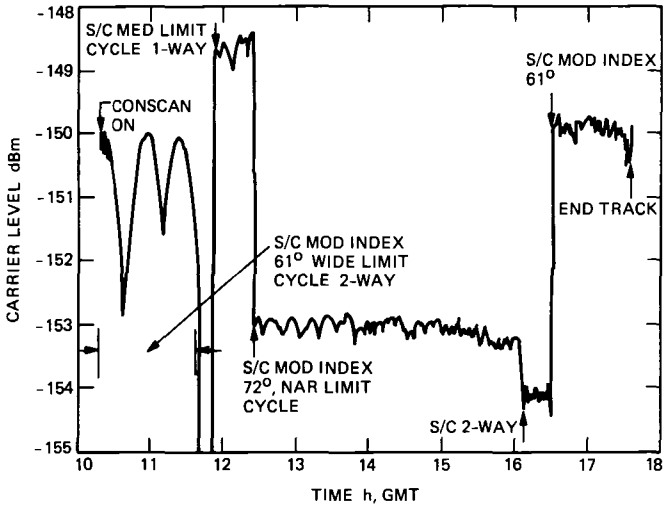

Fig A-1 Carrier signal level Voyager 2, DOY 086

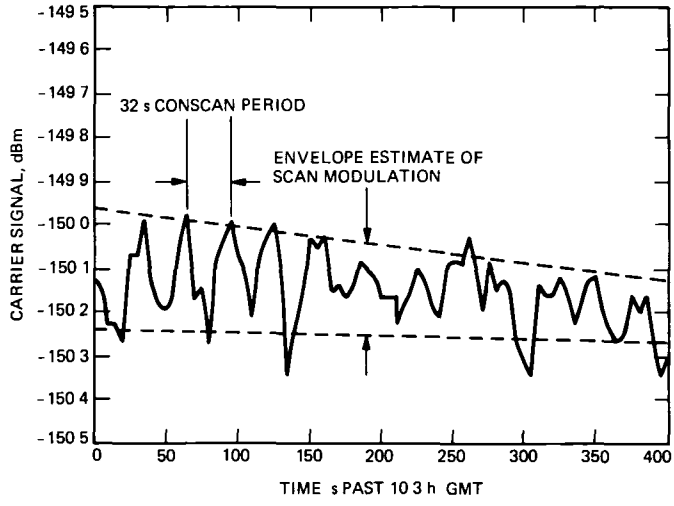

Fig A-3 Carrier signal level vs time during conscan acquisition Voyager 2, DOY 086

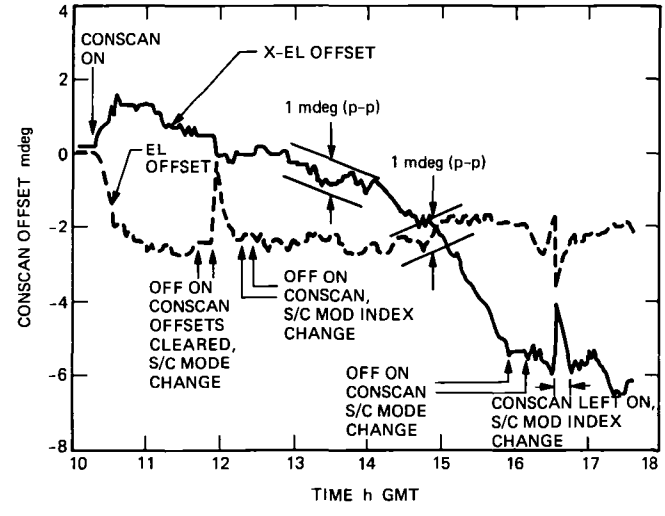

Fig A-2 Conscan offsets Voyager 2, DOY 086

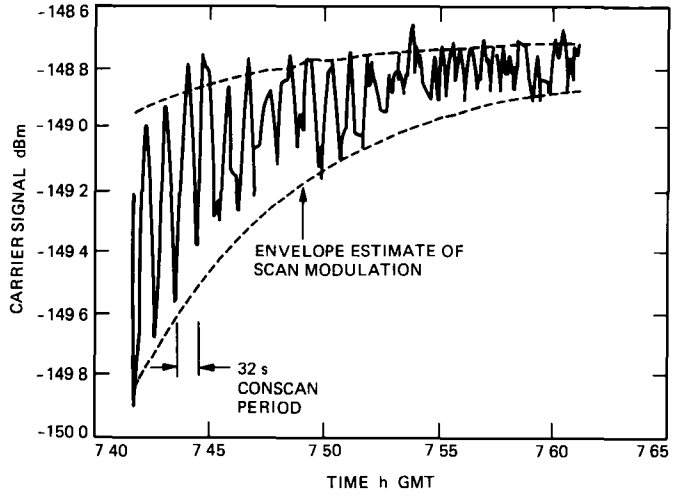

Fig A-4 Carrier signal level vs time during conscan acquisition Voyager 1, DOY 118

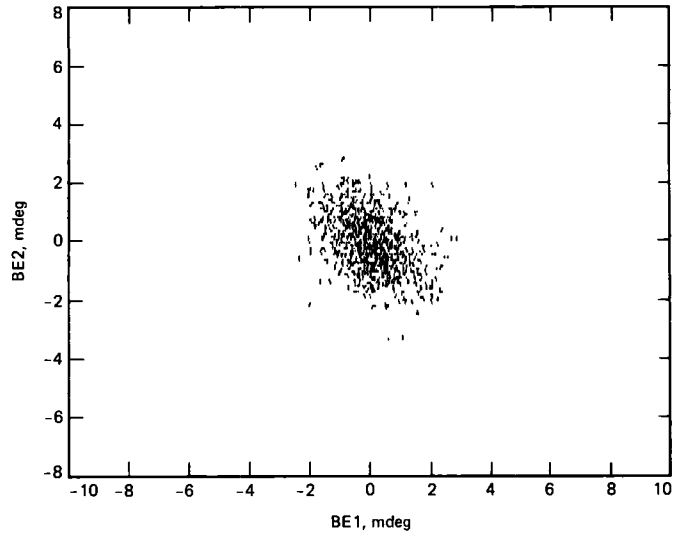

Fig A-5 Angle offsets calculated from modulation on individual scans 1,983 scans from Voyagers 1 and 2, DOY 118, 126, 127, 132, 136

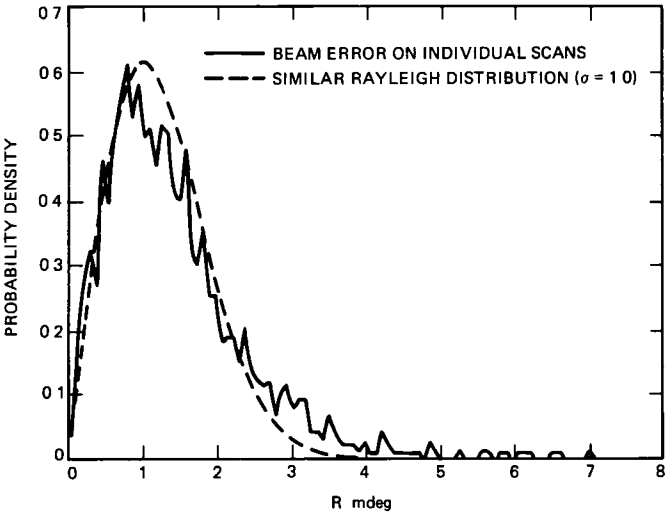

Fig A-6 Probability density

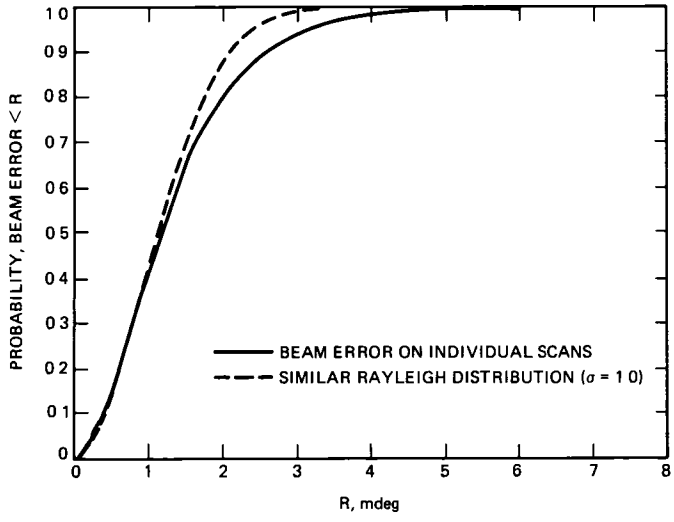

Fig A-7 Cumulative distribution

Appendix B

Atmospheric Refraction Effects on Elevation Pointing

I. Introduction

Atmospheric refraction causes significant bending of radio waves, especially at low elevation angles We review the antenna elevation pointing errors resulting from the bending and the methods used to reduce the magnitude of the errors We also review the importance of the refraction caused errors in performing standard DSN antenna pointing functions

Methods for calculating the radio wave bending depend on the constituents and their distribution in the atmosphere Surface pressure, temperature, and relative humidity are useful in characterizing the atmosphere for such calculations

Presently, the DSN uses a default set of surface atmospheric parameters in the algorithm for calculating refraction correction vs elevation angle The parameters define an average surface atmosphere at a particular DSN complex Use of actual surface atmospheric parameters measured during the epoch of a pass will improve the accuracy of the calculations

We made measurements of the SPC 10 surface atmosphere at frequent intervals during many of the conscan calibration tracks The measurements were used as a basis for calculating current refraction corrections that could be compared with the fixed parameter set calculations The measurements and the results are presented

The discussion of the results shows that more work on this subject is needed by the DSN, particularly in regard to application of the 70- and 34-m antennas at Ka band Specific topics for inquiry are cited

II. Refraction Correction and Its Importance in DSN Applications

A. The DSN Refraction Model

The refraction correction algorithm used in the DSN is the Berman/Rockwell (B/R) model as defined in [B-1] and [B-2] For the SPC 10 average (default) parameters

Pressure = 901 09 mbars
Temperature = 22 07°C
Relative humidity = 31 57 percent

the refraction correction vs elevation is as depicted in Table B-1 Also, Table B-1 shows error estimates derived from results by other investigators [B-3], [B-4] and applied to the B/R model

We will discuss the B/R model and compare it with other models in Section IIC

The values in column (1) of Table B-1 are true elevation angles The calculated B/R model values in column (2) show that the refraction correction is large even to mid-range elevations Column (3) displays the calculated errors in the correction if an average refraction condition for a locale is assumed—it should be representative of our use of default atmospheric parameters Column (4) displays calculated errors if concurrent surface atmospheric observations are used in the refraction calculations—it should be representative of our results obtained in that way We show the 2-σ error estimates because they are relevant to conventional communication link reliability considerations, i e , about 95 percent of the time, the errors would be equal to or less than those shown

B. The Importance of Refraction Caused Pointing Errors in DSN Applications

Table B-2 shows characteristics of DSN antenna beams The logic of the table is Pointing within 0 1 half-power beamwidth (HPBW) in both beam axes, elevation and cross-elevation, produces no more than 0 25 dB degradation or uncertainty in received or transmitted signal level—very satisfactory for all but the most demanding DSN support Pointing within 0 5 HPBW in elevation produces no more than 3 dB degradation—very satisfactory for all normal signal acquisition operations

Based on the error estimates of Table B-1 and the antenna beam characteristics of Table B-2, we make the following general observations

(1) For all normal S-band functions and for normal X-band acquisition, correction for concurrent surface atmospheric conditions *is not necessary* A suitable average of site conditions should suffice for the refraction calculation—refer to Table B-1, column 3, at elevations >10 degrees

(2) For precision pointing at X-band, and for all Ka-band functions, correction for concurrent surface atmospheric conditions *is necessary* The fractional beamwidths for these functions are set boldface in Table

B-2 for emphasis For Ka-band precision pointing at low elevations, the quality of the correction appears marginal—refer to Table B-1, column 4

(3) For antenna pointing calibrations, the accuracy objective is <1 mdeg, and correction for concurrent surface atmospheric conditions *is necessary*

Regarding observation 2, recall that when an antenna is properly functioning in the conscan mode, all pointing errors that are slowly varying compared to the scan period, including refraction effects, are removed

C. Discussion of the Berman/Rockwell and Other Radio Frequency Refraction Models

1 The Berman/Rockwell model The basic approach in the B/R radio refraction model derivation (cf [B-1], [B-2]) is to empirically match a pedigreed tabulation for optical refraction with an analytic function The simplified form of the function (Ropt) applicable for elevation angles >5 degrees is

$$\text{Ropt} = [\text{Fp(surf press)}] \times [\text{Ft(surf temp)}] \times [\text{Fe(el angle)}] \quad \text{(B-1)}$$

Then, the radio refraction model (Rrf) is obtained by multiplying the optical refraction of Eq (B-1) by a "wet" term that includes the effects of water vapor in the atmosphere

$$\text{Rrf} = \text{Ropt} \times [\text{Fw(surf press, temp, rel humidity)}] \quad \text{(B-2)}$$

Equation (B-2) provides a good approximation of the complete B/R algorithm—within approximately 2 mdeg at 5 degrees elevation, 0 6 mdeg at 10 degrees elevation For the SPC 10 default values for surface pressure, temperature, and relative humidity, Eq (B-2) is

$$\text{Rrf(def)} = \text{Fp(901 09 mbar)} \times \text{Ft(22 07°C)} \times \text{Fe(el angle)} \times \text{Fw(901 09 mbar, 22 07°C, 31 57 percent)}$$

Radio refraction values based on current surface observations, Rrf(obs), can be calculated similarly Note that in the simplified B/R model, all elevation dependence is contained in the function Fe, and Fe is independent of atmospheric effects (Eqs (B-1), (B-2)) Thus, a refraction table based on surface observations can be made directly from the default table

$$\text{Rrf(obs)} = \text{Rrf(def)} \times [\text{Fp} \times \text{Ft} \times \text{Fw(obs)} / \text{Fp} \times \text{Ft} \times \text{Fw(def)}] \quad \text{(B-3)}$$

We have used the convenient relationship Eq (B-3) to reduce and analyze our experimental data

To our knowledge, no significant experimental validation of the B/R refraction model and its expected errors has been done In the next paragraphs we compare the B/R model with other models

2 Other radio refraction models Radio refraction studies of Bean and Dutton [B-3] and Crane [B-4] use an approach different from that of Berman/Rockwell Their basic technique is

(1) Collect a large data set of atmospheric parameters vs height above the surface using radiosondes Include concurrent surface observations

(2) Calculate the trajectory of the radio ray through each of the atmospheric profiles provided from the radiosonde observations Each calculation provides an estimate of elevation refraction of a radio signal from above the atmosphere Also, from the set of calculations, some statistics of the elevation refraction are provided

(3) From all the calculations, plot for individual elevation angles the elevation refraction (Rrf) vs the N number of the surface refractive index (Ns), derived from the concurrent surface observations Then, observe that Rrf vs Ns for each elevation angle has the form

$$\text{Rrf} = a + b \times \text{Ns} \quad \text{(B-4)}$$

(4) For each elevation angle, do a straight line least squares best fit of the Rrf vs Ns data and determine the regression coefficients, a and b, in Eq (B-4) Calculate the statistics of the data fit to the lines

Using the above techniques, the individually calculated results of Bean and Dutton, and Crane, are quite consistent Bean and Dutton show some experimental results that support their calculations

Finally, in their theoretical development, Bean and Dutton arrive at a very simple approximation for radio refraction

$$\text{Rrf} = \text{Ns} \times \cot(\text{el}) \times 57\ 3 \times 10 \sim -6 \text{ (mdeg)} \quad \text{(B-5)}$$

Equation (B-5) is useful above 10 degrees elevation

3 Comparison of B/R and the other models We have calculated refraction tables for the SPC 10 default atmospheric parameters using Eq (B-4) and the regression coefficients from

Bean and Dutton ([B-3], Table 9 9), and from Crane ([B-4], Table II) Also, we calculated Eq (B-5)

Figure B-1 compares the complete B/R algorithm with the other refraction models as a function of elevation angle (B/R minus the others) The agreement between the B/R, Bean and Dutton, and Crane models is quite good (<2 mdeg) over the range of elevations presented It lends confidence to our use of the B/R model The range of usefulness of the simple Eq (B-5) is displayed

The statistics cited in paragraphs 2(2) and 2(4) above were taken from Crane ([B-4], Fig 3 and Table II) to develop the estimated errors in our Table B-1, columns (3) and (4)

III. SPC 10 Surface Atmosphere Observations

A. Introduction

We collected surface atmospheric data at regular intervals during most of the Voyager passes that we observed The data were used to upgrade the refraction correction provided by the standard default values The objectives were to provide improved correction of refraction errors during the Saturn radar support, and to provide better data for development of the antenna error model Also, we wanted to develop and demonstrate refraction correction techniques for future use in the operational DSN

The methods of collecting and processing the data are described Summary analyses of the data from DOY 120 to 142 are presented and discussed

B. Data Collection and Processing

All atmospheric data were hand collected by station personnel, typically at 1 hour intervals Barometric pressure was read from the MMA display, wet and dry bulb temperatures were read from a Bendix Friez Psychron, model 566 series psychrometer

Three PC programs were developed to process and apply the atmospheric data REFCORR, HUM-PSY, and CONCORR REFCORR was used for on-site refraction correction, and HUM-PSY and CONCORR were used for off-site antenna model development The functions of the programs are shown in the block diagram, Fig 3 of this article's main text

REFCORR computes the elevation offset error resulting from the use of default rather than current atmospheric weather parameters It requires inputs of wet and dry bulb temperatures, atmospheric pressure, and elevation angle at the time of the readings

From the surface atmospheric observations, REFCORR computes the relative humidity Then, using the complete B/R algorithm, it computes the refraction correction for the observed surface atmosphere Also, it computes the correction for the default surface atmosphere The two corrections are differenced, giving an estimate of the error in elevation at the time of the observations

The results are printed and displayed on the screen A preliminary procedure, "Antenna Pointing Refraction," dated 19 May 1987, describing the operation of REFCORR and the psychrometer, was prepared and issued by M Wert

HUM-PSY makes a file of temperature, pressure, and relative humidity values, time-tagged at 15 minute intervals It requires inputs of wet and dry bulb temperatures, atmospheric pressure, and time of the readings Relative humidity is calculated as in REFCORR The values at the reading times are linearly interpolated to create the 15 minute values HUM-PSY provides inputs to CONCORR

CONCORR is used to provide refraction correction of conscan files for development of improved antenna pointing error models

Surface atmospheric data applicable to a conscan data point is determined by selecting data points from the HUM-PSY file adjacent to the time of the conscan point, and then linearly interpolating between them CONCORR then calculates the refraction correction using the interpolated surface weather data in the complete B/R algorithm It also calculates the default refraction correction

The refraction correction from the surface observations is subtracted from the default correction The result is added to the conscan elevation offset, providing a corrected elevation offset CONCORR stores the data in a file formatted for use in the antenna error model linear least squares fitting program, PHO9, it also provides plots of corrected elevation offsets vs time using the companion plotting program, REFPLOT (cf Fig B-2)

C. Analysis of SPC 10 Surface Atmosphere Data

We have analyzed the surface atmosphere data taken from DOY 120 to DOY 142 During that time, consistent surface atmosphere observations were made concurrently with several good Voyager spacecraft conscan tracks and one Saturn blackbody track The atmosphere data are discussed here, results of use of those data in correcting elevation pointing errors are discussed in the next section

As discussed in Section IIC, a good approximation of the B/R refraction for current surface observations is obtained as the product of the default refraction and the ratio of the surface atmosphere dependent parameters, Fp, Ft, and Fw [from Eq (B-3)]

$$Rrf(obs)/Rrf(def) = Fp \times Ft \times Fw(obs)/Fp \times Ft \times Fw(def)$$

Figure B-2 shows plots of calculated Rrf(obs)/Rrf(def) ratios for the surface observations during the period For example on DOY 120, the ratio varied between 1 045 and 1 08, at 10 degrees elevation, the default refraction correction is 85 0 mdeg, the calculated correction from the surface observations varied between 85 X 1 045 = 88 8 mdeg and 85 X 1 08 = 91 8 mdeg

It is evident that the Fig B-2 ratios are fairly well behaved and slowly varying during any single pass period However, for passes separated by several days, the ratios vary widely One measurement each day is about five times better than none

A representative measure of the sensitivity of the refraction ratios to the surface atmospheric parameters—pressure, temperature, and relative humidity—is available from our measurements The ranges observed of the parameters are

Pressure 895–905 mbar
Temperature 7–27 5°C
Relative Humidity 15–81 percent

Setting two of the parameters to default values, and varying the third over the ranges indicated, show that the angular refraction change caused by the relative humidity variations was about 5 times that from the temperature variations and 30 times that from the pressure variations If humidity changes are forecast, expect significant changes in radio refraction

Figure B-3 shows daily averages of the Rrf(obs)/Rrf(def) ratios The significant changes over several days are clearly illustrated

From the data in Fig B-3, we can calculate the variance of the elevation error resulting from use of the default rather than the observed atmospheric parameters For example, at 10 degrees elevation, the calculated mean (+3 3 mdeg) plus 2-σ error (2 X 5 10 mdeg) is 13 5 mdeg, to be compared to 11 6 mdeg given in column (3) of Table B-1—values at other elevations have the same relative comparison The comparison should be considered qualitative, because our data sample is tiny—the 90 percent confidence interval on sigma is 3 8 to 8 0 mdeg

IV. Elevation Offsets Using Surface Atmospheric Measurements

A. Introduction

We have analyzed elevation offset data from the Voyager conscan and Saturn beam scan passes of DOY 120 to DOY 142 Elevation offsets obtained using the default refraction correction are compared with calculated offsets using concurrent surface atmospheric observations

The results show that the surface observations are useful, but leave some unanswered questions

B. Elevation Offsets From Individual Passes

Observed offsets based on default correction, and calculated offsets based on surface observations, are plotted in Figs B-4 through B-11 Three different antenna systematic error tables (SETBLs) were used during the period, but the plotted offsets have all been adjusted to a common SETBL, 4X31C The calculated offsets are from the simplified B/R algorithm

The figures show that, except for DOY 127, the calculated offsets are of smaller magnitude (closer to zero elevation error) than the default offsets Unfortunately, we don't really know what the true elevation error should be, because of possible errors in the antenna pointing system Examination of the average offsets can provide some insight into the matter

C. Elevation Offset Averages

Figure B-12 shows the pass averages of the default and calculated offsets Globally, the calculated offsets are an improvement However, they are certainly not negligible, especially after DOY 125 After DOY 125 there is an apparent bias in the calculated offsets of about +3 mdeg—about that bias they behave fairly well

The signatures of all offset curves, default and calculated, show increases at low elevation angles (cf Figs B-4 through B-11) Figure B-13 shows the average of all default and calculated offsets vs elevation angle The residual calculated offsets are large at 10 degrees and significant at 15 degrees They are about three times the 2-σ errors expected using concurrent surface atmospheric observations (compare column (4) of Table B-1)

The source of the apparent large errors, especially at low elevation angles, is not understood

(1) The B/R refraction algorithm was shown to agree fairly well with other models down to 5 degrees elevation—can they all be in equal error?

(2) Are we doing something wrong in processing or applying the surface observations?

(3) Is there some unidentified error characteristic of the antenna system that has such a steep angular gradient?

V. Summary Observations on Refraction Effects

(1) Refraction causes large errors in elevation angle Correction based on average site (default) atmospheric parameters is adequate for all S-band and for normal X-band acquisition operations Antenna calibrations, precision X-band, and all Ka-band operations require correction based on concurrent surface atmospheric observations

(2) Results from the DSN's Berman/Rockwell algorithm for calculating refraction from surface atmospheric parameters agree fairly well with other formulations

(3) Large changes in refraction tend to occur over several days, while changes within the length of a pass tend to be very much smaller

(4) The results in improving refraction correction by using concurrent surface atmospheric observations were significantly less accurate than expected At low elevations, the errors are unaccountably large—although that may not be a refraction effect

(5) Further work has been identified to refine and demonstrate the model of the effects of atmospheric refraction on antenna pointing

(a) Use more recent literature on radio refraction models and the experimental results establishing their accuracy (the latest reference used here was from 1976)

(b) Find and remove the cause of the large low elevation errors

(c) Establish a field experimental program to demonstrate refraction corrections of the required accuracy to support antenna pointing calibrations at X-band (8 5 GHz) and future Ka-band (34 GHz), in preparation for a network operational capability

References

[B-1] A L Berman and S T Rockwell, *New Optical and Radio Frequency Angular Tropospheric Refraction Models for Deep Space Applications*, Technical Report 32-1601, Jet Propulsion Laboratory, Pasadena, California, November 1, 1975

[B-2] A L Berman, "Modification of the DSN Radio Frequency Angular Tropospheric Refraction Model," *DSN Progress Report 42-38*, vol January–February 1977, Jet Propulsion Laboratory, Pasadena, California, pp 184–186, April 15, 1977

[B-3] B R Bean and E J Dutton, *Radio Meteorology*, New York Dover Publications, Inc , especially Chapters 1 and 8, 1968

[B-4] R K Crane, "Refraction Effects in the Neutral Atmosphere," *Methods of Experimental Physics*, New York Academic Press, Chapter 2 5, 1976

Table B-1. SPC 10 refraction correction and errors vs. elevation angle

(1) Elevation angle (deg)	(2) Refraction correction[a] (mdeg)	(3) Estimated 2-σ error[b] with average atmospheres (mdeg)	(4) Estimated 2-σ error[b] with surface observations (mdeg)
5 0	156 9	21 3	3 3
10 0	85 0	11 6	1 8
15 0	58 1	7 9	1 2
20 0	43 7	5 9	0 9
30 0	27 2	3 7	0 6
40 0	18 5	2 5	0 4
60 0	9 0	1 2	0 2
90 0	0 0	0 0	0 0

[a] B/R model using SPC 10 default parameters
[b] From interpretation of data by Crane [B-4]

Table B-2. Approximate 0.1 and 0 5 half-power beamwidths (HPBWs) of DSN antennas

Frequency band	70-m 0 1 HPBW/0 5 HPBW (mdeg)	34-m 0 1 HPBW/0 5 HPBW (mdeg)
S	11/57	23/114
X	**3**/15	**6**/30
Ka	**0.8/4**	**1.6/8**

The fractional beamwidths for these functions are set boldface for emphasis

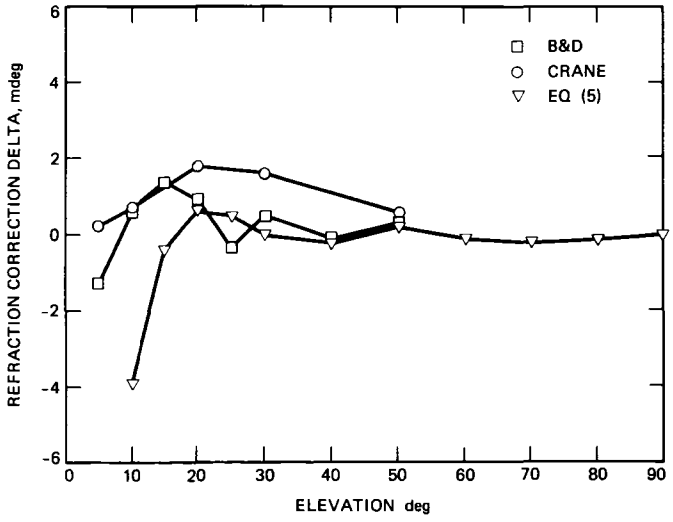

Fig B-1. Deltas (B/R—other models), GDSCC default parameters

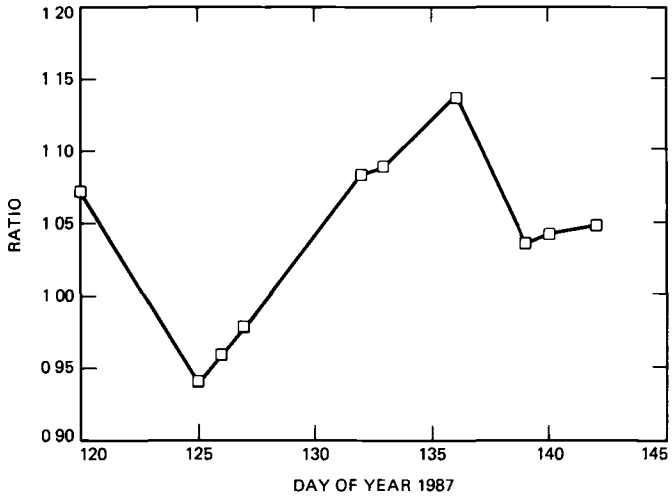

Fig B-3. Daily average observed/default refraction ratios

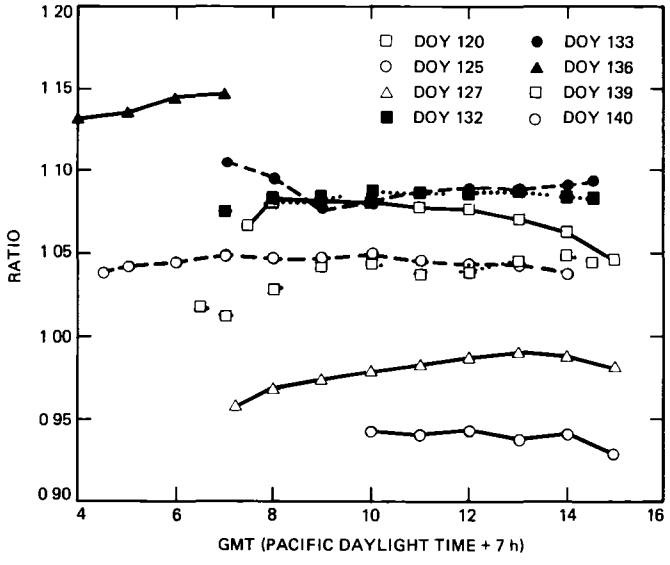

Fig B-2 Hourly observed/default refraction ratios

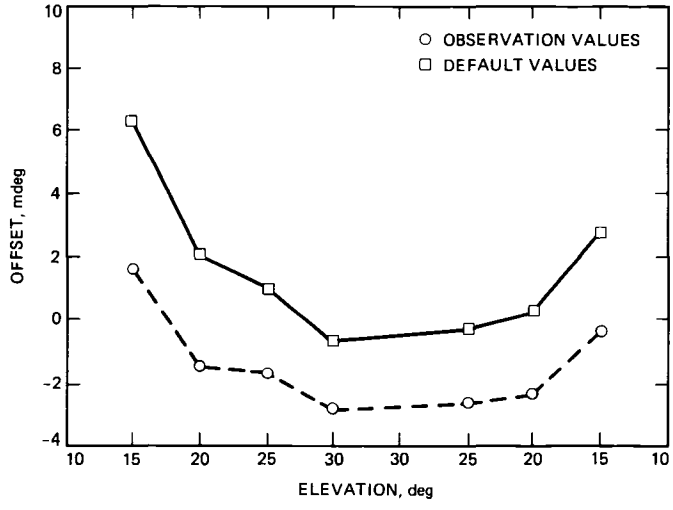

Fig B-4 Elevation offsets Voyager 2 DOY 120 (corrected to SETBL 4X31C)

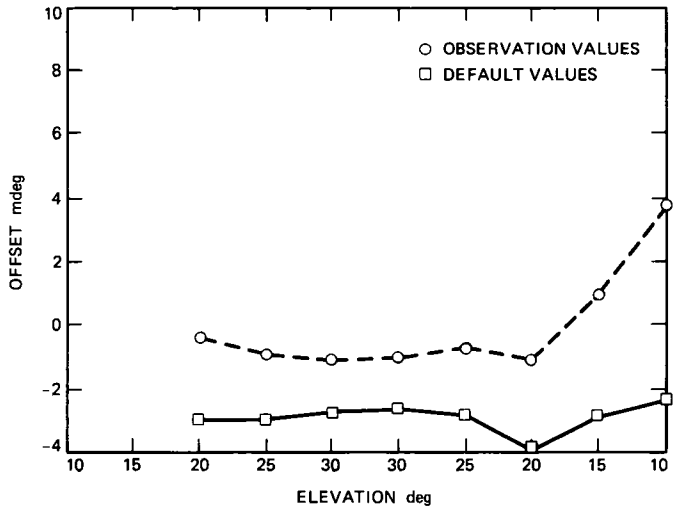

Fig B-5 Elevation offsets Voyager 2 DOY 125 (corrected to SETBL 4X31C)

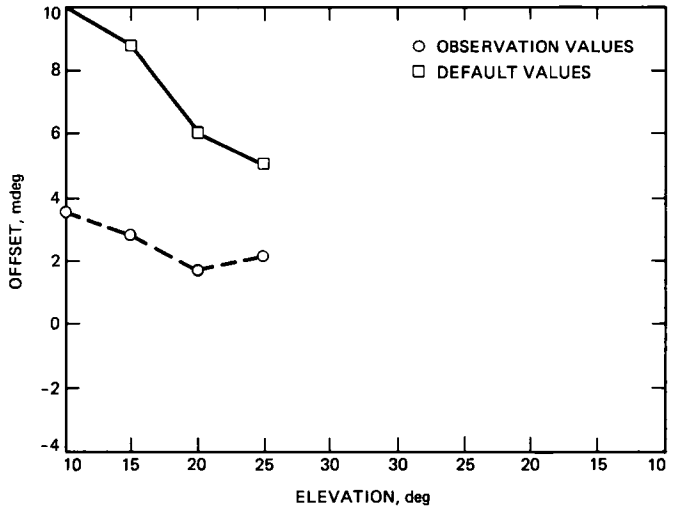

Fig. B-7 Elevation offsets Voyager 2 DOY 133 (corrected to SETBL 4X31C)

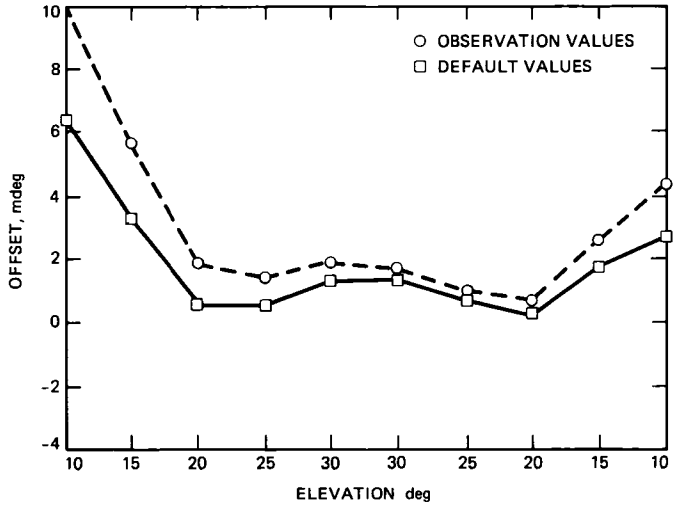

Fig B-6 Elevation offsets Voyager 2 DOY 127 (corrected to SETBL 4X31C)

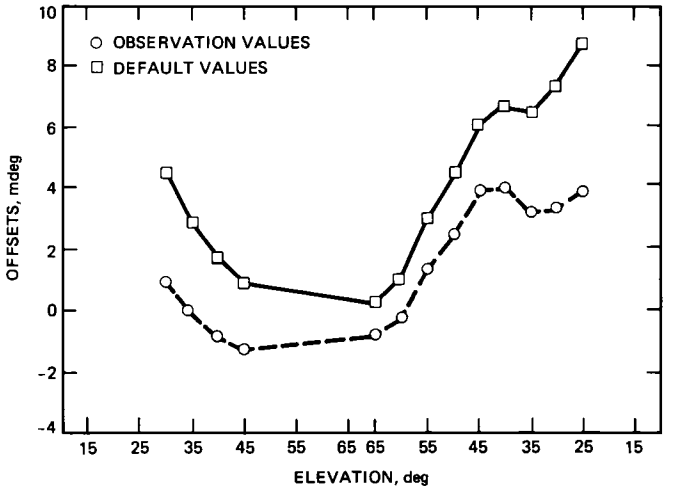

Fig. B-8 Elevation offsets Voyager 1 DOY 136 (corrected to SETBL 4X31C)

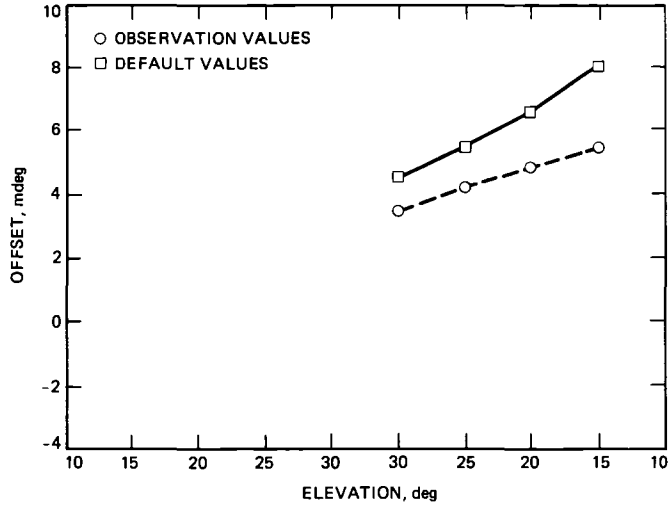

Fig B-9 Elevation offsets. Saturn blackbody scans DOY 139 (SETBL 4X31C)

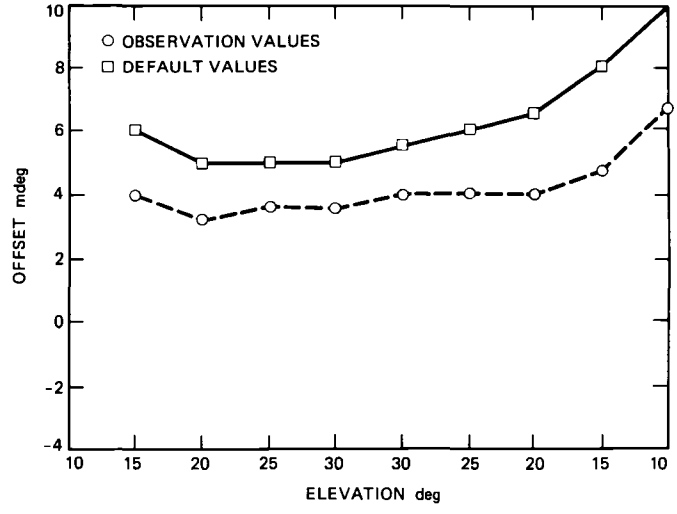

Fig B-11 Elevation offsets. Voyager 2 DOY 142 (SETBL 4X31C)

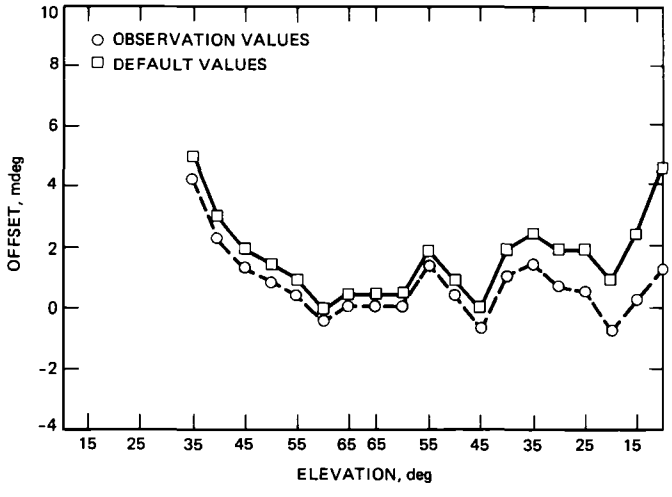

Fig B-10 Elevation offsets Voyager 1 DOY 140 (SETBL 4X31C)

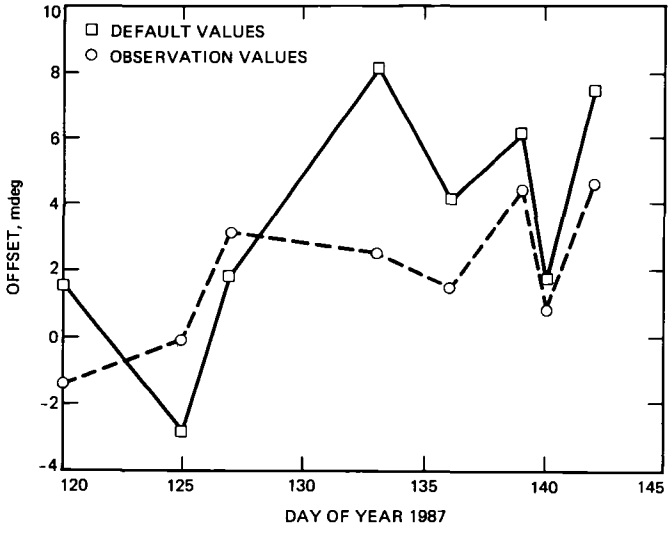

Fig B-12 Average default and corrected elevation offsets (corrected for surface observations and to SETBL 4X31C)

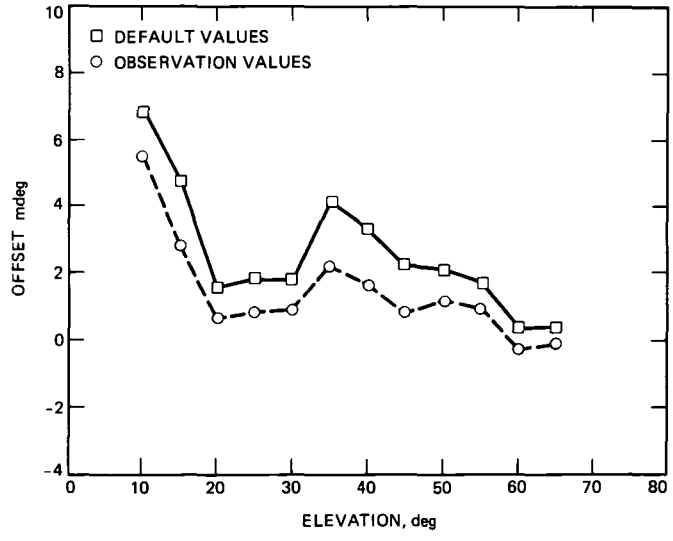

Fig. B-13. Average elevation offsets (corrected to SETBL 4X31C)

End of Document